IPP-Report

Max-Planck-Institut
für Plasmaphysik

Bruce Scott

Low Frequency Fluid Drift Turbulence in Magnetised Plasmas

IPP 5/92
März 2001

Low Frequency Fluid Drift Turbulence in Magnetised Plasmas

Der Mathematisch-Naturwissenschaftlichen Fakultät

der Heinrich-Heine-Universität Düsseldorf

als Habilitationsschrift vorgelegt

von

Bruce Scott

aus Kingsville, Texas, USA

Düsseldorf

June 2000

Table of Contents

Deutsches Vorwort und Zusammenfassung

Diese Arbeit ist eine deutsche Habilitationsschrift zum Thema Fluiddynamik in magnetisierten Plasmen. Sie ist auch entworfen, um die Kluft zwischen dem aktuellen Stand der Kenntnis dieses Faches und den zur Zeit verfügbaren Behandlungen in den Lehrbüchern in etwas zu schliessen. Ein magnetisiertes Plasma ist ein in ein magnetisches Feld eingeführtes und dann ionisiertes Neutralgas. Aufgrund der Kleinheit des Gasdruckes im Vergleich zur Energiedichte des Magnetfeldes bestimmt das Feld die Gasbewegung. Wenn auch entsprechend konfiguiert kann das Magnetfeld das Plasma einschliessen. Die verschiedenen Sorten geladener Teilchen werden als geladene Fluide betrachtet, die sich ineinander und durcheinander bewegen, gekoppelt nur durch elektrische Kräfte und den Stosswiderstand. Magnetisierte Plasmen sind vor allem im Labor wichtig, obwohl viele der Grundlagen auch zum Verständnis astrophysikalischer und extraplanetarischer Probleme wichtig sind.

Der gewohnte Zugang zu solchen Systemen ist die Magnetohydrodynamik, kurz MHD. Im MHD-Bild wird das Plasma als ein einziges Fluid beschrieben, das einen elektrischen Strom in Wechselwirkung mit externen oder selbstkonsistenten elektromagnetischen Feldern tragen kann. Dieses Modell ist relativ bekannt, und einige Lehrbücher sind in den letzten Jahren aufgetaucht, mit deren Hilfe Studenten und Forscher gut in dieses Thema einsteigen können. Wenn das MHD-Modell beim Behandeln von globalen Phänomenen magnetisierter Plasmen auch sehr erfolgreich ist, zeigt es leider erhebliche Defizite wenn es das Ziel ist, die kleinskaligen Bewegungen zu behandeln, die den thermodynamischen Zustand des Plasmas bestimmen. Denn die meisten Laborplasmen sind nicht ruhig sondern ständig von flüssigkeitsähnlicher Turbulenz durchschüttelt. Diese Turbulenz transportiert Wärme und Teilchen vom heissen Plasmakern nach außen und kann in einigen Fällen sogar das Plasma unterbrechen. Diese Bewegungen stellen eine selbstkonsistente Wechselwirkung zwischen dem elektromagnetischen Feld und den Elektronen- und Ionengasen dar. Obwohl der Parameterbereich bei niedriger Frequenz (ein Megahertz und weniger) und kleinen Skalen (Millimeter bis zu Zentimeter) liegt, bleibt es wichtig, jede geladene Teilchensorte getrennt zu modellieren.

Die dafür benötigte Theorie wird Fluiddriftdynamik genannt, deren Hauptthema die Driftwellen sind. Driftwellen sind in Lehrbüchern nur oberflächlich und idealisiert dargestellt, was ausreicht, um zu wissen was sie sind, aber nicht um zu verstehen, wie und warum sie auftreten und wie sie die selbstkonsistente Wechselwirkung besonders zwischen dem Elektronengas, dem Strom, und dem elektrischen Feld vermittelt. Kleinskalige elektrische Feldstörungen sind in der Fluiddriftdynamik wesentlich, weil die turbulenten Wirbel eine zum Magnetfeld senkrechte Driftgeschwindigkeit haben, die durch das fluktuierende

elektrische Feld und das Hintergrund-Magnetfeld gegeben wird. Das Schlüsselkonzept ist Quasineutralität: ein Neutralplasma, aber robuste Aktivität des elektrischen Feldes. In der Tat stellt man häufig die Frage, wie oder warum elektrische Felder in einem neutralen Plasma entstehen. Das Verständnis der Antwort zu dieser Frage bildet die Grundlage dieses Themas. Was man dadurch gewinnt ist ein physikalischer Rahmen, in welchem die Turbulenz und Transportfragen magnetisierter Plasmen angegangen werden können. Denn das MHD-Modell ist nicht in der Lage, die Kopplung von Druck zu Strom zum elektrischen Feld zu beschreiben, was den Kern dieser Dynamik darstellt.

Ein Überblick des Inhalts steht in den vorhergehenden Seiten. Wir beginnen mit den Grundprinzipien der Hydrodynamik und der klassischen Elektrodynamik und finden dann den Parameterbereich der quasineutralen Dynamik, die auch implizit hinter dem MHD-Modell steht. Danach finden wir die Grenzen, in denen das MHD-Modell sich als Spezialfall der Zweiflüssigkeitdynamik und auch der Driftdynamik erweist. Dabei lernen wir auch, wie die Driftdynamik aus der Begrenzung auf ein inkompressibeles Magnetfeld entsteht. In Kapiteln 4 und 5 finden wir den grundlegenden Charakter kleiner Störungen in diesem System. Die Kapitel 6 bis 9 behandeln die verschiedenen Aspekte der Fluid-Driftturbulenz, als Driftwellen-Turbulenz bekannt. Wir fangen mit einfachen Überlegungen zu der da hinterliegenden nichtlinearen Dynamik an, setzen mit einigen Methoden zur statistichen Diagnose numerischer Berechnungen fort und finden dann die nichtlineare Instabilität, welche der Schwerpunkt dieser Physik ist, und die Wechselwirkungen mit großskaligen verscherten Strömungen. Kapitel 10 stellt Austauschturbulenz vor, die der aus der Hydrodynamik weithin bekannten Rayleigh-Taylor Konvektion entspricht. Die Kapitel 11 bis 13 betrachten elektromagnetische Driftwellen-Turbulenz in geschlossener Magnetfeldgeometrie. Wir beginnen zunächst mit einem vereinfachten Modell, das nur den Elektrondruck behandelt; dann folgt die Einbeziehung der Elektronen- und Ionentemperaturen. Kapitel 14 behandelt die grundlegenden Eigenschaften des aus Driftwellen-Turbulenz resultierenden Transportes, der sich grundsätzlich von der besser bekannten kinetischen Diffusion, wie zum Beispiel Wärmeleitung, unterscheidet. Anhänge A und B behandeln die Details der numerischen Methoden und der Modelle der Geometrie des magnetischen Feldes, die notwendig ist, um nicht nur die einfachsten Fälle betrachten zu können. Denn dieses Thema wird durch nichtlineare Physik und folglich numerische Berechnungen beherrscht. Numerische Modelle bilden deswegen von Anfang an einen wesentlichen Bestandteil dieser Arbeit. Die Zitate zur Literatur sind nicht als umfassend beabsichtigt, sondern als Ausgangspunkte für weiteren Studien gedacht. Dafür gibt es in jedem Kapitel einen eigenen Abschnitt. Viele Askepte dieser Arbeit sind sehr neu und sind nur von einer handvoll Autoren behandelt worden. Eines der Ziele ist, die Anzahl der Leute zu erweitern, die sich zu diesem Thema auskennen und damit daran interessiert sind.

Preface

This work is a German Habilitation thesis, also designed to fill a large gap between the state of the art in work on fluidlike dynamics in magnetised plasmas, and currently available treatments in textbooks. A magnetised plasma is a neutral gas introduced into a magnetic field and then ionised. The gas pressure is small compared to the energy density of the magnetic field, so that the magnetic field strongly orders the gas motions and can be constructed so as to confine the plasma. The charged particle populations making up the plasma can be treated as fluids which move through each other, coupled together by electric forces and collisional friction. Magnetised plasmas are important principally in the laboratory, although many of the basic concepts are important to astrophysical and extraplanetary physical problems.

The conventional approach to such a system is called magnetohydrodynamics, or MHD. It treats the plasma as a single fluid which can carry a current, interacting with both externally applied and self consistent electromagnetic fields. This model is relatively well known, and several textbooks have emerged in recent years which are very useful to students and researchers entering the field. Unfortunately, while very successful in treating global phenomena of magnetised plasmas, the MHD model is severely lacking when the aim is to treat the small scale motions which determine the thermodynamic state of the plasma. For most laboratory plasmas are not quiescent at all, but continually churning with fluidlike turbulence which not only carries heat and particles out of the plasma core regions but also in some circumstances leads to its disruption if the temperature is too high. These motions are a self consistent interaction between the electron and ion fluids, and between each of them and the electromagnetic field. Although at low frequencies (below one megahertz) and small scales (a few millimeters to centimeters) charge densities and light wave propagation can be neglected, it is still important to treat each charged species, or at least the electrons and ions, separately.

The class of dynamics required to treat this physical system is called fluid drift dynamics, and its principal paradigm is what are known as drift waves. Drift waves are treated in most textbooks in a very idealised fashion, which is enough to understand what they are, but not enough to understand how they arise, and how they mediate self consistent interaction between especially the electron fluid, the electric current, and the electric field. Small scale, fluctuating electric fields are essential to fluid drift dynamics, because the turbulent eddies have a flow velocity across the magnetic field given by the fluctuating electric field and the background magnetic field. The key concept is quasineutrality: neutral plasma, robust electric field activity. Indeed, one often asks the question: how does, or why should, a neutral plasma develop electric fields. The understanding of the resolution

to that question forms the basis of this subject, and what one gains from that is a physical framework under which the turbulence and transport problems in magnetised plasmas can be addressed. For it is important to understand that they cannot be addressed by the MHD model, because of the fact that the coupling from pressure to current to electric field is one of the things that are discarded in that model.

A general description of the contents of this work can be obtained by the table at the beginning. We start with the first principles of fluid dynamics and classical electrodynamics and then find the regime in which we can reduce to quasineutral dynamics, which also implicitly underlies MHD. Then, we find the limits under which we can specialise to the MHD model as a subset, first of two fluid dynamics, then of the fluid drift dynamics that results when the motions are not vigorous enough to compress the magnetic field. In Chapters 4 and 5 we find the basic character of small disturbances in this system. Chapters 6 through 9 treat various aspects of fluid drift turbulence, also called drift wave turbulence, moving from a simple consideration of the underlying nonlinear dynamics, to some methods by which one can diagnose computations to find out what is going on, and then to the nonlinear instability which is the hallmark of this physics, and then to the interactions with large scale sheared flows. Chapter 10 introduces interchange turbulence, which is the plasma analog of the buoyant convection well known from fluid dynamics. Chapters 11 through 13 treat electromagnetic drift wave turbulence in closed magnetic field geometry, starting with a simplified model treating only the electron pressure and then introducing the electron and ion temperatures. Chapter 14 treats the basic characteristics of the transport that results from fluid drift turbulence, as this is quite different from the kinetic diffusion, such as heat conduction, that is more familiar. Appendices A and B treat the details of the numerical methods and models of magnetic field geometry necessary to treat all but the simplest cases. For this subject is dominated by nonlinear physics and therefore numerical computation. Computations therefore form an integral part of its study right from the beginning. Citations to the literature are not intended to be comprehensive but to serve as starting points for further reading, a section for which is included in every chapter. Much of this work is very new, and has been treated only by a handful of authors. One of the aims is to expand the set of people who know about this subject and might therefore be interested in it.

Acknowledgments

I have to thank the many colleagues and leaders who have introduced me to this field and have made its study so stimulating. For support over the years I would like to specially thank my thesis advisor Adil Hassam, two of my "chiefs" Dieter Pfirsch and Karl Lackner, and also Harold Weitzner, Derek Robinson, Karl-Heinz Spatschek, and William Tang. For continuing interactions, two-way teaching, and the general sort of scientific activity that keeps one inspired, not to mention one or two key bits of help with which one avoids serious pitfalls, special thanks go to Taik-soo Hahm, Ralf Schneider, Wonchull Park, Volker Naulin, Greg Hammett, Wei-li Lee, Alan Glasser, Frank Jenko, Ron Waltz, Andris Dimits, Patrick Diamond, Rainer Grauer, Zhihong Lin, Mike Beer, and Nathan Mattor, in no randomised order and in a certainly incomplete list. May we all keep up the good work.

1. Overview of Fluid Drift Dynamics

B. Scott

Jul 1999

Plasma physics is the study of large populations of charged particles interacting with electric and magnetic fields. Each particle moves according to the equations of motion for a charged point mass in an electromagnetic field, and the electromagnetic field reacts to what the charges do, according to Maxwell's equations. In this sense it is a classical theory; quantum effects enter only when individual particles interact with each other, or in certain instances where packets of electromagnetic energy (photons) interact directly with an atom or one or more of the charged particles.

A gas of charged particles is a plasma when the number of particles involved in any interaction of interest is large enough that they act collectively, rather than simply as individuals. One can think of a cloud of electrons made to contract by some external force. The net electrostatic potential in the cloud will then decrease, and the electric field caused by the gradient of that potential will cause the cloud to expand. If there are two clouds, as shown in Fig. 1.1, each of electrons and ions in equal numbers, then the gas is net neutral, and in this case the electron cloud will oscillate between expansion and contraction, around an equilibrium in which the two clouds would coincide. The individual particles are always in motion if the gas is of a finite temperature, but the plasma dynamics proceeds according to what the populations do in a net sense. The simple situation just described is the basic plasma oscillation between the charge density and the electric field. It is fundamentally a collective interaction, and it is with such collective interactions between particle populations and electric and magnetic fields that plasma physics is concerned.

There is a very wide range of basic interactions in a plasma. Some involve only a specific subset of the particles, those which for example have a velocity in a certain direction that coincides with the frequency of an electromagnetic wave propagating in that direction. Effects such as this are called kinetic, since the details of which particles are at which velocities, or more generally, which particles are in a given region of phase space, is of key importance to the situation. These effects are usually most important on microscopic scales, or on larger scales as damping mechanisms for otherwise dissipation free fluidlike motions. Examples are the conduction of heat by particles scattering back and forth over the distance of a mean free path between collisions, or the absorption of high frequency waves by resonance with particles moving at a velocity equal to the phase velocity of the wave.

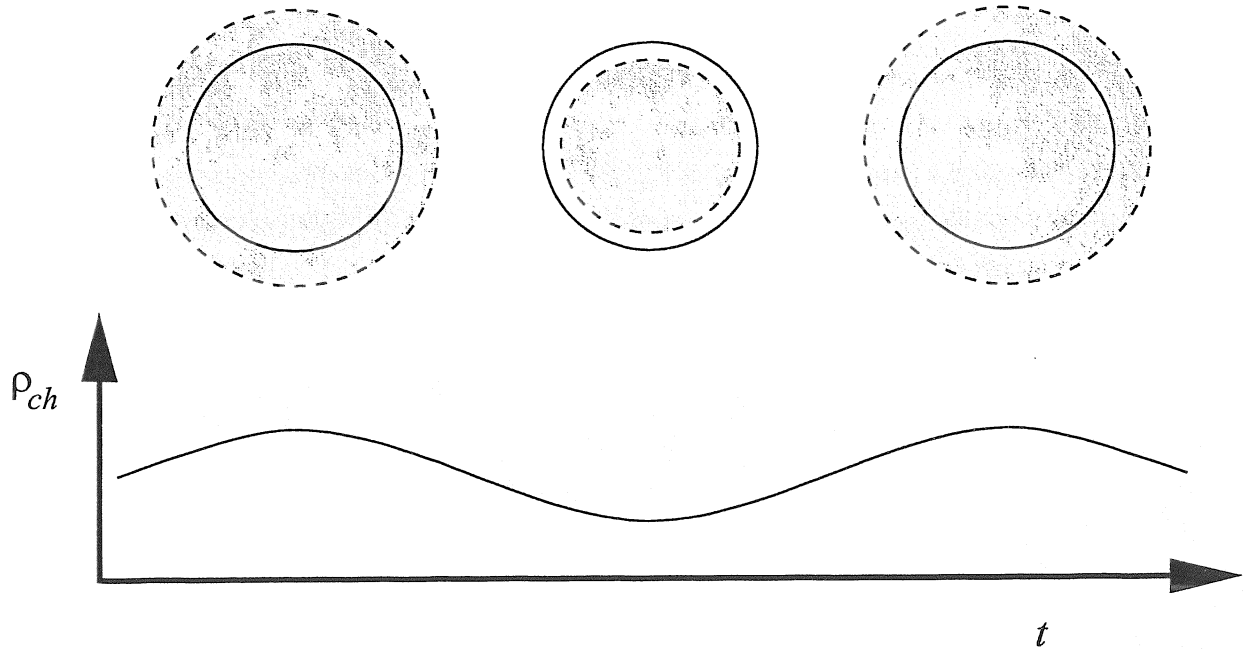

Figure 1.1. The basic oscillation of a plasma consisting of clouds of equal numbers of electrons (dashed circle, filled) and ions (solid circle). When the electron cloud expands, it is pulled back to the ion cloud by the electric field created by the nonzero charge density. When the electron could contracts, it is pushed back by the same force, now of opposite sign. The ion cloud has a motion opposite to the electrons, but smaller by a factor of the square root of the mass ratio. The sinusoidal curve gives the charge density, ρ_{ch}, at the center of the plasma as a function of time, t. The oscillation proceeds at the plasma frequency, ω_{pe}.

Other interactions, particularly macroscopic ones whose spatial scale is comparable to the overall dimensions of the plasma, can be described with a simpler fluid model. In this case the details of particular velocities are unimportant, and one can describe the situation using only the densities, mean velocities, and temperatures of the constituent gases making up the plasma. This situation is obviously relevant to considerations of global stability. But it is also important to a class of smaller scale, fluidlike motions which occur in the form of turbulence, for which kinetic effects provide dissipation channels. These motions are responsible for the transport of particles and energy out of an inhomogeneous system, whenever microscopic processes do not suffice. The situation is analogous to turbulence in a normal fluid such as the Earth's atmosphere, which transports energy from hot regions to colder regions, and does so much more efficiently than microscopic processes. This type of dynamics is the one with which this work is most concerned.

Plasma physics is important to situations found both in nature and in the laboratory. The most familiar case in nature is the outer regions of the solar atmosphere, called the corona. The gas there is very hot, over a million degrees Kelvin. We denote temperatures in terms of the average kinetic energy of random motion per particle, expressed in units of energy. So one million degrees Kelvin corresponds roughly to $k_B T = 100\,\mathrm{eV}$, or an average energy of one hundred electron volts. Here, $k_B = 1.38 \times 10^{-16}$ ergs per degree Kelvin, or equivalently about one electron volt per about $11,600$ degrees Kelvin. One electron volt is the quantity of energy acquired by an electron which is accelerated through a potential change of one volt, that is, 1.6×10^{-12} ergs. In plasma physics we normally express temperatures in eV, with the Boltzmann constant understood. With $T = 100\,\mathrm{eV}$ the average energy of collision between any two particles is $100/13.6$ or about seven times what is necessary to strip an electron away from a proton, thereby ionising a hydrogen atom. Such a hot gas is fully ionised, and the ions in it are simply individual nuclei. Whether it is a plasma or not depends on the density at a given temperature. Charged particles in populations screen each other, such that outside of a distance given by the Debye length, $\lambda_D = T_e/4\pi n_e e^2$ for a neutral plasma with electron density n_e and temperature T_e, the influence of an individual particle is no longer felt and the particles respond to each other collectively through their effects on the electromagnetic field. If the number of charged particles in a Debye sphere is large, $n_e \lambda_D^3 \gg 1$, then the gas behaves as a plasma. This parameter for the solar corona, whose density is very roughly $n_e = 10^6\,\mathrm{cm}^{-3}$, is of order 10^8. Differing regions of the corona are threaded by magnetic fields of varying strength, so depending on the situation the coronal plasma is either magnetised or unmagnetised.

A laboratory plasma is the clearest example of a magnetised plasma. The simplest case is a straight magnetic field set up by means of solenoidal coils which carry an electric current. Within this is a vacuum chamber into which a diffuse gas is admitted and then ionised according to some means, or the gas can be introduced already ionised and hot enough to remain so. Individual particles of mass M and charge state Ze (electrons have $Z = -1$) in a magnetic field of strength B and unit direction $\mathbf{b}$ represented by the continuous vector field, $\mathbf{B} = B\mathbf{b}$, follow orbits around the lines of force, called magnetic field lines, whose orientation is simply given by $\mathbf{b}$. This gyro motion occurs in the plane locally perpendicular to the field line. It follows from the magnetic part of the Lorentz force, which acts at right angles to both the instantaneous velocity, $\mathbf{w}$, and the magnetic field, with magnitude $ZewB/c$. Parallel to the field line the motion is unaffected, but the motion projected onto a plane perpendicular to $\mathbf{B}$ is a circle of radius ρ_L and frequency Ω_L given by

$$\rho_L = \frac{Mcw}{ZeB} \qquad \Omega_L = \frac{ZeB}{Mc} \tag{1.1}$$

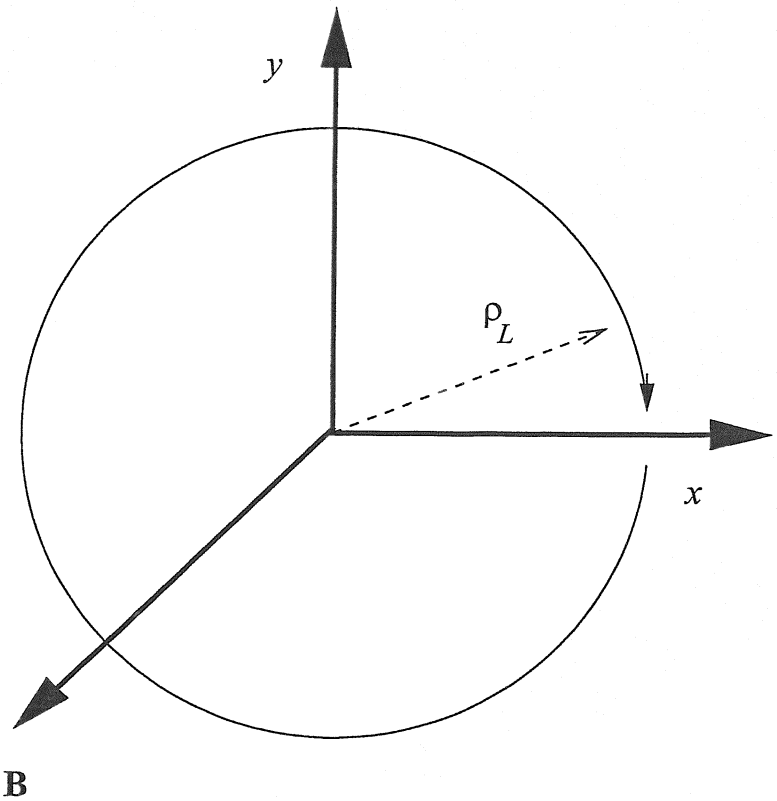

Figure 1.2. Gyro motion of an ion in a magnetic field, **B**. The particle orbits the field lines in the xy-plane, perpendicular to **B**. The radius of the orbit is ρ_L, and the sense of the motion is such that the Lorentz force is centripetal. For positive ions the orbit is clockwise as seen by an observer displaced in the direction of **B**.

These are called the gyroradius and gyrofrequency, respectively.

Thermal populations of charged particles have characteristic values of these scales. A gas of electrons, for example, has an average velocity, or thermal velocity, given in terms of their temperature and mass by

$$V_e = \left(\frac{T_e}{m_e}\right)^{1/2} \tag{1.2}$$

Substituting this velocity in for w in ρ_L and noting that the magnitude of the charge is just e, we find the electron gyroradius and gyrofrequency. We find these quantities similarly for the ions. Together we have

$$\rho_e = \frac{c}{eB}(m_e T_e)^{1/2} \qquad \rho_i(Z) = \frac{c}{ZeB}(M_i T_i)^{1/2} \qquad \Omega_e = \frac{eB}{m_e c} \qquad \Omega_i(Z) = \frac{ZeB}{M_i c} \tag{1.3}$$

where it is important to note that the masses of electrons and ions are very disparate. We always have

$$\mu_e \equiv \frac{m_e}{M_i} \ll 1 \tag{1.4}$$

and for the lightest ions, protons, $\mu_e = 5.4 \times 10^{-4}$. We *usually* have

$$\rho_e \ll \rho_i \tag{1.5}$$

although in some cases the ions are so cold that the mass ratio is overcome. A laboratory plasma is considered magnetised if all of these gyroradii are small compared to its overall dimensions. The limiting case is the ratio between ρ_i and the plasma's scale length perpendicular to **B**. This constraint is well satisfied, particularly for plasmas which are confined by an externally applied magnetic field, which is the usual case of a laboratory plasma.

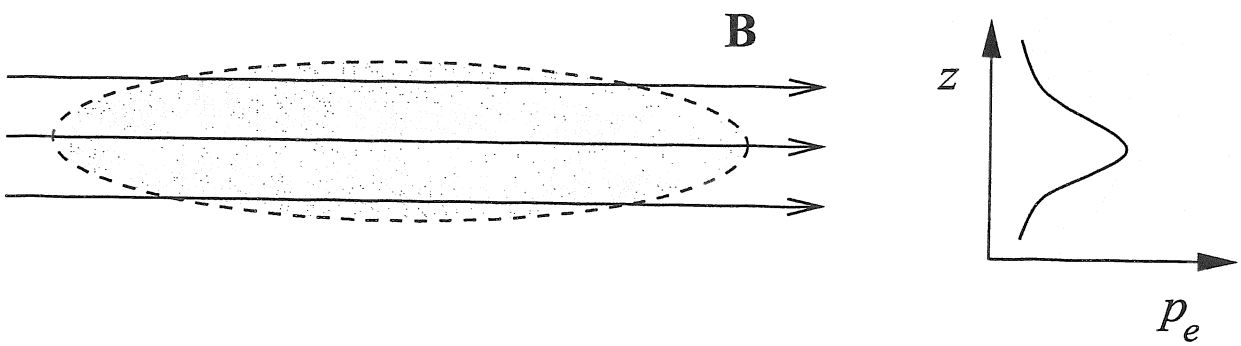

Figure 1.3. Sketch of a linear magnetised plasma. The particle gyroradii are small compared to the perpendicular scale length, which is in this case the plasma radius, a. If there is an edge layer with steep gradients scaling as $L_\perp \ll a$, then the gyroradii would have to be smaller than $L_\perp$ in order for dynamics in that layer to be magnetised.

One of the most important application of plasma physics in the laboratory is to the case in which a plasma is confined by means of an appropriately constructed magnetic field, and heated by external means to a temperature hot enough that the individual nuclei undergo fusion reactions. When the energy responsible for this comes from the random thermal motion, this situation is called thermonuclear fusion. The long range attempt to bring this process to bear under controlled conditions is of obvious importance to the future of energy generation in the prevailing industrialised society. The two main lines of research are called magnetic and inertial fusion. In the first, the plasma is confined

by a magnetic field and expected to undergo fusion under conditions which are steady for times much longer than those characteristic of dynamical stability. In the second, a small pellet of high density frozen material is very suddenly subjected to intense laser energy, such that it implodes to high density under enough temperature to undergo fusion. As far as fusion applications are concerned, this work will treat only the first situation.

A plasma can be confined by a magnetic field due to the Lorentz forces acting on all its particles. If the plasma is magnetised the individual particles cannot simply slip past the magnetic field. But the magnetic field and the plasma together form a dynamical system, and one must take care that it is stable. The study of macroscopic dynamics of a current carrying plasma and a magnetic field is most often done using a model called magnetohydrodynamics, or MHD. The plasma constituents are assumed to be sufficiently well coupled that it can be treated as a single, charge neutral fluid, which due to its makeup can carry an electric current. In a neutral plasma the electric part of the Lorentz force adds up to zero, and the magnetic part adds up in terms of the individual velocities and charges to what is called the J-cross-B (JxB) force, given by the sum over all particles of the magnetic Lorentz force,

$$\sum_j Z_j e_j \frac{\mathbf{v}_j \times \mathbf{B}}{c} = \frac{\mathbf{J} \times \mathbf{B}}{c} \qquad \text{with} \quad \mathbf{J} = \sum_j Z_j e_j \mathbf{v}_j \tag{1.6}$$

This current is in turn given by the spatial gradients of the magnetic field according to Ampere's law

$$\mathbf{J} = \frac{c}{4\pi} \nabla \times \mathbf{B} \tag{1.7}$$

which holds at low enough frequencies that we can ignore propagation delay at the finite speed of light. If we substitute this relation into the JxB force, we find the two types of forces that a magnetic field exerts on a current carrying plasma:

$$\frac{\mathbf{J} \times \mathbf{B}}{c} = -\nabla \left(\frac{B^2}{8\pi} \right) + \frac{\mathbf{B} \cdot \nabla \mathbf{B}}{4\pi} \tag{1.8}$$

A simple picture of the MHD model is one of magnetic field lines as wires, bundles of which exert a pressure in the plane perpendicular to their orientation, and which exhibit tension, that is, a restoring force against bending. These two analogies describe the nature of the two terms in the JxB force. Further expanding the wire analogy is the reaction of the magnetic field to the plasma — the wires are simply dragged along by the plasma and bunched together if the plasma flow is compressional. This gives rise to two types of wave

motion called Alfvén waves, as shown in Fig. 1.4, which propagate at a velocity called the Alfvén speed,

$$v_A = \left(\frac{B^2}{4\pi n_i M_i} \right)^{1/2} \tag{1.9}$$

reflecting the fact that the magnetic forces scale as $B^2/4\pi$ and that $n_i M_i$ is the mass density. Magnetic pressure gives rise to compressional Alfvén waves, and tension leads to shear Alfvén waves, also called torsional Alfvén waves if the perpendicular flow is in the form of localised vortices, or eddies. Motion at global scales is connected to overall stability: if the net magnetic forces are in balance with the pressure force the system is in equilibrium, and if the net reaction to small disturbances is towards restoration of the equilibrium, then the system is stable.

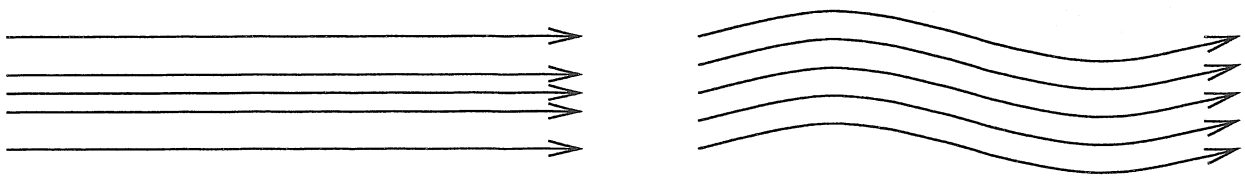

Figure 1.4. The two types of magnetic forces. Magnetic pressure (left) acts perpendicular to the field lines in response to compression of the plasma, which carries the field lines with it. This gives rise to compressional Alfvén waves which propagate longitudinally, perpendicular to the magnetic field. Magnetic tension (right) results from shearing, compression free motion which bends the field lines. The resulting curvature represents a JxB Lorentz force tending to straighten the field lines. This gives rise to shear Alfvén waves, which propagate transverse, parallel to the magnetic field. Both waves propagate at the Alfvén speed, v_A, and constitute the basic characteristics of MHD.

A stable plasma is still subject to smaller scale motion, however, and it is with this that we are most concerned. Magnetised plasmas, whether in nature or in the laboratory, have transport properties due both to kinetic particle motion and also to small scale fluid vortical motion perpendicular to the magnetic field. Particles have a probability to collide with one another through very short range (within a Debye length) interactions, which is characterised by a collision frequency. Coulomb collisions are not like those between hard spheres; the interactions are mediated by the two-particle electromagnetic field. The dominant interactions are small-angle scatterings which add up into a characteristic time

after which a narrow distribution of velocities becomes thermalised. This is expressed in terms of the collision frequencies for electrons and ions,

$$\nu_e = \frac{4\sqrt{2\pi} n_e \lambda e^4}{3 m_e^{1/2} T_e^{3/2}} \qquad \nu_i = \frac{4\sqrt{\pi} n_i \lambda e^4}{3 M_i^{1/2} T_i^{3/2}} \tag{1.10}$$

where it is noted that the characteristic electron-ion collision frequency in a neutral plasma is also ν_e. The factor of λ is the Coulomb logarithm, the logarithm of the ratio between the Debye length and the distance of closest approach, usually the DeBroglie wavelength of the two particles in the center of momentum frame. Collisional transport is a random walk process with the gyroradius as the step size and the inverse collision frequency as the step time. For electrons and ions the characteristic classical diffusion coefficients are therefore

$$D_e = \rho_e^2 \nu_e \qquad D_i = \rho_i^2 \nu_i \sim \left(\frac{T_e}{T_i} \frac{M_i}{m_e} \right)^{1/2} D_e \tag{1.11}$$

The corresponding diffusion rates for dynamics are given by these coefficients divided by the scale of motion squared. If the plasma is hot enough, however, this diffusion rate is slow enough to be largely negligible. A plasma is considered hot if it is fully ionised and these diffusion rates are slower than any of the intrinsic dynamics under consideration.

Instead of collisional transport, what controls confinement in a hot, magnetised plasma is a class of motions called fluid drift dynamics. These are turbulent flows, whose scale is somewhat larger but not much larger than ρ_i, and whose characteristic velocity is well below the sound speed. The standard definition of the sound speed takes into account the possibility of electrons providing pressure and ions providing inertia, through electrostatic coupling between the two fluids. The sound speed c_s in a plasma with singly charged ions is

$$c_s = \left(\frac{T_e}{M_i} \right)^{1/2} \tag{1.12}$$

which is the analog of the value in terms of the pressure and mass density familiar from neutral fluids. The fastest frequencies available for incompressible perpendicular motion are those given by the sound speed and the local scale of inhomogeneity, $L_\perp$, so in setting up models we will assume frequencies of this order:

$$\omega \sim \frac{c_s}{L_\perp} \tag{1.13}$$

In keeping with this relation between electron pressure and ion inertia, we have a drift scale, ρ_s, which has the same form as the ion gyroradius

$$\rho_s = \frac{c_s}{\Omega_e} = \frac{c}{eB} (M_i T_e)^{1/2} \tag{1.14}$$

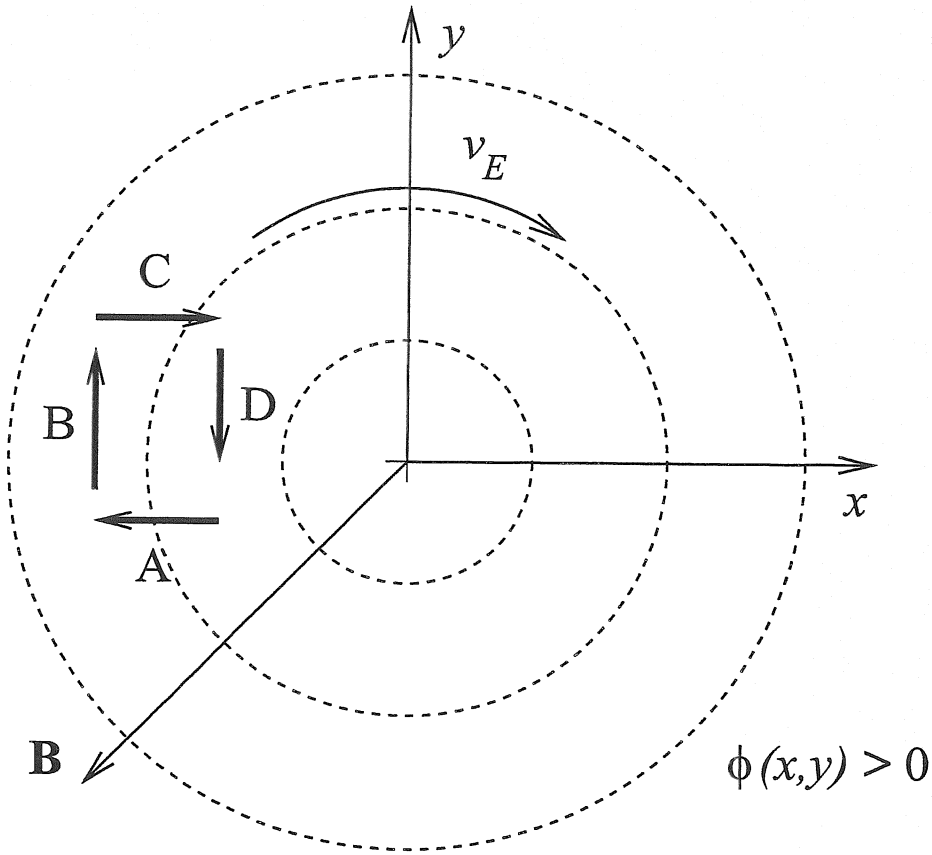

Figure 1.5. The ExB drift in a magnetised plasma. The dashed lines are contours of constant electrostatic potential, ϕ, representing a localised disturbance in the electric field, $\mathbf{E} = -\nabla\phi$ in the xy-plane, perpendicular to the magnetic field, $\mathbf{B}$. The four thick arrows A–D represent phases of the gyro orbit of a positive ion. During phase A, the particle is accelerated by the electric field, so that during phase B it coasts faster. During phase C it is decelerated, so that during phase D it coasts slower. The center of the orbit drifts in a direction mutually perpendicular to $\mathbf{E}$ and $\mathbf{B}$, such that the average net Lorentz force vanishes. The drift velocity, $\mathbf{v}_E$, is therefore the same for all charged particles. It is clockwise around a potential maximum, as seen by an observed displaced in the direction of $\mathbf{B}$. This ExB drift velocity constitutes the basic characteristic of fluid drift motion.

Many laboratory plasmas, especially discharges, have ions at room temperature but electrons at a few to several eV, which gives the motivation for these definitions. If the ions are also hot, their temperature is usually comparable to T_e and so ρ_s and c_s keep their relevance.

Fluid drift dynamics can display a moderately wide range of scales, down to about ρ_s in space and up to about $c_s/L_\perp$ in frequency. The drift concept is relevant if the particles

undergo many gyro orbits in the time that their gyro centers drift over one gyroradius. This requires dynamical frequencies to be small compared to any of the gyrofrequencies, of which Ω_i is the slowest. This can only be satisfied if the drift parameter, defined by

$$\delta \equiv \frac{\rho_s}{L_\perp} \ll 1 \tag{1.15}$$

is small. Another important figure of merit is the ratio of plasma gas pressure to magnetic field pressure,

$$\beta = \frac{8\pi p}{B^2} \tag{1.16}$$

called the plasma beta. Consideration of fluid drift dynamics while neglecting any compressional effects of the magnetic field typically require that $\beta \ll 1$. A related parameter is the electron dynamical beta, which is the square of the ratio of the sound speed to the Alfvén speed,

$$\beta_e = \frac{4\pi p_e}{B^2} \ll 1 \tag{1.17}$$

which must be small in order to separate shear Alfvén from sound wave dynamics. Furthermore, it is β_e, specifically, that must be small to allow the neglect of compressional dynamics and hence the consideration of perpendicular motions as a quasistatic evolution of force balances.

The important consideration for drift dynamics is that we cannot treat the plasma as a single fluid, but must instead use a two fluid (or several fluid) model. The key assumption behind the MHD model is that the Lorentz force for each fluid species approximately vanishes, leaving a plasma velocity of

$$\mathbf{u} = \mathbf{v}_E \equiv c\frac{\mathbf{E}\times\mathbf{B}}{B^2} \tag{1.18}$$

called the E-cross-B (ExB) velocity. For frequencies as low as $c_s/L_\perp$ this no longer holds; instead, the pressures enter the force balance. It then follows that due to their strongly disparate masses, the electrons and ions will have qualitatively different responses to the electromagnetic field. In particular, the forces on the electrons parallel to the magnetic field can balance, leaving a quasistatic evolution. Small disturbances exhibiting this situation are called drift waves, and their nonlinear state is called drift wave turbulence. These waves have been directly measured in linear plasma devices, and there is a large body of circumstantial evidence that they are responsible for the turbulent fluctuations among the ExB velocity and thermodynamic quantities that lead to transport of particles and thermal energy out of magnetically confined plasmas. Drift wave turbulence, and more

generally fluid drift dynamics, is therefore of obvious importance to laboratory plasmas, and it provides the subject of study for this exposition.

The typical scales of fluid drift turbulence are roughly $10\rho_s$ and $2\pi \times 10L_\perp/c_s$, with $\delta \sim 10^{-2}$. In fusion experiments these correspond to roughly 1 cm and 10 μsec, which is small and fast compared to the transport time scales but large compared to most kinetic processes and slow compared to compressional MHD processes. Due to this last property, the perpendicular flow vortices are largely incompressible. The forces across the magnetic field lines are therefore always in approximate balance, which can be regarded as quasistatic. Part of this is the electrostatic nature of the perpendicular electric field, so that the ExB velocity is given in terms of the electrostatic potential as a stream function. The fluid velocities perpendicular to the magnetic field are still similar to the ExB velocity, and due to some subtle properties which are covered in the next two chapters the ExB velocity is still the one according to which thermodynamic quantities are transported, or advected. Shear Alfvén dynamics is still quite important, however, leaving a dynamical system of very rich, electromagnetic character. For those familiar with geophysical fluid dynamics, the situation is not unlike geostrophic flow in character, and there are many analogies between the two models. In a magnetised plasma, small scales across the magnetic field are coupled to long parallel wavelengths, with a parallel/perpendicular scale ratio of order 10^3. This is generally called flute mode character and is due to the fact that the shear Alfvén dynamics tends to eliminate gradients parallel to the magnetic field.

The basic outline of this work is as follows. The model of an ideal fluid is briefly introduced in Chapter 2, which continues with the hierarchy of fluid models culminating in MHD and is concerned mainly with the way the models are derived. The drift approximation and fluid drift dynamics form the subject of Chapter 3. Chapters 4 and 5 treat the basic modes of dynamics within the model, including drift waves and their relatives. The changes wrought by turbulence and ExB flows are very important and take up Chapters 6 through 9. The effects of inhomogeneous magnetic fields are considered by themselves in Chapter 10, and then in Chapter 11 the interplay between drift wave dynamics and the interchange forcing in a magnetic field lying on closed, toroidal flux surfaces is studied. Extensions to the fluid model needed to treat kinetic dissipation mechanisms due to the temperatures are treated in Chapters 12 and 13, and in Chapter 13 we find a new class of dynamics due specifically to the ion temperature gradient. The general nature of the transport due to fluid drift turbulence is considered and contrasted against the classical random diffusion process in Chapter 14. Appendices on numerical methods to treat the dynamics and mathematical methods to treat toroidal magnetic geometry appear at the end. Each chapter closes with a section on further reading.

2. Ideal Fluid Electrodynamics and MHD

B. Scott

Jul 1999

2.1. Introduction

The classical picture of natural phenomena in physics is one of particles and fields. Plasma physics however deals with collective phenomena. The number of particles in any situation of interest is arbitrarily large, and this renders impractical the solution of a Sturm-Liouville equation for each particle. We therefore use a statistical picture, which replaces the discrete particle model with a continuous model of a distribution function in position/velocity phase space for each species of particle. We understand the distribution function as a C^∞ field much like the electromagnetic field itself. A C^∞ field is one which is assumed to be differentiable as many times as deemed necessary; it is a function of several independent variables, position and velocity space for a distribution function or just position space for the dynamical fields, or for a fluid.

The situations which we will describe are strongly ruled by self consistency, especially for the electrons, which are the principal carriers of electric current. This means that the thermodynamics of electrons cannot be separated from the electromagnetic phenomena for which they act as sources. In order to best understand this with a minimum of extra complication we will treat a plasma as a collection of charged fluids. We therefore replace the distribution function with a small number of field quantities which can reflect the overall nature of the dynamics without having to treat what can become enormously complicated details of kinetic phenomena (specialised reactions of particles with particular velocities). In many cases it is possible to work with ideal fluids, in which only a density, velocity, and temperature are retained. At most, we will require a few extra quantities such as conductive heat fluxes. The emphasis will be on the interplay between the thermodynamics of each fluid and the electromagnetic field.

We introduce a hierarchy of three dynamical systems: The first is fluid electrodynamics, in which the fluid motion is considered as ideal and nonrelativistic but the entire electrodynamics is retained. This can treat arbitrary frequencies since the wave propagation part does not require approximation, and allows finite charge densities to appear even if the equilibrium about which one expands is net charge neutral. It is useful in setting the parameter limits on the more restricted cases. The second can be called fluid plasma dynamics. Here, the nonrelativistic approximation is extended to the fields; we

will find that this introduces several simplifications that enter together: the fluid system becomes quasineutral and the fields evolve quasistatically in response to the varying source distributions. By quasineutral we refer to the important property that the total charge density can be neglected but the electric field still has a primary role in the dynamics. The third system is magnetohydrodynamics, also called MHD. This is a much simplified picture which replaces the several charged fluids with a single fluid which can carry current; that is, we retain only one mass density, one velocity field, and one temperature (equivalently, pressure). We discuss MHD at length for two reasons. One, to understand both the incompressible and compressible classes of its dynamics, which will be our road to understand the low frequency approximations in Chapter 3. Two, to note explicitly upon which assumptions this important and widely used model depends. Although it is applicable to many problems of general interest, the fact that it is limited, especially at small scales and in dynamics for which the thermodynamic gradient is the main drive mechanism, is unfortunately overlooked, to the point that untenable treatments still receive attention in the scientific literature. The aim is to give a presentation of the broad scope of fluid plasma dynamical models, so that one understands the conditions under which each is applicable.

2.II. Derivation of Ideal Fluid Equations and Electrodynamics

Ideal fluid equations can be derived heuristically according to very simple considerations. If all we need consider is a closed system with the three field quantities — a scalar density, a vector velocity field, and a scalar pressure — the matter can be reduced to bookkeeping via the conservation of material, momentum, and thermal energy, respectively. Along the way we encounter an important part of fluid dynamics: the velocity can advect ("carry") itself. This property gives the dynamics a nonlinear character which leads to the richness of problems such as shock waves and turbulence, making it quite unusual if one has spent one's time principally with single particle motion.

The density gets its equation from the consideration of material conservation. We specify n as the material density, which is equivalent to a mass density $\rho = nM$ or charge density $\rho_{ch} = ne$ if M and e are the unit mass and charge for the fluid, respectively. At this point we assume that the velocity field at a given time is known, and ask simply how the resulting material flux affects the evolution of the density within a small interval of time. We can look at this in two ways: consider a volume of fluid which is fixed in space and sum up all the material which enters and leaves, or a volume whose bounding surface moves continuously with the fluid. In the first case the volume is fixed but the amount of material changes; in the second the amount of material is fixed but the volume can change.

Either situation tells us how the density changes at a given point, and we can learn about the advection property by showing how they are equivalent.

For the fixed volume, we assume that a fluid in the vicinity of a point $\mathcal{P}$ and time $\mathcal{T}$ has density $n(\mathbf{x}, t)$ and flows with velocity $\mathbf{v}(\mathbf{x}, t)$. Let $\mathcal{V}$ be a fixed volume which contains $\mathcal{P}$ and is bounded by the surface $\mathcal{S}$. Let N be the total amount of material within $\mathcal{V}$ at time $\mathcal{T}$. The total change in the material within the interval δt is then given by the total amount exiting $\mathcal{V}$ through $\mathcal{S}$:

$$\delta N = \oint dV\, \delta n = -\oint \mathbf{dS} \cdot n\mathbf{v}\delta t \tag{2.1}$$

We can let δt go to zero and then rewrite the change in N as a time derivative, which may be exchanged with the integration since $\mathcal{V}$ is fixed. The right side can be reformed with the use of Gauss's theorem as a volume integral over the divergence of the material flux represented by $n\mathbf{v}$,

$$\delta N = -\oint \mathbf{dS} \cdot n\mathbf{v}\delta t = -\oint dV\, \nabla \cdot n\mathbf{v}\delta t \tag{2.2}$$

Finally, we note that $\mathcal{V}$ is arbitrary and so we can shrink its extent to zero and thus neglect second order differentials. Since $\mathcal{P}$ and $\mathcal{T}$ themselves are arbitrary, the integrand then vanishes for all $\mathbf{x}$ and t:

$$\frac{\partial n}{\partial t} + \nabla \cdot n\mathbf{v} = 0 \tag{2.3}$$

The divergence of the material flux vector then gives the time evolution of the material density. This is the general form of a conservation law for field quantities.

Using the comoving volume, the one whose surface elements move with the fluid, we can find the same result but in different language. We now specify $\mathcal{V}$ as a volume in the neighborhood of $\mathcal{P}$ and $\mathcal{T}$, but since it is comoving, no material enters or leaves. Instead, $\mathcal{V}$ deforms. The demand that N not change is expressed as

$$\delta N = 0 = \delta n\, V + n\, \delta V \tag{2.4}$$

From a theorem of differential geometry we can find the change in the volume in terms of the divergence of the surface displacements,

$$\delta V = V \nabla \cdot \delta\mathbf{x} \tag{2.5}$$

Using these two equations we can find the change in the density,

$$\delta n = -n\frac{\delta V}{V} = -n\nabla \cdot \delta\mathbf{x} = -n\, \delta t\, \nabla \cdot \mathbf{v} \tag{2.6}$$

with the help of the relation $\delta\mathbf{x} = \mathbf{v}\delta t$. As before we let $\delta t \to 0$ and then we have the change in the density:

$$\frac{dn}{dt} + n\nabla \cdot v = 0 \tag{2.7}$$

where the symbol d/dt is used to distinguish this case from the one in which $\mathcal{V}$ is fixed. This relation says that as one follows the fluid, the density changes according to how the fluid is compressed.

These two forms of material conservation form the two reference frames used in fluid dynamics. Equations in the fixed volume system are called the Eulerian form and in the comoving system they are called the Lagrangian form. They are related simply through a local coordinate transformation, which is a one-to-one and onto map between the infinitesimal space about a point in space and time, and itself. Since the fluid moves arbitrarily we can only specify such a transform locally, *i.e.*, through the coordinate differentials, not the coordinates themselves. But since we are transforming derivatives, this is sufficient. The transform between the fixed and comoving reference frames is

$$\begin{aligned} dt' &= dt & dt &= dt' \\ d\mathbf{x}' &= d\mathbf{x} - \mathbf{v}dt & d\mathbf{x} &= d\mathbf{x}' + \mathbf{v}dt' \end{aligned} \tag{2.8}$$

where the prime denotes the comoving one. The corresponding transform of the derivatives is

$$\left.\frac{d}{dt'}\right|_{\mathbf{x}'} = \left.\frac{dt}{dt'}\right|_{\mathbf{x}'} \left.\frac{\partial}{\partial t}\right|_{\mathbf{x}} + \left.\frac{d\mathbf{x}}{dt'}\right|_{\mathbf{x}'} \cdot \left.\frac{\partial}{\partial \mathbf{x}}\right|_{t} \qquad \left.\frac{\partial}{\partial \mathbf{x}'}\right|_{t'} = \left.\frac{\partial}{\partial \mathbf{x}}\right|_{t} \tag{2.9}$$

The spatial gradient remains unchanged, but the time derivative is affected:

$$\frac{d}{dt} = \frac{\partial}{\partial t} + \mathbf{v} \cdot \nabla \tag{2.10}$$

This form of the comoving time derivative is called the advective derivative, since it refers to how a field changes when it is carried by a "wind." One can think, for example, of the air at a given place cooling in time when the wind blows from a place which is colder. An advantage of the ability to move back and forth between the fixed and comoving reference systems is that the equations are easier to construct in the comoving frame. We can then use the transformations to convert to the fixed frame, which we need in order to do a computation involving places at which the velocity field is different.

With this to hand we can simply write the next two equations, but first we come to the other property of a fluid: it moves not only according to external forces but also in response to its own pressure. To get the change of the fluid velocity in the comoving reference frame we simply find the acceleration due to the electric force and the pressure —

since the volume is comoving, the local mean velocity is zero and so there is no magnetic force until we transform back to the fixed frame. The acceleration of the fluid element in its local rest frame is

$$NM\frac{d\mathbf{v}}{dt} = Ne\mathbf{E} - \oint \mathbf{dS}\, p \tag{2.11}$$

where the pressure acts on the bounding surface of the comoving volume. Explicitly writing the volume integration and using Stokes's theorem to rewrite the surface integral, we find

$$\oint dV\, nM\frac{d\mathbf{v}}{dt} = \oint dV\, ne\mathbf{E} - \oint dV\, \nabla p \tag{2.12}$$

We once again take the extent of the volume to zero, finding the acceleration in the local rest frame,

$$nM\frac{d\mathbf{v}}{dt} = ne\mathbf{E} - \nabla p \tag{2.13}$$

At this point we note that in transforming frames with the electromagnetic field we always have to use the Lorentz transform, if only to first order in v/c; this is how we pick up the magnetic force. In the fixed frame we then find

$$nM\left(\frac{\partial}{\partial t} + \mathbf{v}\cdot\nabla\right)\mathbf{v} = ne\left(\mathbf{E} + \frac{\mathbf{v}}{c}\times\mathbf{B}\right) - \nabla p \tag{2.14}$$

We see now the two important differences between the dynamics of a fluid and that of a particle. First, the fluid has an internal pressure, whose gradient acts as an additional force. Second, the velocity advects itself. Both of these are consequences of the C^∞ nature of the fluid as a set of field quantities rather than as a set of particles.

The final equation is conservation of thermal energy, simply the first law of thermodynamics for a fluid. We can use either temperature T or pressure p for an ideal fluid, but due to the later necessity of handling dissipation we will use T. We now restrict to an ideal gas, and note that the internal energy per unit of material is $\frac{3}{2}T$ and the pressure is given by $p = nT$, both with temperature written in units of energy. The first law of thermodynamics is in general

$$\delta\mathcal{E} + p\delta V = \delta Q \tag{2.15}$$

which relates changes to the internal energy $\mathcal{E}$ resulting from the pressure doing work on changes in the volume, or from the addition of heat given by δQ. In fluid dynamics it is more usual to work with exit fluxes, so we will rewrite Q in terms of the heat flux $\mathbf{q}$. For a comoving volume the material quantity N does not change, so the internal energy simply changes according to the temperature,

$$\delta\mathcal{E} = \frac{3}{2}N\delta T = \oint dV\, \frac{3}{2}n\delta T \tag{2.16}$$

The change in the volume is given as before in terms of the divergence of the displacements, and the heat change is given by

$$-\delta Q = \oint \mathbf{dS} \cdot \mathbf{q} = \oint dV \, \nabla \cdot \mathbf{q} \tag{2.17}$$

Allowing the extent of the volume to go to zero, we have

$$\frac{3}{2} n \frac{dT}{dt} + p \nabla \cdot \mathbf{v} = -\nabla \cdot \mathbf{q} \tag{2.18}$$

With d/dt as shorthand for the advective derivative, this same equation then holds for the fixed frame:

$$\frac{3}{2} n \left(\frac{\partial}{\partial t} + \mathbf{v} \cdot \nabla \right) T + p \nabla \cdot \mathbf{v} = -\nabla \cdot \mathbf{q} \tag{2.19}$$

But the role of $\mathbf{q}$ is clarified by these considerations: in the comoving frame no fluid material flows past the bounding surface of the volume, so $\mathbf{q}$ is understood as the conductive heat flux, not the total. This is the part of the energy flux that is not carried by advection: if two bodies at rest are brought together at different temperature, the heat will flow from hot to cold by conduction. By writing the equation for the pressure, using the equations for n and T,

$$\frac{\partial}{\partial t} \left(\frac{3}{2} n T \right) + \nabla \cdot \left(\frac{5}{2} p \mathbf{v} + \mathbf{q} \right) = \mathbf{v} \cdot \nabla p \tag{2.20}$$

we find the total flux as the quantity whose divergence appears, and the work done by pressure. In the total heat flux the pressure appears with a factor of $5/2$ instead of $3/2$ due to its ability to do work by compressing the fluid. The alternative form is

$$\frac{\partial}{\partial t} \left(\frac{3}{2} n T \right) + \nabla \cdot \left(\frac{3}{2} p \mathbf{v} + \mathbf{q} \right) = -p \nabla \cdot \mathbf{v} \tag{2.21}$$

If the velocity is divergence free, the total heat flux appears with a factor of $3/2$, since in the absence of compressions the pressure does no work. For an ideal fluid we have $\mathbf{q} = 0$ and heat can only be carried by advection.

The foregoing can also be derived using the Principle of Least Action, using a suitable Lagrangian density. As this is the way one best derives the Maxwell equations of electrodynamics, we present an outline of the method. The usual application is to specify a Lagrangian $L(x^i, \dot{x}^i)$, dependent on path coordinates $x^i(t)$ and their total time derivatives $\dot{x}^i$, such that the action is given by

$$S = \int dt \, L \tag{2.22}$$

where the integral is over the path $x^i(t)$ the system takes between two time points. The action is varied with respect to changes in the $x^i \to x^i + \delta x^i$, keeping the path endpoints fixed. The resulting variation in the action is set to zero in order to find the extremal action:

$$\delta S = \int dt\, \delta x^i \left(\frac{\partial L}{\partial x^i} - \frac{d}{dt} \frac{\partial L}{\partial \dot{x}^i} \right) = 0 \tag{2.23}$$

As the variations δx^i are arbitrary, the quantity in parentheses must vanish. This gives the well known Euler-Lagrange equations for the system.

With fields one expresses the Lagrangian as an integral over all space of a Lagrangian density, $\mathcal{L}$, which now depends on a set of field quantities. For the Maxwell equations these are the potentials (ϕ, A^i) which together form a four-potential in the framework of a relativistic treatment. For a nonrelativistic treatment we can simply write the Lagrangian in terms of the electric and magnetic fields, using the defining relations

$$\mathbf{E} = -\frac{1}{c}\frac{\partial \mathbf{A}}{\partial t} - \nabla\phi \qquad\qquad \mathbf{B} = \nabla \times \mathbf{A} \tag{2.24}$$

For the fluid we treat the thermal energy as a sort of potential energy, and write the Lagrangian density in the usual form of kinetic minus potential energy. The action becomes

$$S = \int dt\, L = \int dt \int d^3x\, \mathcal{L} \tag{2.25}$$

with $\mathcal{L}$ given by

$$\mathcal{L} = nM\frac{v^2}{2} - \frac{3}{2}nT + \frac{E^2 - B^2}{8\pi} + ne\mathbf{v}\cdot\mathbf{A} - ne\phi \tag{2.26}$$

for a single charged fluid whose field variables are the density, velocity, and pressure, with unit mass and charge as given above. The fluid has pressure, and charge density and current given by

$$p = nT \qquad\qquad \rho_{ch} = ne \qquad\qquad \mathbf{J} = ne\mathbf{v} \tag{2.27}$$

The field variables for the Lagrangian density are the fluid element displacements ζ_i and the potentials ϕ and A^i (these are written as covariant and contravariant components, which becomes important not only in relativity but in any system using arbitrary coordinates). When the ζ_i are given, the fluid field quantities vary as

$$\delta n = -\zeta\cdot\nabla n - n\nabla\cdot\zeta \tag{2.28}$$

$$\delta T = -\zeta\cdot\nabla T - \frac{2}{3}p\nabla\cdot\zeta \tag{2.29}$$

$$\delta\mathbf{v} = -\zeta\cdot\nabla\mathbf{v} + \mathbf{v}\cdot\nabla\zeta + \frac{\partial\zeta}{\partial t} \tag{2.30}$$

Varying the ζ_i gives the fluid equations, while varying ϕ and A^i gives the Maxwell equations, as shown by the variation of the action:

$$\delta S = \int dt \int d^3x \times$$
$$\left\{ \delta\zeta \cdot \left[-nM\frac{d\mathbf{v}}{dt} - \nabla p - ne\left(\frac{1}{c}\frac{\partial \mathbf{A}}{\partial t} + \nabla\phi\right) + \frac{ne}{c}\left(\nabla\mathbf{A}\cdot\mathbf{v} - \mathbf{v}\cdot\nabla\mathbf{A}\right)\right] \right. \tag{2.31}$$
$$\left. + \frac{\delta\phi}{4\pi}\left[\frac{1}{c^2}\frac{\partial^2\phi}{\partial t^2} - \nabla^2\phi - 4\pi ne\right] + \frac{\delta\mathbf{A}}{4\pi}\cdot\left[\frac{1}{c^2}\frac{\partial^2\mathbf{A}}{\partial t^2} - \nabla^2\mathbf{A} - \frac{4\pi}{c}ne\mathbf{v}\right] \right\}$$

These yield, respectively, the fluid equation for $\mathbf{v}$,

$$nM\left(\frac{\partial}{\partial t} + \mathbf{v}\cdot\nabla\right)\mathbf{v} = -\nabla p - ne\left(\frac{1}{c}\frac{\partial\mathbf{A}}{\partial t} + \nabla\phi\right) + ne\frac{\mathbf{v}}{c}\times\nabla\times\mathbf{A} \tag{2.32}$$

which is the same as that already given, the scalar field equation for ϕ,

$$\frac{1}{c^2}\frac{\partial^2\phi}{\partial t^2} - \nabla^2\phi = 4\pi\rho_{ch} \tag{2.33}$$

and the vector field equation for $\mathbf{A}$,

$$\frac{1}{c^2}\frac{\partial^2\mathbf{A}}{\partial t^2} - \nabla^2\mathbf{A} = \frac{4\pi}{c}\mathbf{J} \tag{2.34}$$

subject to the condition

$$\frac{1}{c}\frac{\partial\phi}{\partial t} + \nabla\cdot\mathbf{A} = 0 \tag{2.35}$$

called the Lorentz gauge. These equations for ϕ and $\mathbf{A}$ form two of the Maxwell equations:

$$\frac{1}{c}\frac{\partial\mathbf{E}}{\partial t} = \nabla\times\mathbf{B} - \frac{4\pi}{c}\mathbf{J} \qquad \nabla\cdot\mathbf{E} = 4\pi\rho_{ch} \tag{2.36}$$

The other two follow from the way in which we wrote $\mathbf{E}$ and $\mathbf{B}$ in terms of the potentials:

$$\frac{1}{c}\frac{\partial\mathbf{B}}{\partial t} = -\nabla\times\mathbf{E} \qquad \nabla\cdot\mathbf{B} = 0 \tag{2.37}$$

We write again the equations for each charged fluid,

$$\frac{\partial n_j}{\partial t} + \nabla\cdot n_j\mathbf{v}_j = 0 \tag{2.38}$$

$$n_j M_j\left(\frac{\partial}{\partial t} + \mathbf{v}_j\cdot\nabla\right)\mathbf{v}_j = n_j e_j\left(\mathbf{E} + \frac{\mathbf{v}_j\times\mathbf{B}}{c}\right) - \nabla p_j \tag{2.39}$$

$$\frac{3}{2}\left(\frac{\partial p_j}{\partial t} + \mathbf{v}_j \cdot \nabla p_j\right) + \frac{5}{2} p_j \nabla \cdot \mathbf{v}_j = 0 \tag{2.40}$$

where j is the species label, and note that the charge density and current are summed up over all fluid species; explicitly, we have

$$\mathbf{J} = \sum_j n_j e_j \mathbf{v}_j \qquad \rho_{ch} = \sum_j n_j e_j \tag{2.41}$$

and for each species T_j is given by p_j/n_j.

The Maxwell equations (2.36,2.37) and the fluid equations (2.38–2.40) form a closed system, with obvious generalisation to an arbitrary number of charged fluids. We have written these for ideal fluids, and will delay discussion of dissipation until after making the low frequency approximations.

2.III. High Frequency Motion under Fluid Electrodynamics

The dynamical system just presented has a very rich character in its own right, but since our purpose is to proceed to the low frequency regime we will single out the ingredients needed to motivate the necessary approximations. These are the plasma waves, for motion along the field lines, and the compressional magnetosonic waves, for motion across them. Since the associated frequencies are very fast, we can neglect thermal effects and treat the cold fluid system.

We assume a homogeneous background with finite $\mathbf{B}$, zero $\mathbf{E}$, and a neutral two component plasma at rest. For simplicity let this be made of one singly charged ion species, and an equal number density of electrons. We investigate the resulting wavelike motion of small disturbances on this background.

To obtain the first set of waves, we assume that the mass ratio m_e/M_i is very small, and hence that the ions are stationary. We linearise the dynamical system as follows. Let each quantity be given by an equilibrium value and a perturbation thereof; for example the electron density n_e becomes

$$n_e \to n_e + \tilde{n}_e \tag{2.42}$$

with the tilde used to denote the disturbances. In addition, we note that $\mathbf{v}$ and $\mathbf{E}$ belong purely to the disturbances. As the equilibrium is trivial, we need only write the equations for the disturbances, dropping all terms of order higher than one in the disturbance amplitudes (*e.g.*, neglecting terms such as $\mathbf{v} \cdot \nabla \mathbf{v}$ or $\tilde{n}_e \mathbf{E}$). Furthermore, we choose a single degree of freedom of oscillation. Since the equilibrium is homogeneous we may assume

periodicity for small scale motion in time and all three dimensions, and then choose a single Fourier component. Again, for the density we have

$$\widetilde{n}_e = \widetilde{n}_{e\mathbf{k}} \exp[i(\mathbf{k}\cdot\mathbf{x} - \omega t)] \tag{2.43}$$

with the condition $\widetilde{n}_{e-\mathbf{k}} = \widetilde{n}^*_{e\mathbf{k}}$ such that the disturbance is real valued. We may drop the subscripts $\mathbf{k}$ for clarity.

The equations (2.36–2.39) become

$$-\frac{i\omega}{c}\mathbf{E} = i\mathbf{k}\times\widetilde{\mathbf{B}} + \frac{4\pi n_e e}{c}\mathbf{v} \tag{2.44}$$

$$i\mathbf{k}\cdot\mathbf{E} = 4\pi e\widetilde{n}_e \tag{2.45}$$

$$i\mathbf{k}\cdot\widetilde{\mathbf{B}} = 0 \tag{2.46}$$

$$\frac{i\omega}{c}\widetilde{\mathbf{B}} = i\mathbf{k}\times\mathbf{E} \tag{2.47}$$

$$\omega\widetilde{n}_e = n_e\mathbf{k}\cdot\mathbf{v} \tag{2.48}$$

$$\omega\mathbf{v} = -i\frac{e}{m_e}\mathbf{E} + i\frac{e\mathbf{B}}{m_e c}\times\mathbf{v} \tag{2.49}$$

where we note the fundamental role of the electron gyrofrequency,

$$\Omega_e = \frac{eB}{m_e c} \tag{2.50}$$

in the equation for $\mathbf{v}$. There is more generality here than we need; besides choosing a direction for $\mathbf{k}$ we can choose a polarisation, and this reduces the number of independent quantities to manageable levels.

For wave propagation parallel to $\mathbf{B} = B\mathbf{b}$ we let $\mathbf{k} = k_\parallel\mathbf{b}$. The system splits into three sets of modes: For motion along the magnetic field ($\mathbf{v} \parallel \mathbf{B}$), we have $\mathbf{E} \parallel \mathbf{B}$ and hence the magnetic perturbation vanishes. This gives longitudinal propagation ($\mathbf{k} \parallel \mathbf{v}$) involving the charge density and current, with the electric field determined constitutively by the density. There are two waves, each with the electron plasma frequency ω_{pe} regardless of the size of $k_\parallel$,

$$\omega^2 = \omega_{pe}^2 = \frac{4\pi n_e e^2}{m_e} \tag{2.51}$$

For motion across the field ($\mathbf{v} \perp \mathbf{B}$) we have $\mathbf{k}\cdot\mathbf{v} = 0$ and therefore two sets of three incompressible waves (electric field, current, and magnetic field but no density disturbance),

one for each polarisation. Denoting x and y as the two perpendicular coordinates, with $\nabla x \times \nabla y \cdot \mathbf{b} = 1$, we may express the electric field disturbance, for example, as

$$E_{\pm} = E_x \pm iE_y \tag{2.52}$$

For the plus and minus polarisations we find in turn,

$$(\omega \pm \Omega_e)(\omega^2 - k_{\|}^2 c^2) = \omega \omega_{pe}^2 \tag{2.53}$$

In each case there are two limits: $\Omega_e \gg \omega_{pe}$ or vice versa. The interesting case is the only one in which we obtain frequencies slower than light waves ($\omega \sim k_{\|} c$) or plasma waves; this is for $\Omega_e \gg \omega_{pe}$ and $k_{\|} \to 0$, where we find motion at another frequency,

$$\omega = \pm \omega_{pe}^2 / \Omega_e \tag{2.54}$$

for the plus and minus polarisations, respectively.

For wave propagation perpendicular to $\mathbf{B}$ we can choose the plane of propagation. We choose coordinates such that $\mathbf{k} = k_{\perp} \nabla x$. For motion along the field ($\mathbf{v} \parallel \mathbf{B}$) we find the same result as for electromagnetic waves in the unmagnetised case,

$$\omega^2 = k_{\perp}^2 c^2 + \omega_{pe}^2 \tag{2.55}$$

with only two roots since with $\mathbf{k} \perp \mathbf{v}$ the charge density remains zero. For motion across the field ($\mathbf{v} \perp \mathbf{B}$) the system couples compressional motion along ∇x with transverse motion along ∇y, through the finite Ω_e, and so all four remaining roots are coupled. The slowest mode of interest is for $\Omega_e \gg \omega_{pe}$ and $k_{\perp} \to 0$, where we find two modes each at

$$\omega = \pm \omega_{pe}^2 / \Omega_e \qquad \text{and} \qquad \omega = \pm \Omega_e \tag{2.56}$$

The fastest mode is at the upper hybrid frequency ω_{UH} given by $\omega_{UH}^2 = \Omega_e^2 + \omega_{pe}^2$.

These frequencies are very large, involving only two frequencies whose dependence is inverse to the (small) electron mass. If we consider ion motion but still at the stage of high frequencies, we obtain the dynamics which put the limits on what we are to do next. Considering only propagation and motion perpendicular to $\mathbf{B}$, we can reduce the set of equations to three, involving only $\mathbf{E}$ and the two velocities, $\mathbf{v}$ for electrons and $\mathbf{u}$ for ions:

$$\left(k_{\perp}^2 - \frac{\omega^2}{c^2}\right) \frac{ie\mathbf{E}}{M_i} - \mathbf{kk} \cdot \frac{ie\mathbf{E}}{M_i} = i\omega \frac{\omega_{pi}^2}{c^2} (\mathbf{u} - \mathbf{v}) \tag{2.57}$$

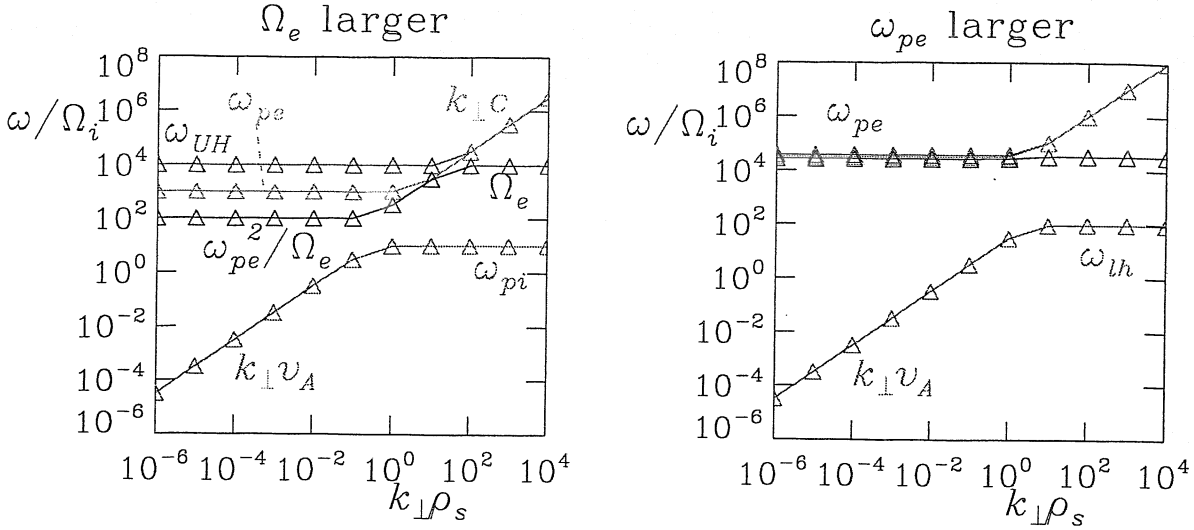

Figure 2.1. Fast perpendicular waves in a magnetised plasma, for the two cases in which either ω_{pe} or Ω_e is the larger. The latter case is more prevalent, such that the magnetosonic waves turn over into non-quasineutral ion plasma waves. For $\omega_{pe} > \Omega_e$ (less magnetised) one finds the more conventional lower hybrid waves at ω_{lh}. Below the lowest of the four curves in each graph, motion is dynamically incompressible perpendicular to the magnetic field and is quasineutral.

$$\mu_e \omega \mathbf{v} = -\frac{ie\mathbf{E}}{M_i} + i\Omega_i \mathbf{b}\times\mathbf{v} \tag{2.58}$$

$$\omega \mathbf{u} = \frac{ie\mathbf{E}}{M_i} - i\Omega_i \mathbf{b}\times\mathbf{u} \tag{2.59}$$

valid for all of $\mathbf{k}$, $\mathbf{E}$, $\mathbf{u}$, and $\mathbf{v}$ perpendicular to $\mathbf{b}$, where μ_e is the mass ratio, Ω_i is the ion gyrofrequency, and ω_{pi} is the ion plasma frequency, respectively given by

$$\mu_e = \frac{m_e}{M_i} \qquad \Omega_i = \frac{eB}{M_i c} \qquad \omega_{pi}^2 = \frac{4\pi n_i e^2}{M_i} \tag{2.60}$$

The two lowest frequency modes of interest are those found by setting

$$\mu_e \to 0 \qquad \text{and} \qquad \omega^2 \ll k_\perp^2 c^2 \tag{2.61}$$

That is, we neglect the four roots found above. It is of interest to note that $n_e e(\mathbf{u}-\mathbf{v})$ gives the total current. What we will want to know is whether we can neglect this in the direction along $\mathbf{k}$; that is, whether we can take the current as divergence free. Choosing $\mathbf{k}$ in the x-direction, we can find a relation between the components of the current,

$$J^x = \frac{i\Omega_i\,\omega}{\omega_{pi}^2 + \Omega_i^2} J^y \tag{2.62}$$

noting the cancellation between k^2 and $\mathbf{kk}$ in Eq. (2.57), and then write the rest of the system for the velocity in the direction along $\mathbf{k}$, and the current in the direction along $\mathbf{b}\times\mathbf{k}$,

$$\omega u^x = i\Omega_i \frac{J^y}{n_e e} \tag{2.63}$$

$$\omega \frac{J^y}{n_e e} = -i\Omega_i \frac{k_\perp^2 c^2}{\omega_{pi}^2}\left(u^x - \frac{J^x}{n_e e}\right) \tag{2.64}$$

where the equation for $\mathbf{v}$ has been used to eliminate $\mathbf{E}$. If J^x can be ignored then the frequency we get is consistent with propagation at the Alfvén velocity along $\mathbf{k}$,

$$\omega^2 = \frac{k_\perp^2 c^2 \Omega_i^2}{\omega_{pi}^2} = k_\perp^2 v_A^2 \qquad \text{where} \quad v_A^2 = \frac{B^2}{4\pi n_i M_i} \tag{2.65}$$

But for progressively smaller scales this frequency rises to the ion gyro and plasma frequencies, J^x becomes significant, and the resulting frequency is modified to

$$\omega^2 = \frac{\left(\omega_{pi}^2 + \Omega_i^2\right) k_\perp^2 v_A^2}{\omega_{pi}^2 + \Omega_i^2 + k_\perp^2 v_A^2} \tag{2.66}$$

For sufficiently small values of k we get waves propagating at v_A but the frequency then turns over at what can be called a low-density generalisation of the lower hybrid frequency:

$$\omega_{LH} = \left(\omega_{pi}^2 + \Omega_i^2\right)^{1/2} \tag{2.67}$$

The textbook lower hybrid wave enters at $\omega_{lh} = (\Omega_i \Omega_e)^{1/2}$ but requires quasineutrality; if $\omega_{pi} < \omega_{lh}$ then quasineutrality is broken. On the other hand, we have neglected the electron motion one needs to derive ω_{lh}. Note that the boundary $\omega_{lh} < \omega_{pi}$ is the same as $\Omega_e < \omega_{pe}$, while it is more common in magnetised plasmas that $\Omega_e > \omega_{pe}$. In the latter limit, coupled with $v_A < c$, the turnover is at the ion plasma frequency ω_{pi}.

The ion plasma frequency is the limit at which space charge effects become important, since it is a reflection that $\nabla \cdot \mathbf{J} = 0$ no longer holds. We finally note that this simplified analysis of compressional magnetosonic waves is only as valid as our two assumptions (Eq. 2.61). For these we require

$$\frac{m_e}{M_i} \ll \frac{v_A^2}{c^2} \ll 1 \tag{2.68}$$

The first decouples the magnetosonic waves from the faster electrons-only motion, thereby also ensuring that $\omega_{pi} < \omega_{lh}$, and the second allows the neglect of light speed effects on the Alfvén waves at low $k_\perp^2$, and furthermore ensures that $\omega_{pi} > \Omega_i$.

2.IV. Quasineutral Motion in a Neutral Plasma

The ion plasma frequency is important because it tells us the slowest time scale on which motion in a plasma involves the charge density as such, which in the cases we will address should be negligible even though we will have fluctuating electric fields. This latter situation is called quasineutrality, so named because the plasma is neutral enough so that the total current is divergence free, but not so much that the electric field has to be divergence free. Adding the fluid continuity equations we have

$$\frac{\partial \rho_{ch}}{\partial t} = -\nabla \cdot (n_i e\mathbf{u} - n_e e\mathbf{v}) = -\nabla \cdot \mathbf{J} \tag{2.69}$$

so the ability to neglect the charge density in wavelike motion requires

$$\frac{\partial \rho_{ch}}{\partial t} \to 0 \implies \nabla \cdot \mathbf{J} = 0 \tag{2.70}$$

On the other hand, the existence of a rotational flow with the electrostatic potential as its stream function requires the existence of a nonvanishing charge density. Let us assume at this point that we have ExB vortices in a homogeneous magnetic field, and that the electric field is static. Then,

$$\mathbf{u} = c\frac{\mathbf{E}\times\mathbf{B}}{B^2} \qquad \mathbf{E} = -\nabla\tilde{\phi} \tag{2.71}$$

and the vorticity is proportional to the charge density,

$$\Omega = \nabla\times\mathbf{u} = \frac{c\mathbf{B}}{B^2}\nabla_\perp^2\tilde{\phi} \tag{2.72}$$

with $\nabla_\perp^2$ the perpendicular components of the Laplacian. Let us further assume that the amplitude of the potential relative to the electron temperature is comparable to disturbances in the density,

$$\frac{e\tilde{\phi}}{T_e} \sim \frac{\tilde{n}_e}{n_e} \tag{2.73}$$

Then, the requirement that the total charge density be small compared to the charge density of just the electrons becomes a space scale restriction:

$$\frac{\rho_{ch}}{n_e e} \ll \frac{\tilde{n}_e}{n_e} \sim \frac{e\tilde{\phi}}{T_e} \implies \frac{\nabla^2\tilde{\phi}}{4\pi n_e e} \ll \frac{e\tilde{\phi}}{T_e} \implies \lambda_D^2\nabla_\perp^2 \ll 1 \tag{2.74}$$

where λ_D is the Debye length given by

$$\lambda_D^2 = \frac{T_e}{4\pi n_e e^2} \tag{2.75}$$

In order for ExB flow dynamics to remain quasineutral, we require that the space scales of interest satisfy

$$\Delta_\perp \gg \lambda_D \tag{2.76}$$

and that the time scales satisfy

$$\tau \gg \omega_{pi}^{-1} \tag{2.77}$$

due to the inability of the ions to keep up with the electron motion beyond that frequency.

It is interesting to note the consequences to the electromagnetic field of making this approximation on the motion of the plasma. The electromagnetic field equations (2.36,2.37) admit a gauge freedom, in the sense that for any scalar field χ we can transform the potentials according to

$$\phi \to \phi - \frac{1}{c}\frac{\partial \chi}{\partial t} \qquad \mathbf{A} \to \mathbf{A} + \nabla\chi \tag{2.78}$$

while leaving the electric and magnetic fields unchanged, and hence the Maxwell equations unchanged. If $\mathbf{A}$ has a divergence, then, we can easily find a χ for which $\nabla^2\chi$ will cancel that divergence. On the other hand, working strictly within the Lorentz gauge, we find by examining Eq. (2.34) that the restriction $\nabla \cdot \mathbf{J} = 0$ leads us to the Coulomb gauge,

$$\nabla \cdot \mathbf{J} = 0 \implies \nabla \cdot \mathbf{A} = 0 \tag{2.79}$$

In some sense, then, $(1/c)\partial\phi/\partial t$ is "small" compared to $\nabla \cdot \mathbf{A}$. This is actually the same sense in which the displacement current is small compared to $(c/4\pi)\nabla\times\mathbf{B}$ and the plasma current $\mathbf{J}$. All together, we then have

$$\nabla \cdot \mathbf{J} \to 0 \implies \begin{cases} \dfrac{1}{c}\dfrac{\partial \mathbf{E}}{\partial t} \ll \dfrac{4\pi}{c}\mathbf{J} \\ \dfrac{1}{c^2}\dfrac{\partial^2 \mathbf{A}}{\partial t^2} \ll \nabla^2\mathbf{A} \\ \dfrac{1}{c^2}\dfrac{\partial^2 \phi}{\partial t^2} \ll \nabla^2\phi \\ \dfrac{1}{c}\dfrac{\partial \phi}{\partial t} \ll \nabla \cdot \mathbf{A} \\ \rho_{ch} \ll n_e e \end{cases} \tag{2.80}$$

all of which requires the time and space scale restrictions in Eqs. (2.76) and (2.77). Quasineutrality is clearly tied together with the requirement that the electromagnetic field itself remains nonrelativistic, since it implies neglect of the displacement current. For this to remain valid we also require that the physical parameters satisfy

$$v_A \ll c \tag{2.81}$$

which means the same thing as

$$\lambda_D \ll \rho_s \tag{2.82}$$

where ρ_s is the drift scale defined in Chapter 1. This ensures quasineutrality by space at scales $\Delta_\perp \sim \rho_s$ and by time for velocities as fast as v_A.

2.V. Fluid Plasma Dynamics under Quasineutrality

Fluid plasma dynamics differs from fluid electrodynamics principally in the sense that the electromagnetic field potentials are statically given by their sources: the small but finite ρ_{ch} gives ϕ while $\mathbf{J}$ gives $\mathbf{A}$. In this sense we can regard the electromagnetic field as nonrelativistic. We also have the dynamics of a plasma in the sense that for a neutral background, space charge effects are not important to the dynamics of disturbances. Although there do arise electric fields, the dynamics of the current and magnetic field is what is most important. This situation still differs from the more familiar MHD, however, since it allows qualitatively different dynamics in the electron and ion pressures, and in their velocities.

With the restriction that all the dynamics under study satisfies quasineutrality, we can simplify the governing equations. We eliminate the density equation for the electrons or one of the ion species, since the requirement that $\nabla \cdot \mathbf{J} = 0$ reduces the number of necessary continuity equations by one. We can find the density whose equation is left out, by solving for its contribution to $\rho_{ch} = 0$. Without the displacement current, we find $\mathbf{J}$ from $\mathbf{B}$, so by using the definition of $\mathbf{J}$ in terms of the fluid velocities we may dispense with the electron equation of motion. The latter is used simply to eliminate $\mathbf{E}$ in the equation for $\mathbf{B}$ and in the equation of motion for each ion species. For an ideal plasma with one ion species of unit charge e we have $n_i = n_e$, and then

$$\frac{\partial n_i}{\partial t} + \nabla \cdot n_i \mathbf{u} = 0 \tag{2.83}$$

$$n_i M_i \frac{d\mathbf{u}}{dt} = -\nabla(p_i + p_e) + \frac{\mathbf{J}\times\mathbf{B}}{c} - n_e m_e \frac{d_e \mathbf{v}}{dt} \tag{2.84}$$

$$\frac{dp_i}{dt} + \frac{5}{3} p_i \nabla \cdot \mathbf{u} = 0 \tag{2.85}$$

$$\frac{d_e p_e}{dt} + \frac{5}{3} p_e \nabla \cdot \mathbf{v} = 0 \tag{2.86}$$

$$\frac{1}{c}\frac{\partial \mathbf{B}}{\partial t} = \nabla\times(\mathbf{v}\times\mathbf{B}) + \nabla\left(\frac{1}{n_e e}\right)\times\nabla p_e + \nabla\times\left(\frac{m_e}{e}\frac{d_e \mathbf{v}}{dt}\right) \tag{2.87}$$

with the plasma current and electron velocity both determined by the magnetic field and ion velocity via

$$\mathbf{J} = \frac{c}{4\pi}\nabla\times\mathbf{B} \qquad\qquad \mathbf{v} = \mathbf{u} - \frac{\mathbf{J}}{n_e e} \tag{2.88}$$

and the advective derivatives given by

$$\frac{d}{dt} = \frac{\partial}{\partial t} + \mathbf{u}\cdot\nabla \qquad\qquad \frac{d_e}{dt} = \frac{\partial}{\partial t} + \mathbf{v}\cdot\nabla \tag{2.89}$$

The dependent variables are the set $\{n_i, \mathbf{u}, p_e, p_i, \mathbf{B}\}$, with n_e, $\mathbf{J}$, and $\mathbf{v}$ as auxiliaries. Note that we could just as easily use the electron density equation instead,

$$\frac{\partial n_e}{\partial t} + \nabla\cdot n_e\mathbf{v} = 0 \tag{2.90}$$

noting that for the single ion species with unit charge we have $\nabla\cdot n_i\mathbf{u} = \nabla\cdot n_e\mathbf{v}$. In some applications it is more expedient to use the electron density, as we will see in the next chapter.

In this form of the equations the electron dynamics is largely submerged, appearing explicitly only in the equation for p_e. This is because it is controlled by the dynamics of the magnetic field, a limit which becomes close to complete if we can neglect the electron mass corrections represented by the two appearances of the electron inertia. In that case we still have an essentially two fluid dynamics, however, because the difference between $\mathbf{u}$ and $\mathbf{v}$ is still present. If this is important, the electron and ion pressures evolve differently, and most importantly the magnetic field responds to $\mathbf{v}$ rather than $\mathbf{u}$. This is the origin of the drift dynamical effects presented in the rest of this work. Under certain circumstances $\mathbf{J}$ can actually cancel $\mathbf{u}$ in the equation for $\mathbf{B}$, removing the field line dragging term (the first one on the right side). Ultimately, this means the same thing as $\mathbf{E}$ cancelling ∇p_e, leaving $\mathbf{v}$ at or close to zero. So even in a situation in which ∇n_e and ∇p_e are parallel (and hence the curl of the ∇p_e term vanishes), we can still have the electrostatic effect in the two fluid motion mentioned in Chapter 1. We will see this more explicitly in Chapter 3.

Fluid plasma dynamics is the starting point for the study of not only low frequency but also dissipative effects treatable by such macroscopic considerations. The step from here to fluid drift dynamics effects is straightforward, but before doing that it is useful to go straight to single fluid MHD and its principal properties to make the relevant time scales most transparent. This will tell us what we have to satisfy in order to take the drift approximation.

2.VI. E Pluribus Unum — The Steps to MHD

"Out of many, one" is a good description of the derivation of MHD from the dynamics of several charged fluids we have just seen. The most familiar picture of plasma dynamics is and remains magnetohydrodynamics, or MHD. Even for those whose work never goes beyond that, however, it is important to know through which assumptions and their associated parameter restrictions the validity of MHD is limited. It is a question of what we have to do to take a plasma made up of several fields and end with a model of a single fluid with a single density, velocity, and temperature, but which due to its make-up of charged particles can carry an electric current. The effect of the current is to force the motion of the fluid by means of the total Lorentz force ($\mathbf{J}\times\mathbf{B}$), while the effect of the fluid back on the current is to advect the lines of force of the magnetic field. Under many applications, the pressure force can be negligible compared to the $\mathbf{J}\times\mathbf{B}$ force and the dynamics is very different from that of a neutral fluid, principally in the ability of the plasma to support transverse waves (the shear Alfvén waves). The opposite situation is kinematic MHD. If the flow is prescribed, or results from fluid motion for which the $\mathbf{J}\times\mathbf{B}$ force is negligible, the magnetic field can evolve without self consistent back reaction on the fluid. This is the typical case of a dynamo plasma.

A cursory list of the assumptions needed to realise this picture is the following: The plasma should be neutral so that the electric field and space charge effects do not dominate the dynamics. The electron mass should be strictly negligible, so as not to affect the inertia or the dynamics of the magnetic field (the two appearances of m_e in the plasma model above). The normalised current should be small, such that we can treat each constituent of the plasma as flowing with the same velocity — the only exception is in the Lorentz force which due to the neutrality of the plasma would otherwise vanish. This allows the thermodynamics of the electron and ion pressures to react equally to the motion of the plasma. Lastly, the pressure gradient should be small compared to the electric field in the forces on any of the fluids, so that each fluid reacts the same way to the Lorentz force. Quantitatively speaking, we require

$$\rho_{ch}\mathbf{E} \ll \frac{\mathbf{J}\times\mathbf{B}}{c} \qquad n_e m_e \ll n_i M_i \tag{2.91}$$

$$\frac{\mathbf{J}}{n_e e} \ll \mathbf{u} \approx \mathbf{v} \qquad \frac{\nabla p_e}{n_e e} \ll \mathbf{E} \approx -\frac{\mathbf{v}}{c}\times\mathbf{B} \tag{2.92}$$

in the case of a single component plasma whose ions have unit charge e.

The first two of these points are easily satisfied for most applications, and so they are the most convincing. The last two points are clearly related: if the pressure forces are

substantially different then the fluids acquire differing velocities, or if the velocities have different properties then the pressures will evolve differently and do different thermodynamic work on each fluid in the plasma. They also present the greatest difficulty, since the changes they bring to an MHD situation cannot be judged from within MHD, which although parametrically limited is a perfectly self consistent model. The procedure we will use here is to outline the basic properties of the single fluid dynamics, most of which are familiar, and then qualify the situation within the framework of drift dynamics, which is where the limitations of MHD are most important in the laboratory or in nature.

Under the above assumptions the steps to MHD from the plasma dynamics of several fluids are straightforward, whether there is one ion species or several. We add the density equations, incorporating the unit masses for each species to get a mass density equation,

$$\frac{\partial \rho}{\partial t} + \nabla \cdot \rho \mathbf{u} = 0 \tag{2.93}$$

where $\mathbf{u}$ is simply the velocity of the entire fluid. We add the equations of motion of all species, including the electrons in order to cancel the electric field

$$\rho \left(\frac{\partial}{\partial t} + \mathbf{u} \cdot \nabla \right) \mathbf{u} = -\nabla p + \frac{\mathbf{J} \times \mathbf{B}}{c} \tag{2.94}$$

This is called the MHD force equation. It is the same as the equation of motion under fluid plasma dynamics except that we neglect the electron inertia, and we write the total pressure as p, simply summing all the pressures including that of the electrons. Finally, we sum the pressure equations after the same fashion,

$$\left(\frac{\partial}{\partial t} + \mathbf{u} \cdot \nabla \right) p + \frac{5}{3} p \nabla \cdot \mathbf{u} = 0 \tag{2.95}$$

noting especially the neglect of the extra terms involving $\mathbf{J}$. This is the complete set for the plasma itself, and it is closed except for the presence of the $\mathbf{J} \times \mathbf{B}$ force.

The most important statement of the electrodynamics part of MHD is that the Lorentz force on each fluid should vanish up to negligible corrections, so that each fluid moves with the ExB velocity:

$$\mathbf{E} + \frac{\mathbf{u}}{c} \times \mathbf{B} = 0 \implies \mathbf{u} = c \frac{\mathbf{E} \times \mathbf{B}}{B^2} \tag{2.96}$$

which we derive by assuming that the electron inertia and ∇p_e are small compared to the magnetic and electric parts of the Lorentz force, respectively, and that $\mathbf{J} \ll n_e e \mathbf{u}$. This fixes $\mathbf{E}$ in terms of $\mathbf{u}$ and $\mathbf{B}$, which immediately gives the equation for the magnetic field:

$$\frac{\partial \mathbf{B}}{\partial t} = \nabla \times (\mathbf{u} \times \mathbf{B}) \tag{2.97}$$

This is called the MHD kinematic equation. The current is again given by

$$\mathbf{J} = \frac{c}{4\pi}\nabla\times\mathbf{B} \tag{2.98}$$

In terms of the density, temperature, and unit mass of each fluid, we have as equations of state

$$\rho = \sum_j n_j M_j \qquad p = \sum_j p_j \qquad p_j = n_j T_j \tag{2.99}$$

where j is the species label (including the electrons). The temperatures are allowed to differ, but only if their relaxation dynamics does not affect the rest of the system. The set of dependent variables reduces to $\{\rho, \mathbf{u}, p, \mathbf{B}\}$ whose equations form a closed system with the help of the constitutive relation for $\mathbf{J}$.

2.VII. MHD Waves — Alfvén Waves

There are three basic types of wave motion in MHD. The first is the sound waves familiar from the neutral fluid. The Lorentz force gives rise to two further types of waves, which act differently depending on whether they propagate along or across the magnetic field. These are the Alfvén waves. Together, sound waves and Alfvén waves determine the basic time scales of MHD.

The two forms of Alfvén waves involve quite different types of dynamics. To see this most clearly we can eliminate $\mathbf{J}$ in the MHD force equation, writing

$$\rho\left(\frac{\partial}{\partial t} + \mathbf{u}\cdot\nabla\right)\mathbf{u} = -\nabla\left(p + \frac{B^2}{8\pi}\right) + \frac{\mathbf{B}\cdot\nabla\mathbf{B}}{4\pi} \tag{2.100}$$

And we can expand the vector operations in the MHD kinematic equation, writing

$$\frac{\partial \mathbf{B}}{\partial t} = -\mathbf{u}\cdot\nabla\mathbf{B} + \mathbf{B}\cdot\nabla\mathbf{u} - \mathbf{B}\nabla\cdot\mathbf{u} \tag{2.101}$$

Plasma flow parallel to the magnetic field does not affect the kinematic equation at all, since $\mathbf{B}\cdot\nabla\mathbf{u}$ cancels the divergence in that case. This yields the sound waves. Motion perpendicular to the magnetic field is of the two types depending on whether it is compressional or not. A squeezing disturbance (both ∇ and $\mathbf{u}\perp\mathbf{B}$) affects the magnetic field strength ($\mathbf{B}\nabla\cdot\mathbf{u}$) and causes it to act as part of a total pressure (∇B^2). This gives rise to the compressional Alfvén waves. A shearing disturbance ($\mathbf{u}\perp\mathbf{B}$ but $\nabla\parallel\mathbf{B}$) does not affect the magnetic field strength, but bends the field lines in the direction of the flow ($\mathbf{B}\cdot\nabla\mathbf{u}$). The restoring force is provided by magnetic field line tension ($\mathbf{B}\cdot\nabla\mathbf{B}$), through which the magnetic field lines act as wires threading the plasma. This yields the shear

Alfvén waves which provide the most characteristic difference between MHD and fluid dynamics, the ability of a magnetised plasma to support transverse waves.

To do this quantitatively we take the same arrangement as before — a homogeneous plasma at rest in the presence of a magnetic field, and linearised disturbances for a single Fourier component. The equations for the disturbances are

$$\omega\widetilde{\rho} = \rho\mathbf{k}\cdot\mathbf{u} \tag{2.102}$$

$$\omega\rho\mathbf{u} = \mathbf{k}\left(\widetilde{p} + \frac{\mathbf{B}\cdot\widetilde{\mathbf{B}}}{4\pi}\right) - \frac{\mathbf{B}\cdot\mathbf{k}}{4\pi}\widetilde{\mathbf{B}} \tag{2.103}$$

$$\omega\widetilde{p} = \frac{5}{3}p\mathbf{k}\cdot\mathbf{u} \tag{2.104}$$

$$\omega\widetilde{\mathbf{B}} = -(\mathbf{B}\cdot\mathbf{k})\mathbf{u} + \mathbf{B}\mathbf{k}\cdot\mathbf{u} \tag{2.105}$$

Since the pressure dynamics is adiabatic the density equation is superfluous. For motion along the magnetic field ($\mathbf{u} \parallel \mathbf{B}$), there is no reaction by $\widetilde{\mathbf{B}}$. If the motion is shearing ($\mathbf{k} \perp \mathbf{u}$) then there is no reaction at all, and if it is compressional ($\mathbf{k} \parallel \mathbf{u}$) then sound waves result,

$$\omega^2 = k_\parallel^2 \frac{5}{3}\frac{p}{\rho} = k_\parallel^2 V_s^2 \qquad V_s^2 = \frac{5}{3}\frac{p}{\rho} \tag{2.106}$$

just like in a neutral fluid.

For motion across the field ($\mathbf{u} \perp \mathbf{B}$) we get the Alfvén waves. If the motion is compressional then we have longitudinal waves with

$$\mathbf{u} \perp \mathbf{B} \qquad \mathbf{k} \perp \mathbf{B} \qquad \mathbf{k} \parallel \mathbf{u} \qquad \widetilde{\mathbf{B}} \parallel \mathbf{B} \tag{2.107}$$

and the pressure and MHD kinematic equations may be combined as

$$\omega\left(\widetilde{p} + \frac{\mathbf{B}\cdot\widetilde{\mathbf{B}}}{4\pi}\right) = \left(\frac{5}{3}p + \frac{B^2}{4\pi}\right)\mathbf{k}\cdot\mathbf{u} \tag{2.108}$$

and the MHD force equation may be rewritten as

$$\omega\rho\mathbf{k}\cdot\mathbf{u} = k_\perp^2\left(\widetilde{p} + \frac{\mathbf{B}\cdot\widetilde{\mathbf{B}}}{4\pi}\right) \tag{2.109}$$

with $\mathbf{k}$ explicitly written as perpendicular to $\mathbf{B}$. This yields the compressional Alfvén waves with both plasma pressure and magnetic pressure contributing to the phase velocity,

$$\omega^2 = k_\perp^2\left(V_s^2 + v_A^2\right) \tag{2.110}$$

This is the low frequency, finite pressure limit of the compressional magnetosonic waves discussed above (cf. Eq. 2.66), and it tells us that the cutoff at $\omega = \omega_\pi$ limits MHD in the same way as it does the plasma dynamics of several fluids — ultimately this is a space scale limitation, as we require

$$\omega \ll \omega_{pi} \implies k_\perp \ll \frac{\omega_{pi}}{v_A} \tag{2.111}$$

for quasineutrality in compressional propagation perpendicular to $\mathbf{B}$.

If the motion across the field is shearing then we have transverse waves with

$$\mathbf{u} \perp \mathbf{B} \qquad \mathbf{k} \parallel \mathbf{B} \qquad \mathbf{k} \perp \mathbf{u} \qquad \widetilde{\mathbf{B}} \perp \mathbf{B} \tag{2.112}$$

Since the flow is divergence free the pressure does not react, and the existence of waves depends entirely on the finite $\mathbf{B}$. Since the magnetic pressure also does not react, we may rewrite the equations as

$$\omega \rho \mathbf{u} = -\frac{B k_\parallel}{4\pi} \widetilde{\mathbf{B}} \tag{2.113}$$

$$\omega \widetilde{\mathbf{B}} = -(B k_\parallel)\mathbf{u} \tag{2.114}$$

with $\mathbf{k}$ explicitly written as parallel to $\mathbf{B}$. This yields the shear Alfvén waves with propagation at the Alfvén velocity,

$$\omega^2 = k_\parallel^2 v_A^2 \tag{2.115}$$

Besides the differing qualitative character of compressional and shearing Alfvén dynamics, the high aspect ratio character of most magnetised plasmas (in nature or in the laboratory) leads to a significant difference in their time scales. The distance across the magnetic field is significantly less than that along the field lines, so the compressional waves are faster. For this reason they are often called "fast Alfvén waves" while the shear waves are called "slow Alfvén waves."

The other important difference between compressional and shear Alfvén waves is that the former go over into sound waves if $B \to 0$. It is interesting to note that the high frequency limit of these sound waves is also the ion plasma frequency, ω_{pi}, limiting ω for $k_\perp \lambda_D > 1$ (take $\Omega_i \to 0$ and $v_A \to c_s$ in Eq. 2.66). Whether the $B \to 0$ limits are reached is a function of the plasma beta, defined as the ratio of plasma to magnetic pressures,

$$\beta = \frac{8\pi p}{B^2} \sim \frac{V_s^2}{v_A^2} \tag{2.116}$$

also related to the ratio of the sound and Alfvén velocities (take $4\pi p_e$ instead, and β becomes β_e). Except for the kinematic regime of natural dynamo phenomena, this parameter is usually smaller than unity, and it is this fact which makes MHD Alfvén waves as important as they are.

For the low frequency drift motion of the rest of this work, the perpendicular dynamics takes place on scales rather smaller than those of the global system size. Aspect ratios in the range of 10^3 in the dynamics are common. Motion across the magnetic field with sound velocities or slower is too slow to effectively excite compressional motion, since $V_s \ll v_A$. On the other hand, the shear Alfvén motion can be excited since the aspect ratio can be comparable to the ratio between v_A and c_s. Expressed as frequencies, we have

$$k_\perp v_A \gg k_\parallel v_A \sim \omega \tag{2.117}$$

If the dynamical frequencies of interest are always much smaller than the minimum of $k_\perp v_A$ and ω_{pi}, then the motion across the field can be treated as dynamically incompressible, even if quasistatic compression (due to an inhomogeneous $\mathbf{B}$) can still enter the dynamics. This leads directly to the fluid drift picture to be introduced in Chapter 3. But before that we treat the energy and momentum conservation properties of the fluid electrodynamic and fluid plasma models, and then dissipation.

2.VIII. Energetics of the Ideal Fluid Dynamical Systems

In the fluid electrodynamic model, energy in total is conserved, but it can be exchanged between fluid and electromagnetic field energy, in addition to its exchange between thermal (random) and kinetic (directed) energy through work done by pressure. Each piece of the total can also be transported from place to place through its own energy flux. We have already seen this type of conservation equation for material and thermal energy densities, during the ideal fluid derivation (Eqs. 2.20 and 2.21). Electromagnetic field energy is carried at the speed of light, while thermal and kinetic energy is carried at the speed of the fluid. In fluid plasma dynamics, the energy content of the electric field becomes negligible along with the charge density, leaving magnetic energy alone, which is now carried at the Alfvén speed since Alfvén waves are the fastest things that model retains. The same is true of single fluid MHD. Otherwise, the form of energy conservation is the same for all three models. Momentum conservation, on the other hand, is progressively more trivial, especially for the electromagnetic field. In MHD the step between Eqs. (2.94) and (2.100) expresses the entire content of electromagnetic momentum conservation.

In electrodynamics the electromagnetic field energy density is given by

$$U_E = \frac{E^2 + B^2}{8\pi} \tag{2.118}$$

Its evolution according to the Maxwell equations (2.36,2.37) is given by

$$\frac{\partial U_E}{\partial t} = \frac{\mathbf{E}}{4\pi} \cdot \frac{\partial \mathbf{E}}{\partial t} + \frac{\mathbf{B}}{4\pi} \cdot \frac{\partial \mathbf{B}}{\partial t} \tag{2.119}$$

in which the gradient operations are manipulated into a total divergence,

$$\frac{\partial U_E}{\partial t} + \nabla \cdot \left(c \frac{\mathbf{E} \times \mathbf{B}}{4\pi} \right) = -\mathbf{E} \cdot \mathbf{J} \tag{2.120}$$

The field energy is transported by the Poynting energy flux, given by c^2 times the Poynting momentum, reflecting transport at the speed of light. The term on the right side gives the transfer to the fluid; it is called the Joule work. The kinetic energy density for each fluid of species j is

$$V_j = n_j M_j \frac{v_j^2}{2} \tag{2.121}$$

Its evolution follows by contracting each Eq. (2.39) with $\mathbf{v}_j$, yielding

$$\frac{\partial V_j}{\partial t} + \nabla \cdot (V_j \mathbf{v}_j) = n_j e_j \mathbf{v}_j \cdot \mathbf{E} - \mathbf{v}_j \cdot \nabla p_j \tag{2.122}$$

where we note here also that the magnetic force is not involved in the transfer between the fluid and the field. The thermal energy density for each fluid of species j is

$$U_j = \frac{3}{2} p_j \tag{2.123}$$

and its evolution follows from Eq. (2.40), to which we can add an arbitrary conductive heat flux $\mathbf{q}_j$

$$\frac{\partial U_j}{\partial t} + \nabla \cdot [(U_j + p_j)\mathbf{v}_j + \mathbf{q}_j] = \mathbf{v}_j \cdot \nabla p_j \tag{2.124}$$

Here, the total heat flux is built up from advective and conductive pieces and the transfer with kinetic energy is through the work done by the pressure, just as for a neutral fluid. In the fluid electrodynamics model the energy transfer between fluids and field is entirely through the electric Lorentz force, with the transfer for each fluid given by its contribution to the total current along $\mathbf{E}$. For the total system of fluids and field the conservation law for energy reads

$$\frac{\partial}{\partial t}(U_E + V + U) + \nabla \cdot \left[c \frac{\mathbf{E} \times \mathbf{B}}{4\pi} + \sum_j (V_j \mathbf{v}_j + [U_j + p_j]\mathbf{v}_j + \mathbf{q}_j) \right] = 0 \tag{2.125}$$

Momentum conservation is derived in similar fashion. The field momentum density is given by the Poynting flux, whose conservation law reads

$$\frac{\partial}{\partial t}\left(\frac{\mathbf{E}\times\mathbf{B}}{4\pi c}\right)+\nabla\cdot\left(U_E\mathbf{g}-\frac{\mathbf{EE}+\mathbf{BB}}{4\pi}\right)=-\left(\rho_{ch}\mathbf{E}+\frac{\mathbf{J}\times\mathbf{B}}{c}\right) \tag{2.126}$$

where $\mathbf{g}$ is the metric tensor and the quantity under the divergence is called the Maxwell stress tensor. All four Maxwell equations and the identity

$$\mathbf{E}\times(\nabla\times\mathbf{E})=\nabla\frac{E^2}{2}-\nabla\cdot(\mathbf{EE})-\mathbf{E}(\nabla\cdot\mathbf{E}) \tag{2.127}$$

for both $\mathbf{E}$ and $\mathbf{B}$ have been used. The exchange with the fluid over the Lorentz force is very clear. For the total system of fluids and field the conservation law for momentum reads

$$\begin{aligned}\frac{\partial}{\partial t}\left[\frac{\mathbf{E}\times\mathbf{B}}{4\pi c}+\sum_j(n_jM_j\mathbf{v}_j)\right]+\\ +\nabla\cdot\left[(p+U_E)\mathbf{g}-\frac{\mathbf{EE}+\mathbf{BB}}{4\pi}+\sum_j(n_jM_j\mathbf{v}_j\mathbf{v}_j)\right]=0\end{aligned} \tag{2.128}$$

Under quasineutrality, the neglect of the displacement current in the dynamics is equivalent to neglecting $\mathbf{E}$ compared to $\mathbf{B}$, so that $\mathbf{E}$ no longer has a role in the energy, except for the Poynting flux and the Joule work. Otherwise, the energy conservation dynamics is largely the same: the contribution by E^2 to U_E is simply dropped. Momentum conservation, however, is greatly simplified. In the case that $v_A \ll c$ we note that since

$$\frac{\mathbf{E}\times\mathbf{B}}{4\pi c}\sim n_iM_ic\frac{\mathbf{E}\times\mathbf{B}}{B^2}\frac{v_A^2}{c^2}\ll n_iM_ic\frac{\mathbf{E}\times\mathbf{B}}{B^2}\sim n_iM_i\mathbf{u} \tag{2.129}$$

the field momentum is rendered negligible. We then have a quasistatic equilibrium between the transfer and the transport of field momentum,

$$\nabla\cdot\left(\frac{B^2}{8\pi}\mathbf{g}-\frac{\mathbf{BB}}{4\pi}\right)=\mathbf{B}\times\frac{\nabla\times\mathbf{B}}{4\pi}=-\frac{\mathbf{J}\times\mathbf{B}}{c} \tag{2.130}$$

which is a simple restatement of Eq. (2.98). In either plasma dynamics or MHD, then, momentum conservation becomes relatively trivial, simply built in by Eq. (2.98). In terms of the energy transport, we compare the Poynting energy flux to the thermal transport,

$$c\frac{\mathbf{E}\times\mathbf{B}}{4\pi}\sim\frac{B^2}{4\pi}c\frac{\mathbf{E}\times\mathbf{B}}{B^2}\sim\frac{B^2}{4\pi}\mathbf{u}\sim\beta^{-1}p\mathbf{u} \tag{2.131}$$

assuming the fluid velocity is comparable to the ExB velocity. The Poynting flux is nominally the larger by a factor of β^{-1}. In the case of motion sufficiently slow that $\nabla \cdot \mathbf{u} \approx 0$, *i.e.*, divergence free perpendicular flows, however, the total force potential of longitudinal motion remains undisturbed, so that we have

$$\widetilde{p} + \frac{B\widetilde{B}}{4\pi} \approx 0 \tag{2.132}$$

and hence rough equality in the divergences, *i.e.*, the actual transport, between the thermal and Poynting energy fluxes. We will see in Chapter 14 that for fluid drift motion the role of the Poynting flux is simply to cancel one factor out of the total 5/2 in the thermal flux, leaving a total of 3/2.

The only real difference in the conservation properties between fluid electrodynamics and fluid plasma dynamics (or MHD), then, is that there are no space charge or light speed effects and hence no propagation of energy or momentum through high frequencies at the speed of light. As long as $v_A \ll c$ the important transfer is through the fluid motions, to which only the Poynting energy flux (momentum times c^2) contributes at a comparable level. Joule work remains as well, as the sole energy transfer mechanism between the fluids and the field.

2.IX. Dissipation — Corrections to the Ideal Plasma

The above model systems are all useful as a framework for understanding how ideal fluid dynamics and related systems for plasmas are derived and how their fundamental properties compare. For lower frequency motion however, we need to introduce dissipation, and the methods used to derive the ideal systems are not sufficient for that. Although simple models can be heuristically constructed, we will find that there are several important properties of the corrections to ideal dynamics that are not easily understood without a formal derivation which starts with collections of particles which are described by distribution functions in position/velocity phase space. A simple example is the fact that an electric field can cause a conductive heat flux, or that a temperature gradient can cause a current. A not so simple example is the existence of special dissipation-free momentum and thermal fluxes directed perpendicular both to the magnetic field and to the gradients of the quantities giving rise to them. Besides these, it is desirable to know how the fluid model is related to the underlying kinetic physics.

There are two main procedures by which fluid equations can be rigorously derived from the kinetic model. Each is most useful for a certain purpose. For actual dissipation such as friction and conduction, we start with a Maxwellian distribution function which

due to its maximal entropy is not changed by a statistical collision process. We then find corrections which are assumed to be small in an ordering parameter which gives the ratio of the time scales between the dynamics of interest and the relaxation time on which the collision process forces the distribution function back towards the Maxwellian. Afterwards, the parameter regime is found from the requirements that the corrections be small. This is called the Chapman-Enskog procedure, after its inventors who applied it to the viscosity of neutral fluids.

For the non-dissipative fluxes which arise from the corrections due a finite particle gyroradius in the presence of an inhomogeneity, the moment approach is most transparent. The details of the distribution function are not followed, but the lower order moments are calculated in a hierarchy which is then closed at some level. A moment of the distribution function is an integral of it times powers of the velocity coordinate over the velocity part of the phase space. The density is the zeroth moment, simply an average. The velocity is the first moment, and the pressure is the isotropic second moment. The hierarchy arises due to the presence of factors of the velocity coordinate in the kinetic equation, so that the equation for the n-th moment is determined at least partly by the $(n+1)$-th or higher moments. A closure approximation enters, by which one expresses the moments at some level and higher as the result which would obtain if the distribution function were Maxwellian. An example here is the ideal fluid, in which off diagonal second and all third moments are taken to vanish, leaving a closed set of equations for the density, velocity, and pressure (or temperature). For collisional processes the moment approach is equivalent to but more difficult to carry out than the Chapman-Enskog procedure. For gyroradius corrections, especially in nontrivial magnetic geometries, the Chapman-Enskog procedure is in turn more difficult.

2.X. The Chapman-Enskog Procedure for Dissipative Corrections

For a collisional process between electrons and ions we apply the Chapman-Enskog procedure to find the conductive heat flux and the resistive friction which we need to put into the fluid equations. We start with a collision process which is assumed to take place faster than any dynamical scale of interest — the usefulness of this principally for low frequency motion is clear. The time scale comparison applies to the rest frame of the particles, so we require both a fast collision frequency and a short mean free path:

$$\frac{\partial}{\partial t} \sim v_t \nabla_\parallel \ll \nu \implies \lambda_{mfp} \nabla_\parallel \ll 1 \qquad \lambda_{mfp} = \frac{v_t}{\nu} \tag{2.133}$$

where v_t is the particle thermal velocity, giving the mean free path λ_{mfp}. Here, we take the maximal ordering on the dissipation free part of the dynamics, implicitly assuming

all "ideal" terms in the fluid equations to be equally important. Since what we expect to obtain are parallel fluxes, a spatially one dimensional treatment is sufficient to outline the method. For most applications the perpendicular fluxes arising from collisional dissipation are so limited by the gyro motion as to be negligibly small.

This is an ordering procedure in the small parameter ν/ω. An additional ingredient to the ordering hierarchy is the application of consistency conditions at each level of the expansion. At each level the solution is not a single distribution function but a class of them whose parameters are constrained by the consistency conditions — application of operators which "annihilate" the largest term, the collision operator. An example is simple averaging over velocity space, since the collision process conserves particles.

The form of the kinetic equation is

$$\mathcal{L}\left[f^{(n-1)}\right] = \mathcal{C}\left[f^{(n)}\right] \tag{2.134}$$

where $f = f(\mathbf{x}, \mathbf{w})$ is a distribution function of the six phase space coordinates $\{\mathbf{x}, \mathbf{w}\}$ and time, (n) is the current order of the expansion, $\mathcal{L}$ is the operator containing all terms except $\mathcal{C}$, and $\mathcal{C}$ is the collision operator which is assumed to conserve particles and energy, and at most transfer momentum between the particle species.

The logic of the procedure is the establishment of *a priori* statements about f at each order in the expansion, which are then further qualified by the consistency conditions. This is done by placing the f at the current order into $\mathcal{L}$ and the f at the next order into $\mathcal{C}$ and then applying operations whose action on $\mathcal{C}$ vanishes for any f; this further constrains what the f at the current order can be. At the end of the calculation, all outstanding assumptions are checked *a posteriori*.

The steps up to second order take place according to the following sequence.

1. To zeroth order $\mathcal{C}[f]$ must vanish, This tells us that the form of $f^{(0)}$ to zeroth order is that of a Maxwellian in the particle velocity $\mathbf{w}$, with parameters n_e, $\mathbf{v}$, and T_e. At zeroth order there is no current since for a relative friction $\mathcal{C}$ vanishes only if $\mathbf{v} - \mathbf{u} = 0$, where as before $\mathbf{v}$ and $\mathbf{u}$ are the velocities of the electron and ion fluids and hence the mean velocities of their distributions. The existence of a current at zeroth order would imply interesting dynamics on the scale of ν, which is excluded. With $\mathbf{v} = \mathbf{u}$, we can do the calculation in the local rest frame of the ion fluid.

2. Write the equation at first order, inserting $f^{(0)}$ into $\mathcal{L}[f]$ and the still unknown $f^{(1)}$ into $\mathcal{C}[f]$.

3. With momentum conservation already satisfied, the consistency conditions which constrain n_e and T_e are conservation of particles and energy. Through application of the annihilation operators represented by integrating $\mathcal{C}[f]$ times 1 and $m_e w^2/2$, respectively, we find the equations for n_e and T_e at order zero.

4. Solve the equation for $f^{(1)}$.

5. Steps 2) and 3) at first order give the dissipative fluxes represented by the current and conduction and hence the equations for n_e and T_e at order one. At this point the procedure stops if we are satisfied with the equations at first order.

To illustrate this procedure it is sufficient to specify a particle and energy conserving collision operator describing frictional drag of the electrons against the ions. To lowest order in $\mu_e = m_e/M_i$, the corresponding operator is the simple Lorentz one describing elastic pitch angle scattering. With $\mu_e \ll 1$ the collision process is one of electrons scattering against a fixed ion background. Momentum is transferred conservatively from the electrons to the ions, tending to relax the relative drift towards zero. With the ion temperature satisfying $m_e T_i \ll M_i T_e$ the velocities of the ions can be neglected. One can show that the energy is largely conserved in the electrons by considering a head-on collision between a fixed ion and an electron moving with velocity v_1. With the change in the electron momentum given by $2m_e v_1$ the ion acquires velocity $u_1 = 2(m_e/M_i)v_1$. The corresponding kinetic energy is $M_i u_1^2/2 = 2m_e v_1^2 \mu_e$, that is, one order down in μ_e from the electron energy. To this order we can neglect the energy transfer (which however is necessary if we want to consider collisional relaxation of a temperature difference). The collision process is described as pitch angle scattering because the degree of freedom which changes for the electron is the angle between its velocity vector and the magnetic field. For a distribution of electrons this represents a diffusion in velocity space, which for $\nu \ll \Omega_e$ is described by

$$\mathcal{C}[f_e] = \frac{\nu_0 v_t^3}{w^3} \frac{\partial}{\partial \zeta}(1-\zeta^2)\frac{\partial f_e}{\partial \zeta} \tag{2.135}$$

where

$$\nu_0 = \frac{3}{8}\sqrt{\pi}\nu_e \tag{2.136}$$

is the scattering rate for thermal electrons and $\zeta = w_\parallel/w$ is the pitch angle. The w^{-3} dependence arises from the inverse square nature of the Coulomb force. Since we are taking $\nu \ll \Omega_e$, the distribution function has dependence on two degrees of freedom in velocity space; we denote these as the total and parallel velocities, w and $w_\parallel$. Since only

$w_\parallel$ is directed, we can illustrate the procedure by doing a one dimensional calculation considering only parallel dynamics.

To zeroth order we have

$$\mathcal{C}[f_e^{(0)}] = 0 \tag{2.137}$$

and $f_e^{(0)}$ is a Maxwellian with zero drift relative to the ions

$$f_e^{(0)} = \left(\frac{n_e}{\pi^{3/2} v_t^3}\right) \exp\left[-w^2/v_t^2\right] \tag{2.138}$$

where $v_t^2 = 2T_e/m_e$ is specifically the electron thermal velocity

The first order equation is

$$\mathcal{C}[f_e^{(1)}] = \left(\frac{\partial}{\partial t} + w_\parallel \nabla_\parallel - \frac{e}{m_e} E_\parallel \frac{\partial}{\partial w_\parallel}\right) f_e^{(0)} \equiv \mathcal{L}[f_e^{(0)}] \tag{2.139}$$

a drift kinetic equation describing dynamics parallel to the magnetic field. The operator $\mathcal{L}$ is found by considering moving particles forced upon by the electric field, in such a way that phase space volume is conserved. The characteristics of $\mathcal{L}$ are simply the particle trajectories.

The consistency conditions are the averages over particle number and kinetic energy, which yield the density and thermal energy since at lowest order there is no velocity (we assume that $u_\parallel \ll v_t$),

$$\int d^3w\, \mathcal{C}[f] = 0, \qquad \int d^3w\, \frac{m_e w^2}{2} \mathcal{C}[f] = 0 \tag{2.140}$$

These conditions are satisfied by arbitrary f, which is why we can apply them at each order. At zeroth order they provide constraints on n_e and T_e,

$$\frac{\partial n_e}{\partial t} = 0 \qquad \frac{3}{2} n_e \frac{\partial T_e}{\partial t} = 0 \tag{2.141}$$

which simply say that n_e and T_e do not change on the collision time scale.

We now expand the equation to first order by inserting $f^{(0)}$ into $\mathcal{L}$ under the consistency constraints on n_e and T_e,

$$\mathcal{C}[f_e^{(1)}] = w_\parallel \left[\frac{\nabla_\parallel n_e}{n_e} + \left(\frac{w^2}{v_t^2} - \frac{3}{2}\right) \frac{\nabla_\parallel T_e}{T_e} + \frac{eE_\parallel}{T_e}\right] f_e^{(0)} \tag{2.142}$$

The solution for f at first order is trivial, since we know the eigenfunctions of the Lorentz operator are the Legendre polynomials, and the right side depends on ζ only through

$$w_\parallel = w\zeta = wP_1(\zeta) \tag{2.143}$$

Since the Legendre polynomials form an orthogonal basis for real functions on $[-1,1]$, only the first eigenfunction has a nonzero coefficient. This means that

$$f_e^{(1)} = -\frac{1}{2\nu_0}\frac{w^3}{v_t^3}w_\parallel\left[\frac{\nabla_\parallel n_e}{n_e} + \left(\frac{w^2}{v_t^2} - \frac{3}{2}\right)\frac{\nabla_\parallel T_e}{T_e} + \frac{eE_\parallel}{T_e}\right]f_e^{(0)} \tag{2.144}$$

The formal step of inserting $f_e^{(1)}$ into $\mathcal{L}$ and applying the consistency constraints is simply a matter of finding the current and heat flux resulting from this $f_e^{(1)}$. These integrals are given by

$$J_\parallel = -\int d^3w\, ew_\parallel f_e^{(1)} \qquad q_{e\parallel} = \int d^3w\, \frac{mw^2}{2}w_\parallel f_e^{(1)} + \frac{5}{2}T_e\frac{J_\parallel}{e} \tag{2.145}$$

subtracting off the advective part and assuming that $u_\parallel \ll v_t$. We find

$$J_\parallel = n_e e\left(u_\parallel - v_\parallel\right) = \eta^{-1}n_e e\frac{V_e^2}{\nu_e}\left[\frac{\nabla_\parallel p_e}{p_e} - \frac{eE_\parallel}{T_e} + \alpha\frac{\nabla_\parallel T_e}{T_e}\right] \tag{2.146}$$

for the current and

$$q_{e\parallel} = -\kappa n_e T_e\frac{V_e^2}{\nu_e}\frac{\nabla_\parallel T_e}{T_e} - \alpha\frac{T_e}{e}J_\parallel \tag{2.147}$$

for the heat flux.

Placing these fluxes into the fluid equations for n_e and T_e, and transforming back to the laboratory frame, we find

$$\frac{\partial n_e}{\partial t} + \nabla_\parallel n_e v_\parallel = 0 \tag{2.148}$$

$$\frac{3}{2}n_e\left(\frac{\partial}{\partial t} + v_\parallel\nabla_\parallel\right)T_e + n_e T_e\nabla_\parallel v_\parallel = -\nabla_\parallel q_{e\parallel} \tag{2.149}$$

$$-n_e eE_\parallel = n_e\frac{e}{c}\frac{\partial A_\parallel}{\partial t} + n_e e\nabla_\parallel\phi = \nabla_\parallel p_e + \alpha n_e\nabla_\parallel T_e - n_e e\eta_\parallel J_\parallel \tag{2.150}$$

where $A_\parallel$ and $J_\parallel$ are related by Ampere's law and $v_\parallel$ is given in terms of $u_\parallel$ and $J_\parallel$ as

$$-\nabla^2 A_\parallel = \frac{4\pi}{c}J_\parallel \qquad v_\parallel = u_\parallel - \frac{J_\parallel}{n_e e} \tag{2.151}$$

and $\eta_\parallel$ is the resistivity given by

$$\eta_\parallel = \eta\frac{m_e\nu_e}{n_e e^2} \tag{2.152}$$

These relations are general, with constant coefficients η, κ, and α given by the specific model. They are also dependent on the charge state of the ions. For this simple Lorentz model we have

$$\eta = \frac{3\pi}{32} \qquad \kappa = \frac{128}{3\pi} = \frac{4}{\eta} \qquad \alpha = \frac{3}{2} \tag{2.153}$$

for charge state $Z = +1$. For the more detailed, and standard, Braginskii model we have

$$\eta = 0.51 \qquad \kappa = 3.2 \qquad \alpha = 0.71 \tag{2.154}$$

also for charge state $Z = +1$, and we note that the definition of the thermal collision frequency

$$\nu_e = \frac{4\sqrt{2\pi} n_e \lambda e^4}{3 m_e^{1/2} T_e^{3/2}} \tag{2.155}$$

comes from that model. For different charge states the numerical constants change but the behaviour does not.

It is interesting to note the presence of the cross terms represented by α. This is called the thermoelectric effect, whereby a temperature gradient causes a current, and the reverse situation of a conductive heat flux caused by a current is guaranteed by Onsager symmetry. It is the result of the collision frequency's dependence on the particles' relative velocity, a feature of the Coulomb interaction. If the above calculation is repeated without the factor of $(v_t/w)^3$ in Eq. (2.135), the result is $\alpha = 0$. The physical origin of this effect is that particles imparting momentum to an ion at a given point originate from another point generally one mean free path away, and the mean free path is longer for faster particles. In the presence of a temperature gradient the faster particles therefore come from places where the temperature difference is greater, and hence they add more to the total impulse than would be the case if the distribution had the same Maxwellian everywhere. Faster particles are in a sense overcounted, then, when adding up the impulses. Had we simply constructed the resistive and conductive dissipation terms from the usual simple considerations of a frictional drag and a finite but small mean free path in a temperature gradient, we would have missed these cross terms. The extra term proportional to $\alpha \nabla_\parallel T_e$ in Eqs. (2.146) and (2.150) is also called the thermal force.

The above analysis is just an illustration of how this procedure is used to find the dissipative fluxes. A more realistic effort takes into account a finite ratio between ν_e and Ω_e, and also includes collisions between like particles, but this requires a level of detail beyond the scope of this outline; the interested reader can consult the references under Further Reading. The version presented here follows Hassam (1980), who was the one to point out that the electron inertia term is second order in ω/ν_e; that is, an arbitrary $v_\parallel - u_\parallel$ cannot appear to lowest order. Furthermore, several other important effects enter at second order along with the electron inertia. The standard among detailed versions is the one by Braginskii (1965), whose definition of ν_e is standard.

In the more realistic applications, one must face the fact that ω/ν_e is almost never small enough to make these collisional models rigorously valid. Nevertheless, they form a

useful starting point in understanding the physics of the dissipative fluxes. Extensions to the collisional fluid model which are designed to treat the more important kinetic effects will be discussed in Chapters 12 and 13.

2.XI. The Moment Approach — Diamagnetic Fluxes

The moment approach has the same basis as the Chapman-Enskog procedure, that of a distribution function in phase space. But instead of direct manipulation of f, a hierarchy of moments are built up. The quantities conserved in ideal fluid dynamics form the starting point,

$$n = \int d^3w\, f \tag{2.156}$$

$$nM\mathbf{v} = \int d^3w\, M\mathbf{w}f \tag{2.157}$$

$$\frac{3}{2}nT + nM\frac{v^2}{2} = \int d^3w\, M\frac{w^2}{2}f \tag{2.158}$$

We find the equations these quantities satisfy by performing the same integrations on the kinetic equation, since they commute with $\partial/\partial t$. In doing this, however, we find that the advection term in the kinetic equation, $\mathbf{w}\cdot\nabla f$, introduces in each equation the moments of correspondingly higher order; these are the fluxes for the conserved quantities,

$$n\mathbf{v} = \int d^3w\, \mathbf{w}f \tag{2.159}$$

$$\mathbf{P} + M\mathbf{v}\mathbf{v} = \int d^3w\, M\mathbf{w}\mathbf{w}f \tag{2.160}$$

$$\mathbf{q} + \left(\frac{3}{2}nT + p + nM\frac{v^2}{2}\right)\mathbf{v} = \int d^3w\, M\frac{w^2}{2}\mathbf{w}f \tag{2.161}$$

And then, writing the equations for these introduces quantities of still higher degree in $\mathbf{w}$ in the integrand. Here, a closure scheme is implemented, according to which one simply declares that moments at a certain level are functions of those already determined. In the simplest models, the pressure is assumed to be isotropic and the fourth moment is assumed to result from a Maxwellian. These last two statements imply the following relations:

$$p = \frac{1}{3}\int d^3w'\, Mw'^2 f \qquad \mathbf{\Pi} = \int d^3w'\, M\left(\mathbf{w}'\mathbf{w}' - \frac{1}{3}w'^2\mathbf{g}\right)f = \mathbf{P} - p\mathbf{g} \tag{2.162}$$

where

$$\mathbf{w}' = \mathbf{w} - \mathbf{v} \tag{2.163}$$

and

$$R_{\|} = \int d^3w' \, M \frac{w'^2}{2} w_{\|}'^2 f = \frac{5}{2} \frac{pT}{M} \tag{2.164}$$

For an ideal fluid, these moments are simply what results from using a Maxwellian for f, that is, $p = nT$ and $\mathbf{\Pi} = \mathbf{q} = 0$. The corrections to this situation then give the dissipative fluxes.

The term dissipative flux is often used for any correction that arises from the (small) departure of f from the Maxwellian. However, in a magnetised plasma we find a further class of corrections which do not involve dissipation *per se* (that is, a process which increases entropy). These are the diamagnetic fluxes, and they arise from the finite gyroradius of the particles in the presence of inhomogeneities in the lower order moments. From the pressure gradient we have an corresponding velocity, called the diamagnetic particle flux, or flow, which due to the opposite reaction of electrons and ions by this process to a pressure gradient gives rise to a diamagnetic current. From the temperature gradient we get a diamagnetic heat flux. And from the velocity gradient we get a diamagnetic momentum flux, historically called gyroviscosity because it has the form of a viscosity tensor. For dynamics much slower than the gyrofrequencies, $\omega \ll \Omega$ for each species, we can form a quasistatic balance between the spatial gradients which provide force terms in the equations, and the Lorentz force which provides a reaction. To lowest order in ω/Ω, and ultimately also the ratio between the gyroradius and the spatial scale of the gradient, we can use this balance to solve for the diamagnetic flux corresponding to a particular gradient.

The simplest example is the diamagnetic flow, which results in the same way the $\mathbf{E}\times\mathbf{B}$ velocity does in MHD: setting the sum of the relevant forces to zero. In a several fluids setting, we do not take the MHD approximation that $ne\mathbf{E} \gg \nabla p$ for each species. Instead, we set $\mathbf{E} = 0$ to isolate the diamagnetic part, and then set the magnetic Lorentz force equal to the pressure force. For example, for electrons we have

$$n_e e \frac{\mathbf{v}\times\mathbf{B}}{c} + \nabla p_e = 0 \tag{2.165}$$

which we solve for the diamagnetic flow,

$$\mathbf{v}_* = -\frac{1}{n_e e} \frac{c}{B^2} \mathbf{B}\times\nabla p_e \tag{2.166}$$

The flow for the ions, $\mathbf{u}_*$, has similar form but opposite sign, and so we also have a diamagnetic current due to the gradient of the total pressure,

$$\mathbf{J}_* = \frac{c}{B^2} \mathbf{B}\times\nabla p \tag{2.167}$$

valid for an arbitrary number of species. We note that this is the same as the perpendicular part of the current in an MHD equilibrium, and that this type of force balance consideration is what leads us to low frequency motion, which we will cover in Chapter 3. We also note that the condition that this flow is small compared to the thermal velocity is a condition on the gyroradius:

$$\frac{\mathbf{v}_*}{V_e} = -\mu_e^{1/2}\frac{cT_e}{eB^2}\mathbf{B}\times\frac{\nabla p_e}{p_e} \sim \rho_e \nabla \log p_e \tag{2.168}$$

The gyroradii must therefore be small compared to the perpendicular scale length, which means simply that these fluxes are only relevant to a magnetised plasma, and then to low frequency motion (slower than the gyrofrequencies). This limitation applies to each of the diamagnetic fluxes, not only the flow.

As another example we can take the heat flux which arises from the temperature gradient, which we illustrate for ions of charge state Ze. We isolate the diamagnetic part by setting $\mathbf{E} = 0$ in the kinetic equation, and also assume that $M_i |\mathbf{u}_*|^2 \ll T_i$. Forming the third moment of the kinetic equation, we have

$$\nabla \cdot \int d^3w\, M_i \frac{w^2}{2}\mathbf{w}\mathbf{w}f = \frac{Ze}{M_i c}\int d^3w\, M_i \frac{w^2}{2}\mathbf{w}\,(\mathbf{w}\times\mathbf{B})\cdot\frac{\partial f}{\partial \mathbf{w}} \tag{2.169}$$

We solve the right side via integration by parts, and following from $\rho_i \nabla \ll 1$ we set the Maxwellian into the left side. The fourth moment is evaluated as in Eq. (2.164) since for a Maxwellian it is an isotropic, diagonal tensor. We now have

$$\nabla\left(\frac{5}{2}\frac{p_i T_i}{M_i}\right) = \frac{Ze}{M_i c}\left(\frac{5}{2}p_i\mathbf{u}_* + \mathbf{q}_{i\wedge}\right)\times\mathbf{B} \tag{2.170}$$

By operation with $\mathbf{B}\times$ from the left, we find

$$\frac{5}{2}p_i\mathbf{u}_* + \mathbf{q}_{i\wedge} = \frac{c}{ZeB^2}\mathbf{B}\times\nabla\left(\frac{5}{2}p_i T_i\right) \tag{2.171}$$

and hence, using the result for $\mathbf{u}_*$, we have

$$\mathbf{q}_{i\wedge} = \frac{5}{2}\frac{p_i}{Ze}\frac{c}{B^2}\mathbf{B}\times\nabla T_i \tag{2.172}$$

A similar result holds for the velocity field, but it is much more complicated. Following the method used to find $\mathbf{q}_{i\wedge}$ we set up the equation for the off-diagonal second moment and again balance the gradients involving the Maxwellian, $\nabla\mathbf{u}$ as a tensor, with the magnetic Lorentz force. After a symmetrising operation, this yields

$$p_i\mathbf{W} = \frac{Ze}{M_i c}\left(\mathbf{\Pi}_*\times\mathbf{B} - \mathbf{B}\times\mathbf{\Pi}_*\right) \tag{2.173}$$

where $\mathbf{\Pi}_*$ is the diamagnetic momentum flux, and $\mathbf{W}$ is the strain tensor given by

$$\mathbf{W} = \nabla\mathbf{u} + (\nabla\mathbf{u})^T - \frac{2}{3}(\nabla\cdot\mathbf{u})\mathbf{g} \tag{2.174}$$

with the superscript denoting the transpose. Solution of this equation gives $\mathbf{\Pi}_*$, which is usually displayed in terms of its components perpendicular and parallel to the magnetic field,

$$\mathbf{\Pi}_{*\perp\perp} = \frac{n_i M_i}{4}\frac{cT_i}{ZeB^2}(\mathbf{B}\times\mathbf{W}_{\perp\perp} - \mathbf{W}_{\perp\perp}\times\mathbf{B}) \tag{2.175}$$

$$\mathbf{\Pi}_{*\perp\parallel} = n_i M_i \frac{cT_i}{ZeB^2}\mathbf{B}\times\mathbf{W}_{\perp\parallel} \tag{2.176}$$

noting that due to the cross operations the parallel-parallel component is zero.

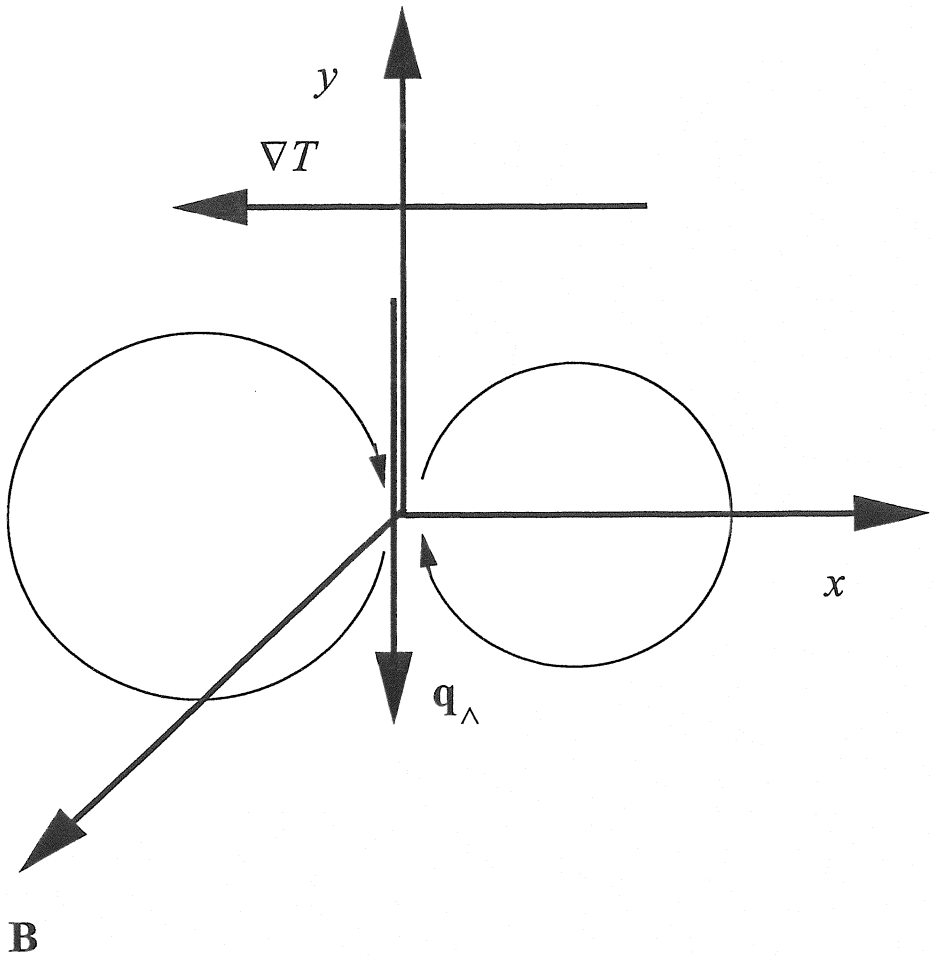

Figure 2.2. The diamagnetic heat flux. Gyro motion occurs in the xy-plane, perpendicular to the magnetic field, $\mathbf{B}$. For ions it is clockwise. A temperature gradient towards $-\nabla x$ results in a net heat flux $\mathbf{q}_{i\wedge}$ towards $-\nabla y$, generally towards $\mathbf{B}\times\nabla T/Ze$, due to the fact that the up-gradient particles are moving faster.

The moment approach is a viable alternative to the Chapman-Enskog procedure for calculating the dissipative transport equations for a plasma, and it can be shown that an expansion in a finite set of moments is equivalent to an expansion in a finite set of orthogonal polynomials in the Chapman-Enskog procedure (required for realistic collision operators). In both cases, the complications arise from the w^{-3} dependence of the Coulomb interaction, which couples all moments. More details can be found in the references under Further Reading.

The particle view of these diamagnetic fluxes is noteworthy. If we take a simple situation in which there is a temperature gradient, but the plasma is otherwise homogeneous and at rest, we isolate $\mathbf{q}_{i\wedge}$, illustrated in Fig. 2.2. Drawing the diagram such that the magnetic field is toward the observer and the gradient is toward the observer's left, the ions follow gyro orbits in a clockwise sense, and the electrons orbit counterclockwise. Examining all the particles which are incident on a given reference point in space, the particles arriving from the left have a higher temperature than those arriving from the right. The faster ions are seen by the observer to move downward, and the faster electrons are seen to move upward. This gives rise to both a net flow and a net conductive flux, since due to the dependence of the particle gyroradius on velocity the faster of the particles on both sides have their gyrocenters farther away. So if the observer places a probe at the reference point, a net ion flow, a net current, and a net ion conductive heat flux will all be measured in the downward direction, and a net electron flow and conductive heat flux will be measured in the upward direction. However, no gyrocenters are in motion. The reconciliation with the measurement of a flow but no gyrocenters in motion, and therefore no actual transport of conserved quantities follows from a subtle result called the diamagnetic cancellation. This is the fact that all diamagnetic flux terms conspire to cancel each other out of the fluid equations to lowest order in the gyroradius, up to terms arising from any inhomogeneity in the magnetic field. For example, we have

$$\frac{3}{2}n_e\mathbf{v}_*\cdot\nabla T_e + p_e\nabla\cdot\mathbf{v}_* + \nabla\cdot\mathbf{q}_{e\wedge} = -\frac{1}{n_e e}\frac{c}{B^2}\mathbf{B}\times\nabla\left(\frac{5}{2}p_eT_e\right) \tag{2.177}$$

in the electron temperature equation which vanishes for homogeneous $\mathbf{B}$, so that $\mathbf{v}_*$ does not directly advect T_e. By the same result for ions, $\mathbf{u}_*$ does not directly advect T_i. Similar results concerning $\mathbf{v}_*$ and $\boldsymbol{\Pi}_*$ prevent $\mathbf{v}_*$ and $\mathbf{u}_*$ from directly advecting n_e and $\mathbf{u}$, respectively. Due to these cancellations, diamagnetic fluxes affect the fluid equations only through inhomogeneity in $\mathbf{B}$. But such a variation in $\mathbf{B}$ leads precisely to motion of the gyrocenters, through the finite drifts one calculates from single particle motion in an inhomogeneous magnetic field.

The consideration of fluid motion in terms of net drifts leads naturally to the main subject of this work, namely, fluid drift dynamics of a magnetised plasma. The main assumptions needed to contemplate the diamagnetic fluxes are the same as those needed to move from the fluid plasma model, and its MHD subset, to the fluid drift model: the gyroradius should be small compared to the perpendicular scale, and the frequencies of interest should be small compared to the gyrofrequency. We will further require the motion to be free of dynamical compression, and so the compressional Alfvén/magnetosonic waves form the parameter boundary. However, the main MHD assumption that the electric field should be larger than the pressure force is usually violated in this parameter regime, so our starting point will be the low frequency limit of the fluid plasma model. Under these restrictions the perpendicular dynamics is in force balance, which is the consideration used to derive fluid drift dynamics. That is the subject of the next chapter.

Further Reading

The derivation of Maxwell's equations from the Principle of Least Action is standard and appears in many texts, including *The Classical Theory of Fields*, by L. D. Landau and E. M. Lifshitz (Pergamon, 1972). For ideal fluids see *Fluid Dynamics*, also by Landau and Lifshitz (Pergamon, 1972).

High frequency wave properties of fluid electrodynamics is covered in many introductory texts of plasma physics, including *Basic Principles of Plasma Physics*, by S. Ichimaru (Benjamin, London,1973), *Principles of Plasma Physics*, by N. A. Krall and A. W. Trivelpiece (McGraw Hill, 1973), *Plasma Physics*, by K. Nishikawa and M. Wakatani (new edition: Springer, 2000), and *Theoretische Plasmaphysik*, by K.-H. Spatschek (Teubner, Stuttgart, 1990).

Ideal magnetohydrodynamics also has an extensive literature. A good introductory text is *Ideal Magnetohydrodynamics*, by J. P. Freidberg (Plenum Press, New York, 1987). A good text for further study of the basic phenomena (especially reconnection and MHD turbulence) is *Nonlinear Magnetohydrodynamics*, by D. Biskamp (Cambridge, 1993). The standard text for astrophysical MHD applications is *Cosmical Magnetic Fields*, by E. N. Parker (Clarendon Press, Oxford, 1979). A tokamak-oriented text which includes the basic MHD problems as well as the more complicated phenomena one encounters is *Theory of Tokamak Plasmas*, by R. B. White (North Holland, Amsterdam, 1989).

The Chapman-Enskog and moment hierarchy procedures fall under the domain of collisional transport theory, reviewed by R. Balescu, *Transport Processes in Plasmas*, 2 Vols., (North Holland, Amsterdam, 1988). See also *The Mathematical Theory of Non-Uniform Gases* by S. Chapman and T. G. Cowling (Cambridge, 1952).

The original references for the Chapman-Enskog procedure are S. Chapman, "On the law of distribution of molecular velocities, and on the theory of viscosity and thermal conduction, in a nonuniform, simple, monatomic gas," *Phil. Trans. Roy. Soc. London* A216 (1916) 279, and D. Enskog, *Kinetische Theorie der Vorgänge in mässig verdünnten Gasen* (Almqvist and Wiskell, Uppsala, 1917).

For a plasma of several fluids, one of which is electrons, the standard reference is S. I. Braginskii, in *Reviews of Plasma Physics*, M. A. Leontovich, ed. (Consultants Bureau, New York, 1965), Vol. 1, p. 205. The more introductory treatment presented in Section X follows A. B. Hassam, "Higher-order Chapman-Enskog theory for electrons," *Phys. Fluids* 23 (1980) 38, who pointed out that the electron inertia is formally an order down from resistive friction and therefore should not appear in the lowest order collisional regime.

For the moment approach the main reference is H. Grad, in *Communications of Pure and Applied Mathematics* 2 (1949) 311. The most realistic collision operator is the one of Landau, reviewed by both Braginskii and Balescu, above. Common simplified models are the pitch angle scattering model of Lorentz, discussed by Balescu, or the damping/relaxation BGK model generalised by J. Greene, "Improved Bhatnagar-Gross-Krook model of electron-ion collisions," *Phys. Fluids* 16 (1973), 2022.

The diamagnetic cancellation for temperature and heat flux was shown by S.-T. Tsai, F. W. Perkins, and T. H. Stix, in *Phys. Fluids* 13 (1970) 2108, and the one for velocity and gyroviscosity was shown by F. L. Hinton and C. W. Horton, Jr., in *Phys. Fluids* 14 (1971) 116.

3. The Drift Approximation and Fluid Drift Equations

B. Scott

Jul 1999

3.I. Introduction

We have seen in the previous chapter that fluid plasma dynamics admits both compressional and shear Alfvén oscillations, through its MHD subset. In situations where the disturbances have very disparate length scales parallel and perpendicular to the background magnetic field, the frequencies of the corresponding Alfvén oscillations are also disparate, as both types of oscillation have simple dispersion relations describing propagation at the Alfvén speed. If the dynamics of a long, thin flux tube are to occur at low frequencies commensurate with the flux tube's shear Alfvén time, it is reasonable to expect that the compressional waves are not appreciably excited, and the motion remains dynamically incompressible. In such a situation, the perpendicular forces should remain in quasistatic balance, with finite time derivatives but without compressional waves. Fluid plasma dynamics under this restriction becomes fluid drift dynamics, with flows and thermal fluxes given in terms of associated stream functions which are scalar quantities among the dependent variables. This chapter explains the qualitative nature of the drift approximation and the conditions under which it is expected to be valid. Perpendicular force balance is discussed with respect to the total current as well as the flows of each fluid species. The finite ion inertia gives rise to the correction which mediates the quasistatic evolution of the force balance — the polarisation drift of the ions, which represents the polarisation current. Following this, a detailed derivation of the fluid drift equations for nonlinear disturbances on an inhomogeneous background is presented. Following that, the free energy theorem governing these equations is constructed, with discussion on the role of the background gradients as sources. Derivation of the fluid drift equations for more generally global dynamics is deferred to Chapter 14, which treats the particle and energy transport due to the fluid drift turbulence.

3.II. What the Drift Approximation Is

We expect dynamical disturbances on a magnetised plasma background to consist of strongly anisotropic flux tubes, such that the scale of motion perpendicular to the magnetic field, $\mathbf{B}$, is several orders of magnitude smaller than the parallel scale, so that in terms of wavenumbers we have

$$k_\perp \gg k_\parallel \tag{3.1}$$

We further expect shear Alfvén dynamics to be important, so that the relevant frequencies are in the range of

$$\omega \sim k_\parallel v_A \tag{3.2}$$

These two relations therefore imply

$$\omega \ll k_\perp v_A \tag{3.3}$$

If we further specify that $\omega \ll \Omega_i$ for all $k_\perp$ of interest, then it follows that the time scales of motion are much slower than those of compressional waves, and so these are not appreciably excited. The drift approximation consists of a formalism which removes these fast time scales from the governing equations, leaving only the dynamics of interest.

The drift approximation is usually associated with two other inequalities in addition to (3.1). The plasma should be magnetised, which means that the spatial scale associated with the gradient, $L_\perp$, be large compared to the drift scale, ρ_s,

$$\delta \equiv \frac{\rho_s}{L_\perp} \ll 1 \tag{3.4}$$

so that it is possible to have dynamics on scales comparable to ρ_s which is local in the sense that the background can be taken as a set of constant parameters. The dynamical plasma beta should also be low,

$$\beta_e \equiv \frac{4\pi p_e}{B^2} = \frac{c_s^2}{v_A^2} \ll 1 \tag{3.5}$$

so that motion which strongly perturbs the gas pressure remains incompressible due to the much stronger magnetic pressure. We will see how these enter below. Both δ and β_e are available as small parameters in a formal expansion.

These inequalities give rise to a quasistatically evolving force balance across magnetic field lines; quasistatic, since although not static it evolves without dynamical oscillations (compressional Alfvén or lower hybrid waves) involved in its restoration. Rather, the inertia gives rise to the small correction which continually acts to enforce the balance to

lowest order in the small parameter δ. The characteristics of that force balance are that the perpendicular and parallel dynamics largely separate, such that the perpendicular electric field is electrostatic and any disturbances in the magnetic field are perpendicular to the background field (*i.e.*, of the shear Alfvén type).

The drift approximation works with both the several fluids and single fluid (MHD) versions of the fluid plasma dynamics model; in the latter case the model it gives rise to is usually called "reduced MHD" in the literature. We will see that reduced MHD is wholly contained within fluid drift dynamics in the same sense that MHD is contained within the plasma dynamics model of several fluids.

3.III. Perpendicular Force Balance — Diamagnetic Current

To elucidate the character of the quasistatic force balance we start with the MHD force equation,

$$\rho\frac{d\mathbf{u}}{dt} = -\nabla p + \frac{\mathbf{J}\times\mathbf{B}}{c} \tag{3.6}$$

which we formally solve for the perpendicular component of $\mathbf{J}$,

$$\mathbf{J}_\perp = \mathbf{J} - \frac{\mathbf{B}\mathbf{B}\cdot\mathbf{J}}{B^2} = \frac{c}{B^2}\mathbf{B}\times\nabla p + \frac{c}{B^2}\mathbf{B}\times\rho\frac{d\mathbf{u}}{dt}, \tag{3.7}$$

by operation with $(c/B^2)\mathbf{B}\times$, often called the drift operator.

Due to the smallness of the inertia we expect that to $O(1)$ the force balance holds,

$$\mathbf{J}_\perp{}^{(0)} = \mathbf{J}_* \equiv \frac{c}{B^2}\mathbf{B}\times\nabla p \tag{3.8}$$

and then the inertial correction appears at $O(\delta)$,

$$\mathbf{J}_\perp{}^{(1)} = \frac{c}{B^2}\mathbf{B}\times\rho\frac{d\mathbf{u}}{dt} \tag{3.9}$$

The smaller piece is called the polarisation current, since it emerges from the polarisation drift flows in each charged fluid, as we shall see shortly. The larger piece simply reflects approximate MHD equilibrium in the disturbances. As it holds during temporal changes in the pressure, the force balance is referred to as quasistatic.

The parallel component of the MHD force equation is simply

$$\rho\frac{du_\parallel}{dt} = -\nabla_\parallel p \tag{3.10}$$

Here it is important to note the approximation that the scale of the magnetic field is large enough, and the perturbations to it are small enough, that $\mathbf{B}$ may be commuted through the advective time derivative to form

$$u_\parallel = B^{-1}\mathbf{B}\cdot\mathbf{u} \tag{3.11}$$

with the parallel gradient given in terms of the total (background plus disturbances) field,

$$\nabla_{\|} = B^{-1}\mathbf{B}\cdot\nabla \tag{3.12}$$

Although the disturbances in $\mathbf{B}$ are small, they combine with the perpendicular components of ∇, denoted $\nabla_{\perp}$, which are by the same order (one order in δ) much larger than $\nabla_{\|}$. We therefore have

$$\mathbf{B}\cdot\nabla \sim \widetilde{\mathbf{B}}\cdot\nabla \tag{3.13}$$

with the consequence that all three components of $\nabla_{\|}$ are of the same order.

3.IV. Perpendicular Force Balance — Fluid Drifts

To obtain more insight into the consequences of quasistatic force balance, as well as to evaluate the polarisation drift, we turn to the equation of motion for each charged fluid separately. Assuming a one component plasma with singly charged ions with $n_i = n_e$ and $m_e \ll M_i$, the equations of motion are

$$n_i M_i \frac{d\mathbf{u}}{dt} + \nabla\cdot\mathbf{\Pi}_* = -\nabla p_i + n_e e\left(\mathbf{E} + \frac{\mathbf{u}}{c}\times\mathbf{B}\right) \tag{3.14}$$

$$0 = -\nabla p_e - n_e e\left(\mathbf{E} + \frac{\mathbf{v}}{c}\times\mathbf{B}\right) \tag{3.15}$$

with $\mathbf{u}$ the ion flow and $\mathbf{v}$ the electron flow, and

$$\frac{d}{dt} = \frac{\partial}{\partial t} + \mathbf{u}\cdot\nabla \tag{3.16}$$

the ion advective derivative. We retain the diamagnetic part of Π to cancel part of the advection, as noted in the previous chapter. We assume *a priori* that the left side of the ion equation is one order smaller in δ than the right side.

We assume that $\mathbf{E}_{\perp}$ is electrostatic, so that

$$\mathbf{E}_{\perp} = -\nabla_{\perp}\phi \qquad E_{\|} = -\frac{1}{c}\frac{\partial A_{\|}}{\partial t} - \nabla_{\|}\phi \tag{3.17}$$

Neglecting inertia, the lowest order flows are then given in terms of ϕ and the pressures as stream functions,

$$\mathbf{u}_{\perp}{}^{(0)} = \frac{c}{B^2}\mathbf{B}\times\nabla\phi + \frac{1}{n_e e}\frac{c}{B^2}\mathbf{B}\times\nabla p_i \tag{3.18}$$

$$\mathbf{v}_{\perp} = \frac{c}{B^2}\mathbf{B}\times\nabla\phi - \frac{1}{n_e e}\frac{c}{B^2}\mathbf{B}\times\nabla p_e \tag{3.19}$$

where the perpendicular electron flow is finished because we are neglecting perpendicular electron inertia. In turn, the pieces of these flows are,

$$\mathbf{v}_E = \frac{c}{B^2}\mathbf{B}\times\nabla\phi \qquad \mathbf{v}_* = -\frac{1}{n_e e}\frac{c}{B^2}\mathbf{B}\times\nabla p_e \qquad \mathbf{u}_* = \frac{1}{n_e e}\frac{c}{B^2}\mathbf{B}\times\nabla p_i \tag{3.20}$$

the ExB velocity, and the electron and ion diamagnetic velocities, respectively.

If we take these $O(1)$ flows and form the resulting lowest order current, we find

$$\mathbf{J}_\perp{}^{(0)} = n_e e\left(\mathbf{u}_\perp{}^{(0)} - \mathbf{v}_\perp\right) = \frac{c}{B^2}\mathbf{B}\times\nabla\left(p_i + p_e\right) \tag{3.21}$$

which is the same as Eq. (3.8). This is just the diamagnetic current $\mathbf{J}_*$, because the diamagnetic flows and fluxes are found by neglecting the inertial corrections. The ExB flows vanish in the current since they are the same for all charged fluids, and we have assumed a neutral plasma.

We find the polarisation drift by inserting the lowest order $\mathbf{u}_\perp{}^{(0)}$ and inserting it into the corrections at $O(\delta)$,

$$\mathbf{u}_\perp{}^{(1)} = \frac{1}{n_e e}\left[n_i M_i \frac{c}{B^2}\mathbf{B}\times\frac{d\mathbf{u}_\perp{}^{(0)}}{dt} + \mathbf{\Pi}_*^{(0)}\right] \qquad \mathbf{u}_p \equiv \frac{M_i}{e}\frac{c}{B^2}\mathbf{B}\times\frac{d_E}{dt}\mathbf{u}_\perp{}^{(0)} \tag{3.22}$$

where the diamagnetic flow is cancelled by $\mathbf{\Pi}_*$, leaving perpendicular advection only by $\mathbf{v}_E$ as noted in the previous chapter. The ExB advective derivative is then given by

$$\frac{d_E}{dt} = \frac{\partial}{\partial t} + \mathbf{v}_E\cdot\nabla \tag{3.23}$$

Parallel advection is neglected due to the ordering

$$k_\parallel c_s \ll \omega \sim \mathbf{v}_E\cdot\nabla \tag{3.24}$$

which we discuss further in Section V.

It remains to explain why indeed we must keep the polarisation drift at all. This is due to the fact that although $\mathbf{u}_p$ itself is one order down in δ compared to $\mathbf{v}_E$ and $\mathbf{u}_*$,

$$\mathbf{u}_p = \frac{M_i c}{eB^2}\mathbf{B}\times\frac{d_E}{dt}\mathbf{u}_\perp = \frac{1}{\Omega_i}\mathbf{b}\times\frac{d_E}{dt}\mathbf{u}_\perp \tag{3.25}$$

its divergence is not. We note now that the divergence of any expression of the form given by taking the drift operator to the gradient of a scalar vanishes unless the magnetic field is inhomogeneous. For example, the divergence of the ExB flow is

$$\nabla\cdot\frac{c}{B^2}\mathbf{B}\times\nabla\phi = \nabla\times\left(\frac{c\mathbf{B}}{B^2}\right)\cdot\nabla\phi \tag{3.26}$$

Although the divergence of $\mathbf{u}_*$ by itself has a contribution arising from $\nabla p_i \times \nabla n_e$, these pieces vanish in all situations through the appropriate diamagnetic cancellations. So the perpendicular flow and flux divergences enter only through the scale of the background magnetic field. By contrast, the divergence of the polarisation drift enters through the perpendicular scale of motion, *e.g.*,

$$-\nabla \cdot \mathbf{J}_p = \nabla \cdot \frac{n_i M_i c^2}{B^2} \frac{d_E}{dt} \nabla_\perp \phi \sim \frac{n_i M_i c^2}{B^2} \frac{d_E}{dt} \nabla_\perp^2 \phi \tag{3.27}$$

In terms of the ordering, this means

$$\nabla \cdot \mathbf{J}_* \sim \frac{\mathbf{J}_*}{L_B} \sim \frac{\delta^{-1} \mathbf{J}_p}{\delta^{-1} \Delta_\perp} \sim \frac{\mathbf{J}_p}{\Delta_\perp} \sim \nabla \cdot \mathbf{J}_p \tag{3.28}$$

Effectively, the divergence operator drops the lowest order flows by one order in δ, setting the divergences each at $O(\delta)$.

The same holds when comparing advection by $\mathbf{u}_\perp$ to the polarisation divergence. If the scale of motion is comparable to ρ_s and the dynamical frequency is comparable to $c_s/L_\perp$, then advection of the density by the ExB velocity,

$$\mathbf{v}_E \cdot \nabla n_e \sim \frac{c}{B} \frac{\phi}{\rho_s} \frac{n_e}{L_\perp} \tag{3.29}$$

and the divergence of the polarisation drift times the density,

$$n_e \nabla \cdot \mathbf{u}_p \sim \frac{n_e}{\rho_s} \frac{c_s/L_\perp}{\Omega_i} \frac{c}{B} \frac{\phi}{\rho_s} \sim \frac{n_e}{L_\perp} \frac{c}{B} \frac{\phi}{\rho_s} \tag{3.30}$$

will be comparable, since $\rho_s \Omega_i = c_s$. This is how small scale drift wave disturbances and their associated turbulence scale, so in general we must retain $\mathbf{u}_p$ when it appears under the divergence operator.

3.V. Drift Ordering

The foregoing considerations, treated loosely and without formal justification, leads directly to the question of how we should set up the ordering in the expansion so as to make it systematic. As in the cases of the successively simpler models presented in the previous chapter, this involves some assumptions about the space and time scales of interest. Loosely speaking, we wish to include frequencies, ω, as fast as $c_s/L_\perp$ and space scales as small as ρ_s, and we wish to exclude the faster compressional or gyro frequencies. So in ordering the various terms in the equations we assume

$$\frac{\partial}{\partial t} \sim \omega \sim \frac{c_s}{L_\perp} \ll \Omega_i \tag{3.31}$$

for the time derivative. Note that this inequality requires a magnetised background plasma, since c_s/Ω_i is just ρ_s.

Since the dynamics of interest is gradient driven instabilities and turbulence, we have some guidance concerning the amplitude of motion at a given perpendicular space scale, $\Delta_\perp$. Any disturbances should satisfy (*e.g.*, for the density)

$$\nabla\widetilde{n}_e \sim \nabla n_e \qquad \Longrightarrow \qquad \frac{\widetilde{n}_e}{n_e} \sim \frac{\Delta_\perp}{L_\perp} \tag{3.32}$$

If the space scale is global then we expect $O(1)$ disturbances. If the space scale is ρ_s then we expect $O(\delta)$ disturbances. In either case, this ordering of the amplitudes is called "mixing level" since the dynamics is assumed to be just strong enough to equilibrate the background gradient.

If $\Delta_\perp \sim L_\perp$ then the equations become very complicated due to the need to keep all the operations by the advective derivative, the drift operator, and the divergence in their proper order, especially when considering the polarisation drift. This is still a matter of current research and we will delay discussion of it until Chapter 14. By far the more important applications of fluid drift dynamics have been in situations where the dynamics is local: $\Delta_\perp \ll L_\perp$. Most models, and all of the ones we will discuss before Chapter 14, will take this assumption. It is important to note that we do not thereby linearise the dynamics; we can still treat mixing level turbulence so long as it occurs at small scales. For mixing level turbulence the nonlinear ExB advection is ordered comparable to the linear contribution arising from advection of the background gradient by the ExB eddy disturbances. For example,

$$\mathbf{v}_E \cdot \nabla\widetilde{n}_e \sim \mathbf{v}_E \cdot \nabla n_e \tag{3.33}$$

Both in turn are ordered comparable to the time derivative, following the expectation that advection of the background, also called "gradient drive," is responsible for the dynamics. In general,

$$\frac{\partial}{\partial t} \sim \mathbf{v}_E \cdot \nabla \sim v_A \nabla_\parallel \tag{3.34}$$

and we keep quadratic nonlinearities involving the appearances of $\widetilde{\phi}$ and $\widetilde{\mathbf{B}}_\perp$ in $\mathbf{v}_E \cdot \nabla$ and $\nabla_\parallel$, respectively. The dynamics is therefore allowed to be nonlinear.

We do not, however, keep direct nonlinear contributions to the coefficients of the various terms. For example, the smallness of the amplitudes coupled with the small scale of motion guarantees that

$$\nabla \cdot n_i \nabla_\perp \phi = n_i \nabla_\perp^2 \phi + \nabla_\perp n_i \cdot \nabla_\perp \phi = n_i \nabla_\perp^2 \phi + O(\delta) \tag{3.35}$$

so the appearance of the density in the polarisation divergences is merely as a coefficient. Similarly, we neglect direct advection by the parallel velocity, because

$$\nabla \cdot n_i u_\parallel \mathbf{b} = n_i \nabla \cdot u_\parallel \mathbf{b} + u_\parallel \nabla_\parallel n_i = n_i \nabla \cdot u_\parallel \mathbf{b} + O(\delta) \tag{3.36}$$

due to the fact that the background has no $O(1)$ variation along the field lines, and that for the parallel dynamics there is no scale disparity; the dynamics tends to involve the longest parallel wavelengths allowed by the geometry of the background (cf. Eq. 3.24).

All of this amounts to a two scale expansion: we are following nonlinear disturbances on an at most slowly varying background, not the global approach to equilibrium of that background. Collecting all of it together, we expect that the relative amplitudes of all the disturbances scale together,

$$\frac{e\widetilde{\phi}}{T_e} \sim \frac{\widetilde{n}_e}{n_e} \sim \frac{u_\parallel}{c_s} \sim \frac{\widetilde{\mathbf{B}}_\perp}{B} \sim \delta = \frac{\rho_s}{L_\perp} \ll 1 \tag{3.37}$$

that the perpendicular scale of motion follows ρ_s although it may be several ρ_s,

$$\rho_s \lesssim \Delta_\perp \ll L_\perp \tag{3.38}$$

and that the time scale follows from advection or Alfvén wave motion,

$$\frac{\partial}{\partial t} \sim \mathbf{v}_E \cdot \nabla \sim \{v_A, c_s\} \nabla_\parallel \sim \frac{c_s}{L_\perp} \ll \Omega_i \tag{3.39}$$

All inequalities in these expressions imply smallness by one order in δ. In the literature, this is often called "drift ordering" or "gyrokinetic ordering."

We also expect the dynamical plasma beta to be small,

$$\beta_e = \frac{4\pi p_e}{B^2} = \frac{c_s^2}{v_A^2} \ll 1 \tag{3.40}$$

because we are neglecting compression of the magnetic field while allowing the pressure to evolve arbitrarily. Although this does mean that the values of c_s and v_A in Eq. (3.37) are disparate, we are taking a "maximal ordering" designed to retain both Alfvén and acoustic dynamics parallel to the magnetic field. This is because they involve different subsets of the dependent variables and also different parallel scales of motion. Both together are responsible for limiting the range of excited parallel wavelengths, as we will see in the next chapter. Due to the subsidiary ordering on β_e, which is taken at each level of the expansion in δ, we neglect the disturbances of $\mathbf{B}$ in the drift operator, $(c/B^2)\mathbf{B}\times$.

3.VI. Derivation of the Fluid Drift Equations

The starting point is the fluid plasma dynamics model of Chapter 2. We assume a single component plasma of singly charged ions and electrons. As dissipative fluxes we retain the heat flux $\mathbf{q}$ and momentum flux $\mathbf{\Pi}$ for each fluid species. The only other source of dissipation treated is resistive friction between the electrons and ions. Diamagnetic heat and momentum fluxes are retained for each species.

The outline of the derivation is the procedure involved by the drift approximation. The perpendicular electric field is taken as electrostatic, so that only the parallel component of the magnetic vector potential is retained. Perpendicular flows and diamagnetic heat and fluxes are given to $O(1)$ in terms of scalar dependent variables. The polarisation drift and diamagnetic momentum fluxes are retained as $O(\delta)$ corrections. The electron mass remains finite although the $m_e \ll M_i$ limit is taken to neglect small corrections to terms which would still exist for $m_e \to 0$. The formulae for the perpendicular flows and fluxes are inserted into the rest of the equations to form a closed set which determines the set of scalar variables formed by the densities, temperatures, and parallel flows for each species and the electrostatic and parallel magnetic potentials. Closure is achieved by specifying formulae or additional equations for the parallel heat and momentum fluxes (those which represent true dissipation). The simplest form of this is the procedure given by the Chapman-Enskog expansion in Chapter 2. The neglect of the perpendicular magnetic potential (equivalently, disturbances in the strength of the magnetic field) is checked *a posteriori* by calculating it from the diamagnetic and polarisation currents.

The first step is the electric field. Taking the perpendicular components as electrostatic, we have through Faraday's law,

$$E_{\|} = -\frac{1}{c}\frac{\partial A_{\|}}{\partial t} - \nabla_{\|}\phi \qquad \mathbf{E}_{\perp} = -\nabla_{\perp}\phi \tag{3.41}$$

where the scalar functions ϕ and $A_{\|}$ become two of the dynamical variables. This effectively replaces the vector equations for $\mathbf{E}$ and $\mathbf{B}$ with scalar equations for ϕ and $A_{\|}$.

The second step is specification of the lowest order perpendicular flows and fluxes; collectively, the drifts. The flows are found by solving the equations of motion by applying the drift operator and neglecting the inertia,

$$\mathbf{u}_{\perp} = \mathbf{v}_E + \mathbf{u}_* = \frac{c}{B^2}\mathbf{B}\times\nabla\phi + \frac{1}{n_e e}\frac{c}{B^2}\mathbf{B}\times\nabla p_i \tag{3.42}$$

$$\mathbf{v}_{\perp} = \mathbf{v}_E + \mathbf{v}_* = \frac{c}{B^2}\mathbf{B}\times\nabla\phi - \frac{1}{n_e e}\frac{c}{B^2}\mathbf{B}\times\nabla p_e \tag{3.43}$$

Here, the diamagnetic and dissipative momentum fluxes are ordered with the inertia. The perpendicular heat fluxes are found using the moment approach explained in Chapter 2,

$$\mathbf{q}_{e\perp} = -\frac{5}{2}\frac{p_e}{e}\frac{c}{B^2}\mathbf{B}\times\nabla T_e \qquad \mathbf{q}_{i\perp} = \frac{5}{2}\frac{p_i}{e}\frac{c}{B^2}\mathbf{B}\times\nabla T_i \tag{3.44}$$

The polarisation drift is found by inserting the lowest order $\mathbf{u}_\perp$ into the inertia, with the diamagnetic momentum flux cancelling out the advection of $\mathbf{u}_\perp$ by $\mathbf{u}_*$, leaving

$$\mathbf{u}_p = -\frac{M_i c^2}{eB^2}\frac{d_E}{dt}\left(\nabla_\perp\phi + \frac{\nabla_\perp p_i}{n_e e}\right) \tag{3.45}$$

Here, we have taken the correction to $O(\delta)$ only, neglecting $O(\delta^2)$ and $O(\beta_e\delta)$ corrections due to the variation of $\mathbf{B}$.

A subtle point regarding the parallel and perpendicular components of a vector arises when taking divergences. In general, $\mathbf{B}$ is not homogeneous, so we must be careful with the order of the operations. Using $\mathbf{u}$ as an example, what we have done is to split the perpendicular and parallel parts,

$$\mathbf{u} = \mathbf{u}_\perp + \mathbf{b}u_\parallel = (\mathbf{g} - \mathbf{bb})\cdot\mathbf{u} + \mathbf{bb}\cdot\mathbf{u} \tag{3.46}$$

where $\mathbf{g}$ is the metric tensor (all derivatives are in general covariant, and $\nabla\mathbf{g} = 0$; this is important when using curvilinear coordinates, especially when they are nonorthogonal). The divergence of $\mathbf{u}$ contains both parallel and perpendicular contributions,

$$\nabla\cdot\mathbf{u} = \nabla_\perp\cdot\mathbf{u}_\perp + \nabla\cdot\mathbf{b}u_\parallel \tag{3.47}$$

Under drift ordering, the scale of $\mathbf{B}$ is larger than that of $\mathbf{u}_\perp$ in the perpendicular directions, so $\mathbf{B}$ may be commuted at will through the perpendicular gradient or the perpendicular divergence. The parallel scale however is the same for both, namely, the inverse of $k_\parallel$. Noting that $\nabla\cdot\mathbf{B} = 0$, the divergence of $\mathbf{b}$ is finite,

$$\nabla\cdot\mathbf{b} = \nabla\cdot\frac{\mathbf{B}}{B} = \mathbf{B}\cdot\nabla\frac{1}{B} = B\nabla_\parallel\frac{1}{B} \tag{3.48}$$

and so the parallel gradient of B enters the parallel divergence:

$$\nabla\cdot\mathbf{u} = \nabla_\perp\cdot\mathbf{u}_\perp + B\nabla_\parallel\frac{u_\parallel}{B} \tag{3.49}$$

The density equation for a single component, singly ionised, neutral plasma can be derived either from the ion or electron densities. Here, we take the electron one due to the ability to neglect the polarisation drift. The material continuity equation for electrons is

$$\frac{\partial n_e}{\partial t} + \nabla\cdot n_e\mathbf{v} = 0 \tag{3.50}$$

The velocity is split into parallel and perpendicular components,

$$\frac{\partial n_e}{\partial t} + \nabla \cdot n_e \mathbf{v}_\perp + \nabla \cdot n_e v_\parallel \mathbf{b} = 0 \tag{3.51}$$

The perpendicular velocity is further split into the ExB and diamagnetic parts, and the divergence of the ExB velocity is set together with the diamagnetic divergence,

$$\frac{\partial n_e}{\partial t} + \mathbf{v}_E \cdot \nabla n_e + n_e \nabla \cdot \mathbf{v}_E + \nabla \cdot n_e \mathbf{v}_* + B\nabla_\parallel \frac{n_e v_\parallel}{B} = 0 \tag{3.52}$$

Instead of the parallel electron velocity directly, we will retain the parallel current,

$$J_\parallel = n_e e(u_\parallel - v_\parallel) \tag{3.53}$$

as a dynamical variable. It is related to $A_\parallel$ through Ampere's law,

$$J_\parallel = -\frac{c}{4\pi}\nabla_\perp^2 A_\parallel \tag{3.54}$$

where to $O(1)$ only the perpendicular components of ∇^2 contribute. The particular choice of the divergence forms results from the diamagnetic cancellation discussed in Chapter 2, according to which these fluxes enter only through divergence combinations which vanish unless $\mathbf{B}$ is inhomogeneous. The diamagnetic divergence operator is defined for any scalar f as

$$\mathcal{K}(f) \equiv -\left(\nabla \times \frac{c\mathbf{B}}{B^2}\right) \cdot \nabla f = -\nabla \cdot \frac{c}{B^2}\mathbf{B}\times\nabla f \tag{3.55}$$

so the divergence of the diamagnetic material flux is

$$\nabla \cdot n_e \mathbf{v}_* = -\nabla \cdot \frac{1}{e}\frac{c}{B^2}\mathbf{B}\times\nabla p_e = \frac{1}{e}\mathcal{K}(p_e) \tag{3.56}$$

The divergence of $\mathbf{v}_E$ is also of this form,

$$\nabla \cdot \mathbf{v}_E = \nabla \cdot \frac{c}{B^2}\mathbf{B}\times\nabla\phi = -\mathcal{K}(\phi) \tag{3.57}$$

Finally, putting the ExB advection together with the time derivative, we have

$$\frac{d_E n_e}{dt} = \frac{B}{e}\nabla_\parallel \frac{J_\parallel}{B} - n_e B \nabla_\parallel \frac{u_\parallel}{B} - \frac{1}{e}\mathcal{K}(p_e) + n_e \mathcal{K}(\phi) \tag{3.58}$$

This is the equation for the electron density, but due to quasineutrality it also governs the ions. Note that due to the ordering we can use $\nabla_\parallel J_\parallel$ or $n_e e \nabla_\parallel (u_\parallel - v_\parallel)$ interchangeably, as the contribution in this term from $\nabla_\parallel n_e$ is at higher order in δ.

The role of the polarisation drift on the ions is next, and it is easiest to see it by considering the quasineutrality condition,

$$\nabla \cdot \mathbf{J} = 0 \tag{3.59}$$

As with the velocities, we separate the parallel and perpendicular parts, and in the perpendicular part we retain the polarisation drift of the ions,

$$-\nabla \cdot n_i e \mathbf{u}_p = \nabla \cdot J_{\|} \mathbf{b} + \nabla \cdot \mathbf{J}_* = B \nabla_{\|} \frac{J_{\|}}{B} + \nabla \cdot (n_i e \mathbf{u}_* - n_e e \mathbf{v}_*) \tag{3.60}$$

In this case, all of the subtleties have been taken care of in writing down the polarisation drift, in Eq. (3.45). Inserting the formulae for $\mathbf{u}_*$ and $\mathbf{v}_*$, we have

$$\nabla \cdot \frac{n_i M_i c^2}{B^2} \frac{d_E}{dt} \left(\nabla_{\perp} \phi + \frac{\nabla_{\perp} p_i}{n_e e} \right) = B \nabla_{\|} \frac{J_{\|}}{B} + \mathcal{K}(p_e + p_i) \tag{3.61}$$

We can see the relation between the electron and ion density equations, since the differences are all in these contributions to $\nabla \cdot \mathbf{J} = 0$. One can use Eqs. (3.58) and (3.61) within drift ordering to find

$$\frac{d_E n_i}{dt} = -n_i B \nabla_{\|} \frac{u_{\|}}{B} + \frac{1}{e} \mathcal{K}(p_i) + n_i \mathcal{K}(\phi) - \nabla \cdot n_i \mathbf{u}_p \tag{3.62}$$

Since $\mathbf{u}_p$ contains its own time derivative, the electron equation (3.58) is more suitable for computations. Using Eq. (3.61) to eliminate $\mathbf{u}_p$ simply recovers Eq. (3.58). We will use a similar manipulation to eliminate $\nabla \cdot \mathbf{u}_p$ in the ion temperature equation.

The temperatures are manipulated in similar fashion to the densities. For the electrons we start with

$$\frac{3}{2} n_e \left(\frac{\partial}{\partial t} + \mathbf{v} \cdot \nabla \right) T_e + p_e \nabla \cdot \mathbf{v} = -\nabla \cdot \mathbf{q}_e \tag{3.63}$$

Explicitly neglecting advection by $v_{\|}$ and separating $\mathbf{v}_E$ from $\mathbf{v}_*$, we have

$$\begin{aligned} \frac{3}{2} n_e \left(\frac{\partial}{\partial t} + \mathbf{v}_E \cdot \nabla \right) T_e + p_e \nabla \cdot \mathbf{v}_E + p_e \nabla \cdot v_{\|} \mathbf{b} = \\ -\frac{3}{2} n_e \mathbf{v}_* \cdot \nabla T_e - p_e \nabla \cdot \mathbf{v}_* - \nabla \cdot \mathbf{q}_{e\perp} - \nabla \cdot q_{e\|} \mathbf{b} \end{aligned} \tag{3.64}$$

The first three terms on the right side combine to form the diamagnetic cancellation for the heat flux, whereupon

$$\begin{aligned} \frac{3}{2} n_e \left(\frac{\partial}{\partial t} + \mathbf{v}_E \cdot \nabla \right) T_e + p_e \nabla \cdot \mathbf{v}_E + p_e B \nabla_{\|} \frac{v_{\|}}{B} = \\ -T_e \nabla \cdot n_e \mathbf{v}_* - p_e \nabla \cdot \frac{\mathbf{q}_{e\perp}}{p_e} - B \nabla_{\|} \frac{q_{e\|}}{B} \end{aligned} \tag{3.65}$$

The parallel velocity is eliminated in favor of the parallel current,

$$\frac{3}{2}n_e\left(\frac{\partial}{\partial t}+\mathbf{v}_E\cdot\nabla\right)T_e=\frac{T_eB}{e}\nabla_\parallel\frac{J_\parallel}{B}-p_eB\nabla_\parallel\frac{u_\parallel}{B}-B\nabla_\parallel\frac{q_{e\parallel}}{B}\\-p_e\nabla\cdot\mathbf{v}_E-T_e\nabla\cdot n_e\mathbf{v}_*-p_e\nabla\cdot\frac{\mathbf{q}_{e\perp}}{p_e} \tag{3.66}$$

Finally, we express the magnetic divergences in terms of the $\mathcal{K}$ operator,

$$\frac{3}{2}n_e\frac{d_ET_e}{dt}=\frac{T_eB}{e}\nabla_\parallel\frac{J_\parallel}{B}-p_eB\nabla_\parallel\frac{u_\parallel}{B}-B\nabla_\parallel\frac{q_{e\parallel}}{B}\\-\frac{5}{2}\frac{p_e}{e}\mathcal{K}(T_e)-\frac{T_e}{e}\mathcal{K}(p_e)+p_e\mathcal{K}(\phi) \tag{3.67}$$

Similar manipulation of the ion temperature equation leads to the intermediate form involving the polarisation drift,

$$\frac{3}{2}n_i\frac{d_ET_i}{dt}=-p_iB\nabla_\parallel\frac{u_\parallel}{B}-p_i\nabla\cdot\mathbf{u}_p+\frac{5}{2}\frac{p_i}{e}\mathcal{K}(T_i)+\frac{T_i}{e}\mathcal{K}(p_i)+p_i\mathcal{K}(\phi)-B\nabla_\parallel\frac{q_{i\parallel}}{B} \tag{3.68}$$

We then use Eq. (3.61) to eliminate $\mathbf{u}_p$, leaving

$$\frac{3}{2}n_i\frac{d_ET_i}{dt}=\frac{T_i}{e}B\nabla_\parallel\frac{J_\parallel}{B}-p_iB\nabla_\parallel\frac{u_\parallel}{B}+\frac{5}{2}\frac{p_i}{e}\mathcal{K}(T_i)-\frac{T_i}{e}\mathcal{K}(p_e)+p_i\mathcal{K}(\phi)-B\nabla_\parallel\frac{q_{i\parallel}}{B} \tag{3.69}$$

The curious appearances of $J_\parallel$ and $\mathcal{K}(p_e)$ in this equation is simply due to their relation to $\mathbf{u}_p$ under the divergences. The same applies to p_e and p_i under $\mathcal{K}$ in $\mathbf{J}_*$.

The parallel divergences appear in the equations for the scalar quantities; the parallel gradients appear in those for the parallel fluxes. At this point we need the equations for the parallel velocities. For the ions we contract the equation of motion with the (total) magnetic field, to eliminate the magnetic Lorentz force,

$$\mathbf{B}\cdot\left[n_iM_i\frac{d_E}{dt}\mathbf{u}=-\nabla p_i+n_ee\mathbf{E}+n_ee\frac{\mathbf{u}}{c}\times\mathbf{B}-\nabla\cdot\left(\Pi_\parallel\mathbf{b}\right)-\mathbf{R}_{ei}\right] \tag{3.70}$$

where $\mathbf{R}_{ei}=R_{ei}\mathbf{b}$ is retained as parallel resistive friction, $\Pi_\parallel\mathbf{b}=\mathbf{bb}\cdot\boldsymbol{\Pi}$ is the parallel part of viscous dissipation, and the diamagnetic (gyroviscous) cancellation and drift ordering are invoked to write the advective derivative only with $\mathbf{v}_E$. Neglecting higher order corrections, we carry the contraction with $\mathbf{B}$ through d_E/dt such that it operates only on $\mathbf{u}$ and substitute $n_i=n_e$ in the electric force,

$$n_iM_i\frac{d_E}{dt}u_\parallel=-\nabla_\parallel p_i+n_eeE_\parallel-B\nabla_\parallel\frac{\Pi_\parallel}{B}-R_{ei} \tag{3.71}$$

By similar operation on the electron equation of motion we have

$$n_e m_e \frac{d_E}{dt} v_{\parallel} = -\nabla_{\parallel} p_e - n_e e E_{\parallel} + R_{ei} \tag{3.72}$$

where we neglect electron viscosity. Adding the two and neglecting the electrons' contribution to the total inertia, we find the equation for $u_{\parallel}$,

$$n_i M_i \frac{d_E}{dt} u_{\parallel} = -\nabla_{\parallel}(p_e + p_i) - B\nabla_{\parallel}\frac{\Pi_{\parallel}}{B} \tag{3.73}$$

to which R_{ei} does not contribute since like $E_{\parallel}$ it cancels in the subtraction, conserving total momentum. Forming an equation for the relative drift velocity, $u_{\parallel} - v_{\parallel}$, we have

$$n_e m_e \frac{d_E}{dt}\left(u_{\parallel} - v_{\parallel}\right) = \nabla_{\parallel} p_e + n_e e E_{\parallel} - R_{ei} + O(\mu_e) \tag{3.74}$$

where as before $\mu_e = m_e/M_i$ is the electron ion mass ratio. Putting in Faraday's law (Eq. 3.41) for $E_{\parallel}$ and dropping the $O(\mu_e)$ corrections we have

$$\frac{n_e e}{c}\frac{\partial A_{\parallel}}{\partial t} + n_e m_e \frac{d_E}{dt}\left(u_{\parallel} - v_{\parallel}\right) = \nabla_{\parallel} p_e - n_e e \nabla_{\parallel}\phi - R_{ei} \tag{3.75}$$

Finally, under drift ordering the factor of n_e appearing in the inertia may be commuted through the advective derivative, neglecting $O(\delta)$ corrections, to yield the Ohm's law,

$$\frac{n_e e}{c}\frac{\partial A_{\parallel}}{\partial t} + \frac{m_e}{e}\frac{d_E}{dt} J_{\parallel} = \nabla_{\parallel} p_e - n_e e \nabla_{\parallel}\phi - R_{ei} \tag{3.76}$$

If we provide constitutive relations for the dissipation effects, $q_{e\parallel}$, $q_{i\parallel}$, R_{ei}, and $\Pi_{\parallel}$, in terms of the dependent variables $\{\phi, A_{\parallel}, n_e, T_e, T_i, u_{\parallel}\}$, with $J_{\parallel}$ already given by Ampere's law (Eq. 3.54) and n_i by n_e, we then have a closed set. The simplest form of this (aside from neglecting thermal effects altogether and all dissipation except for resistive friction, as we will do for simplified, explanatory treatments) is the Chapman-Enskog formalism of Chapter 2, Section X. In the literature these are sometimes called the reduced Braginskii equations, since a procedure very similar to that leading to reduced MHD is being applied to the two fluid Braginskii equations (see Further Reading, Chapter 2). That set amounts to the dynamical equations (Eqs. 3.58,3.61,3.67,3.69,3.73,3.76), plus the constitutive relations

$$R_{ei} = n_e e \eta_{\parallel} J_{\parallel} - 0.71 n_e \nabla_{\parallel} T_e \qquad \eta_{\parallel} = 0.51 \frac{m_e \nu_e}{n_e e^2} \tag{3.77}$$

$$q_{e\parallel} = -0.71 \frac{T_e}{e} J_{\parallel} - n_e \kappa_{\parallel e} \nabla_{\parallel} T_e \qquad \kappa_{\parallel e} = 3.2 \frac{T_e}{m_e \nu_e} \tag{3.78}$$

$$q_{i\parallel} = -n_i \kappa_{\parallel i} \nabla_\parallel T_i \qquad \kappa_{\parallel i} = 3.9 \frac{T_i}{M_i \nu_i} \tag{3.79}$$

$$\Pi_\parallel = -n_i M_i \mu_\parallel \nabla_\parallel u_\parallel \qquad \mu_\parallel = 0.96 \frac{T_i}{M_i \nu_i} \tag{3.80}$$

and Ampere's law (Eq. 3.54) for $J_\parallel$. Note that the term $\nabla_\parallel u_\parallel$ in $\Pi_\parallel$ is not a divergence, but a gradient.

This set can be generalised by taking models for the coefficients $\eta_\parallel, \kappa_{\parallel e}, \kappa_{\parallel i}, \mu_\parallel$ which are more realistic in the weakly collisional regime, or by extending the model to retain $q_{e\parallel}$ and $q_{i\parallel}$ as dynamical variables. Electron viscosity ($\mu_{\parallel e}$) is usually neglected because the electron inertia itself only enters in the weakly collisional regime (in a Chapman-Enskog expansion it enters only at second order as noted in Chapter 2, Further Reading). Perpendicular dissipative effects (scaling as $\rho_i^2 \nu_i$ for the ions and $\rho_e^2 \nu_e$ for the electrons) are neglected because they are typically very weak at ρ_s scales in strongly hot, magnetised plasmas (since ν_i is usually much smaller than $c_s/L_\perp$, and $\mu_e \nu_e$ is smaller still).

The *a posteriori* check involving the neglect of $\mathbf{A}_\perp$ can be done by estimating $\nabla p_e \sim p_e (e/T_e) \nabla \phi$, and then using Ampere's law to obtain $\mathbf{A}_\perp$ from the dominant perpendicular current, $\mathbf{J}_*$, which is determined by $p = p_e + p_i$ via Eq. (3.21). We find that $\mathbf{J}_\perp \sim n_e e \mathbf{v}_E$. The effective compressibility of the magnetic field lines (perpendicular to $\mathbf{B}$) can then be determined by taking the curl of $\mathbf{A}_\perp$. One finds that the field strength disturbance $\widetilde{B}/B$ is of order $\beta_e \delta$, in agreement with the simple postulate that $\nabla_\perp (p + B^2/8\pi)$ remains close to zero. Estimation of the magnitude ratio $A_\parallel / A_\perp$ is more complicated since it depends on estimation of $J_\parallel$, but if we assume that $J_\parallel / n_e e c_s \sim \delta$, then we find that since $\mathbf{v}_E / c_s \sim \delta$ we have $J_\parallel \sim J_\perp$ and hence $A_\parallel \sim A_\perp$, so that while $\omega A_\parallel / c$ can compete with $\nabla_\parallel \phi$, the inductive perpendicular electric field $\omega \mathbf{A}_\perp / c$ is small compared to $\nabla_\perp \phi$ by the flute mode ordering factor $k_\parallel / k_\perp \sim \delta$. It is therefore a good approximation to neglect $\mathbf{A}_\perp$ in the perpendicular electric field in fluid drift dynamics whenever both β_e and δ are small compared to unity.

3.VII. Energetics of the Fluid Drift Equations

The drift equations form an expansion of the fluid plasma model to lowest order in δ, and as a result they only conserve total energy up to $O(\delta)$ corrections. To achieve the usual goal — expansion of the equations up to $O(\delta)$ corrections with an energy theorem up to $O(\delta^2)$ corrections — one has to do better than this. The fluid drift equations are customarily used, however, in a different context than this. Rather than evolving a global system through $O(1)$ changes, one follows the dynamics of small scale, small amplitude disturbances, even if nonlinear, on a prescribed background which is at most slowly

varying compared to the disturbances. In this case we are not interested in total energy conservation but in the conservation of fluctuation free energy. That is, the background gradient itself should appear as a source, while the usual dissipation mechanisms appear as sinks. By contrast, in a global system such as those presented in Chapter 2, there are no sources or sinks unless these are either specified as external forcing mechanisms or as fluxes entering or leaving through boundaries. In a global system a gradient is not a source, but energy is moved from place to place. Similarly, a dissipation mechanism is merely a transfer process between ordered motion (*e.g.*, wave energy or fluid kinetic energy) and random motion (temperature). In a local system one does not follow the relaxation of the gradient by the disturbances, nor the heating which results from a dissipation mechanism like friction or viscosity.

In order to see why the local drift equations do not conserve global energy completely, consider how advection and compression work together in conserving and transferring thermal and kinetic energy (refer to Section VIII of Chapter 2). In the total advective heat flux of $(5/2)p_i\mathbf{u}$, a factor of $3/2$ of that comes from advection of n_i and T_i, so far as the action of the divergence on n_i and T_i is concerned, but for the velocity divergence a factor of $3/2$ comes from $\nabla \cdot n_i\mathbf{u}$ in the density equation and the other factor of 1 comes from $p_i\nabla \cdot \mathbf{u}$ in the temperature equation. So for each contribution to $\mathbf{u}$, both advection and compression are involved. But for $u_\parallel$ and $\mathbf{u}_p$, the advection pieces have been dropped, and so we cannot have complete conservation unless these are retained. We will pick up this issue again in Chapter 14, when we discuss particle and thermal energy transport by fluid drift turbulence.

As far as fluctuation free energy is concerned, however, there are no problems. We must construct an energylike quantity which is quadratic in the disturbances. The way to do this is to generalise the kinetic energy, which takes care of the velocities, to a free energy expression which incorporates the state variables, which collectively refer to those which appear under gradient operators as force terms for the velocities. These are ϕ in addition to n_e, T_e, and T_i. The potential ϕ already appears through the ExB kinetic energy, and a term proportional to ϕ^2 should not appear, because of quasineutrality. The potential is therefore already taken care of. For the others, it suffices to take their squares and adjust the coefficients such that (1) energy sinks such as $\eta_\parallel J_\parallel^2$ appear properly, and (2) compression and work terms such as $u_\parallel \nabla_\parallel p_i$ appear as transfer couplings and not as sources or sinks. Denoting the disturbances with the tilde symbol and adjusting the units, we have

$$U = n_i M_i \left[\frac{(\mathbf{v}_E + \mathbf{u}_*)^2 + \widetilde{u}_\parallel^2}{2}\right] + \frac{\widetilde{\mathbf{B}}^2}{8\pi} + n_e m_e \frac{(\widetilde{J}_\parallel/n_e e)^2}{2} + \frac{p_e}{2}\frac{\widetilde{n}_e^2}{n_e^2} + \frac{3}{2}\frac{p_e}{2}\frac{\widetilde{T}_e^2}{T_e^2} + \frac{p_i}{2}\frac{\widetilde{n}_e^2}{n_e^2} + \frac{3}{2}\frac{p_i}{2}\frac{\widetilde{T}_i^2}{T_i^2} \tag{3.81}$$

for the free energy density U, where $\mathbf{v}_E$ and $\mathbf{u}_*$ are given in terms of $\nabla_\perp\widetilde{\phi}$ and $\nabla_\perp\widetilde{p}_i$, with $\widetilde{p}_i = n_i\widetilde{T}_i + T_i\widetilde{n}_e$ noting $\widetilde{n}_i = \widetilde{n}_e$, and $\widetilde{\mathbf{B}}$ is given in terms of $\nabla_\perp\widetilde{A}_\parallel$. Note that the density enters twice, once each for electrons and ions. The polarisation drift does not appear, due to the drift ordering.

In keeping with the ordering, we find the time evolution of U through the equations for the disturbances. In order to do this properly we must separate the gradient drive terms which are introduced by the appearance of the background under $\mathbf{v}_E\cdot\nabla$ and $\nabla_\parallel$. Writing the equations explicitly in terms of the disturbances, we have

$$\nabla\cdot\frac{n_iM_ic^2}{B^2}\frac{d_E}{dt}\left(\nabla_\perp\widetilde{\phi}+\frac{\nabla_\perp\widetilde{p}_i}{n_ee}\right)=B\nabla_\parallel\frac{\widetilde{J}_\parallel}{B}+\mathcal{K}(\widetilde{p}_e+\widetilde{p}_i) \tag{3.82}$$

$$\frac{d_E\widetilde{n}_e}{dt}=-\mathbf{v}_E\cdot\nabla n_e+\frac{B}{e}\nabla_\parallel\frac{\widetilde{J}_\parallel}{B}-n_eB\nabla_\parallel\frac{\widetilde{u}_\parallel}{B}-\frac{1}{e}\mathcal{K}(\widetilde{p}_e)+n_e\mathcal{K}(\widetilde{\phi}) \tag{3.83}$$

$$\begin{aligned}\frac{3}{2}n_e\frac{d_E\widetilde{T}_e}{dt}=&-\frac{3}{2}n_e\mathbf{v}_E\cdot\nabla T_e+\frac{T_eB}{e}\nabla_\parallel\frac{\widetilde{J}_\parallel}{B}-p_eB\nabla_\parallel\frac{\widetilde{u}_\parallel}{B}-B\nabla_\parallel\frac{\widetilde{q}_{e\parallel}}{B}\\&-\frac{5}{2}\frac{p_e}{e}\mathcal{K}(\widetilde{T}_e)-\frac{T_e}{e}\mathcal{K}(\widetilde{p}_e)+p_e\mathcal{K}(\widetilde{\phi})\end{aligned} \tag{3.84}$$

$$\begin{aligned}\frac{3}{2}n_i\frac{d_E\widetilde{T}_i}{dt}=&-\frac{3}{2}n_i\mathbf{v}_E\cdot\nabla T_i+\frac{T_i}{e}B\nabla_\parallel\frac{\widetilde{J}_\parallel}{B}-p_iB\nabla_\parallel\frac{\widetilde{u}_\parallel}{B}-B\nabla_\parallel\frac{\widetilde{q}_{i\parallel}}{B}\\&+\frac{5}{2}\frac{p_i}{e}\mathcal{K}(\widetilde{T}_i)+\frac{T_i}{e}\mathcal{K}(\widetilde{p}_e)+p_i\mathcal{K}(\widetilde{\phi})\end{aligned} \tag{3.85}$$

$$n_iM_i\frac{d_E}{dt}\widetilde{u}_\parallel=-\nabla_\parallel(p_e+p_i)-\nabla_\parallel(\widetilde{p}_e+\widetilde{p}_i)-B\nabla_\parallel\frac{\widetilde{\Pi}_\parallel}{B} \tag{3.86}$$

$$\frac{n_ee}{c}\frac{\partial\widetilde{A}_\parallel}{\partial t}+\frac{m_e}{e}\frac{d_E}{dt}\widetilde{J}_\parallel=\nabla_\parallel p_e+\nabla_\parallel\widetilde{p}_e-n_ee\nabla_\parallel\widetilde{\phi}-\widetilde{R}_{ei} \tag{3.87}$$

It is important to do this for the heat fluxes as well, should they be given in terms of constitutive relations; for example, Eqs. (3.78,3.79) become

$$\widetilde{q}_{e\parallel}=-0.71\frac{T_e}{e}\widetilde{J}_\parallel-n_e\kappa_{\parallel e}\nabla_\parallel T_e-n_e\kappa_{\parallel e}\nabla_\parallel\widetilde{T}_e \tag{3.88}$$

$$\widetilde{q}_{i\parallel}=-n_i\kappa_{\parallel i}\nabla_\parallel T_i-n_i\kappa_{\parallel i}\nabla_\parallel\widetilde{T}_i \tag{3.89}$$

in the Braginskii model. In these equations, the background quantities are regarded as parameters unless they appear as gradient forcing terms under either $\mathbf{v}_E\cdot\nabla$ or $\nabla_\parallel$, and, of course, pressures under gradients appear with density and temperature pieces separately, *e.g.*,

$$\mathcal{K}(\widetilde{p}_e)=T_e\mathcal{K}(\widetilde{n}_e)+n_e\mathcal{K}(\widetilde{T}_e)\qquad\qquad\nabla_\parallel p_e=T_e\nabla_\parallel n_e+n_e\nabla_\parallel T_e \tag{3.90}$$

In forming the evolution equation for U, many terms form pairs which can be recast in the form of total divergences. These are transfer mechanisms, just like their similar counterparts in the global energy theorems discussed in Chapter 2. For example, multiplying Eq. (3.86) with $\widetilde{u}_\parallel$, we obtain a piece involving $\widetilde{u}_\parallel$ and $\nabla_\parallel \widetilde{p}_e$,

$$n_i M_i \frac{d_E}{dt}\frac{\widetilde{u}_\parallel^2}{2} = \cdots - \widetilde{u}_\parallel \nabla_\parallel \widetilde{p}_e \tag{3.91}$$

In both the density and temperature equations, in each case multiplying with the relative fluctuations, we find the corresponding pieces which involve $\nabla_\parallel$ acting on $\widetilde{u}_\parallel$,

$$n_e T_e \frac{d_E}{dt}\frac{\widetilde{n}_e^2}{n_e^2} = \cdots - T_e \widetilde{n}_e B \nabla_\parallel \frac{\widetilde{u}_\parallel}{B} \tag{3.92}$$

$$\frac{3}{2} n_e T_e \frac{d_E}{dt}\frac{\widetilde{T}_e^2}{T_e^2} = \cdots - n_e \widetilde{T}_e B \nabla_\parallel \frac{\widetilde{u}_\parallel}{B} \tag{3.93}$$

The right sides of these equations combine into the following total divergence,

$$\frac{\partial U}{\partial t} = \cdots - B\nabla_\parallel \frac{\widetilde{p}_e \widetilde{u}_\parallel}{B} = \cdots - \mathbf{B}\cdot\nabla \frac{\widetilde{p}_e \widetilde{u}_\parallel}{B} = \cdots - \nabla\cdot\mathbf{B}\frac{\widetilde{p}_e \widetilde{u}_\parallel}{B} \tag{3.94}$$

Similarly, the $\mathbf{v}_E\cdot\nabla$ part of the advective derivative becomes a total divergence, because we are keeping only the lowest order, divergence free part of it. For example, the ordering follows

$$\mathbf{v}_E\cdot\nabla\widetilde{n}_e \sim \mathbf{v}_E\cdot\nabla n_e \sim n_e \nabla\cdot\mathbf{v}_E \gg \widetilde{n}_e\nabla\cdot\mathbf{v}_E \tag{3.95}$$

noting that the $n_e\nabla\cdot\mathbf{v}_E$ term is already accounted for in $\mathcal{K}(\widetilde{\phi})$. The action of $\mathbf{v}_E\cdot\nabla$ on U simply enters a divergence,

$$\frac{d_E U}{dt} = \frac{\partial U}{\partial t} + \mathbf{v}_E\cdot\nabla U = \frac{\partial U}{\partial t} + \nabla\cdot U\mathbf{v}_E + O(\delta) \tag{3.96}$$

The corrections of order δ are further dropped by treating the velocity in $\mathbf{v}_E\cdot\nabla$ as exactly incompressible, leaving the quasistatic compression given by $\mathcal{K}(\widetilde{\phi})$ as a separate set of terms. Within this model, conservation by both $\mathbf{v}_E\cdot\nabla$ and $\mathcal{K}(\widetilde{\phi})$ is exact.

The gradient drive terms however do not vanish in this fashion of integration over total divergences, but remain as sources. For example,

$$\frac{\partial U}{\partial t} = \cdots - \widetilde{u}_\parallel \nabla_\parallel p_e = \cdots - \frac{\widetilde{u}_\parallel}{B}\widetilde{\mathbf{B}}\cdot\nabla p_e \tag{3.97}$$

which simply means that a flow along a perturbed field line down a pressure gradient will lead to the driving of the parallel flow. The same holds for ExB advection of the

background gradients. For example, the gradient forcing terms in Eqs. (3.83) and (3.84) give rise to

$$\frac{\partial U}{\partial t} = \cdots - T_e \frac{\widetilde{n}_e}{n_e} \mathbf{v}_E \cdot \nabla n_e - n_e \frac{3}{2} \frac{\widetilde{T}_e}{T_e} \mathbf{v}_E \cdot \nabla T_e \tag{3.98}$$

and so the transport of $\widetilde{n}_e$ and $\widetilde{T}_e$ by the ExB velocity down their respective gradients leads to the excitation of free energy in the form of just these fluctuations.

Similarly, a heat flux down a temperature gradient along a perturbed field line will drive the temperature disturbances. With the dissipative model of Eqs. (3.78,3.79) this is somewhat subtle, since the contribution due to the gradient must be extracted from a second order $\nabla_\parallel$ operation which is a divergence and a gradient. For the electrons this is manipulated as follows. Writing the contribution to the energy theorem as

$$\frac{\partial U}{\partial t} = \cdots - \frac{\widetilde{T}_e}{T_e} B \nabla_\parallel \frac{\widetilde{q}_{e\parallel}}{B} \tag{3.99}$$

we add the heat flux equation (3.88) times $\widetilde{q}_{e\parallel}/n_e T_e \kappa_{\parallel e}$, to obtain

$$\frac{\partial U}{\partial t} = \cdots - B \nabla_\parallel \left(\frac{\widetilde{T}_e}{T_e} \frac{\widetilde{q}_{e\parallel}}{B} \right) - \frac{\widetilde{q}_{e\parallel}}{\kappa_{\parallel e} n_e T_e} \left(\widetilde{q}_{e\parallel} + 0.71 \frac{T_e}{e} \widetilde{J}_\parallel \right) - \widetilde{q}_{e\parallel} \nabla_\parallel (\log T_e) \tag{3.100}$$

where the first term is a total divergence and the last one is the gradient drive term for $\widetilde{q}_{e\parallel}$. Now, we complete the square on the combination involving $\widetilde{q}_{e\parallel}$ and $\widetilde{J}_\parallel$ by considering the Ohm's law's contribution to the energy, whose relevant terms involving dissipation are the ones from R_{ei} in Eq. (3.77),

$$\frac{\partial U}{\partial t} = \cdots - \eta_\parallel \left(\widetilde{J}_\parallel \right)^2 + \frac{\widetilde{J}_\parallel}{n_e e} 0.71 n_e \nabla_\parallel (\widetilde{T}_e + T_e) \tag{3.101}$$

We then substitute for the term involving 0.71 using Eqs. (3.77,3.78) and combine the two sets of terms neglecting the divergence term, to find

$$\frac{\partial U}{\partial t} = \cdots - \eta_\parallel \left(\widetilde{J}_\parallel \right)^2 - \frac{p_e}{\kappa_{\parallel e}} \left(\frac{\widetilde{q}_{e\parallel}}{p_e} + 0.71 \frac{\widetilde{J}_\parallel}{n_e e} \right)^2 - \widetilde{q}_{e\parallel} \nabla_\parallel (\log T_e) \tag{3.102}$$

We now have two negative definite sinks, respectively representing resistivity and thermal conduction, and the gradient drive term arising from conductive heat flows along perturbed field lines down the background temperature gradient.

In all cases, the corrections incurred by the operation of $\nabla_\parallel$ or $\mathbf{v}_E \cdot \nabla$ on the background quantity are down by one order in δ from the same operation on the disturbance; *e.g.*,

$$\mathbf{v}_E \cdot \nabla \frac{\widetilde{T}_e}{T_e} = \frac{\mathbf{v}_E \cdot \nabla \widetilde{T}_e}{T_e} + \widetilde{T}_e \mathbf{v}_E \cdot \nabla \frac{1}{T_e} = \frac{\mathbf{v}_E \cdot \nabla \widetilde{T}_e}{T_e} + O(\delta) \tag{3.103}$$

Equations for the disturbances are scaled against the local parameters n_e, T_e, and T_i, and then the parameters are assumed to be constants except where operated upon by $\mathbf{v}_E \cdot \nabla$ or $\nabla_\parallel$, and then these gradients are taken to be separate drive terms, as in Eqs. (3.82–3.89). The energy theorem is then exact without these $O(\delta)$ corrections.

The combined energy theorem of Eqs. (3.83) to (3.87) under the dissipative flux formulae of Eqs. (3.77) to (3.80) is

$$\begin{aligned}\frac{\partial}{\partial t}\int d^3x\, U = \int d^3x \Bigg\{ \Bigg[& -\widetilde{q}_{e\parallel}\nabla_\parallel(\log T_e) - \widetilde{q}_{i\parallel}\nabla_\parallel(\log T_i) - \widetilde{u}_\parallel \nabla_\parallel(p_e+p_i) \\ & - (T_e+T_i)\frac{\widetilde{n}_e}{n_e}\mathbf{v}_E\cdot\nabla n_e - \frac{3}{2}n_e\frac{\widetilde{T}_e}{T_e}\mathbf{v}_E\cdot\nabla T_e - \frac{3}{2}n_e\frac{\widetilde{T}_i}{T_i}\mathbf{v}_E\cdot\nabla T_i \Bigg] \\ - \Bigg[& \eta_\parallel\left(\widetilde{J}_\parallel\right)^2 + \frac{p_e}{\kappa_{\parallel e}}\left(\frac{\widetilde{q}_{e\parallel}}{p_e} + 0.71\frac{\widetilde{J}_\parallel}{n_e e}\right)^2 + \frac{p_i}{\kappa_{\parallel i}}\left(\frac{\widetilde{q}_{i\parallel}}{p_i}\right)^2 + \mu_\parallel\left(\nabla_\parallel \widetilde{u}_\parallel\right)^2 \Bigg] \Bigg\}\end{aligned} \tag{3.104}$$

for a localised system, in which the total divergences vanish under the integral. Note the scaling against p_e, especially for $\widetilde{T}_i/T_e$. The first two lines on the right side give the sources, all gradient drive terms, and the last line gives the sinks, all resulting from collisional dissipation. Drive terms due to $J_\parallel\nabla_\parallel(p_e+p_i)$ vanish due to the relationship between $\widetilde{J}_\parallel$ and $\widetilde{\mathbf{B}}$ via $\widetilde{A}_\parallel$. We note the mutual cancellation of all $\mathcal{K}()$ terms, which proceeds similarly to the $\nabla_\parallel$ terms as both represent compression phenomena: $\mathcal{K}()$ is the quasistatic remnant of compression due to an inhomogeneous magnetic field, which is left behind after the drift approximation removes dynamical (wavelike) compression from the system. The operator $\mathcal{K}()$ is a first order differential operator, which possesses the linearity property. One therefore ends with expressions of the form $\mathcal{K}(f)$, with f a scalar, and these are total divergences, by Eq. (3.55).

3.VIII. Summary

To summarise this chapter, we have defined the drift approximation as a parameter limit in which we can take $k_\parallel/k_\perp$, δ, and β_e as arbitrarily small, and the frequencies Ω_i and $k_\perp v_A$ as arbitrarily fast. This leads to quasistatic, dynamically incompressible perpendicular dynamics while retaining compressibility along the magnetic field, hence allowing frequencies as fast as $k_\parallel v_A$. It follows that the electric field splits into an electrostatic $\mathbf{E}_\perp$ and an electromagnetic $E_\parallel$. Due to the smallness of δ the dynamics is allowed to be nonlinear at small relative amplitude, with disturbances obeying $\widetilde{n}_e/n_e \ll 1$ but $\nabla\widetilde{n}_e \sim \nabla n_e$. All $O(\delta)$ corrections are neglected, except for the polarisation drift, which under divergences reverts to $O(1)$. The gradient operator on disturbances is always an order larger than

on the background except for the first operation involving background gradients, so that although $\nabla\widetilde{n}_e \sim \nabla n_e$ we have $\nabla n_i \cdot \nabla\phi \ll n_i\nabla_\perp^2\phi$. Due to the flute mode ordering we can use ∇^2 and $\nabla_\perp^2$ interchangeably. The parallel structure of $\mathbf{B}$ is retained since all parallel wavelengths are comparable. A local model of nonlinear, turbulent dynamics is derived under the drift approximation, and the model satisfies a fluctuation free energy theorem in which background gradients appear as sources. Global energy is only conserved to first order in δ. A proper energy theorem and a model which conserves global energy exactly is deferred to Chapter 14, in which the properties of transport by fluid drift turbulence are considered.

Further Reading

Drift dynamics was considered for linear instabilities in the late 1950s and early 1960s, for which one can see S. S. Moiseev and R. Z. Sagdeev, *Sov. Phys. JETP* 17 (1963) 515, but the procedure for nonlinear dynamics involving polarisation was first systematically worked out by F. L. Hinton and C. W. Horton, Jr., in *Phys. Fluids* 14 (1971) 116, in which the diamagnetic cancellation involving gyroviscosity was demonstrated. The diamagnetic cancellation involving the heat flux was shown by S.-T. Tsai, F. W. Perkins, and T. H. Stix, in *Phys. Fluids* 13 (1970) 2108. The similar operations leading to reduced MHD were systematised by H. R. Strauss, in *Phys. Fluids* 20 (1976) 1354.

Systematic fluid drift equations involving the self consistent electron dynamics were developed by J. F. Drake and T. M. Antonsen, Jr., in *Phys. Fluids* 27 (1984) 898, following earlier work by D. A. Monticello and R. B. White, in *Phys. Fluids* 23 (1980) 366. The local forms were developed by B. Scott, A. B. Hassam, and J. F. Drake, in *Phys. Fluids* 28 (1985) 275, and by R. E. Waltz, in *Phys. Fluids* 28 (1985) 577.

Fluctuation free energy was developed as a concept to study drift waves, which will form the centerpiece of Chapter 5. It grew out of the first drift wave model to incorporate electron dynamics, by M. Wakatani and A. Hasegawa, in *Phys. Fluids* 27 (1984) 611, and was developed to diagnose the turbulence by B. Scott, in *Phys. Rev. Lett.* 65 (1990) 3289 and in *Phys. Fluids B* 4 [1992] 2468), and by R. E. Waltz, in *Phys. Fluids B* 2 (1990) 2118. This concept is descended from theorems which treat accessibility to free energy in rotating shear flows in geophysical fluid dynamics. Two excellent texts are *Atmosphere-Ocean Dynamics*, by A. Gill (Academic Press, 1982), and *Geophysical Fluid Dynamics*, by J. Pedlosky (Springer, 1987).

4. Parallel Dynamics — Alfvén and Sound Waves

B. Scott

Jul 1999

4.1. Introduction

The simplest way to examine the relationship between MHD and fluid drift dynamics, is to compare the properties of wavelike disturbances on a homogeneous background in both models. We encountered the sound waves and compressional and shear Alfvén waves in MHD in Chapter 2. Herein we study them under the fluid drift model and its reduced MHD subset in detail, especially the roles of the various terms in the free energy theorem for each system. In both cases, a sound wave is an oscillation of free energy between pressure disturbances and parallel (ion) mass flows, and a shear Alfvén wave is such an oscillation between magnetic field energy and (ion) ExB kinetic energy. The ions are referred to in parentheses, because the much less massive electrons contribute negligibly to the fluid kinetic energy. In the case of shear Alfvén waves, a substantial component of the energy which oscillates against the magnetic field can come from the pressure disturbances rather than the ExB flows. This is the case in which the single fluid MHD model breaks down, since under MHD the fluid pressure is not coupled to the magnetic field energy (equivalently, the electric current) at all in a homogeneous magnetic field. Alfvén waves whose parallel dynamics is coupled to the electron pressure in this fashion are called kinetic shear Alfvén waves, or simply kinetic Alfvén waves, due to their original derivation from kinetic theory. The excitation of a parallel current by the imbalance of the pressure and electrostatic forces is called an adiabatic response, since it tends towards maintenance of the state of adiabatic electrons, or force balance, so named due to its quasistatic nature on slower time scales.

The MHD model usually treats the most basic shear Alfvén waves as plane waves, as shown in Fig. 4.1. Under both reduced MHD and fluid drift dynamics, the basic mode is a torsional Alfvén wave, following from the description of incompressible velocity and magnetic field disturbances in terms of their stream functions, or potentials, as in Fig. 4.2. The basic motion is described by an oscillating ExB vortex which has different phases at different positions along the field lines. Drift dynamics departs from MHD by taking into account the coupling between this Alfvén dynamics and the electron pressure, as we develop in this chapter.

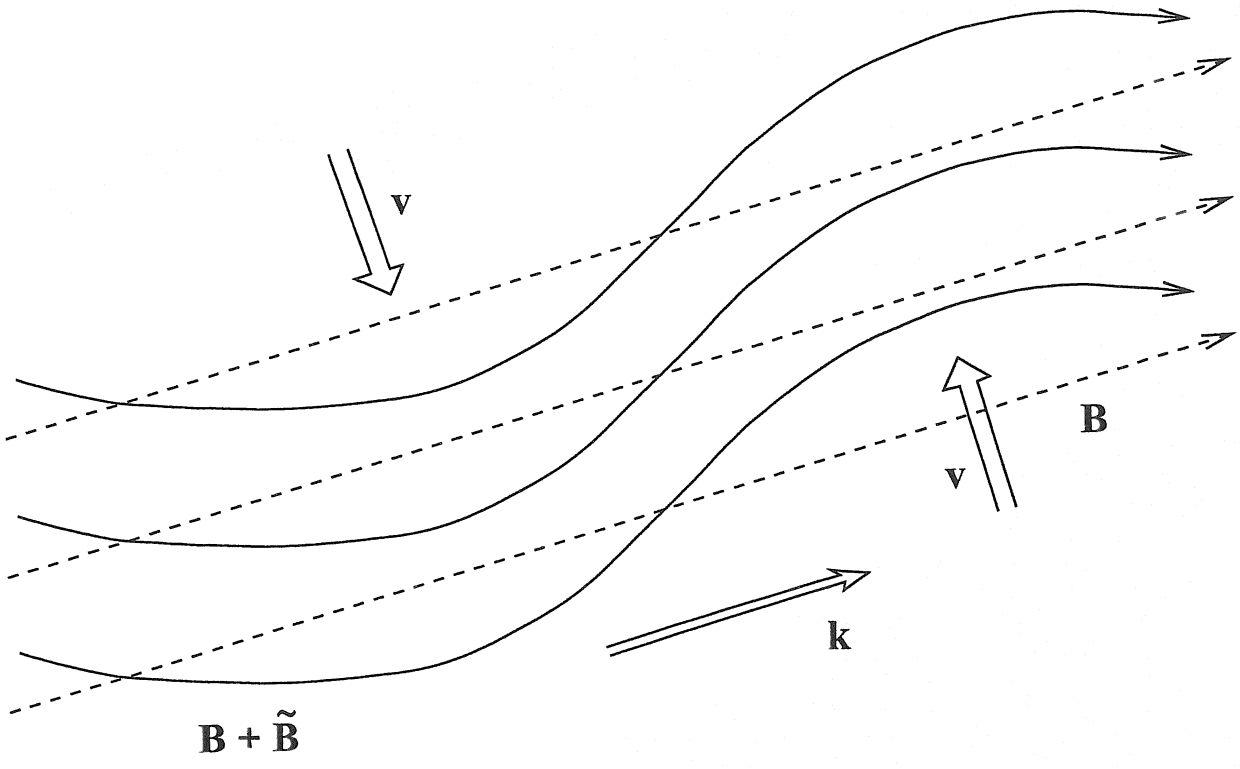

Figure 4.1. The conventional shear Alfvén wave under MHD, as a plane wave oscillation. The dashed lines show the undisturbed magnetic field lines, $\mathbf{B}$. Under the influence of the plasma flow ($\mathbf{v}$) across the magnetic field, the field lines are bent into the positions shown by the solid lines, $\mathbf{B}+\widetilde{\mathbf{B}}$. The effect of magnetic tension to oppose this deformation leads to transverse wave propagation ($\mathbf{k}$) along $\mathbf{B}$.

4.II. The Four Field Model of Fluid Drift Dynamics

In this and the next few chapters we will study the fundamental properties of the fluid drift dynamical model in qualitative form using the simplest possible model which still incorporates the necessary physics, that is, perpendicular ExB flows and parallel electron and ion dynamics, but neglecting the details of dissipation and some extra instabilities that go with the specific dynamics of the temperatures. Electron and ion temperature effects are deferred to Chapters 12 and 13, respectively.

We assume a single component plasma with singly charged ions and equal electron and ion densities. The key feature of the two fluids which gives them differing responses to a fluctuating electromagnetic field is their disparate unit masses; the electron/ion mass ratio is small, so that the inertia of the electrons in response to the field can often be neglected. This means that the faster electron response will govern how the plasma responds to

electric fields and currents, while the ion inertia will govern how the plasma responds to neutral flows. The principal examples of these are the shear Alfvén waves and sound waves, respectively. The dependent variables we need to keep are $\{\phi, p_e, A_{\|}, u_{\|}\}$, with $J_{\|}$ determined from $A_{\|}$ via Ampere's law. This is a situation in which the electrons provide the dynamics through their finite temperature (hence pressure), while the ions provide the inertia through their finite mass.

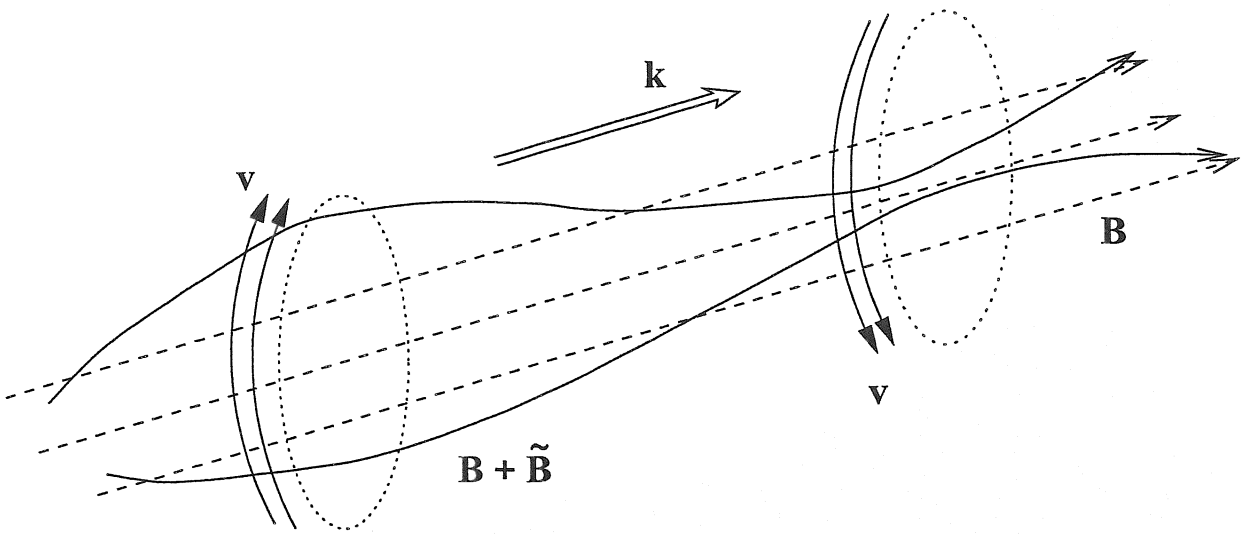

Figure 4.2. The same shear Alfvén wave oscillation, but localised to a flux tube with a finite radius in the perpendicular plane. The flow is now vortical, representing ExB eddy motion. The field lines are twisted, and again their curvature leads to magnetic tension which opposes the deformation. The magnetic disturbance ($\widetilde{\mathbf{B}}$) and ExB flow ($\mathbf{v}$) may be replaced by their respective stream functions, $\widetilde{A}_{\|}$ and $\widetilde{\phi}$. The result is the representation in terms of potentials under drift dynamics or reduced MHD, rather than in terms of vector fields as under pure MHD.

To find the model equations, we start with the dissipative drift dynamics model of Chapter 3, Sections VI and VII, and then set the temperature and heat flux disturbances to zero. We then eliminate the background gradient and magnetic divergence terms. The resulting four field model for small scale disturbances on a homogeneous background with resistive friction and ion viscosity appears as

$$\frac{d_E}{dt}\rho_s^2\nabla_\perp^2\frac{e\widetilde{\phi}}{T_e} = c_s\nabla_{\|}\frac{\widetilde{J}_{\|}}{nec_s} \tag{4.1}$$

$$\frac{d_E}{dt}\frac{\widetilde{p}_e}{p_e} = \Gamma c_s \nabla_\parallel \left(\frac{\widetilde{J}_\parallel}{nec_s} - \frac{\widetilde{u}_\parallel}{c_s} \right) \tag{4.2}$$

$$\beta_e \frac{\partial}{\partial t}\frac{\widetilde{A}_\parallel}{B\rho_s\beta_e} + \mu_e \frac{d_E}{dt}\frac{\widetilde{J}_\parallel}{nec_s} = c_s \nabla_\parallel \left(\frac{\widetilde{p}_e}{p_e} - \frac{e\widetilde{\phi}}{T_e} \right) - 0.51\mu_e\nu_e \frac{\widetilde{J}_\parallel}{nec_s} \tag{4.3}$$

$$\frac{d_E}{dt}\frac{\widetilde{u}_\parallel}{c_s} = -c_s \nabla_\parallel \frac{\widetilde{p}_e}{p_e} + \mu_\parallel \nabla_\parallel^2 \frac{\widetilde{u}_\parallel}{c_s} \tag{4.4}$$

with Ampere's law

$$\frac{\widetilde{J}_\parallel}{nec_s} = -\rho_s^2 \nabla_\perp^2 \frac{\widetilde{A}_\parallel}{B\rho_s\beta_e} \tag{4.5}$$

where the mass ratio and dynamical beta, assumed to be small, are

$$\mu_e = \frac{m_e}{M_i} \qquad \beta_e = \frac{c_s^2}{v_A^2} = \frac{4\pi p_e}{B^2} \tag{4.6}$$

and for the purposes of modelling we simply take the parallel viscosity, $\mu_\parallel$, and ratio of specific heats, Γ as free parameters. This is a convenient way to scale the equations, showing the symmetries among the various interactions. The nonlinear effects in d_E/dt and $\nabla_\parallel$ are still generally present, but for the purposes of studying waves, we will neglect them until they take center stage in Chapter 6.

To isolate the properties of wavelike motion we will first neglect dissipation entirely. Then, considering the initial value problem with some specific numerical examples we will reintroduce resistive friction and ion viscosity, showing how they act differently on the various waves.

4.III. Wavelike Motion Under Fluid Drift Dynamics

We saw in Chapter 2 how linearised wave oscillations on a homogeneous background are treated in the context of several different dynamical models, one of which was MHD. We now do the same for the simplified four field fluid drift model. All we need do to the above set of equations is to eliminate the nonlinear terms by taking

$$\frac{d_E}{dt} \to \frac{\partial}{\partial t} \qquad \nabla_\parallel \to \frac{\partial}{\partial s} \tag{4.7}$$

where s is a coordinate along the magnetic field given by $\mathbf{B} = B\nabla s$. The perpendicular plane may be represented by x and y, which are equivalent in the absence of gradients. The perpendicular operator $\nabla_\perp^2$ then becomes

$$\nabla_\perp^2 = \left(\frac{\partial^2}{\partial x^2} + \frac{\partial^2}{\partial y^2} \right) \tag{4.8}$$

These equations represent wave dynamics parallel to the magnetic field involving the state variables $\widetilde{\phi}$ and $\widetilde{p}_e$ and parallel flux variables $\widetilde{A}_{\parallel}$ and $\widetilde{u}_{\parallel}$, which are localised in the xy-plane such that

$$\nabla_{\perp}^2 \gg \nabla_{\parallel}^2 \tag{4.9}$$

and therefore (following the drift approximation) do not exhibit oscillatory wave dynamics perpendicular to the magnetic field.

A set of four equations for four dependent variables implies four distinct modes of oscillation — four eigenfunctions and their frequencies. In the case that both β_e and μ_e are small, we can split them into two pairs of two waves each. For frequencies much faster than $c_s \nabla_{\parallel}$ we can neglect $u_{\parallel}$ and combine $\widetilde{p}_e$ and $\widetilde{\phi}$ to form the following set of equations for the two faster waves,

$$\frac{\partial}{\partial t}\rho_s^2 \nabla_{\perp}^2 \left(\frac{\widetilde{p}_e}{p_e} - \frac{e\widetilde{\phi}}{T_e} \right) = \left(1 - \Gamma \rho_s^2 \nabla_{\perp}^2\right) c_s \nabla_{\parallel} \frac{\widetilde{J}_{\parallel}}{nec_s} \tag{4.10}$$

$$\beta_e \frac{\partial}{\partial t} \frac{\widetilde{A}_{\parallel}}{B\rho_s \beta_e} + \mu_e \frac{\partial}{\partial t} \frac{\widetilde{J}_{\parallel}}{nec_s} = c_s \nabla_{\parallel} \left(\frac{\widetilde{p}_e}{p_e} - \frac{e\widetilde{\phi}}{T_e} \right) \tag{4.11}$$

Using Eqs. (4.3,4.5) to eliminate $\widetilde{A}_{\parallel}$, we may further combine the two first order equations into one that is second order,

$$\left(\beta_e - \mu_e \rho_s^2 \nabla_{\perp}^2\right) \rho_s^2 \nabla_{\perp}^2 \frac{\partial^2}{\partial t^2} \left(\frac{\widetilde{p}_e}{p_e} - \frac{e\widetilde{\phi}}{T_e} \right) = \left(1 - \Gamma \rho_s^2 \nabla_{\perp}^2\right) \rho_s^2 \nabla_{\perp}^2 c_s^2 \nabla_{\parallel}^2 \left(\frac{\widetilde{p}_e}{p_e} - \frac{e\widetilde{\phi}}{T_e} \right) \tag{4.12}$$

We note that since $k_{\perp}^2$ is finite, we can cancel the common factor of $\rho_s^2 \nabla_{\perp}^2$ from both sides. This is now in the form of a wave equation, but the coefficients still depend on $\nabla_{\perp}^2$. What this means is that the speed of the wave in the parallel direction is dependent on the scale of motion in the perpendicular plane. Clearly, then, we still have three dimensional character to the dynamics: with $\widetilde{\phi}$ and $\widetilde{A}_{\parallel}$ serving as stream functions for $\mathbf{v}_E$ and $\widetilde{\mathbf{B}}_{\perp}$, we have vortical ExB motion and magnetic fluctuations in the perpendicular plane, coupled together by currents which flow in the parallel direction. However, as shown in Fig. 4.3, we have the situation that this Alfvénic activity, represented by the pair $(\mathbf{v}_E, \widetilde{\mathbf{B}}_{\perp})$, or $(\widetilde{\phi}, \widetilde{A}_{\parallel})$, is now coupled to the electron pressure disturbances, $\widetilde{p}_e$. This is seen in Eqs. (4.10–4.12), as it is the difference between $\widetilde{p}_e/p_e$ and $e\widetilde{\phi}/T_e$ to which $\widetilde{J}_{\parallel}$ interacts, not just $e\widetilde{\phi}/T_e$. The forces on the electrons are given by the pressure gradient as well as the electric field, and the imbalance drives the current. The stream function is now $e\widetilde{\phi}/T_e - \widetilde{p}_e/p_e$, for the perpendicular electron flow including the diamagnetic component, $\mathbf{v} = \mathbf{v}_E + \mathbf{v}_*$. The

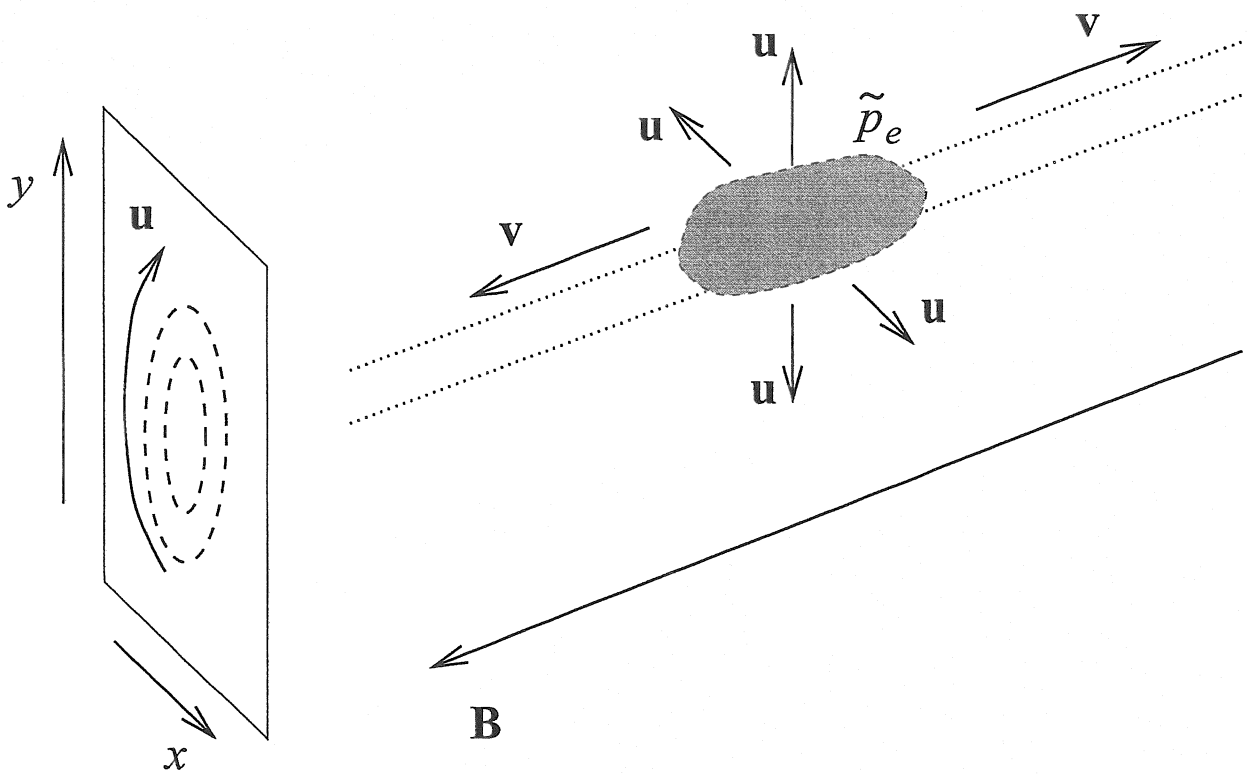

Figure 4.3. The kinetic shear Alfvén wave oscillation, localised to a flux tube in the xy-plane, caused by an initial electron pressure disturbance. The parallel pressure gradient gives rise to parallel electron flows ($\mathbf{v}$) which are balanced by the ion polarisation drift ($\mathbf{u}$). Both species have their ExB drifts, which do not cause a net current. As the electron current oscillates in the direction of $\mathbf{B}$, the ion flow spirals into and out of the flux tube as a correction to the ExB flow, which is along the dashed circles drawn in the xy-plane. The response of the pressure disturbance depends on the perpendicular scale of the flux tube; if this scale is close to ρ_s, substantial parallel displacement of the pressure disturbance results. Under MHD or reduced MHD, there would be no response of the pressure to the Alfvén dynamics, and the pressure disturbance would not give rise to ExB flows. There would be no response to an initial pressure disturbance, other than sound waves.

existence of $\widetilde{J}_{\parallel}$ with the finite $\nabla_{\parallel}$ with which it is excited drives both $\widetilde{p}_e$ and $\widetilde{\phi}$ so as to restore balance between the two forces. The polarisation current arises to balance $\widetilde{J}_{\parallel}$, preserving $\nabla \cdot \mathbf{J} = 0$ overall.

If we Fourier decompose the disturbances in the perpendicular plane, we find that

each component has its own wave speed. The wave equation becomes

$$\frac{\partial^2}{\partial t^2}\left(\frac{\widetilde{p}_e}{p_e}-\frac{e\widetilde{\phi}}{T_e}\right)=V_a^2\nabla_\parallel^2\left(\frac{\widetilde{p}_e}{p_e}-\frac{e\widetilde{\phi}}{T_e}\right) \tag{4.13}$$

with the wave speed V_a given by

$$V_a^2=\frac{1+\Gamma k_\perp^2\rho_s^2}{\beta_e+\mu_e k_\perp^2\rho_s^2}\,c_s^2=\frac{1+\Gamma k_\perp^2\rho_s^2}{1+k_\perp^2\sigma_0^2}\,v_A^2 \tag{4.14}$$

where σ_0 is the collisionless skin depth given by

$$\sigma_0^2=\frac{c^2}{\omega_{pe}^2}=\frac{m_e c^2}{4\pi n e^2}=\frac{\mu_e}{\beta_e}\,\rho_s^2 \tag{4.15}$$

If we take the limit $k_\perp^2\rho_s^2\to 0$, we find propagation at the Alfvén speed

$$\lim_{k_\perp^2\to 0} V_a = v_A \tag{4.16}$$

This limit corresponds to the single fluid MHD torsional shear Alfvén waves, for which all scales propagate at v_A. We note the possibility of $k_\perp^2\rho_s^2\to 0$ within the drift approximation, so long as we still satisfy $\nabla_\perp^2 \gg \nabla_\parallel^2$ and hence that parallel (shear) Alfvén motion is arbitrarily slow compared to perpendicular (compressional) Alfvén motion. If on the other hand we take $k_\perp^2\rho_s^2\to\infty$, we find propagation at the electron thermal speed

$$\lim_{k_\perp^2\to\infty} V_a = V_e \tag{4.17}$$

corresponding to electrostatic dynamics with electromagnetic induction ($\widetilde{A}_\parallel$) now negligible compared to electron inertia ($\widetilde{J}_\parallel$).

The dependence of the wave propagation parallel to the magnetic field on the scale of motion perpendicular to the field is apparent in this dispersion relation, as shown in Fig. 4.4. The two velocities, v_A and V_e, represent the limits of the fastest and slowest speeds at which kinetic shear Alfvén waves propagate, but which is the faster depends on whether β_e is larger or smaller than μ_e. The waves with the largest perpendicular scales propagate at v_A, reflecting ideal MHD behaviour, with $\widetilde{\phi}$ and $\widetilde{A}_\parallel$ interacting such that $E_\parallel = 0$, that is, the wave is an oscillation between the inductive and static parts of the electric field, or similarly between the parallel and polarisation currents. At the smallest perpendicular scales the waves propagate at V_e, reflecting electrostatic dynamics between $\widetilde{p}_e$ and $\widetilde{J}_\parallel$. The existence of this electrostatic limit is possible only within the drift model, as it results from the coupling between the electron pressure and the Alfvénic activity.

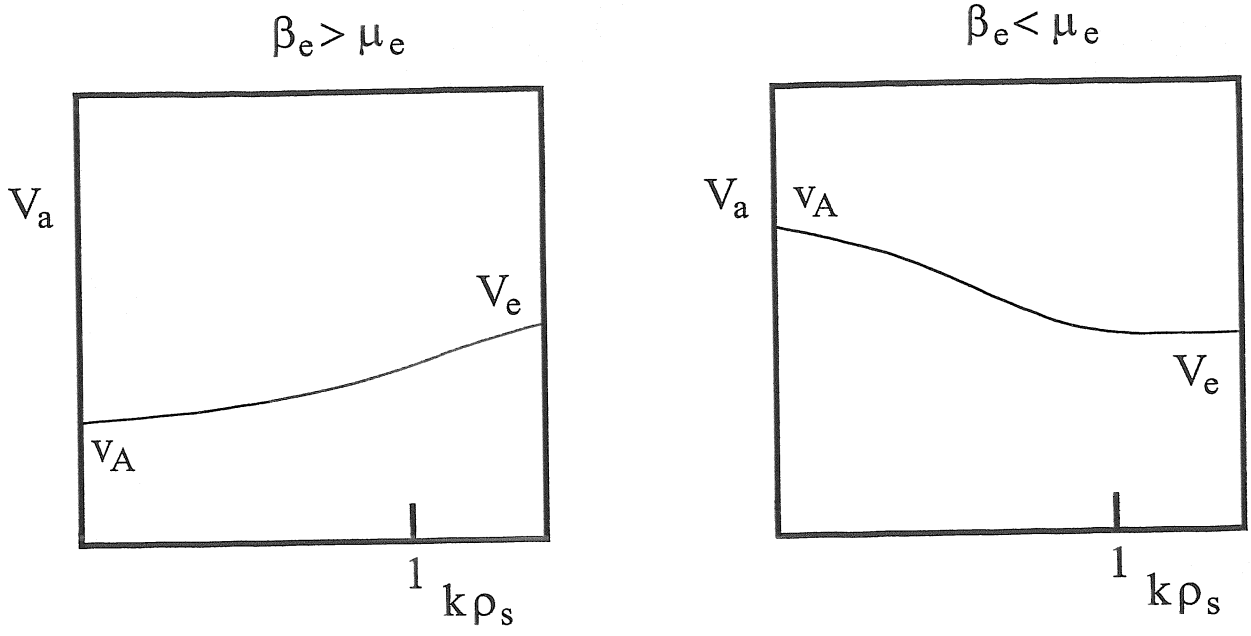

Figure 4.4. The kinetic shear Alfvén wave dispersion relation, showing the propagation velocity, V_a, as a function of the inverse perpendicular scale, $k_\perp$. For $\beta_e > \mu_e$ (left) V_a rises with $k_\perp$, and for $\beta_e < \mu_e$ (right) it falls with rising $k_\perp$. In both cases, the large scale limit is the Alfvén speed, v_A, reflecting ideal MHD between $\widetilde{\phi}$ and $\widetilde{A}_\parallel$, and the small scale limit is the electron thermal speed, V_e, reflecting electrostatic dynamics between $\widetilde{p}_e$ and $\widetilde{J}_\parallel$. The speed of parallel electron dynamics is always between these two limits.

The two perpendicular scales, ρ_s and σ_0, therefore place limits on whether the single fluid MHD model with massless electrons is applicable to the treatment of parallel dynamics. The skin depth merely brings in finite electron inertia to control the propagation speed, but the drift scale brings in the part of the dynamics which involves the electron thermodynamics through $\widetilde{p}_e$. If $k_\perp^2 \rho_s^2$ is finite, then the interaction between the electron pressure and the compression along $\mathbf{B}$ is important in distinguishing electron and ion dynamics. Plasma pressure does not couple to shear Alfvén dynamics in single fluid MHD, but it in general it does so.

The other two waves in the four field model are found by assuming slower frequencies, such that the two kinetic shear Alfvén waves are not excited. We find this limit by assuming the state often referred to as "adiabatic electrons"

$$\frac{\widetilde{p}_e}{p_e} = \frac{e\widetilde{\phi}}{T_e} \tag{4.18}$$

which results from the demand that the eigenfunctions of the kinetic shear Alfvén waves are at zero amplitude, hence that both sides of Eqs. (4.10–4.12) vanish. The name "adiabatic" refers to the quasistatic evolution of the electric fields, with the electrons progressing through successive states of force balance. We subtract Eq. (4.1) from Eq. (4.2) and insert Eq. (4.18) to find

$$\left(1 - \rho_s^2 \nabla_\perp^2\right) \frac{\partial}{\partial t} \frac{\widetilde{p}_e}{p_e} = -\Gamma c_s \nabla_\parallel \frac{\widetilde{u}_\parallel}{c_s} \tag{4.19}$$

$$\frac{\partial}{\partial t} \frac{\widetilde{u}_\parallel}{c_s} = -c_s \nabla_\parallel \frac{\widetilde{p}_e}{p_e} \tag{4.20}$$

having also assumed that $\widetilde{J}_\parallel \to 0$ due to its coupling to departures from Eq. (4.18) via the kinetic shear Alfvén dynamics. Performing the Fourier decomposition of the xy-plane and combining the two equations into one, we find another wave equation,

$$\left(1 + \Gamma k_\perp^2 \rho_s^2\right) \frac{\partial^2}{\partial t^2} \frac{\widetilde{p}_e}{p_e} = \Gamma c_s^2 \nabla_\parallel^2 \frac{\widetilde{p}_e}{p_e} \tag{4.21}$$

Propagation of these sound waves occurs at the velocity V_p given by

$$V_p^2 = \frac{\Gamma}{1 + \Gamma k_\perp^2 \rho_s^2} c_s^2 \tag{4.22}$$

This reveals c_s as the isothermal, cold ion sound speed, since for isothermal electrons we would have $\Gamma = 1$.

In the single fluid MHD limit ($k_\perp^2 \to 0$) the sound waves and shear Alfvén waves propagate with velocities given by V_s and v_A, respectively, with c_s the isothermal limit of V_s. When $k_\perp^2 \rho_s^2$ becomes finite, both velocities are altered. The sound waves slow down with $k_\perp^2 \rho_s^2$, while the kinetic Alfvén waves go towards propagation at V_e as both $k_\perp^2 \rho_s^2$ and $k_\perp^2 \sigma_0$ become larger than unity (note that V_e^2 is β_e/μ_e times v_A^2, as ρ_s^2 is β_e/μ_e times σ_0^2). In all cases, these two pairs of waves form a complete set of eigenmodes for the four field model on a homogeneous background. The propagation speed in the parallel direction depends on $k_\perp$ rather than $k_\parallel$, giving the dispersion an interesting character: for propagation of waves within a thin flux tube, differing Fourier modes propagate at differing speeds, so that an initial structure will "dephase" if its perpendicular extent is comparable to ρ_s. It is important to note that while the mathematics is suggestive of longitudinal wave propagation — scalar variables depending on s and propagating along ∇s — the ExB fluid motion and the magnetic disturbances have directions in the perpendicular plane. The scalar variables ϕ and $A_\parallel$ are only useful in describing shear Alfvén propagation if their perpendicular extent is limited; *i.e.*, we require $\nabla_\perp^2 \gg \nabla_\parallel^2$. But this is the usual situation.

On fast time scales, with $\tau \sim (k_\parallel V_a)^{-1}$, the sound waves appear as zero frequency modes. The two quantities that change only slowly are $\widetilde{u}_\parallel$, which is clear, and something which sometimes goes by the name of total enstrophy,

$$\frac{\partial}{\partial t}\left(\frac{\widetilde{p}_e}{p_e} - \Gamma\rho_s^2\nabla_\perp^2\frac{e\widetilde{\phi}}{T_e}\right) = 0 \tag{4.23}$$

This is the third equation we find if we set $\widetilde{u}_\parallel$ to zero in Eqs. (4.1–4.4). Although $\widetilde{p}_e$ and $\widetilde{\phi}$ vary rapidly, through their difference $\widetilde{p}_e - \widetilde{\phi}$, the pressure and ExB vorticity always vary together. What this represents is a variation of the density, here $\widetilde{p}_e/T_e$, in response to the divergence in the current carries by one of the species. For electrons this is $\nabla_\parallel \widetilde{J}_\parallel$. For ions it is the polarisation divergence, which balances $\widetilde{J}_\parallel$ such that the total $\nabla \cdot \mathbf{J}$ remains zero. We will return to this point when discussing the transport of density/pressure by the electric current, below.

4.IV. Energetics of Kinetic Shear Alfvén and Sound Waves, Dissipation

The four field model has a relatively simple free energy theorem in the absence of background gradients. Its construction follows the same procedure as in Chapter 3, Section VII. The free energy density is

$$\frac{U}{p_e} = \frac{\mathbf{v}_E^2 + \widetilde{u}_\parallel^2}{2c_s^2} + \frac{\widetilde{\mathbf{B}}^2}{8\pi p_e} + \frac{\mu_e}{2}\left|\frac{\widetilde{J}_\parallel}{nec_s}\right|^2 + \frac{1}{2\Gamma}\left|\frac{\widetilde{p}_e}{p_e}\right|^2 \tag{4.24}$$

Explicitly substituting the definitions of $\mathbf{v}_E$ and $\widetilde{\mathbf{B}}$, this becomes

$$\frac{U}{p_e} = \frac{1}{2}\left|\rho_s\nabla_\perp\frac{e\widetilde{\phi}}{T_e}\right|^2 + \frac{1}{2}\left|\frac{\widetilde{u}_\parallel}{c_s}\right|^2 + \frac{\beta_e}{2}\left|\rho_s\nabla_\perp\frac{\widetilde{A}_\parallel}{B\rho_s\beta_e}\right|^2 + \frac{\mu_e}{2}\left|\frac{\widetilde{J}_\parallel}{nec_s}\right|^2 + \frac{1}{2\Gamma}\left|\frac{\widetilde{p}_e}{p_e}\right|^2 \tag{4.25}$$

If for purposes of clarity we simply re-express these scaled units as normalised quantities, we find for the linearised equations

$$\frac{\partial}{\partial t}\nabla_\perp^2\widetilde{\phi} = \nabla_\parallel\widetilde{J}_\parallel \tag{4.26}$$

$$\frac{\partial\widetilde{p}_e}{\partial t} = \Gamma\nabla_\parallel\widetilde{J}_\parallel - \Gamma\nabla_\parallel\widetilde{u}_\parallel \tag{4.27}$$

$$\beta_e\frac{\partial\widetilde{A}_\parallel}{\partial t} + \mu_e\frac{\partial\widetilde{J}_\parallel}{\partial t} = \nabla_\parallel\widetilde{p}_e - \nabla_\parallel\widetilde{\phi} - 0.51\mu_e\nu_e\widetilde{J}_\parallel \tag{4.28}$$

$$\frac{\partial\widetilde{u}_\parallel}{\partial t} = -\nabla_\parallel\widetilde{p}_e + \mu_\parallel\nabla_\parallel^2\widetilde{u}_\parallel \tag{4.29}$$

with $\widetilde{J}_\parallel = -\nabla_\perp^2 \widetilde{A}_\parallel$, where $\nabla_\perp^2$ is normalised in terms of ρ_s^2. For the free energy density we find

$$U = \frac{1}{2}\left(\left|\nabla_\perp \widetilde{\phi}\right|^2 + \frac{\widetilde{p}_e^2}{\Gamma} + \beta_e \left|\nabla_\perp \widetilde{A}_\parallel\right|^2 + \mu_e \widetilde{J}_\parallel^2 + \widetilde{u}_\parallel^2\right) \tag{4.30}$$

which satisfies

$$\frac{\partial U}{\partial t} = -0.51 \mu_e \nu_e \widetilde{J}_\parallel^2 - \mu_\parallel \left|\nabla_\parallel \widetilde{u}_\parallel\right|^2 + \nabla \cdot (\cdots) \tag{4.31}$$

The total free energy is the integral of U over the spatial domain, and in a periodic domain the divergence terms vanish under the integral. That is, the free energy decays according to resistive and viscous dissipation only, and there are no sources. These equations are normalised in terms of the periodicity length in the parallel direction given by $2\pi/K_\parallel$, with the time scaled against $K_\parallel c_s$, since in the neglect of background gradients the only important perpendicular scales are ρ_s and σ_0.

We can examine the various transfer effects by looking at the pieces of $\partial U/\partial t$ together. Variously, we find them by multiplying the equation for $\nabla_\perp^2 \widetilde{\phi}$ with $-\widetilde{\phi}$, the equation for $\widetilde{p}_e$ with $\widetilde{p}_e$, the equation for $\widetilde{A}_\parallel$ and $\widetilde{J}_\parallel$ with $\widetilde{J}_\parallel$, and the equation for $\widetilde{u}_\parallel$ with $\widetilde{u}_\parallel$. We note that the effective electron inertia is actually only one piece, due to Ampere's law,

$$\widetilde{J}_\parallel = -\nabla_\perp^2 \widetilde{A}_\parallel \qquad \beta_e \frac{\partial \widetilde{A}_\parallel}{\partial t} + \mu_e \frac{\partial \widetilde{J}_\parallel}{\partial t} = \left(\beta_e - \mu_e \nabla_\perp^2\right) \frac{\partial \widetilde{A}_\parallel}{\partial t} \tag{4.32}$$

These pieces of the free energy theorem appear as

$$\frac{\partial}{\partial t} \frac{1}{2} \left|\nabla_\perp \widetilde{\phi}\right|^2 = \widetilde{J}_\parallel \nabla_\parallel \widetilde{\phi} \tag{4.33}$$

$$\frac{\partial}{\partial t} \frac{\widetilde{p}_e^2}{2\Gamma} = -\widetilde{J}_\parallel \nabla_\parallel \widetilde{p}_e + \widetilde{u}_\parallel \nabla_\parallel \widetilde{p}_e \tag{4.34}$$

$$\frac{\partial}{\partial t} \frac{\beta_e}{2} \left|\nabla_\perp \widetilde{A}_\parallel\right|^2 + \frac{\partial}{\partial t} \frac{\mu_e \widetilde{J}_\parallel^2}{2} = \widetilde{J}_\parallel \nabla_\parallel \widetilde{p}_e - \widetilde{J}_\parallel \nabla_\parallel \widetilde{\phi} - 0.51 \mu_e \nu_e \widetilde{J}_\parallel^2 \tag{4.35}$$

$$\frac{\partial}{\partial t} \frac{\widetilde{u}_\parallel^2}{2} = -\widetilde{u}_\parallel \nabla_\parallel \widetilde{p}_e - \mu_\parallel \left|\nabla_\parallel \widetilde{u}_\parallel\right|^2 \tag{4.36}$$

neglecting several terms which appear as total divergences. Terms appearing in two different equations with opposite sign represent transfer mechanisms, while terms appearing only once represent sources and sinks. The divergence terms represent transport of free energy due to fluxes, which does not concern us at the moment.

There are three pathways of free energy coupling, all of which go through the terms with one factor of $\nabla_\parallel$. Two of them appear also in single fluid MHD: the shear Alfvén coupling between $\widetilde{\phi}$ and $\widetilde{J}_\parallel$ over $\widetilde{J}_\parallel \nabla_\parallel \widetilde{\phi}$ and the sound wave coupling between $\widetilde{p}_e$ and $\widetilde{u}_\parallel$

over $\widetilde{u}_{\|}\nabla_{\|}\widetilde{p}_e$. As noted above, there is no direct coupling between $\widetilde{\phi}$ or $\widetilde{J}_{\|}$ and $\widetilde{p}_e$ in single fluid MHD, due to the absence of $\nabla_{\|}\widetilde{p}_e$ in Ohm's law and $\nabla_{\|}\widetilde{J}_{\|}$ in the pressure equation. But in drift dynamics these two terms create a third coupling, between $\widetilde{p}_e$ and $\widetilde{J}_{\|}$ over $\widetilde{J}_{\|}\nabla_{\|}\widetilde{p}_e$, which we can refer to as the kinetic shear Alfvén transfer mechanism. As $\widetilde{\phi}$ and $\widetilde{J}_{\|}$ are already coupled through the basic shear Alfvén dynamics, this ultimately represents a coupling through the parallel electron dynamics between $\widetilde{\phi}$ and $\widetilde{p}_e$. In terms of transport of thermodynamic quantities by the ExB velocity, this represents a coupling between the principal transported quantity and the advective velocity doing the transporting. As we will see in later chapters (especially Chapters 7 and 11), this gives fluid drift turbulence some very important distinctions when compared to such simple concepts as random mixing. Simply put, this kinetic shear Alfvén coupling is the hallmark feature of fluid drift dynamics in general, and drift wave physics in particular.

4.V. Initial Value Problem with Dissipation

We can further emphasise the kinetic shear Alfvén coupling between pressure and ExB flows by considering the transient response of the plasma to an initial pressure disturbance. We assume that $\beta_e \ll 1$ and $\mu_e \ll 1$, while ν_e and $\mu_{\|}$ are finite. The initial disturbance $\widetilde{p}_e(x,y,s)$ is set up such that $\nabla_{\perp}^2 \gg \nabla_{\|}^2$; that is, it is a flute mode disturbance localised in all three dimensions, with most of the dynamics occurring in a thin flux tube of radius $\Delta_{\perp} \gtrsim \rho_s$ and length $\Delta_{\|}$, dimensions basically set by those of the initial $\widetilde{p}_e$. We set this up such that $\widetilde{p}_e$ is the only nonzero disturbance; the other three dependent variables start at zero. A simple example of this is

$$\widetilde{p}_e(x,y,s,t=0) = \widetilde{p}_0 \exp\left[-\left(x^2+y^2\right)/\Delta_{\perp}^2\right] \exp\left[-s^2/\Delta_{\|}^2\right] \tag{4.37}$$

where $\widetilde{p}_0$ is the initial amplitude. For a periodic domain the disturbance is considered well localised if $K_{\|}\Delta_{\|}$ is well larger than unity.

In single fluid MHD the only response would be sound waves: $\widetilde{p}_e$ forces $\widetilde{u}_{\|}$ and $\widetilde{u}_{\|}$ re-forces $\widetilde{p}_e$. There would be no Alfvénic activity, as $\widetilde{\phi}$ and $\widetilde{J}_{\|}$ would be zero for all time. But what actually happens is that the finite pressure gradient forces the electron fluid such that $\widetilde{J}_{\|}$ rises away from zero, starting the shear Alfvén activity. It is important to note that with the initial finite $\widetilde{p}_e$ we always get shear Alfvén waves, no matter what the parameters; basically, no matter how small $\rho_s^2\nabla_{\perp}^2$ is. If we are in the MHD regime because $\Delta_{\perp} \gg \rho_s$, we do not get a kinetic shear Alfvén oscillation, because in that case $\nabla_{\|}\widetilde{J}_{\|}$ is a negligible force on $\widetilde{p}_e$. However, the finite $\widetilde{p}_e$ always launches the Alfvén waves, whose amplitude is given by the adiabatic response: $e\widetilde{\phi}/T_e \sim \widetilde{p}_e/p_e$.

Dissipation of the Alfvénic activity proceeds through resistivity ($0.51\mu_e\nu_e$) in the four field model, while the sound wave response is damped by the parallel viscosity ($\mu_\parallel$). The viscous damping rate is simply $\mu_\parallel\nabla_\parallel^2$, or somewhat faster than $\mu_\parallel\Delta_\parallel^{-2}$. The resistive damping rate is complicated by the presence of β_e; the kinetic shear Alfvén response damps roughly as $0.51\mu_e\nu_e\Delta_\perp^{-2}/\beta_e$, or about $\sigma_0^2/\Delta_\perp^2$ times ν_e, in physical units. If oscillations are forced at a given frequency ω, the quantity $\sigma_0(\nu_e/\omega)^{1/2}$ is often referred to as the collisional skin depth.

4.VI. Numerical Examples

We illustrate the combined action of kinetic shear Alfvén waves and sound waves by taking two example sets of parameters, and looking at large and small perpendicular scale responses for each. Large and small scales are taken to be $K = k_\perp\rho_s = 0.1$ and 1.0, respectively, for single Fourier components in the perpendicular plane. The parallel direction is assumed to be periodic on a length $2\pi/K_\parallel$. The initial state for the Fourier component $k_\perp$ is given by

$$p_e(\mathbf{k}_\perp) = \exp\left[-\left(6K_\parallel s\right)^2\right] \tag{4.38}$$

and we solve Eqs. (4.26–4.29) with $\nabla_\perp^2$ replaced by $-K^2$ and with $\Gamma = 1$. Since in this model $\nabla_\perp$ always appears in the form of $\nabla_\perp^2$, all coefficients of the equations are real and we can therefore use $\widetilde{p}_e$ and $p_e(\mathbf{k}_\perp)$ interchangeably, so long as we recall that we are keeping only one Fourier component.

For this study the equations were discretised on a uniform grid of 128 nodes in the s-direction with step size $h_s = 2\pi/128K_\parallel$, and the time step was set to $\tau = 0.8h_s/V_a$. The numerical scheme was the one detailed in Appendix A.

A warm plasma case, appropriate to the outer regions of magnetically confined fusion plasma experiments, is given by

$$\beta_e = 5\times10^{-4} \qquad \mu_e = 3670^{-1} \qquad \nu_e = 1000K_\parallel c_s \qquad \mu_\parallel = 0.1c_sK_\parallel^{-1} \tag{4.39}$$

with the value of μ_e reflecting deuterium ions. A hot plasma case, appropriate to the core regions of such experiments, is given by

$$\beta_e = 10^{-2} \qquad \mu_e = 3670^{-1} \qquad \nu_e = 1.0K_\parallel c_s \qquad \mu_\parallel = 0.1c_sK_\parallel^{-1} \tag{4.40}$$

The resulting transient activity for the two cases with $K = 0.1$ is shown in Figs. 4.5(a–c). In each frame (on a separate page) the free energy pieces in Eqs. (4.33–4.36) are shown in the left column and the total free energy, the resistive and sound wave damping rates, and the total damping rate and numerical error are shown in the right column. On the

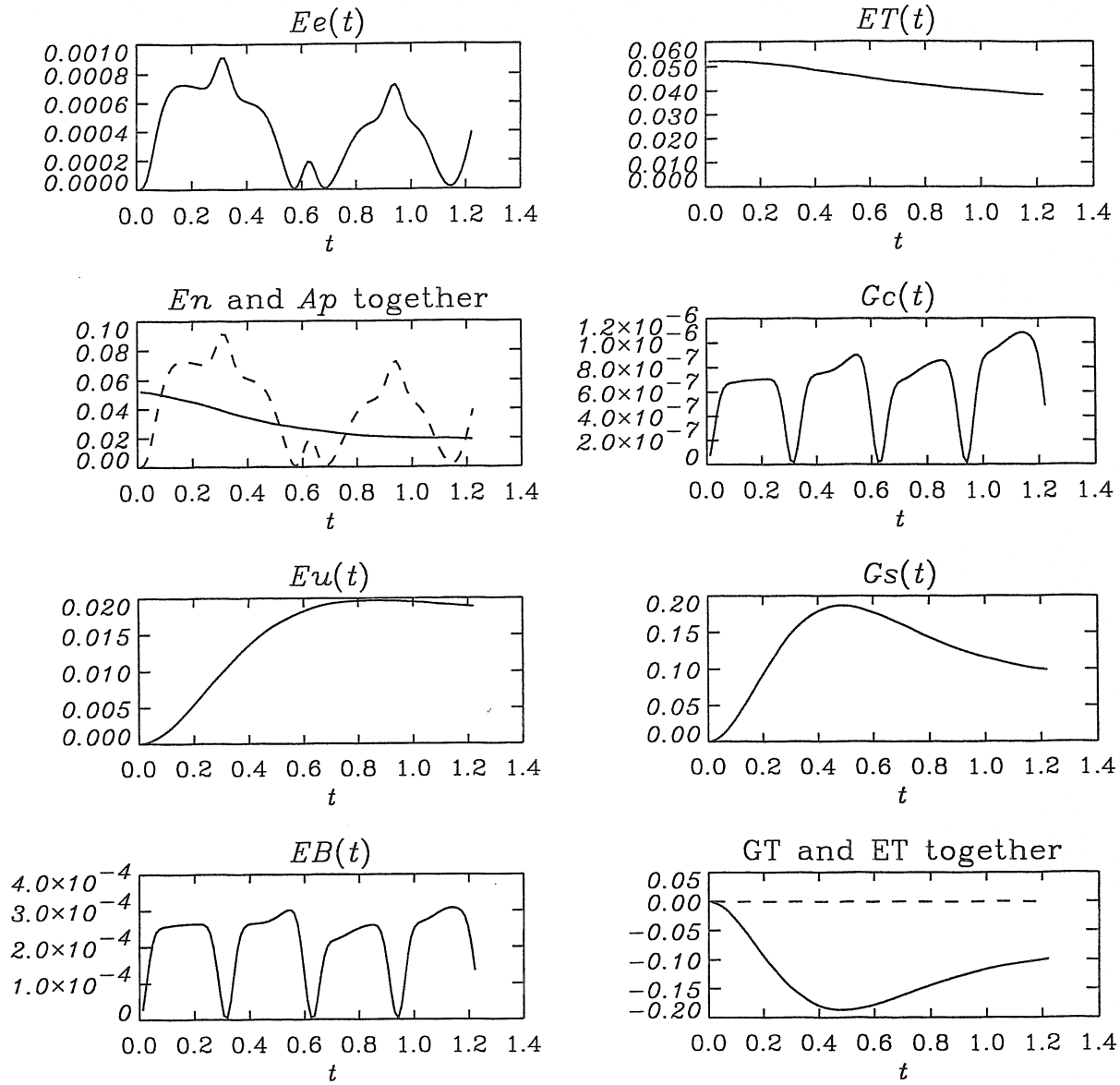

Figure 4.5a. Time evolution of the energetic quantities in a kinetic shear Alfvén wave oscillation, for the hot plasma case with $K = 0.1$, on the Alfvén time scale. The potential and magnetic field oscillate together, and the sound waves begin to oscillate and damp. The quantities Ee, En, Eu, and EB give the contributions of $\widetilde{\phi}$, $\widetilde{p}_e$, $\widetilde{u}_{\|}$, and $\widetilde{A}_{\|}$ to the total energy (ET), respectively. The integrated squared amplitude of $\widetilde{\phi}$ (Ap) follows that of $\widetilde{p}_e$ (En). The damping rates Gc and Gs are due to resistivity and viscosity, respectively. The total growth rate (GT) is much larger than the error (GE).

fast time scale for the hot case (a) we find the initial Alfvénic response, with the ExB and magnetic energies rising to peak values within about $\Delta t = 0.3$. The complicated waveforms reflect the excitation of several $k_{\|}$ values. The resistive damping follows the

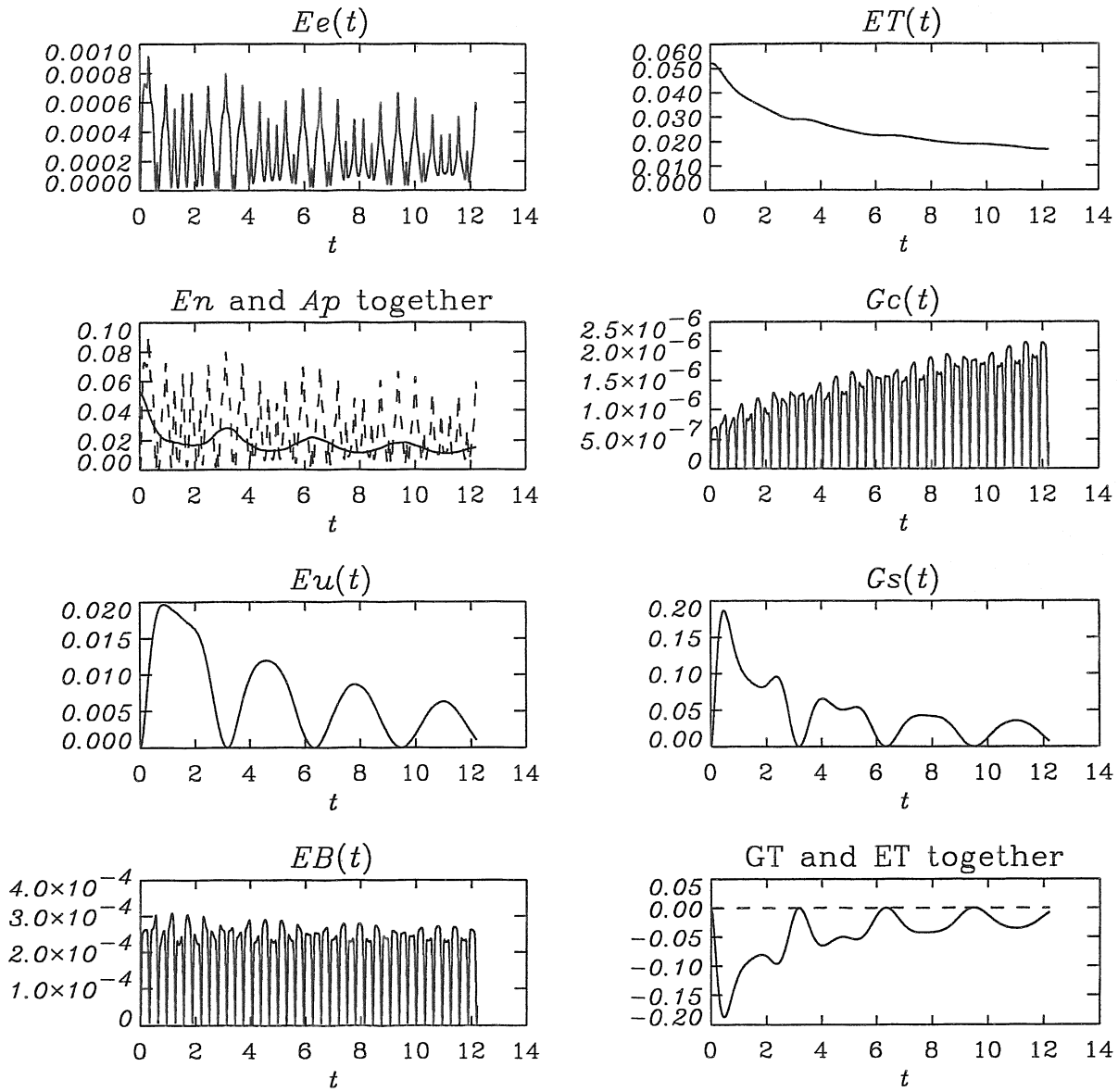

Figure 4.5b. Time evolution of the energetic quantities in a kinetic shear Alfvén wave oscillation, for the hot plasma case with $K = 0.1$, as in Fig. 4.5a, but on the sound time scale. The pressure and parallel ion velocity oscillate together as Alfvén waves proceed through many periods. Essentially all of the damping is due to the viscosity.

magnetic energy, through $\widetilde{J}_{\|}$. The sound wave damping follows $\widetilde{u}_{\|}$. On the slow time scale for the same case (b) we find very weak damping of the Alfvén activity, due to the relatively high β_e and small K. We find the sound wave activity damping actually faster, with the total energy damping unsteadily due to the oscillation of $\widetilde{u}_{\|}$. For the warm plasma case (c) we find the faster Alfvénic activity damping resistively, while sound waves with

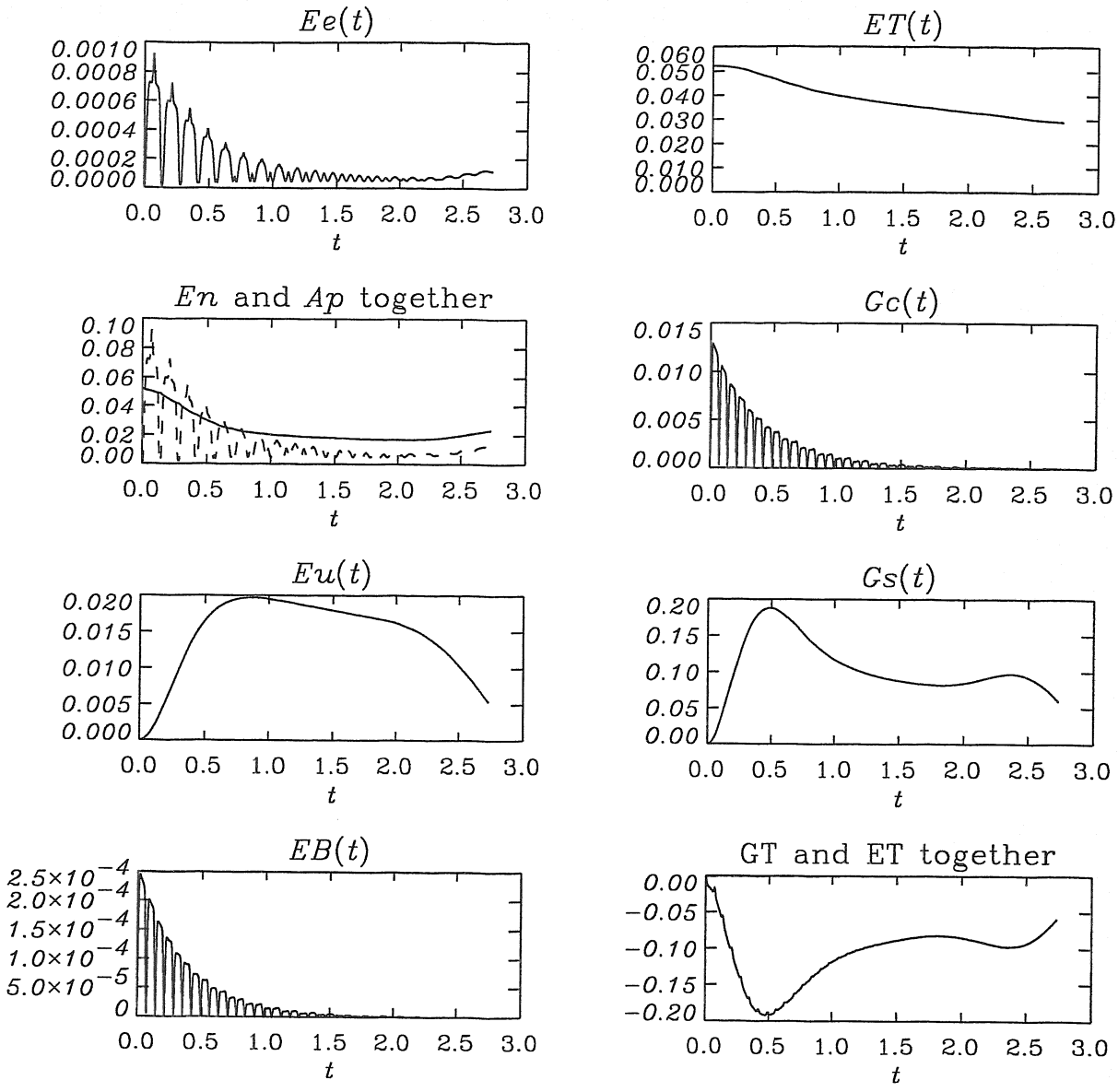

Figure 4.5c. Time evolution of the energetic quantities in a kinetic shear Alfvén wave oscillation, for the warm plasma case with $K = 0.1$, on the sound time scale. Although even here most of the damping is due to the viscosity, the resistivity is what damps the Alfvénic activity. Ee and Ap remain finite, as the sound waves evolve with adiabatic electrons, but EB drops away to zero.

adiabatic electrons survive for longer periods, still viscously damped. The $K = 1.0$ cases are not shown, but they are similar except for one important fact: the oscillation between $\widetilde{p}_e$ and the Alfvénic activity is stronger, with the result that $\widetilde{p}_e$ is actually transported by this activity. We display this for the hot plasma case in the next section.

In all cases we find that most of the damping in terms of energy is through $\mu_{\|}$, *i.e.*,

the sound waves. This is damping on $\widetilde{u}_{\parallel}$ and by extension on $\widetilde{p}_e$. The Alfvén dynamics, however, proceeds independently of this, damped only through the resistivity. The overall damping rate follows the sound waves since with $K < 1.0$ the ExB flow energy is smaller than the pressure disturbance free energy even with similar amplitudes in $\widetilde{\phi}$ and $\widetilde{p}_e$. For the hot plasma case, this Alfvén damping rate is very small, due to the largeness of β_e/μ_e, especially for $K = 0.1$ as the damping scales as K squared.

4.VII. Transport of Density/Pressure by the Electric Current

A very interesting question posed by the foregoing results is the prospect that disturbances in the plasma density and pressure may be spread out along the magnetic field lines by this Alfvénic activity rather than by the sound waves. In MHD this is anathema, since the plasma thermodynamical quantities behave in parallel dynamics just like a fluid. We can illustrate this contrast very well by taking the hot plasma case and restricting to a pure kinetic shear Alfvén case by neglecting Eq. (4.29) and setting the sound wave activity $(\nabla_{\parallel}\widetilde{u}_{\parallel})$ to zero in Eq. (4.27).

The resulting evolution for $K = 0.1$ is shown in Fig. 4.9. Apart from the fact that it is a pressure disturbance doing the initial launching, we find the familiar shear Alfvén waves of MHD, with negligible effect on $\widetilde{p}_e$. If ρ_s takes its typical tokamak core value of 1 mm, this corresponds to a pellet with a diameter of about 3 cm. For $K = 0.3$ (pellet diameter 1 cm) we have a marginal case; the density/pressure disturbance changes only slightly, but we see a visible pulse in it which follows $\phi(\mathbf{k}_{\perp})$, in other words, the Alfvén waves. Finally, the result for $K = 1.0$, corresponding to a small but not tiny pellet diameter of 3 mm is displayed in Fig. 4.10. We find about half the density disturbance taking direct part in the Alfvénic activity. The fraction scales roughly as $K^2/\left(1+K^2\right)$, following from the absence of a $\nabla_{\perp}^2$ factor between $\widetilde{p}_e$ and $\widetilde{J}_{\parallel}$ in Eqs. (4.27,4.28). On the short time scale represented in these two Figures, the re-introduction of the sound waves was found to have negligible effect.

In the case with K^2 close to unity, the density/pressure spreads out via Alfvén wave activity, not sound waves. This is made possible by how small amounts of charge enter and leave the pieces of the flux tube at various positions along the s-axis. For a localised disturbance of the form in Eq. (4.37), we can consider the single flux tube it occupies. At $s = 0$ the initial response is a parallel current according to which electrons leave the region in both directions along s. By quasineutrality the ions spiral out of the region in the xy-plane: while both species undergo circular ExB motion the ions have a finite slip in the radial direction, $\nabla r = (x\nabla x + y\nabla y)/r$, where $r^2 = x^2 + y^2$, represented by the polarisation drift. At positions on the s-axis at distance from $s = 0$ (up and down the

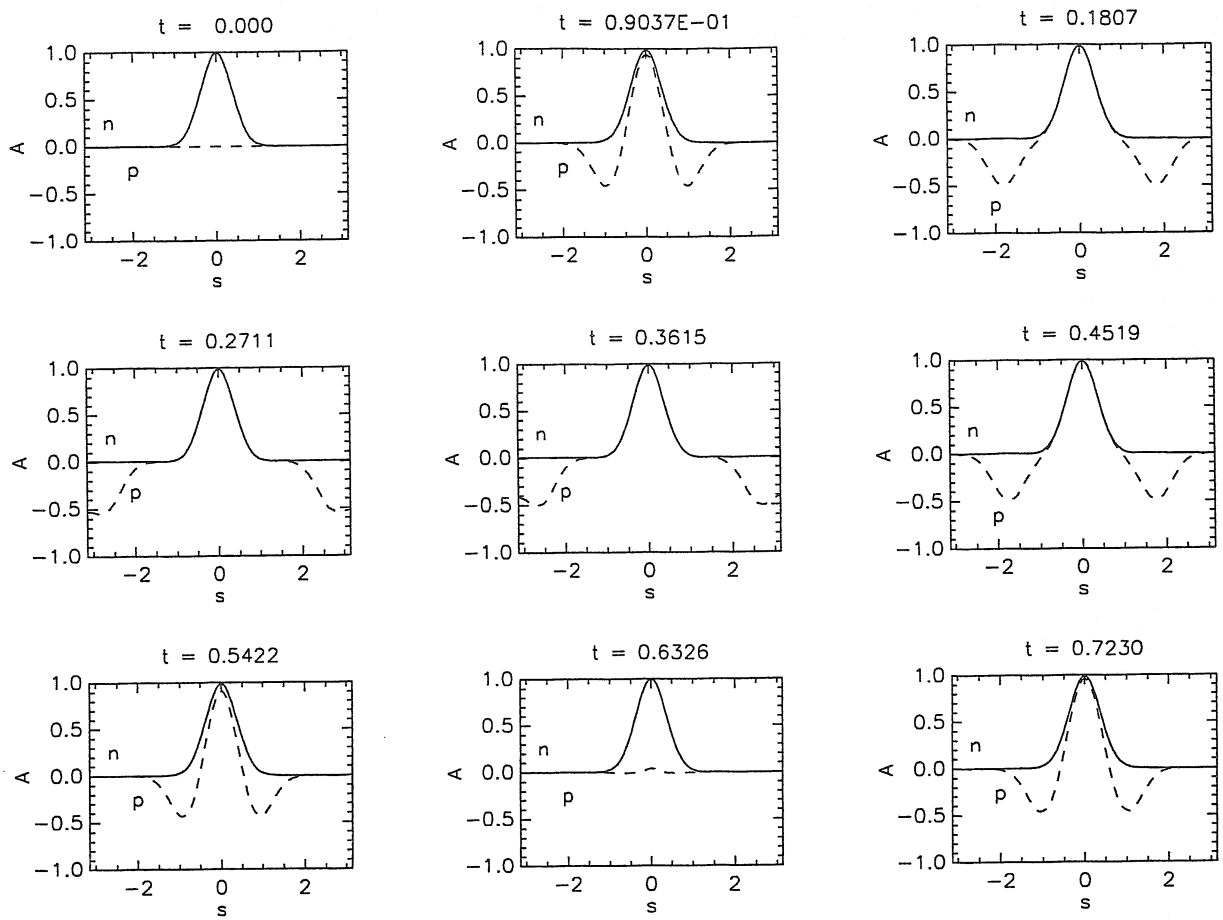

Figure 4.9. A kinetic shear Alfvén wave oscillation, for the hot plasma case with $K = 0.1$. The wave is excited by $\widetilde{p}_e$ (labelled as 'n'), but most of the motion involves $\widetilde{\phi}$ ('p').

magnetic field lines from the initial disturbance; consult Fig. 4.3), what happens is that electrons enter the region along the field lines ($\widetilde{J}_{\|}$) while ions spiral radially inward ($\widetilde{\mathbf{u}}_p$). This is the Alfvén activity represented by $\widetilde{\phi}$ and $\widetilde{J}_{\|}$ both responding to $\widetilde{p}_e$. The mass flow follows the fate of $\widetilde{p}_e = T_e\widetilde{n}_e$, which is proportional to $\widetilde{\rho} = M_i\widetilde{n}_e$. If $\Delta_\perp > \rho_s$, then the mass flow follows sound waves, while if $\Delta_\perp < \rho_s$ it follows from the redistribution of ions due to the polarisation drift; *i.e.*, ultimately from the kinetic Alfvén waves. All of this is decided by the relative sizes of the effective coefficients in front of the time derivatives of $\widetilde{\phi}$ and $\widetilde{p}_e$ in Eqs. (4.26,4.27).

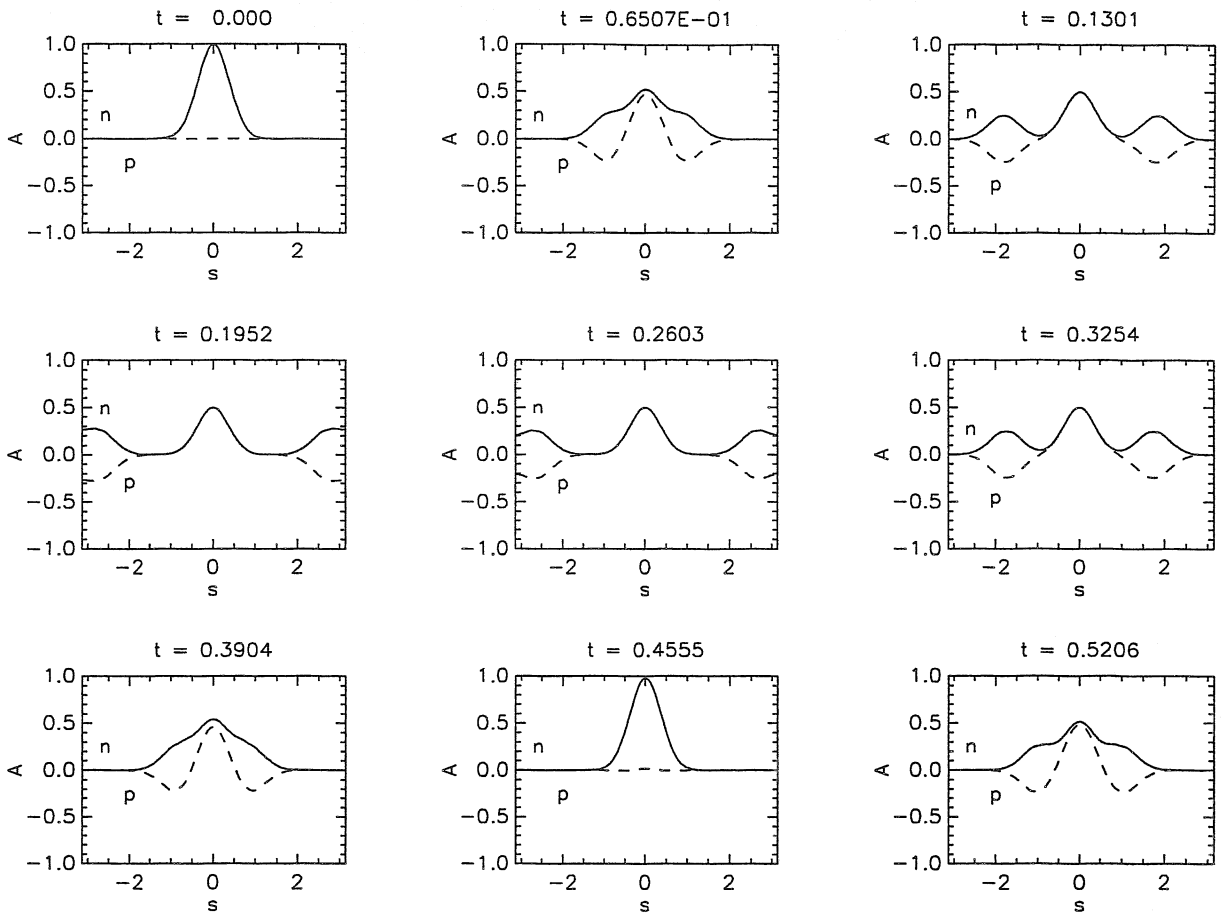

Figure 4.10. A kinetic shear Alfvén wave oscillation, for the hot plasma case with $K = 1.0$. The wave is excited by $\widetilde{p}_e$ (labelled as 'n'), and now due to the thinness of the flux tubes about half of the pressure disturbance is involved in the Alfvén wave along with $\widetilde{\phi}$ ('p'). Note also that the frequency is a little faster than the case in Fig. 4.9.

We note that there is no response at all to a pressure disturbance under the reduced MHD model neglecting sound waves, whose equations for are found by neglecting $\widetilde{u}_{\|}$ and the two terms involved in the kinetic shear Alfvén coupling mechanism, leaving

$$\frac{\partial}{\partial t}\nabla_{\perp}^2\widetilde{\phi} = \nabla_{\|}\widetilde{J}_{\|} \tag{4.41}$$

$$\frac{\partial \widetilde{p}_e}{\partial t} = 0 \tag{4.42}$$

$$\beta_e \frac{\partial \widetilde{A}_{\parallel}}{\partial t} + \mu_e \frac{\partial \widetilde{J}_{\parallel}}{\partial t} = -\nabla_{\parallel} \widetilde{\phi} - 0.51 \mu_e \nu_e \widetilde{J}_{\parallel} \tag{4.43}$$

If the current or electrostatic potential are not initially excited, there is no evolution in this system at all. Given the results just presented we therefore conclude that the initial response to a pressure disturbance is incorrectly predicted by MHD at all scales, not just those near $k_\perp \rho_s \sim 1$.

4.VIII. Thermal Effects on Parallel Dynamics

We are deferring the discussion of temperature effects in general until Chapters 12 and 13, because of some additional complications that require expansion of the scope of the model equations. However, we note that in the context of homogeneous parallel dynamics, the character of the wave dynamics does not change as a result of adding the temperatures. Rather, energy equipartition and the dissipation mechanisms are affected, which restricts the overall effect to the level of details: quantitative effects on both the wave speeds and the damping rates of kinetic shear Alfvén and sound waves. Results to this effect will be shown in Chapter 13, where the effects of the finite ion gyroradius on the Alfvén dynamics will form a central topic. The important result for the present purpose is merely to note that for $k_\perp \rho_i$ up to unity there are no qualitative effects on kinetic shear Alfvén waves and sound waves due to the physics of the temperatures. In particular, the efficacy of transport of density/pressure by the Alfvén dynamics for $K \lesssim 1$ survives.

4.IX. Summary

The drift approximation removes the compressional Alfvén waves of MHD but leaves the shear Alfvén waves alone. Applied solely to the MHD model, the drift approximation becomes the reduced MHD model, in which the shear Alfvén waves are mathematically described by $(\widetilde{\phi}, \widetilde{A}_{\parallel})$ instead of $(\mathbf{v}_E, \widetilde{\mathbf{B}}_\perp)$ although their physics is the same. When two fluid behaviour is retained, the drift approximation leads to the fluid drift dynamics model, which takes the pressure gradient into account in the electron force balance, forming the adiabatic response of the electrons. To conserve energy, the parallel current is retained in the parallel thermodynamics of the electrons, with the combination $(\widetilde{u}_{\parallel} - \widetilde{J}_{\parallel}/ne)$ describing the parallel electron motion. Correspondingly, the combination $\mathbf{v}_E + \mathbf{v}_*$, for which the scaled potential/pressure difference is the stream function, describes the perpendicular electron motion. The pressure forces and the difference between the electron and ion fluid velocities therefore go together, and the Alfvénic activity follows the total electron velocity, not the ion velocity or the ExB drift. Under drift dynamics, the electrons have an adiabatic response, and therefore disturbances in the electron pressure launch Alfvén

waves. If $\beta_e \ll 1$, the resulting kinetic shear Alfvén waves oscillate on relatively fast time scales, while the sound wave activity is slower. Given moderate resistivity, the Alfvénic activity damps, leaving the sound waves to oscillate with adiabatic electrons and dissipate viscously. If the collisionality is very low, then we have to treat the temperatures and their associated kinetic dissipation mechanisms. We will do this in Chapters 12 and 13.

Further Reading

Kinetic shear Alfvén waves are described by A. B. Mikhailovskii, in *Theory of Plasma Instabilities* (Consultants Bureau, New York, 1974). They were described using kinetic theory by A. Hasegawa and L. Chen, in *Phys. Fluids* 19 (1976) 1924. The wave energetics was discussed by B. Scott, in *Plasma Phys. Contr. Fusion* 39 (1997) 1635. Kinetic shear Alfvén waves as transients to instabilities and turbulence, which we will cover in the next few chapters, were discussed in these references, and by K. T. Tsang, J. C. Whitson, J. D. Callen, P. J. Catto, and J. Smith, in *Phys. Rev. Lett.* 41 (1978) 557, and by S. Camargo, B. Scott, and D. Biskamp, in *Phys. Plasmas* 3 (1996) 3912.

5. Perpendicular Dynamics — Drift Waves

B. Scott

Jul 1999

5.1. Introduction

In studying the part of fluid drift dynamics which involves wave propagation parallel to the magnetic field, we have already encountered one very subtle part of the dynamics which takes place in the plane locally perpendicular to the magnetic field. This is the polarisation drift. When other perpendicular drifts excepting the ExB velocity are absent, the polarisation drift is responsible for allowing parallel currents which can have a divergence. Charge neutrality is then maintained by a balance between the divergences of these two currents, with the reaction of the polarisation drift to the other divergences controlling the evolution of the perpendicular electric field, and hence the ExB velocity.

In this chapter we are also concerned by the effects of advection by the ExB velocity. In a homogeneous background the ExB advection is a purely nonlinear effect — advection of a disturbance by a velocity whose stream function is also a disturbance. When there is a background gradient, however, we encounter linear effects arising from the advection of the background by the ExB disturbances. Flows down the gradient of a given quantity drive disturbances in that same quantity (*e.g.*, the pressure). The interaction between this perpendicular ExB advection and the self consistent adiabatic response parallel to the magnetic field forms the dynamical structure which we call the drift wave. Drift wave turbulence is what transpires when the advection is strong enough that the nonlinear and linear effects are comparable; this we defer to Chapter 6. Herein, we treat drift waves as linear modes of oscillation, or as instabilities, which occur in a magnetised plasma in which there is a pressure gradient and a finite parallel scale.

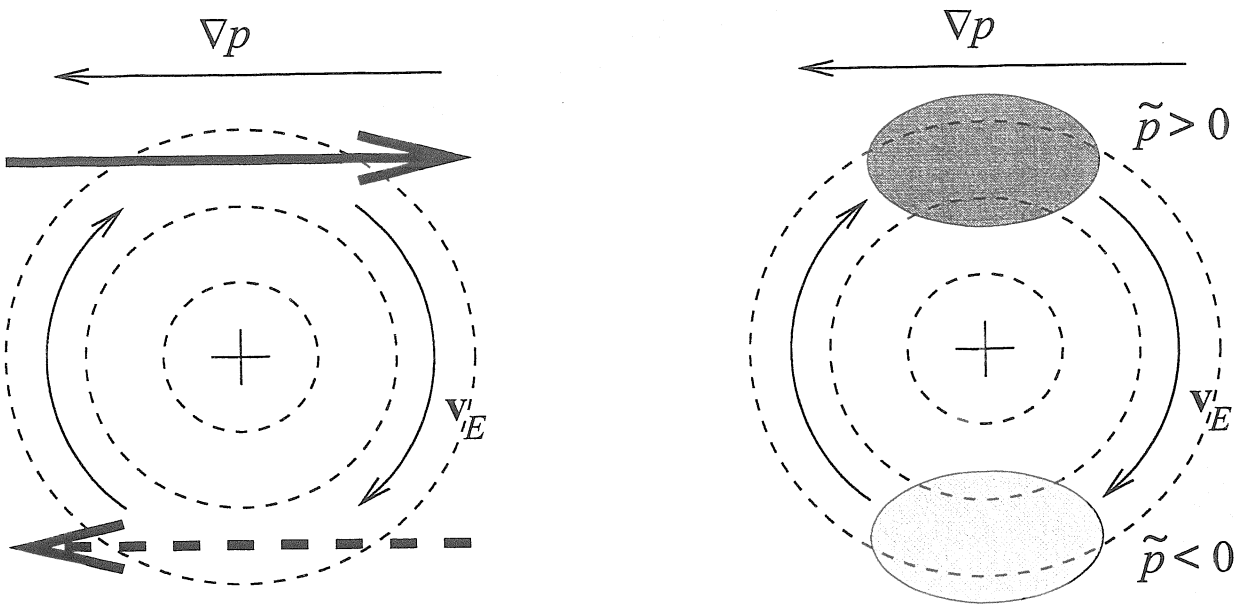

Figure 5.1. ExB advection in a background pressure gradient. The dashed circles are contours of $\tilde{\phi}$, representing a localised ExB flow vortex, clockwise around the potential maximum. The ExB flow, $\mathbf{v}_E$, is shown by the solid arrow arcs, and where it is down or up the gradient it is shown (left frame) by the thick solid and dashed arrows, respectively. These flows excite the pressure disturbances, $\tilde{p}_e$, positive where the flow is down-gradient, and negative where the flow is up-gradient (right frame). The resulting $\tilde{p}_e$ is driven on the leading edge of the $\tilde{\phi}$ maximum, in the drift direction (towards the top of the picture). For a vortex wave train, the pressure is therefore driven with a phase ahead of the potential.

5.II. ExB Advection in a Gradient — The Drift Frequency

The simplest process by which advection in a background gradient drives the associated disturbance is given simply by the model in which the total ExB advection of that quantity is zero:

$$\frac{d_E p_e}{dt} = \frac{\partial p_e}{\partial t} + \mathbf{v}_E \cdot \nabla p_e = 0 \tag{5.1}$$

If we linearise this equation, replacing p_e by the background p_e and the disturbance $\tilde{p}_e$, we neglect the action of $\mathbf{v}_E \cdot \nabla$ on $\tilde{p}_e$, and note that with a fixed background we advance only the disturbance. This says that

$$\frac{\partial \tilde{p}_e}{\partial t} = -\mathbf{v}_E \cdot \nabla p_e \tag{5.2}$$

A sketch of the process is shown in Fig. 5.1. We set a right handed coordinate system $\{x, y, s\}$ such that $\mathbf{B} = B\nabla s$ and $\nabla \log p_e = -L_p^{-1}\nabla x$, with B and L_p constants. The ExB velocity in the x-direction is

$$\mathbf{v}_E \cdot \nabla x = \frac{c}{B^2}\mathbf{B}\times\nabla\tilde{\phi} \cdot \nabla x = -\frac{c}{B}\frac{\partial\tilde{\phi}}{\partial y} \tag{5.3}$$

Scaling the disturbances in terms of $\tilde{p}_e/p_e$ and $e\tilde{\phi}/T_e$, we have the evolution of the pressure disturbance,

$$\frac{\partial}{\partial t}\frac{\tilde{p}_e}{p_e} = -\frac{cT_e}{eBL_p}\frac{\partial}{\partial y}\frac{e\tilde{\phi}}{T_e} \tag{5.4}$$

This is the usual expression in any situation where the adiabatic response of the electrons is relevant, tending to keep $e\tilde{\phi}/T_e$ close to $\tilde{p}_e/p_e$. It leads to the typical time scale associated with drift dynamics in which the free energy source is the background gradient. One expression of the definition of ρ_s is as the scale which combines with the sound speed to produce cT_e/eB as a diffusion coefficient; *i.e.*,

$$\rho_s c_s = \frac{cT_e}{eB} \qquad \text{since} \quad c_s^2 = \frac{T_e}{M_i} \quad \text{and} \quad \rho_s^2 = \frac{c^2 T_e M_i}{e^2 B^2} \tag{5.5}$$

Combining the factor of ρ_s with the y-derivative, we obtain the background drift frequency, c_s/L_p. For a particular wavenumber k_y, we have the frequency with the associated wavelength $2\pi/k_y$,

$$\omega_* = \frac{cT_e k_y}{eBL_p} = \frac{k_y \rho_s c_s}{L_p} \tag{5.6}$$

This is called the diamagnetic frequency, due to the fact that the wave propagation velocity multiplying k_y is simply the diamagnetic drift velocity, v_D, given by

$$v_D = \frac{cT_e}{eBL_p} = \frac{\rho_s c_s}{L_p} = |\mathbf{v}_*| \tag{5.7}$$

Motion of this type represents a drift in the y-direction, which is the electron drift direction, $-\mathbf{B}\times\nabla p_e$, given by the orientation of the $\mathbf{v}_*$ of the background. Such motion is called a diamagnetic drift.

5.III. Drift Waves — The Very Simplest Model

The foregoing considerations give rise to the picture of drift waves one most often finds in textbooks. We know that there is an adiabatic response in the electrons parallel to the magnetic field, but we discard the details and simply assume that it takes place on a much faster time scale than that of the diamagnetic drift. We also have to assume that the effects of parallel ion dynamics is negligible, and so the diamagnetic drift must in turn take place much faster than sound wave time scales. We therefore assume a nonvanishing parallel wavenumber, $k_\parallel$, and demand that

$$k_\parallel V_a \gg \omega \sim \omega_* \gg k_\parallel V_s \tag{5.8}$$

where V_a and V_s are the generalised Alfvén and sound speeds encountered in the previous chapter. We note here that V_a is not necessarily V_e as written in some texts; that is true only when the adiabatic response is purely electrostatic, which would require $v_A > V_e$, or $\beta_e < \mu_e k_\perp^2 \rho_s^2$. In any case, however, if we can say that the time scale for the adiabatic response is arbitrarily fast, *and* the parallel gradient does not vanish, we may replace further consideration of the parallel dynamics with the condition that the electrons be adiabatic:

$$\frac{e\widetilde{\phi}}{T_e} = \frac{\widetilde{p}_e}{p_e} = \frac{\widetilde{n}_e}{n_e} \tag{5.9}$$

The last equality is due to the fact that the parallel electron dynamics also relaxes the temperature disturbances, and if it is arbitrarily fast then $\widetilde{T}_e$ will go to zero. At this point, electron pressure and density become synonymous, as in the four field model with $\Gamma = 1$. Specification of the details of the parallel dynamics is very vague, no more involved than the simple arguments just given. Among other things, the polarisation drift of the ions is neglected, and quasineutrality is guaranteed by having the electrons adiabatic, so that not only is the current divergence free, it is also zero.

Advection of the background density by ExB disturbances under these conditions leads to the very simple dispersion relation,

$$\omega = \omega_* = k_y v_D \tag{5.10}$$

which we find by substituting the adiabatic state, Eq. (5.9), into the advection equation, Eq. (5.4), yielding

$$\left(\frac{\partial}{\partial t} + v_D \frac{\partial}{\partial y}\right) \frac{e\widetilde{\phi}}{T_e} = 0 \tag{5.11}$$

and taking the appropriate Fourier transforms in space and time. The physical picture of this is very simple. The disturbances have spatial variation in at least two directions,

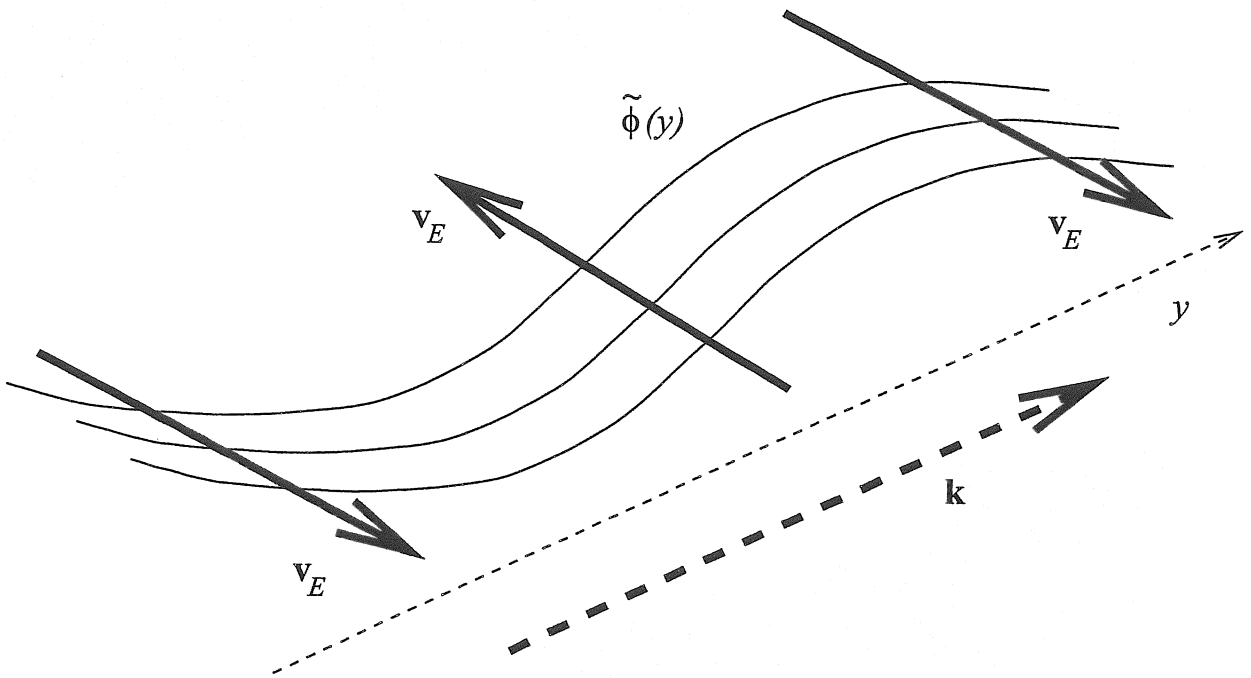

Figure 5.2. Sketch of a simple one dimensional drift wave. The implied vertical axis is $\tilde{\phi}$, and the sinusoidal curves represent a wave train $\tilde{\phi}(y)$. The ExB flow, $\mathbf{v}_E$, is up or down the pressure gradient according to the direction of the thick solid arrows. Flow to the right is down-gradient, and there the pressure disturbance tends to be excited positive. But the arbitrarily fast adiabatic response ties $\tilde{\phi}$ back to $\tilde{p}_e$, giving a drift propagation in the y-direction, with $\mathbf{k} = k_y \nabla y$. Spatially, $\mathbf{B}$ is in the direction of the vertical axis.

y and s, the drift and parallel directions, respectively. At this level of simplicity, any x-dependence has no effect. Even the s-dependence makes no difference, except for the prescription that the ordering in Eq. (5.8) be maintained. The simplest case is a sinusoidal wave in the y-direction, a sketch of which is shown in Fig. 5.2. At all places where there is y-variation in $\tilde{\phi}$, the pressure disturbance is driven. On the "leading edge" of the wave, the ExB flow in the x-direction is positive, that is, down the gradient, and $\tilde{p}_e$ is driven positive there. Since the adiabatic response is effectively instantaneous, $\tilde{\phi}$ follows $\tilde{p}_e$ and the structure simply propagates in the y-direction with the diamagnetic drift velocity. It is important to note that this propagation does not result from a proper wave equation; Eq. (5.11) is only a first order equation, so there is no counterpart propagating in the opposite direction. An initial disturbance simply moves unidirectionally.

5.IV. Drift Waves — Polarisation and Dispersion

There are two principal features of the very basic drift wave model: there is no instability, because the frequency is purely real, and there is no dispersion, because the propagation velocity is independent of the wavelength. Systems which have this property are called "self similar" because there is no preferred scale of motion as long as the assumptions and restrictions leading up to the model are satisfied. However, we have already seen that in the parallel dynamics, both for the adiabatic (kinetic shear Alfvén) and sound wave responses, the wave speeds for *parallel* motion depend on the *perpendicular* wavenumbers. This is still true for purely adiabatic sound waves, so we ought to watch out for its emergence for drift waves. This is done by taking the polarisation current into account. Here, we assume that the parallel current is not zero, although it is still negligible enough that we can assume adiabatic electrons. But the small but finite parallel divergence now requires the finite polarisation current.

This is a second version of drift waves one can encounter in textbooks: we start with the equation for the ion density in a plasma with a density gradient but a homogeneous magnetic field. With $\mathbf{B}$ constant we have $\nabla \cdot \mathbf{v}_E = 0$ and no diamagnetic flux effects, but there is still the polarisation drift to watch out for. We have

$$\frac{\partial n_i}{\partial t} + \mathbf{v}_E \cdot \nabla n_i + \nabla \cdot n_i \mathbf{u}_p = 0 \tag{5.12}$$

where now the polarisation drift, given by

$$n_i \mathbf{u}_p = -\frac{n_i M_i c^2}{eB^2} \left(\frac{\partial}{\partial t} + \mathbf{v}_E \cdot \nabla \right) \nabla_\perp \phi \tag{5.13}$$

(here neglecting the parallel ion motion), breaks the situation of pure ExB advection. Linearising these equations and applying drift ordering, by which the factors in Eq. (5.13) are taken as constant, we find

$$\frac{\partial}{\partial t} \frac{\widetilde{n}_i}{n_i} + v_D \frac{\partial}{\partial y} \frac{e\widetilde{\phi}}{T_e} - \rho_s^2 \nabla_\perp^2 \frac{\partial}{\partial t} \frac{e\widetilde{\phi}}{T_e} = 0 \tag{5.14}$$

The other consideration is quasineutrality, which allows replacement of $\widetilde{n}_i$ by $\widetilde{n}_e$; *i.e.*, in the disturbances as well as the background. Finally, we prescribe adiabatic electrons, Eq. (5.9), in this case also, to find

$$\left[\left(1 - \rho_s^2 \nabla_\perp^2\right) \frac{\partial}{\partial t} + v_D \frac{\partial}{\partial y} \right] \frac{e\widetilde{\phi}}{T_e} = 0 \tag{5.15}$$

The only difference between this and Eq. (5.11) is the appearance of the factor of $\rho_s^2 \nabla_\perp^2$. If we again take the appropriate Fourier transforms in space and time, we find the modification to the dispersion relation of Eq. (5.10) caused by the polarisation drift,

$$\omega = \frac{\omega_*}{1 + k_\perp^2 \rho_s^2} = \frac{c_s}{L_p} \frac{k_y \rho_s}{1 + k_\perp^2 \rho_s^2} \equiv \omega_L \tag{5.16}$$

This is the origin of the name of ρ_s as the "drift wave dispersion scale." At this scale the propagation starts to slow down, with ω_L giving the basic drift wave frequency and representing the slowing of the time scale as $k_\perp \rho_s$ approaches unity. Otherwise the physical picture does not change from that of the previous section; we have simply been slightly more careful in setting up the model. If ρ_s is arbitrarily small, we recover the simplest self similar model.

In both of these simple models, we still have the problem that the result describes only pure propagation; there is no instability. This is related to the absence of driving and dissipation: there is no concept of energetics. Even the dissipation-free transfer phenomena require a more careful description of the dynamics than simple specification of adiabatic electrons; we have already encountered some of this in contemplating the kinetic shear Alfvén waves. Fortunately, having done that already, it is a simple step to arrive at a complete description of drift waves, not only how their structure is established and maintained, but also how free energy is tapped from the background and then transferred through the dynamical system until it ends at dissipation. All we have to do is to add the extra phenomenon of ExB advection in a gradient to what we have already done in deriving the kinetic shear Alfvén waves.

5.V. Perpendicular versus Parallel Dynamics — Self Consistent Drift Waves

In order to really understand the drift wave structure, one has to investigate how it is initially established. The adiabatic electron state has to be maintained, even if it is the initial state. More generally, the departures from the adiabatic state must be found by considering the self consistent electron dynamics following from the adiabatic response. We have already seen, however, that adiabatic electrons is the end state of dissipative Alfvén activity, regardless of how the system is initialised. So we know that the time scale on which the adiabatic state is itself established is that on which the Alfvén waves die out. Here, we investigate the ExB advection and kinetic shear Alfvén waves interacting together, and show that this is the mechanism by which drift waves are set up and maintained. We simply add the extra terms arising from the background gradient to the linearised four field model we have already seen in Chapter 4, Section II. There are two such terms, one from

the ExB advection of the gradient, and one from the parallel derivative of the quantity with a gradient:

$$\mathbf{v}_E \cdot \nabla p_e = \frac{c}{B^2}\mathbf{B}\times\nabla\widetilde{\phi}\cdot\left(-\frac{p_e}{L_p}\nabla x\right) = p_e\frac{c_s}{L_p}\rho_s\frac{\partial}{\partial y}\frac{e\widetilde{\phi}}{T_e} \tag{5.17}$$

$$\widetilde{\mathbf{B}}\cdot\nabla p_e = -\frac{1}{B^2}\mathbf{B}\times\nabla\widetilde{A}_{\parallel}\cdot\left(-\frac{p_e}{L_p}\nabla x\right) = -p_e\frac{c_s}{L_p}\beta_e\rho_s\frac{\partial}{\partial y}\frac{\widetilde{A}_{\parallel}}{\beta_e B\rho_s} \tag{5.18}$$

If we add these two terms to the linearised four field model where appropriate, we have

$$\frac{\partial}{\partial t}\rho_s^2\nabla_\perp^2\frac{e\widetilde{\phi}}{T_e} = c_s\nabla_{\parallel}\frac{\widetilde{J}_{\parallel}}{nec_s} \tag{5.19}$$

$$\frac{\partial}{\partial t}\frac{\widetilde{p}_e}{p_e} + \frac{c_s}{L_p}\rho_s\frac{\partial}{\partial y}\frac{e\widetilde{\phi}}{T_e} = \Gamma c_s\nabla_{\parallel}\left(\frac{\widetilde{J}_{\parallel}}{nec_s} - \frac{\widetilde{u}_{\parallel}}{c_s}\right) \tag{5.20}$$

$$\beta_e\frac{\partial}{\partial t}\frac{\widetilde{A}_{\parallel}}{B\rho_s\beta_e} + \mu_e\frac{\partial}{\partial t}\frac{\widetilde{J}_{\parallel}}{nec_s} = c_s\nabla_{\parallel}\left(\frac{\widetilde{p}_e}{p_e} - \frac{e\widetilde{\phi}}{T_e}\right) - \frac{c_s}{L_p}\beta_e\rho_s\frac{\partial}{\partial y}\frac{\widetilde{A}_{\parallel}}{\beta_e B\rho_s} - 0.51\mu_e\nu_e\frac{\widetilde{J}_{\parallel}}{nec_s} \tag{5.21}$$

$$\frac{\partial}{\partial t}\frac{\widetilde{u}_{\parallel}}{c_s} = -c_s\nabla_{\parallel}\frac{\widetilde{p}_e}{p_e} + \frac{c_s}{L_p}\beta_e\rho_s\frac{\partial}{\partial y}\frac{\widetilde{A}_{\parallel}}{\beta_e B\rho_s} + \mu_{\parallel}\nabla_{\parallel}^2\frac{\widetilde{u}_{\parallel}}{c_s} \tag{5.22}$$

with Ampere's law

$$\frac{\widetilde{J}_{\parallel}}{nec_s} = -\rho_s^2\nabla_\perp^2\frac{\widetilde{A}_{\parallel}}{\beta_e B\rho_s} \tag{5.23}$$

These equations can be simply normalised in the way suggested by the scaled units, but we now have a choice to resolve, namely, that of the parallel versus perpendicular scale. This provides the opportunity to motivate the normalisation scheme for drift wave dynamics in its entirety. The first step is the choice between $L_{\parallel}$ and $L_\perp$ for the system scale for the time. On traditional grounds we choose $L_\perp$ as the one ω_* depends on. We choose it independently of L_p in order to be able to turn the gradient on and off in a computation. Time is therefore normalised against $c_s/L_\perp$. The state variables, $\widetilde{\phi}$ and $\widetilde{p}_e$, serving as stream functions and parallel force potentials, are normalised in terms of the scaled units suggested by the adiabatic response, appropriate to any situation in which that response controls the amplitude of $\widetilde{\phi}$. The flux variables, $\widetilde{A}_{\parallel}$ and $\widetilde{u}_{\parallel}$, and also $\widetilde{J}_{\parallel}$, are normalised in terms of c_s. The parallel gradient is still normalised against the wavenumber of the parallel scale, $2\pi/L_{\parallel}$, and an extra factor of the ratio $L_{\parallel}/2\pi L_\perp$ is folded into the flux variables and will appear in the dimensionless parameters of the system, reflecting the interaction between the parallel and perpendicular dynamics. The factor of β_e can be placed either in Ampere's law or in Faraday's law. We place it in Faraday's law such that

$\widetilde{A}_\parallel$ always appears with β_e, so that in the limit $\beta_e \to 0$ we revert back to an electrostatic system which still has a finite $\widetilde{J}_\parallel$ due either to electron inertia or dissipation. Finally, $\nabla_\perp$ is normalised against ρ_s when acting on a dependent variable.

The normalised quantities are

$$\frac{e\widetilde{\phi}}{T_e} \qquad \frac{\widetilde{p}_e}{p_e} \qquad \frac{\widetilde{A}_\parallel}{\hat{\beta}B\rho_s}\frac{2\pi L_\perp}{L_\parallel} \qquad \frac{\widetilde{u}_\parallel}{c_s}\frac{2\pi L_\perp}{L_\parallel} \qquad \frac{\widetilde{J}_\parallel}{n_e e c_s}\frac{2\pi L_\perp}{L_\parallel} \tag{5.24}$$

Ampere's law and Faraday's law then become

$$\widetilde{J}_\parallel = -\nabla_\perp^2 \widetilde{A}_\parallel \qquad\qquad E_\parallel = -\hat{\beta}\frac{\partial \widetilde{A}_\parallel}{\partial t} - \nabla_\parallel \widetilde{\phi} \tag{5.25}$$

The normalised equations appear as

$$\frac{\partial}{\partial t}\nabla_\perp^2 \widetilde{\phi} = \nabla_\parallel \widetilde{J}_\parallel \tag{5.26}$$

$$\frac{\partial \widetilde{p}_e}{\partial t} = -\omega_p \frac{\partial \widetilde{\phi}}{\partial y} + \Gamma\nabla_\parallel \widetilde{J}_\parallel - \Gamma\nabla_\parallel \widetilde{u}_\parallel \tag{5.27}$$

$$\hat{\beta}\frac{\partial \widetilde{A}_\parallel}{\partial t} + \hat{\mu}\frac{\partial \widetilde{J}_\parallel}{\partial t} = \nabla_\parallel\left(\widetilde{p}_e - \widetilde{\phi}\right) - \omega_p\hat{\beta}\frac{\partial \widetilde{A}_\parallel}{\partial y} - 0.51\hat{\mu}\nu\widetilde{J}_\parallel \tag{5.28}$$

$$\hat{\epsilon}\frac{\partial \widetilde{u}_\parallel}{\partial t} = -\nabla_\parallel \widetilde{p}_e + \omega_p\hat{\beta}\frac{\partial \widetilde{A}_\parallel}{\partial y} + \mu_\parallel \nabla_\parallel^2 \widetilde{u}_\parallel \tag{5.29}$$

The main parameters are the ones controlling the kinetic shear Alfvén dynamics, that is, the adiabatic response,

$$\hat{\beta} = \beta_e\left(\frac{L_\parallel}{2\pi L_\perp}\right)^2 \qquad \hat{\mu} = \mu_e\left(\frac{L_\parallel}{2\pi L_\perp}\right)^2 \qquad \nu = \frac{\nu_e L_\perp}{c_s} \tag{5.30}$$

where we note the scaling against the parallel to perpendicular scale ratio for the background. Replacing β_e and μ_e, $\hat{\beta}$ and $\hat{\mu}$ respectively give the effective inertia of the adiabatic response on drift wave time scales. The two parameters ω_p and $\hat{\epsilon}$ are free switches. Their nominal values are

$$\omega_p = |L_\perp \nabla \log p_e| \qquad\qquad \hat{\epsilon} = \left(\frac{L_\parallel}{2\pi L_\perp}\right)^2 \tag{5.31}$$

but we can set them arbitrarily, to turn the gradient on and off or to speed up the sound waves in a computation, respectively.

The parameters controlling the parallel wave speeds determine the competition between the ExB perpendicular dynamics and the generalised parallel dynamics. They may also be written as

$$\hat{\beta} = \left(\frac{c_s/L_\perp}{K_\parallel v_A}\right)^2 \qquad \hat{\mu} = \left(\frac{c_s/L_\perp}{K_\parallel V_e}\right)^2 \qquad \hat{\epsilon} = \left(\frac{c_s/L_\perp}{K_\parallel c_s}\right)^2 \tag{5.32}$$

where $K_\parallel = 2\pi/L_\parallel$ is the nominal value of the parallel wavenumber. In situations dominated by resistivity we can express the combination

$$C = 0.51\hat{\mu}\nu = 0.51\frac{\nu_e L_\perp}{c_s}\frac{m_e}{M_i}\left(\frac{L_\parallel}{2\pi L_\perp}\right)^2 \tag{5.33}$$

as the basic collisionality for drift waves. Traditional drift ordering in terms of these parameters is

$$\left(\hat{\beta}, \hat{\mu}, C\right) \ll 1 \ll \hat{\epsilon} \tag{5.34}$$

reflecting an almost adiabatic balance in the electrons and the neglect of sound waves for the ions. If we replace the factor of unity by the square of $k_y\rho_s$, and take the square root, we recover Eq. (5.8).

To concentrate on the drift wave dynamics we will neglect sound wave dynamics, but before doing so there is an interesting relationship between the two to take note of. In a homogeneous plasma under the four field model, one has four eigenmodes for each Fourier component, which we saw in the previous chapter. These are the kinetic shear Alfvén and sound waves, one pair of each. When the background gradient is introduced, one of the sound waves gets transformed into a drift wave. We can see this by subtracting Eqs. (5.26,5.27) to find,

$$\frac{\partial}{\partial t}\left(\widetilde{p}_e - \Gamma\nabla_\perp^2\widetilde{\phi}\right) + \omega_p\frac{\partial\widetilde{\phi}}{\partial y} = -\Gamma\nabla_\parallel\widetilde{u}_\parallel \tag{5.35}$$

If we set $\Gamma = 1$, replacing $\widetilde{p}_e$ with $\widetilde{n}_e$, and note that $\widetilde{n}_i = \widetilde{n}_e$, we recover Eq. (5.14), except for the sound wave term on the right side. We can estimate the size of the sound wave term using Eq. (5.29), to find

$$\frac{\partial}{\partial t}\left(\widetilde{p}_e - \Gamma\nabla_\perp^2\widetilde{\phi}\right) + \omega_p\frac{\partial\widetilde{\phi}}{\partial y} \sim \Gamma\nabla_\parallel^2\widetilde{p}_e\left(\hat{\epsilon}\frac{\partial}{\partial t}\right)^{-1} \tag{5.36}$$

With everything besides $\hat{\epsilon}$ of order unity, we now see that the sound wave physics is preempted by the drift waves, so long as we retain flute mode ordering, $\hat{\epsilon}^{-1} \ll 1$. This is why the sound waves can be neglected in a linear analysis. If we neglect the sound wave

term and set the gradient to zero, we recover the zero frequency mode in the pure kinetic shear Alfvén system, which we saw in the previous chapter.

$$\frac{\partial}{\partial t}\left(\frac{\widetilde{p}_e}{p_e} - \rho_s^2 \nabla_\perp^2 \frac{e\widetilde{\phi}}{T_e}\right) = 0 \tag{5.37}$$

This zero frequency mode becomes part of the sound wave system on its slower frequencies. With the gradient present, however, it becomes the drift wave described in Eqs. (5.14,5.15), if the electrons are adiabatic.

We now allow the electrons to respond self consistently, through the interaction between the parallel and perpendicular dynamics. As we saw in the previous chapter, the parallel dynamics tends towards an adiabatic state, with $\widetilde{p}_e = \widetilde{\phi}$. But the ExB advection tends to excite $\widetilde{p}_e$ at extremal locations of $\mathbf{v}_E \cdot \nabla x = -\partial\widetilde{\phi}/\partial y$, that is, the x-component of the ExB velocity, not $\widetilde{\phi}$. The actual state of the electrons, the relationship between $\widetilde{p}_e$ and $\widetilde{\phi}$, is determined from these differing tendencies. Any difference of the actual response from $\widetilde{p}_e = \widetilde{\phi}$ will give the corrections to the adiabatic dispersion relation, and hence any instability.

In fact, Eq. (5.14), or better its generalisation Eq. (5.35), is the starting point for discussing drift waves at this level. We may define a "nonadiabatic pressure" by combining the terms in Eq. (5.15) on the left side and everything else on the right. We define

$$\frac{\widetilde{h}_e}{n_e} = \frac{\widetilde{p}_e}{p_e} - \frac{e\widetilde{\phi}}{T_e} \qquad \text{normalised to} \quad \widetilde{h}_e = \widetilde{p}_e - \widetilde{\phi} \tag{5.38}$$

which is the state variable for the kinetic shear Alfvén waves, and rewrite Eq. (5.35) as

$$\left[\left(1 - \Gamma\nabla_\perp^2\right)\frac{\partial}{\partial t} + \omega_p \frac{\partial}{\partial y}\right]\widetilde{\phi} = -\frac{\partial \widetilde{h}_e}{\partial t} \tag{5.39}$$

If we Fourier transform this in time and space we have

$$\omega\left(1 + \Gamma k_\perp^2\right) + \omega_p k_y = -\omega\left(\widetilde{h}_{e\mathbf{k}}/\widetilde{\phi}_{\mathbf{k}}\right) \tag{5.40}$$

for a given Fourier component $\mathbf{k} = (k_x, k_y, k_\parallel)$, and frequency ω, noting that in normalised units $\omega_* \to \omega_p k_y$. The nonadiabatic response on the right side is determined by the Ohm's law, which we can express by Fourier transforming and placing all terms except the nonadiabatic forcing on the left side,

$$\hat{\beta}\left(\omega - \omega_*\right)\widetilde{A}_{\parallel\mathbf{k}} + \left(\hat{\mu}\omega + iC\right)\widetilde{J}_{\parallel\mathbf{k}} = -k_\parallel \widetilde{h}_{e\mathbf{k}} \tag{5.41}$$

Substituting $k_\perp^2 \widetilde{A}_{\|\mathbf{k}} = \widetilde{J}_{\|\mathbf{k}}$ from Ampere's law, we find

$$\left[\hat{\beta}\left(\omega - \omega_*\right) + \left(\hat{\mu}\omega + iC\right) k_\perp^2\right] \widetilde{J}_{\|\mathbf{k}} = -k_\perp^2 k_\| \widetilde{h}_{e\mathbf{k}} \tag{5.42}$$

We write the Fourier transformed vorticity equation as

$$\omega k_\perp^2 \widetilde{\phi}_{\mathbf{k}} = k_\| \widetilde{J}_{\|\mathbf{k}} \tag{5.43}$$

From the three equations (5.26,5.27,5.28) we have Eqs. (5.43,5.40,5.42), respectively. Now we combine the latter two to write the self consistent electron response,

$$k_\|^2 \widetilde{h}_{e\mathbf{k}} = -\omega \left[\hat{\beta}\left(\omega - \omega_*\right) + \left(\hat{\mu}\omega + iC\right) k_\perp^2\right] \widetilde{\phi}_{\mathbf{k}} \tag{5.44}$$

Here we can see why it is important that $k_\|$ not vanish. If it could do so, the mode could not be determined in this fashion, for there would be no response path from $\widetilde{p}_e$ back to $\widetilde{\phi}$ — we would have to look for additional physics, as we will do in Chapter 10. On the other hand, if $k_\|$ is relatively large (parallel wavelength much shorter than $L_\|$), then the adiabatic response is fast enough to render the departures from $\omega = \omega_L$ negligible. So the most important Fourier components, or "modes" in a homogeneous magnetic field are those with $k_\| = \pm 1$, from the standpoint of instability or dissipation.

5.VI. The Role of Dissipation — Phase Shifts and Drift Wave Energetics

By examination of Eq. (5.40) we note that instability or dissipation — a finite imaginary part to the mode frequency — is possible only if the nonadiabatic response, $\widetilde{h}_e$, is out of phase with $\widetilde{\phi}$. More generally, there must be a phase shift of $\widetilde{p}_e$ ahead of $\widetilde{\phi}$ in order for there to be an instability. To see this, we can assume we already know that there is such a phase shift, α, in the Fourier components,

$$\widetilde{p}_{e\mathbf{k}} = \widetilde{\phi}_{\mathbf{k}} \exp(-i\alpha) \approx \widetilde{\phi}_{\mathbf{k}}(1 - i\alpha) \tag{5.45}$$

with the latter form valid if $\alpha \ll 1$. Then, we find from Eq. (5.40) that

$$\omega\left(1 + \Gamma k_\perp^2\right) - \omega_* = -\omega(-i\alpha) = i\alpha\omega \tag{5.46}$$

If $\alpha \ll 1$ we may solve this by expansion,

$$\omega = \omega_L + i\alpha \frac{\omega_L}{1 + \Gamma k_\perp^2} \tag{5.47}$$

with ω_L defined in Eq. (5.16), noting that in normalised units $\omega_* \to \omega_p k_y$.

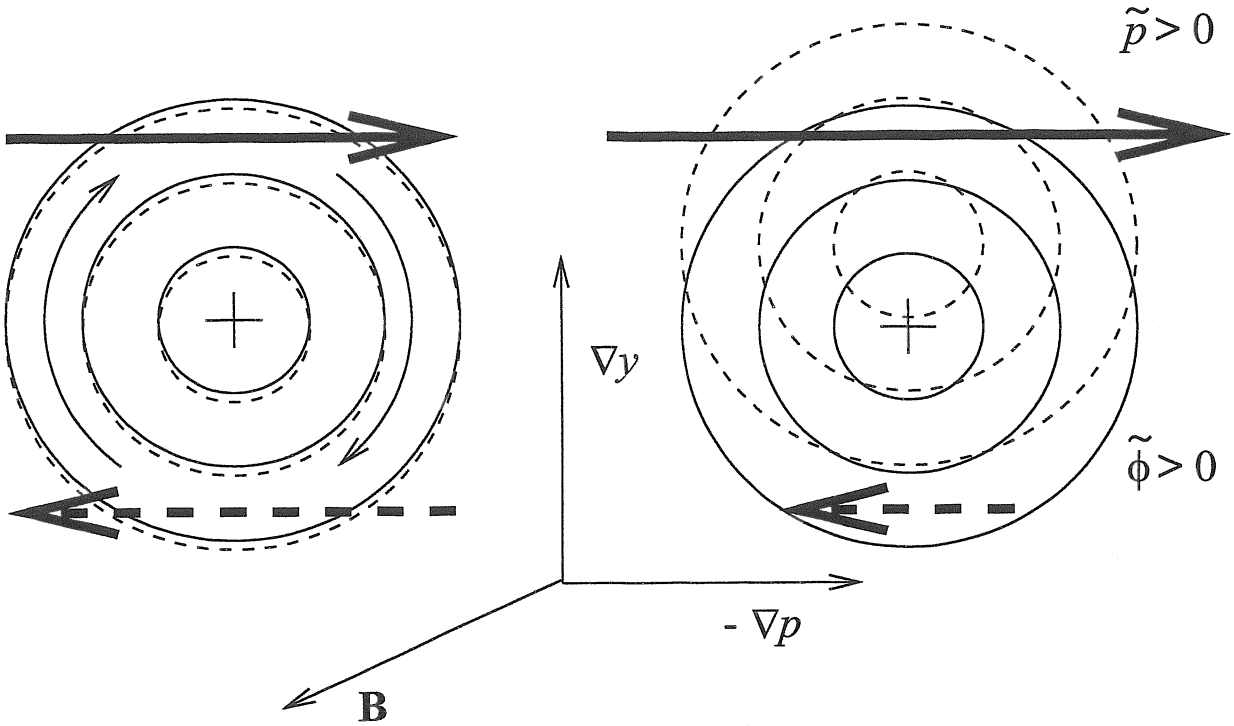

Figure 5.3. The role of the phase shift for drift waves. The orientation is given by the three axes, where ∇y gives the drift direction. Solid and dotted circles represent the positive disturbances $\tilde{\phi}$ and $\tilde{p}_e$, respectively. The arrow arcs on the left figure show the sense of the ExB velocity associated with $\tilde{\phi}$. The thick solid and dashed arrows represent the down-gradient and up-gradient contributions to the net transport. For nearly adiabatic electrons (left figure), the phase shift is negligible and the net transport is nearly zero. If there is a substantial phase shift of $\tilde{p}_e$ ahead of $\tilde{\phi}$, then the net transport is down-gradient, there is a tapping of the free energy in the gradient, and hence growth of the disturbances.

Now, we examine Eq. (5.42). Assuming that $k_\parallel^2 = O(1)$ and that $(\hat{\beta}, \hat{\mu}, C) \ll 1$, we find that $\tilde{h}_e \ll \tilde{\phi}$ and hence that the correction on the left side of Eq. (5.40) is indeed small. If $C = 0$, that is, there is no dissipation, then this correction is purely real — $\tilde{p}_e$ differs from $\tilde{\phi}$ in amplitude but not in phase. This means that inertia by itself amounts purely to a real frequency shift and hence cannot cause instability (unless it is very large, enough to cause reactive instabilities; see Section 5.X for what this means). The other limit is the classic case of the collisional drift wave: assume that C is much larger than $\hat{\beta}$ or $\hat{\mu}$, so that $\tilde{J}_\parallel$ is a purely resistive response to $\tilde{h}_e$. If this is true we find that

$$\tilde{h}_{e\mathbf{k}} = -iC\frac{\omega k_\perp^2}{k_\parallel^2}\tilde{\phi}_\mathbf{k} \qquad \Longrightarrow \qquad \alpha = C\frac{\omega k_\perp^2}{k_\parallel^2} \tag{5.48}$$

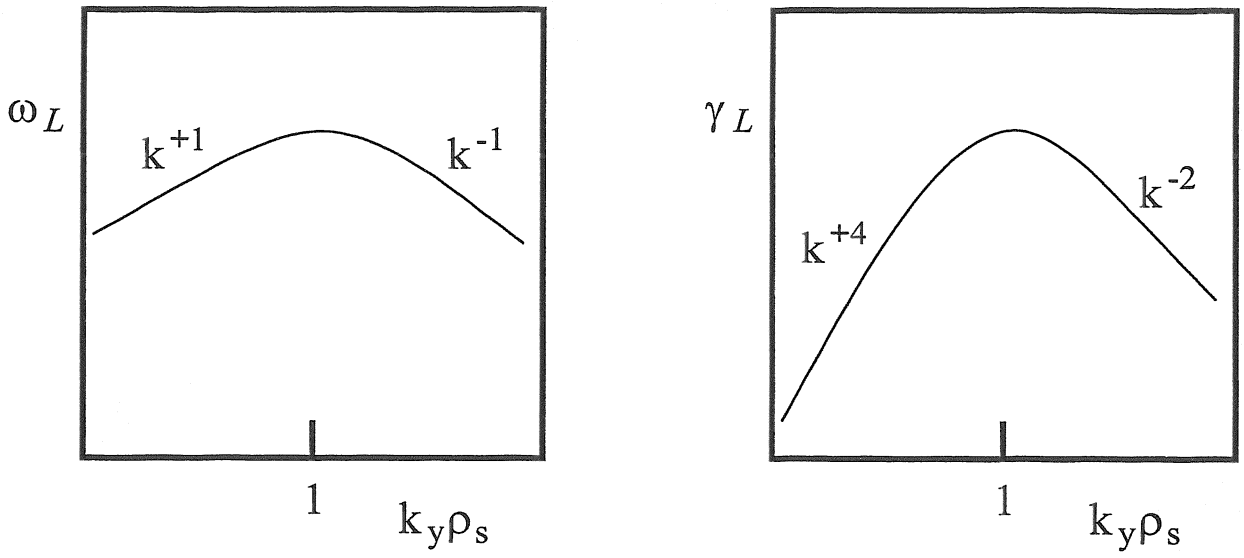

Figure 5.4. The simple collisional drift wave dispersion relation, showing the mode frequency, ω_L, and growth rate, γ_L, as a function of the drift wavenumber, k_y. The phase shift is caused by resistive friction acting as a drag on the adiabatic response. In the four field model, all scales yield $\gamma_L > 0$, that is, instability, with the fastest growth rates at $k_y\rho_s = 1$. The maximum frequency is $c_s/2L_p$. The maximum growth rate is proportional to the phase shift, which in this case is proportional to C.

Dissipation therefore leads to instability, with waves propagating at $\omega = \omega_L$ but growing at a rate proportional to C. In the simple case of pure collisional drift waves with $C \ll 1$, we find a growth rate spectrum given by

$$\gamma = \alpha \frac{\omega_L}{1+\Gamma k_\perp^2} = C\frac{\omega_L^2}{k_\parallel^2}\frac{k_\perp^2}{1+\Gamma k_\perp^2} = C\frac{\omega_p^2}{k_\parallel^2}\frac{k_y^2}{(1+\Gamma k_\perp^2)^2}\frac{k_\perp^2}{1+\Gamma k_\perp^2} \tag{5.49}$$

For $C \ll 1$ and $k_\parallel$ quantised at $[\ldots,-2,-1,0,1,2,\ldots]$ the fastest growing modes are at $k_\parallel^2 = 1$ and $k_\perp^2 \approx 1$. That is, perpendicular scales near the drift scale ρ_s and parallel wavelengths comparable to the system length $L_\parallel$.

The phase shift is related to the net transport down the background gradient done by the disturbances, and therefore to the tapping of the free energy represented by the gradient. We build the energy theorem for drift waves in exactly the same fashion as for kinetic shear Alfvén waves, except that now in addition to the transfer effects and sinks we have the gradient as a source, which enters through the extra terms arising from Eqs. (5.17,5.18). Following the procedure of Chapter 4, Section IV, and applying the

Fourier transforms in space but not in time, the pieces of the free energy theorem including the sound wave dynamics appear as

$$\frac{\partial}{\partial t} k_\perp^2 \left|\widetilde{\phi}_{\mathbf{k}}\right|^2 = 2\,\mathrm{Re}\left[\widetilde{J}_{\parallel\mathbf{k}}^* i k_\parallel \widetilde{\phi}_{\mathbf{k}}\right] \tag{5.50}$$

$$\frac{\partial}{\partial t}\frac{1}{\Gamma}\left|\widetilde{p}_{e\mathbf{k}}\right|^2 = 2\,\mathrm{Re}\left[-\widetilde{J}_{\parallel\mathbf{k}}^* i k_\parallel \widetilde{p}_{e\mathbf{k}} + \widetilde{u}_{\parallel\mathbf{k}}^* i k_\parallel \widetilde{p}_{e\mathbf{k}} - \frac{\omega_p}{\Gamma}\widetilde{p}_{e\mathbf{k}}^* i k_y \widetilde{\phi}_{\mathbf{k}}\right] \tag{5.51}$$

$$\frac{\partial}{\partial t}\left(\hat{\beta} + \hat{\mu} k_\perp^2\right) k_\perp^2 \left|\widetilde{A}_{\parallel\mathbf{k}}\right|^2 = 2\,\mathrm{Re}\left[\widetilde{J}_{\parallel\mathbf{k}}^* i k_\parallel \widetilde{p}_{e\mathbf{k}} - \widetilde{J}_{\parallel\mathbf{k}}^* i k_\parallel \widetilde{\phi}_{\mathbf{k}} - C\left|\widetilde{J}_{\parallel\mathbf{k}}\right|^2\right] \tag{5.52}$$

$$\frac{\partial}{\partial t}\hat{\epsilon}\left|\widetilde{u}_{\parallel\mathbf{k}}\right|^2 = 2\,\mathrm{Re}\left[-\widetilde{u}_{\parallel\mathbf{k}}^* i k_\parallel \widetilde{p}_{e\mathbf{k}} + \hat{\beta}\omega_p \widetilde{u}_{\parallel\mathbf{k}}^* i k_y \widetilde{A}_{\parallel\mathbf{k}} - \mu_\parallel k_\parallel^2 \left|\widetilde{u}_{\parallel\mathbf{k}}\right|^2\right] \tag{5.53}$$

noting the application of the condition that the physical disturbances be real-valued, for example, $\widetilde{\phi}_{-\mathbf{k}} = \widetilde{\phi}_{\mathbf{k}}^*$, and that the electromagnetic source in Ohm's law, given proportional to the real part of $\hat{\beta}\omega_p \widetilde{J}_{\parallel\mathbf{k}}^* i k_y \widetilde{A}_{\parallel\mathbf{k}}$, vanishes since $\widetilde{J}_{\parallel\mathbf{k}} = k_\perp^2 \widetilde{A}_{\parallel\mathbf{k}}$. The transfer effects and sinks are the same as those in the homogeneous case, but now the gradient introduces the sources, which we can identify as the terms multiplied by ω_p,

$$\Gamma_n = U^{-1}\,\mathrm{Re}\left[-\frac{\omega_p}{\Gamma}\widetilde{p}_{e\mathbf{k}}^* i k_y \widetilde{\phi}_{\mathbf{k}}\right] \qquad \Gamma_m = U^{-1}\,\mathrm{Re}\left[\hat{\beta}\omega_p \widetilde{u}_{\parallel\mathbf{k}}^* i k_y \widetilde{A}_{\parallel\mathbf{k}}\right] \tag{5.54}$$

The first of these is the ExB gradient drive, and the second is the sound wave magnetic drive; almost all interesting cases have $\Gamma_m \ll \Gamma_n$. The sinks are given by the negative definite terms,

$$\Gamma_c = U^{-1}\,\mathrm{Re}\left[C\left|\widetilde{J}_{\parallel\mathbf{k}}\right|^2\right] \qquad \Gamma_s = U^{-1}\,\mathrm{Re}\left[\mu_\parallel k_\parallel^2 \left|\widetilde{u}_{\parallel\mathbf{k}}\right|^2\right] \tag{5.55}$$

giving the resistive and viscous damping. As for the kinetic shear Alfvén wave model, the resistivity acts only on the adiabatic response, and the viscosity acts only on the sound waves. The total energy, U, is given by

$$U = k_\perp^2 \left|\widetilde{\phi}_{\mathbf{k}}\right|^2 + \frac{1}{\Gamma}\left|\widetilde{p}_{e\mathbf{k}}\right|^2 + \left(\hat{\beta} + \hat{\mu} k_\perp^2\right) k_\perp^2 \left|\widetilde{A}_{\parallel\mathbf{k}}\right|^2 + \hat{\epsilon}\left|\widetilde{u}_{\parallel\mathbf{k}}\right|^2 \tag{5.56}$$

representing ExB, thermal, electromagnetic, and sound wave free energy, respectively. These sources and sinks are normalised in terms of a total growth rate,

$$\gamma = \frac{1}{2U}\frac{\partial U}{\partial t} = \Gamma_n + \Gamma_m - \Gamma_c - \Gamma_s \tag{5.57}$$

which in this case is simply the linear growth rate. The mode frequency is measured from the phase of the disturbance,

$$\omega = -\frac{\partial}{\partial t}\,\mathrm{Im}\log \widetilde{p}_{e\mathbf{k}} \tag{5.58}$$

correcting for the branch cut at $\pm\pi$.

The principal ExB source which we have been discussing is Γ_n. If we go back to the spatial representation, we find that it is given as net down-gradient transport times the gradient strength,

$$\frac{\partial}{\partial t}\frac{1}{2\Gamma}\widetilde{p}_e^2 = \cdots + \frac{\omega_p}{\Gamma}\left\langle -\widetilde{p}_e\frac{\partial\widetilde{\phi}}{\partial y}\right\rangle = \cdots + \frac{\omega_p}{\Gamma}\left\langle \widetilde{p}_e\widetilde{\mathrm{v}}_E\right\rangle \tag{5.59}$$

where the angle brackets denote the average over the spatial domain. We can see where the phase shifts are relevant by returning to the Fourier representation, noting that the domain average gives Γ_n, and then substituting $\widetilde{p}_{e\mathbf{k}} = (1-i\alpha)\widetilde{\phi}_{\mathbf{k}}$, to find

$$\Gamma_n = U^{-1}\frac{\omega_p k_y}{\Gamma}\,\alpha\left|\widetilde{\phi}_{\mathbf{k}}\right|^2 \tag{5.60}$$

If the details of the adiabatic response give rise to a positive phase shift, then we have positive net down-gradient transport and a growing disturbance.

5.VII. Alfvénic Transients — The Initial Value Problem for Drift Waves

We have three equations (or four, with the sound waves) but so far have looked at only one mode at the given $(k_x, k_y, k_\parallel)$. In a real initial value problem we cannot simply pick out the eigenmode of choice but must allow the dynamical system to evolve from an initial state. That is, we are not allowed to Fourier transform time. Our usual scenario for this is the initial pressure disturbance localised in all three dimensions. As in the cases we looked at in the previous chapter, the linear nature of the problem allows restriction to a single spatial Fourier component, so it is sufficient to start with the appropriate periodic initial state. The evolution is described by that of each linear eigenmode, of which there are three if we neglect the sound waves. We can find all three of these modes by combining the methods above to find the drift wave and those of the previous chapter to find the two kinetic shear Alfvén waves. Neglecting $\widetilde{u}_\parallel$, we may manipulate Eqs. (5.26,5.27,5.28) into the following form for the Fourier components,

$$\left(\frac{\partial}{\partial t} + i\frac{\omega_p k_y}{1+\Gamma k_\perp^2}\right)\widetilde{\phi}_{\mathbf{k}} = -\frac{1}{1+\Gamma k_\perp^2}\frac{\partial\widetilde{h}_{e\mathbf{k}}}{\partial t} \tag{5.61}$$

$$\left(\frac{\partial}{\partial t} \pm iV_a k_\parallel\right)\left[\widetilde{h}_{e\mathbf{k}} \mp V_a\left(\hat{\beta}\widetilde{A}_{\parallel\mathbf{k}} + \hat{\mu}\widetilde{J}_{\parallel\mathbf{k}}\right)\right] = -i\omega_p k_y\left(\widetilde{\phi}_{\mathbf{k}} \mp iV_a\hat{\beta}\widetilde{A}_{\parallel\mathbf{k}}\right) \pm V_a C\widetilde{J}_{\parallel\mathbf{k}} \tag{5.62}$$

where V_a is the kinetic shear Alfvén phase velocity given in these units by

$$V_a^2 = \frac{1+\Gamma k_\perp^2}{\hat{\beta}+\hat{\mu}k_\perp^2} \tag{5.63}$$

The first equation is the same as Eq. (5.40), which gives the drift wave with $\widetilde{h}_e$ as a correction, as we have seen. The second combines the two adiabatic response equations, in which $\partial/\partial t \sim \hat{\beta}^{-1/2} \gg 1$, leaving the ω_* terms on the right as corrections, and the C term for resistive damping. This latter pair of equations describes the two kinetic shear Alfvén waves to which the drift wave is coupled. Together, these are the three eigenmodes in terms of which the initial state evolves. Since $\widetilde{\phi}_{\mathbf{k}}$ starts at zero, all the modes are excited (including the drift mode, since we may replace $\widetilde{\phi}_{\mathbf{k}}$ by $\widetilde{p}_{e\mathbf{k}}$ in its eigenmode equation, adjusting the correction on the right side accordingly). If $k_\perp^2 \ll 1$ in addition to $(\hat{\beta}, \hat{\mu}, C) \ll 1$, the evolution is relatively simple: the Alfvén waves' zero frequency mode, $\widetilde{p}_{e\mathbf{k}} - \Gamma k_\perp^2 \widetilde{\phi}_{\mathbf{k}}$, does not evolve on the short time scales, $\tau \sim \hat{\beta}^{1/2}$, on which the two Alfvén transients propagate and dissipate. On the slower time scale of $\tau \sim (\omega_p k_y)^{-1}$, the nearly adiabatic structure is well established and drift wave begins to propagate. At late times the transients are long dead, leaving the drift mode which propagates with $\omega \approx \omega_L$ and slowly grows on the time scale of $\tau \sim (\omega_L \alpha)^{-1}$. This is the eventual solution, justifying the simpler procedure of finding the sole mode with a positive growth rate. At very late times, the drift mode interacts with the remaining sound wave, which is damped in the four field model through parallel viscosity.

5.VIII. Numerical Examples

It is instructive to take the same numerical examples we did for kinetic shear Alfvén and sound waves, and include the background gradient effects, and with them the drift wave. We take a single $k_\parallel = 1$, and set $\Gamma = 1$ and $k_x = 0$ for simplicity, and examine the spectrum of modes of various k_y. Each of these is followed from the initial disturbance until the final mode structure is established and the growth rate and mode frequency can be measured. For this purpose we also include the sound waves, so that the equations to be solved are the four ordinary differential equations,

$$\frac{\partial \widetilde{\phi}_{\mathbf{k}}}{\partial t} = -ik_\parallel \widetilde{A}_{\parallel \mathbf{k}} \tag{5.64}$$

$$\frac{\partial \widetilde{p}_{e\mathbf{k}}}{\partial t} = -i\omega_p k_y \widetilde{\phi}_{\mathbf{k}} + ik_\parallel \left(k_\perp^2 \widetilde{A}_{\parallel \mathbf{k}} - \widetilde{u}_{\parallel \mathbf{k}} \right) \tag{5.65}$$

$$\left(\hat{\beta} + \hat{\mu} k_\perp^2 \right) \frac{\partial \widetilde{A}_{\parallel \mathbf{k}}}{\partial t} = ik_\parallel \left(\widetilde{p}_{e\mathbf{k}} - \widetilde{\phi}_{\mathbf{k}} \right) - i\omega_p \hat{\beta} k_y \widetilde{A}_{\parallel \mathbf{k}} - C k_\perp^2 \widetilde{A}_{\parallel \mathbf{k}} \tag{5.66}$$

$$\hat{\epsilon} \frac{\partial \widetilde{u}_{\parallel \mathbf{k}}}{\partial t} = -ik_\parallel \widetilde{p}_{e\mathbf{k}} + i\omega_p \hat{\beta} k_y \widetilde{A}_{\parallel \mathbf{k}} - \mu_\parallel k_\parallel^2 \widetilde{u}_{\parallel \mathbf{k}} \tag{5.67}$$

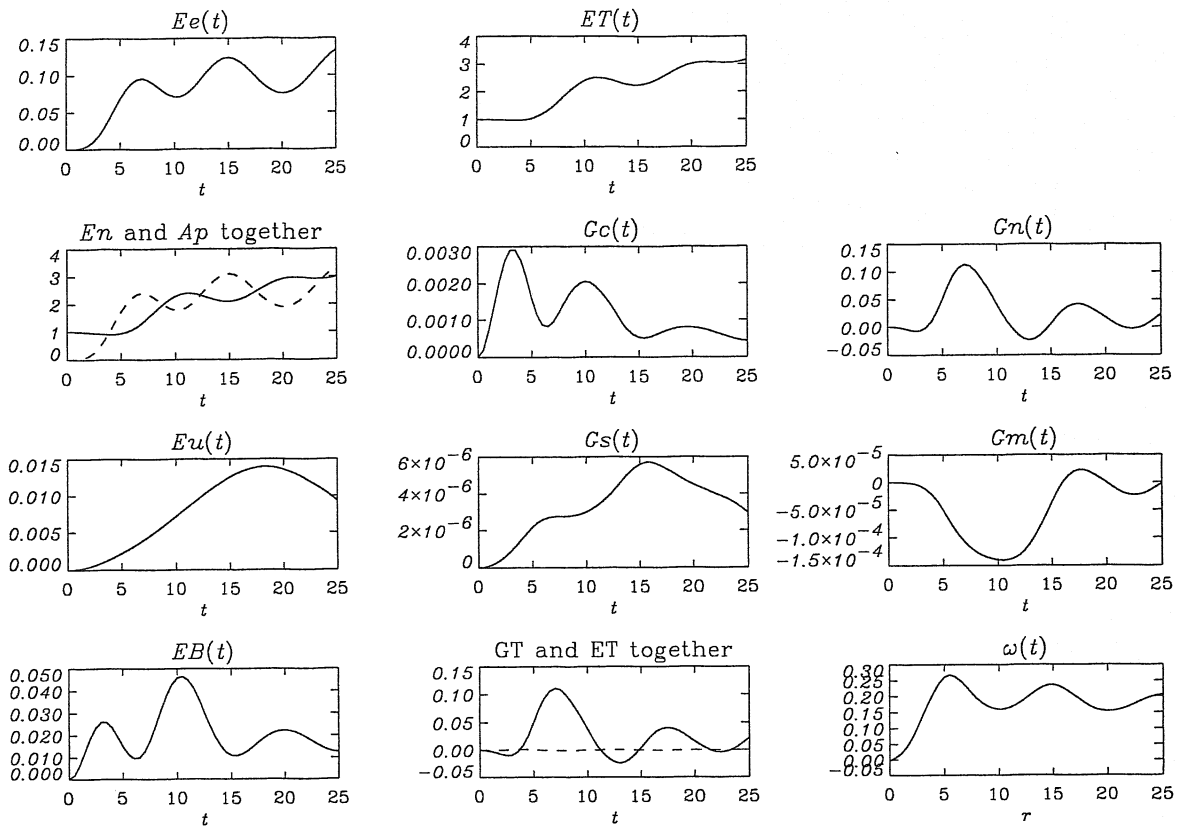

Figure 5.5a. Transient response to the initial pressure disturbance, for the warm plasma case with $K = 0.2$. The Alfvénic transients are excited and then $\widetilde{\phi}_{\mathbf{k}}$ and $\widetilde{p}_{e\mathbf{k}}$ oscillate about each other at similar amplitude. The quantities Ee, En, Eu, and EB give the contributions of $\widetilde{\phi}_{\mathbf{k}}$, $\widetilde{p}_{e\mathbf{k}}$, $\widetilde{u}_{\|\mathbf{k}}$, and $\widetilde{A}_{\|\mathbf{k}}$ to the total energy (ET), respectively. The squared amplitude of $\widetilde{\phi}_{\mathbf{k}}$ (Ap) is shown together with En. The sink rates Gc and Gs are due to resistivity and viscosity, and the source rates Gn and Gm give the ExB and magnetic parts of the pressure gradient drive, respectively. The total growth rate (GT) is much larger than the error (GE). The instantaneous mode frequency, ω, is also shown.

for the four dependent variables $(\widetilde{\phi}_{\mathbf{k}}, \widetilde{p}_{e\mathbf{k}}, \widetilde{A}_{\|\mathbf{k}}, \widetilde{u}_{\|\mathbf{k}})$, which follow from Eqs. (5.25–5.29). The initial state for all cases is $\widetilde{p}_{e\mathbf{k}} = 1.0$ and $\widetilde{\phi}_{\mathbf{k}} = \widetilde{A}_{\|\mathbf{k}} = \widetilde{u}_{\|\mathbf{k}} = 0$.

This is a very simple task easily taken care of by use of the second order Runge-Kutta scheme. The general form of the equations is $\dot{\mathbf{x}} = \mathbf{A} \cdot \mathbf{x}$, that is, a set of ordinary differential equations with a matrix of coefficients. One time step is given by

$$\mathbf{x}^* \leftarrow \mathbf{x} + \frac{1}{2}\tau \mathbf{A} \cdot \mathbf{x} \qquad \mathbf{x} \leftarrow \mathbf{x} + \tau \mathbf{A} \cdot \mathbf{x}^* \tag{5.68}$$

The time step in all cases was set to $\tau = 0.01$. Computed numbers are sampled 250 times between $0 < t < 125$, and averaged over the last 100 samples.

The warm plasma case, appropriate to the outer regions of magnetically confined fusion plasma experiments, is given by

$$\hat{\beta} = 5 \qquad \hat{\mu} = 2.7 \qquad \nu = 10 \qquad \mu_{\|} = 10 \qquad \hat{\epsilon} = 10^4 \tag{5.69}$$

reflecting deuterium ions and a scale ratio of $K_{\|}L_{\perp} = 10^{-2}$. The hot plasma case, appropriate to the core regions of such experiments, is given by

$$\hat{\beta} = 1 \qquad \hat{\mu} = 0.027 \qquad \nu = 0.1 \qquad \mu_{\|} = 1 \qquad \hat{\epsilon} = 10^2 \tag{5.70}$$

reflecting a scale ratio of $K_{\|}L_{\perp} = 10^{-1}$. We also examine an electrostatic case, given by the warm plasma parameters but with $\hat{\beta} = 0.1$.

The warm plasma case with $K = 0.2$ is exemplary for the transient phase and establishment of the drift wave mode structure, starting from the initial pressure disturbance. The mode frequency and growth rate finish at 0.186 and 0.0212, and the nominal resistive damping rate $\hat{\mu}K^2C/\hat{\beta}$ is about 0.01. In Fig. 5.5a, we see the transient phase, to $t = 25$, too short for the resistive damping to have been completely effective, but long enough for about two kinetic shear Alfvén periods. The amplitudes of $\widetilde{p}_{e\mathbf{k}}$ and $\widetilde{\phi}_{\mathbf{k}}$ are already comparable, reflecting the adiabatic response. Sound waves are negligible on this time scale. The ExB drive rate (Gn, which is Γ_n), oscillates, showing that the mode structure has not found itself. The mode frequency, however, has found its eventual value and is settling there. The emergence of the drift wave from this transient state is shown in Fig. 5.5b, with the evolution to $t = 125$. Here we find all pieces of the electron dynamics (Γ_n and Γ_c), as well as the mode frequency and growth rate, pinned to their eventual values. Only the sound wave component has not settled, but this is of negligible impact. For all intents and purposes, the drift wave structure is well established, and the disturbance is growing as an instability.

A sketch of the basic process is shown in Fig. 5.6, which repeats the kinetic shear Alfvén structure of Fig. 4.3 of the previous chapter, but then adds the background gradient. The initial adiabatic response is the same, and the rest of the dynamics sets in more slowly. The adiabatic response tends to keep $\widetilde{\phi}_{\mathbf{k}}$ close to $\widetilde{p}_{e\mathbf{k}}$ as for the kinetic shear Alfvén waves, but now the advection of the gradient also tends to push $\widetilde{p}_{e\mathbf{k}}$ ahead of $\widetilde{\phi}_{\mathbf{k}}$, as in Fig. 5.1. The resulting structure, the drift wave, reflects the combination of these two processes, and drifts in the y-direction. If the phase shift is not small, the simple models of Sections 5.III and 5.IV, and even the small phase shift expansion of Section 5.V, break down, and

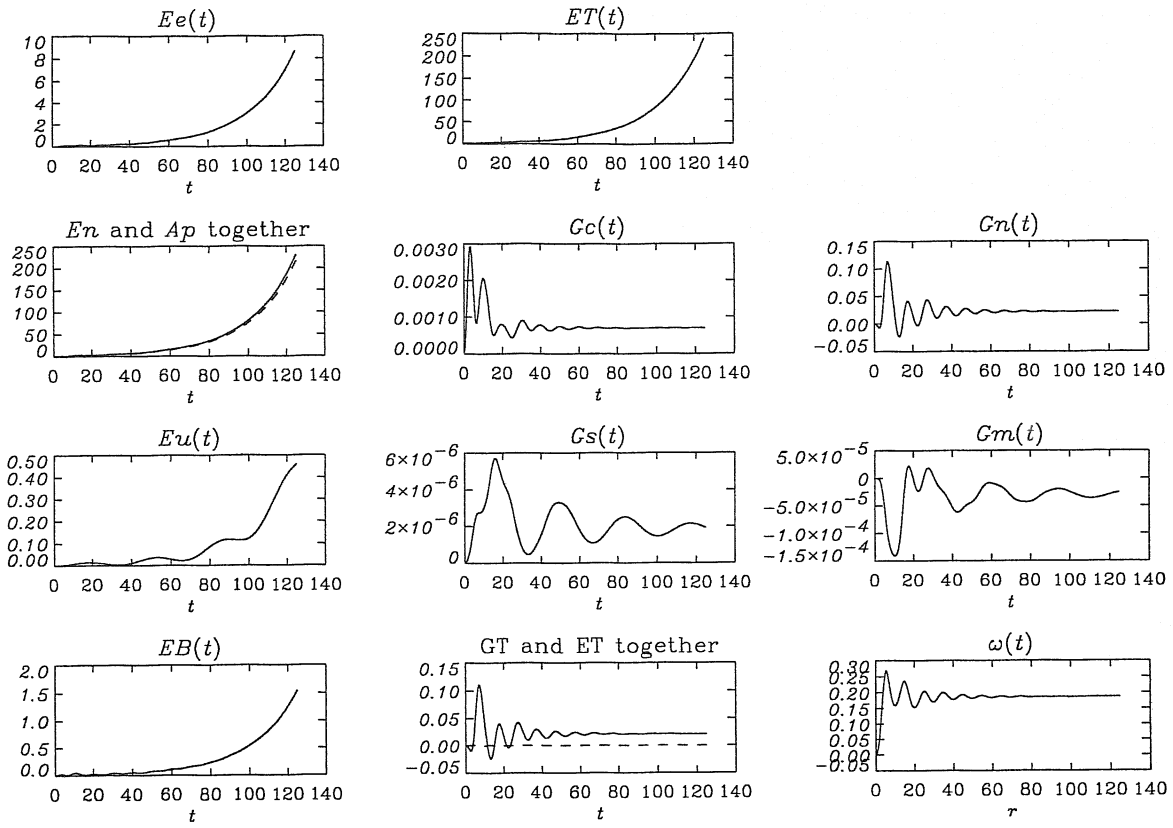

Figure 5.5b. Development of the drift wave structure from the initial pressure disturbance, for the warm plasma case with $K = 0.2$. The Alfvénic transients are excited and then decay on a time scale of about $\Delta t = 50$. Both the mode frequency and growth rate settle out on this same scale, as the drift wave emerges from the initial state of all four eigenmodes. The sound wave energy and damping are very small, due to the small $K_\parallel L_\perp$; a companion case run without the sound waves gave nearly identical results for the other quantities. The only important free energy source is the ExB transport (Gn), and the only significant sink is resistivity (Gc), although the small K^2 keeps $\Gamma_c \ll \Gamma_n \approx \gamma$.

we have to consider the general problem. This is already apparent in the departure of the mode frequency of the previous case, 0.186, from its nominal value of 0.192. Generally, the mode frequency slows down as the structure becomes more nonadiabatic, and the growth rate is also reduced.

The reduction of the mode frequency below ω_L is evident for the electrostatic case, shown in Fig. 5.7, chosen such that the resistive damping term in the Ohm's law is easily the largest, leaving the dynamics in the collisional regime. But the value of C large enough to ensure this also produces a strong nonadiabatic response, with growth rates above 0.1

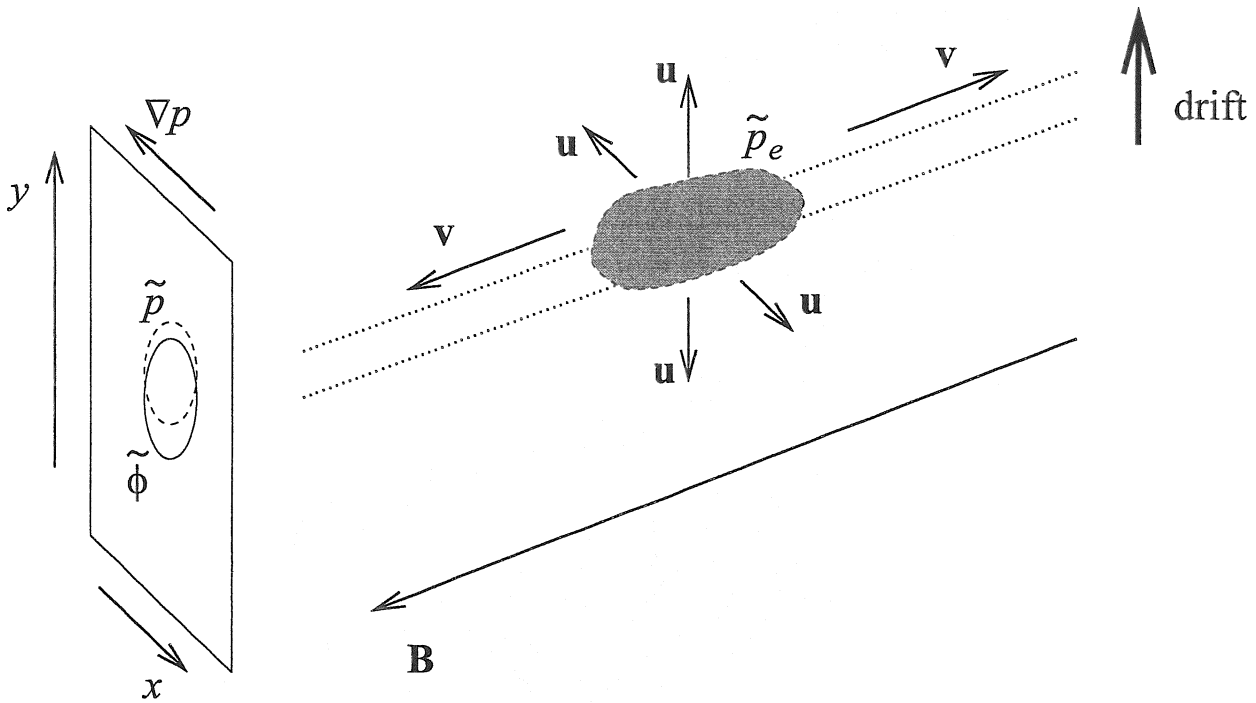

Figure 5.6. The drift wave structure, localised to a flux tube in the xy-plane, caused by an initial electron pressure disturbance, showing how it is formed by the kinetic shear Alfvén wave oscillation. The adiabatic response consists of the pressure disturbance ($\widetilde{p}_{e\mathbf{k}}$) launching the Alfvénic activity, tends to force $\widetilde{\phi}_{\mathbf{k}}$ towards $\widetilde{p}_{e\mathbf{k}}$, with the polarisation (ions, $\mathbf{u}$) and parallel (electrons, $\mathbf{v}$) currents balancing to maintain quasineutrality. When a background gradient is present, the ExB vortex in the xy-plane represented by $\widetilde{\phi}_{\mathbf{k}}$ (contour given by the solid circle) continually excites $\widetilde{p}_{e\mathbf{k}}$ (contour given by the dashed circle) where the ExB flow is down-gradient, that is, phase shifted in the forward drift direction (y). The combination of these two effects results in a net drift of the entire structure in the y-direction. When the Alfvénic transients have damped away, the result is a drift wave.

in the last half decade before $k_y = 1$. Nevertheless, the overall behaviour does follow the simple near-adiabatic model, defined by the regime in which the corrections on the right sides of Eqs. (5.65,5.66) are small.

Turning to the warm plasma case, we find that the finite electromagnetic behaviour has minimal effect. Although $\hat{\beta} > \hat{\mu}$, we still have $CK^2 > \hat{\beta}$ for all but the longest wavelength range. The growth rates are lowered by the perturbative effect of the magnetic flutter effect ($\widetilde{\mathbf{B}} \cdot \nabla p_e$) on the phase shifts, as we will explore in the next section. But for this value of $\hat{\beta}$ the effect is not large.

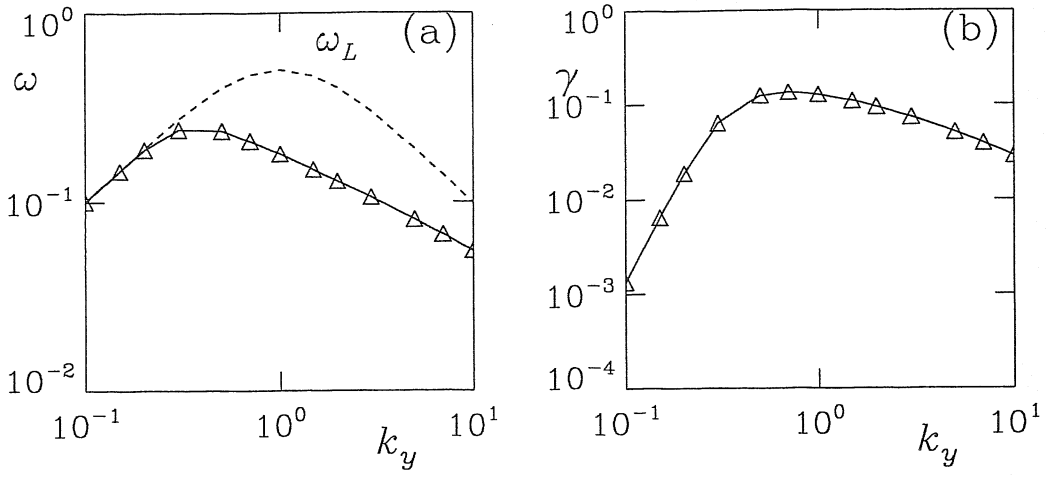

Figure 5.7. Spectra of the mode frequency (a) and growth rates (b), for the electrostatic case. The near-adiabatic model is closely followed until about $k_y = 0.3$, beyond which the nonadiabatic response is substantial. The spectrum for γ is still much steeper on the long-wave side of the peak.

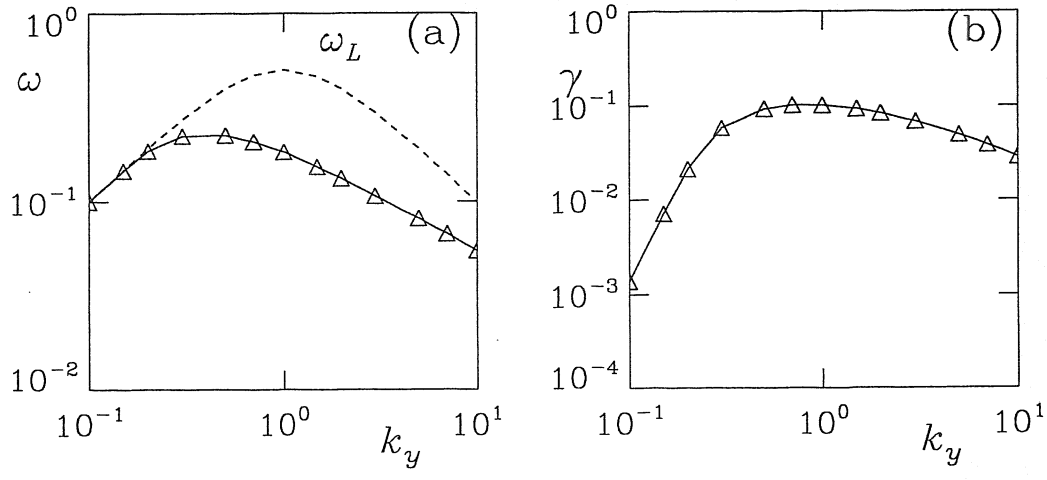

Figure 5.8. Spectra of the mode frequency (a) and growth rates (b), for the warm plasma case. The difference to Fig. 5.7 is minimal, with the growth rates very slightly lower in the peak range. The spectrum for γ does not strongly feel the electromagnetic effects. This follows from the relatively high collisionality.

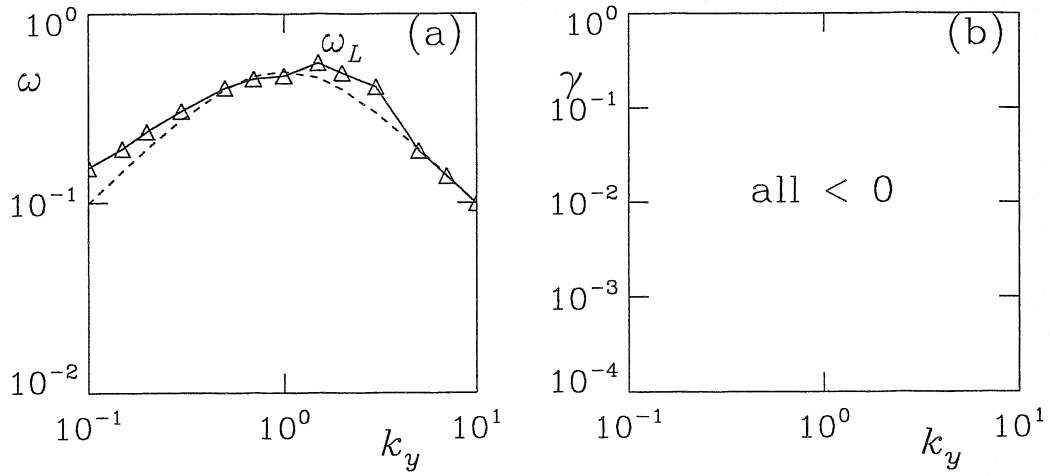

Figure 5.9. Spectra of the mode frequency (a) and growth rates (b), for the hot plasma case. The growth rates are all indistinguishable from zero, but the oscillation of the mode amplitudes and energetics is observed to have a small decay. The very low collisionality is not strong enough to cause an instability on a system undergoing rapid, nearly undamped kinetic shear Alfvén oscillations. To treat this case properly requires the electron temperature physics of Chapter 12.

The hot plasma case is quite different. Here, $\hat{\beta} \gg \hat{\mu}$ and furthermore C is small enough to make $\hat{\beta}\omega_* \gg Ck_\perp^2$ unless K is unrealistically large. This is a reactive case, where we could more or less set C to zero. The growth rates are uncertain but the total energy does drop with time. The mode frequency spectrum is shown in Fig. 5.9, together with the finding that the time averaged growth rates are negative. The nonadiabatic effects are small on average, which is why ω follows ω_L, but the temporal excursions are large and do not die out. This property is shown in Fig. 5.10, in which we can see that the total energy and ExB drive rate oscillate dramatically about a value much closer to zero than the standard deviation. We will discuss reactive dynamics in Section 5.X; it typically points to the need for additional physics, which for this case requires the electron temperature as treated in Chapter 12.

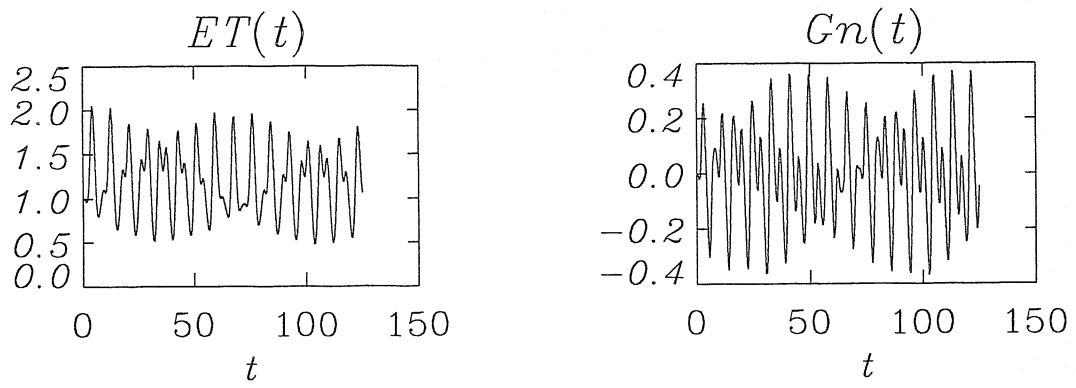

Figure 5.10. Development of the drift wave structure from the initial pressure disturbance, for the hot plasma case with $K = 0.5$. The Alfvénic transients are excited but then do not decay effectively, since the collisionality is so low. Oscillations in the total energy (ET) and gradient drive rate (Gn) are large, but there is a discernible long term drop in ET. See Figure 5.9.

5.IX. Drift Alfvén Waves — The Magnetic Flutter Effect

When the electromagnetic effects entering through $\widetilde{A}_{\|}$, hence the finite β_e, start to have significant effect on the drift wave, the drift wave becomes a drift Alfvén wave, since the particular properties of the Alfvénic transients as such start to alter the structure of the drift wave mode, and therefore the mode frequency and growth rate. The place in the dynamics this happens is in the response of the parallel current $\widetilde{J}_{\|}$ to its force potential $\widetilde{h}_e$. If the situation is collisional and electrostatic, the the response is dissipative, with $\widetilde{J}_{\|}$ exactly $\pi/2$ out of phase with $\widetilde{h}_e$. In this limit the parallel dynamics acts as a resistive diffusion of the force potential along the magnetic field. When the magnetic effects enter, this phase relation alters, with effect on the phase shift $\widetilde{h}_e \leftrightarrow \widetilde{\phi}$ of the drift wave.

There are two electromagnetic effects to consider. One is induction, represented by $\partial \widetilde{A}_{\|}/\partial t$ in the Ohm's law. The other is magnetic flutter, arising from the parallel gradient of the background electron pressure, $\widetilde{\mathbf{B}} \cdot \nabla p_e$, also in the Ohm's law. This comes from the fact that the disturbances to the magnetic field lines can give them a down-gradient component. The causal chain for this is the dependence of the drift wave state variables in the drift direction ($\partial \widetilde{h}_e/\partial y$), so that the current they generate has the same dependence, due to the linearity of the electrostatic, dissipative part of the Ohm's law. Ampere's law, which is also linear, therefore yields a magnetic potential, $\widetilde{A}_{\|}$, with the same y-dependence as $\widetilde{h}_e$. This in turn yields a disturbance in the magnetic field which is in the x-direction, down or up the gradient, depending on the sign.

Each of these effects carries with it a particular perpendicular scale. These are the collisional and collisionless skin depths, σ_0 and σ_c respectively, given by

$$\sigma_0^2 = \frac{\mu_e}{\beta_e}\rho_s^2 \qquad \sigma_c^2 = \frac{0.51\mu_e\nu_e}{\beta_e\omega_*}\rho_s^2 \tag{5.71}$$

in physical units. The first follows from the competition between electron inertia ($\partial\widetilde{J}_\parallel/\partial t$) and magnetic induction ($\beta_e\omega$); the second follows from the competition between resistivity and magnetic flutter ($\beta_e\omega_*$). When both of these scales are smaller than the perpendicular scale of motion, these finite β_e effects significantly influence the response of $\widetilde{J}_\parallel$ to $\widetilde{h}_e$.

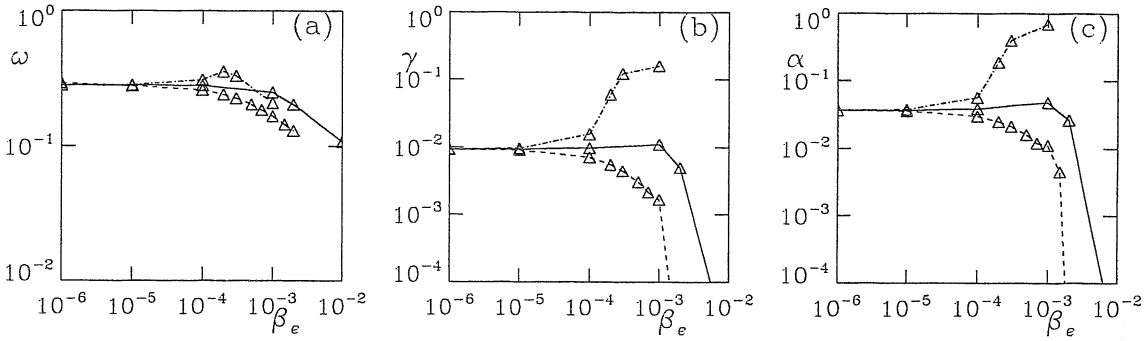

Figure 5.11. Scalings of the mode frequency (a) and growth rates (b), and phase shifts (c), versus β_e, for the warm plasma case with the collisionality reduced to $\nu = 1$. Note that $\hat{\beta} = 10^4\beta_e$ for these parameters. The solid curve is nominal, the dashed curve is with the magnetic flutter effect ($\widetilde{\mathbf{B}} \cdot \nabla p_e$) doubled, and the dash-dot curve is with the flutter effect turned off. The role of the flutter effect is to cancel the magnetic induction in the Ohm's law, with the induction destabilising and the flutter effect stabilising. If the flutter effect is doubled, a clear stabilising tendency results, explained by the phase shifts rather than the more frequencies, as in the text.

The electromagnetic effects have opposite tendencies, reflected by the entrance of $\hat{\beta}$ in the response equation for the Fourier components, Eq. (5.44). The physical explanation for this, in the regime that the finite $\hat{\beta}$ effects are weak, is that when a current starts to flow, the field line is tipped from its equilibrium position towards the direction of the gradient. The resulting pressure force opposes the induced current, leaving the resistive dynamics unperturbed if $\omega = \omega_*$. But this is the real frequency part of $\omega - \omega_*$, which doesn't directly affect the phase shift anyway. Eq. (5.44) may be rewritten as

$$k_\parallel^2 \widetilde{h}_{e\mathbf{k}} = \omega\left[\hat{\beta}\left(\omega_* - \omega\right) - \left(\hat{\mu}\omega + iC\right)k_\perp^2\right]\widetilde{\phi}_{\mathbf{k}} \tag{5.72}$$

Setting the factor of ω to ω_L, assuming that $\widetilde{h}_e$ is a correction, we find that the imaginary part of the response $\widetilde{h}_{e\mathbf{k}}/\widetilde{\phi}_{\mathbf{k}}$ is affected only by C, that is, dissipation. But especially when the growth rate is substantial, there is also an imaginary correction due to γ multiplied by $\hat{\beta}(\omega_* - \omega)$. If $\omega_* > \omega$, the usual case even for the isothermal model, the imaginary part of the finite $\hat{\beta}$ correction actually subtracts from the phase shift represented by C. We may rewrite Eq. (5.72) in terms of the (real) mode frequency and growth rate, obtaining

$$k_{\|}^2 \widetilde{h}_{e\mathbf{k}} = (\omega_R + i\gamma)\left[\hat{\beta}\,(\omega_* - \omega_R) - (\hat{\mu}\omega_R + iC)\,k_{\perp}^2\right]\widetilde{\phi}_{\mathbf{k}} \tag{5.73}$$

where ω_R, γ, and ω_* are all real coefficients. The correction due to $\hat{\beta}\omega_*\gamma$ is obviously stabilising since it acts to reduce the phase shift in the self consistent electron response. If ω_R is close to ω_*, the magnetic induction and flutter effects cancel, but if (as usual) $\omega_R < \omega_*$, then the net effect is stabilisation by magnetic flutter. We note as well the destabilising tendency of the electron inertia, $\hat{\mu}$, which has the same physical role as the magnetic induction.

We can find if this is the actual mechanism for the finite $\hat{\beta}$ stabilisation we saw marginally in the warm plasma case but clearly in the hot plasma case, by setting C to something intermediate between the two cases and varying $\hat{\beta}$. We do this for the model equations unaltered (the same ω_* in the magnetic flutter effect as in the ExB gradient drive), for the flutter effect doubled, and then for the flutter effect removed entirely. Varying the flutter effect in this fashion amounts to placing a constant coefficient in front of the two $\hat{\beta}\omega_p$ terms in Eqs. (5.66,5.67), setting it to 1.0, 2.0, and 0, respectively. The parameters for these cases were set to

$$\hat{\mu} = 2.7 \qquad \nu = 1 \qquad \mu_{\|} = 10 \qquad \hat{\epsilon} = 10^4 \qquad K = 0.3 \tag{5.74}$$

and β_e was swept between 10^{-6} and 10^{-2}, noting that $\hat{\beta} = 10^4\beta_e$. The results are shown in Fig. 5.11, and it is clear that the lack of a strong $\hat{\beta}$ effect for the nominal case is due to the cancellation between the magnetic induction and flutter effects, because when we double the flutter effect we find a clear stabilisation. With no flutter we find a reactive instability, discussed in the next section. Clearly, magnetic induction is destabilising, and magnetic flutter is stabilising. We note that this cannot be explained by the effects on the real frequency, which does not exhibit strong changes with which we could explain the effects on γ. What does change with the magnetic flutter effect, however, is the drift wave phase shift. We therefore find that the magnetic flutter effect does its work indirectly, on the phase shift of a growing instability, rather than directly through the real frequency effects associated with the skin depths.

5.X. Reactive Instabilities

In the previous two sections we found another curious effect. This is that when the effective inertia of the adiabatic response, $\hat{\beta} + \hat{\mu}k_\perp^2$, is large enough we found instabilities which do not depend on dissipation. We referred to this briefly in Section VI, after Eq. (5.47), that is, that the effect of the real part of the self consistent response cannot cause instability if it is a correction. However, with substantial $\hat{\beta}$, we start to find reactive instabilities, termed as such because they are not catalysed by dissipation. Reactive instabilities are similar to such textbook ideal fluid results as the Kelvin-Helmholtz and firehose instabilities. They are part of a system which is perfectly conservative, and in the simple examples the equation to be solved involves Hermitian operators whose eigenvalues are purely real. These eigenvalues are squared frequencies, so that when they are negative the eigenmode becomes a purely growing instability. In the present case, we have four eigenmodes although they do not come in pairs, but when $\hat{\beta} + \hat{\mu}k_\perp^2$ is large enough two of the eigenfrequencies are nevertheless purely imaginary, one of which represents a purely growing instability. For fluid dynamics these are physically real instabilities, but for a plasma they usually signify that we are missing some important physics. For drift waves that is indeed the case. The clearest example of a reactive instability in the drift wave system arises when $\hat{\beta}$ is small but $\hat{\mu}k_\perp^2$ is larger than unity, and C is not large enough to control the dynamics. This is an instability caused by parallel dynamics of a finite electron mass, and that is always a sign that we need to extend the dynamical model to incorporate Landau damping, an expressly kinetic effect. We will not go further to address such effects in this chapter, but it is useful to keep the general concept in mind. In this case it means we cannot use the four field model for low collisionality (even if the reactive instability is removed by the magnetic flutter effect), but must include the electron temperature and the associated kinetic effects. We will return to this point in Chapter 12.

5.XI. Summary

Drift waves represent a fundamental interaction between parallel and perpendicular dynamics which occurs in a magnetised plasma with an electron pressure gradient. Advection of the background gradient liberates free energy, which is then dissipated through the adiabatic response. The advection effect tends to drive the phase shift of the pressure disturbance ahead of the electrostatic potential disturbance by a quarter wavelength, while the adiabatic response tends to reduce it to zero. The phase shift and free energy tapping, and net transport, all go together. In the most idealised case the kinetic shear Alfvén oscillations, and their dissipation, are arbitrarily fast, so that the electrons are almost adiabatic, and the phase shift and growth rate are small. For interesting parameters,

however, the corrections rapidly become too large for this implied expansion to be valid, and a computation which involves the damped transients is necessary. It is possible to do an eigenvalue analysis to find the maximum growth rate, but the physics of the drift wave dynamics is more transparent in the initial value problem for which the instability has to evolve. The initial state of a pressure disturbance is exemplary in showing the relationship of drift waves to kinetic shear Alfvén waves. By the same token, one could not study drift waves with an MHD model, since the coupling of Alfvénic dynamics to the electron pressure would then be missing. Drift waves are dissipative instabilities, requiring either resistivity or kinetic dissipation effects, so that if the resistivity is too small one would have to keep the electron temperature dynamics. When the dynamical beta, β_e, is large enough, the adiabatic response becomes electromagnetic, and the drift wave becomes a drift Alfvén wave. Magnetic induction, part of the effective inertia of the adiabatic response, is generally destabilising, and magnetic flutter, which is a parallel gradient of the background along disturbed field lines, is generally stabilising, in both cases due to indirect effects on the drift wave phase shift. The details of stability or instability then follow from the relative size of these two effects. Drift wave stability in general is sensitive to the details of the cancellation between the mode frequency and the diamagnetic frequency.

Further Reading

Drift wave instabilities have an extensive literature, most of which is concerned on the details introduced by particular magnetic geometric or electron kinetic effects. The original reference for the isothermal collisional model is S. S. Moiseev and R. Z. Sagdeev, *Sov. Phys. JETP* 17 (1963) 515. The collisionless model used to be called the universal instability. Two reviews of the linear work are W. M. Tang, *Nucl. Fusion* 18 (1978) 1089, and P. C. Liewer, *Nucl. Fusion* 25 (1985) 543.

The electromagnetic generalisation, usually called the drift Alfvén wave, goes back to L. V. Mikhailovskaya and A. B. Mikhailovskii, *Sov. Phys. JETP* 18 (1964) 1077, and is treated by A. B. Mikhailovskii, in *Theory of Plasma Instabilities* (Consultants Bureau, New York, 1974). See also J. T. Tang and N. C. Luhmann, Jr., *Phys. Fluids* 19 (1976) 1935, for a very clear exposition.

The relationship of the drift wave to the transient electron parallel dynamics is almost never treated by papers on linear instabilities. The general importance of this became clear only in recent studies focussing on turbulence, such as S. Camargo, B. Scott, and D. Biskamp, *Phys. Plasmas* 3 (1996) 3912.

See also the Further Reading sections of the previous and next few chapters.

6. Nonlinear ExB Flow Dynamics and Drift Wave Turbulence

B. Scott

Jul 1999

6.1. Introduction — Turbulence as Incoherent Nonlinearity

In general situations the dynamical system is not comprised solely of a single wave or instability. This is due to the nonlinearity of the more general system when two or more eigenfunctions are excited; in general the various waves are coupled together and interact with each other as well as the background. Drift wave systems have as their dominant coupling mechanism a quadratic nonlinearity. Quadratic nonlinearities exhibit a phenomenon known as three wave coupling: each Fourier component $\mathbf{k}$ interacts with the other ones $\mathbf{k}'$ through beat waves $\mathbf{k}''$ satisfying the constraint $\mathbf{k} + \mathbf{k}' + \mathbf{k}'' = 0$. One can consider this as a process of modes $\mathbf{k}'$ and $\mathbf{k}''$ beating together to drive mode $\mathbf{k}$ (in the shorthand in which the word "mode" is used to signify an individual eigenmode, wave, or Fourier component).

We can distinguish between quasilinear and nonlinear effects. Quasilinear dynamics refers to a single wave interacting with the background; in other words, modes zero and $-\mathbf{k}$ driving mode $\mathbf{k}$, as in a linear system, but now together with modes $\mathbf{k}$ and $-\mathbf{k}$ driving mode zero. The waves excite changes in the background which affect the subsequent evolution of the waves. When many modes are excited, the dynamics could still be quasilinear if this particular wave/background interaction were still dominant. Such dynamics tends to produce relaxation oscillations in conservative systems: the action of the wave on the background is stabilising but overshoots the point at which the growth rate goes to zero, and then the free energy in the wave all goes back to the background, reestablishing the original unstable state, and so on. The interaction typically has a coherent character, with long term memory of initial conditions.

True nonlinear effects are different from this. The same three wave coupling mechanism works as well between all possible triplets in the full set of waves. Each three wave interaction works independently of all the others, but many such interactions affect each individual wave. The dynamics involves many degrees of freedom ("modes") all exchanging energy, and while each three wave interaction tends towards coherence, the fact that there are many of them going on simultaneously results in a weak degree of overall coherence between waves at differing $\mathbf{k}$ (we are careful to note that at each $\mathbf{k}$ there are as many eigenmodes as dependent variables). When these three wave interactions are as

strong as the quasilinear interactions, they result in an incoherent type of dynamics, which is fundamentally nonperiodic. Moreover, it has a short time memory: dynamics at the same spatial point but separated in time become uncorrelated beyond a time range called the correlation time. The correlation time is somewhat longer than the time required for individual eddies to turn over, but it is shorter than the time required for the collective disturbance free energy to respond to changes in the background parameters. The dynamics therefore quickly loses memory of any initial state, and somewhat more slowly reaches a state called saturation: the individual waves fluctuate vigorously in amplitude and phase, but their free energy (or amplitude) level remains statistically stationary over time scales of several correlation times. This type of dynamics is what we call turbulence. It is a nonequilibrium, dissipative system with many degrees of freedom, with short correlation times and lengths. It is characterised by its statistical properties, not so much by the evolutionary fate of individual structures. For those familiar with geophysical fluid dynamics, the distinction between individual eddies, or structures, within the turbulence and the statistical properties of the fluctuating dynamics is analogous to the distinction between weather and climate.

Turbulence in fluids is generally three dimensional, but in a magnetised plasma the magnetic field orders the dynamics such that its nonlinear part is essentially two dimensional. The fluid part of the dynamics occurs in what we can call the drift plane: the plane locally perpendicular to the magnetic field, in which the drift velocities and fluxes occur. The dynamics in the third dimension, along the magnetic field, is shaped principally by the electrons, through their adiabatic response. Drift wave turbulence therefore differs from its fluid counterpart by this tendency towards coupling between the flow eddies themselves and the quantities they transport. It does however share an important property of two dimensional fluid turbulence, the dual cascade of energy and enstrophy. Enstrophy is a generalised quantity sensitive to higher order derivatives of the flow potential than those present in the energy; for fluid turbulence it is the square of the flow vorticity while the energy is the square of the flow velocity. With both energy and enstrophy conserved by the nonlinear interactions of two dimensional turbulence, the energy is preferentially transferred inversely to larger scales in a local cascade each step of which involves similar scales of motion, and the enstrophy cascades in direct fashion to smaller scales.

Over the next four chapters, we will be investigating drift wave turbulence. In this chapter we study the basic three wave interactions and the properties they have in transferring free energy between different scales of motion, within the simplest two dimensional models which contain this dynamics. Chapter 7 covers the basic statistical features of drift wave turbulence, collectively called mode structure. Chapter 8 introduces the sheared

magnetic field, and the important property that while linear drift waves are stable under magnetic shear, the turbulence is robustly self sustaining if initialised at nonlinear amplitude, due to the way the nonlinear self-advection of ExB flow eddies changes the mode structure. Three dimensional turbulence is also introduced, and then two and three dimensional mode structure is compared. The turbulence is very similar in the two and three dimensional models because the nonlinear effects take place in the two dimensional plane locally perpendicular to the magnetic field. For these three chapters we study the nonlinear three wave interactions by themselves by turning off the effect the dynamics has on the background. In Chapter 9 we then study these background effects, the most important of which is what are called zonal flows: ExB flows perpendicular to both the magnetic field and the background gradient, with dependence only on the coordinate following the background gradient. These flows have a strong back reaction on the turbulence and are important both as an external forcing mechanism and as a suppression mechanism which is self generated by the turbulence.

6.II. Three Wave Coupling and Turbulence in the Drift Plane

Generally, as we have already seen for linear waves, the dynamics in the two dimensions perpendicular to the magnetic field is very different from that parallel to the field. The true wave motion involved in kinetic shear Alfvén and sound waves occurs only in the parallel direction. All drifts, including the ExB advection which in combination with the Alfvénic dynamics gives rise to drift waves, are strictly perpendicular to the magnetic field. Their dynamics is therefore two dimensional, and takes place in the plane everywhere locally perpendicular to the magnetic field. This plane we can call the drift plane. Although the drift dynamics is perpendicular to the total magnetic field including the disturbances, the difference this makes to the perpendicular drift operator given by $(c/B^2)\mathbf{B}\times$ is negligible under drift ordering. The parallel direction, by contrast, is strongly affected by the magnetic disturbances because the corrections act in the dimensions perpendicular to the background magnetic field (the magnetic disturbances are perpendicular under drift ordering). Both the drift dynamics and the magnetic flutter part of the parallel dynamics therefore occur effectively in this drift plane.

The special property of the nonlinear terms which are kept under drift ordering is that they are quadratic. If we set up the coordinates for drift wave dynamics in a homogeneous magnetic field as in Chapter 5, Section V, and in Chapter 4, Section III,

$$\mathbf{B} = B\nabla s \qquad \nabla p_e = -\frac{p_e}{L_p}\nabla x \qquad \mathbf{B}\times\nabla p_e = -B\frac{p_e}{L_p}\nabla y \tag{6.1}$$

then the drift plane is simply the xy-plane. As nonlinearities we have (for example, on the pressure)

$$\mathbf{v}_E \cdot \nabla \widetilde{p}_e = \frac{c}{B}\left(\frac{\partial \widetilde{\phi}}{\partial x}\frac{\partial \widetilde{p}_e}{\partial y} - \frac{\partial \widetilde{p}_e}{\partial x}\frac{\partial \widetilde{\phi}}{\partial y}\right) \tag{6.2}$$

for the ExB advection, and

$$\widetilde{\mathbf{B}} \cdot \nabla \widetilde{p}_e = -\frac{1}{B}\left(\frac{\partial \widetilde{A}_\parallel}{\partial x}\frac{\partial \widetilde{p}_e}{\partial y} - \frac{\partial \widetilde{p}_e}{\partial x}\frac{\partial \widetilde{A}_\parallel}{\partial y}\right) \tag{6.3}$$

for the part of the parallel gradient due to the disturbances of the magnetic field lines. These are called the ExB and magnetic flutter nonlinearities, respectively. For this chapter we are concerned with the simplest electrostatic models, and so we only have the ExB nonlinearities to consider, one per dynamical equation.

Quadratic nonlinearities have the property that they are built up of couplings between three waves. In the equation for each perpendicular wave $\mathbf{k}$, given by

$$\mathbf{k} = k_x \nabla x + k_y \nabla y \tag{6.4}$$

we have contributions from two other waves $\mathbf{k}'$ and $\mathbf{k}''$, subject to the constraint

$$\mathbf{k} + \mathbf{k}' + \mathbf{k}'' = 0 \tag{6.5}$$

This constraint arises from the orthogonality of the Fourier transforms. Given a simple advection equation for $\widetilde{p}_e$ assuming that $\widetilde{\phi}$ is given,

$$\frac{\partial \widetilde{p}_e}{\partial t} = -\mathbf{v}_E \cdot \nabla \widetilde{p}_e = \frac{c}{B}\nabla s \cdot \left(\nabla \widetilde{p}_e \times \nabla \widetilde{\phi}\right) \tag{6.6}$$

(here neglecting the linear driving and coupling terms), we form the equation for the wave $\mathbf{k}$ using the Fourier transform relations

$$\widetilde{p}_e = \sum_{\mathbf{k}} e^{i\mathbf{k}\cdot\mathbf{x}} \widetilde{p}_{e\mathbf{k}} \qquad \widetilde{p}_{e\mathbf{k}} = \oint \frac{k^2 d^2 x}{4\pi^2} e^{-i\mathbf{k}\cdot\mathbf{x}} \widetilde{p}_e \qquad \widetilde{p}_{e-\mathbf{k}} = \widetilde{p}^*_{e\mathbf{k}} \tag{6.7}$$

to obtain

$$\frac{\partial \widetilde{p}_{e\mathbf{k}}}{\partial t} = \frac{c}{B}\nabla s \cdot \oint \frac{k^2 d^2 x}{4\pi^2} e^{-i\mathbf{k}\cdot\mathbf{x}} \sum_{-\mathbf{k}'} \sum_{-\mathbf{k}''} e^{-i\mathbf{k}'\cdot\mathbf{x}} e^{-i\mathbf{k}''\cdot\mathbf{x}} (i\mathbf{k}') \times (i\mathbf{k}'') \widetilde{p}_{e-\mathbf{k}'} \widetilde{\phi}_{-\mathbf{k}''} \tag{6.8}$$

The integral on the right side vanishes except for triplets $\{\mathbf{k}, \mathbf{k}', \mathbf{k}''\}$ for which Eq. (6.5) is satisfied.

Three wave models are constructed using a single triplet for explanatory purposes. The model consists of an evolution equation for each (complex) Fourier component which is a member of the triplet. In the simplest prototype there is only one field, and therefore only three degrees of freedom. If we set $\widetilde{p}_{e\mathbf{k}} = \widetilde{\phi}_{\mathbf{k}}$ we would have an identically vanishing nonlinearity, so we would have to go to the next level of complexity and set $\widetilde{p}_{e\mathbf{k}} = F(k)\widetilde{\phi}_{\mathbf{k}}$. We will treat a well known example of this, the two dimensional Euler equation for which instead of $\widetilde{p}_e$ we have the vorticity associated with $\widetilde{\phi}$, in the next section.

The property of three wave couplings which is most interesting is that they represent a conservative mutual transfer of energy from wave to wave. For Eq. (6.6), for example, one can easily verify that

$$\frac{\partial}{\partial t}\left(\frac{\widetilde{p}_{e\mathbf{k}}^{*}\widetilde{p}_{e\mathbf{k}} + \widetilde{p}_{e\mathbf{k}'}^{*}\widetilde{p}_{e\mathbf{k}'} + \widetilde{p}_{e\mathbf{k}''}^{*}\widetilde{p}_{e\mathbf{k}''}}{2}\right) = 0 \tag{6.9}$$

for any arbitrary triplet. This equation is built up of transfers among the three pieces,

$$\frac{\partial}{\partial t}\frac{|\widetilde{p}_{e\mathbf{k}}|^2}{2} = C_{\mathbf{k}\mathbf{k}'}\,\mathrm{Re}\left[\widetilde{p}_{e\mathbf{k}}\widetilde{\phi}_{\mathbf{k}'}\widetilde{p}_{e\mathbf{k}''} - \widetilde{p}_{e\mathbf{k}}\widetilde{p}_{e\mathbf{k}'}\widetilde{\phi}_{\mathbf{k}''}\right] \tag{6.10}$$

$$\frac{\partial}{\partial t}\frac{|\widetilde{p}_{e\mathbf{k}'}|^2}{2} = C_{\mathbf{k}\mathbf{k}'}\,\mathrm{Re}\left[\widetilde{p}_{e\mathbf{k}}\widetilde{p}_{e\mathbf{k}'}\widetilde{\phi}_{\mathbf{k}''} - \widetilde{\phi}_{\mathbf{k}}\widetilde{p}_{e\mathbf{k}'}\widetilde{p}_{e\mathbf{k}''}\right] \tag{6.11}$$

$$\frac{\partial}{\partial t}\frac{|\widetilde{p}_{e\mathbf{k}''}|^2}{2} = C_{\mathbf{k}\mathbf{k}'}\,\mathrm{Re}\left[\widetilde{\phi}_{\mathbf{k}}\widetilde{p}_{e\mathbf{k}'}\widetilde{p}_{e\mathbf{k}''} - \widetilde{p}_{e\mathbf{k}}\widetilde{\phi}_{\mathbf{k}'}\widetilde{p}_{e\mathbf{k}''}\right] \tag{6.12}$$

where the nonlinearities have been symmetrised and the coupling constant, which due to Eq. (6.5) is mutual, is given by

$$C_{\mathbf{k}\mathbf{k}'} = \frac{1}{2}\frac{c}{B}\nabla s\cdot(\mathbf{k}\times\mathbf{k}') \tag{6.13}$$

noting the cancellation in the cross products,

$$\nabla s\cdot(\mathbf{k}\times\mathbf{k}') = \nabla s\cdot(\mathbf{k}'\times\mathbf{k}'') = \nabla s\cdot(\mathbf{k}''\times\mathbf{k}) \tag{6.14}$$

since $\mathbf{k}'' = -\mathbf{k} - \mathbf{k}'$.

As in the case for the linear transfer effects we studied in the previous two chapters, equal terms appearing in two different equations with opposite sign represent a conservative transfer between those two pieces of the total free energy. This can be a coherent transfer, in which the relative phase of each pair of waves is a constant, and the coupling represents a coherent structure, as is the case for a linear eigenmode in which the couplings occur between several dependent variables belonging to the same $\mathbf{k}$. In a nonlinear system it is more usual, however, that the couplings are incoherent because many of them are simultaneously active among waves at a similar set of scales. This is what takes place in turbulence.

6.III. The Dual Cascade Property in Two Dimensional Turbulence

The important property of the turbulence part of the drift wave dynamical system is that it is two dimensional. The entire dynamics is three dimensional, but the dimension parallel to the magnetic field involves the Alfvén dynamics. The other two dimensions describe the drift plane. The ExB flows which lead to turbulence take place in drift planes, and the dynamics of these flows under the drift approximation is incompressible, due to the neglect of compressional Alfvén waves. The prototypical model for the study of two dimensional incompressible flows is called the 2D Euler equation,

$$\frac{\partial \mathbf{v}}{\partial t} + \mathbf{v} \cdot \nabla \mathbf{v} = 0 \qquad \nabla \cdot \mathbf{v} = 0 \tag{6.15}$$

The special property of two dimensional flows is that the flow vorticity is always perpendicular to the flow itself. The flow and its vorticity are respectively given by

$$\mathbf{v} = \hat{\mathbf{s}} \times \nabla \phi \qquad \Omega = \hat{\mathbf{s}} \cdot \nabla \times \mathbf{v} = \nabla_\perp^2 \phi \tag{6.16}$$

where keeping to our usual notation $\hat{\mathbf{s}} = \nabla s$ is the unit vector normal to the plane of motion, and the direction of the vorticity is $\hat{\mathbf{s}}$. We can take the curl of Eq. (6.15) and dot with $\hat{\mathbf{s}}$ to find

$$\left(\frac{\partial}{\partial t} + \mathbf{v} \cdot \nabla \right) \Omega = 0 \tag{6.17}$$

This is the same equation satisfied by ExB flows if all other interactions are neglected, and the only difference is the units in which ϕ is expressed. We can therefore think of ϕ interchangeably as the ExB stream function, or the electrostatic potential.

The important consequence of Eq. (6.17) as a nonlinear equation for a single field and its derivatives is that the enstrophy, or mean squared flow vorticity, is conserved along with the energy. To get the energy equation we multiply by $-\phi$ and integrate over the plane, and to get the enstrophy equation we multiply by Ω and integrate over the plane. Assuming no boundary contributions, we find

$$\frac{\partial}{\partial t} \int dx\, dy\, \frac{1}{2} |\nabla_\perp \phi|^2 = 0 \tag{6.18}$$

$$\frac{\partial}{\partial t} \int dx\, dy\, \frac{1}{2} \left| \nabla_\perp^2 \phi \right|^2 = 0 \tag{6.19}$$

In all of the above expressions, the gradient operator involves only the two coordinates within the drift plane,

$$\nabla_\perp = (\nabla x) \frac{\partial}{\partial x} + (\nabla y) \frac{\partial}{\partial y} \qquad \nabla_\perp^2 = \frac{\partial^2}{\partial x^2} + \frac{\partial^2}{\partial y^2} \tag{6.20}$$

written with the perpendicular symbol to distinguish from their three dimensional counterparts. Although there is no assumed dependence in the direction normal to the plane, this direction is the one in which the vorticity is aligned and is also the one about which the sense of rotation (and the curl operator) is defined.

The Euler equation looks exactly like our prototypical advection equation, Eq. (6.6), but with Ω substituted for $\widetilde{p}_e$. In terms of Fourier components, we have

$$\frac{\partial \Omega_{\mathbf{k}}}{\partial t} = \sum_{-\mathbf{k}'} \sum_{-\mathbf{k}''} \frac{1}{2} \hat{\mathbf{s}} \cdot (\mathbf{k} \times \mathbf{k}') \left(\Omega_{-\mathbf{k}''} \phi_{-\mathbf{k}'} - \Omega_{-\mathbf{k}'} \phi_{-\mathbf{k}''} \right) \tag{6.21}$$

where $\Omega_{\mathbf{k}} = -k^2 \phi_{\mathbf{k}}$ is the vorticity component, subject to the constraint that $\mathbf{k} + \mathbf{k}' + \mathbf{k}'' = 0$. If we take a particular triplet $\{\mathbf{k}, \mathbf{k}', \mathbf{k}''\}$ then the terms in the equations for $\phi_{\mathbf{k}}$, $\phi_{\mathbf{k}'}$, and $\phi_{\mathbf{k}''}$ are given by

$$\frac{\partial \Omega_{\mathbf{k}}}{\partial t} = C_{\mathbf{k}\mathbf{k}'} \left(\Omega_{-\mathbf{k}''} \phi_{-\mathbf{k}'} - \Omega_{\mathbf{k}'} \phi_{-\mathbf{k}''} \right) \tag{6.22}$$

$$\frac{\partial \Omega_{\mathbf{k}'}}{\partial t} = C_{\mathbf{k}\mathbf{k}'} \left(\Omega_{-\mathbf{k}} \phi_{-\mathbf{k}''} - \Omega_{\mathbf{k}''} \phi_{-\mathbf{k}} \right) \tag{6.23}$$

$$\frac{\partial \Omega_{\mathbf{k}''}}{\partial t} = C_{\mathbf{k}\mathbf{k}'} \left(\Omega_{-\mathbf{k}'} \phi_{-\mathbf{k}} - \Omega_{\mathbf{k}} \phi_{-\mathbf{k}'} \right) \tag{6.24}$$

which we can form by simple permutation among the members of the triplet. The coupling constant is given by

$$C_{\mathbf{k}\mathbf{k}'} = \frac{1}{2} \hat{\mathbf{s}} \cdot (\mathbf{k} \times \mathbf{k}') \tag{6.25}$$

Using these forms we can build the energy equations for each of the three components (and their complex conjugates) in the triplet, noting that for each mode we have the reality condition, $\phi_{\mathbf{k}} = \phi^*_{-\mathbf{k}}$. For each energy component given by

$$U_{\mathbf{k}} = |\mathbf{k}\phi_{\mathbf{k}}|^2 = -\phi_{\mathbf{k}} \Omega_{-\mathbf{k}} \tag{6.26}$$

we obtain

$$\frac{\partial U_{\mathbf{k}}}{\partial t} = 2 C_{\mathbf{k}\mathbf{k}'} \, \mathrm{Re} \left[\phi_{\mathbf{k}} \Omega_{\mathbf{k}'} \phi_{\mathbf{k}''} - \phi_{\mathbf{k}} \phi_{\mathbf{k}'} \Omega_{\mathbf{k}''} \right] \tag{6.27}$$

$$\frac{\partial U_{\mathbf{k}'}}{\partial t} = 2 C_{\mathbf{k}'\mathbf{k}'} \, \mathrm{Re} \left[\phi_{\mathbf{k}'} \Omega_{\mathbf{k}''} \phi_{\mathbf{k}} - \phi_{\mathbf{k}'} \phi_{\mathbf{k}''} \Omega_{\mathbf{k}} \right] \tag{6.28}$$

$$\frac{\partial U_{\mathbf{k}''}}{\partial t} = 2 C_{\mathbf{k}\mathbf{k}'} \, \mathrm{Re} \left[\phi_{\mathbf{k}''} \Omega_{\mathbf{k}} \phi_{\mathbf{k}'} - \phi_{\mathbf{k}''} \phi_{\mathbf{k}} \Omega_{\mathbf{k}'} \right] \tag{6.29}$$

Pairs of equal terms appearing with opposite sign give the energy transfers. Considering the equations as a permutation among the three modes in the triplet, the second term in each equation gives the energy transfer from the equation below it, and the first term

in each equation gives the energy transfer from the equation above it. For example, the energy transfer from mode $\mathbf{k}'$ to mode $\mathbf{k}$ is given by

$$T_U(\mathbf{k} \leftarrow \mathbf{k}') = 2C_{\mathbf{k}\mathbf{k}'} \operatorname{Re}\left[-\phi_{\mathbf{k}}\phi_{\mathbf{k}'}\Omega_{\mathbf{k}''}\right] = 2C_{\mathbf{k}\mathbf{k}'} \operatorname{Re}\left[(k'')^2\phi_{\mathbf{k}}\phi_{\mathbf{k}'}\phi_{\mathbf{k}''}\right] \tag{6.30}$$

Similarly, for each enstrophy component given by

$$W_{\mathbf{k}} = |\Omega_{\mathbf{k}}|^2 = k^4 |\phi_{\mathbf{k}}|^2 \tag{6.31}$$

we build the enstrophy transfer equations,

$$\frac{\partial W_{\mathbf{k}}}{\partial t} = 2C_{\mathbf{k}\mathbf{k}'} \operatorname{Re}\left[\Omega_{\mathbf{k}}\phi_{\mathbf{k}'}\Omega_{\mathbf{k}''} - \Omega_{\mathbf{k}}\Omega_{\mathbf{k}'}\phi_{\mathbf{k}''}\right] \tag{6.32}$$

$$\frac{\partial W_{\mathbf{k}'}}{\partial t} = 2C_{\mathbf{k}\mathbf{k}'} \operatorname{Re}\left[\Omega_{\mathbf{k}'}\phi_{\mathbf{k}''}\Omega_{\mathbf{k}} - \Omega_{\mathbf{k}'}\Omega_{\mathbf{k}''}\phi_{\mathbf{k}}\right] \tag{6.33}$$

$$\frac{\partial W_{\mathbf{k}''}}{\partial t} = 2C_{\mathbf{k}\mathbf{k}'} \operatorname{Re}\left[\Omega_{\mathbf{k}''}\phi_{\mathbf{k}}\Omega_{\mathbf{k}'} - \Omega_{\mathbf{k}''}\Omega_{\mathbf{k}}\phi_{\mathbf{k}'}\right] \tag{6.34}$$

Hence, the transfer of enstrophy from mode $\mathbf{k}'$ to mode $\mathbf{k}$ is given by

$$T_W(\mathbf{k} \leftarrow \mathbf{k}') = 2C_{\mathbf{k}\mathbf{k}'} \operatorname{Re}\left[-\Omega_{\mathbf{k}}\Omega_{\mathbf{k}'}\phi_{\mathbf{k}''}\right] = 2C_{\mathbf{k}\mathbf{k}'} \operatorname{Re}\left[-k^2(k')^2\phi_{\mathbf{k}}\phi_{\mathbf{k}'}\phi_{\mathbf{k}''}\right] \tag{6.35}$$

A dynamical system of many three wave interactions which satisfies both energy and enstrophy conservation exhibits a property known as a dual cascade. When energy in some range of spatial scales is distributed to larger and smaller scales in three wave interactions, the statistically most likely interactions are those which spread the energy preferentially towards larger scales and the enstrophy preferentially towards smaller scales. With no constraint on the distribution of the energy, we would see a transfer to smaller scales because there are many more available states there. But when the enstrophy is also conserved, it takes over this direct cascade, and then the energy, which appears with two fewer factors of $k_\perp$, is constrained to go to larger scales. The transfer process is referred to as a cascade because it is a local interaction between similar scales of motion. So for energy or enstrophy to get from one scale to another, it passes successively through the intermediate scales. When the turbulence is saturated (statistically stationary over intermediate times at each range of scales), one can speak of this cascading energy transfer as a throughput. We note that in the spectrum of wavenumbers $\mathbf{k}$, a range of scales corresponds to a range $|\mathbf{k}| \sim k$, which we can call the spectral range k. A direct cascade proceeds towards higher k, while an inverse cascade proceeds towards lower k. In a dual cascade, two quantities associated with some field variable proceed in opposite directions

in the spectrum, generally the energy and enstrophy. For the Euler equation, enstrophy is simply mean squared vorticity.

The existence of a dual cascade has been proven within various statistical models as well as demonstrated in simple computations, some of which we will illustrate in the next section, but we can observe that for interactions which spread energy and enstrophy out of some intermediate spectral range, the energy and enstrophy must go in opposite directions. Examining Eqs. (6.30) and (6.35), assuming that $k < k' < k''$, we find that the signs of the transfer out of mode $\mathbf{k}'$ are opposite. Combining Eqs. (6.30) and (6.35), with the transfers from mode $\mathbf{k}'$ to mode $\mathbf{k}''$,

$$T_U(\mathbf{k}'' \leftarrow \mathbf{k}') = 2C_{\mathbf{k}\mathbf{k}'} \,\mathrm{Re}\left[-k^2 \phi_{\mathbf{k}} \phi_{\mathbf{k}'} \phi_{\mathbf{k}''}\right] \tag{6.36}$$

$$T_W(\mathbf{k}'' \leftarrow \mathbf{k}') = 2C_{\mathbf{k}\mathbf{k}'} \,\mathrm{Re}\left[(k')^2 (k'')^2 \phi_{\mathbf{k}} \phi_{\mathbf{k}'} \phi_{\mathbf{k}''}\right] \tag{6.37}$$

In each transfer pair, T_U and T_W are of opposite sign, assuming a preferred sign of the triple correlation given by the average of the triple product. A cascade is a transfer chain which goes from mode to mode, so for one of the quantities the transfers from $\mathbf{k}''$ to $\mathbf{k}'$ and from $\mathbf{k}'$ to $\mathbf{k}$ have one sign, and those of the other quantity they have the opposite sign. Noting the symmetry of the transfer, we find that for a given sign of the triple correlation and that $k < k' < k''$, both the transfers for a given quantity are in the same direction. Since the enstrophy favours higher $\mathbf{k}$ due to its extra wavenumber factors, we expect it to go to high k and the energy to go to low k. But we have to show this in computations of the actual nonlinear behaviour, to which we now turn.

6.IV. The Hydrodynamic and Adiabatic Limits

The difference between a simple scalar quantity which is passively advected by the flow and the stream function for an incompressible 2D flow is well illustrated by a simple 2D drift turbulence model in which there are assumed to be no dependences parallel to the magnetic field but the advected scalar and the stream function for the flow are nevertheless allowed to evolve independently. This is called the hydrodynamic limit, since it is simply a freely evolving 2D Euler equation for the ExB flow, whose stream function is the electrostatic potential, $\widetilde{\phi}$, with a transported quantity, $\widetilde{p}_e$, whose evolution has no effect on that of the flow. Using the same coordinate system as before, and keeping the ExB nonlinearities in both equations for the ExB vorticity and the electron pressure, but for now neglecting the gradient drive term, we have

$$\left(\frac{\partial}{\partial t} + \mathbf{v}_E \cdot \nabla\right) \nabla_\perp^2 \widetilde{\phi} = \frac{d_E}{dt} \nabla_\perp^2 \widetilde{\phi} = 0 \tag{6.38}$$

$$\left(\frac{\partial}{\partial t} + \mathbf{v}_E \cdot \nabla\right) \widetilde{p}_e = \frac{d_E \widetilde{p}_e}{dt} = 0 \tag{6.39}$$

where we have defined the advective derivative in terms of the ExB flows,

$$\frac{d_E}{dt} = \frac{\partial}{\partial t} + \mathbf{v}_E \cdot \nabla \tag{6.40}$$

and the ExB nonlinearities have the basic 2D form

$$\mathbf{v}_E \cdot \nabla = \frac{\partial \widetilde{\phi}}{\partial x}\frac{\partial}{\partial y} - \frac{\partial \widetilde{\phi}}{\partial y}\frac{\partial}{\partial x} \tag{6.41}$$

The derivation of these equations follows from the four field model of Chapter 4, Section II, but setting the parallel dynamics ($\widetilde{A}_\parallel$, $\widetilde{J}_\parallel$, $\widetilde{u}_\parallel$, $\nabla_\parallel$) to zero. To study the properties of the ExB advection we leave out the gradient drive terms as well. The disturbances have been normalised in the same way as before, with an extra factor of $\delta = \rho_s / L_\perp$

$$\widetilde{\phi} \leftarrow \delta^{-1} \frac{e\widetilde{\phi}}{T_e} \qquad \widetilde{p}_e \leftarrow \delta^{-1} \frac{\widetilde{p}_e}{p_e} \tag{6.42}$$

which combines with the normalisation of the time and space coordinates,

$$t \leftarrow t L_\perp / c_s \qquad x \leftarrow x/\rho_s \qquad y \leftarrow y/\rho_s \tag{6.43}$$

to eliminate constant factors from the nonlinear terms. At this point, $L_\perp$ is any macroscopic scale assumed to be large compared to ρ_s.

The opposite model to the above assumes that the parallel electron dynamics is not only present but so efficient that the electrons are strictly adiabatic. The parallel ion dynamics is still neglected, so that the quantities ($\widetilde{A}_\parallel$, $\widetilde{J}_\parallel$, $\widetilde{u}_\parallel$, $\nabla_\parallel$) are still zero. The equations for $\widetilde{p}_e$ and $\widetilde{\phi}$ are subtracted, with $\widetilde{p}_e$ then set equal to $\widetilde{\phi}$, as in the simple drift wave models in Chapter 5, Section IV, to form

$$\frac{d_E}{dt}\left(1 - \nabla_\perp^2\right)\widetilde{\phi} = 0 \tag{6.44}$$

This is called the adiabatic limit, as opposite from the hydrodynamic limit. There is now no net transport in the drift plane of pressure at all, since the phase shifts between $\widetilde{p}_e$ and $\widetilde{\phi}$ are zero for all waves (cf. Chapter 5, Section VI). The pointwise instantaneous transport,

$$\mathbf{v}_E \cdot \nabla \widetilde{p}_e = \mathbf{v}_E \cdot \nabla \widetilde{\phi} = \frac{\partial \widetilde{\phi}}{\partial x}\frac{\partial \widetilde{\phi}}{\partial y} - \frac{\partial \widetilde{\phi}}{\partial y}\frac{\partial \widetilde{\phi}}{\partial x} = 0 \tag{6.45}$$

vanishes in the adiabatic case. The "external" mechanism of the adiabatic coupling keeps $\widetilde{\phi}$ tied to $\widetilde{p}_e$ arbitrarily efficiently. Eq. (6.44) has very similar properties to the 2D Euler

equation, Eq. (6.15), except for the fact that the extra factor of unity in the enstrophy operator $\left(1 - \nabla_\perp^2\right)$ suppresses the nonlinear interactions at scales much larger than ρ_s.

The computation in which we can study these equations consists of a finite difference method on an equidistant, isotropic grid in the xy-plane. All quantities are assumed to be periodic in x and y, in both of which the domain size is 20π with 64 grid nodes. The time step is 0.05. The initial state consists of a random phase distribution with adiabatic electrons, whose Fourier components are given by

$$\widetilde{p}_{e\mathbf{k}} = \widetilde{\phi}_{\mathbf{k}} = a_0 \left[1 + (k_\perp^2/0.32)^4\right]^{-1/2} e^{i\Theta} \tag{6.46}$$

with Θ a phase which is uniformly random on $[0, 2\pi]$, and a_0 set such that the maximum absolute value of the resulting $\widetilde{p}_e(x, y)$ is 3, which gives a marginally nonlinear start. The initial spectrum is chosen so as to observe the change in dominant scales of the two quantities, away from the logarithmic center of the spectrum. Since each of the equations is already in characteristic form, representing simple advection of two scalar quantities by $\mathbf{v}_E$, the MUSCL scheme of Appendix A is applied to update the quantities under the $\partial/\partial t$ operators. Then, the vorticity operator for each system ($\nabla_\perp^2$, or $1 - \nabla_\perp^2$) is solved via two dimensional fast Fourier transforms (FFT). The $k_y = 0$ component, which represents the background, is frozen by setting its time derivative to zero, as remarked in the Introduction.

We study the hydrodynamic and adiabatic models with the same initial state. This allows easy distinction between their dynamical character, as in the hydrodynamic model we can watch $\widetilde{p}_e$ and $\widetilde{\phi}$ evolve apart, and in the adiabatic model we can observe the suppression of nonlinear interactions for the larger scales by the presence of the extra factor of unity in the vorticity operator.

6.V. Results for the Hydrodynamic Model

Due to the fact that there is no coupling from $\widetilde{p}_e$ back to $\widetilde{\phi}$ in the hydrodynamic model, the two dynamical fields evolve separately. The ExB eddies tracked by $\widetilde{\phi}$ evolve according to the Euler equation and $\widetilde{p}_e$ is passively advected.

The amplitudes and decay rate are shown in Fig. 6.1. They show monotonic decay of all quantities, with the damping rate given for the total energy (average total energy density, $U_E + U_n$). Although the model equation is conservative, it makes a difference whether an energy sink at high $k_\perp$ (small scale) is present. The basic assumption is not one of zero dissipation, but of high Reynolds number. Generally, the Reynolds number for decaying turbulence gives the ratio of the rate at which nonlinear interactions scatter the free energy among the various degrees of freedom, to the rate at which the free energy is

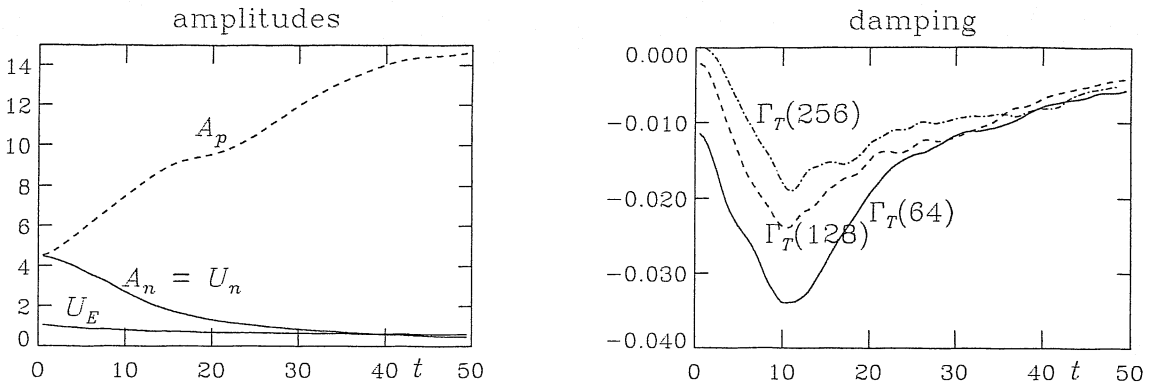

Figure 6.1. Time evolution of the hydrodynamic model. (left) Initial decay of half squared amplitudes of $\widetilde{p}_e$ and $\widetilde{\phi}$, denoted A_n and A_p, respectively. The free energy density components are also given, U_E for the ExB eddies ($\widetilde{\phi}$) and U_n for the density (also pressure in this model), noting that U_n is also A_n. (right) Energetic losses (mostly in $\widetilde{p}_e$ due to the direct cascade) for three values of the resolution.

dissipated. Characterising the nonlinear dynamical time scale by an eddy turnover time, or V/L for given velocity V and scale length L, and a diffusive damping rate of μ/L^2, we find the classical definition of the Reynolds number, $R = VL/\mu$. In the hydrodynamic model, the direct cascade in U_n is the most powerful nonlinear interaction, and we see that in the faster decay of U_n compared to U_E. We see also that the average half squared amplitude of $\widetilde{\phi}$, shown by A_p, actually rises, as the inverse cascade in U_E moves the ExB energy to larger scales where the factor of $k_\perp^2$ is smaller. The decay rates are shown for each of three resolutions, the nominal 64×64, and two companion cases with 128×128 and 256×256. The initial transient phase, during which the nonlinear transfer dynamics destroys the alignment between $\widetilde{p}_e$ and $\widetilde{\phi}$, shows a virulent cascade in which free energy is thrown to the highest $k_\perp$ and hence to the numerical dissipation. At later times, however, the decay rates are comparable, since most of the energy resides at lower $k_\perp$, and there are several factors of two over which the local cascade operates.

A high Reynolds number means that there is enough spectral separation between the largest scales and the dissipation range for the nonlinear interactions to operate unconstrained, whether the dissipation is physical or numerical. The high Reynolds number limit is characterised by an dissipation rate which is independent of the resolution, that is, the Reynolds number. Fig. 6.2 shows the evolution of the $\widetilde{\phi}$ and $\widetilde{p}_e$ spectra, and the vorticity spectrum, out of the initial state. Over the short time interval of $0 < t < 10$, most of the redistribution occurs. The spectra of A_n and A_w become much flatter, but that of A_p

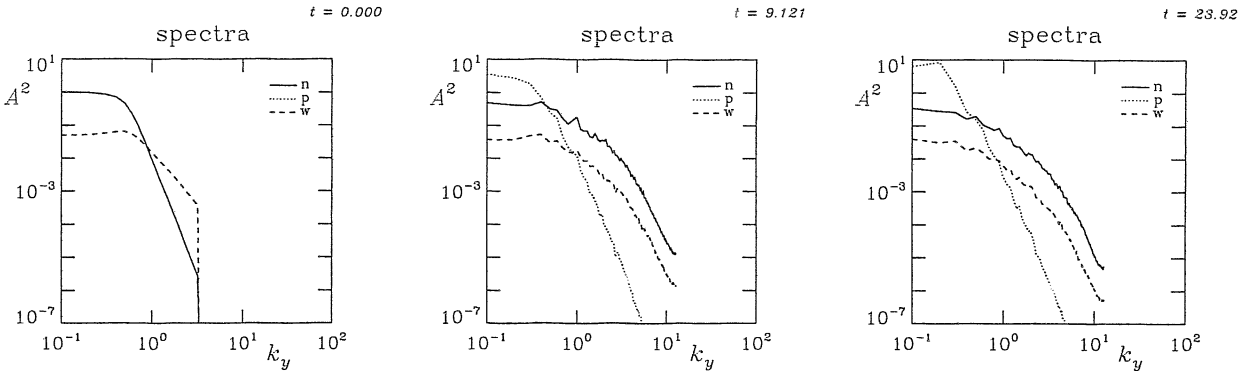

Figure 6.2. Amplitude spectra in the hydrodynamic model, for $\widetilde{p}_e$, $\widetilde{\phi}$, and the vorticity, labelled by 'n', 'p', and 'w', respectively. The times of the snapshots are $t = 0$ (left), $t = 9.8$ (center), and $t = 24$ (right). The spectra evolve rapidly apart due to the differing cascade dynamics for $\widetilde{p}_e$ and $\widetilde{\phi}$.

steepens. This follows from the cascade dynamics for each of these three quantities. Once most of the ExB energy is at larger scales, the cascade dynamics in the middle range slows down, and then the decaying turbulence enters the high Reynolds number regime.

The evolution of the disturbances themselves is shown in Fig. 6.3, in which the top row of frames gives the initial state. The physical nature of the nonlinear interactions is vortex merger for the ExB eddies and shearing apart of the structures for the quantities directly advected by the eddies. As this includes the vorticity, the $\widetilde{\phi}$ disturbances are involved in both the flows and the advected quantities. The Euler equation's dynamics is essentially this merger/shearing process, until at late times (if the Reynolds number is high enough) one is left with a shear-free flow field. The fate of a passively advected quantity, usually called a passive scalar, in this case $\widetilde{p}_e$, is for the disturbances to be sheared apart into sheets, much like the vorticity in the Euler equation, whose narrowness is limited only by the Reynolds number. These interactions represent the physical manifestations of the cascade dynamics in the hydrodynamic model.

6.VI. Results for the Adiabatic Model

In the adiabatic model the two fields do not evolve apart because they are constrained to be equal. This eliminates the direct cascade in the free energy associated with $\widetilde{p}_e$ since the ExB nonlinearity on that quantity vanishes. We are left with the dual ExB energy/enstrophy cascade we would have with the Euler equation by itself, but now there is a new twist. The vorticity operator carries the extra factor of unity, coming from the

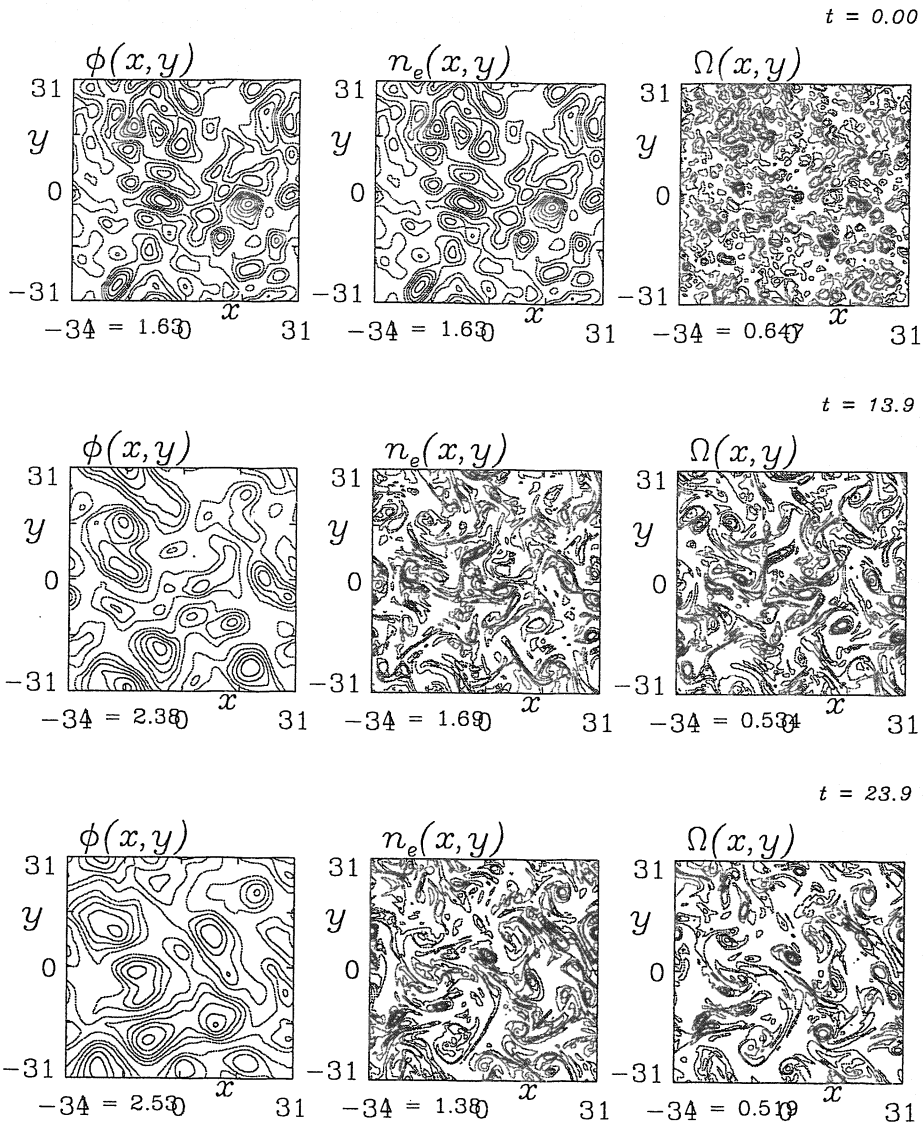

Figure 6.3. Evolution of the disturbances for the hydrodynamic model. The nonlinear interactions represent ExB vortex merger and shearing apart of advected quantities, including the ExB flow vorticity itself.

adiabatic constraint $\widetilde{p}_e = \widetilde{\phi}$, and at low $k_\perp$ this factor is the larger. Consequently, the nonlinear interactions are strongly suppressed as $k_\perp^2$ drops away from unity. The dual cascade stops at about $k_\perp \sim 0.3$.

The amplitudes and decay rate are shown in Fig. 6.4. As in the hydrodynamic model, they show monotonic decay of all quantities, with the damping rate given for the total energy (average total energy density, $U_E + U_n$). There are several differences. First, the decay is very slow since the direct cascade in U_n is suppressed. Second, the fact that the dual cascade keeps the energy mostly at low $k_\perp$, the high Reynolds number limit is

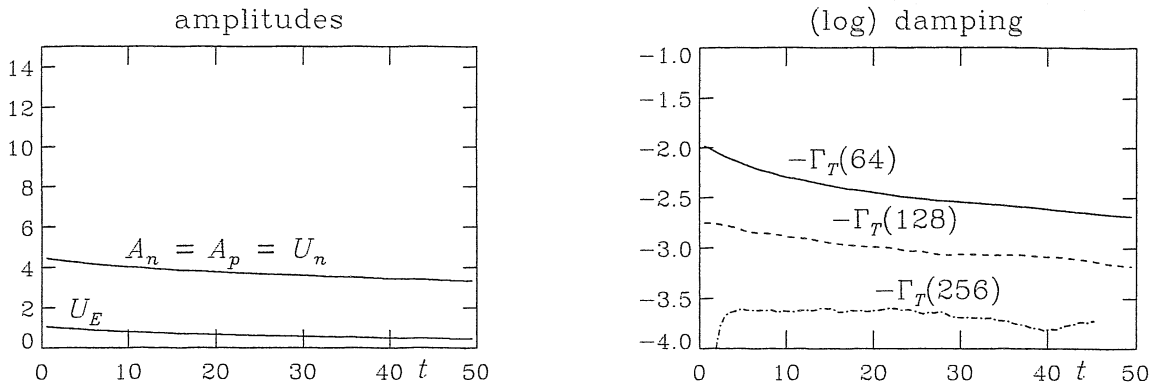

Figure 6.4. Time evolution of the adiabatic model. (left) Initial decay of half squared amplitudes of $\widetilde{p}_e$ and $\widetilde{\phi}$, and the energy components, on the same vertical scale as in Fig. 6.1, for comparison. (right) Energetic losses (all in $\widetilde{\phi}$, which has the inverse energy cascade) for three values of the resolution. Decay is much slower in this case, and A_p does not grow, due to the weakness of the nonlinearity at low $k_\perp$. Because the principal energy cascade is towards low $k_\perp$, the high Reynolds number limit is not reached.

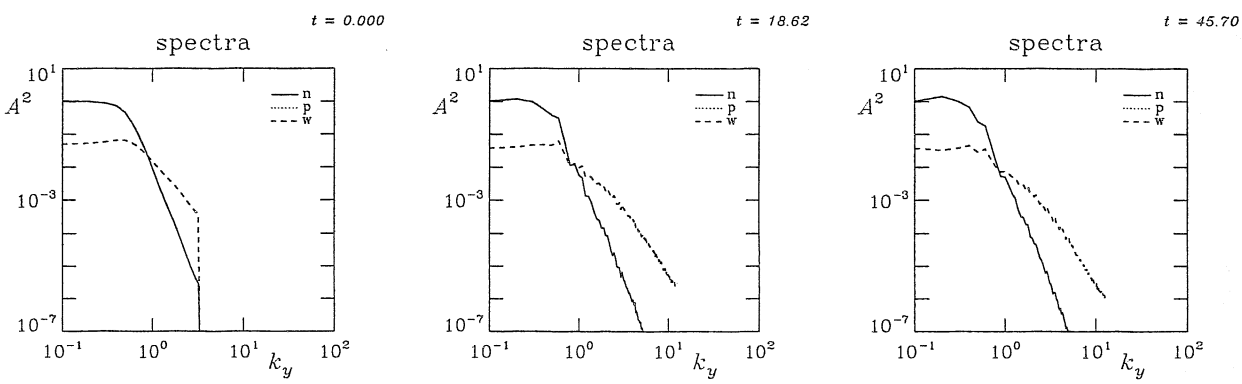

Figure 6.5. Amplitude spectra in the adiabatic model, for $\widetilde{p}_e = \widetilde{\phi}$, and the vorticity, labelled by 'n' (or 'p'), and 'w', respectively. The times of the snapshots are $t = 0$ (left), $t = 19$ (center), and $t = 46$ (right). The spectra evolve slowly, with slight steepening of $\widetilde{\phi}$ and flattening of $\nabla_\perp^2 \widetilde{\phi}$ due to the dual cascade, but with suppression at low $k_\perp$ by the adiabatic constraint (the vorticity operator becomes $1 - \nabla_\perp^2$) and little activity at higher $k_\perp^2$ due to the weaker nonlinear dynamics of the vorticity at immediately larger scales.

not reached. Third, the suppression of even the vorticity nonlinear advection at low $k_\perp$

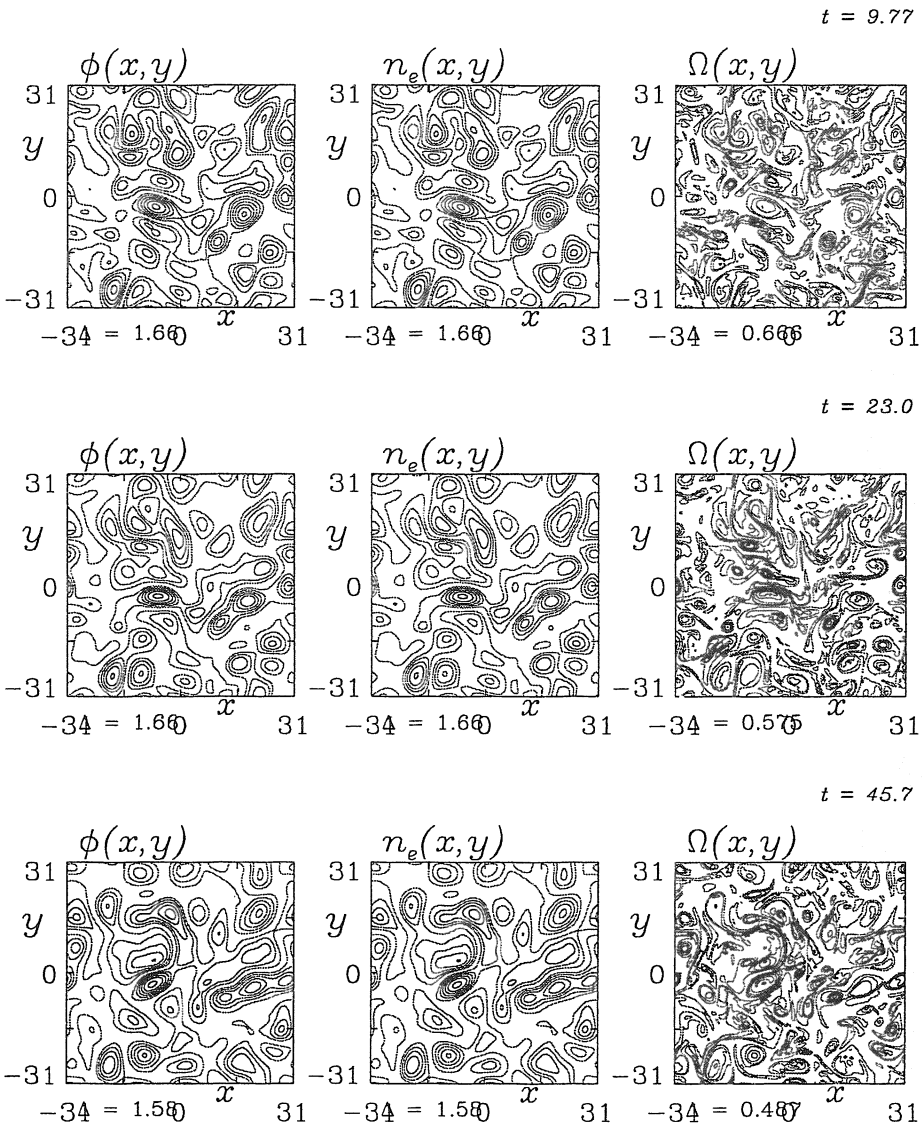

Figure 6.6. Evolution of the disturbances for the adiabatic model, with the same initial state as in Fig. 6.3. The ExB vortex merger process is largely suppressed once the eddies are all larger than several ρ_s ($\rho_s = 1$ in these units), and the vortex sheet formation is weaker following suppression of the vorticity nonlinearity where the flow energy resides.

prevents $\widetilde{\phi}$ from reaching large amplitudes in a generally decaying system.

The evolution of the amplitude spectra of $\widetilde{\phi} = \widetilde{p}_e$ and $\nabla_\perp^2 \widetilde{\phi}$ is shown in Fig. 6.5. The behaviour we saw for the hydrodynamic model in Fig. 6.2 is suppressed by the effect of the adiabatic constraint on the vorticity operator, for the ExB cascade dynamics, and by the associated removal of the passive scalar nonlinearity. If we look at scales below ρ_s (unity in these units) we see more evolution, but only until all the energy finds itself at lower

$k_\perp$ (about $k_\perp = 0.3$). Subsequent evolution is very slow, and there is little evolution of spectra or even the shapes of the contours showing the spatial morphology.

A computation must involve scales near ρ_s or not much happens in the adiabatic model. Runs with smaller domain sizes (10π) show much stronger evolution before this slowly evolving end state is reached, and runs with larger domain sizes (40π) show even less activity than the case detailed above. In either of the cases there is little spectrum evolution for $k_y < 0.3$. The inverse cascade via vortex merger stops when the scales get too large, that is, when the nonlinearity is no longer sizeable compared to the energy content. The enstrophy content at high $k_\perp$ drops faster with time than the energy content, which in turn drops faster than the squared amplitude of $\widetilde{\phi}$. The hydrodynamic model by contrast always sees the inverse $\widetilde{\phi}$ cascade continue until the last vortex merger allowed by the boundary conditions takes place, if the computations are run long enough.

6.VII. The Dissipative Coupling Model for 2D Drift Wave Turbulence

We now examine what a continuous level of driving and dissipation has on these purely decaying dynamical systems. With this continuous forcing, there are always energy sources and sinks available to the turbulence. The free energy will therefore redistribute itself among the available degrees of freedom until these forcing effects are all in statistical balance. This balanced state is called saturation, and in a dissipatively forced system such as drift wave turbulence one is mostly interested in the maintenance of this saturated state. The approach to this state is not as important as the properties the turbulence has once it is statistically stationary. This is why we have not been more concerned with the Reynolds number effects encountered in the previous section. As we will see, this concern is much less pronounced when the dynamics is heavily forced.

The simplest two dimensional drift wave model is derived analogously to the hydrodynamic and adiabatic limits. Here, we retain the gradient drive term and allow the parallel coupling between the state variables to be finite. The simplest model containing all these effects arises from the three dimensional four field model with the drive terms, but with the parallel dynamics replaced by the dissipative coupling model. In the resistive limit the Ohm's law is simply a constitutive relation between the current and the static forces along the magnetic field,

$$\widetilde{J}_\parallel = \eta_\parallel^{-1} \left(\frac{\nabla_\parallel \widetilde{p}_e}{n_e e} - \nabla_\parallel \widetilde{\phi} \right) \tag{6.47}$$

where $\eta_\parallel = 0.51 m_e \nu_e / n_e e^2$ is the collisional resistivity, here in physical units. It is the parallel gradient of this current that appears in the other equations, and so in those equations the difference of the static forces is simply two factors of $\nabla_\parallel$ acting on the nonadiabatic

response, $\widetilde{h}_e$, whose central role we saw in Chapter 5. To get the two dimensional dissipative coupling model of drift wave turbulence, we simply replace $-\nabla_\parallel^2$ by a constant, which together with the resistivity becomes the coupling parameter,

$$D = 1.96 \frac{k_\parallel^2 V_e^2}{\nu_e c_s / L_\perp} \tag{6.48}$$

In these terms the dissipative coupling model becomes

$$\frac{\partial}{\partial t} \nabla_\perp^2 \widetilde{\phi} = -\mathbf{v}_E \cdot \nabla \left(\nabla_\perp^2 \widetilde{\phi} \right) + D \left(\widetilde{\phi} - \widetilde{p}_e \right) \tag{6.49}$$

$$\frac{\partial \widetilde{p}_e}{\partial t} = -\mathbf{v}_E \cdot \nabla \left(\widetilde{p}_e + p_e \right) + D \left(\widetilde{\phi} - \widetilde{p}_e \right) \tag{6.50}$$

also called the Hasegawa-Wakatani model, after its original authors. Here, the gradient drive term is expressed as the background piece in the advection, with $p_e = -x$, so that the numerical scheme advects the disturbance and background together.

This is the prototypical drift wave turbulence model, and it is a useful model for learning the physical character of drift wave turbulence. We will study it in more detail as such in the next chapter, but for now the purpose is to show the persistence of the basic nonlinear ExB flow and passive scalar dynamics in a situation with dissipative forcing. The constant D is merely a method for continuous transition between the deep hydrodynamic ($D = 0$) and adiabatic ($D = \infty$) limits. We have also set $L_\perp = L_p$ to eliminate the coefficients in front of the gradient term in the equation for $\widetilde{p}_e$. In all other respects, the computations to be done in this model follow those for the hydrodynamic and adiabatic models. The vorticity and pressure are advected as in the hydrodynamic model, with the $k_y = 0$ component eliminated, leading to the auxiliaries defined by

$$S_w = \nabla_\perp^2 \widetilde{\phi} - \tau \, \mathbf{v}_E \cdot \nabla \left(\nabla_\perp^2 \widetilde{\phi} \right) \qquad S_n = \widetilde{p}_e - \tau \, \mathbf{v}_E \cdot \nabla \left(\widetilde{p}_e + p_e \right) \tag{6.51}$$

Then, the dissipative coupling is solved implicitly, along with the $\nabla_\perp^2$ operator, in $k_\perp$-space according to

$$\left(\frac{\tau D}{1 + \tau D} - \nabla_\perp^2 \right) \widetilde{\phi} = \frac{\tau D \, S_n}{1 + \tau D} - S_w \tag{6.52}$$

and

$$\widetilde{p}_e = \frac{\tau D \, \widetilde{\phi} + S_n}{1 + \tau D} \tag{6.53}$$

and then the vorticity is recovered via

$$\nabla_\perp^2 \widetilde{\phi} = S_w - \frac{\tau D}{1 + \tau D} \left(S_n - \widetilde{\phi} \right) \tag{6.54}$$

avoiding operation by $\nabla_\perp^2$ directly.

6.VIII. Results for the Driven Dissipative System

We highlight an intermediate case with $D = 0.1$ in order to show how the various pieces of the dynamics interact, and then examine the energy transfer dynamics in all limits. The case with $D = 0.1$ is referred to as nominal. The turbulence evolved initially as it would do in the hydrodynamic limit, but then the dissipative coupling prevents $\widetilde{p}_e$ and $\widetilde{\phi}$ from separating completely. One interesting result is that the cases with various resolution do not differ to the extent they do in the two decaying cases discussed above. Most of the activity is in a driven range of the spectrum, and the action of the dissipation involving D prevents the "long term" forms of the decaying systems from establishing themselves. The turbulence approaches saturation after about $t = 100$, and averaged quantities are measured over the interval $200 < t < 400$. More detail on how these averages are computed is presented in the next chapter.

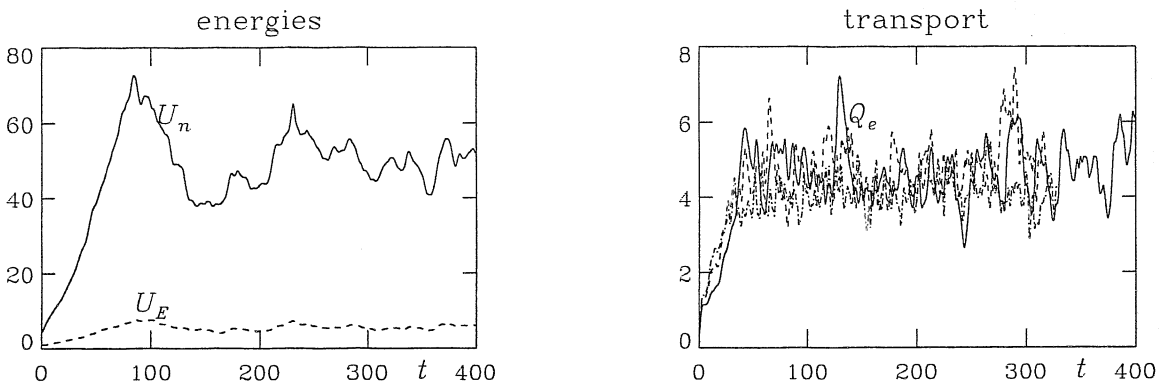

Figure 6.7. Time evolution of the dissipative coupling model, for the nominal case of $D = 0.1$. (left) Half squared amplitudes of $\widetilde{p}_e$ and $\widetilde{\phi}$, denoted A_n and A_p, respectively, and the free energy density components, U_E for the ExB eddies ($\widetilde{\phi}$) and U_n for the density, noting that U_n is also A_n. (right) The transport caused by the turbulence, for three values of the resolution. For 64^2, 128^2, and 256^2 grid nodes, the values are 4.69 ± 0.80 and 4.89 ± 0.74 and 4.14 ± 0.51, respectively.

Time traces of the free energy components of the turbulence are shown in Fig. 6.7, and in the right frame the resulting transport (Q_e, which is the average of $\widetilde{p}_e \widetilde{v}_E^x$) is given for the three values of the resolution. The values of Q_e are about one standard deviation apart. It is also noteworthy that the numerical dissipation rate, Γ_E, was 0.028, 0.028, and 0.026, for 64^2, 128^2, and 256^2 grid nodes, respectively. This shows that the high Reynolds limit has been reached, and so the resolution consideration is not grievous. A grid of 64^2

nodes is sufficient to study phenomenology as we are doing here. The main result from the time traces is that most of the free energy resides in $\widetilde{p}_e$, and so the main dissipation process is actually the direct cascade of the associated free energy component, U_n, to arbitrarily short wavelengths.

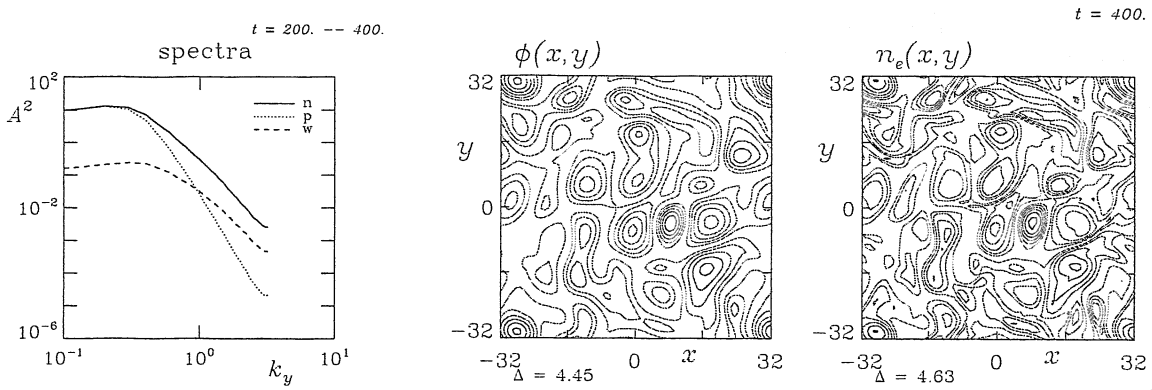

Figure 6.8. (right) Averaged amplitude spectra in the dissipative coupling model, with $D = 0.1$, for $\widetilde{p}_e$, $\widetilde{\phi}$, and the vorticity, labelled by 'n', 'p', and 'w', respectively. (center, left) Contours of $\widetilde{\phi}$ and $\widetilde{n}_e = \widetilde{p}_e$ at $t = 400$, showing the close coupling at larger scales but differences on smaller scales, corresponding to the spectra. The nonlinear interactions affecting $\widetilde{p}_e$ are stronger relative to the coupling at higher $k_\perp$.

The amplitude spectra and the disturbances themselves are shown in Fig. 6.8. Here we can easily see the varying effectiveness of the dissipative coupling at larger and smaller scales. The spectra look more like the adiabatic limit at low k_y but then separate at smaller scales for which the nonlinear interactions are more able to compete with the coupling. The high degree of correlation between $\widetilde{p}_e$ and $\widetilde{\phi}$ is clear from the spatial distributions, but a the level of details there is more to see in $\widetilde{p}_e$. The tendency to form sheets is still evident at the smaller scales, and the adiabatic coupling reduces the basic tendency for all the ExB energy to go to larger scales.

The energy transfer dynamics is shown in Fig. 6.9. In each case the transfer is defined as positive if the free energy leaves a spectral range k' and enters the spectral range k. For the thermal free energy U_n given by the average of $\widetilde{p}_e^2/2$ and the enstrophy given by the average of $(\nabla_\perp^2\widetilde{\phi})^2/2$, the formulae for each three wave triplet are given by Eq. (6.35), with $\widetilde{p}_e$ or $\nabla_\perp^2\widetilde{\phi}$ put in for Ω. For the ExB energy U_E given by the average of $|\nabla_\perp\widetilde{\phi}|^2/2$, the formula is given by Eq. (6.30) with $\nabla_\perp^2\widetilde{\phi}$ put in for Ω. The spectral range k is defined as

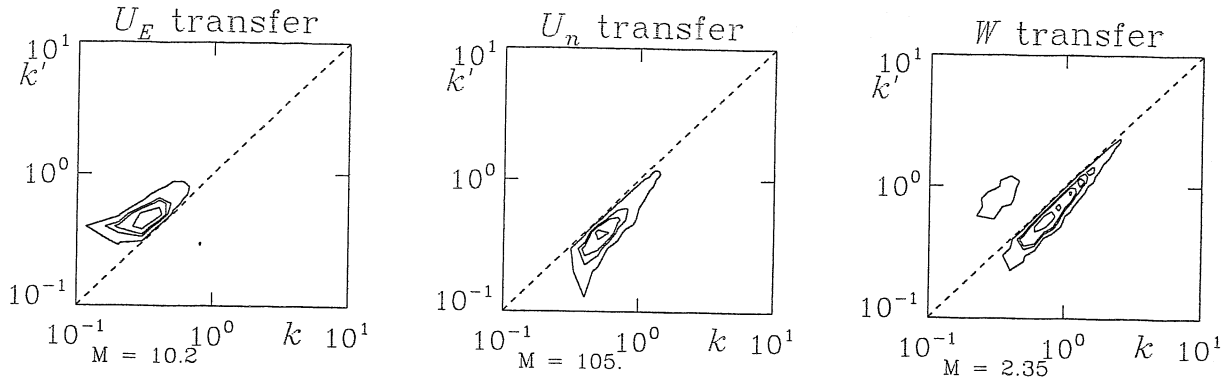

Figure 6.9. Energy and enstrophy transfer in the dissipative coupling model, with $D = 0.1$. Left to right, the transfer from spectral range k' to k is shown for the ExB energy U_E, the thermal free energy U_n, and the enstrophy. The maximum value for each frame is given by M. Contours are drawn only where the transfer is positive, noting the symmetry about $k' = k$, so that activity above the dashed line shows an inverse transfer while activity below the dashed line shows a direct transfer. The cascade is local, with most of the activity near $k' = k$.

the set of all Fourier pairs (k_x, k_y) for which the resulting $k_\perp$ is within 0.5 of k, normalised to the minimum wavenumber on which the spectrum is quantised ($2\pi/L$ for system size L) and noting that $k_\perp^2 = k_x^2 + k_y^2$. The symmetry about $k' = k$ is obvious, and so the contours are drawn only where they are positive. Activity above the line $k' = k$ indicates an inverse transfer tendency, while a direct transfer would appear below the line. The quantitative level of each transfer is given by its maximum value, denoted M in the figures. A local cascade is a successive transfer between spectral ranges corresponding to scales within a factor of two of each other, and indeed this is where we find the activity. As argued above, the transfer is clearly an inverse cascade in the ExB energy (energy associated with $\widetilde{\phi}$, or U_E), and a direct cascade in the mean squared vorticity (fluid enstrophy) and the thermal free energy (energy associated with $\widetilde{p}_e$, or U_n).

The above introductory results show that the basic properties of the adiabatic and hydrodynamic limits are present generally, and both cascade tendencies, dual for the ExB energy and enstrophy, and direct for the passive scalar quantity, are still active when the turbulence is severely forced by either or both of drive and dissipation. It is useful to demonstrate that the simultaneous presence of the nonlinear transfer dynamics for $\widetilde{\phi}$ and $\widetilde{p}_e$ is present for all values of D except the extreme adiabatic limit. In Fig. 6.10 we find the transfer dynamics for $D = 0.01$, 0.03, 0.3, and 1.0, from top to bottom. We find

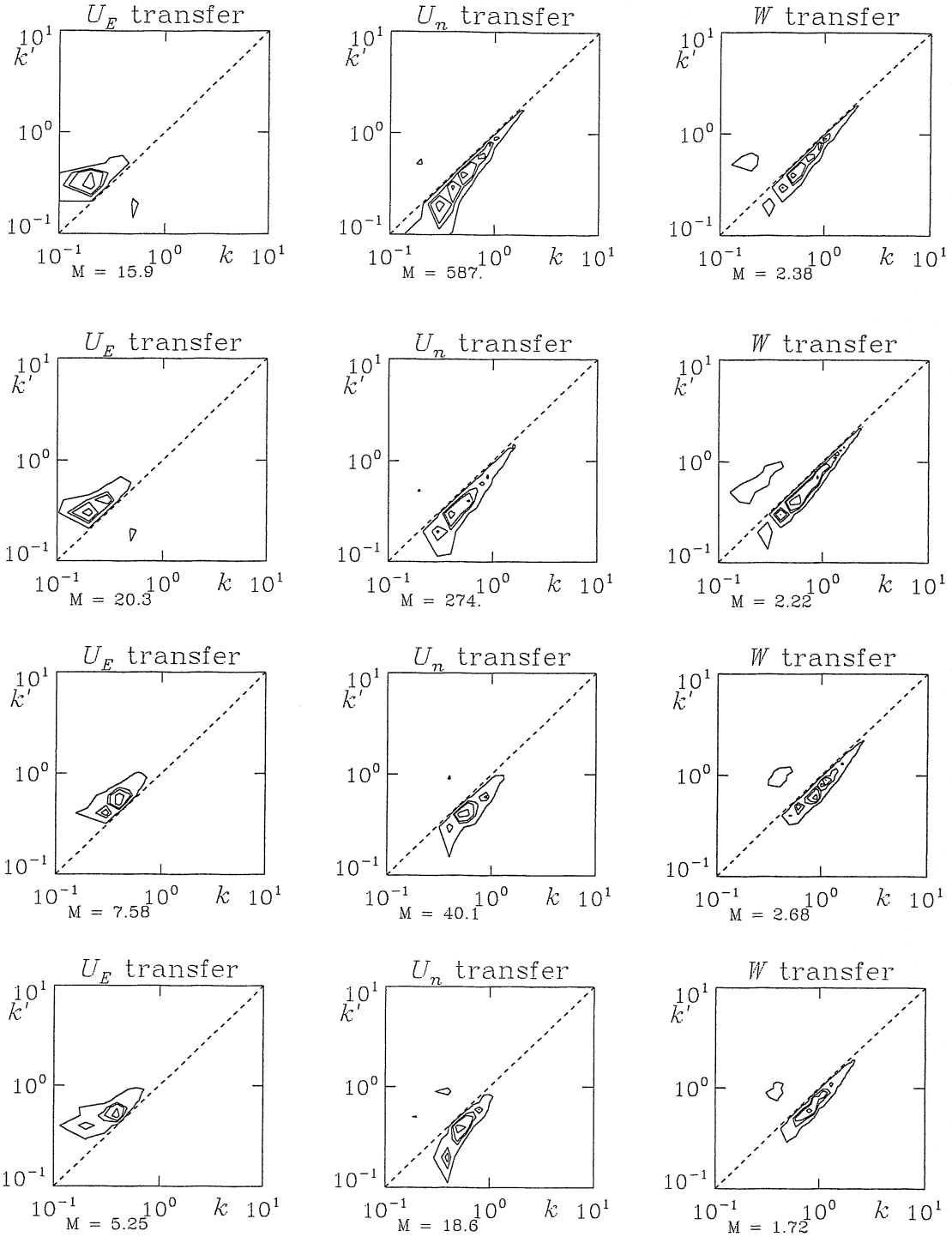

Figure 6.10. Energy and enstrophy transfer in the dissipative coupling model, from top to bottom with $D = 0.01$, 0.03, 0.3, and 1.0, respectively. Labelling is as in Fig. 6.9. These cases serve to show that the same basic transfer dynamics is present for all $D < 1.0$, with only the levels changing.

the same morphology in all cases, with the hydrodynamic regime (small D) showing the strongest dynamics along with the strongest turbulence (a wider range of the spectrum is hydrodynamic). For all cases shown the direct transfer in U_n is stronger than the inverse transfer in U_E. Larger values of D are necessary to find the true adiabatic limit, as in Section VI, above. But as we will see in subsequent chapters, drift wave turbulence is either more nonadiabatic than in the $D > 1.0$ cases or it is too weak to be of consequence. We therefore always find that in cases of interest that both Euler fluid and passive scalar nonlinear dynamics is simultaneously present in drift wave turbulence.

6.IX. Summary

Turbulence is a phenomenon involving mostly conservative interactions among a large number of statistically independent degrees of freedom. It involves nonlinear interactions among various accessible states of the disturbances, rather than quasilinear interactions between disturbances and background (profile) quantities. For fluid turbulence the principal nonlinearities are quadratic, with the result that the interactions are three wave triplets each following their own transfer dynamics. The number of such triplets, and the number of triplets of which each degree of freedom is a member, is arbitrarily large.

Three wave interactions transfer energy mostly locally in the spectrum of scales of motion. For most nonlinearities the tendency is to transfer free energy from larger scales towards smaller scales, where there are more accessible states. A spectrally local transfer chain is called a cascade, termed direct for transfer to smaller scales and inverse for transfer to larger scales. A two dimensional, incompressible fluid such as the ExB velocity exhibits a dual cascade due to the simultaneous conservation of energy and enstrophy (mean squared vorticity for a homogeneous fluid), with the enstrophy going to smaller scales and the energy to larger. This dual cascade is a basic consequence of the three wave constraint on the vorticity nonlinearity.

Dissipative coupling reaches limits in which it can be treated as the presence or absence of the adiabatic constraint. Conventional fluid turbulence in the presence of a thermal gradient is hydrodynamic, and always develops motion at the very largest scales due to the dual cascade. When the adiabatic constraint is important the dominant scales of motion approach the drift scale, ρ_s, at which the dynamics loses the self similarity enjoyed by purely hydrodynamics turbulence. In deeply adiabatic dynamics, the direct cascade through the transported quantity is shut off, leaving the vorticity nonlinearity to act alone. Dissipative drift wave turbulence is always somewhere between these two limits, and in all regimes the basic transfer dynamics of each nonlinearity retains its character.

Further Reading

Basic textbooks on fluid turbulence include those by U. Frisch, *Turbulence: the Legacy of A.N. Kolomogorov*, (Cambridge, 1995), M. Lesieur, *Turbulence in Fluids*, (3rd ed, Kluwer Academic Publishers, 1997), and A. S. Monin and A. M. Yaglom, *Statistical Fluid Mechanics: Mechanics of Turbulence*, Vol 2 (MIT Press, Cambridge, USA 1975). The standard cascade model is the one by A. N. Komolgorov, in *C. R. (Dokl.) Akad. Sci. URSS* 30 (1941) 301 [*J. Fluid Mech.* 13 (1962) 82], covered in all the basic texts. The dual cascade property of two dimensional turbulence was shown and explained by R. H. Kraichnan, in *Phys. Fluids* 10 (1967) 1417.

The adiabatic and hydrodynamic limits for drift wave turbulence arise from the earliest standard models, developed by A. Hasegawa and H. Mima, in *Phys. Rev. Lett.* 39 (1977) 205 and *Phys. Fluids* 21 (1978) 87, and by M. Wakatani and A. Hasegawa, in *Phys. Fluids* 27 (1984) 611, respectively. Statistical equilibrium models to investigate the cascade properties analytically were developed by D. Montgomery and L. Turner, in *Phys. Fluids* 23 (1980) 264 for the Hasegawa-Mima model, and by F. Y. Gang, B. D. Scott, and P. H. Diamond, in *Phys. Fluids B* 1 (1989) 1331 for the Wakatani-Hasegawa model, both of which are known by those names. A general review of the self organising property of flows with dual cascades is given by A. Hasegawa, in *Adv. Phys.* 34 (1985) 1. Citations to the literature for the energy transfer diagnostics are given in the next chapter.

7. Computational Diagnostics and Drift Wave Mode Structure

B. Scott

Jul 1999

7.I. Introduction

In the previous chapter we have seen that the basic tendency of the nonlinear ExB dynamics to exhibit the dual energy/enstrophy cascade preserves its character in all regimes of the dissipative coupling parameter. That is, whether the passive scalar quantity is closely tied to the transporting eddies by the coupling, or not, the inverse energy cascade in ExB energy and the direct cascades in the enstrophy and the passive scalar free energy maintain their qualitative form. Even the locality of the cascade process — that most of the transfer occurs within a factor of two of any given spectral range k — is preserved. Only the quantitative level is changed, as for stronger coupling the dynamics is more adiabatic and the nonlinear transfer of the passive scalar quantity is therefore inhibited. This state of affairs is not obvious in the more heuristic diagnostics, such as the transport rates, disturbance amplitudes, visualisations, or even the spatial scale of motion. A detailed diagnostic was necessary to show that the cascade dynamical character is universal: the two dimensional energy transfer spectrum showing the transfer rates between spectral ranges k and k'. In subsequent chapters we will find that more than one type of eigenmode is potentially present in the overall turbulent system; in some cases there will be as many as four different eigenmode types. Whether the turbulence is actually more of the character of one of these eigenmodes than of the others can only be decided by detailed diagnosis, as will become clear. Herein, we introduce the basic statistical diagnostics of disturbances in turbulence, a nonlinear, nonequilibrium state which does not lend itself to exact analytical solution, or even modelling beyond very heuristic considerations. Together, these diagnostics show the fundamental character of drift wave turbulence: how its different pieces are coupled, how it transfers energy from source to sink. This experience will be very useful in sorting out the dynamical character of turbulence in the more complicated situations we will see in later chapters.

7.II. Temporal Diagnostics

The first diagnostic of use is the average saturated amplitude of the disturbances and the average transport they cause. It is important to define what we mean by an average in this context. If we measure the transport, for example, as a function of time, then we can say that it is saturated if the average measured for it in some interval of time is statistically equal to that measured over some other interval of time. This interval should be long compared to the dynamical time scale of individual vortices or other disturbances, but short compared to the time we would expect the background to evolve as a result of the transport. In a local computation such as the ones we have dealt with so far, the background is either held fixed, or due to the boundary conditions (periodic, Neumann, or Dirichlet in the x-direction) the average profile gradient is held fixed. We may therefore take arbitrarily long intervals, limited by reasonable computational resources. The shortest interval we should use is that given by the longer of the eddy turnover time or the correlation time of the turbulence. The eddy turnover time is the typical dynamical time scale on which energy is transferred between similar spatial scales; one can define it in terms of the average vorticity. The correlation time is that on which two signals displaced in time begin to lose relation to each other; for this one can take the width of the correlation function in terms of the time displacement. In practice we must use a time rather longer than either of these in order to obtain a good statistical sample.

If we have a time series $Q_e(t)$ of the transport averaged over space,

$$Q_e(t) = \int \frac{d^2x}{L_x L_y} \widetilde{p}_e \widetilde{v}_E^x \tag{7.1}$$

where L_x and L_y are the domain dimensions in x and y, respectively, we may express the average and standard deviation of it in the usual way,

$$Q_e = \int \frac{dt}{T} Q_e(t) \qquad \delta Q_e = \left(\int \frac{dt}{T} \left[Q_e(t) - Q_e \right]^2 \right)^{1/2} \tag{7.2}$$

where T is the extent of the time interval. In a computation, all of these are discrete samples, with the averaged integrals replaced by sums of the samples divided by the number of samples. The quantity Q_e is statistically stationary if for differing intervals of fixed T the standard deviation of the measures of Q_e is less than the standard deviation δQ_e itself. The turbulence is temporally saturated if not only the average transport but

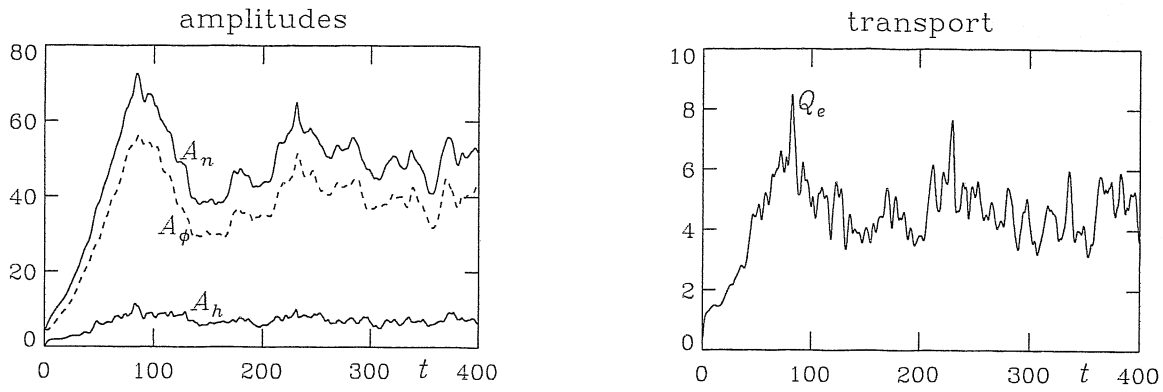

Figure 7.1. (left) Time traces of the half squared amplitudes of $\widetilde{n}_e$, $\widetilde{\phi}$, and $\widetilde{h}_e$, respectively labelled by A_n, A_p, and A_h. (right) Time trace of the transport, Q_e. These quantities are averaged over the spatial domain. The substantial transport reflects strong nonadiabatic electron dynamics, even though the adiabatic response leads to $\widetilde{n}_e$ and $\widetilde{\phi}$ of similar size.

also the average amplitude of each dependent variable is statistically stationary by this definition.

A computation of turbulence involving several dependent variables yields correspondingly several time series, and therefore a wealth of information even simply in these time traces. It would not do justice to such a dynamical system if understanding of it were limited to the average transport or the average amplitude of a single dependent variable. The first step beyond that is the ratio between two of these amplitudes. If the density and electrostatic potential amplitudes were always equal, for example, we would have a strong indication that the electrons might be adiabatic. If these amplitudes differ such that the nonadiabatic part of the density disturbances, $\widetilde{h}_e = \widetilde{n}_e - \widetilde{\phi}$, is comparable by amplitude to $\widetilde{n}_e$ or $\widetilde{\phi}$, the electrons are surely quite strongly nonadiabatic. By convention we use the half squared amplitudes as diagnostics, since some of them also appear as parts of the free energy. For example, the time trace of the half squared amplitude of $\widetilde{\phi}$ is given by

$$A_p(t) = \int \frac{d^2x}{L_x L_y} \frac{\widetilde{\phi}^2}{2} \tag{7.3}$$

In a similar manner, we have $A_n(t)$ and $A_h(t)$ for $\widetilde{n}_e$ and $\widetilde{h}_e$. These time traces of the amplitudes and the transport are shown for the case $D = 0.1$ of the Hasegawa-Wakatani dissipative coupling model, in Fig. 7.1 (we recall that $\widetilde{p}_e = \widetilde{n}_e$ in this model). This is our first indication of how "drift wave like" the turbulence is: the amplitudes of $\widetilde{n}_e$ and

$\widetilde{\phi}$ always track each other, at least moderately closely, even when the dynamics of $\widetilde{h}_e$ is strong enough to lead to substantial transport.

7.III. Spectral Diagnostics

Besides the amplitudes, we also want to know information about the basic scale of motion: where most of the free energy resides, whether the large or small scales are important even if not dominant. Moreover, the dynamical character of the turbulence may vary with the scale of motion. The simplest way to get a this is through the amplitude spectrum of the disturbances. As for the averaged amplitudes themselves, these spectra will tell us more if we compare them for the various dependent variables in a given computation. Taking the potential as an example, the amplitude spectrum is defined as the set of squared magnitudes of the Fourier amplitudes. At a given point in x and time, we can set up a spectrum in the wavenumber space k_y,

$$A_p(k_y, x, t) = \left|\widetilde{\phi}(k_y, x, t)\right|^2 \tag{7.4}$$

noting the reality condition between positive and negative modes. In a turbulent process these values vary too rapidly to be of much use, so we resort to two levels of averages: the average instantaneous spectrum, which is the average of A_p over x, and the average of that over time,

$$A_p(k_y) = \int \frac{dt}{T} \int \frac{dx}{L_x} \left|\widetilde{\phi}(k_y, x, t)\right|^2 \tag{7.5}$$

which we can use in the case that the turbulence is statistically stationary. The transport spectrum is measured in similar fashion,

$$Q_e(k_y) = \int \frac{dt}{T} \int \frac{dx}{L_x} \widetilde{p}_e^*(k_y, x, t)\widetilde{v}_E^x(k_y, x, t) \tag{7.6}$$

where $\widetilde{v}_E^x$ is the x-component of the ExB velocity. These last forms, by averaging over as much of the statistical fluctuation as possible, tell us the most about the mode structure.

It is interesting to look at the differences between $A_p(k_y)$ and $A_n(k_y)$, which is the amplitude spectrum of $\widetilde{n}_e$ (we use 'p' as a label for $\widetilde{\phi}$, with 'n' and 't' reserved for $\widetilde{n}_e$ and $\widetilde{T}_e$; only in the models in which $\widetilde{n}_e = \widetilde{p}_e$ is $\widetilde{p}_e$ shown in the diagnostics directly). For moderate levels of dissipative coupling the electrons are close to adiabatic at the larger scales but less so at the smaller scales. This tells us that the nonlinear advection of the vorticity, $\mathbf{v}_E \cdot \nabla\nabla_\perp^2\widetilde{\phi}$, is more able at smaller scales where the factors of $k_\perp$ are larger to compete with the dissipative coupling, $D(\widetilde{n}_e - \widetilde{\phi})$, since D is independent of k_y in this model. This is also reflected in $A_h(k_y)$, the amplitude spectrum of $\widetilde{h}_e$ itself, which follows

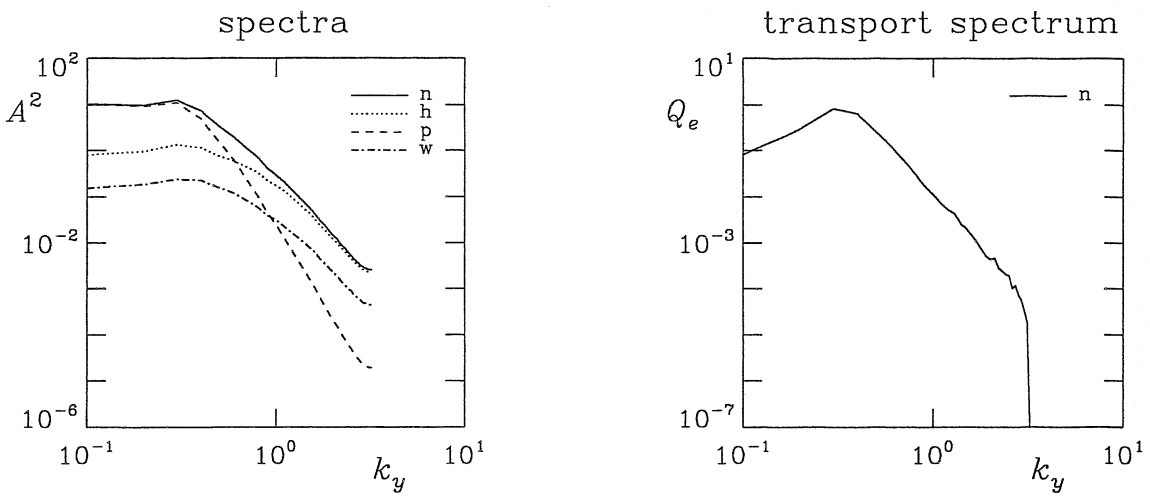

Figure 7.2. (left) Amplitude spectra of $\widetilde{n}_e$, $\widetilde{h}_e$, $\widetilde{\phi}$, and $\nabla_\perp^2\widetilde{\phi}$, respectively labelled by 'n', 'h', 'p', 'w'. (right) Spectrum of the transport, Q_e. These quantities are averaged over time and the x-direction. The characteristics of note are that $\widetilde{\phi}$ and $\widetilde{n}_e$ track each other at low k_y, with $\widetilde{h}_e$ small, but that the small scales see mostly density disturbances, with $\widetilde{\phi}$ small. For weak to moderate coupling, $\widetilde{h}_e$ and $\nabla_\perp^2\widetilde{\phi}$ also tend to track each other. This follows from the competition between the dissipative coupling and a strongly $k_\perp$-dependent excitation mechanism, which is dependent on the polarisation nonlinearity (ExB advection of the vorticity). The resulting transport peaks at intermediate wavelength.

that of $\widetilde{n}_e$ at small scales where the direct cascade sends enough free energy into $\widetilde{n}_e$ so that $A_n > A_p$. At the larger scales, though, we have $A_h \ll A_n \approx A_p$, the signature of nearly adiabatic electrons. Due to these characteristics, we also find that the transport spectrum has a peak displaced to the short wavelength side of most of the free energy. These results are shown in Fig. 7.2.

It is also interesting to note the spectrum of the vorticity,

$$A_w(k_y) = \int \frac{dt}{T} \int \frac{dx}{L_x} \left| \nabla_\perp^2 \widetilde{\phi}(k_y, x, t) \right|^2 \tag{7.7}$$

shown in Fig. 7.2 together with the other amplitudes. As expected due to the fact that it contains more factors of $k_\perp$ than A_p, the vorticity has a flatter spectrum than the state variables $\widetilde{\phi}$ and $\widetilde{n}_e$. This is important to keep in mind, as the nonlinear vorticity dynamics is important to drift wave turbulence overall, and therefore spatial resolution of the density or electrostatic potential is not sufficient to ensure an adequately resolved

computation. In this model the vorticity and $\widetilde{h}_e$ have very similar dynamics, due to the constancy of the coupling mechanism, and exhibit similar spectra. Finally, the fact that the high-k_y decay of the vorticity spectrum proceeds right to the last mode indicates a well behaved numerical scheme (*i.e.*, there are no sharp upward or downward turns, except for the tendency towards flatness at the last mode).

7.IV. Energetics

Beyond the amplitudes and spectra of the disturbances we may apply these same diagnostics to the terms corresponding to the major processes in the energetics — each step in the pathway from source to sink. Drift wave energetics take the pathway

$$\text{gradient drive} \rightarrow \widetilde{p}_e \leftrightarrow \widetilde{J}_{\parallel} \rightarrow \widetilde{\phi} \rightarrow \widetilde{J}_{\parallel} \rightarrow \text{dissipation} \tag{7.8}$$

The path through $\widetilde{\phi}$ is necessary to get the first of these arrows, which represents the source, simply the product of the gradient and the transport. The second arrow is the kinetic shear Alfvén transfer given by $\widetilde{J}_{\parallel}\nabla_{\parallel}\widetilde{p}_e$. The third and fourth arrows represent the more familiar MHD Alfvén transfer, $\widetilde{J}_{\parallel}\nabla_{\parallel}\widetilde{\phi}$. Both these transfers go either way as they are of indefinite sign and represent a coupling. Finally, the dissipation is simply $\eta_{\parallel}\widetilde{J}_{\parallel}^2$ in the resistive models with no temperature dynamics. In a drift wave computation like the ones shown so far this transfer pathway is all there is between $\widetilde{p}_e$ and $\widetilde{\phi}$, but in more general situations more than one pathway is available. Diagnosis of the energetics is important for proper understanding of the dynamics in such situations.

The energetics of the dissipative coupling model is given by

$$-\widetilde{\phi}\frac{d_E\nabla_{\perp}^2\widetilde{\phi}}{dt} = \widetilde{\phi}D\widetilde{h}_e \tag{7.9}$$

$$\widetilde{n}_e\frac{d_E\widetilde{n}_e}{dt} = -\omega_n\widetilde{n}_e\frac{\partial\widetilde{\phi}}{\partial y} - \widetilde{\phi}D\widetilde{h}_e - D\widetilde{h}_e^2 \tag{7.10}$$

where ω_n is the normalised gradient strength (unity in the models of the previous chapter), arranging the current together with the pressure in the energetics, following the fact that the vorticity equation itself contains only transfer terms in the models with parallel dynamics (see Chapter 5, Section VI). We normalise the various processes in terms of twice the energy, expressing them in terms which can be compared to growth rates of linear instabilities. The gradient drive, kinetic shear Alfvén transfer, and resistive dissipation are given by

$$\Gamma_n = \frac{1}{2U}\int d^2x\left[-\omega_n\widetilde{n}_e\frac{\partial\widetilde{\phi}}{\partial y}\right] \tag{7.11}$$

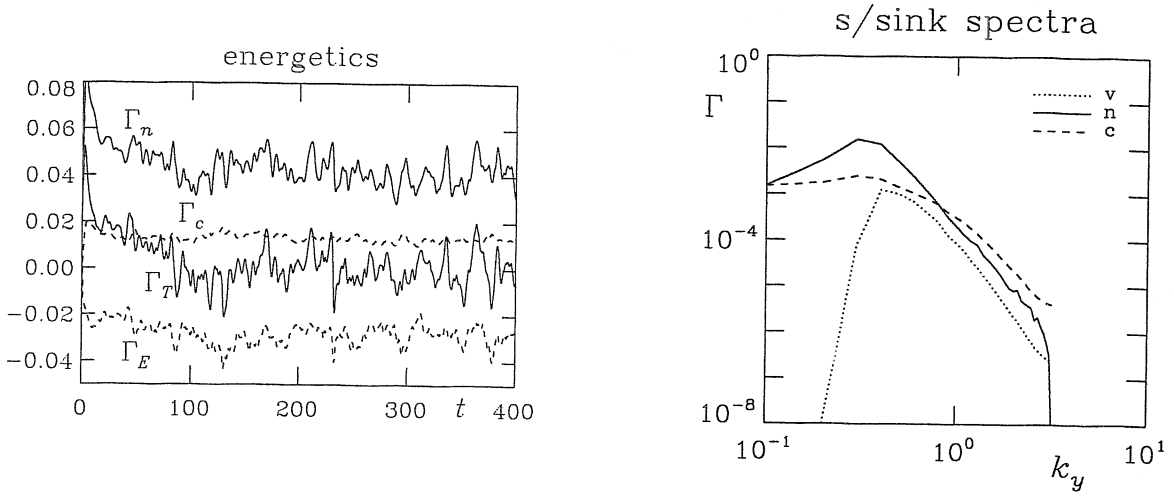

Figure 7.3. (left) Time traces of the source (Γ_n) and sink (Γ_c) rates, compared to the total growth rate (Γ_T) and the numerical dissipation (Γ_E). The cascade dynamics dump significant energy into the smallest scales which are dissipated through the numerical scheme. The close agreement with a case with twice the resolution indicates that this is the onset of the high Reynolds number regime, in which details of the very smallest scales are lost but without significant impact on the main results. These curves reach saturation before the amplitudes do (see Fig. 7.1). (right) Spectra of the source (n), transfer (v), and sink (c) rates. The sink spectrum is the flattest, reflecting the $k_\perp$-independent coupling mechanism. The source spectrum follows from the transport (Fig. 7.1). The transfer spectrum is positive at high k_y but negative at low k_y, balancing the inverse ExB energy cascade.

$$T_{jp} = \frac{1}{2U}\int d^2x \left[\tilde{\phi} D\tilde{h}_e\right] \tag{7.12}$$

$$\Gamma_c = \frac{1}{2U}\int d^2x \left[D\tilde{h}_e^2\right] \tag{7.13}$$

respectively, where U is the total free energy given by

$$U = \int d^2x \frac{1}{2}\left(\left|\nabla_\perp \tilde{\phi}\right|^2 + \tilde{n}_e^2\right) \tag{7.14}$$

noting that the gradient drive is proportional to the transport times the gradient strength. The spectra of the source, transfer, and sink are then given by

$$\Gamma_n(k_y) = \frac{1}{U}\int \frac{dt}{T}\int \frac{dx}{L_x}\ \mathrm{Re}\left[-\omega_n i k_y \tilde{n}_e^*(k_y,x,t)\tilde{\phi}(k_y,x,t)\right] \tag{7.15}$$

$$T_{jp}(k_y) = \frac{1}{U}\int \frac{dt}{T}\int \frac{dx}{L_x}\ \mathrm{Re}\left[D\widetilde{\phi}^*(k_y,x,t)\widetilde{h}_e(k_y,x,t)\right] \tag{7.16}$$

$$\Gamma_c(k_y) = \frac{1}{U}\int \frac{dt}{T}\int \frac{dx}{L_x}\ \mathrm{Re}\left[D\widetilde{h}_e^*(k_y,x,t)\widetilde{h}_e(k_y,x,t)\right] \tag{7.17}$$

These energetics quantities are shown for the dissipative coupling model, for $D = 0.1$, in Fig. 7.3. The time traces of the energetics saturate sooner than the amplitudes do (see also Fig. 7.1), which is very often the case. The cascade dynamics proceeds in both directions, which tends to result in the spectrum of the sink to be flatter than that of the source, as the energy balance of the ranges on both sides of the drive peak are affected by the nonlinear transfer. The driven modes have a particular structure, but the randomness of the cascade phenomenon results in the creation of modes of arbitrary structure at lower and higher k. This keeps all the damped eigenmodes alive, and they do most of the dissipation. In a linear computation these damped eigenmodes are absent at late times, and all one sees is the structure of the most (or only) unstable eigenmode. But in turbulence with the incoherent nature of the scattering taking place between all the possible three wave triplets, all modes are continually excited whether they are linearly damped or not. The transfer spectrum is positive at high k_y on average because of the inverse cascade in the ExB energy. The direct cascade in the other state variables (here, $\widetilde{n}_e$) ensures that there is always activity at high k_y, and then the linear coupling feeds that into the ExB eddies. Even in this simplified model there are several cycles acting at once, and with the turbulence in statistical saturation, all of them have to be in balance. The short correlation time we will see in the next section shows that the nonlinear interactions are mostly incoherent, even if the linear coupling by itself would produce coherent eigenmodes.

7.V. Correlations

In some cases it is important to know the correlation time and lengths, especially when comparing with the predictions of a simple model based on scaling a set of equations or on the typical scales of a linear instability. Analytical models may make assumptions about the scales based on isotropy as well as the wavelength and growth rate of the strongest instability. Measuring the correlation length in both the x and y-directions indicates how isotropic the turbulence is, and these lengths and the correlation time may be compared to the wavelength and the growth time of the linear instability. Measuring the correlation time indicates how important the incoherent part of the dynamics is to the whole.

In each case the correlation length or time is given by the $1/e$ width of the corresponding correlation function. We take the time as an example. The correlation function of the density disturbances is given by

$$F(\tau) = \left[\int \frac{dt}{T}\,\widetilde{n}_e(t)\widetilde{n}_e(t+\tau)\right]\left[\int \frac{dt}{T}\,\widetilde{n}_e(t)\widetilde{n}_e(t)\right]^{-1} \tag{7.18}$$

with each integral actually an averaged sum over the time interval T. If T is long enough then $F(\tau)$ is symmetric about zero. The curve is normally smooth enough that $F(\tau)$ is equal to e^{-1} only for two values of τ of roughly equal magnitude; the correlation time τ_c may be defined as the average of these two magnitudes.

The correlation lengths may be measured in similar fashion, but if the coordinate domain is periodic the integrals may be replaced by sums over the spectra. For example, using the Fourier decomposition of the y-direction,

$$\widetilde{n}_e(y) = \sum_l \widetilde{n}_{el} e^{ily} \tag{7.19}$$

the correlation function becomes

$$F(\Delta y) = \left[\sum_l |\widetilde{n}_{el}|^2 \cos l\Delta y\right] \left[\sum_l |\widetilde{n}_{el}|^2\right]^{-1} \tag{7.20}$$

which is obviously both symmetric about zero and periodic. It is expected that λ_y is significantly smaller than L_y so that this artifact does not affect the measurement of λ_y. Similar considerations apply for the x-direction whether or not it is periodic.

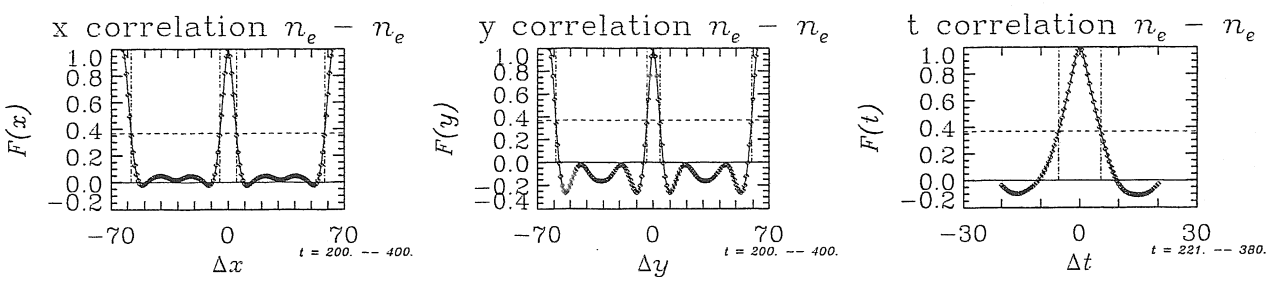

Figure 7.4. From right to left, the correlation functions for $\widetilde{n}_e$ against x, y, and t, in each case averaged over the other two variables. The dynamics is periodic in space but not in time. The horizontal dashed line is drawn at the level $1/e$, and the vertical lines then give the corresponding correlation length or time. The correlation lengths and time are much shorter than the domain size or the duration of the saturation phase, respectively.

To improve the statistics, the integrals in each of these correlation functions may be averaged over the other two independent variables; that is, they become average sums over all spatial coordinates and time points of the integrands; for example, $\widetilde{n}_e(t)\widetilde{n}_e(t+\tau)$ becomes averaged over (x, y, t) rather than just t. In a three dimensional computation it may be averaged over (x, y, s, t).

In Fig. 7.4 the correlation functions for $\widetilde{n}_e$ in the dissipative coupling model with $D = 0.1$ are shown for each independent variable (x, y, t), averaged in each case over the other two (the time correlation function is averaged only over y). The periodic expressions (Eq. 7.20) were used for x and y, and for t the time interval in Eq. (7.18) was $T = 40$ with 160 samples. The correlation lengths are $\lambda_x = 4.8$ and $\lambda_y = 3.8$, and the correlation time is $\tau_c = 5.3$. This feature of $\lambda_x > \lambda_y$ is common in this model, in which there is no x-dependence in the dissipation and linear modes with $k_x < k_y$ are slightly favoured. We will see this change as the models get more complicated. The correlation time is short, reflecting the dominance of small scales in the dynamics. In three dimensional models the scales will get slightly larger but otherwise the tendency to scale with ρ_s and $c_s/L_\perp$ will remain.

7.VI. Randomness

One of the things to understand about turbulence is that it is a nonperiodic phenomenon involving an effectively arbitrarily large number of degrees of freedom. Both correlation times and lengths are expected to be limited in some sense, and the above examples show that they are. How random the phenomenon is can be characterised by looking at the distribution of amplitudes as well as their averages. The rms amplitude of a signal is the standard deviation relative to the mean. For disturbance amplitudes sampled over the entire spatial domain the mean is usually very close to zero, but even if in a more limited sampling the mean may be subtracted away and then the signal normalised to its standard deviation,

$$\bar{f} = N^{-1}\sum_i f_i \qquad \delta f = \left[N^{-1}\sum \left(f_i - \bar{f}\right)^2\right]^{1/2} \qquad A_i = \frac{f_i - \bar{f}}{\delta f} \tag{7.21}$$

We then measure the distribution of amplitudes of A_i; typically four standard deviations about zero are enough. The one dimensional space with A as a coordinate is split up into equal bins over the interval $[-4, 4]$ for an odd number of bins evaluated as cell centered volumes in this phase space (*i.e.*, one is centered at the origin). For each point in the sample, the bin into which A_i falls is incremented by one, and then all bins are divided by the number of points. The resulting histogram is graphed as $P(A)$.

For a random sampling it is well known that the distribution $P(A)$ is given by a Gaussian in A, or $(2/\pi)^{1/2}e^{-A^2}$. One can also find $P(A)$ for a perfectly coherent sine wave by sampling it at equal intervals; the result is a double hump curve with a minimum at zero and maxima at the wave amplitude. There is also a model for a passively advected quantity in a random flow field, according to which $P(A)$ should have more of a Lorentzian character

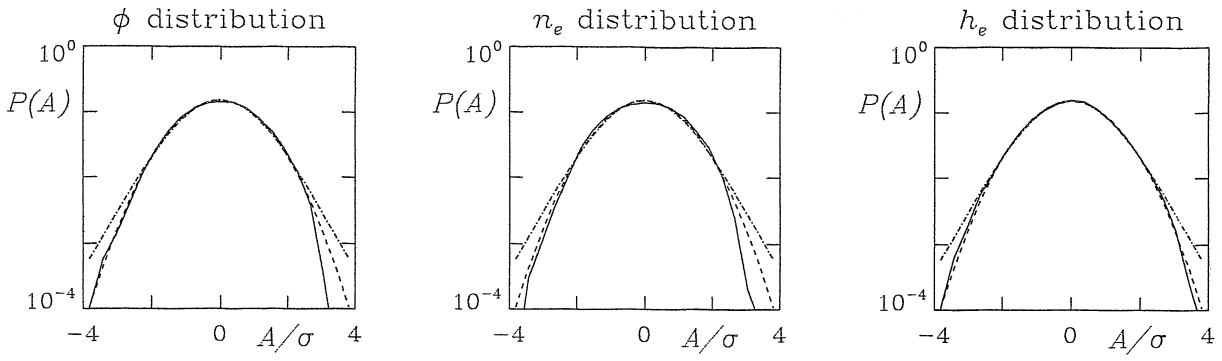

Figure 7.5. Amplitude probability distributions of $\widetilde{\phi}$ (left), $\widetilde{n}_e$ (center), and $\widetilde{h}_e$ (right), for the case with $D = 0.1$. Noise sets in due to the finite sample size at about 2.5 standard deviations. The distributions do not differ significantly from Gaussian.

which has significantly extended tails compared to a Gaussian due to the tendency towards spatial intermittency (the passive scalar distribution is given by $c[1 + kA^2]^{-\gamma}$, with $c = 1.38624\sqrt{\pi}$, $k = 0.08$, and $\gamma = 1 + 1/2k$; see Further Reading, below). The amplitude distributions for $\widetilde{\phi}$, $\widetilde{n}_e$, and $\widetilde{h}_e$, are shown in Fig. 7.5, for the case with $D = 0.1$. As we can see, the distributions are indistinguishable from Gaussian. They are definitively different from the coherent distribution, as befits the short correlation time and lengths. They are closer to Gaussian than to the passive scalar curve, although these are not very distinct at the level of two standard deviations.

The transport dynamics shows somewhat more interesting behaviour. In Fig. 7.6 we display the distributions of the down-gradient ExB velocity, $\widetilde{v}_E^x$, for the case with $D = 0.1$, and the transport, $\widetilde{h}_e\widetilde{v}_E^x$, for the cases with $D = 0.1$ and a more adiabatic case with $D = 1.0$. Both the pieces in the transport, $\widetilde{h}_e$ and $\widetilde{v}_E^x$, are Gaussian, but the transport is not. This largely reflects the increased probability of smaller amplitudes in the product of Gaussian quantities, but the distribution of the transport is also skewed towards positive values. The skewness results from the energetic favouring (through the gradient drive) of any disturbances which happen to find themselves aligned with down-gradient flows of the same sign. These ones tap the free energy and do the transport. A nonzero net transport reflects their dominance. The same signal for the more adiabatic cases shows little skewness, following from the comparatively weaker gradient drive.

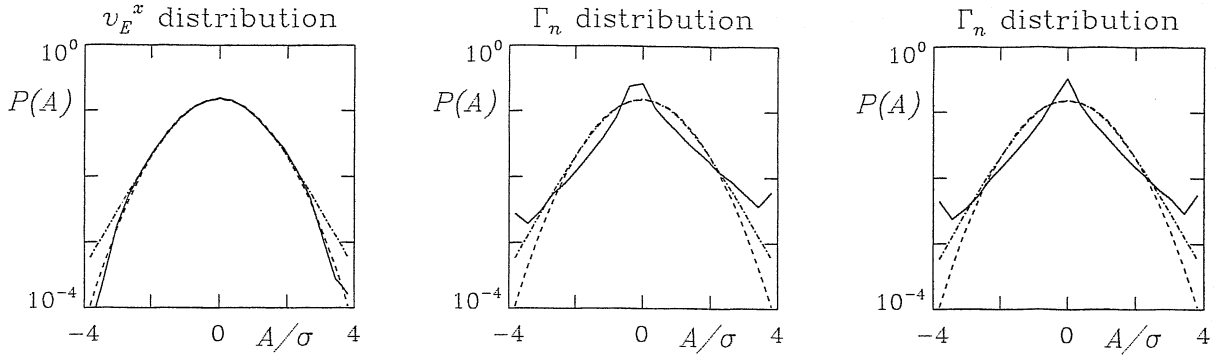

Figure 7.6. Amplitude probability distributions of $\widetilde{v}_E^x$ (left) and Q_e (center) for $D = 0.1$, and and Q_e for $D = 1.0$ (right). The skewness of the Q_e distribution reflects the transport by the nonadiabatic part of the dynamics. The sharper peak results from the product of two random variables favouring the smaller values. The dependence of the skewness on energetic favouring is shown by the fact that it is less pronounced for the more adiabatic case.

7.VII. Cross Coherence

Randomness in a single amplitude may mask a significant degree of correlation between the amplitudes of two different quantities, each of which may have a Gaussian distribution. The most obvious case is that of adiabatic electrons in otherwise random turbulence: both $\widetilde{n}_e$ and $\widetilde{\phi}$ have a Gaussian distribution but they are perfectly correlated because they are held equal to each other by arbitrarily strong cross coupling. We may quantify this through two measurements. One is the cross coherence. Each sampled quantity is normalised to its standard deviation and zero mean as shown above. Then, each point in the sample contains two numbers, the normalised amplitudes of each quantity, and may be placed in a two dimensional space with these two amplitudes, call them A_1 and A_2, as the coordinate axes. If the two quantities are perfectly correlated the points lie on the line $A_2 = A_1$, or if they are anticorrelated they lie on the line $A_2 = -A_1$. If they are perfectly uncorrelated then the points will be scattered with a density independent of the angle about the coordinate origin, $A_2 = A_1 = 0$.

We measure this as a sort of two dimensional histogram. The space (A_1, A_2) is binned in the same way as the one dimensional axis A for single quantity distributions, and then each point is placed into the bin in which A_1 and A_2 fall for that point, and the corresponding bin number incremented. Contours of $P(A_1, A_2)$ are drawn in the left frame of Fig. 7.7 for the case with $D = 0.1$. These are ellipses oriented along the line $A_2 = A_1$, reflecting a cross coherence intermediate between the two extremes of perfect correlation

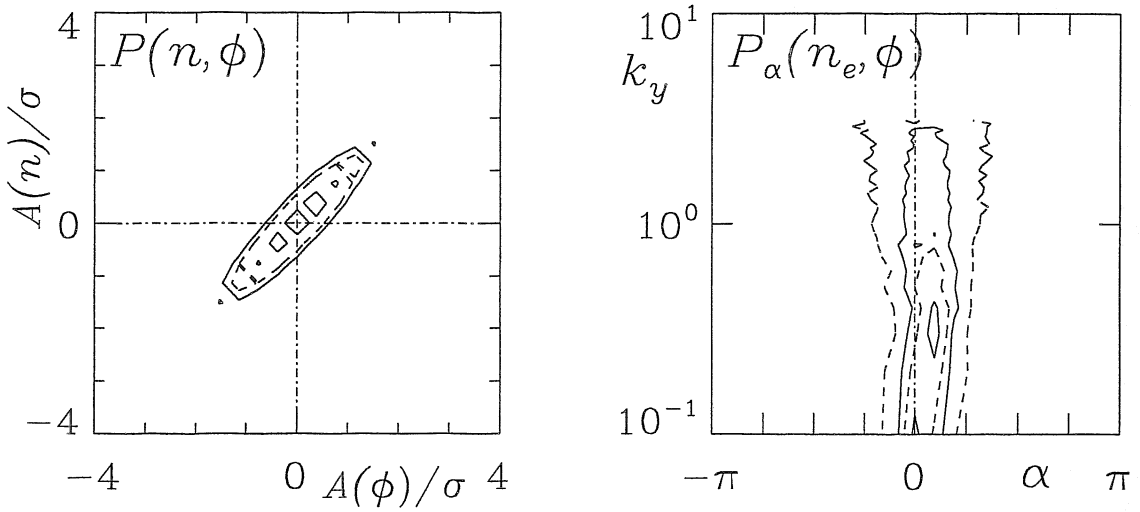

Figure 7.7. Cross coherence (left) and phase shift distributions (right), between $\widetilde{n}_e$ and $\widetilde{\phi}$ for $D = 0.1$. These forms reflect the general trend of the adiabatic response, which persists in turbulence with robust transport.

and perfect relative randomness. The ellipses are typically thin for drift wave turbulence, reflecting the tendency towards an incompletely adiabatic response. As we will see in later chapters, the ellipses become circles when the coupling between $\widetilde{p}_e$ and $\widetilde{J}_{||}$ is left out, which reflects a character of passive advection.

The second measure is the relative phase between the two Fourier components for each given wavenumber. Taking the Fourier decomposition in the y-direction as in Eq. (7.19), for both $\widetilde{n}_e$ and $\widetilde{\phi}$ for example, we define the relative phase as

$$\alpha_l(\widetilde{n}_e, \widetilde{\phi}) = \mathrm{Im}\log\left(\widetilde{n}_{el}^{*}\widetilde{\phi}_l\right) \tag{7.22}$$

assuming that $\widetilde{n}_{el} = a_l\widetilde{\phi}e^{-i\alpha_l}$ with both a_l and α_l real. We then assemble the distribution $P(\alpha_l)$ as a one dimensional histogram over the interval $[-\pi, \pi]$ for each wavenumber l. Contours of $P(\alpha_l)$ are drawn in the right frame of Fig. 7.7 for the case with $D = 0.1$, and again these do better than the simple average to reflect the character of the phase shift distribution. For adiabatic electrons $P(\alpha_l)$ would be a delta function at zero for each l, while a perfectly uncorrelated distribution would be a flat line whose level is the inverse number of bins in the histogram. Perfectly driven linear instabilities would show a narrow distribution at $\pi/2$, reflecting a down-gradient flow through a disturbance with positive amplitude. As we see, for intermediately nonadiabatic drift wave turbulence we find that the distribution is still quite well localised near zero even though it is shifted to positive

values of α. Most of the signal for $P(\alpha)$ is well below $\pi/2$, and this may be taken as a signature for drift wave mode structure.

7.VIII. Inter Scale Transfer

We have already seen the nonlinear transfer, but we mention it here again as is it part of the energetics. In addition to the transfers terms such as $\widetilde{p}_e \leftrightarrow \widetilde{J}_{\|}$, which for electrostatic turbulence is a linear process at each k, we have the interscale transfers $T(k_\perp \leftarrow k'_\perp)$ for each quantity, reflecting the scattering in wavenumber space by the nonlinear ExB advection. This builds a picture of drift wave energetics which involves longer and shorter wavelengths as well as the $\widetilde{\phi}$ and $\widetilde{n}_e$ (or $\widetilde{p}_e$) disturbances. For all limits of the dissipative coupling we have the picture as shown at the end of Chapter 6; the qualitative tendencies persist, and only their strengths scale with the parameters. The simultaneous, oppositely directed nonlinear transfer dynamics in the ExB energy U_E and the thermal free energy U_n is compensated for by the linear transfer, which we saw in Fig. 7.3. The flow of energy is therefore circular, from low-$k_\perp$ U_n to high-$k_\perp$ U_n through the direct cascade of turbulent mixing, then through the linear kinetic shear Alfvén transfer to high-$k_\perp$ U_E, to low-$k_\perp$ U_E through the inverse energy cascade of vortex merger, and then through the linear transfer back to low-$k_\perp$ U_n. At all scales the gradient drive and nonadiabatic (Alfvénic) dissipation are operative, with the intermediate range of positive net drive determined self consistently by the dynamics. A diagram of this is shown in Fig. 7.8.

7.IX. Summary — The Mode Structure of Drift Wave Turbulence

The basic properties of drift wave turbulence, as measured through the mode structure, are as follows. It is a process of incompressible, two dimensional ExB drift turbulence occurring in drift planes, locally perpendicular to the background magnetic field, with the drift planes coupled together by the parallel dynamics, especially the adiabatic response of the electrons. The ExB flow disturbances follow an Eulerian equation and the thermodynamic quantities they transport would attempt to follow passive scalar dynamics. The basic character of this part of the dynamics is a turbulent local cascade process. This is shown by the energy transfer spectra, which measure the interscale exchanges to occur within about a half decade of wavenumber space, and by the short space and time correlations, and by the fact that the instantaneous spectra are much noisier than the average spectra, which are always smooth. This ExB drift plane turbulence is acted upon by dissipative coupling strongly enough that the potential and pressure disturbances, or more generally the flow eddies and the quantities they transport, are always highly correlated. The coupling is however not generally so strong that the electrons are adiabatic;

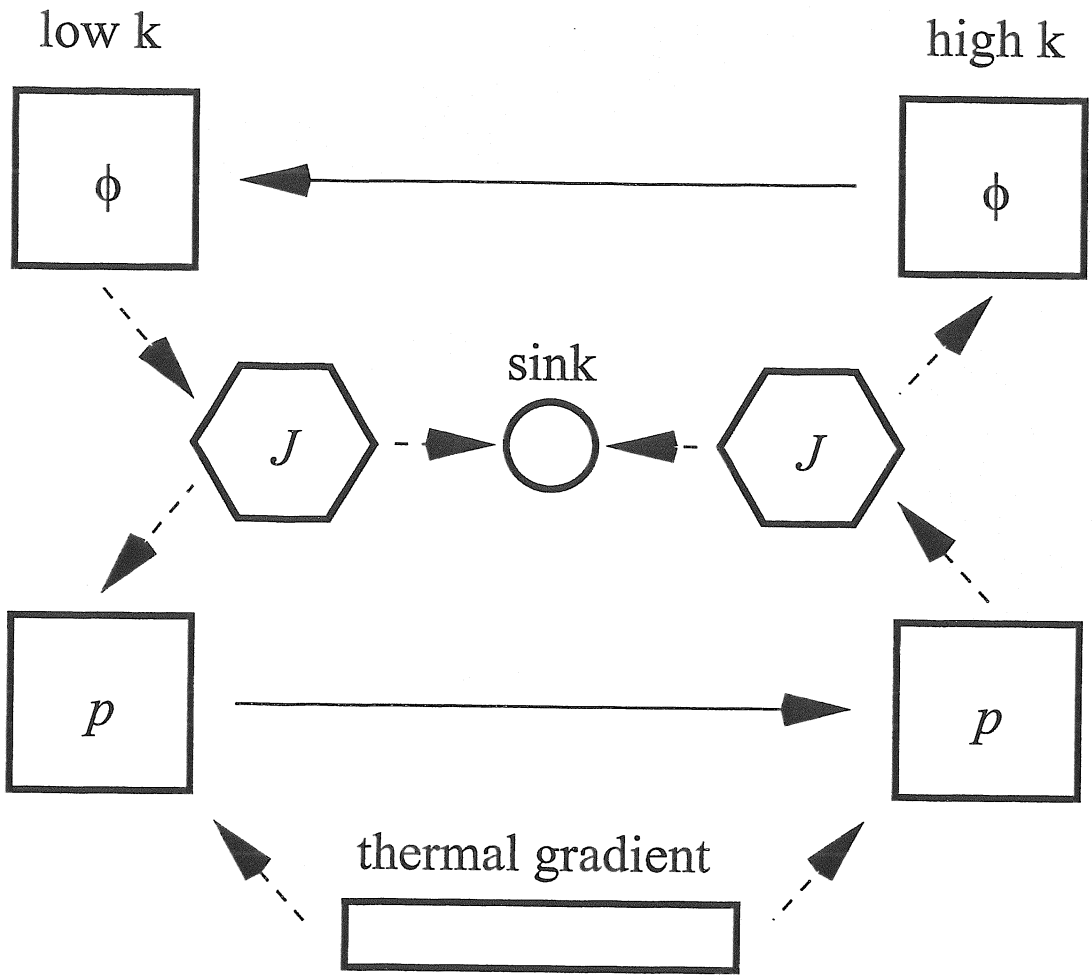

Figure 7.8. Diagram of the energy transfer dynamics in drift wave turbulence. Nonlinear transfer via unsteady ExB advection is between scales, shown with solid lines. The scale transfer is dominantly through $k_\perp$ although in three dimensions $k_\parallel$ is also involved. Linear transfer, shown with dashed lines, includes coupling between the state variables ϕ and p (collectively $\widetilde{n}_e$ and $\widetilde{T}_e$) mediated by the current, denoted J. The thermal gradient drives p and the parallel dynamics is dissipative at all scales. Due to the bi-directional nonlinear transfer, the sink spectrum is always wider than the drive spectrum, and an intermediate spectral range becomes dominant. Where this range falls depends on the relative strengths of all the interactions, self consistently, eventually determined by the parameters.

rather, the size of $\widetilde{h}_e$ is usually at least a sizeable fraction of the size of $\widetilde{n}_e$. Drift wave turbulence is therefore well described as a competition between ExB turbulence in the drift plane, excited by the background gradient, and dissipative Alfvénic dynamics (treated in

the simplest model as a relaxation, but proceeding through kinetic shear Alfvén waves generally) along the magnetic field. The importance of the dual ExB/pressure cascade is reflected in the fact that the spectra of the sinks are flatter than those of the sources. The vorticity spectrum is always flatter than that of any other advected quantity. The statistics is almost always indistinguishable from Gaussian, showing that (1) the system is turbulent and (2) the passive scalar character of the thermodynamic quantities is felt only in the energy transfer properties, that is, the parallel coupling is strong enough that the thermodynamic quantities do not depart statistically from the ExB flow disturbances. This is also seen in the phase shift distributions, specifically in the absence of a region in wavenumber space in which the influence of the coupling is lost.

Finally, it is worth emphasising that this information comes from a rather involved statistical diagnosis of the turbulence, not from superficial information such as linear growth rates, the saturated transport scaling, or visualisations of the disturbances in any of the dependent variables. What is important to understanding at this stage is the qualitative character of the dynamics, not the quantitative results, and not how things look to the eye. Drift wave turbulence is a complicated system which does not lend itself well to simple, heuristic analytical modelling, except perhaps in an *ad hoc* explanatory mode. But we can do that just as well with this fully developed package of diagnostics, which has the advantage of operating on actual nonlinear solutions to the equations as they stand.

Further Reading

This chapter concentrates on energetics because for gradient driven systems the key question is how the turbulence maintains itself against dissipation, and because the free energy source is in the gradient of a thermodynamic state variable while it is liberated by flow eddies, and the energy transfer channel from transported quantity back to flow stream function is of central importance. Cross correlation among the variables is the most useful diagnostic. The cross coherence diagnostic is standard for more than one variable and is covered in the texts cited below. The phase shift diagnostic was developed for drift wave turbulence by B. Scott, in *Plasma Phys. Contr. Fusion* 39 (1997) 471. The energy transfer diagnostics originally come from neutral fluid turbulence, *e.g.*, used by A. J. Domaradzki to demonstrate local cascade dynamics in three dimensional incompressible turbulence, in *Phys. Fluids* 31 (1988) 2747. It was expanded for drift wave turbulence by S. Camargo, D. Biskamp, and B. Scott, in *Phys. Plasmas* 2 (1995) 48, and *Phys. Plasmas* 3 (1996) 3912.

A large volume of literature exists on the statistical characterisation of a single fluctuating variable, and much of statistical diagnosis of turbulence actually falls into this area. For drift wave turbulence see the review by W. Horton, in *Reviews of Modern Physics*,

Vol. 7, No. 3, April 1999. For experimental data on disturbances in fusion plasmas see E. Sánchez *et al*, in *Phys. Plasmas* 7 (2000) 1408. Standard techniques are treated in many texts on turbulence, including U. Frisch, *Turbulence: the Legacy of A.N. Kolomogorov*, (Cambridge, 1995), M. Lesieur, *Turbulence in Fluids*, (3rd ed, Kluwer Academic Publishers, 1997), and A. S. Monin and A. M. Yaglom, *Statistical Fluid Mechanics: Mechanics of Turbulence*, Vol 2 (MIT Press, Cambridge, USA 1975).

8. Magnetic Shear and Drift Wave Turbulence
Self Sustained Turbulence — The Nonlinear Instability

B. Scott

Jul 1999

8.1. Introduction

Having introduced drift wave turbulence and its mode structure in the previous two chapters, we now turn to the first major effect of magnetic field line geometry: magnetic shear on closed flux surfaces. In a magnetically confined plasma in equilibrium, the magnetic field lies in closed surfaces which are called flux surfaces. The magnetic field is further generally sheared, which means that any regular, simply connected region in the drift plane becomes deformed by shearing if each point in it is transported along the magnetic field. The magnetic field has this property if the surfaces it lies in are shaped or the plasma lying in it it carries a current. Generally, any finite pressure equilibrium guarantees the presence of currents, due to the necessary magnetic forces. Drift wave dynamics and turbulence is most relevant in systems with magnetic field lines which lie in closed surfaces. The reason for this is that we have been implicitly assuming that the parallel wavenumber does not vanish. The finite parallel gradient, $\nabla_\parallel$, is the path to dissipation through the kinetic shear Alfvén channel, and so whether $\nabla_\parallel$ is in general allowed to vanish or not is important. It is a theorem of topology that if a vector field should lie within a closed, unbounded domain (*e.g.*, a sphere or torus) and is everywhere nonvanishing, then the domain must be toroidal. For a magnetic field in three dimensional Euclidean space this means that the surfaces must be two dimensional tori. These surfaces are called flux surfaces.

There are two very important results of this geometric change to the dynamics of drift waves. First, drift waves as such become linearly stable. In the simple linear models of Chapter 5, we found that for most parameters the linear modes had substantial growth rates. But when $\nabla_\parallel$ becomes a secular function of the position across flux surfaces, which is the effect of shear, we find that the eigenmodes are all stable. Second, the turbulence can persist nevertheless, if it is initialised at finite amplitude. It sustains itself by altering the linear mode structure into something which can support much stronger nonadiabatic dynamics, with both larger drive and dissipation rates. The basic dynamics of this is already present in the simple dissipative coupling model of the previous two chapters, but there it is overshadowed by the fact that the linear modes can grow by themselves. In a sheared magnetic field, these nonlinear interactions become the reason we find turbulence

at all. Stabilisation of drift waves by magnetic shear and self destabilisation of drift wave turbulence form the focus of this chapter.

8.II. Field Line Connection and Magnetic Shear

If the background is an MHD equilibrium, we may use pressure as the coordinate tracking displacements across flux surfaces. The basic condition of MHD equilibrium with no mass flows is that the right side of the MHD force equation vanish, or (cf. Chapter 2)

$$\frac{\mathbf{J}\times\mathbf{B}}{c} = \nabla p \tag{8.1}$$

If we take the dot product of this with either $\mathbf{J}$ or $\mathbf{B}$, we find that both of these vector fields must lie in surfaces of constant p. This defines the direction across flux surfaces as the direction down the pressure gradient. The obvious choice of coordinate directions is what we have been using: ∇p, $\mathbf{B}$, and their cross product.

We now allow the magnetic field to be sheared, and what this means is that its direction is a function of the coordinate across flux surfaces. The very simplest model of this situation is the three dimensional periodic slab, which treats toroidal topology and magnetic shear, but no other complication of closed flux surfaces (these we will investigate in subsequent chapters). It is this combination of periodicity and shear which carries the important result that the parallel gradient does not in general vanish. We model the magnetic field and background pressure as

$$L_p \nabla \log p = -\nabla x \qquad\qquad \mathbf{B} = B_0 \left(\nabla s - \frac{x}{L_s} \nabla y \right) \tag{8.2}$$

in a domain with at least the y and s-coordinates periodic, reflecting the topology of the ys-surfaces, which are the flux surfaces. The contravariant components of $\mathbf{B}$ are given by $B^s = \mathbf{B} \cdot \nabla s$, *etc.*, or

$$B^x = 0 \qquad\qquad B^y = -B_0 \frac{x}{L_s} \qquad\qquad B^s = B_0 \tag{8.3}$$

We assume periodicity lengths of L_y and $L_\parallel$, respectively,

$$f(x, y + L_y, s) = f(x, y, s + L_\parallel) = f(x, y, s) \tag{8.4}$$

The pressure scale length is L_p, and the degree of shear is given by the shear length L_s, which gives the distance one would have to move across surfaces to get the magnetic field direction to rotate about the x-direction by 45 degrees. In a local computation, L_y, $L_\parallel$, L_p, B_0, and L_s are all constant parameters.

The parallel gradient of any scalar quantity f is given by

$$\frac{1}{B_0}\mathbf{B}\cdot\nabla f \equiv \nabla_{\|} f = \frac{\partial f}{\partial s} - \frac{x}{L_s}\frac{\partial f}{\partial y} \tag{8.5}$$

The periodicity within the surfaces leads to a Fourier representation for f,

$$f(x,y,s) = \sum_l \sum_m f_{lm}(x) \exp\left(2\pi i l \frac{y}{L_y} + 2\pi i m \frac{s}{L_{\|}}\right) \tag{8.6}$$

The parallel gradient can be evaluated in terms of a set of wavenumbers,

$$\begin{aligned}\nabla_{\|} f &= \sum_l \sum_m \left(\frac{2\pi i m}{L_{\|}} - \frac{2\pi i l}{L_y}\frac{x}{L_s}\right) f_{lm}(x) \exp\left(2\pi i l \frac{y}{L_y} + 2\pi i m \frac{s}{L_{\|}}\right) \\ &\equiv \sum_l \sum_m i k_{\|} f_{lm}(x) \exp\left(2\pi i l \frac{y}{L_y} + 2\pi i m \frac{s}{L_{\|}}\right)\end{aligned} \tag{8.7}$$

where due to the finite domain size, the set of available parallel wavenumbers,

$$k_{\|} = \frac{2\pi}{L_{\|}}\left(m - l\frac{L_{\|}}{L_y}\frac{x}{L_s}\right) \tag{8.8}$$

with l and m integers, is discrete. The parallel gradient can only vanish if either the Fourier component f_{lm} itself vanishes, or if l and m are chosen such that

$$\left(m - l\frac{L_{\|}}{L_y}\frac{x}{L_s}\right) = 0 \tag{8.9}$$

where the quantity multiplying l can be called a field line pitch parameter. Flux surfaces on which $k_{\|}(l,m)$ vanishes are called rational surfaces, and flux surfaces on which $k_{\|}(l,m)$ can vanish for every l allowed by the computational domain are called main rational surfaces.

Obviously, if the pitch parameter is irrational then not only this particular $k_{\|}$ cannot vanish, but neither can any other, so long as l, hence k_y, does not vanish (in this representation, $k_y = 2\pi l/L_y$). That is, not all surfaces are rational. If there is finite shear ($L_s^{-1} \neq 0$), then the pitch parameter is in general irrational because it is continuously varying, and the set of rational numbers on the real line is a set of measure zero. This is why the assumption that $k_{\|}$ and hence $\nabla_{\|}$ does not vanish for typical situations is a good one, so long as the background magnetic field lies in closed surfaces and there is finite shear. This combined property of periodicity and magnetic shear is called field line connection.

8.III. The Sheared Slab Model

A simple way to treat magnetic shear is to take into account the field line connection property, and examine the dynamics in the neighborhood of a major rational surface of a closed domain with toroidal topology. The radial coordinate x gives the distance across magnetic flux surfaces from this rational surface, the y-coordinate is perpendicular to the magnetic field within the $x = 0$ surface, and the s-coordinate is taken along the magnetic field at the $x = 0$ surface. We expect the parallel dynamics to favour the longest possible wavelengths, so within this model we prescribe $\partial/\partial s = 0$. The magnetic field is given by $\mathbf{B} = B_0\{0, -x/L_s, 1\}$ in $\{x, y, s\}$, respectively. The parallel gradient is therefore tied to the y-coordinate,

$$\mathbf{B} \cdot \nabla f = -B_0 \frac{x}{L_s} \frac{\partial f}{\partial y} \tag{8.10}$$

for any scalar quantity $f = f(x, y)$. The corresponding parallel wavenumbers are therefore tied to those in the drift direction,

$$k_\parallel = -\frac{x}{L_s} k_y \tag{8.11}$$

The parallel wavenumber is however a valid statistical parameter distinct from k_y, as due to the ability of disturbances to alter their extent in the x-direction, the $k_\parallel$ spectrum can change independently of the k_y spectrum. Additionally, this secular dependence of the geometry on x now forbids periodic boundary conditions in the x-direction.

Other than these changes in the geometry, the basic dynamics we will examine is that of the previous two chapters, that is, electrostatic drift wave turbulence within the simplest possible dynamical model. A result of the dependence of $k_\parallel$ on x is that there is coupling to parallel sound wave motion in addition to currents, so the set of dependent variables is widened to $\{\widetilde{\phi}, \widetilde{p}_e, \widetilde{u}_\parallel\}$. The pressure is synonymous with the density; $\widetilde{p}_e = \widetilde{n}_e$. Nonadiabatic dynamics is represented by $\widetilde{h}_e = \widetilde{n}_e - \widetilde{\phi}$, which acts as a force potential for the parallel current and is required for the gradient drive to be nonzero. It is also required for the pressure/density nonlinearity $\mathbf{v}_E \cdot \nabla \widetilde{p}_e$ to be nonzero, because $\mathbf{v}_E \cdot \nabla \widetilde{\phi}$ vanishes. As in the two dimensional dissipative coupling model, the current is given by resistive friction,

$$\widetilde{J}_\parallel = \eta_\parallel^{-1} \left(\frac{\nabla_\parallel \widetilde{p}_e}{n_e e} - \nabla_\parallel \widetilde{\phi} \right) \tag{8.12}$$

where $\eta_\parallel = 0.51 m_e \nu_e / n_e e^2$ is the collisional resistivity. Otherwise, we take the same normalisation procedure as before, to obtain

$$\frac{d_E}{dt} \nabla_\perp^2 \widetilde{\phi} = C^{-1} \nabla_\parallel^2 \left(\widetilde{p}_e - \widetilde{\phi} \right) \tag{8.13}$$

$$\frac{d_E\widetilde{p}_e}{dt} = -\frac{\partial\widetilde{\phi}}{\partial y} + C^{-1}\nabla_\parallel^2\left(\widetilde{p}_e - \widetilde{\phi}\right) - L\nabla_\parallel\widetilde{u}_\parallel \tag{8.14}$$

$$\frac{d_E\widetilde{u}_\parallel}{dt} = -L\nabla_\parallel\widetilde{p}_e + \mu_\parallel\nabla_\parallel^2\widetilde{u}_\parallel \tag{8.15}$$

where the principal parameter is the collisionality,

$$C = 0.51\frac{\nu_e L_p}{c_s}\frac{m_e}{M_i}\frac{L_s^2}{L_p^2} \tag{8.16}$$

reflecting the competition between perpendicular drift wave excitation and parallel resistive dissipation. A low collisionality implies strong dissipative coupling, and vice versa. The collisionality plays the same role as the inverse of the coupling constant, D, in the dissipative coupling model, but the dissipation and coupling are now spatially dependent, with D replaced by $C^{-1}k_\parallel^2$, and $k_\parallel = -k_y x$. The other parameters control the sound wave response,

$$L = \frac{L_p}{L_s} \qquad \mu_\parallel \leftarrow \frac{\mu_\parallel L_s^{-2}}{c_s/L_p} \tag{8.17}$$

and can be chosen artificially as long as they are significantly less than unity.

In this normalisation the differential operators are

$$\nabla_\perp^2 = \frac{\partial^2}{\partial x^2} + \frac{\partial^2}{\partial y^2} \qquad \nabla_\parallel = -x\frac{\partial}{\partial y} \qquad \frac{d_E}{dt} = \frac{\partial}{\partial t} + \left(\frac{\partial\widetilde{\phi}}{\partial x}\frac{\partial}{\partial y} - \frac{\partial\widetilde{\phi}}{\partial y}\frac{\partial}{\partial x}\right) \tag{8.18}$$

Dependent variables are functions of (x, y), with y periodic on an interval of $2\pi/K$, with K giving the minimum value of $k_y\rho_s$. The domain in x is localised to $-x_L < x < x_L$, and all dependent variables vanish for $x = \pm x_L$.

8.IV. Linear Stability of Electrostatic Drift Waves in a Sheared Magnetic Field

An important result of field line connection in closed surfaces is that the simple drift waves we have been studying are all linearly stable. We recall that if $k_\parallel^2$ may be taken as a constant in the dissipative coupling model, then every Fourier component in the entire set is linearly unstable — the imaginary part of the frequency eigenvalue is positive. We saw this in Chapter 5. There have been several attempts in the past to prove linear stability of the sheared slab to drift waves, but this problem cannot be solved exactly. The solutions in the literature are numerical, and most are approximate. Here we will recover this result with the well defined initial value problem. It will prove especially important to do this without resorting to eigenmodes, because for many situations there is no localised eigenmode which keeps its structure. Due to the secular x-dependence of

$k_\parallel$, the initial disturbance launches a wavelike component whose propagation velocity is partly in the x-direction, and therefore some of the activity will propagate away from the rational surface.

One point should be kept in mind. We are spending time with a two dimensional model while a three dimensional one is generally more germane. However, the linear eigenmodes of a sheared slab are the same in both two and three dimensions, since they are only active in the vicinity of their rational surfaces, and which plane we take in the space of Fourier components in s (the set of m's) is arbitrary. We can therefore set $m = 0$ without loss of generality, at least for the linear problem.

The definition of the problem is as above, with the nonlinear terms set to zero. We have a single Fourier component k_y, defined for $0 < t < \infty$ and $-x_L < x < x_L$, subject to the boundary condition that all dependent variables vanish for $x = \pm x_L$. The dependent variables are $\widetilde{\phi}$, $\widetilde{p}_e$, and $\widetilde{u}_\parallel$ taking complex values, satisfying the set of equations given by

$$\frac{\partial}{\partial t}\left(\frac{\partial^2}{\partial x^2} - k_y^2\right)\widetilde{\phi} = C^{-1}k_y^2 x^2\left(\widetilde{\phi} - \widetilde{p}_e\right) \tag{8.19}$$

$$\frac{\partial \widetilde{p}_e}{\partial t} = -ik_y\widetilde{\phi} + C^{-1}k_y^2 x^2\left(\widetilde{\phi} - \widetilde{p}_e\right) + iLk_y x\widetilde{u}_\parallel \tag{8.20}$$

$$\frac{\partial \widetilde{u}_\parallel}{\partial t} = iLk_y x\widetilde{p}_e - \mu_\parallel k_y^2 x^2 \widetilde{u}_\parallel \tag{8.21}$$

with k_y, C, L, and $\mu_\parallel$ constant parameters.

We first see what happens if $C = 0$ and $\mu_\parallel = 0$, that is, the interaction between drift waves and sound waves in the adiabatic limit with no dissipation. The equations then reduce to

$$\frac{\partial}{\partial t}\left(1 + k_y^2 - \frac{\partial^2}{\partial x^2}\right)\widetilde{\phi} = -ik_y\widetilde{\phi} + iLk_y x\widetilde{u}_\parallel \tag{8.22}$$

$$\frac{\partial \widetilde{u}_\parallel}{\partial t} = iLk_y x\widetilde{\phi} \tag{8.23}$$

with $\widetilde{p}_e = \widetilde{\phi}$. We start with a simple adiabatic disturbance with $\widetilde{\phi} = 3\exp -x^2/4$, set parameters to $k_y = 0.3$ and $L = 0.01$, and allow the system to evolve. The grid consists of 128 equidistant nodes in a domain bounded by $x_L = 32$. The time step is 0.05.

What happens is shown in Fig. 8.1. The initial disturbance, localised to within ± 2 of the rational surface, spreads out, losing amplitude such that the total free energy remains the same. When the disturbances reach positions at which $k_\parallel c_s > \omega_*$, or

$$x_s = \frac{\omega_*}{k'_\parallel c_s} \to L^{-1} \tag{8.24}$$

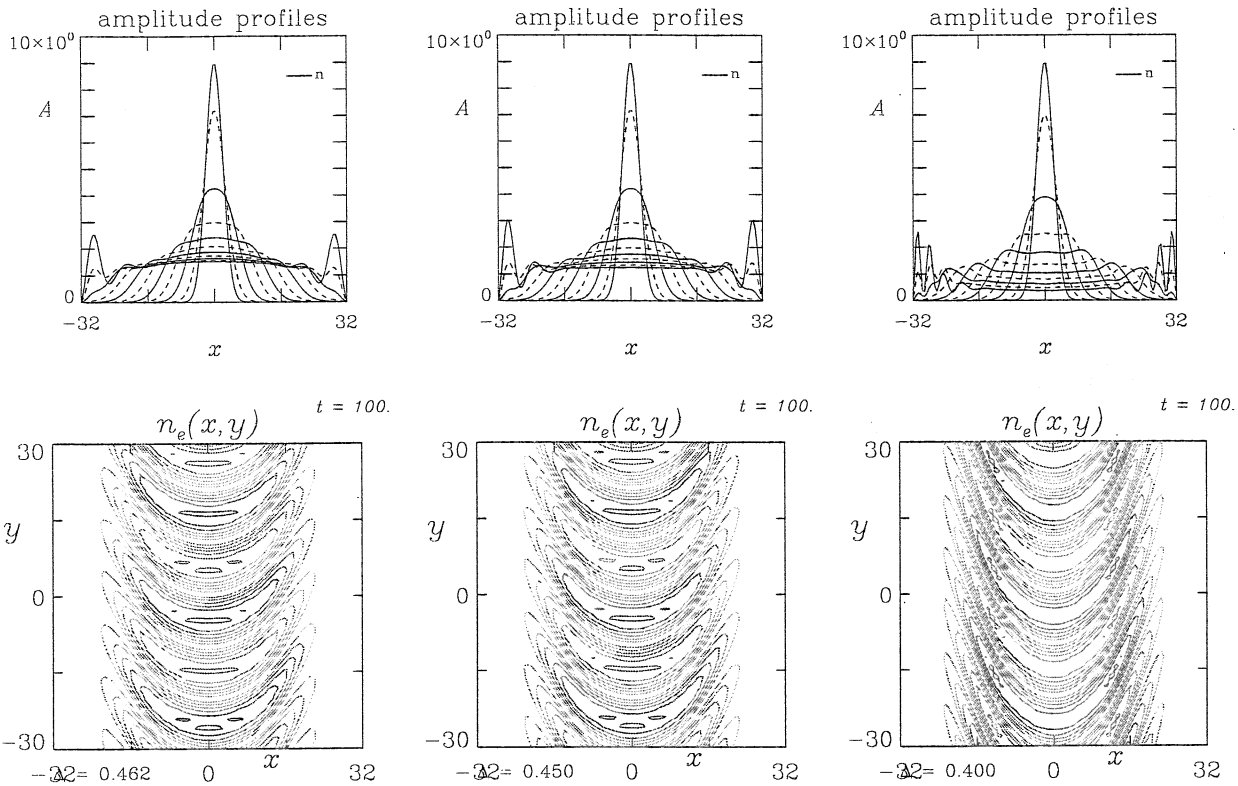

Figure 8.1. (left to right) Spread of adiabatic linear drift waves away from the rational surface, for $L = 0$, 0.01, and 0.03. (top row) pressure/density envelope lines are shown at intervals of $\Delta t = 20$, to $t = 200$. (bottom row) Spatial structure of $\widetilde{p}_e$ at $t = 100$.

(where $k'_{\|} = k_y/L_s$ and the second value is the one in normalised units), the wave energy goes over into sound waves. For a domain of $x_L = 32$ this turnover is only reached before hitting the boundary for the case with $L = 0.1$. It is interesting to note that the actual spreading is not actually due to the sound waves, but to the x-dependence of the effective k_x of the disturbance. Although we did not do this in Chapters 6 and 7, one can verify using the homogeneous dissipative coupling model in the adiabatic limit, and the same domain dimensions and initial state we just used here, that the initial spreading of the disturbances also occurs in that model. However, with a periodic domain in x the disturbances eventually run into each other, and the fastest growing eigenmode has $k_x = 0$. Here, with the unbounded x-domain, the spreading continues indefinitely, and in the computations it is halted only when the disturbances hit the limit $x = \pm x_L$. The spatial manifestation of this is the formation of the meniscus shapes as shown in the bottom row of Fig. 8.1.

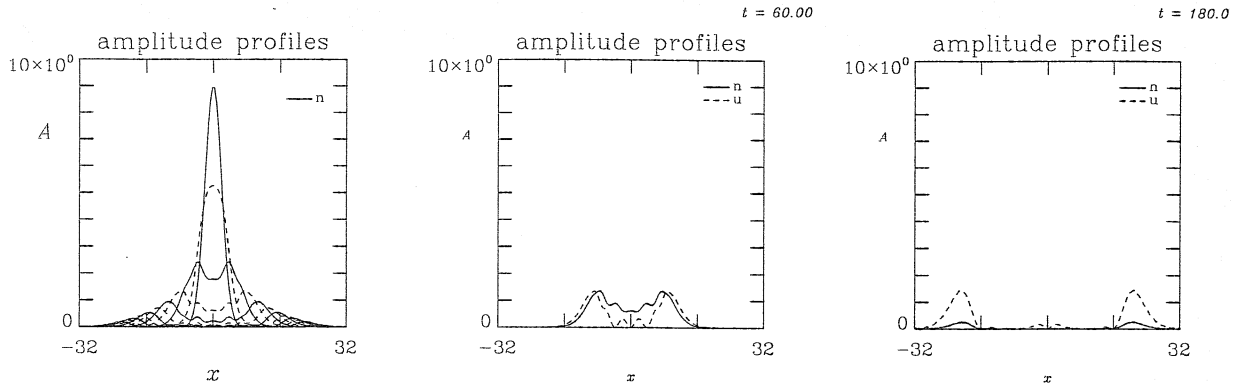

Figure 8.2. (left) Spread of adiabatic linear drift waves away from the rational surface, for $L = 0.1$, as in Fig. 8.1. (center and right) Shown for $t = 60$ and 180, the density ($\widetilde{p}_e$, solid lines) drops and converts into sound waves ($\widetilde{u}_\parallel$, dashed), and the spreading continues.

As the case with $L = 0.1$ shows (Fig. 8.2), however, the resonance with the sound waves does not by itself limit the spreading. The sound waves themselves continue until they either pile up at the computational boundary or they are dissipated. A simple way to do the dissipation is to reintroduce $\mu_\parallel$. We find that if we set $\mu_\parallel = 0.01$ the spreading does not go beyond about $x = \pm 15$. This is then an effective way to contain the dynamics to the part of the possible domain in x actually carried in the computations.

Now allowing the disturbances to be nonadiabatic, and therefore potentially able to tap enough free energy from the background gradient in order to grow, we set $C = 10$ and again take the several values of L. There is a channel centered upon $x = 0$ in which ω_* is larger than either of $k_\parallel c_s$ and $k_\parallel^2 V_e^2/\nu_e$. The width of this layer is given by

$$\Delta_D^2 = \frac{0.51\omega_*\nu_e}{(k_\parallel' V_e)^2} \qquad \rightarrow \qquad \Delta_D = \left(\frac{C}{k_y}\right)^{1/2} \tag{8.25}$$

with the second value the one in normalised units (note we usually have $\Delta_D < x_s$). This is called the hydrodynamic layer, since within it the dissipative coupling is smaller than the wave frequency, and outside of it the electron response becomes adiabatic. The waves tap the free energy well, within this channel, but then they spread to the adiabatic region $|x| > \Delta_D$.

If the waves are disallowed to spread by setting $\mu_\parallel = 0.01$ we find that the cases with $L \leq 0.03$ do not grow. However, for $L \geq 0.1$ a central spike appears in the density disturbance at $x = 0$. The spike is much narrower than Δ_D; in fact, it is typically one

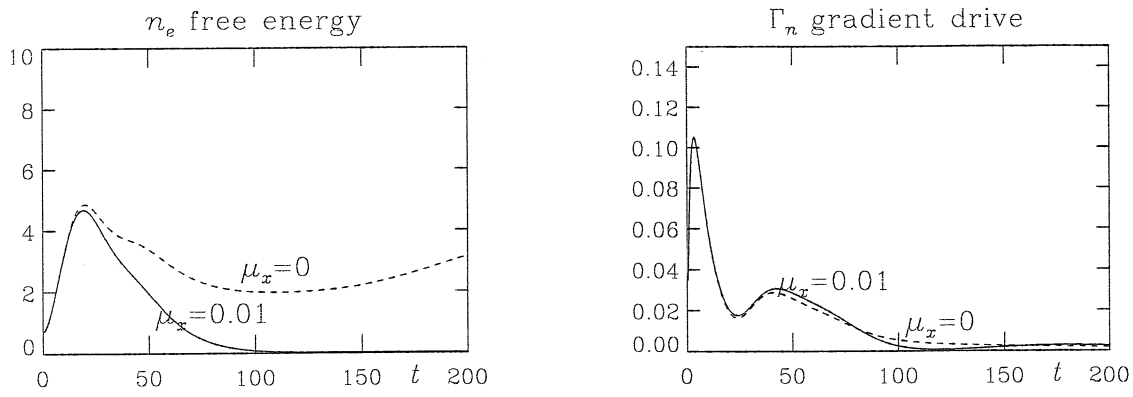

Figure 8.3. The effect of a spurious numerical solution, referred to as the density spike in the text, shown for $L = 0.1$ and $\mu_{||} = 0.01$, in both free energy (left) and drive rate (right). The spike is removed by setting an artificial x-diffusion to $\mu_x = 0.01$ (solid lines).

or two grid points wide. We find by testing with up to 1024 grid nodes in the x-direction that this is nearly independent of the resolution. At late times we have $\widetilde{p}_e \gg \widetilde{\phi}$ arbitrarily, in the spike. Since it goes with the grid resolution and not with some physical scale we judge the spike to be an artifact. A very small amount of dissipation in the x-direction is sufficient to eliminate it; we add a term

$$\frac{\partial \widetilde{p}_e}{\partial t} = \cdots + \mu_x \frac{\partial^2 \widetilde{p}_e}{\partial x^2} \tag{8.26}$$

to the pressure/density equation. At early times, before the spike develops, we find no effect on the initial spreading of the wave energy. After about $t = 100$ however, the spike begins to dominate the density, even though $\widetilde{\phi}$ has largely disappeared. This is shown in Fig. 8.3. The initial rise of the wave energy and its peak are not affected, but the decay of the free energy is, since the spike becomes a significant fraction of the activity after this decay phase sets in. It is interesting to note, however, that the drive rate is largely unaffected.

The effect of the density spike and its elimination can be seen in the spreading of the wave energy away from the rational surface for the case with $L = 0.03$, shown in Fig. 8.4. The snapshots are all at $t = 120$, near the transient peak before the wave energy begins to decay. As also inferred from Fig. 8.3, the energetic effect of the spike is nonnegligible at this time. However, the behaviour of the part of the system not involved in the spike is more strongly affected by $\mu_{||}$, the parallel viscosity. The elimination of the spike by setting $\mu_x = 0.01$ is achieved at the acceptable cost of slightly damping the actual solution, with the effect seen in Fig. 8.3.

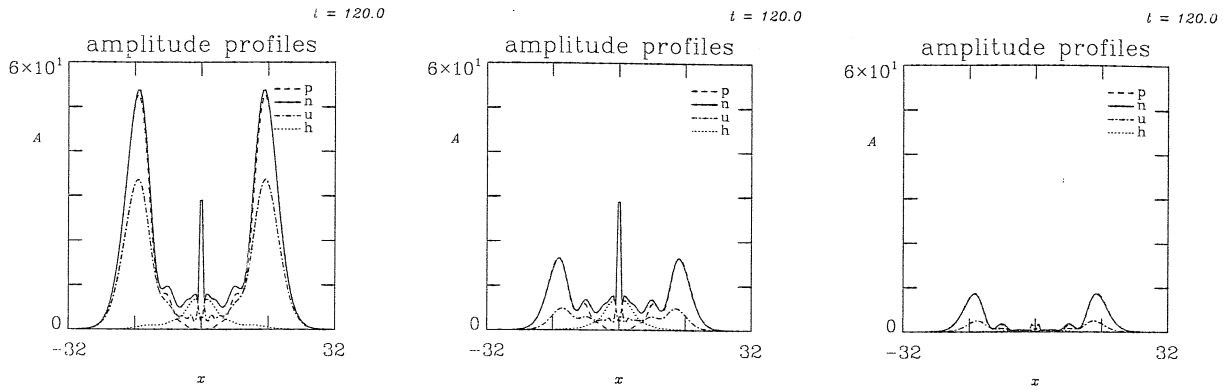

Figure 8.4. Spread of nonadiabatic linear drift waves away from the rational surface, shown for $t = 120$, for $L = 0.03$ with $\mu_\parallel = 0$ (left) and $\mu_\parallel = 0.01$ (center and right). The rightmost frame also has an x-viscosity of $\mu_x = 0.01$, sufficient to eliminate the density spike at $x = 0$. The sound layer width is $x_s = 30$ and the hydrodynamic layer width is $\Delta_D = 5.5$, shown by the mode structure; the labels are 'p' for $\widetilde{\phi}$, 'n' for $\widetilde{p}_e = \widetilde{n}_e$, 'u' for $\widetilde{u}_\parallel$, and 'h' for $\widetilde{h}_e = \widetilde{p}_e - \widetilde{\phi}$. These values of $\mu_\parallel$ and μ_x are sufficient to strongly damp the wave after about $t = 150$.

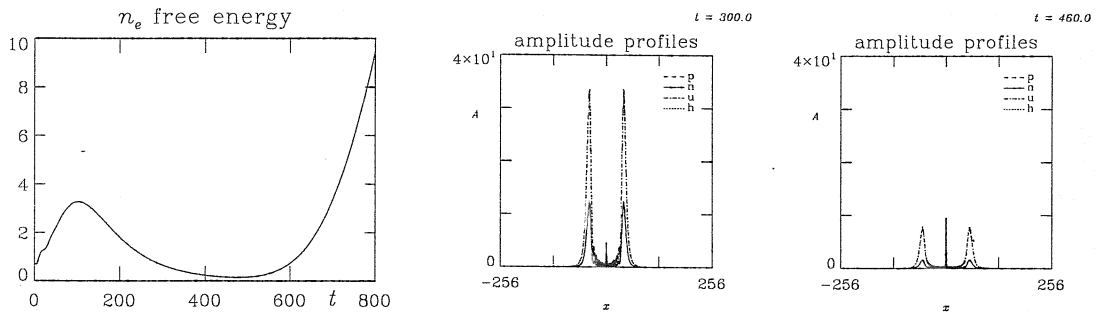

Figure 8.5. (left) Stability of linear drift waves, shown for $L = 0.03$ and $\mu_\parallel = \mu_x = 0$ on a larger grid with $x_L = 256$, in the free energy. (center and right) Snapshots of the disturbances at $t = 300$ and 460, showing the density spike at late times. This is with a different initial state than the cases on the smaller grids.

The issue of drift wave stability is further settled by taking the case with $L = 0.03$ and no dissipation other than the resistivity; the parameters are set to $C = 10$, $\mu_\parallel = \mu_x = 0$, and $k_y = 0.3$. The grid is expanded to 1024 equidistant nodes on a domain with $x_L = 256$, that is, holding the resolution constant. The energetics and two snapshots are shown in

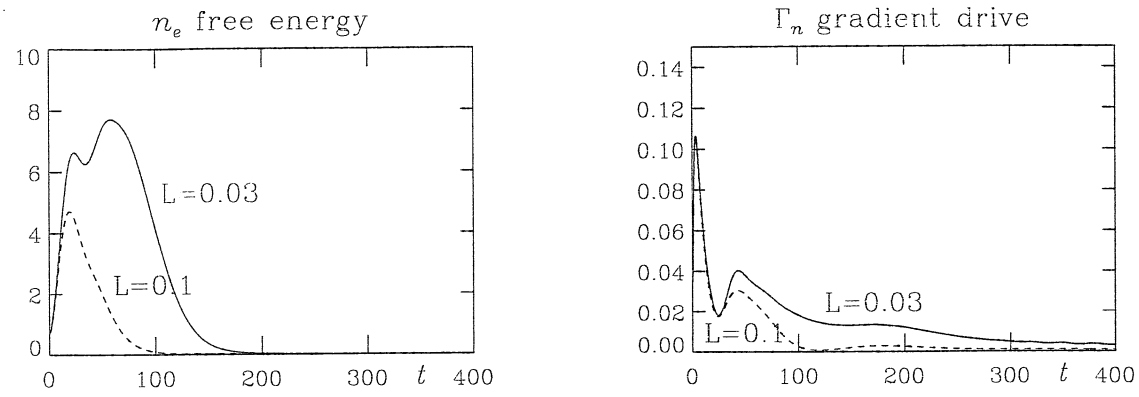

Figure 8.6. Stability of linear drift waves, shown for $L = 0.03$ and 0.1, in both free energy (left) and drive rate (right). With $\mu_{\|} = \mu_x = 0.01$ the damping is strong and the initial disturbances do not persist.

Fig. 8.5. Up to about $t = 450$ all components of the free energy are falling, but even here the density spike becomes noticeable after $t = 300$ and gives a positive growth rate later. Given the properties of the spike — narrowness, no connection from $\widetilde{n}_e$ to $\widetilde{\phi}$, extremely slow emergence — we conclude that it really is spurious and should be eliminated. Returning to the grid with 128 nodes and $x_L = 32$, and setting $\mu_{\|} = \mu_x = 0.01$, we find that the cases with $L = 0.03$ and $L = 0.1$ are definitively stable. We will use the $L = 0.1$ case when looking at the turbulence in the next section.

This has illustrated a very important property of numerical systems when no physically growing eigenmode is present: the grid often contains its own eigenmodes which exist solely due to its discrete nature. Stability computations done by other means also include some form of spurious mode elimination; one uses a semi analytical variational principle to assume a mode of regular structure, or in an eigenvalue computation one will assume a certain symmetry at the rational surface and specify that wave energy should be outgoing at $x = \pm x_L$. In some cases the elimination of spurious modes depends on the form of the grid spacing. Generally, it is important to use all the diagnostics at our disposal when undertaking numerical investigations of such delicate systems as linear drift waves, so as to distinguish physical from spurious effects.

8.V. Turbulence in the Sheared Slab – the Nonlinear Drift Wave Instability

We now reintroduce the nonlinear terms, and address the nonlinear initial value problem. At the initial time, we prescribe the disturbances to be in an adiabatic state, with $\widetilde{u}_{\|}$ and $\widetilde{J}_{\|}$ both zero. The disturbances are given a random phase form as in Chapter 6, with $\widetilde{p}_e = \widetilde{\phi}$. We prescribe the initial amplitude by rescaling such that the average value of $|\widetilde{p}_e|^2$ is given by the parameter A_0. We then run computations with identical physical parameters, but with different initial amplitudes. In this case we choose $C = 10$, $L = 0.1$, $\mu_{\|} = \mu_x = 0.01$, $K = 0.05$, and $x_L = 10\pi$ on a 128×256 grid in $\{x, y\}$, such that the grid cells are square. We choose initial amplitudes $A_0 = 3.0 \times 10^{-8}$, and 3.0×10^{-2}, and 3.0×10^{-1}, and 3.0. The case with $A_0 = 3.0 \times 10^{-8}$ is included to recover the linear stability result with this finite difference computation.

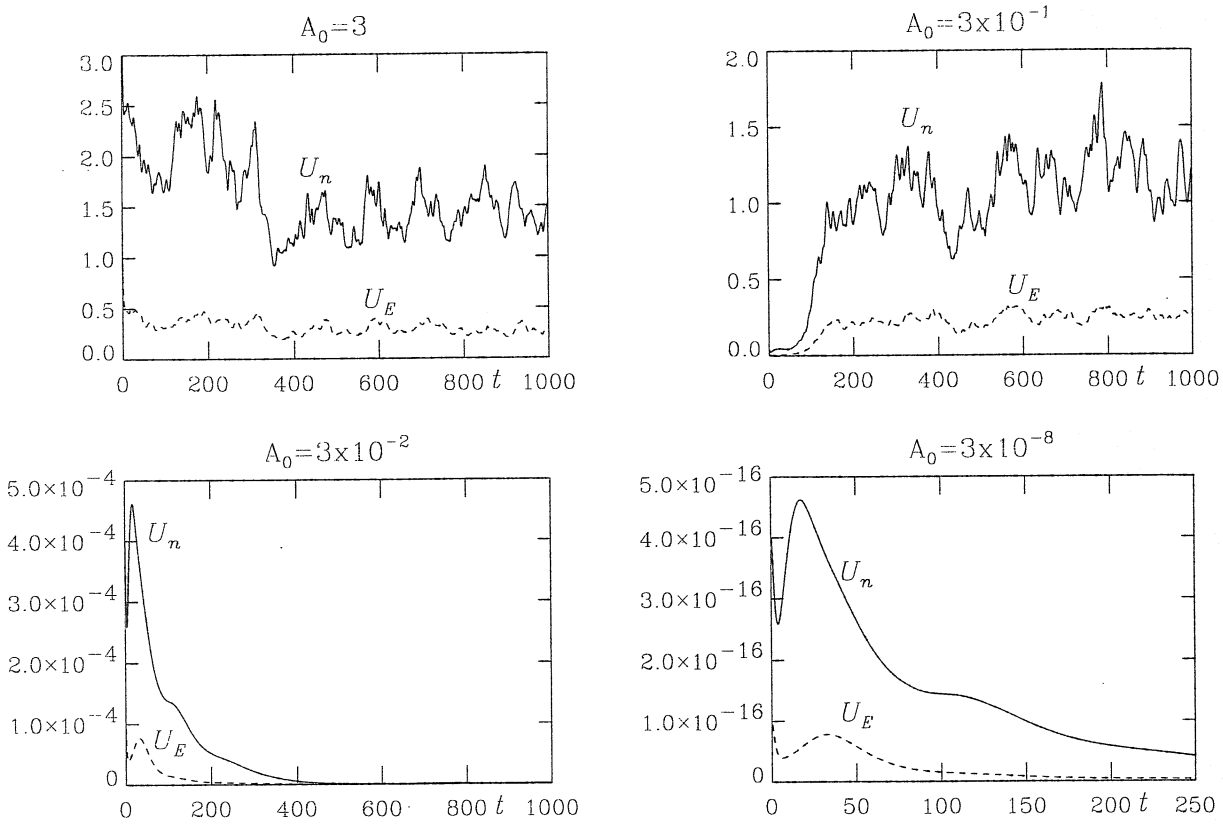

Figure 8.7. The nonlinear drift wave instability, as self sustaining turbulence if the initial disturbance amplitude is high enough for the nonlinear interactions to excite enough nonadiabatic activity to tap the available free energy. Each frame shows the evolution of the free energy components in the pressure/density (U_n) and the ExB eddies (U_E), for the indicated initial amplitude, A_0. The two self sustaining cases eventually find convergence.

The basic fact of a nonlinear instability is what is shown in Fig. 8.7. The four cases with differing initial amplitudes find differing fates. The nonlinear interactions, which scale as the square of the amplitude, are required for the turbulence to maintain itself against the fact that it is linearly stable. We find from the energetics, shown in Fig. 8.8, that the degree of nonadiabaticity is much greater in the self sustaining cases than in those which decay. What the turbulence is doing is opposing the tendency of the current (Eq. 8.12) to dissipate to zero and leaving the disturbances in a more or less adiabatic state. In Eq. 8.13, we find that the only agent which can maintain $\nabla_{\|}^2(\widetilde{p}_e - \widetilde{\phi})$ away from zero is the polarisation drift divergence on the left side, and what this information about the energetics tells us is that the nonlinear vorticity dynamics is much more effective in exciting the nonadiabatic dynamics than is the linear inertial effect of the vorticity. The fact that the energetics is normalised in terms of a dynamical rate makes the diagnostic independent of the amplitude of the disturbances, leaving the conclusion that the average nonadiabaticity has to have grown. The turbulence leads to much more robust activity than linear waves exhibit at the same parameters.

Two things tell us that this is a nonlinear instability. First, we ran the same case which gave no linear instabilities, but with a finite initial amplitude in the presence of nonlinear effects we found fully developed, statistically stationary turbulence. Second, there is a threshold in this initial amplitude level. If the disturbances are too small at $t = 0$, the nonlinearities are too small to affect the linear dynamics, and the disturbances decay. If the initial disturbances are strong enough, however, the turbulence sustains itself. The cause of this must be one of the nonlinearities, and in this case there are only three of them, namely, the ExB advection terms on the three dependent variables. To find out which one is important, we switch them off in turn at $t = 500$ of the saturated state and watch the subsequent evolution. The results for a run with $C = 50$ are shown in Fig. 8.9, which is a sufficient summary. In each frame we have the full system of equations, or all nonlinearities, run from $t = 0$ to 1000. In the leftmost frame, we restart at $t = 500$ leaving out the vorticity nonlinearity only. In the center frame, we restart leaving out all nonlinearities except the vorticity nonlinearity. In the rightmost frame, we restart leaving out all nonlinearities, leaving the linear dynamics with saturated turbulence as its initial state. Not surprisingly, this linear case decays. Interestingly, the case without the vorticity nonlinearity only also decays. Even more interestingly, the case keeping only the vorticity nonlinearity not only does not decay, but grows much more robustly to much higher amplitude. The conclusion is obvious: the nonlinear instability is caused by turbulent ExB advection of the vorticity, and the other nonlinear effects are stabilising. In some other cases the stabilising effect of $\mathbf{v}_E \cdot \nabla \widetilde{p}_e$ is offset by the fact that it still causes

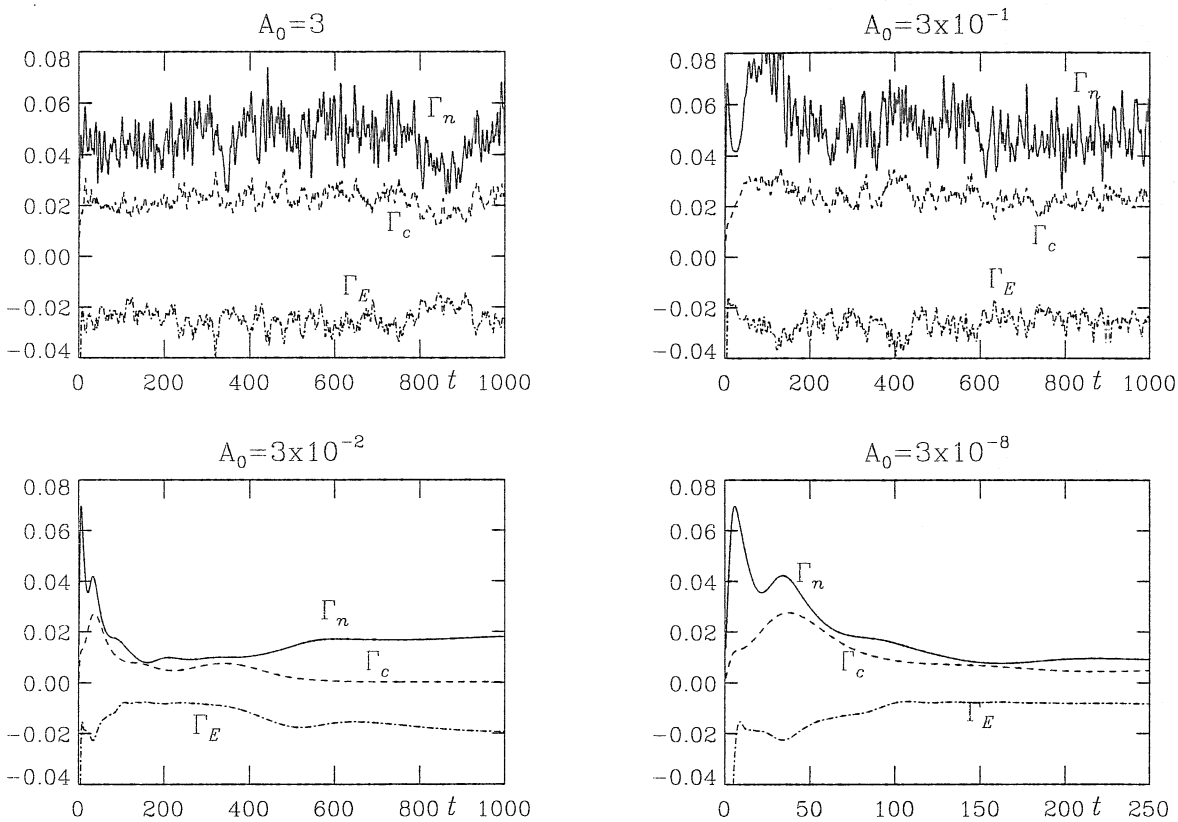

Figure 8.8. Gradient drive (Γ_n), collisional dissipation (Γ_c), and grid dissipation (Γ_E, including the effects of both $\mu_\parallel$ and μ_x) rates for the four cases shown in Fig. 8.7. We find that the collisional dissipation, and therefore nonadiabatic activity in general, is robustly maintained by the turbulence.

vigorous activity in the pressure/density equation, which carries over to the polarisation drift through the linear $\partial/\partial t$ term. Nevertheless, in all cases investigated to date, the vorticity nonlinearity is by far the most destabilising effect.

Nonlinear stabilisation is a familiar effect for linear instabilities: the initially small disturbances grow to finite amplitude, and then the nonlinear effects act as a mixing process, cascading the disturbance free energy to regions of the spectrum where they are damped. For this reason, nonlinear effects are often modelled as an effective diffusion, a procedure which is very familiar in the study of fluid turbulence. The nonlinearities involving the density and the sound waves are of this form: their effect is to cascade energy from each region in the spectrum to the next region roughly a factor of two to higher wavenumbers, as we saw in Chapter 6. Eventually, they reach a dissipation range, and if the numerical spectrum is wide enough it does not matter how far towards high wavenumbers this is.

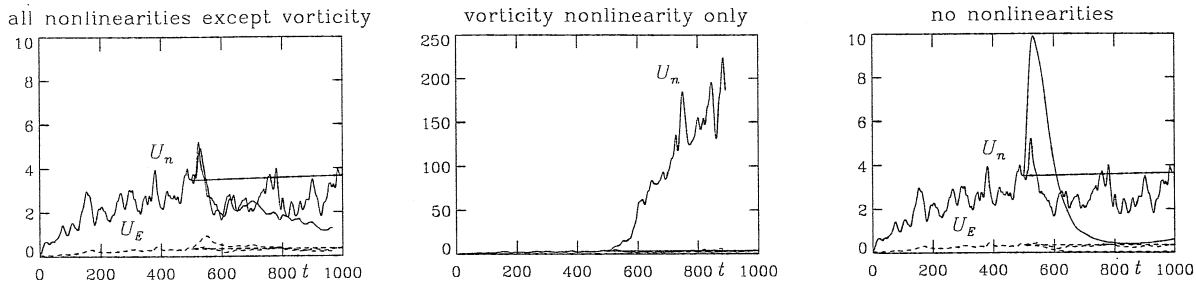

Figure 8.9. Free energy levels for a case with $C = 50$ run to $t = 1000$ and then restarted at $t = 500$ and repeated to $t = 1000$ with various nonlinearities shut off. This shows that the vorticity nonlinearity is the principal agent responsible for the self sustained nature of the turbulence.

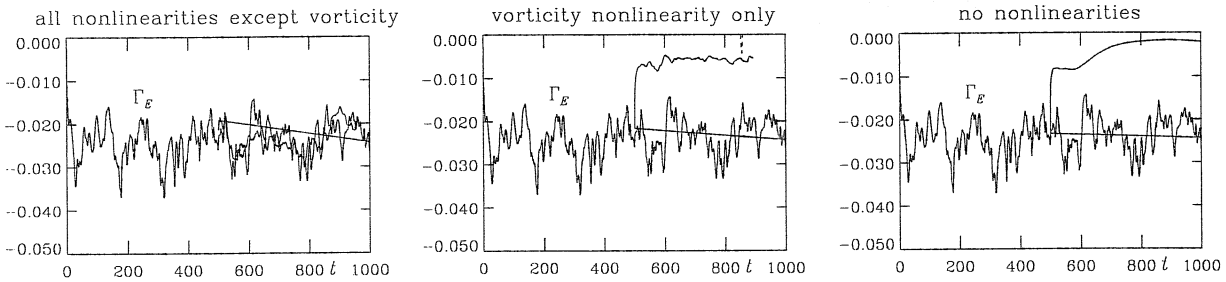

Figure 8.10. Grid dissipation rates for the cases shown in Fig. 8.9. This shows that the pressure/density nonlinearity acts mostly to excite small scale grid dissipation by robustly transferring free energy to high $k_\perp$.

The vorticity nonlinearity clearly has a different character than this. In Fig. 8.10, the numerical dissipation is shown for the cases in the $C = 50$ run of Fig. 8.9. We find that when the pressure/density nonlinearity is left in, most of the dissipation remains, but when it is absent the dissipation drops away suddenly, even when the vorticity nonlinearity is still present. This results from the inverse cascade tendency, which keeps most of the ExB energy away from the dissipation range at high wavenumbers. What the vorticity nonlinearity actually does is simply to scatter the disturbance free energy back and forth, widening the range of available phase shifts, which are necessary for accessing the free energy in the pressure gradient. This test also shows that the grid dissipation is mostly due to high Reynolds number turbulent mixing through $\mathbf{v}_E \cdot \nabla \widetilde{p}_e$ rather than $\mu_\parallel$ or μ_x, because it drops so substantially when the nonlinearity is removed.

We now investigate whether these effects, most easily studied in the two dimensional sheared slab model, carry over to the more realistic three dimensional situation. We immediately encounter the problem of resolution. We have seen that the necessary grid for capturing the nonlinear drift wave instability has of order 10^4 nodes. If we add the third dimension, we would like to have this resolution for each rational surface we have in the computation, not just the single one in the two dimensional model. But there are a great number of rational surfaces. In general, the distance between rational surfaces for each $k_y = 2\pi l/L_y$ is given by the distance between rational surfaces for modes (l, m) and $(l, m \pm 1)$. This distance is given by the shear; we require $k_\parallel(l, m) = 0$ for the rational surface for mode (l, m), with $k_\parallel$ given by Eq. (8.8) and the rational surfaces defined by Eq. (8.9). For modes $m = 0$ and $m = \pm 1$ these locations are found at $x = 0$ and $x = \pm(L_s/L_\parallel)(L_y/l)$, respectively. With $k_y = l/L_y$ we have the spacing between rational surfaces for each k_y,

$$\Delta_{rs} = \frac{1}{\hat{s}k_y} \tag{8.27}$$

where $\hat{s}$ is the shear parameter given by

$$\hat{s} = \frac{L_\parallel}{L_s} \tag{8.28}$$

With typical values in a sheared magnetic field of $\hat{s} = O(1)$, we have the spacing as $1/k_y$ for each k_y.

This gives rise to the three dimensional resolution problem, since we must resolve rational surfaces not only for k_y close to K, but also for $k_y \sim 1$, that is, physical wavenumbers close to the inverse of ρ_s. Their spacing is in turn of order ρ_s, so in a computation with a domain size of order $10^2\rho_s$, we will have of order 10^2 rational surfaces for each k_y, and with of order 10^2 k_y-modes we therefore have of order 10^6 grid nodes, actually closer to 10^7 if we follow the fact that the grid in m-space would have to be the largest in order to resolve the range of modes resonant near each boundary.

The only remedy for this problem is to align the coordinates to the magnetic field, not at only one flux surface, but everywhere. The resolution problem is caused by the fact that the parallel gradient involves two coordinates, since two contravariant components of $\mathbf{B}$ are nonzero. What we need is a coordinate transformation which removes this problem by leaving only one nonzero $B^\mu = \mathbf{B} \cdot \nabla x^\mu$ among the $x^\mu \in \{x, y, s\}$. The simplest transformation which does this is

$$y_k = y + \hat{s}x(s - s_k) \qquad\qquad y = y_k - \hat{s}x(s - s_k) \tag{8.29}$$

where the back transformation is also given, and x and s remain unchanged. The quantity s_k is a constant which sets the reference point of the transform to a given location in s. The meaning of this reference point is that the transformed coordinate cells are square only at the reference point; the field aligned coordinate system is generally nonorthogonal because of the shear. The inverse metric coefficients for the untransformed coordinate system are given by

$$g^{xx} = 1 \qquad g^{yy} = 1 \qquad g^{ss} = 1 \qquad \text{others} = 0 \tag{8.30}$$

For the field aligned system they are given by

$$g^{xx} = 1 \qquad g_k^{xy} = \hat{s}(s - s_k) \qquad g^{yy} = 1 + \hat{s}^2(s - s_k)^2 + \hat{s}^2 x^2 \tag{8.31}$$

$$g^{xs} = 0 \qquad g_k^{ys} = \hat{s}x \qquad g^{ss} = 1 \tag{8.32}$$

We evaluate these at $x = 0$ due to the drift ordering, leaving

$$g^{xx} = 1 \qquad g_k^{xy} = \hat{s}(s - s_k) \qquad g^{yy} = 1 + \hat{s}^2(s - s_k)^2 \qquad g^{ss} = 1 \qquad \text{others} = 0 \tag{8.33}$$

The element g^{xy} tells us that the coordinate cells are indeed square only at $s = s_k$. The usefulness of this is that each member of this family of transformations is equivalent in the sense that it covers the whole space. So we can use the one referenced at a given location in s for evaluation of the perpendicular drift dynamics, keeping care when taking parallel derivatives to include the shift in y introduced by the fact that for two members of the family of transformations, the s_k values, and hence the y_k-coordinate reference, are different.

One can verify that this coordinate system is indeed aligned by finding the contravariant components of $\mathbf{B}$:

$$B^x = 0 \qquad B_k^y = 0 \qquad B_s = B_0 \tag{8.34}$$

Due to the fact that only one of the B^μ is nonvanishing, the parallel gradient involves only that coordinate:

$$\mathbf{B} \cdot \nabla f = B^\mu \frac{\partial f}{\partial x^\mu} = B^s \frac{\partial f}{\partial s} \tag{8.35}$$

The flute mode condition of drift ordering shows that derivatives with respect to s are small, since

$$\nabla_\parallel^2 = B^{-2}(\mathbf{B} \cdot \nabla)^2 = \frac{\partial^2}{\partial s^2} \qquad \nabla_\perp^2 = g^{xx}\frac{\partial^2}{\partial x^2} + 2g^{xy}\frac{\partial^2}{\partial x \partial y} + g^{yy}\frac{\partial^2}{\partial y^2} \tag{8.36}$$

While the multiplicative factors are all of order unity, the condition that $k_\parallel \ll k_\perp$ results in the fact that

$$\frac{\partial}{\partial s} \ll \frac{\partial}{\partial x} \sim \frac{\partial}{\partial y} \tag{8.37}$$

We are back to the plan which led to the two dimensional model, and have succeeded in generalising it to three dimensions, adding additional nodes in the third dimension only to the extent that we need a small range of $k_{||}$ values at each location in x, for each k_y.

This transformation affects the boundary conditions. Although the flux surface itself is still physically periodic in both y and s, the fact that we have replaced y with y_k means that perfect periodicity in s is lost. In the untransformed coordinate system we have

$$f(x, y + L_y, s) = f(x, y, s) \qquad f(x, y, s + L_{||}) = f(x, y, s) \tag{8.38}$$

for periodicity in the y and s-directions, respectively. To express these conditions in the field aligned coordinate system we merely apply the transformation in Eq. (8.29) to them, obtaining

$$f(x, y_k + L_y, s) = f(x, y_k, s) \qquad f(x, y_k + 2\pi\hat{s}x, s + L_{||}) = f(x, y_k, s) \tag{8.39}$$

Periodicity in y is maintained, since the differing meanings of y and y_k appear only when we vary s. The other condition, though, becomes one of what we can call pseudo-periodicity, since when we apply the Fourier decomposition in y_k (allowed because we still have periodicity in y), we obtain a phase shifted periodicity in s:

$$f(x, k_y, s + L_{||}) = f(x, k_y, s)e^{-2\pi i\hat{s}k_y x} \tag{8.40}$$

which we obtain by multiplying Eq. 8.39 by $\exp(-ik_y y)$ and integrating over y (taking care not to confuse y_k, the k-th member of the family of field aligning transformations, with the drift direction wavenumber k_y). The phase factor in Eq. (8.40) shows where the rational surfaces are: the locations where $\hat{s}k_y x$ is an integer. On these rational surfaces we have true periodicity in s as well as y, and so $k_{||}$ can vanish even for finite k_y. Elsewhere, however, $k_{||}$ cannot vanish for finite k_y, and so we have the conclusion that $k_{||}$ is in general finite on closed magnetic surfaces. This recovers the important property of shear and periodicity, once more, by which $k_{||}$ is in general finite on topologically toroidal surfaces when there is magnetic shear. This property is why we get drift wave dynamics.

The shifting transformation implied by a nonzero s_k in Eq. (8.29) affects the boundary conditions and the parallel derivatives. All of the above equations hold, but we want to express them for differing members of the family of transforms for different locations in s. At $s = s_1$ we use $s_k = s_1$, while at $s = s_2$ we use $s_k = s_2$. In general, the k value will track the s-node being used, and parallel derivatives and the parallel boundary conditions involve differing s-nodes. The parallel derivative for a given s_k is given by

$$2h_s \frac{\partial f}{\partial s}(x, y_k, s_k) = f(x, y_k, s_k + h_s) - f(x, y_k, s_k - h_s) \tag{8.41}$$

where h_s is the node spacing in s. Setting $s_{k\pm1} - s_k = h_s$, we reexpress this derivative such that each location in s uses the field aligned transform referenced there,

$$2h_s \frac{\partial f}{\partial s}(x, y_k, s_k) = f(x, y_{k+1} - \Delta^+, s_{k+1}) - f(x, y_{k-1} - \Delta^-, s_{k-1}) \tag{8.42}$$

with the shifts given by

$$\Delta^\pm = \pm \hat{s} x h_s \tag{8.43}$$

This is merely a matter of taking the shift implied in Eq. (8.40) over an entire periodicity length $L_\parallel$, and distributing it among all the s-nodes. The parallel boundary condition becomes

$$f(x, y_{k+N}, s_{k+N}) = f(x, y_k, s_k) \tag{8.44}$$

where N is the number of s-nodes, and therefore $s_{k+N} - s_k$ is $L_\parallel$. Each location along a field line is now treated numerically equivalently, which is in order with the property of the slab geometry that all locations along the field line are equivalent. For more details of the numerical treatment which also evaluates quantities in between the grid nodes, and the special requirements when a periodic domain is used in x, see Appendix B, Sections A and B.

8.VII. The Nonlinear Drift Wave Instability in Three Dimensions

We use this coordinate treatment to address this three dimensional sheared slab drift wave turbulence under the four field model. Following from the two dimensional model we have just used, we expand to the three dimensional model at the same parameters for one set of the cases to make a comparison possible, and then expand further to allow for a finite electromagnetic response. The four field model in slab geometry appears as

$$\frac{d_E}{dt} \nabla_\perp^2 \widetilde{\phi} = \nabla_\parallel \widetilde{J}_\parallel \tag{8.45}$$

$$\frac{d_E \widetilde{p}_e}{dt} = -\frac{\partial \widetilde{\phi}}{\partial y} + \nabla_\parallel \widetilde{J}_\parallel - \nabla_\parallel \widetilde{u}_\parallel \tag{8.46}$$

$$\hat{\beta} \frac{\partial \widetilde{A}_\parallel}{\partial t} + \hat{\mu} \frac{d_E \widetilde{u}_\parallel}{dt} = \nabla_\parallel \left(\widetilde{p}_e - \widetilde{\phi} \right) - C \widetilde{J}_\parallel - \hat{\beta} \frac{\partial \widetilde{A}_\parallel}{\partial y} \tag{8.47}$$

$$\hat{\epsilon} \frac{d_E \widetilde{u}_\parallel}{dt} = -\nabla_\parallel \widetilde{p}_e + \mu_\parallel \nabla_\parallel^2 \widetilde{u}_\parallel + \hat{\beta} \frac{\partial \widetilde{A}_\parallel}{\partial y} \tag{8.48}$$

where $\widetilde{J}_\parallel$ and $\widetilde{A}_\parallel$ are related through Ampere's law,

$$\widetilde{J}_\parallel = -\nabla_\perp^2 \widetilde{A}_\parallel \tag{8.49}$$

The numerical scheme is detailed in Appendix A. The three dimensional model uses the same normalisation convention we developed in Chapter 5. We note that $\hat{\epsilon}$ means the same thing as L^{-2}, and that $\widetilde{u}_{\|}$ appears in the energy theorem for these equations as $\hat{\epsilon}\widetilde{u}_{\|}^2/2$ rather than $\widetilde{u}_{\|}^2/2$. We recover the dissipative electrostatic model by setting $\hat{\beta} = \hat{\mu} = 0$, but the three dimensional numerics does not allow that. For the electrostatic limit it is sufficient to reduce to $\hat{\beta} = \hat{\mu} = 0.03$. By contrast to the two dimensional model we keep the $k_y = 0$ component, as it is important to show the nonlinear instability survives in this more realistic case. In the two dimensional model it was merely necessary to examine the physical effects; here, we have to prove existence.

The first set of cases we look at is the electromagnetic model, with $\hat{\beta} = \hat{\mu} = 1$ and $C = 1$. This is a low collisionality case with a finite time dependence in the adiabatic response. The same coupling to sound waves is kept by setting $\hat{\epsilon} = 100$. We set the shear parameter to $\hat{s} = 1$. The first thing we encounter is another numerical problem with linear modes, and this time it is an easily identifiable problem with the computational grid. The parallel boundary condition in Eq. (8.40) is what does field line connection in this model, and it prescribes a phase shift each Fourier component must have at displacements of one connection length. The distance between neighboring rational surfaces is given by $1/k_y\hat{s}$. If the computational grid is square, then the highest k_y is π/h_x. The distance to the next rational surface for this mode is $h_x/\pi\hat{s}$, which is less than h_x itself! In fact, since for periodic boundaries in x we have the condition that the x-domain size must be an integral multiple of the distance between *main* rational surfaces (cf. Section A of Appendix B), it follows that there is a mode for which the grid spacing h_x is an integral number of the rational surface spacing for some small scale k_y mode. Generally, for an isotropic grid with $h_x = h_y$, the mode whose wavelength is Nh_y will be equally resonant on every grid node, for $\hat{s} = N/2\pi$. In order to avoid this we acquire another resolution problem, namely, that for $\hat{s} = 1$ we require that h_y/h_x be at least about 8 in order to avoid these grid modes, whose consequence is rapid growth of small scale clutter representing modes which do not feel the field line connection effect. We will not do this for every run, but it is important to do it once to show that the grid mode problem really can be avoided. Unlike the two dimensional model above, it was not possible to solve this problem by applying a viscosity, for reasonable viscosity levels. It is important to note that the turbulence turns out to be insensitive to these grid modes, since they are coherent structures with no or almost no s-dependence and as such are destroyed by the turbulence faster than they can grow.

Two runs are compared, and as in the previous cases they differ only in the initial amplitude. The initial state is the same as before, equal on every drift plane except for a random variation of the amplitude between 0.9 and 1.1 times the nominal level, sufficient

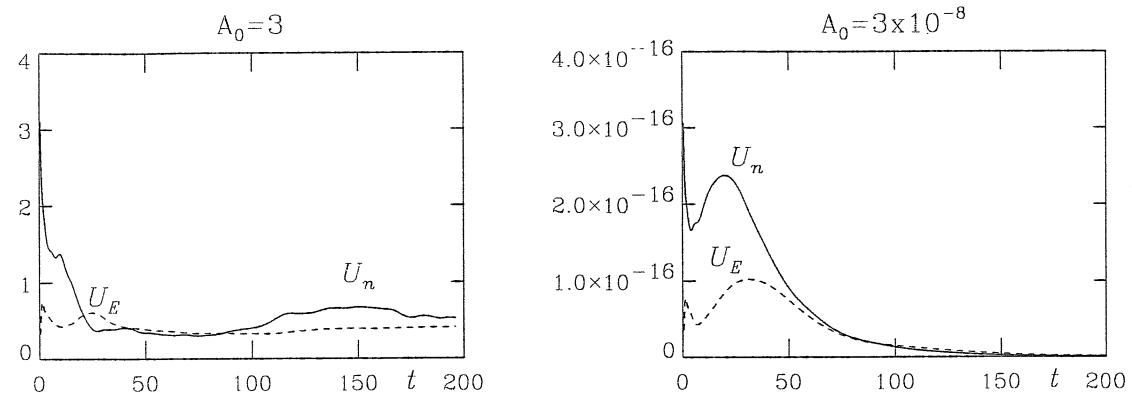

Figure 8.11. Free energy levels for two cases with different initial amplitudes, showing the nonlinear instability in the three dimensional model. Parameters $\hat{\beta}$, $\hat{\mu}$, C, and $\hat{s}$ were all unity. Labelling is as in Fig. 8.7.

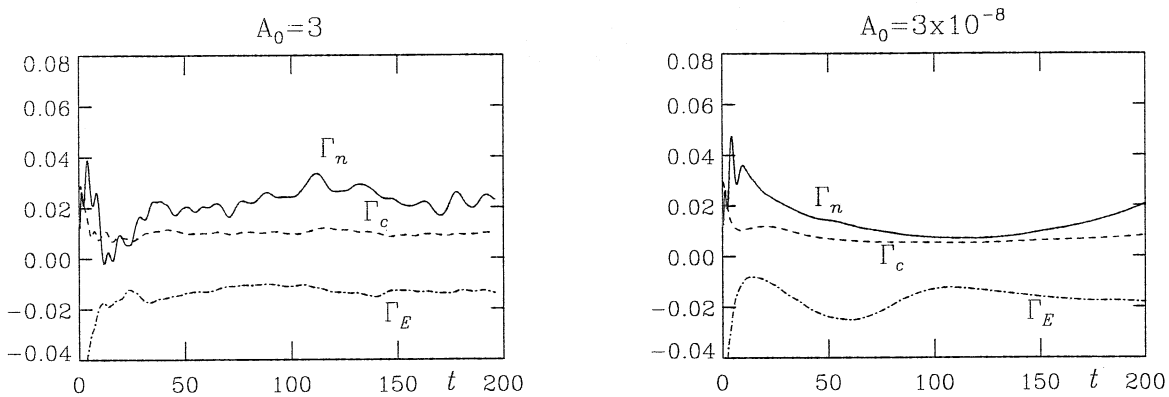

Figure 8.12. Gradient drive (Γ_n), collisional dissipation (Γ_c), and grid dissipation (Γ_E) rates for the four cases shown in Fig. 8.11. We find that the collisional dissipation, and therefore nonadiabatic activity in general, is robustly maintained by the turbulence, although the differences are less pronounced at this low collisionality. Labelling is as in Fig. 8.8.

along with the shear to excite the Alfvénic dynamics (the shifting in the grid represented by the various y_k at each s_k guarantees a strong initial adiabatic response). For one case, termed linear, the nominal level was $A_0 = 3 \times 10^{-8}$, and for the other, nonlinear case it was $A_0 = 3$. Time traces of the free energy are shown in Fig. 8.11. This first result is the stable, damped nature of the disturbances in the linear case, and the basic existence of the nonlinear instability for the nonlinear case. The runs were taken to $t = 200$ to ensure that the results are not simply initial transients. These two cases are sufficient to demonstrate

the nonlinear instability for the three dimensional model including the $k_y = 0$ component; in other words, realistic dynamics.

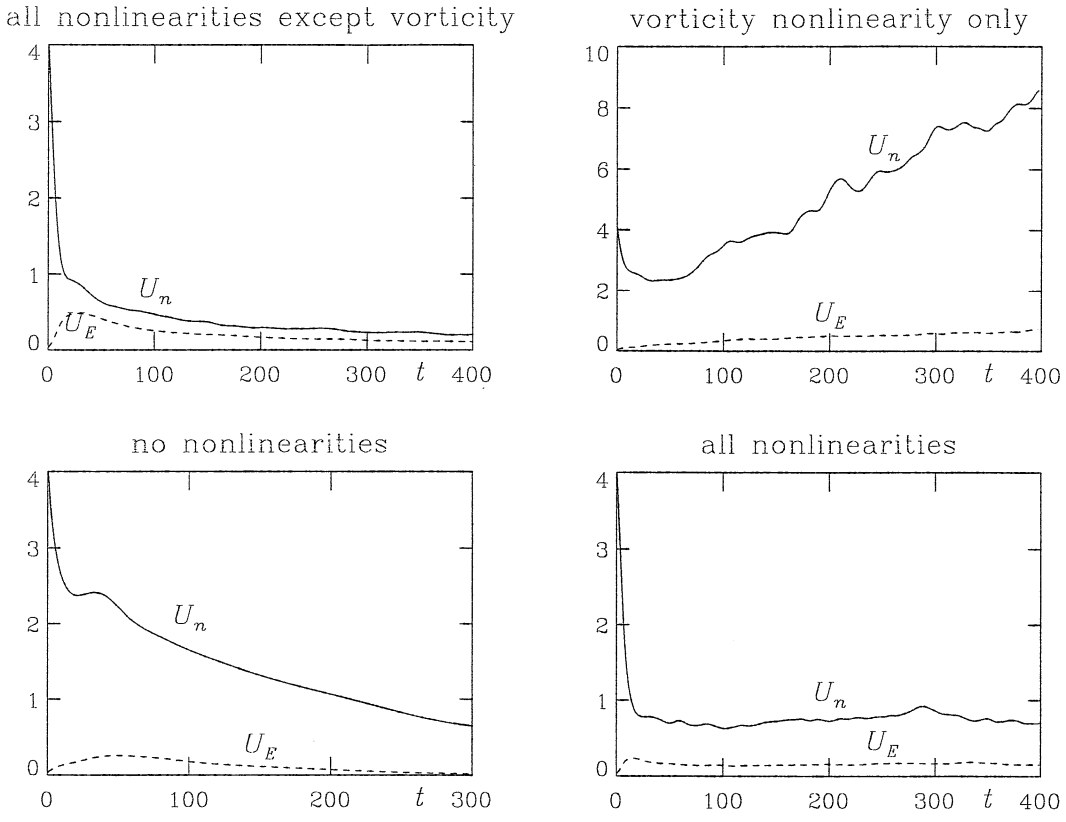

Figure 8.13. Free energy levels for an electrostatic case with $C = 3$, with all terms present and with various nonlinearities shut off. In three dimensions as well as two, the vorticity nonlinearity is the principal agent responsible for the self sustained nature of the turbulence.

The next set of cases we look at is the electrostatic model, with $\hat{\beta} = \hat{\mu} = 0.03$ and $C = 3$. The resolution ratio h_y/h_x was only 4, leading to a mild grid mode at the end of the spectrum for linear cases; this grid mode was nevertheless eliminated by the turbulence. The initial state is the same as for the nonlinear electromagnetic case, and here we compare runs with all terms present to those with some or all of the nonlinearities shut off, as we did for the two dimensional case. The resulting time traces, shown in Fig. 8.13, reflect the same conclusion we had before. The cases with no vorticity nonlinearity damp, the case with all nonlinearities saturates, and the case with the vorticity nonlinearity by itself grows to much higher amplitude. In Fig. 8.14, the grid dissipation rates are shown for these cases. The separation between the cases with and without the pressure/density nonlinearity is

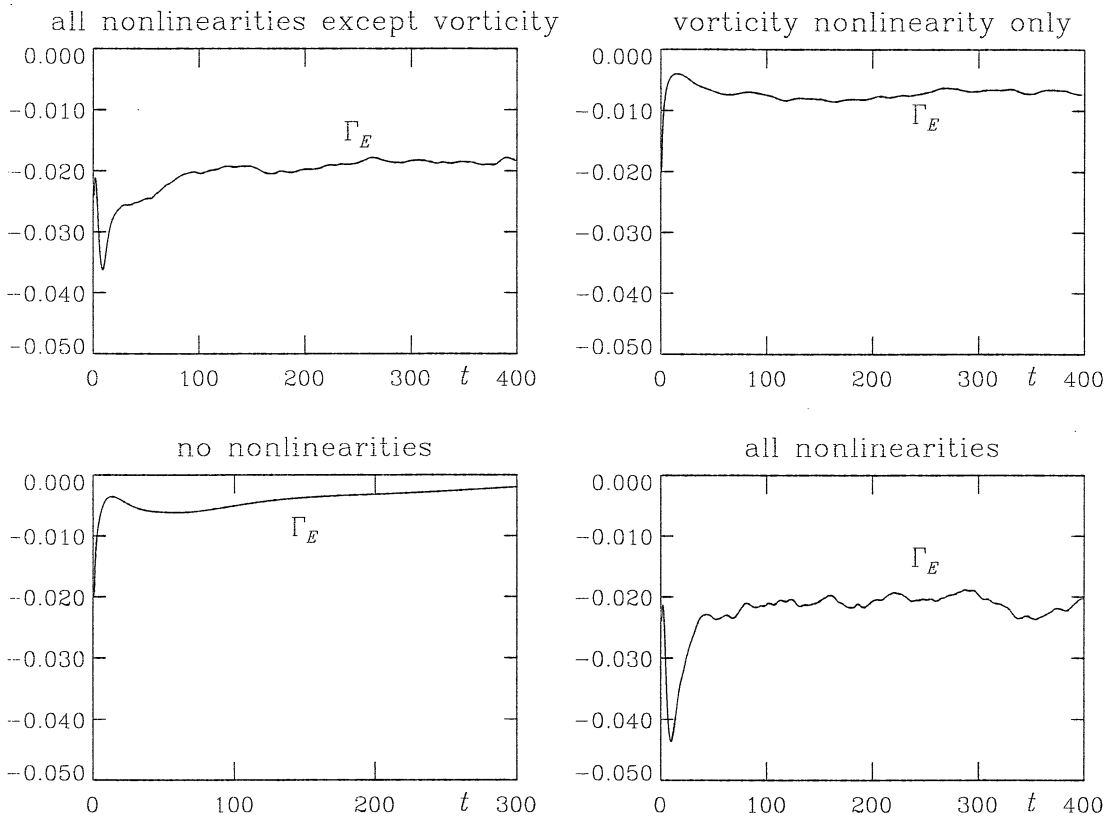

Figure 8.14. Grid dissipation rates for the cases shown in Fig. 8.13. In three dimensions as well as two, the pressure/density nonlinearity acts mostly to excite small scale grid dissipation by robustly transferring free energy to high $k_\perp$.

clear, showing that the direct cascade of free energy through $\mathbf{v}_E \cdot \nabla \widetilde{p}_e$ remains important in saturating drift wave turbulence. Taken together, these tests show that the physics of self sustained drift wave turbulence as a nonlinear instability is the same in both the two and three dimensional slab models. The reason is that the competition between perpendicular and parallel dynamics is present in both models. While the parallel coordinate is missing in the two dimensional model, the ability of the parallel gradient to wax and wane according to how much it is excited by the turbulence is still present, due to the ability of the nonadiabatic part of the turbulence to increase or decrease its average domain widths in the x-direction (cf. Eq. 8.18).

Taking these results concerning how the vorticity nonlinearity excites the turbulence generally, we examine some details in the mode structure which show how it acts. We take the four cases shown in Figs. 8.13 and 8.14, and plot the spectra of the mean squared vorticity nonlinearity and the mean squared parallel current divergence, $\mathbf{v}_E \cdot \nabla \nabla_\perp^2 \widetilde{\phi}$ and

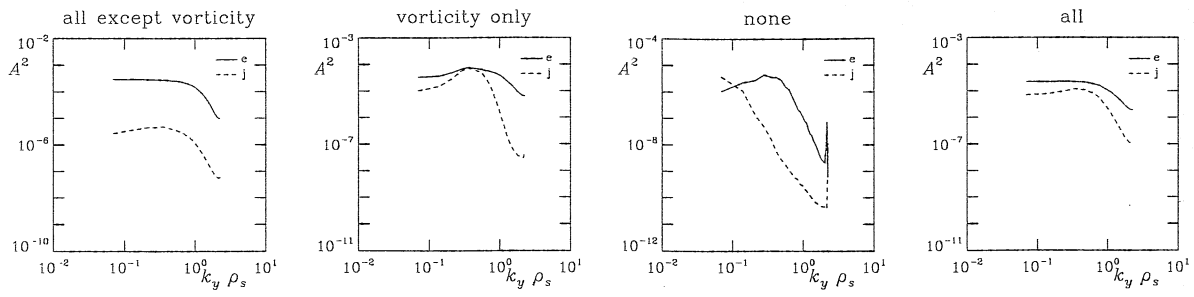

Figure 8.15. Dynamical spectra for the ExB vorticity, for the cases shown in Fig. 8.13. The solid and dashed curves show the average sizes of $\mathbf{v}_E \cdot \nabla \nabla_\perp^2 \widetilde{\phi}$ and $\nabla_\parallel \widetilde{J}_\parallel$ for all k_y, respectively. Note that in the two cases which do not contain the vorticity nonlinearity (first and third form left), the solid curve shows how strong this would be if it were switched back on. Small scale nonadiabatic activity ($\nabla_\parallel \widetilde{J}_\parallel$) is robustly excited by the vorticity nonlinearity but is weak without it. The nonadiabatic activity is strongest when so excited but in the absence of the pressure/density nonlinearity. This further highlights the vorticity nonlinearity as the basic catalytic effect for drift wave turbulence, exciting nonadiabaticity in general so that the portion with larger phase shifts can be more strongly driven. The high-k_y spike in the linear case is the grid mode, which in the other cases is eliminated by the turbulence.

$\nabla_\parallel \widetilde{J}_\parallel$, respectively. It is important to take the mean squared values and not the averages, since we are looking at a process whose role is to keep $\nabla_\parallel \widetilde{J}_\parallel$ from vanishing, not to keep it at a particular value. This opens up the range of accessible states with nonadiabatic electrons, namely, larger possible values of $\nabla_\parallel \widetilde{J}_\parallel$. Taking the spectra for the case with all terms as a benchmark, we find that the linear dynamics acting by itself (no nonlinearities) produces very weak nonadiabaticity, especially at medium to high k_y. The vorticity nonlinearity produces very strong nonadiabaticity, as the removal of $\mathbf{v}_E \cdot \nabla \widetilde{p}_e$ and $\mathbf{v}_E \cdot \nabla \widetilde{u}_\parallel$ leads to less direct cascading of the pressure/density — and we recall that only the nonadiabatic part contributes to the nonlinearity, since $\mathbf{v}_E \cdot \nabla \widetilde{\phi}$ vanishes. The case with all nonlinearities except $\mathbf{v}_E \cdot \nabla \nabla_\perp^2 \widetilde{\phi}$ still shows a flat spectrum for the nonadiabaticity, but it is much smaller than in either of the other two nonlinear cases. Indeed, whatever nonadiabaticity is left in the linear case results solely from the linear time derivative of the vorticity. These are the nonlinear and linear polarisation current effects, and the whole of this has shown that the nonlinear polarisation current is very much stronger than its linear counterpart in producing electron nonadiabaticity. This is why we have a nonlinear instability.

The vorticity nonlinearity has a special structure, due to the fact that it has the inverse cascade tendency. The nonlinear term is much larger relative to the linear term, compared

to the same relation in the other equations. This is due to the extra factors of $k_\perp$ in this term and its transfer effects (cf. Chapter 6). The two beat waves driving a particular $k_\perp$ in three wave coupling triplets with $\mathbf{k}+\mathbf{k}'+\mathbf{k}''=0$ tend to come from higher $k'_\perp$ rather than lower, and this gives larger than usual factors of $k'_\perp$ and $k''_\perp$ in comparison to the three wave interactions in the other nonlinearities, as well as two additional factors of either $k'_\perp$ or $k''_\perp$. This extra large nonlinear effect arises precisely where it is needed to expand the set of accessible nonadiabatic states, whether larger $k_\parallel^2$ for a given $\widetilde{h}_e$ or a larger $\widetilde{h}_e$ for a given $k_\parallel^2$. With larger $\widetilde{h}_e$ possible, there is more gradient drive (Γ_n), and with larger $k_\parallel^2$ there is more dissipation (Γ_c). Both changes occur in turbulence in this fashion, in contrast to the linear waves. As a result, the central features of drift wave turbulence are something one cannot tell from linear drift wave analysis.

8.VIII. Magnetic Shear and Drift Wave Mode Structure

The mode structure of nonlinear drift wave turbulence is similar in both two dimensional homogeneous and slab models, and it is similar still in three dimensional turbulence. This is because the basic role of dissipative coupling between the two state variables is present in all three models (recall once more how all three are set up such that $\nabla_\parallel$ cannot vanish for finite k_y). We here list the important features of three dimensional drift wave mode structure, noting the comparisons to and contrasts against the contents of Chapter 7.

The case from which these measurements come is one with robust, electromagnetic turbulence, with parameters $\hat{\beta}=1$, $\hat{\mu}=5$, $C=25$, $\hat{\epsilon}=1835$, $\hat{s}=1$, and $K=0.025$, on a $32\times 128\times 16$ grid in $\{x,y,s\}$, with time step 0.05. The domain was periodic in x on an interval of $-40<x<40$, twice the main rational surface spacing. The case was run very long, to $t=5000$, and averages were taken over the last $\Delta t=1000$. The transport was $Q_e=0.58$. The spectra of the amplitudes and energetics are shown in Fig. 8.16, where we find the same properties as before: $\widetilde{\phi}$ and $\widetilde{n}_e$ track each other especially at low k_y and then diverge, with $\widetilde{n}_e$ larger at higher k_y. The vorticity has the flattest spectrum. The cross coherence is shown in Fig. 8.17, which indicates the strong coupling we saw before. The density and potential are well correlated, and the phase shift distributions are narrow and closer to zero than to $\pi/2$. The amplitude probability distributions show the same near-Gaussian form as in Chapter 7, and are not repeated here. The spatial form of the disturbances in shown in Fig. 8.18, and here we see something new, the strong presence of $k_y=0$ ExB flow layers. These are sheared, since $\widetilde{v}_E^y=\partial\widetilde{\phi}/\partial x$, and this results in the deformation of the disturbances. The vorticity (labelled as Ω) is still dominated by the

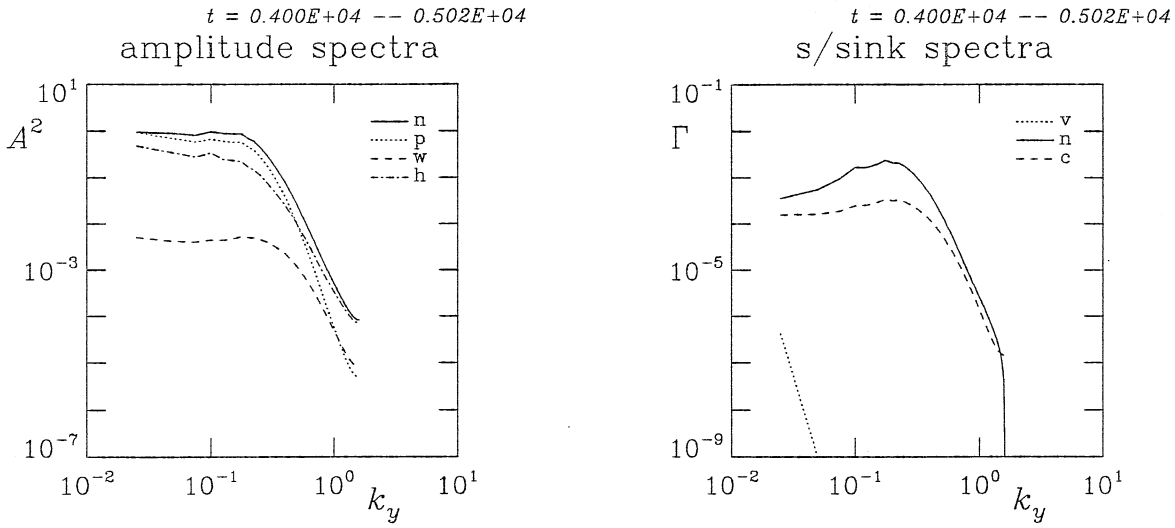

Figure 8.16. (left) Amplitude spectra of $\widetilde{n}_e$, $\widetilde{\phi}$, $\nabla_\perp^2\widetilde{\phi}$, and $\widetilde{h}_e$, respectively labelled by 'n', 'p', 'w', and 'h'. (right) Spectra of the ExB gradient drive ('n'), dissipation ('c'), and the magnetic flutter drive ('v'). The latter is always small for drift wave turbulence. These quantities are averaged over time and the x and s-directions. Compare with Fig. 7.2.

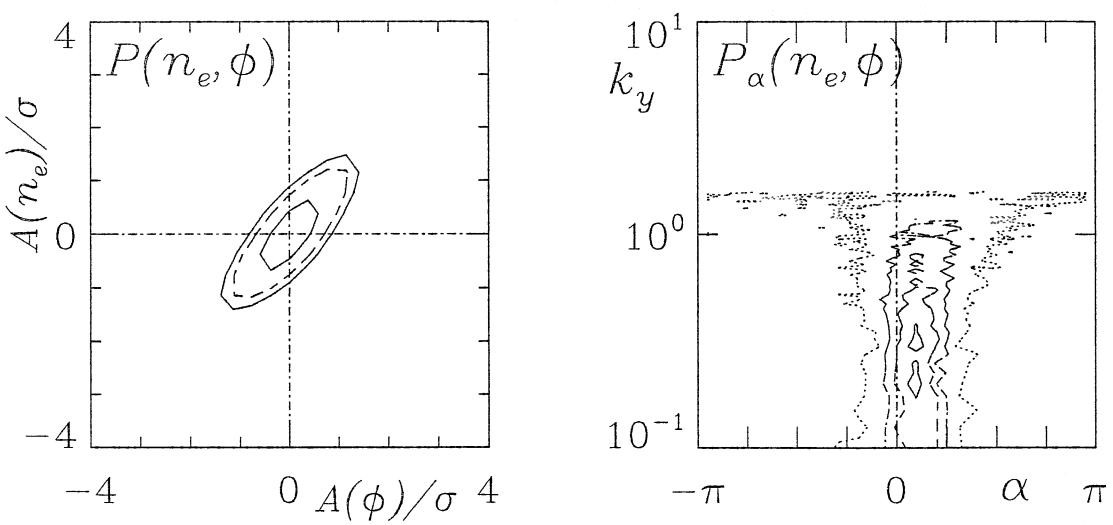

Figure 8.17. Cross coherence (left) and phase shift distributions (right), between $\widetilde{n}_e$ and $\widetilde{\phi}$. These forms reflect the general trend of the adiabatic response, which persists in turbulence with robust transport. Compare with Fig. 7.7.

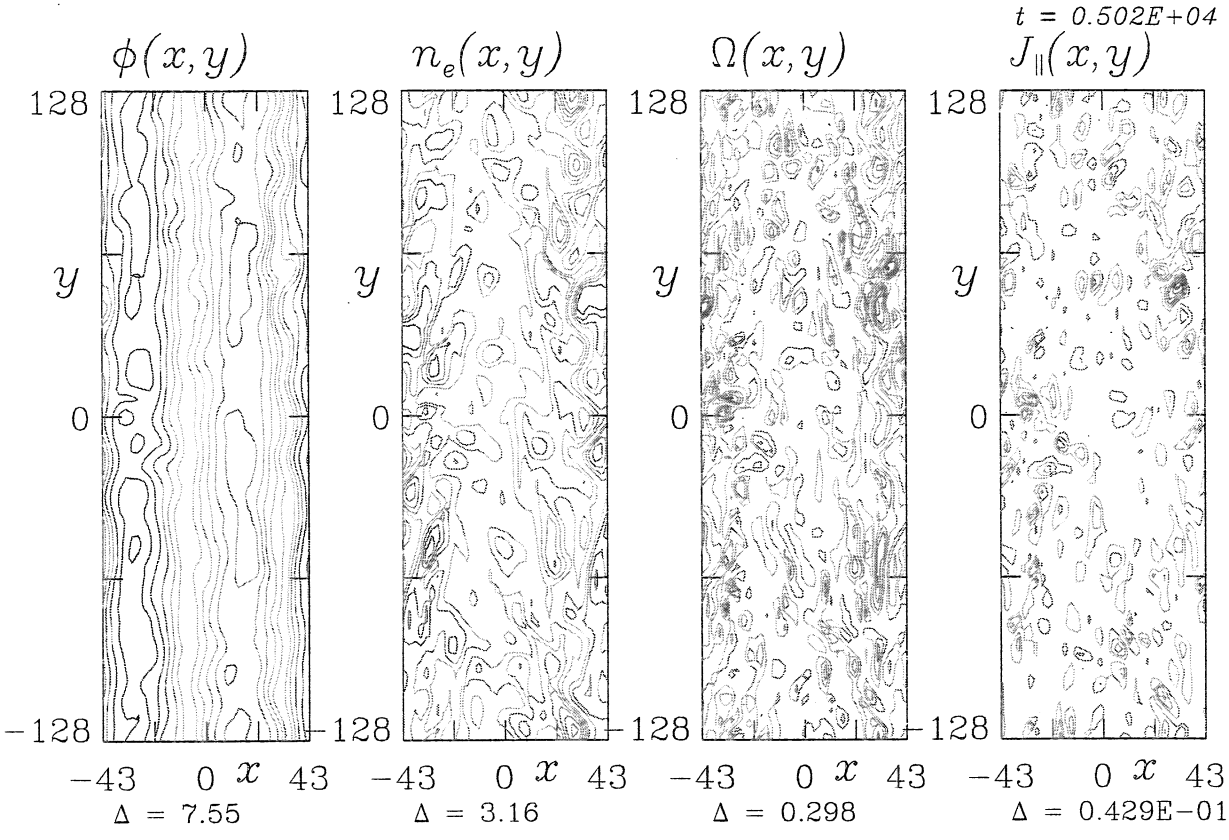

Figure 8.18. Spatial morphology of the disturbances. The $k_y = 0$ mode is very pronounced, developing the ExB flow layers to be discussed in the next chapter. The disturbances are dragged along with the flows but they are otherwise similar to those seen in Fig. 8 of Chapter 6, small scale eddies and disturbances several ρ_s in size.

turbulence. We will see this structure in the two dimensional model as well in the next chapter, when these flow layers take center stage.

The three dimensional structure is something which cannot appear in a two dimensional model, but it also forms part of the mode structure. The amplitude and transport envelopes are shown in Fig. 8.20. They show no dependence on s, as should be the case. It is necessary to apply the shifting transformations discussed at the end of Section VI to get this result, as otherwise the strong grid deformation would lead to spurious structure in the s-direction (cf. Appendix B). The parallel spectra of the amplitudes and energetics are shown in Fig. 8.21. These show the manifestation in $k_\parallel$-space of the spatial structure for slab drift waves seen in Fig. 8.4, in which we find $\widetilde{h}_e$ occupying a smaller space in x than $\widetilde{n}_e$ and $\widetilde{\phi}$; outside the $x \sim \Delta_D$ region noted in Eq. (8.25) the dynamics is adiabatic. The same holds for $k_\parallel$ in the three dimensional model, which follows since in the two

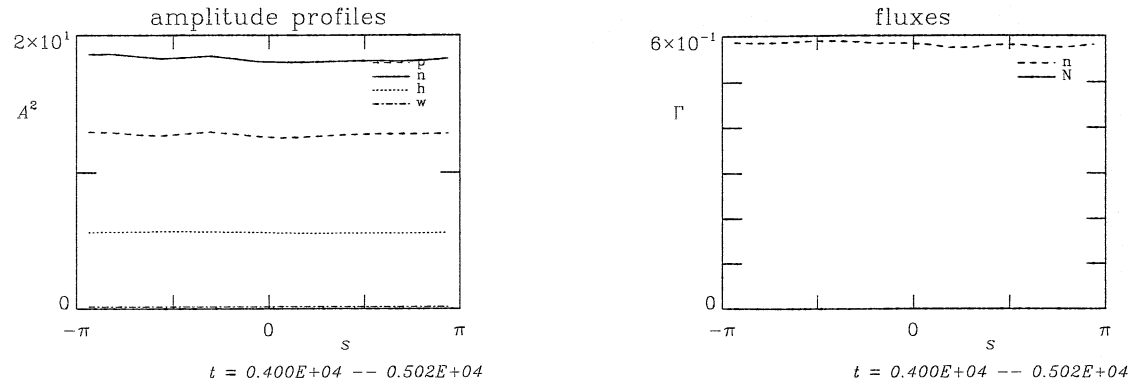

Figure 8.20. (left) Amplitude envelopes of $\widetilde{n}_e$, $\widetilde{h}_e$, $\widetilde{\phi}$, and $\nabla_\perp^2\widetilde{\phi}$, respectively labelled by 'n', 'h', 'p', and 'w'. This amplitude ordering $\widetilde{n}_e > \widetilde{\phi} > \widetilde{h}_e$ is a general feature of drift wave turbulence; to get $\widetilde{\phi} > \widetilde{n}_e$ requires the temperature. (right) Amplitude envelope of the ExB transport ('n'). The magnetic flutter transport is negligible on this scale.

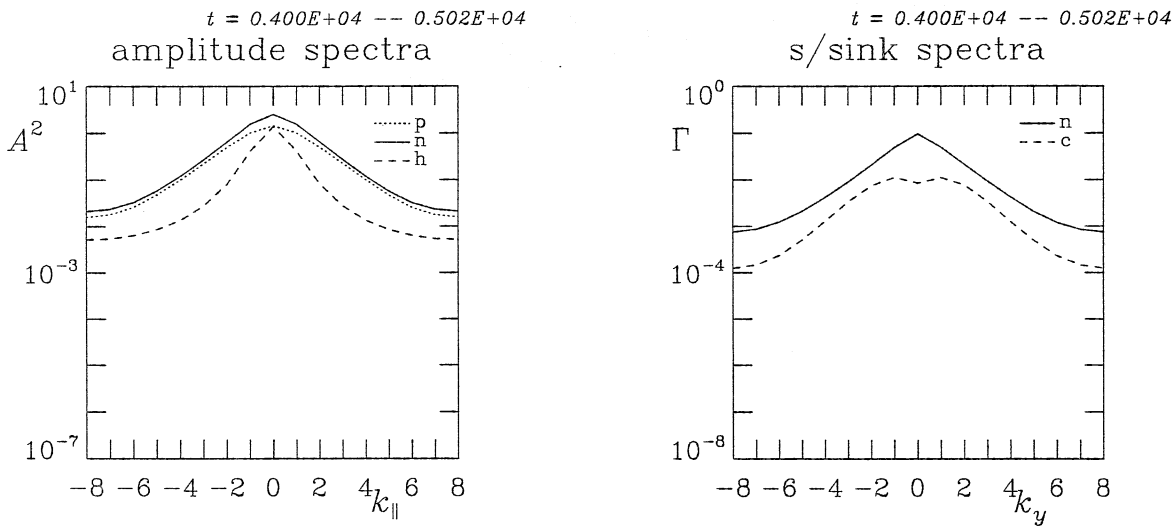

Figure 8.21. (left) Parallel spectra of the amplitudes of $\widetilde{\phi}$, $\widetilde{n}_e$, and $\widetilde{h}_e$, respectively labelled by 'p', 'n', and 'h'. (right) Spectra of the ExB gradient drive ('n') and collisional dissipation ('c'). The nonadiabatic dynamics occupies a smaller space than the whole, especially apparent in the contrast in the spectra of $\widetilde{n}_e$ and $\widetilde{h}_e$.

dimensional model $k_\parallel = -k_y x$, and k_y is fixed for each mode. So as we noted above, x in the two dimensional model plays the same role as $k_\parallel$ in the three dimensions, which is

possible since x is a free coordinate in the three dimensional model, acting only to add more degrees of freedom to the statistics.

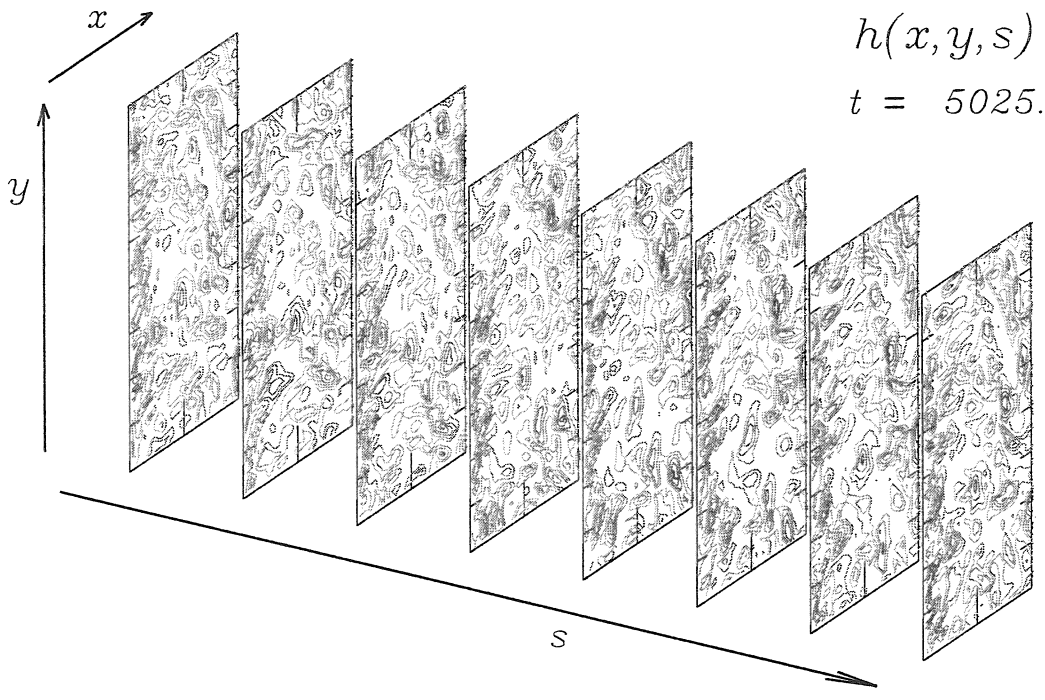

Figure 8.22. Three dimensional morphology of the nonadiabatic density, $\widetilde{h}_e = \widetilde{n}_e - \widetilde{\phi}$, with the flux surface average subtracted out. Every second drift plane is shown. There is a general tendency to follow the field lines, but enough structure remains to obscure it. Note that the field lines are sheared, in the s-direction but tilting towards negative y, for positive x.

The three dimensional morphology is shown in Fig. 8.22. There are 16 drift planes in all, and 8 are shown. One sees a general tendency to follow the field lines, but since disturbances are born at all locations in s with equal probability it is moderately obscured. The profiles, which are not simply the $k_y = 0$ part but the $k_y = k_\parallel = 0$ flux surface averages, have been subtracted out in order to highlight the disturbances.

8.IX. Transport Scaling of Drift Wave Turbulence

Simple quantitative scaling is not the way to understand the physics of a turbulent system, since as we have seen the physical character can persist in the presence of widely varying quantitative variation. An example is the energy transfer dynamics discussed at the end of Chapter 6. Simply looking at total energy levels or even total transfer would have obscured the fact that each individual transfer mechanism keeps its form throughout the parameter range. But we do need to know the quantitative information after all, and in this case we are going to find out something very interesting. Several runs were performed in the three dimensional model with the same setup as in the previous section. The nominal case was with parameters $\hat{\beta} = 1$, $\hat{\mu} = 5$, and $\nu = 1.0$, giving $C = 2.5$. The other parameters were $\hat{\epsilon} = 18350$, $\hat{s} = 1$, and $K = 0.025$. The grid resolution was $64 \times 256 \times 16$ in $\{x, y, s\}$, with Dirichlet boundary conditions in x.

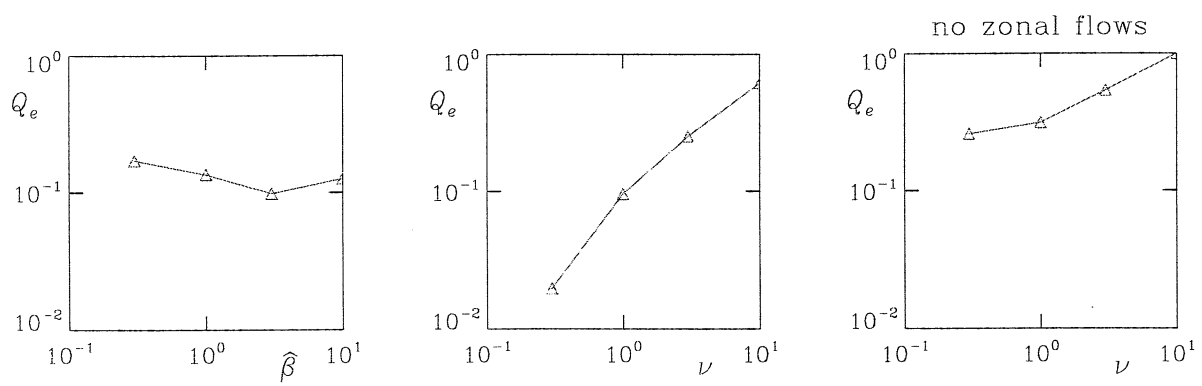

Figure 8.23. Transport scaling of drift wave turbulence, as a function of $\hat{\beta}$ and ν. Note that $C = 0.51\hat{\mu}\nu$. In the rightmost frame the $k_y = k_{||} = 0$ component of $\mathbf{v}_E \cdot \nabla\nabla_\perp^2\tilde{\phi}$ is shut off, removing the tendency of ExB flow layers to build up. These flows, to be discussed in the next chapter, suppress the turbulence especially at low collisionality.

The main scalings are those against $\hat{\beta}$ and ν, with $C = 0.51\hat{\mu}\nu$. These are shown in Fig. 8.23, and the interesting result is the one in the rightmost frame, showing the effect of switching off that flux surface averaged flow we saw in Fig. 8.18, by setting the $k_y = k_{||} = 0$ component of $\mathbf{v}_E \cdot \nabla\nabla_\perp^2\tilde{\phi}$ to zero in each time step. The first result is that the beta dependence is relatively flat. We will investigate this further in Chapter 12, when we look at the combined effect of magnetic flutter and ∇T_e, but we note here that it reflects the cancellation noted for magnetic flutter in Chapter 5, Section IX. The second result is

what we would expect, that the transport scales with collisionality in roughly proportional measure. We might also expect that it should be shut off at very low ν. But the mere collisionality effect is complicated; at very low ν enough of the dynamics is adiabatic that the stabilising effect of the pressure/density nonlinearity is weakened, leaving the vorticity nonlinearity in a more pronounced role. This leads to the flattening of the scaling in the rightmost frame. The central frame shows that it is the effect of the ExB flow layers which sharply suppress the turbulence and reduce the transport at low collisionality. These flows, called zonal flows, form the main topic of the next chapter, and we will investigate them there.

One other point of interest is the effect of the sound waves. Both these and the ExB advection causing the pressure/density cascade to small scales form dissipation channels, along with the parallel currents. We find that for values above about 10^3, corresponding to $L = 0.03$ in the two dimensional slab model, the parameter $\hat{\epsilon}$ has little effect on the transport. To get the nominal value we have been setting $\hat{\epsilon} = 3670\hat{\mu}$, for whatever $\hat{\mu}$ we choose. This reflects the deuterium/electron mass ratio in the respective inertias. For values of 183.5, 551, 1835, and 5505, for the case discussed in Section VIII, the transport values were 0.250 ± 0.017, 0.515 ± 0.039, 0.579 ± 0.042, and 0.597 ± 0.062. Weaker sound waves allow a larger space for the interaction between nonadiabatic and adiabatic drift wave dynamics, but beyond the point at which $k_{\|}c_s$ can no longer affect the longer wavelengths, the sound waves have little to no effect. This is basically a question of how steep the gradients are, and in laboratory plasmas they are steep. The nominal cases we have been using correspond well to the edge regions of magnetically confined fusion experiments, but to treat that seriously we need the temperature and geometric complications to be introduced in later chapters.

8.X. Conclusion – the Irrelevance of Linear Stability

The first conclusion of this chapter is that linear drift waves are stabilised by magnetic shear and the eigenmode structure it introduces in the direction across flux surfaces. The mechanism is field line connection, which depends on the combined effect of periodicity (toroidal topology) and magnetic shear. If either of these are absent then the linear eigenmodes are unstable again.

The second conclusion is that turbulence can exist in the absence of any linear instabilities. It sustains itself by changing the basic structure of the linear eigenmodes, so that much more robust nonadiabatic, dissipative electron activity and therefore electron pressure gradient drive are possible for a given set of parameters. The agent responsible for this change is the vorticity nonlinearity, which represents self advection of ExB eddies

or equivalently the nonlinear polarisation drift. This nonlinearity has the property of an incoherent scattering, which expands the space of available states without appreciable diffusivity. The other nonlinearities are mostly stabilising and act more conventionally as turbulent mixing diffusion. The fundamental cause of this difference between the nonlinearities is their differing cascade character; inverse for the ExB energy, direct for everything else.

The implication of these results is that linear stability analysis is not useful in determining whether drift wave turbulence will result, or if it does what its mode structure or transport scaling will be. For practical results one must turn to self consistent computation. It may well be possible to model this nonlinear instability given its properties as revealed by those computations, but the basic requirements of self consistency (at least a two field model is needed) and a statistical analysis (with the differing character of the nonlinearities) make that a difficult prospect, one whose predictive value is questionable. The computations by themselves are sufficient to understand the physics.

Linear mode structure is too constrained; oscillations in the solution depend too much on the order of the system of equations and the factors of x^2 that appear. The presence of a randomising agent like turbulence break these constraints and allow a wider accessibility to the space of possible degrees of freedom.

Further Reading

With this chapter we encounter results which are usefully discussed only in the scientific literature. A few pointers are presented.

"Shear damping" of linear drift waves became known in the 1960s and quickly became a central theme in magnetic fusion research. The earlier work is reviewed by W. M. Tang, in *Nucl. Fusion* 18 (1978) 1089. Linear drift waves in sheared slab geometry were definitively found stable by D. W. Ross and S. M. Mahajan, in *Phys. Rev. Lett.* 40 (1978) 324, and by K. T. Tsang, P. J. Catto, J. C. Whitson, and J. Smith, in *Phys. Rev. Lett.* 40 (1978) 327.

Immediately afterward, the delicate nature of the linear stability problem, and its sensitivity to very small scale structure across the rational surface, was noted by S. P. Hirshman and K. Molvig, who proposed the nonlinear instability in *Phys. Rev. Lett.* 42 (1979) 648. In the adiabatic sheared slab model with drift and sound waves, with an external drive parameter, D. Biskamp and M. Walter found the mode structure changes which eventually lead to the nonlinear instability; the analytical model in that work merits further study.

Self sustained turbulence in the self consistent dissipative drift wave system was demonstrated by B. Scott, in *Phys. Rev. Lett.* 65 (1990) 3289, and the mode structure

changes and the importance of the simultaneous action of the two nonlinearities were detailed by B. Scott, H. Biglari, P. W. Terry, and P. H. Diamond, in *Phys. Fluids B* 3 (1991) 51, and by B. Scott, in *Phys. Fluids B* 4 (1992) 2468. Three dimensional mode structure was presented by B. Scott, in *Plasma Phys. Contr. Fusion* 39 (1997) 1635, and parts of the results of this chapter demonstrating the three dimensional nonlinear instability in *Phys. Plasmas* 7 (2000) 1845. Drift wave computation in general is reviewed by W. Horton, in *Reviews of Modern Physics*, Vol. 7, No. 3, April 1999, without having much to say about the nonlinear instability.

Field aligned coordinates were proposed by K. V. Roberts and J. B. Taylor, in *Phys. Fluids* 8 (1965) 315, and expanded for toroidal flux tube models by S. C. Cowley, R. M. Kulsrud, and R. N. Sudan, in *Phys. Fluids B* 3 (1991) 2767, and by M. A. Beer, S. C. Cowley, and G. W. Hammett, in *Phys. Plasmas* 2 (1995) 2687. The global consistency requirement was noted by J. W. Connor, R. J. Hastie, and J. B. Taylor, in *Phys. Rev. Lett.* 40 (1978) 396, and was first properly worked out for flux tube models by B. Scott, in *Phys. Plasmas* 5 (1998) 2334. For the global version, see R. L. Dewar and A. H. Glasser, *Phys. Fluids* 26 (1983) 3038, as well as Appendix B.

9. Drift Wave Turbulence and ExB Zonal Flows

B. Scott

Jul 1999

9.I. Introduction — Eddies and Flows

In Chapter 6 we investigated the basic properties of the ExB nonlinearities present in drift wave turbulence. We isolated these by deliberately switching off the component of the disturbances which has no dependence in the drift direction; that is, we have been neglecting the quasilinear modifications of the background profiles. The component varying only in the direction of the profile gradient has two properties which distinguish it from the turbulence: it does not participate in adiabatic coupling, and it does not participate in transport. Once excited, therefore, it can exist independently of the dissipation even though it does interact with the turbulence. A flow with this property is called a zonal flow, borrowing the concept from geophysical fluid dynamics of a flow in the direction of changing longitude, within a given band of latitudes; hence it is constant within arbitrarily thin zones (the term given to intervals of latitude, independent of longitude). The flow is zonal, or purely in the drift direction, because its stream function depends only on the down-gradient direction, the only other dimension in the drift plane.

If this zonal flow is sheared, then it can influence individual eddies and disturbances in the turbulence in a special way. Transport down the gradient represents a statistical wandering of the transported quantity in that direction, whether or not there is any displacement of the disturbances in the drift direction. If there is a strongly sheared zonal flow, a mean gradient in the kinetic energy of ExB flow is present. Transport of flow momentum down this gradient is called Reynolds stress, and if positive it leads to the well known Kelvin-Helmholtz instability. Under certain conditions and for certain scales of motion this instability is eliminated: If the background vorticity is constant, there is no vorticity extremum and the Rayleigh criterion for instability is therefore not satisfied. Generally, the instability has a threshold expressed in terms of a ratio between the wavelength of a cross-flow disturbance and the scale of the flow shear; for a ratio well below unity the disturbances are stable. The special influence the sheared flow then has on disturbances maintained by other means (*e.g.*, drift waves) is to literally rip them apart; both correlation times and lengths are reduced.

A sheared ExB flow can therefore either drive or suppress drift wave turbulence, depending on the situation. Furthermore, we have the issue of the origin of the sheared flow.

Not only are externally applied flows important (*i.e.*, those which are part of the background equilibrium), but the turbulence could itself actually drive or generate flows due to the intrinsic connection between electron pressure and electrostatic potential disturbances, and the tendency of the ExB flow eddies associated with those potential disturbances to transfer their energy towards ever larger scales. On energy conservation grounds alone, suppression of disturbances by flows implies a transfer of energy from disturbances to flows. The investigations outlined in this chapter will clarify the relationship between drift wave turbulence and ExB flows. We will see that not only the parameters but also the geometry of the background magnetic field has a strong effect on the fate of the turbulence and the flows.

9.II. Kelvin-Helmholtz Stability

We here review the basic textbook results concerning the stability of sheared flows. The first of these is the Rayleigh theorem, according to which there must be a vorticity extremum in order for there to be an instability. The second is the existence of a threshold, by which only disturbances of sufficiently long wavelength along the flow but reflecting motion perpendicular to the flow, are stable.

The classic Kelvin-Helmholtz problem consists of a two dimensional Euler equation in the xy-plane, with a mean flow in the y-direction having a profile in the x-direction: $\mathbf{v}_0 = \{0, v_0^y\}$ with $v_0^y = V(x)$. The vorticity profile is given by $\Omega_0(x) = \partial V/\partial x$. The linearised equation for disturbances is

$$\left(\frac{\partial}{\partial t} + V\frac{\partial}{\partial y}\right)\widetilde{\Omega} + \widetilde{v}_x\frac{\partial^2 V}{\partial x^2} = 0 \tag{9.1}$$

where the flow and vorticity disturbances are given in terms of the perturbed stream function,

$$\widetilde{v}_x = -\frac{\partial\widetilde{\phi}}{\partial y} \qquad\qquad \widetilde{\Omega} = \frac{\partial^2\widetilde{\phi}}{\partial x^2} + \frac{\partial^2\widetilde{\phi}}{\partial y^2} \tag{9.2}$$

As befits a linear problem with no y-dependence in the background, we may assume a dependence in y and t of the form $\exp[i(ky - \omega t)]$, and obtain

$$\frac{\partial^2\widetilde{\phi}}{\partial x^2} - k^2\widetilde{\phi} = \frac{kV''}{kV - \omega}\widetilde{\phi} \tag{9.3}$$

To find a useful criterion for stability we may multiply both sides by the complex conjugate $\widetilde{\phi}^*$ and take the imaginary part,

$$\gamma\int dx\,\frac{kV''}{(\omega_R - kV)^2 + \gamma^2}\left|\widetilde{\phi}\right|^2 = 0 \tag{9.4}$$

where $\omega = \omega_R + i\gamma$. This equation says that for general form of the disturbance $\widetilde{\phi}(x)$ the growth rate γ must vanish unless there is a point within the domain (here, the entire x-line) in which V'' vanishes, so that it can change sign. That is, there must be an inflection point in the velocity profile, or equivalently an extremum in the vorticity profile, in order for there to be an instability. This is the Rayleigh theorem for the stability of sheared flows.

If we take the real part we find

$$\int dx \, \frac{(\omega_R - kV)kV''}{(\omega_R - kV)^2 + \gamma^2} \left|\widetilde{\phi}\right|^2 = \int dx \left|\frac{\partial \widetilde{\phi}}{\partial x}\right|^2 + \int dx \, k^2 \left|\widetilde{\phi}\right|^2 \tag{9.5}$$

Given Eq. (9.4) for finite γ the quantity involving ω_R in the numerator vanishes, and we can combine the rest into

$$\int dx \left|\frac{\partial \widetilde{\phi}}{\partial x}\right|^2 + \int dx \, k^2 \left[1 + \frac{VV''}{(\omega_R - kV)^2 + \gamma^2}\right] \left|\widetilde{\phi}\right|^2 = 0 \tag{9.6}$$

This condition can be satisfied generally for localised flows whose product VV'' is negative. However, a lower bound on the growth rate can be found by noting that the size of the second term in the brackets must be larger than unity. Taking into account that we used $\gamma \neq 0$ to find this equation, we now have

$$\text{either} \quad \gamma = 0 \quad \text{or} \quad (\omega_R - kV)^2 + \gamma^2 < |VV''| \sim \frac{V^2}{\Delta_V^2} \tag{9.7}$$

where Δ_V can be taken to be the width of the flow. This implies in general that for $\gamma \neq 0$ the wavenumber k cannot be too large; there is a threshold involving k and Δ_V such that

$$\gamma \neq 0 \quad \text{only for} \quad k\Delta_V < O(1) \tag{9.8}$$

What this threshold exactly is depends on the detailed profile of V, but the existence of the threshold is true generally.

9.III. Shear Flow Suppression via Decorrelation

The above results concern direct interactions between disturbances and flows, for which the only free energy source is the gradient of the mean flow energy. But the main interest for magnetised plasma turbulence is what a sheared flow can do to turbulence caused by other means; specifically, the thermal gradient. Simple arguments involving two point correlation lead to a result that the imposition of a large scale sheared flow should interfere with the transport of passive scalar quantities by random scatter. Suppose we have a diffusive process, in which the average separation of two points grows with the square root of the elapsed time. In either the x- or y-directions, this distance will evolve as

$$\Delta_x = (2Dt)^{1/2} \qquad \Delta_y = (2Dt)^{1/2} \tag{9.9}$$

In a sheared flow, the separation of two points grows secularly. If the separation in the x-direction is Δ_x, then the separation in the y-direction will grow according to the flow shear V' as

$$\Delta_y = V'\Delta_x t \tag{9.10}$$

Expressing these infinitesimally, we have

$$\frac{\partial \Delta_x}{\partial t} = \frac{D}{\Delta_x} \qquad \frac{\partial \Delta_y}{\partial t} = \frac{D}{\Delta_y} + V'\Delta_x \tag{9.11}$$

Given a definite correlation length λ_y in the y-direction, the correlation time τ_c is reduced by the fact that with the flow shear the inter-point separation reaches λ_y sooner than it would if only the diffusive process were present. As a result, we therefore find a smaller separation Δ_x, due to the smaller time interval. This is the correlation length λ_x in the x-direction. If the overall transport is a random walk process, its diffusion coefficient will scale as λ_x^2/τ_c. If the flow shear is weak enough that λ_y is reached by Δ_y comparably fast as λ_x is reached by Δ_x, then the flow shear has little effect. Beyond a threshold, however, roughly given by

$$V' > D/\lambda_y^2 \tag{9.12}$$

the two-point correlation is limited by the flow shear rather than the diffusion.

The drive of disturbances by a background thermal gradient is given by the average transport times the gradient, as we have seen in previous chapters. If the correlation implied in the transport average is reduced, so is therefore the drive, and so perhaps the amplitude of the disturbances. This is a simple heuristic argument, however, and even if it is dressed by more sophisticated theory, the assumptions into the character behind it (that the transport process should be diffusive, with no correlative effect of the transported

quantity back to the eddy disturbances doing the transport) remain. Whether this process is actually active is something which must be checked by statistical diagnosis of a given situation, be it experimental data or computations.

9.IV. Energetics of Shear Flow Suppression

There is another way to think about suppression of turbulence by a sheared flow, which how the imposed flow and the disturbances exchange energy. If the flow suppresses the turbulence directly, it follows that the turbulence loses energy to the flow. Conversely, if the flow were Kelvin-Helmholtz unstable, it should serve as a free energy source. Returning to Eq. (9.1) for disturbances on a zonal flow, we form the equation for the energy of the disturbances by multiplying by $\widetilde{\phi}$ and integrating over the entire plane to find

$$\frac{\partial}{\partial t}\frac{1}{2}\int dx \left(\left| \frac{\partial \widetilde{\phi}}{\partial x} \right|^2 + k^2 \left| \widetilde{\phi} \right|^2 \right) = -\int dx\, V' \left(\widetilde{v}_x \widetilde{v}_y \right) \tag{9.13}$$

This term on the right side multiplying V' is the Reynolds stress. If $Re = \widetilde{v}_x \widetilde{v}_y$ is positive in the presence of positive V', the flow eddies are tilting with the flow, and they yield energy to the flow. In this situation, they are directly suppressed by the flow. In the opposite case, the eddies are tilting against the flow, taking energy from it. In this case they are directly driven by the flow, as in the case of a Kelvin-Helmholtz instability. We already know, however, that if there is no maximum in the mean vorticity or if the scale of variation of the flow shear is larger than the disturbances (*i.e.*, in this case we imagine a constant background vorticity), then there is no direct drive. The flow either has no effect or it suppresses the disturbances. In the case of a complicated set of model equations, the measurement of the average product of the Reynolds stress and the background vorticity can tell us how vigorously the disturbances are driven or suppressed by the mean flow.

The mechanism of flow drive or suppression conserves energy: if the disturbances are driven, then the flow is locally reduced; if the disturbances are suppressed, then their energy goes into the flow. The equation for the effect of the disturbances on the mean flow is

$$\frac{\partial}{\partial t}\frac{1}{2}\int dx\, V^2 = -\int dx\, V \mathbf{v} \cdot \nabla \widetilde{v}_y = \int dx\, V' \left(\widetilde{v}_x \widetilde{v}_y \right) \tag{9.14}$$

using $\nabla \cdot \widetilde{\mathbf{v}} = 0$ in the integration by parts. Eqs. 9.13 and 9.14 reflect the basic conservation of kinetic energy, as the Reynolds stress merely mediates transfer between the mean flow and the disturbances. We have already seen the tendency of two dimensional flow dynamics to cascade energy inversely to the largest available scales. It follows that there is a natural

tendency of flows in the absence of a Kelvin-Helmholtz instability to energetically suppress turbulence, as the turbulence transfers its energy into the flows.

Whether a suppressive effect of a background flow on the turbulence proceeds via decorrelation or energetically is something that can be measured in a computation. Cross coherence of the flow eddies and the transported quantities (*i.e.*, simply $\widetilde{p}_e$ in the simplest drive wave model), correlation lengths, and Reynolds stresses are all directly accessible, and the measurement of these will tell us by which mechanism the disturbances are affected by background flows.

9.V. Effect of Imposed Background Shear in the Dissipative Coupling Model

To see the basic effect of a sheared zonal flow on drift wave turbulence, we can take the simple dissipative coupling model of Chapter 6 as a starting point, and then impose a constant background vorticity. At this point we still remove the $k_y = 0$ component of the disturbances, namely, the back reaction of the turbulence on the background. At this level the sheared ExB flow is strictly part of the background.

We take the case $D = 0.1$ of the dissipative coupling model and add the background flow component to the ExB advection term. The equations are otherwise unaltered. The dependent variables are $\widetilde{p}_e$ and $\widetilde{\phi}$, satisfying the following equations,

$$\frac{\partial}{\partial t}\nabla_\perp^2 \widetilde{\phi} = -\mathbf{v}_E \cdot \nabla \left(\nabla_\perp^2 \widetilde{\phi}\right) + D\left(\widetilde{\phi} - \widetilde{p}_e\right) \tag{9.15}$$

$$\frac{\partial \widetilde{p}_e}{\partial t} = -\mathbf{v}_E \cdot \nabla \left(\widetilde{p}_e + p_e\right) + D\left(\widetilde{\phi} - \widetilde{p}_e\right) \tag{9.16}$$

where D is the dissipative coupling parameter and $\nabla p_e = -\nabla x$ is the background gradient. The ExB velocity is given by the potential disturbances plus the background vorticity:

$$\mathbf{v}_E = \nabla s \times \nabla \phi - V' x \nabla y \tag{9.17}$$

where ∇s is the direction normal to the drift plane and V' is the normalised flow shear parameter. In physical units, we have

$$V' = \frac{L_\perp}{c_s}\frac{\partial v_0^y}{\partial x} \tag{9.18}$$

where v_0^y is the background flow, assumed to be in the y-direction. As before, x and y are the down gradient and drift directions, and we have taken $L_\perp = L_p$. To solve these equations numerically we take the same scheme as in Chapter 6, Section VII, and do the upwind advection with the combined $\mathbf{v}_E$.

It is important to note that a constant background vorticity is incompatible with periodic boundary conditions in the x-direction. This is because the background flow has opposite sign at the limiting values of $x = \pm L_x/2$, where L_x is the x-domain size. One remedy is to take a shearing coordinate system, but the rebuilding of the solver for operations involving $\nabla_\perp^2$ is not trivial, although the way to do it is well known. We therefore take the same Dirichlet boundary conditions as in the previous chapter, namely, setting the dependent variables to zero at the x-boundaries. Without the $k_y = 0$ component, no special handling is necessary. The y-coordinate is periodic on a length of $L_y = 20\pi$, and $L_x = L_y$.

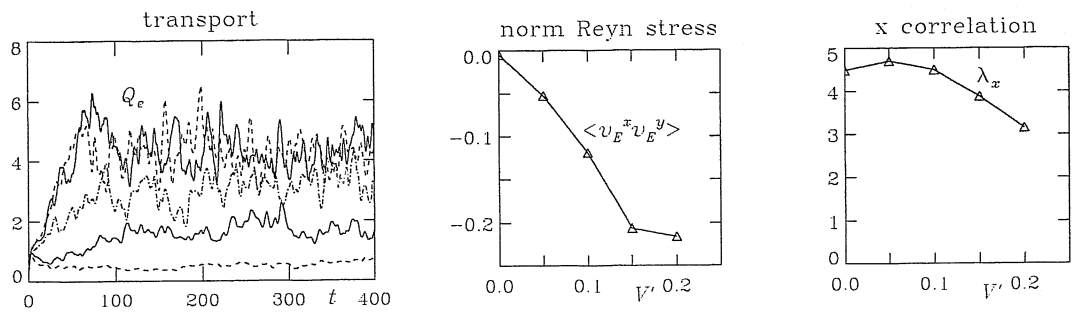

Figure 9.1. (left) Transport in the dissipative coupling model with $D = 0.1$, as a function of imposed ExB flow shear. The top solid curve is for $V' = 0$, the top dashed curve is for $V' = 0.05$, and further curves are for 0.1, 0.15, and 0.2 towards the bottom. (center) Correlation between $\tilde{v}_E^x$ and $\tilde{v}_E^y$, showing the onset of Reynolds stress. (right) Reduction of correlation length in the x-direction with increasing V', reflecting the shearing apart of the disturbances. No other aspect of the mode structure is affected.

In Fig. 9.1, we show the time evolution of the cases with $D = 0.1$ and V' taking the set of values $\{0, 0.05, 0.1, 0.15, 0.2\}$. The amplitudes and transport are both reduced by the background ExB shear, and it is important to note that the rate of numerical dissipation at small scales (Γ_E) does not change with V'. This suppression is a physical effect, but we must search into the mode structure for the underlying dynamics; there are no strong changes to either the source (Γ_n) or sink (Γ_c) rates. The values of Γ_n, Γ_c, and Γ_E are all close to 0.045, 0.014, and 0.030, respectively. There are also no strong changes in any of the features of the mode structure we discussed in Chapter 7. The only signpost is a weak dependence of the correlation lengths on V', where we find a reduction in the λ_x and an enlargement in λ_y with increasing V'. Examining further, we find an increase of the Reynolds stress with V', which arises from a strengthening correlation between $\tilde{v}_E^x$ and $\tilde{v}_E^y$

since their amplitudes decrease along with everything else, with increasing V'. The rate of shear flow suppression is therefore quadratic in V', since it is the product between Re and V'.

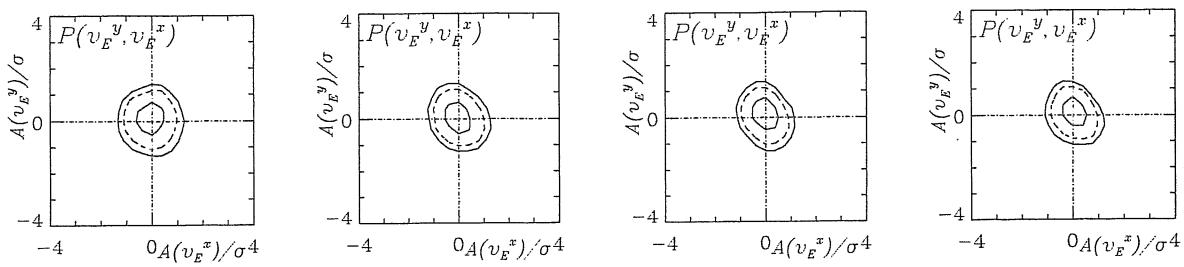

Figure 9.2. (left to right) Cross correlation between the y and x-components of the ExB velocity components associated with $\widetilde{\phi}$, for $V' = 0.05$, 0.1, 0.15, and 0.2. The onset of Reynolds stress follows this correlation. The actual amplitude of the Reynolds stress peaks near $V' = 0.1$, due to the falling overall amplitude with rising V'.

This Reynolds stress departs from zero only when the background ExB shear is imposed. In Fig. 9.2 we find the cross correlation between $\widetilde{v}_E^x$ and $\widetilde{v}_E^y$ as a function of V'. For small V' the correlation is not visible, although Fig. 9.1 shows that it is indeed nonzero even for $V' = 0.05$. Here, though, the flow shear is too weak to suppress the turbulence in the face of its general nonlinearity. Only when the threshold is reached, here about $V' = 0.1$, is there actual suppression. In the suppression regime, all quantities are reduced together, basically preserving the mode structure, although there is a measurable effect on the down gradient correlation length. This shows that the ExB shear suppression effect is basically perturbative, affecting the ExB vorticity disturbances directly but the rest of the dynamics only indirectly. Since the Reynolds stress correlation is linear in the background velocity shear until suppression is reached, we can conclude that the effect of the background velocity shear is to simply tilt the flow eddies, such that they begin to lose energy to the background flow. Only when this energy loss rate is large enough to compete with Γ_n is there an effect on the overall amplitude.

We find suppression when V' is as large as Γ_n, the overall rate of excitation of the turbulence. This basically means that the rate at which the disturbances are sheared apart, or decorrelated, is as large as the rate at which they are generated in the first place. Energetic suppression and decorrelation are therefore related. Models in the literature

based on linear modes express a suppression criterion in terms of the linear growth rate, simply as

$$V'_{\text{crit}} = \gamma_L \tag{9.19}$$

What the above results indicate is that we simply replace the linear growth rate with the overall nonlinear excitation rate, which we can call Γ_+,

$$V'_{\text{crit}} = \Gamma_+ \tag{9.20}$$

In this case we have simply $\Gamma_+ = \Gamma_n$.

9.VI. Zonal Flows in the Dissipative Coupling Model

The results of Section V showed that a background ExB vorticity is capable of suppressing drift wave turbulence quite dramatically, and that the mechanism by which it does so is to excite a Reynolds stress by tilting the flow eddies in the drift plane with the flow shear. In this state the sign of the Reynolds stress is such that the net transfer of energy is from turbulence to the background flow. In a sense we can think of this as merely part of the general inverse cascade or nonlinear transfer tendency of the essentially Eulerian flow field. But the vorticity is itself a dependent variable. We therefore ask whether the turbulence can excite this background flow by itself, and the once excited background flow can then give rise to a Reynolds stress that further drives, or spins up, the background flow. To investigate this in the dissipative coupling model we set $V' = 0$ and return to periodic boundary conditions in the x-direction to avoid boundary layer effects on the flows.

One point to note is that the coupling constant only acts on the $k_y \neq 0$ components, since it arises from a model in which $k_\parallel$ is not allowed to vanish, and as explained in Chapter 8 and in Appendix B, this is a result of finite k_y on closed magnetic surfaces. To properly capture this effect, we set $D = 0$ for the $k_y = 0$ component in the operations in which the combinations of D and $\nabla_\perp^2$ are solved. For $k_y \neq 0$ we keep the value of D and proceed normally.

There is a difference between removing all $k_y = 0$ components and removing the zonal flows. Removing of the zonal flows is done by discarding the y-average of $\mathbf{v}_E \cdot \nabla \nabla_\perp^2 \widetilde{\phi}$ but taking no other modifications. This last case is referred to as that without zonal flows, while the case with all $k_y = 0$ components present is referred to as that with zonal flows. The cases with all $k_y = 0$ components removed are referred to as such.

In Fig. 9.3, we show the saturated transport as a function of D, that is, the adiabaticity of the electrons, for all three cases: one without any $k_y = 0$ components, one without zonal flows, and one with zonal flows. With the $k_y = 0$ modification of $\widetilde{p}_e$ we find slightly lower

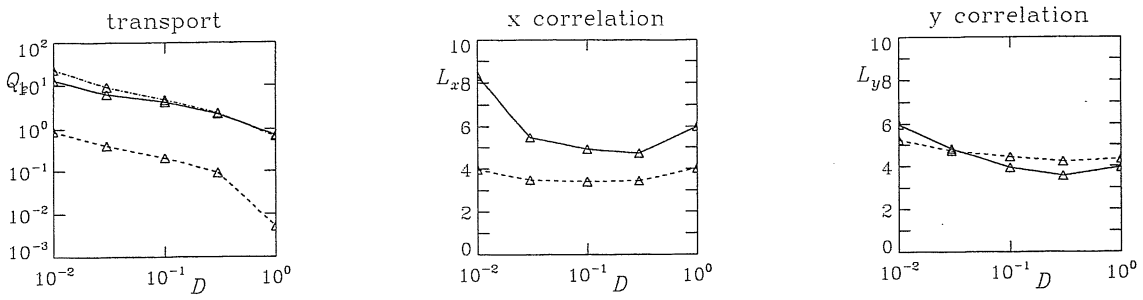

Figure 9.3. Transport (left) and x and y correlation lengths (center and right) in the dissipative coupling model as a function of D, for cases with zonal flows (dashed), without zonal flows (solid), and without all $k_y = 0$ components (dash-dot). The suppression of the turbulence by zonal flows is dramatic. The action of these flow shear layers to chop up disturbances extended in the x-direction is shown by the much larger effect on λ_x. The changes in λ_y are all within the error bars.

transport, due to local, transient modifications of the background due to the turbulence. This effect is most pronounced in the hydrodynamic regime ($D < 0.1$) where it is larger than the error bars of about 25 percent for $D = 0.01$ dropping to about 15 percent for $D = 1.0$. With all $k_y = 0$ components present, the tendency of the zonal flows to suppress the turbulence is dramatic, and takes place for all values of D and amounts to a complete suppression for $D = 1.0$. Energy residing in the $k_y = 0$ component cannot contribute to the transport because $\widetilde{v}_E^x = -\partial\widetilde{\phi}/\partial y$, but that is not the entire reason for the suppression. We also show the x and y-correlation lengths in Fig. 9.3, and here the most visible effect is for the x-correlation lengths to be reduced by the zonal flows, while the correlation lengths in the y-direction are largely unaffected (the visible differences are comparable to statistical scatter). The new effect on the mode structure is that in the presence of zonal flows we now have $\lambda_y > \lambda_x$. While the linear growth rates are almost independent of x but weakly favour $k_x = 0$, the zonal flow dynamics clearly preferentially suppresses the $k_x > k_y$ components. Free energy is exchanged between eddies ($k_y \neq 0$) and flows ($k_y = 0$), but the total direct effect on the energetics is not large. Indirectly, we find that the values of Γ_n are also reduced, but not as much as the squared amplitudes themselves. Zonal flows have a mainly perturbative effect, similar to background flows, in that an energetic/decorrelation suppression is added to an existing turbulent state. Their effect on the overall transport is to lower it by reducing the turbulence amplitudes, not so much by changing the mode structure. Only when the suppression is nearly total, as it is in some of these two dimensional cases, are there any changes in the mode structure.

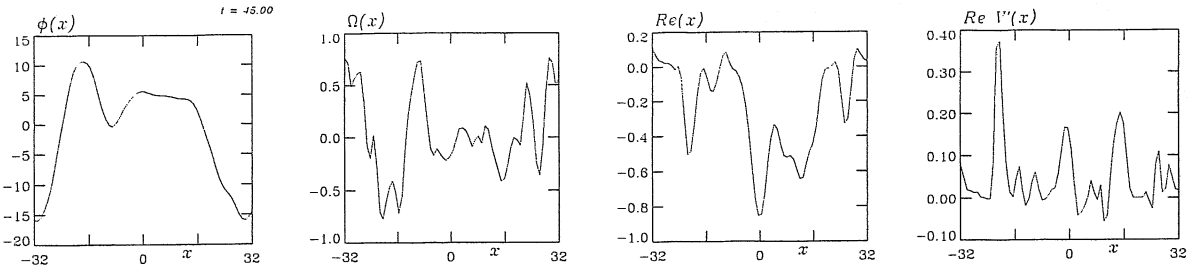

Figure 9.4. Profiles of the potential (ϕ), vorticity (Ω), Reynolds stress (Re), and suppression product ($Re\,V'$) for the case with zonal flows with $D = 0.1$, taken at $t = 45$ in the phase during which suppression is very abrupt. The Reynolds stress on average is zero, but it has a profile which lines up with the vorticity. As in the imposed mean flow case in Fig. 9.1, the Reynolds stress is excited by flow vorticity and acts to energetically suppress the turbulence.

We also find from the diagnostics in Figs. 9.1 and 9.2 that the average Reynolds stress for the cases with zonal flows is zero, and we can see that from the profiles, shown in Fig. 9.4. The zonal flows are built up by the Reynolds stress, which although zero on average as for any other profile quantity with periodic boundary conditions, fluctuates between quite large values on spatial scales comparable to the x-direction correlation length. This serendipitous localised Reynolds stress gives rise to a type of instability in which once a vorticity sheet, or flow shear layer, forms it then further shears the eddies such that it is amplified. The profile of the Reynolds stress starts out as random but we can see the correlation with the vorticity by plotting the product, as done in Fig. 9.4. We find that this product too fluctuates, but is mostly positive on average, which tends to build the small flow shear layers into a larger flow profile structure. Once the strong flow layers are formed, they evolve slowly since the much weaker turbulence can only yield a small Reynolds stress.

At late times the profile of ϕ tends to end in a sinusoidal form if the turbulence is hydrodynamic. Nonlinear interactions can continue even when most of the ExB energy is at this large scale (cf. Chapter 6, Section VI). The strong suppression by ExB shear can also be inferred from the magnitude of the vorticity profile. This shearing rate averages at least 0.2 and reaches values of up to 0.5, much larger than the other dynamical rates of the turbulence. The flow structure does not continue evolving beyond a certain point at which the tendency to become Kelvin-Helmholtz stable ($Re\,V' < 0$) balances the tendency of the smaller scales to regenerate the flow layer ($Re\,V' > 0$). The average suppression product $Re\,V'$ is therefore small at late times.

The fact that the turbulence tends to drive the zonal flows at high-k_y but would then tend towards Kelvin-Helmholtz instability at low-k_y is shown by the Reynolds stress

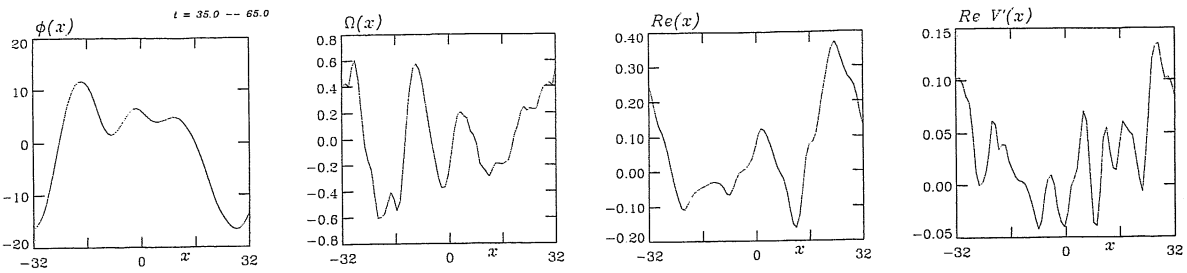

Figure 9.5. Profiles of the potential (ϕ), vorticity (Ω), Reynolds stress (Re), and suppression product ($Re\,V'$) for the case with zonal flows with $D = 0.1$, averaged over the suppression phase $35 < t < 65$. Though the strongest events are ephemeral, the same observations as in Fig. 9.4 apply.

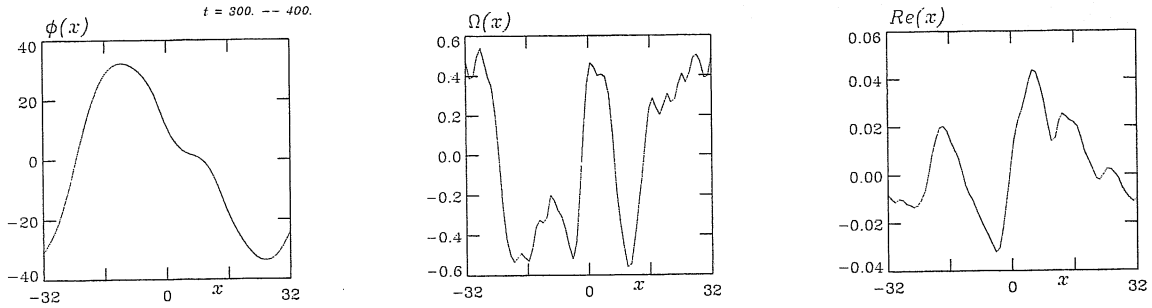

Figure 9.6. Profiles drawn as in Fig. 9.5, averaged over $300 < t < 400$, well after the suppression phase. The turbulence survives but with the morphology altered by the zonal flows. The flow shear layer has widened to consume the entire domain, and the average zonal flow generation is now small. The flow generation process is less efficient when the scales of the turbulence and of the vorticity profile are disparate.

spectrum for the cases from the previous section, with all $k_y = 0$ suppressed but with the applied background ExB shear. These are shown in Fig. 9.7. When the flow is applied, the Reynolds stress is increasingly negative (Fig. 9.1), and the position where it does so is in the region of the spectrum where the gradient drive is strongest. At the longest wavelengths, the sign turns around and the largest scale eddies tend towards Kelvin-Helmholtz instability. But the flow is stabilising to the turbulence, overall. Note that the sign of the applied shear is negative, so that a negative Reynolds stress implies a transfer of ExB energy from eddies to background flow. Although the reduction of Γ_n overall is not significant, as noted in the discussion of Fig. 9.1, its peak values for the most strongly driven wavelengths is reduced. So the suppression of turbulence by background and zonal

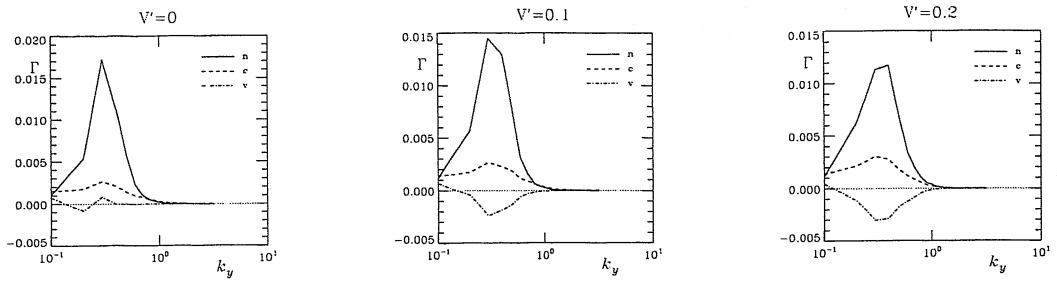

Figure 9.7. Reynolds stress ('v') and energetics ('n' and 'c') spectra for the cases with all $k_y = 0$ components removed but with the applied shear layer parameterised by V', as in Figs. 9.1 and 9.2. The sign of the shear in Eq. 9.17 is such that the flows are driven by negative Reynolds stress. For larger V' the energetic suppression by Reynolds stress is sufficient to compete with the rest of the energetics, and the turbulence is suppressed. Note that Γ_n is also reduced by the flow shear.

flows is not merely a matter of decorrelation, but also of energetics, both directly through the transfer effect in Eqs. 9.13 and 9.14 and indirectly through the effect on the peak of the gradient drive spectrum.

In the dissipative coupling model, then, the turbulence spins up its own mean, sheared ExB flow, and then this flow profile suppresses the turbulence. The flow emerges from the turbulence because the Reynolds stress is not zero but fluctuates randomly around zero. When and where the Reynolds stress profile is extremal, the vorticity profile builds with the same form, thereby reinforcing the Reynolds stress profile due to its action on the turbulent eddies. The zonal flow begins as a set of flow layers which have a scale in the x-direction comparable to the turbulence. On long time scales, however, the larger scale component in the x-direction (driven inefficiently by finite-k_x components beating against each other to drive the $k_x \approx 0$ component) continues evolving the zonal flow towards an end state of a single vorticity sheet.

9.VII. Shear Suppression in the Three Dimensional Model

The results in the dissipative coupling model form a starting point, not an end, for the consideration of zonal flow dynamic in drift wave turbulence. The two dimensional model is useful in showing the basic character of the interaction between ExB turbulence and background flows, but we have to see how well these effects survive in more realistic situations. We already presented the result for drift wave turbulence in a sheared but otherwise homogeneous magnetic field in Chapter 8. Results from the toroidal magnetic

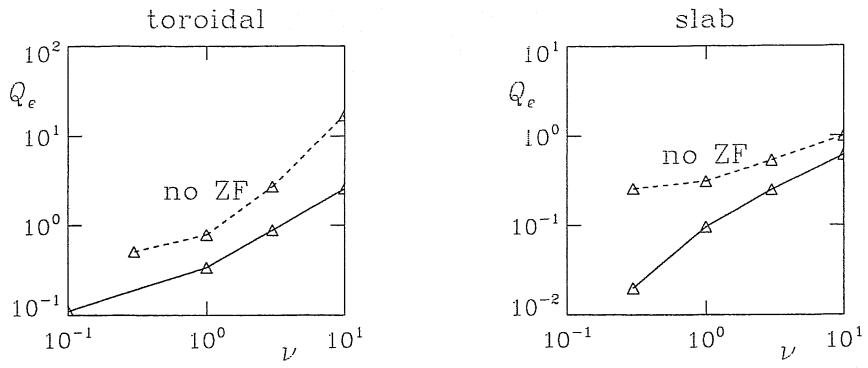

Figure 9.8. Transport scaling of three dimensional drift wave turbulence, as a function of ν, with $C = 0.51\hat{\mu}\nu$, for cases with and without zonal flows and in slab and toroidal magnetic geometry with magnetic shear. The zonal flow effects are noticeable for both models but are stronger in the slab at low ν, and in the torus at high ν.

field geometry model from Chapter 11 are also available, and both are shown together in Fig. 9.8. We find that the zonal flow effects are more substantial for the slab geometry cases than for toroidal geometry. Especially the tendency towards shutting the turbulence off entirely at low collisionality disappears in the toroidal model. This is due to the fact that forcing of the turbulence by interchange effects is significant in the latter model, as will be developed starting with the next chapter.

9.VIII. Summary

Sheared flows have been known for more than a century to be unstable to the Kelvin-Helmholtz phenomenon of vortex rollup. The basic instability has a threshold based on the width of the vorticity layer, according to which disturbances of shorter wavelength along the flow than this width are stable. The classic form of this is the Rayleigh criterion for a vortex extremum. Rotating shear layers add other constraints based on the transport of angular momentum by the disturbances. The classic case is Couette flow, known since the early 20th Century. Basic criteria for instability on energy principal lines like that of Section II have been derived for most systems under study. Sheared flows are usually considered as the cause of an instability, or neutrally stable.

It is when disturbances and turbulence are driven by other means that the sheared flow can be stabilising. A Kelvin-Helmholtz stable flow layer whose scale is large compared to the disturbances acts like a background vorticity which shears the eddies apart and suppresses the turbulence. The suppression is also energetic, as the main energy generation of the spectrum feels the flow shear as a sink. Energy is conserved between the eddies and

the background flow, so that the inverse cascade tendency manifests itself as a transfer from eddies to flow. In the presence of a background vorticity, the eddies build a Reynolds stress which effects this transfer, so the flow shear acts as a sink.

Zonal flows are the time dependent vorticity sheets which are directly generated by the turbulence. They form a sort of instability, in which the random but large amplitude fluctuations in the zonal Reynolds stress give rise to vorticity sheets which further amplify the Reynolds stress so as to transfer energy from eddies to flows with the same mechanism as for background flows. Zonal flows are part of the turbulence even when they do not suppress it, so the turbulence amplitude in saturation is usually lowered by the action of the flows.

Further Reading

The criteria for Kelvin-Helmholtz stability discussed in Section II are treated in most fluid dynamics textbooks, including *Hydrodynamic and Hydromagnetic Stability*, by S. Chandrasekhar (repr. Dover, 1981), and *Hydrodynamic Stability*, by P. G. Drazin and W. H. Reid (Cambridge, 1981). Extended criteria for flows in rotating or stratified systems are treated in most geophysical fluid dynamics textbooks, including *Atmosphere-Ocean Dynamics*, by A. E. Gill (Academic Press, 1982).

Shear flow suppression of plasma turbulence is a central topic of magnetic fusion energy research, reviewed along with fluid counterparts by P. W. Terry, *Phys. Plasmas* 7 (2000) 1653. Shear flow suppression via energetic means as a result of tilting of the turbulence eddies was first shown for drift wave turbulence by B. Scott, in *Plasma Phys. Contr. Fusion* 34 (1992) 1977.

The importance of zonal flow modification of low frequency turbulence was found by Z. Lin, T. S. Hahm, W. W. Lee, W. M. Tang, R. B. White, in Science 281 (1998) 1835. Zonal flow generation as time dependent shear flow suppression is treated analytically by T. S. Hahm, M. A. Beer, Z. Lin, G. W. Hammett, W. W. Lee, and W. M. Tang, in *Phys. Plasmas* 6 (1999) 922.

10. Inhomogeneous Magnetic Fields – Interchange Effects

B. Scott

Jul 1999

10.I. Introduction

In many situations the drift wave paradigm we have been developing does not apply. We have seen the important dependence of the dynamics upon the adiabatic response of the electrons, and of this in turn upon finite parallel wavelengths. It then follows that if in our physical situation parallel dynamics has no role, the something else must be invoked to explain the dynamics we see. This can happen if the parallel length scale is arbitrarily long, so that not only sound waves but also kinetic shear Alfvén waves are too slow to affect the perpendicular dynamics. It can also happen if the parallel dynamics is arbitrarily fast but the magnetic geometry allows a mode of oscillation with $k_{||} = 0$ for finite drift wavelength. In this latter case the dynamics is strictly two dimensional, and even the finite $k_{||}$ portion which involves drift wave dynamics is of negligible importance. We have seen some of this two dimensional element in Chapter 6 but will complete its development herein. It is also relevant to the three dimensional situation in which perpendicular forcing overwhelms the parallel responses and so dominates the action. This is the realm of interchange mode dynamics, and the cause of it is an inhomogeneous magnetic field, which gives rise to the perpendicular diamagnetic fluxes and a nonzero ExB divergence. These create an alternative pathway of energetic coupling between pressure disturbances and ExB flows, and hence to new instabilities, commonly called interchange modes.

The relationship between these interchange modes and drift waves is sufficiently subtle — and important — that we will leave it to the next chapter. For the present, the interchange dynamics takes center stage. We first study it in the simpler two dimensional model, and compare it to the Rayleigh Taylor forcing for neutral fluids. By contrast to that latter case, the interchange forcing conserves energy exactly and so forms a coupling mechanism, rather than a potential energy source as gravity would do, even if the mechanism for destabilisation is very similar. We next study the three dimensional version under the reduced MHD model, keeping the Alfvén dissipation of ExB flows but neglecting the pressure/current coupling which gives rise to drift waves. If the interchange forcing varies more or less sinusoidally in the direction along the magnetic field, then the basic 2D interchange mode is only excited where the gradients of the pressure and the magnetic field strength line up. In a toroidal magnetic field, the gradient of the magnetic field strength

and the radius of curvature are closely equivalent, so these are commonly called curvature effects. The modes they give rise to are called ballooning modes, because the region on which they are excited is localised to the outboard midplane of the torus, or where the alignment just described takes place. We need to understand the physics of these modes before comparing them to drift waves.

The model magnetic geometries discussed in this and the next chapter are very simple — we require consideration only of magnetic shear and curvature. More realistic geometry falls into the province of modelling rather than of fundamental physics, so we leave it to Appendix B.

10.II. Magnetic Divergences and the Interchange Model

We review the origin of the diamagnetic flux and ExB divergences and the new terms they introduce to the basic conservation laws, this time with specific attention to how they build the physical model for interchange dynamics. When the magnetic field is inhomogeneous, the drift operator is no longer divergence free. The drift operator is

$$\frac{c}{B^2}\mathbf{B}\times\nabla \tag{10.1}$$

acting on scalar quantities to produce vectors which are essentially axial. Acting on the electrostatic potential, it gives the ExB velocity, and acting on the total pressure it gives the diamagnetic current,

$$\mathbf{v}_E = \frac{c}{B^2}\mathbf{B}\times\nabla\phi \qquad\qquad \mathbf{J}_* = \frac{c}{B^2}\mathbf{B}\times\nabla p \tag{10.2}$$

The divergence of the drift operator, which we will call the curvature operator, is defined as

$$\mathcal{K} \equiv -\nabla\cdot\frac{c}{B^2}\mathbf{B}\times\nabla = -\left(\nabla\times\frac{c\mathbf{B}}{B^2}\right)\cdot\nabla \tag{10.3}$$

As the second form shows, $\mathcal{K}$ is only nonzero if the magnetic field is inhomogeneous. The simplest model magnetic field which gives rise to these magnetic divergence terms is a straight field with a perpendicular gradient in the field strength,

$$\mathbf{B} = B_0\left(1-\frac{x}{L_B}\right)\nabla s \tag{10.4}$$

in the same $\{x, y, s\}$ coordinate system we have been using. In the same spirit as for the background pressure, we may neglect the variation of B under drift ordering everywhere except where its gradient makes a term nonzero; in this case, the magnetic divergence

terms. The two vector fields $\mathbf{v}_E$ and $\mathbf{J}_*$ written above acquire finite divergences through this variation of $\mathbf{B}$,

$$\nabla \cdot \mathbf{v}_E = -\mathcal{K}(\phi) \qquad \nabla \cdot \mathbf{J}_* = -\mathcal{K}(p) \tag{10.5}$$

Under the simple slab model in Eq. (10.4) the curvature operator becomes

$$\mathcal{K} = -\left(\nabla\times\frac{c}{B}\nabla s\right)\cdot\nabla = -\frac{1}{L_B}\frac{c}{B}\left(\nabla x\times\nabla s\right)\cdot\nabla y = \frac{1}{L_B}\frac{c}{B}\frac{\partial}{\partial y} \tag{10.6}$$

If we scale the units of $\widetilde{\phi}$ and $\widetilde{p}$ as disturbances, we find, for example, that

$$\nabla \cdot \mathbf{v}_E = -\mathcal{K}(\widetilde{\phi}) = -\frac{cT_e}{eBL_B}\frac{\partial}{\partial y}\frac{e\widetilde{\phi}}{T_e} \tag{10.7}$$

Similarly, the divergence of the diamagnetic current becomes

$$\frac{1}{n_e e}\nabla \cdot \mathbf{J}_* = -\frac{1}{n_e e}\mathcal{K}(\widetilde{p}) = -\frac{cT_e}{eBL_B}\frac{\partial}{\partial y}\frac{\widetilde{p}}{p_e} \tag{10.8}$$

In a model with cold ions, the total pressure becomes p_e, and its fluctuation becomes $\widetilde{p}_e$. In an isothermal model, we have $\widetilde{p}_e = T_e\widetilde{n}_e$.

The simplest model for interchange dynamics consists of the four field model we have been studying, with the magnetic divergences but without the parallel dynamics. The parallel flows, $\widetilde{u}_{\|}$ and $\widetilde{J}_{\|}$ are therefore set to zero, leaving only $\widetilde{p}_e$ and $\widetilde{\phi}$ as dependent variables. Since we are deferring the diamagnetic heat flux until the discussion of temperature effects in Chapters 12 and 13, we are restricted to an isothermal model, with $\Gamma = 1$ and therefore $\widetilde{p}_e = T_e\widetilde{n}_e$. With $\widetilde{u}_{\|} = \widetilde{J}_{\|} = 0$ we have the hydrodynamic limit of the perpendicular dynamics, with addition of the magnetic divergences. The normalised equations appear as

$$\frac{d_E}{dt}\nabla_\perp^2\widetilde{\phi} = -\omega_B\frac{\partial\widetilde{p}_e}{\partial y} \tag{10.9}$$

$$\frac{d_E\widetilde{p}_e}{dt} = -\omega_n\frac{\partial\widetilde{\phi}}{\partial y} - \omega_B\frac{\partial}{\partial y}\left(\widetilde{p}_e - \widetilde{\phi}\right) \tag{10.10}$$

All terms are as in Chapter 6, with the profile scale given by $L_\perp$ and the pressure gradient given by

$$\omega_n = \frac{L_\perp}{L_p} \tag{10.11}$$

where L_p is the pressure scale length. The new parameter is the interchange forcing, entering through L_B and $\mathcal{K}$,

$$\mathcal{K} = \omega_B\frac{\partial}{\partial y} \qquad \omega_B = \frac{L_\perp}{L_B} \tag{10.12}$$

In a computation of two dimensional interchange dynamics, the only parameters are ω_n, usually set to unity, and ω_B, which for a low-beta plasma is smaller. We additionally have the system size, since the disturbance perpendicular length scale is normalised to ρ_s.

These new terms give rise to a energetic coupling between $\widetilde{p}_e$ and $\widetilde{\phi}$ which the purely hydrodynamic drift wave model lacks. The interesting property is that the coupling is reactive; that is, it is dissipation free. Interchange dynamics follows from the quasistatic compression of perpendicular flows, which although dynamically incompressible (since we still have $\omega \ll k_\perp v_A$) have a finite divergence through the drift motion in the inhomogeneous magnetic field. This compression mechanism must conserve energy during their transfer of energy between $\widetilde{\phi}$ (kinetic energy of ExB motion) and $\widetilde{p}_e$ (thermal energy), in the same way that parallel sound waves do. Multiplying Eq. (10.9) by $-\widetilde{\phi}$ and Eq. (10.10) by $\widetilde{p}_e$, and integrating over all space, we find

$$\frac{\partial}{\partial t}\int d^2x\,\frac{1}{2}\left|\nabla_\perp\widetilde{\phi}\right|^2 = \int d^2x\,\omega_B\,\widetilde{\phi}\,\frac{\partial\widetilde{p}_e}{\partial y} \tag{10.13}$$

$$\begin{aligned}\frac{\partial}{\partial t}\int d^2x\,\frac{1}{2}\left|\widetilde{p}_e\right|^2 &= -\int d^2x\,\omega_n\,\widetilde{p}_e\,\frac{\partial\widetilde{\phi}}{\partial y} + \int d^2x\,\omega_B\,\widetilde{p}_e\frac{\partial\widetilde{\phi}}{\partial y} \\ &= -\int d^2x\,\omega_n\,\widetilde{p}_e\,\frac{\partial\widetilde{\phi}}{\partial y} - \int d^2x\,\omega_B\,\widetilde{\phi}\,\frac{\partial\widetilde{p}_e}{\partial y}\end{aligned} \tag{10.14}$$

The total energy theorem is therefore

$$\frac{\partial}{\partial t}\int d^2x\,\frac{1}{2}\left(\left|\nabla_\perp\widetilde{\phi}\right|^2 + \left|\widetilde{p}_e\right|^2\right) = -\int d^2x\,\omega_n\,\widetilde{p}_e\,\frac{\partial\widetilde{\phi}}{\partial y} \tag{10.15}$$

So all we have is the gradient as a source, and the interchange effects cancel. The energy theorem is the same as that for the hydrodynamic limit of two dimensional drift waves, except we have the interchange coupling mechanism. There is no dissipation in the model at all, so instabilities tend to grow until the free energy source is depleted nonlinearly — if we do not allow this then the turbulence will never saturate. We can still study interchange turbulence qualitatively, but we will have to invoke an artificial dissipation mechanism to keep it stationary. Due to the inverse cascade dynamics in $\widetilde{\phi}$ we will find that high-$k_\perp$ dissipation does not suffice; we will have to add low-$k_\perp$ dissipation.

10.IV. The Ideal Interchange Mode

We here introduce the ideal interchange as a linear instability. The linearised equations are those of Eqs. (10.9,10.10) without the nonlinear terms,

$$\frac{\partial}{\partial t}\nabla_\perp^2\widetilde{\phi} = -\omega_B\frac{\partial\widetilde{p}_e}{\partial y} \tag{10.16}$$

$$\frac{\partial\widetilde{p}_e}{\partial t} = -\omega_n\frac{\partial\widetilde{\phi}}{\partial y} - \omega_B\frac{\partial}{\partial y}\left(\widetilde{p}_e - \widetilde{\phi}\right) \tag{10.17}$$

Taking a single Fourier component,

$$\widetilde{p}_e(x,y,t) = \widehat{p}_e\exp[i(k_x x + k_y y - \omega t)] \tag{10.18}$$

where $\widehat{p}_e$ is now the complex amplitude, we solve Eq. (10.17) for $\widehat{p}_e$ in terms of $\widehat{\phi}$,

$$\widehat{p}_e = \frac{\omega_* - \omega_c}{\omega - \omega_c}\widehat{\phi} \tag{10.19}$$

where $\omega_* = \omega_n k_y$ and $\omega_c = \omega_B k_y$ are the diamagnetic and interchange drift frequencies. Using this we can eliminate $\widehat{p}_e$ in Eq. (10.16) and then solve it for ω,

$$\omega k_\perp^2(\omega - \omega_c) = -\omega_c(\omega_* - \omega_c) \tag{10.20}$$

If we take the large scale limit ($k_\perp^2 \to 0$ and $k_y \to 0$ but with the aspect ratio $k_y^2/k_\perp^2$ finite), we find

$$\gamma^2 = -\omega^2 = \frac{k_y^2}{k_\perp^2}\omega_B(\omega_n - \omega_B) \tag{10.21}$$

which is a purely growing mode if $\omega_n > \omega_B > 0$. That is, the gradient of B must be aligned with that of p, but it must not be too large (we note however that if $\omega_B > \omega_n$ then the low beta assumption of the equilibrium would break down). The maximum value of this growth rate is known as the ideal interchange growth rate,

$$\gamma_I = \frac{c_s}{(L_p L_B)^{1/2}} \tag{10.22}$$

in physical units. This is the classic interchange instability of MHD, since we derived it without any effect from the parallel current (with $\widetilde{J}_\parallel = 0$ the drift wave regime is not invoked) and we see that an instability results for arbitrarily large scale.

The long wavelength limit is particularly similar to the classic Rayleigh Taylor instability of a stratified fluid under gravity, since the main forcing term for the flows themselves has the same form. For the governing equations we take the two dimensional Boussinesq

ideal fluid model, which starts with the ideal fluid equations but then neglects compressional effects everywhere except where the density disturbance multiplies gravity,

$$\rho\left(\frac{\partial \mathbf{v}}{\partial t}+\mathbf{v}\cdot\nabla\mathbf{v}\right)=-\nabla p+\widetilde{\rho}g\nabla x \tag{10.23}$$

$$\frac{\partial p}{\partial t}+\mathbf{v}\cdot\nabla p=0 \tag{10.24}$$

with ρ the mass density, $\widetilde{\rho}$ its disturbance, and $g\nabla x$ the gravity vector. The gravity vector is down the background gradient, in the x-direction, and motion is in the xy-plane. Taking the stream function and vorticity defined as

$$\mathbf{v}=\hat{\mathbf{s}}\times\nabla\phi \qquad\qquad \Omega=\hat{\mathbf{s}}\cdot\nabla\times\mathbf{v}=\nabla_\perp^2\phi \tag{10.25}$$

with $\hat{\mathbf{s}}=\nabla x\times\nabla y$ the normal to the plane, we find

$$\left(\frac{\partial}{\partial t}+\mathbf{v}\cdot\nabla\right)\Omega=\hat{\mathbf{s}}\cdot\nabla\times(\widetilde{\rho}g\nabla x)=-\hat{\mathbf{s}}\times g\nabla x\cdot\nabla\widetilde{\rho} \tag{10.26}$$

The linearised form of this replaces $\widetilde{\rho}$ by $(\rho/\Gamma p)\widetilde{p}$, where Γ is the ratio of specific heats, finding

$$\frac{\partial}{\partial t}\nabla_\perp^2\widetilde{\phi}=-\frac{g}{\Gamma p}\frac{\partial\widetilde{p}}{\partial y} \qquad\qquad \frac{\partial\widetilde{p}}{\partial t}=-\frac{p}{L_p}\frac{\partial\widetilde{\phi}}{\partial y} \tag{10.27}$$

The forcing by gravity in the Boussinesq fluid model is the same as the forcing by curvature in the plasma interchange model, and except for the extra y derivatives in the latter model the two are basically the same. However, gravity functions as a potential energy source in the Boussinesq fluid model, while in the plasma interchange model the interchange forcing is merely a transfer mechanism. Hence, the analogy, while useful for understanding, should not be overdone. What actually takes place in the plasma interchange model is that the pressure disturbance in a magnetised plasma gives rise to a diamagnetic current, and then if there is a magnetic field gradient (equivalently, curvature) this current has a nonzero divergence. Charges would build up but in this case of low frequency dynamics what does build up is ExB vorticity, as the polarisation current compensates the divergence of the diamagnetic current. This ExB vorticity represents flow both down and up the gradient, but if $\nabla p\cdot\nabla B>0$ the down gradient flow is through a pressure enhancement, so there is net transport. In other words, the phase shift of the pressure ahead of the electrostatic potential in the electron drift direction is $\pi/2$, or the ideal value for an instability. The reason for the energetic difference is that gravity forms a true potential energy, while compression is generally a conservative transfer mechanism.

We now investigate the turbulence. A simple case will suffice to show that it does not saturate unless we include some form of long wavelength dissipation. We take $\omega_n = 1$ and $\omega_B = 0.1$, and start a simple initial pressure disturbance with

$$\widetilde{p}_e = A_0 \exp\left(-\frac{x^2+y^2}{\Delta_\perp^2}\right) \qquad \widetilde{\phi} = 0 \tag{10.28}$$

parameterised by an initial amplitude and scale, which we set to $A_0 = 10^{-8}$ and $\Delta_\perp = 6$. We let the domain size be given by a minimum wavenumber $K = 0.1$, with $L_x = L_y = 2\pi/K$ on a 64×64 grid. As a form of long wavelength damping, we take a cue from the results of the dissipative coupling model in Chapter 6, and dissipate $\widetilde{\phi}$ homogeneously in the vorticity equation with a constant coefficient, γ_d, set to 0.01. The equations to solve are

$$\frac{\partial}{\partial t}\nabla_\perp^2\widetilde{\phi} = -\mathbf{v}_E \cdot \nabla\left(\nabla_\perp^2\widetilde{\phi}\right) - \omega_B\frac{\partial \widetilde{p}_e}{\partial y} + \gamma_d\widetilde{\phi} \tag{10.29}$$

$$\frac{\partial \widetilde{p}_e}{\partial t} = -\mathbf{v}_E \cdot \nabla\left(\widetilde{p}_e + p_e\right) - \omega_B\left(\frac{\partial \widetilde{p}_e}{\partial y} - \frac{\partial \widetilde{\phi}}{\partial y}\right) \tag{10.30}$$

with $p_e = -x$ representing the background gradient. The numerical methods are those of the hydrodynamic Eulerian model of Chapter 6, Section IV, with the ExB advection using the MUSCL scheme of Appendix A and the terms involving ω_B and γ_d evaluated explicitly as external drives, using centered differences for $\partial/\partial y$.

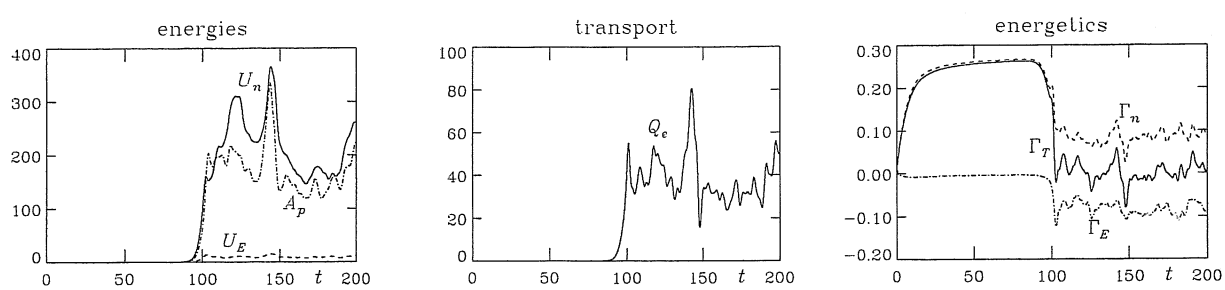

Figure 10.1. Time evolution of the 2D interchange model, for the case with $\omega_B = 0.1$ and $\gamma_d = 0.01$. (left) Half squared amplitude of $\widetilde{\phi}$, denoted A_p and the free energy density components, U_E for the ExB eddies ($\widetilde{\phi}$) and U_n for the density, noting that U_n is also A_n. (center) The transport caused by the turbulence. (right) Growth rate (Γ_T), gradient drive rate (Γ_n), and total dissipation rate (Γ_E). The linear growth phase proceeds until the rapid saturation after about $t = 100$.

This model can be described as two dimensional interchange turbulence with saturation due to long wavelength damping. The time traces in Fig. 10.1 show a linear growth phase which develops after the most unstable eigenmodes emerge near $t = 20$. This proceeds to about $t = 90$ whereupon the total growth rate crashes to zero. The drive rate, eventually settling near $\Gamma_n = 0.1$, is balanced mostly by the high Reynolds number numerical dissipation (as discussed in Chapter 6), with a slight contribution from γ_d more noticeable in the linear phase as the difference between Γ_n and Γ_T. The rise of the transport from the linear regime to saturation shows how rapid the nonlinear interactions are, and how limited the linear growth phase can be, even with the initial amplitude of 10^{-8} and an initial disturbance which is very far from filling the xy-domain.

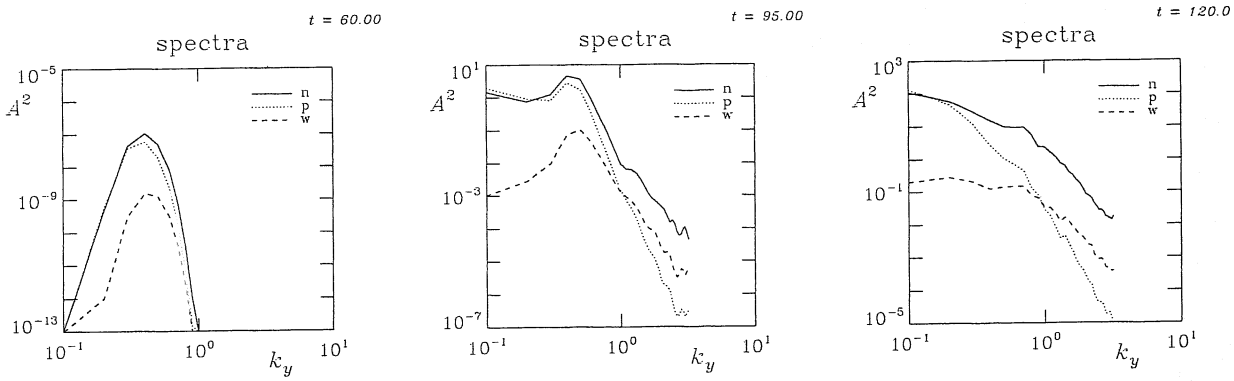

Figure 10.2. Amplitude spectra of the disturbances for $\widetilde{\phi}$, $\widetilde{p}_e$, and the vorticity, drawn with dotted, solid, and dashed lines, respectively. The time frames are from the linear growth (left), initial saturation (center), and turbulence (right) phases at $t = 60$, 95, and 120, respectively. Nonlinear interactions start spreading ExB energy towards longer wavelengths before any other nonlinear change is noticeable, and then the spreading of the spectrum at saturation is very rapid.

The spectrum, shown in Fig. 10.2, spreads out after about $t = 90$ from the initially dominant unstable range of about $0.3 < k_y < 0.5$, filling out as saturation is reached near $t = 100$, and is then stationary after about $t = 120$. The first two k_y components are dominant in the saturated phase. The first nonlinear change that is noticeable is the spreading of ExB energy towards longer wavelengths, here seen in the slight upturn of low-k_y vorticity even at $t = 60$, and then the spreading of the spectrum at saturation is very rapid. The near equality of the amplitudes of $\widetilde{\phi}$ and $\widetilde{p}_e$ is fortuitous, due to this choice of γ_d, as there is no special mechanism forcing $\widetilde{\phi}$ and $\widetilde{p}_e$ towards each other.

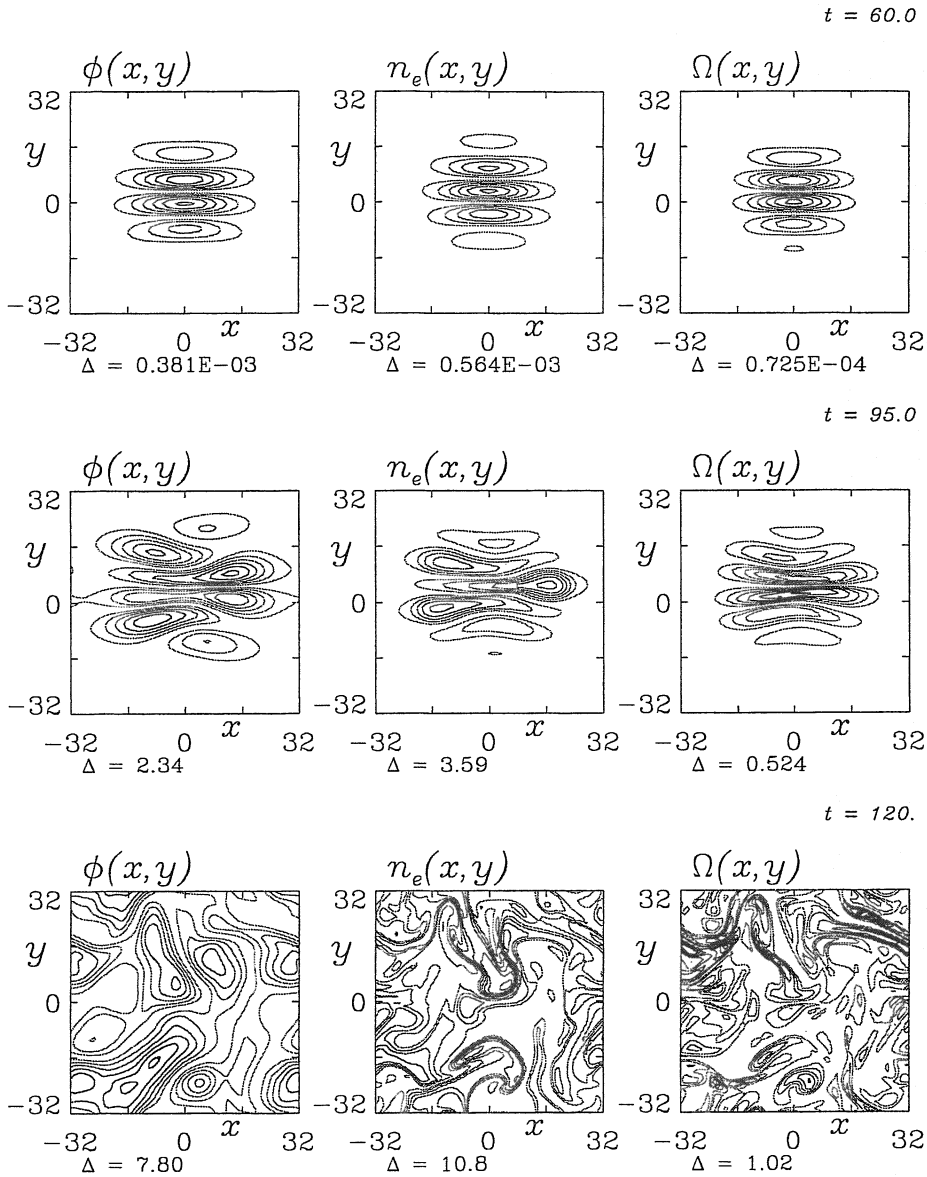

Figure 10.3. Evolution of the disturbances of $\widetilde{\phi}$, $\widetilde{p}_e$, and the vorticity (left to right), for the 2D interchange model, for the case with $\omega_B = 0.1$ and $\gamma_d = 0.01$. The time frames are from the linear growth (top), initial saturation (center), and turbulence (bottom) phases at $t = 60$, 95, and 120, respectively. The nonlinear interactions represent ExB vortex merger and shearing apart of advected quantities, including the ExB flow vorticity itself.

The contours of the disturbances are shown in Fig. 10.3, for the same three snapshots as the spectra in Fig. 10.2. The linear growth phase describes an eigenmode with a phase shift of a quarter wavelength of $\widetilde{p}_e$ ahead of $\widetilde{\phi}$, representing maximum growth and transport. A completely developed linear eigenmode of a single Fourier component would fill out the y-

domain, but before that happens the nonlinear interactions start. The actual displacement of the $\widetilde{p}_e$ disturbances by the ExB eddies is of course nonlinear, resulting from $\widetilde{\mathbf{v}}_E \cdot \nabla \widetilde{p}_e$. The nonlinearities spread the spectrum out, and then each eigenmode accesses free energy on its own, leading to the rapid saturation seen in Fig. 10.1. The fully developed turbulent state fills the entire domain, and the hydrodynamic nature of the interchange turbulence is seen in the sheetlike nature of $\widetilde{p}_e$ and the vorticity. The peculiar morphology of the interchange turbulence is the mushroom cloud appearance of the pressure/density disturbances as the flows driving them form fronts.

10.VI. Radial Flows versus Zonal Flows

We will return to this case to discuss interchange mode structure below, but first we have to address the role of this long wavelength damping we have artificially set, and the fact that it is what causes the saturation in the two dimensional model. The general parlance for the down-gradient flows which drive interchange turbulence is "radial flows" since the physical systems in which convecting flows are usually discussed are gravitationally confined spherical stars or spherical-shell atmospheres, and flows from core regions towards edge regions in a cylindrical or toroidal plasma. These radial flows appear explicitly in the energy theorem (Eq. 10.15), as the term $-\partial\widetilde{\phi}/\partial y$ multiplying $\widetilde{p}_e$ and the gradient strength ω_n. In a nonlinear system, however, we have at the same time the tendency to drive zonal flows, which are perpendicular to the radial flows, by means of the inverse cascade of ExB flow energy. These two mechanisms act against each other, and one or the other will take control. In the case just discussed, zonal flows are present but they are effectively damped by γ_d, as we see no tendency of the amplitude of $\widetilde{\phi}$ to rise with time in Fig. 10.1.

If we remove γ_d and the zonal flows as well, we find that the turbulence grows without bound. Interestingly, this is not simply the case of a linear instability which does not saturate. The disturbances do experience the onset of saturation during the same time interval $60 < t < 95$ as in Fig. 10.1, but the nonlinear interactions serve merely to dump most of the free energy into the lowest $k_y \neq 0$ eigenmode, which then grows as in the linear phase, and without the zonal flows the eigenmode with $k_x = 0$ and $k_y = 1$ (normalised to K) is the lowest mode into which the ExB energy can be transferred. It is also the mode which is most strongly driven, with $\gamma_d = 0$.

Now, we turn the zonal flows back on but keep $\gamma_d = 0$, advancing Eqs. (10.9,10.10) with no artificial effects. What we find now is that the competition between linear drive and nonlinear transfer is won by the zonal flows. The turbulence grows and rapidly saturates as in the other cases but now the nonlinear interactions place energy into the eigenmode

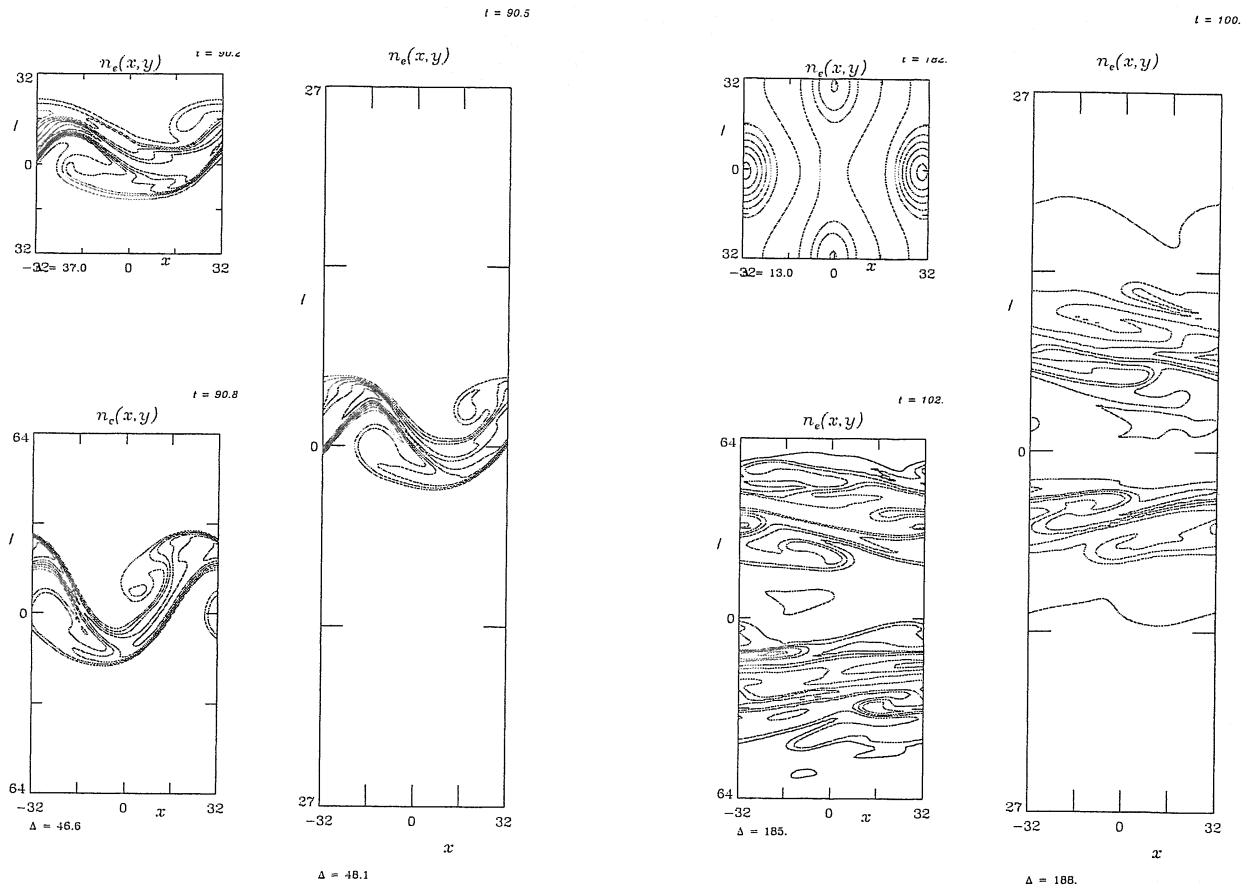

Figure 10.4. (left) Density contours showing the initial breakup of the radial jet for the case $\omega_B = 0.1$, no damping, and with zonal flows, for the three domain aspect ratios $L_y/L_x = 1$, 2, and 4. The times are slightly different due to the run details, but the breakup does not feel the y-boundaries because the region it occupies is small. (right) End state of the three cases. The case with aspect ratio unity collapses into a zonal flow as the diagonal pattern of the jet breakup leads to a coherent state dominated by the two Fourier components $(1,0)$ and $(1,1)$. But the spurious nature of that result is shown by the other two cases, which develop a radial flow wide enough not to be Kelvin-Helmholtz unstable.

with $k_x = 1$ and $k_y = 0$ unimpeded by either γ_d or by the elimination of the zonal flow component ($\widetilde{\phi}$ with $k_y = 0$). This zonal flow then rips apart the dominantly radial eddies with $k_y > k_x$, immediately shutting off the free energy access. What remains is a nonlinear state with all the energy in the components with $k_x = 1$ and $k_y = 0$ or ± 1, dynamically aligned ($\widetilde{p}_e$ and $\nabla_\perp^2 \widetilde{\phi}$ functions of $\widetilde{\phi}$) such that the nonlinearities are zero and such that the net drive is zero — $\widetilde{p}_e$ and $\widetilde{\phi}$ are antialigned with a phase shift of π. The initial breakup and end states are shown in Fig. 10.4. In the case of the random phase initial state used

Table 10.1. Saturated amplitudes, transport, and energetics for the damped case with $\omega_B = 0.1$ and $\gamma_d = 0.01$, for the three aspect ratios of the computational domain. The results show good convergence.

L_y/L_x	U_E	U_n	Q_e	Γ_n	Γ_E	Γ_T
4	12.0 ± 1.6	303 ± 58	50.5 ± 10.3	0.0804 ± 0.009	-0.0806 ± 0.008	-0.0001 ± 0.014
2	12.2 ± 1.8	295 ± 59	49.7 ± 10.8	0.0813 ± 0.012	-0.0815 ± 0.014	-0.0002 ± 0.018
1	11.7 ± 3.2	284 ± 86	48.5 ± 17.5	0.0826 ± 0.019	-0.0827 ± 0.016	-0.0002 ± 0.025

in Chapter 6, the nonlinear interactions place enough energy into the $k_x = 1$, $k_y = 0$ component that the $k_y = \pm 1$ component is negligible.

So for computations done in a 1×1 doubly periodic domain, the zonal flows will emerge nonlinearly to shut the turbulence and associated transport off. But this result, as it happens, is for most situations of physical interest entirely spurious.

10.VII. Aspect Ratio Effects for Interchange Flows

One very important consideration is the fate of the flow dynamics according to the aspect ratio we take for the domain size. If the domain is square, that is, the aspect ratio is unity, the radial flows drive the system but the nonlinear transfer dynamics will drive the zonal flows strongly enough for these to shear apart and shut off the eddies with dominantly radial flow, such that a radial flow does not emerge and the turbulence is essentially aborted. But we must remember the results from the Kelvin-Helmholtz instability when discussing the fate of flows in realistic systems. The key feature of a periodic square domain is that a radial flow can only be half as wide as it is long. Going back to the outline of the Kelvin-Helmholtz problem in Chapter 9, Section II, we note that this radial flow can be broken up by secondary disturbances, or those that grow on the primary disturbance which is the radial flow. For a radial flow in a square domain, the longest possible wavelength of a secondary disturbance is larger than the width of the widest possible radial flow. In this case the widest radial flow is mode $(k_x, k_y) = (0, 1)$ which has a half width from peak to zero of $\Delta = L_y/4$, and the most dangerous secondary disturbance has $k_x = 2\pi/L_x$. We find that $k_x\Delta = \pi/2$, and for a sinusoidal flow profile this is sufficient for the Kelvin-Helmholtz instability (the second derivative enters with two factors of π).

In physical situations with convective type flows causing the instabilities and driving the disturbances, the zonal/radial aspect ratio is always large. In the terrestrial atmosphere, for example, the height is about 10 km and the available width for mid-latitude

cyclonic disturbances is of order 1000 km. In the solar convection zone, the pressure scale height is less than 0.1 times the solar radius, to which the horizontal scale is comparable. These aspect ratios are larger than 10. In a cylindrical or toroidal plasma, the zonal periodicity length is at least as large as the radius (for a torus, the minor radius), while the profile scale length in the important regions is much smaller. In order to ascertain the relative importance of radial and zonal flows for any type of instability or turbulence we wish to apply to such situations, we have to make sure the results do not depend on this aspect ratio. We must go to larger aspect ratios until we find convergence.

We take the same damped case above, with $\omega_B = 0.1$ and $\gamma_d = 0.01$, with the same domain size in the x-direction, but with various sizes in the y-direction, with the aspect ratio L_y/L_x set to 1, 2 and 4, respectively. To keep the same small scale dynamics, we let the number of grid points in the y-direction go with the aspect ratio, using grids of 64×64, 128, and 256, respectively. This corresponds to a minimum $k_y\rho_s$ of 0.1, 0.05, and 0.025, respectively, where the above case with $L_y = L_x$ has 0.1; all cases have a minimum $k_x\rho_s$ of 0.1. Statistics are averaged over the interval $200 < t < 600$. The saturated amplitudes, transport, and energetics are listed in Table 10.1, and these show no dependence on the aspect ratio. The approach to saturation is different because of the initial state — it takes longer for the turbulence to fill the entire domain in the case of a larger aspect ratio. But the saturated state has no memory of this.

In the cases with no damping ($\gamma_d = 0$) but with zonal flows, the results are different, as shown by the other frames in Fig. 10.4. We found above that for the case with aspect ratio unity the zonal flows enter to shut the instability and the turbulence off. However, with larger aspect ratios this scenario is not found. Instead, the radial flows continue indefinitely. In all three cases the initial transition to nonlinearity is the same, since the initial state and the jet it produced occupy a region quite smaller than L_y even for the case with aspect ratio unity. But as we saw, the component with $k_yL_y = 2\pi$ (the lowest k_y) eventually dominates if the radial flows persist. The initial jet breaks up due to the Kelvin-Helmholtz process, but then the subsequent radial flow attempts to fill the domain. If the aspect ratio is unity, even this wider radial flow breaks up and turns into a zonal flow. But with aspect ratios of 2 and larger, the widest possible radial flow is no longer Kelvin-Helmholtz unstable. The fate of interchange turbulence therefore depends on the domain aspect ratio, whether or not other eigenmode types are present. An aspect ratio of at least two is required to find if a radial flow will emerge and take over the dynamics, even if cases without dominant radial flows converge well for aspect ratio unity. We will have to keep this in mind while investigating the three dimensional cases involving several eigenmode types, in the next few chapters.

Table 10.2. Saturated amplitudes, transport, and energetics for the damped case with $\omega_B = 0.1$ and $\gamma_d = 0.01$, for the unity aspect ratio case with three grid resolutions. The results show moderate convergence, within the error bars but with a noticeable trend, especially in U_n, as discussed in the text.

N_xN_y	U_E	U_n	Q_e	Γ_n	Γ_E	Γ_T
64^2	11.7 ± 3.2	284 ± 86	48.5 ± 17.5	0.0826 ± 0.019	-0.0827 ± 0.016	-0.0002 ± 0.025
128^2	12.5 ± 3.0	242 ± 84	41.0 ± 16.0	0.0808 ± 0.016	-0.0814 ± 0.016	-0.0006 ± 0.026
256^2	12.9 ± 2.3	225 ± 48	36.3 ± 10.2	0.0764 ± 0.013	-0.0784 ± 0.010	-0.0020 ± 0.018

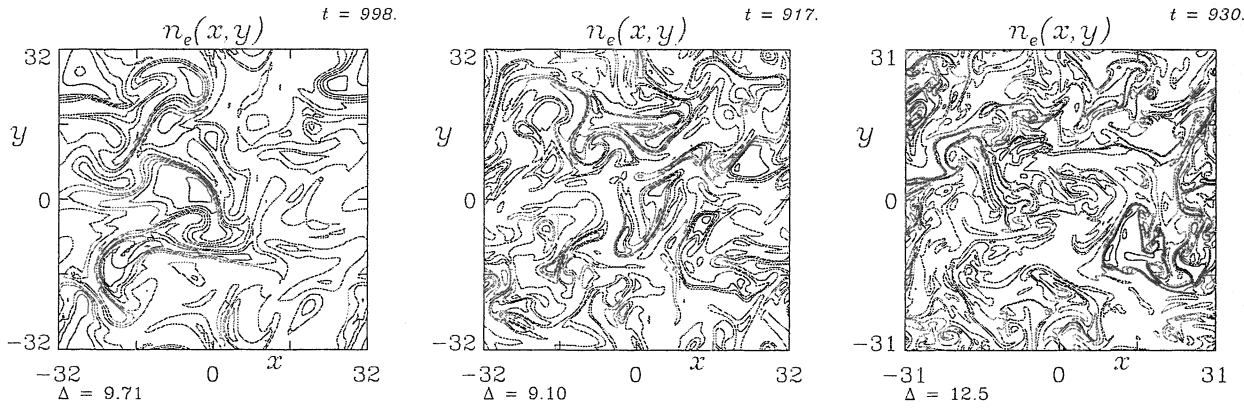

Figure 10.5. Structure of pressure/density disturbances in saturated interchange turbulence with $\omega_B = 0.1$ and $\gamma_d = 0.01$, for 64^2 (left), 128^2 (center), and 256^2 grid nodes, showing the effects of finite resolution. This is very demanding since pure interchange turbulence has no short wavelength sinks and therefore builds a broad $\widetilde{p}_e$ spectrum through the direct cascade. The width of the sheet structures is the clearest effect, and we find a less "bursty" turbulence and transport for the higher resolution. The average transport values are 44.4 ± 15.4, and 39.4 ± 14.4, and 32.2 ± 8.0, respectively.

10.VIII. The Mode Structure of Interchange Turbulence

For the comparisons needed in the next few chapters we need to establish what the mode structure of interchange turbulence is, in order to distinguish it from the drift wave turbulence diagnosed in Chapter 7. A simple summary is sufficient. The mode structure was taken from the cases leading to saturated turbulence, namely, the damped cases with $\omega_B = 0.1$ and $\gamma_d = 0.01$, aspect ratios unity, and three values of the grid resolution, 64^2, 128^2, and 256^2.

The time traces and spectra, and the spatial morphology, have already been shown in Figs. 10.1–10.3. The three cases on the unity aspect ratio grid with the three resolutions are shown in Fig. 10.5. These show extremely nonadiabatic dynamics, as befits the lack of dissipative coupling in the pure interchange model. The energetics for the four aspect ratios $L_y/L_x = 1$, 2, and 4 appear in Table 10.1, showing the obvious result that gradient driving balances the cascade to small scales and on to dissipation, through $\mathbf{v}_E \cdot \nabla \widetilde{p}_e$. The effect of the grid resolution on these quantities for $L_y/L_x = 1$ appears in Table 10.2. Here we find moderate convergence, with all quantities within the error bars, but with a noticeable trend downward in the transport (Q_e) and thermal free energy content (U_n) for higher resolution. This is due to the tendency to form very fine sheets in the absence of strong cross coupling between $\widetilde{p}_e$ and $\widetilde{\phi}$, that is, the coupling through the curvature is quite weak, since $\omega_B \ll \mathbf{v}_E \cdot \nabla$. With higher resolution we find less "bursty" time traces; a large transport event involving a thin structure is more quickly broken up. This accounts for a lower average — apart from the large excursions in the less well resolved cases the transport in the three cases is about the same. The turbulence is close to the high Reynolds number regime, saturated via direct cascade even in the absence of explicit sinks in the equations, but the resulting drive spectrum is wide enough to require higher resolution than similar drift wave cases. We do however find that resolution does not affect the growth of the radial flows in the cases with no saturation.

The source/sink spectra and the amplitude distributions of the x-component of $\widetilde{\mathbf{v}}_E$ and of the transport are shown in Fig. 10.6. There is no sink, and the source peaks at low k_y. The transfer spectrum for $\widetilde{\phi}\mathcal{K}(\widetilde{p}_e)$ is also shown. It is identical to the source spectrum but a factor of 10 lower, since the source contains a factor of $\omega_n = 1$ while the transfer has the same form but replaces the factor with $\omega_B = 0.1$. This source maintains the disturbances against the transfer via cascade to ever smaller scales through $\widetilde{p}_e$. The extreme hydrodynamic character of the turbulence is reflected in the passive scalar distribution of $\widetilde{v}_E^x$ and in the skewness of the distribution of Γ_n. Compared to the linear drive term, the nonlinearities are almost 10 times stronger than they are for the dissipative drift wave case shown in Fig. 7.1, following the size of $U_n = A_n$. The cross coherence and phase shift distribution for the case with resolution 64^2 are shown in Fig. 10.7. These show a lack of cross coherence and a very wide phase shift distribution centered about the maximum driving value of $\pi/2$, forming a clear contrast to the pure drift wave cases discussed in Chapter 7.

The fact that most of the nonlinear transfer goes through $\mathbf{v}_E \cdot \nabla \widetilde{p}_e$ is shown in the spectral transfer diagrams shown in Fig. 10.8, which look very like the most hydrodynamic cases for the dissipative drift waves shown in Fig. 6.10. The transfers are all local cascades,

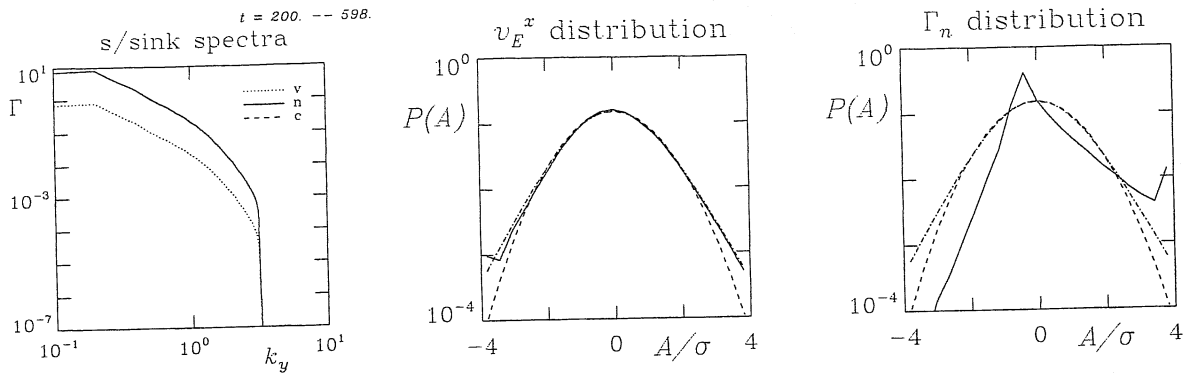

Figure 10.6. Source/sink spectra (left) and amplitude probability distributions of $\widetilde{v}_E^x$ (center) and the transport (right) for saturated interchange turbulence with $\omega_B = 0.1$ and $\gamma_d = 0.01$. The transfer over the curvature ('v') has the same form as the gradient drive, as they are both proportional to the transport but with factors of ω_n (unity) and ω_B, respectively. The down gradient velocity appears more passive scalar like than Gaussian, and the transport/drive is extremely skewed due to the strong driving. Contrast these with the drift wave mode structure in Figs. 7.3 and 7.6. Amplitude probability distributions for the state variables (not shown) look similar to those in Fig. 7.5.

and the direct cascade through $\widetilde{p}_e$ is by far the larger (in each diagram, M gives the maximum). With linear transfer minimal compared to the linear drive, the energetics for interchange turbulence is very simple: gradient drive at long wavelength, enough coupling to $\widetilde{\phi}$ with the same spectrum to maintain the ExB flows, and direct cascade through $\widetilde{p}_e$ to arbitrarily small scales where the disturbances are dissipated. This is very like the classic cases of fluid turbulence driven by stirring at the largest scales, and due to the absence of strong, adiabatic coupling it is very unlike drift wave turbulence.

10.IX. A Simple Model of a Toroidal Magnetic Field

We now turn to three dimensional interchange turbulence, in a model geometry which we can use to treat either slab geometry with interchange effects or a magnetic field lying in closed, toroidal surfaces. This will be kept very simple and heuristic here because we derive it in more detail in the next chapter. The model magnetic field is axisymmetric, with the toroidal component of the field the larger but with a poloidal component which is assumed not to vanish. A general model for such a field is given by the form

$$\mathbf{B} = I\nabla\phi + \nabla\Psi\times\nabla\phi \tag{10.31}$$

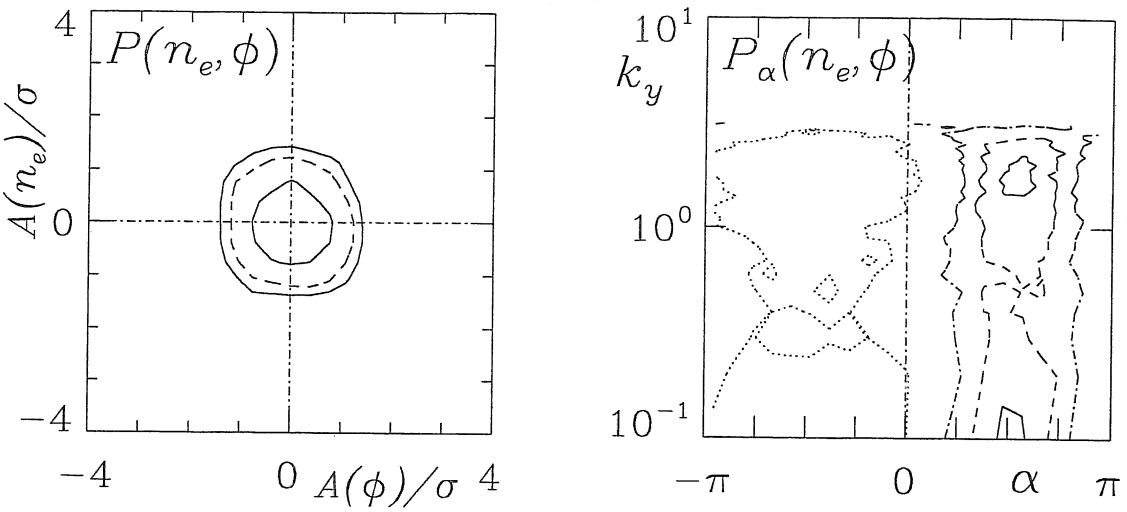

Figure 10.7. Cross coherence (left) and phase shift distributions (right), between $\widetilde{n}_e$ and $\widetilde{\phi}$ for saturated interchange turbulence with $\omega_B = 0.1$ and $\gamma_d = 0.01$. There is no cross coherence. The phase shifts peak at $\pi/2$ and the distribution is very wide, extending beyond the zero and wrapping around the branch cut at $\pm\pi$. These forms reflect the absence of an adiabatic response, since there is no parallel current dynamics in the interchange model. This is the most important contrast to drift wave mode structure as shown in Fig. 7.7.

where $\Psi = \Psi(R,z)$ is the poloidal flux function, $I = I(\Psi)$ gives the toroidal field, and (R,z,ϕ) is a simple, right handed, cylindrical coordinate system, in which the domain $0 < R < \infty$ and $-\infty < z < \infty$ may be called the poloidal plane. The condition that $I = I(\Psi)$ reflects the axisymmetry — there must be no $\mathbf{J}\times\mathbf{B}$ force along $\nabla\phi$. The condition that the equilibrium pressure $p = p(\Psi)$ reflects the MHD equilibrium, that is, since $\mathbf{J}\times\mathbf{B} = c\nabla p$ we must have $\mathbf{B}\cdot\nabla p = 0$. A magnetic field of this form has a field strength which is generally proportional to R^{-1}. The field gradient ∇B is therefore directed along $-\nabla R$, that is, towards the symmetry axis. The radius of curvature is the same, given by R with curvature towards the symmetry axis. This is why interchange turbulence is often referred to as curvature driven, since the curvature and field gradient are synonymous, as they also are for a cylinder with a purely azimuthal magnetic field.

The toroidal field geometry has a property which is different from a cylinder or slab, however — the interchange forcing is in the direction of the major radius but the pressure force is in the direction of the minor radius. These line up so as to cause the interchange instability on the outboard midplane of the torus, but on the inboard midplane they are antialigned, so that the curvature effects are stabilising. The magnetic field connects these

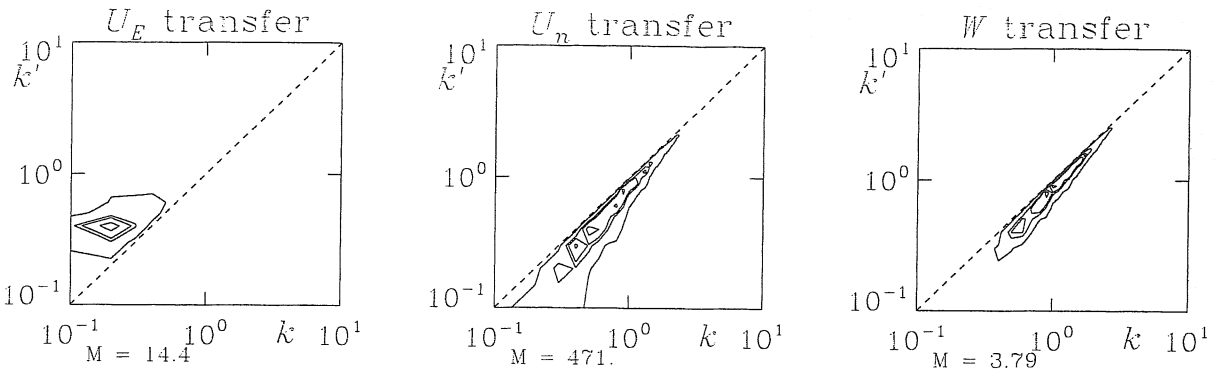

Figure 10.8. Energy and enstrophy transfer for saturated interchange turbulence with $\omega_B = 0.1$ and $\gamma_d = 0.01$. Left to right, the transfer from spectral range k' to k is shown for the ExB energy U_E, the thermal free energy U_n, and the enstrophy. Contours are drawn only where the transfer is positive, noting the symmetry about $k' = k$, so that activity above the dashed line shows an inverse transfer while activity below the dashed line shows a direct transfer. The cascade is local, with most of the activity near $k' = k$. This transfer dynamics is the same as in drift wave turbulence, as seen in Chapter 6.

two regions, so that on the same field lines there are locations where the interchange mechanism for instability is positive and others where it is negative. It is interesting to note that a negative interchange effect by itself does not imply damping, just neutral stability — from Eq. (10.20) one finds a real eigenmode frequency and therefore neutrally stable oscillation. If there is no magnetic shear to complicate the situation, we will have strong instability.

For the computational model, a thin flux tube is built from a small region in the drift plane on the outboard midplane side and then extended in each direction until the inboard midplane is reached. There, a matching condition is applied. For the same reason as in the periodic slab treated in Chapter 8, one cannot extend the flux tube beyond this periodicity length without violating global consistency. We demonstrate this result in the next chapter, and further in Appendix B, but for now we avoid its complication by neglecting magnetic shear and taking the pitch parameter of the field lines to be an integer. The pitch parameter is given by $q = L_\parallel/2\pi R$ with $L_\parallel$ the length traversed from the inboard midplane around to the bottom of the torus to the outboard midplane to the top of the torus continuing around until the inboard midplane is reached again. That is, $L_\parallel$ is the connection length and q gives the number of toroidal cycles for one poloidal cycle. The domain of the s-coordinate is $-\pi qR < s < \pi qR$, corresponding to the poloidal angle

domain $-\pi < \theta < \pi$. With q an integer we may apply simple periodicity at the $\theta = \pm\pi$ positions, where we use the same coordinate system as in Chapter 8. This situation is the same as the periodic, unsheared slab, with the sole addition of the curvature operator.

For the curvature operator we take into account the rotation of the curvature vector about the field line away from the radial (x) direction as one moves away from the $s = 0$ position at the outboard midplane. At $s = 0$ it is directed as in the two dimensional model in Eq. (10.12). As a function of position along s it varies sinusoidally with a wavelength of $2\pi qR$. We therefore have

$$\mathcal{K} = \mathcal{K}^x \frac{\partial}{\partial x} + \mathcal{K}^y \frac{\partial}{\partial y} = \frac{c}{B}\frac{2}{R}\left(\sin\theta \frac{\partial}{\partial x} + \cos\theta \frac{\partial}{\partial y}\right) \tag{10.32}$$

where $\theta = s/qR$. Working in a field aligned coordinate system, it is a simple matter to jump back and forth between a slab and a toroidal model. We will develop this further with all the complications of magnetic shear and boundary conditions in the next chapter.

10.X. Interchange in Three Dimensions — The Ballooning Mode

Since we do not treat any complications of toroidal geometry beyond this version of $\mathcal{K}$, we may merely add the necessary magnetic divergence, or in a toroidal magnetic field, curvature terms as in Eqs. (10.9,10.10) to the three dimensional slab model we looked at zonal flows in, in the previous chapter. However, we remove the two terms in the equations for the current and pressure, which do the drift wave coupling mechanism. In keeping with MHD ordering, we also remove the diamagnetic velocity in the pressure equation. The resulting model is the one which often goes by the name of reduced MHD. The equations are

$$\frac{d_E}{dt}\nabla_\perp^2 \widetilde{\phi} = \nabla_\parallel \widetilde{J}_\parallel - \mathcal{K}\left(\widetilde{p}_e\right) \tag{10.33}$$

$$\frac{d_E \widetilde{p}_e}{dt} = -\frac{\partial \widetilde{\phi}}{\partial y} - \nabla_\parallel \widetilde{u}_\parallel + \mathcal{K}\left(\widetilde{\phi}\right) \tag{10.34}$$

$$\hat{\beta}\frac{\partial \widetilde{A}_\parallel}{\partial t} + \hat{\mu}\frac{d_E \widetilde{u}_\parallel}{dt} = -\nabla_\parallel \widetilde{\phi} - C\widetilde{J}_\parallel - \hat{\beta}\frac{\partial \widetilde{A}_\parallel}{\partial y} \tag{10.35}$$

$$\hat{\epsilon}\frac{d_E \widetilde{u}_\parallel}{dt} = -\nabla_\parallel \widetilde{p}_e + \mu\nabla_\parallel^2 \widetilde{u}_\parallel + \hat{\beta}\frac{\partial \widetilde{A}_\parallel}{\partial y} \tag{10.36}$$

with $\widetilde{J}_\parallel$ and $\widetilde{A}_\parallel$ related through Ampere's law,

$$\widetilde{J}_\parallel = -\nabla_\perp^2 \widetilde{A}_\parallel \tag{10.37}$$

The ideal ballooning mode is found by neglecting the sound waves and taking only the part of Eq. 10.35, which says that $\widetilde{E}_{\parallel} = 0$, and then linearising Eqs. (10.33–10.35). The behaviour of $\widetilde{\phi}$ and $\widetilde{A}_{\parallel}$ is then the ideal MHD shear Alfvén response to the interchange forcing, and the dispersion relation is

$$\omega^2 = k_{\parallel}^2 v_A^2 - \gamma_I^2 \tag{10.38}$$

in physical units, where γ_I is the ideal interchange growth rate in Eq. (10.22). Instability results when $\omega^2 < 0$. If $k_{\parallel} = 0$ then we revert to the two dimensional ideal interchange instability. This is reduced by the Alfvén response, leading to a threshold in the pressure gradient in the case that $k_{\parallel}^2$ is set by the geometry. In a toroidal magnetic field $k_{\parallel}^2$ usually scales as $(qR)^{-2}$, yielding the standard ideal ballooning limit for the pressure gradient,

$$\alpha_M = -q^2 R \nabla \beta \tag{10.39}$$

with $\beta = 8\pi p/B^2$ the plasma beta with the total gas pressure. In the four field model the limit is

$$\alpha_M = \hat{\beta}\omega_B \tag{10.40}$$

with a critical value of unity. However, if there is no magnetic shear, then $k_{\parallel}$ is allowed to vanish, and we find instability and turbulence at all $\hat{\beta}$ for $\omega_B > 0$.

The initial state for the computations of Eqs. (10.33–10.36) was the same as in Chapter 8. The parameters were $\hat{\beta} = 1$, $\hat{\mu} = 1$, and $\nu = 1.0$, giving $C = 0.5$. The other parameters were $\hat{\epsilon} = 3670$ and $K = 0.025$. The domain size in the x-direction was 20π, giving an aspect ratio of $L_y/L_x = 4$. As in the similar case above, the grid was 32×128 grid nodes in the drift plane, and then the parallel direction was covered by 16 nodes, as in the sheared slab cases of Chapter 8. The boundary condition in the x-direction was Dirichlet, with the profile handling discussed in Chapter 9, Section VI. This is the only way to get a saturated state without resorting to the damping with γ_d as above.

The transport quickly rises to a high level and saturates after about $t = 200$. The runs were taken to $t = 1000$, and the mode structure was averaged over $500 < t < 1000$. The amplitude and energetics spectra are shown in Fig. 10.9. Very comparable to the end state in Figs. 10.2 and 10.6, the dynamics is dominated by the lower-k_y range of the spectrum, and $\widetilde{\phi}$ tends towards the steep spectrum of the extreme hydrodynamic limit. Interestingly, the magnetic flutter transport is present, but in this model it is always small as it comes solely from the ion sound waves through $\left\langle \widetilde{u}_{\parallel} \widetilde{B}^x \right\rangle$. The peak in the drive spectrum for Γ_n results from the aspect ratio, as mode 4 for the y-direction corresponds to mode 1 for the x-direction.

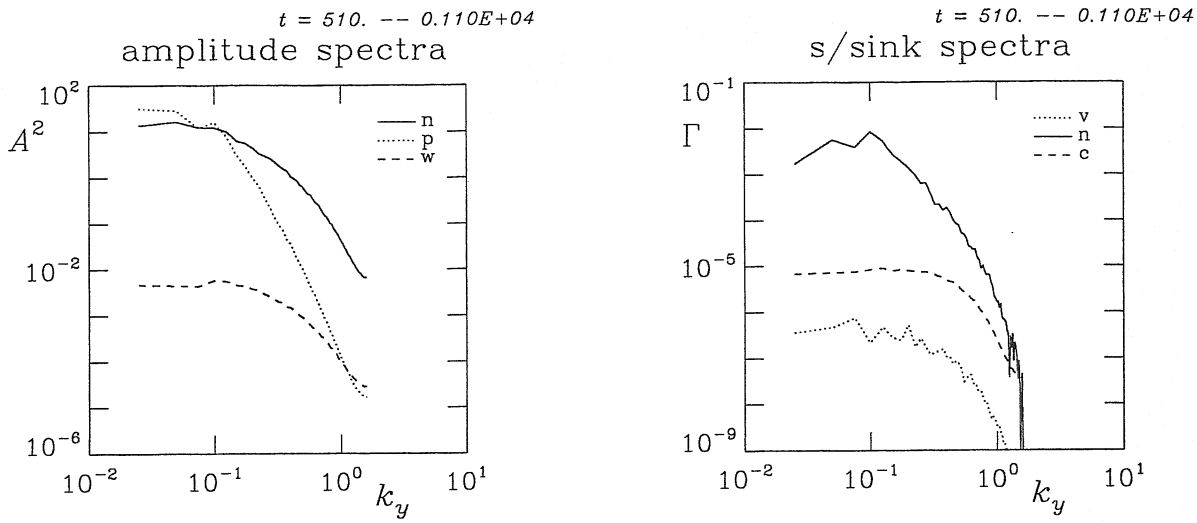

Figure 10.9. (left) Amplitude spectra of $\widetilde{n}_e$, $\widetilde{\phi}$,and $\nabla_\perp^2\widetilde{\phi}$, respectively labelled by 'n', 'p', and 'w'. (right) Spectra of the ExB gradient drive ('n'), dissipation ('c'), and the magnetic flutter drive ('v'). Compare with Figs. 10.2 and 10.6. Interchange turbulence has the same mode structure in two dimensions as in three.

What will turn out to be of great interest in the next chapter is the ingredients of the mode structure which make a clear difference between drift wave and interchange (ballooning) turbulence. The first of these is spectra of the vorticity dynamics, which we showed for drift wave turbulence in Chapter 8, Section VIII. In drift wave turbulence the size of $\nabla_\parallel \widetilde{J}_\parallel$ is controlled by the polarisation drift, which is the only possibility as there are no other effects in slab geometry. For interchange turbulence we also have the interchange forcing. In Fig. 10.10, the spectra are shown both for the vorticity dynamics (the rms levels of the terms themselves) and the energy transfer dynamics (the rms levels of the transfer terms in the energetics). The polarisation drift (recall this is merely the ion fluid inertia) is now negligible, both linearly and nonlinearly, and the interchange forcing closely balances the resulting size of $\nabla_\parallel \widetilde{J}_\parallel$, which is still relevant to interchange turbulence as although $\widetilde{\phi}$ is not coupled to $\widetilde{p}_e$ its finite amplitude now by itself depends on a finite $\nabla_\parallel \widetilde{J}_\parallel$.

The next two important diagnostics are the ones we already saw for two dimensional interchange turbulence in Section VIII, and for drift wave turbulence in Chapter 7 and Section VIII of Chapter 8. These are the cross correlation and phase shift diagnostics, shown for the ballooning case in Fig. 10.11. We find the same result as above for the two dimensional case, that $\widetilde{p}_e$ and $\widetilde{\phi}$ are uncorrelated and that the phase shifts are all close to $\pi/2$. There is a lot of scatter in the phase shifts, however, indicative of strong, randomised

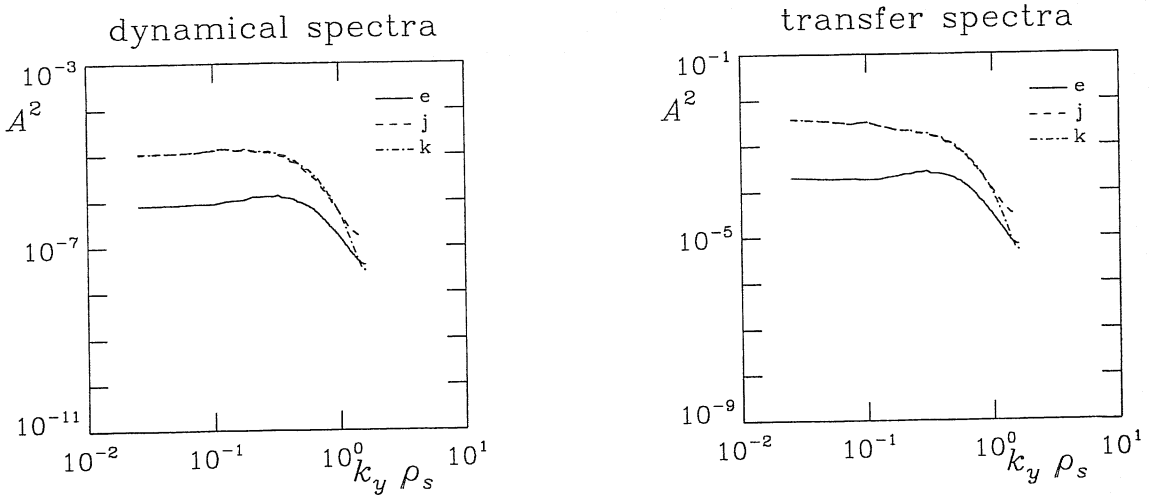

Figure 10.10. Dynamical and transfer spectra for the ExB vorticity, for three dimensional interchange turbulence. The solid, dashed, and dash-dot curves show the average sizes of $\mathbf{v}_E \cdot \nabla \nabla_\perp^2 \widetilde{\phi}$ and $\nabla_\parallel \widetilde{J}_\parallel$, and $\mathcal{K}(\widetilde{p}_e)$, and their associated transfer effects, for all k_y, respectively. The interchange forcing and the parallel current dynamics are in close balance, showing how the system maintains the flute mode character shown in subsequent figures. The vorticity nonlinearity (polarisation drift) plays a negligible role in interchange turbulence, by contrast to drift wave turbulence.

turbulence on top of the main plume structures which cause most of the transport. Only three contour levels are shown, in contrast to the drift wave cases where we can show four without too much clutter (the levels are 0.8, 0.5, 0.3, and 0.1 times the maximum in each case). The dominant effect in the pressure equation is simply ExB advection, which is the same randomising phenomenon leading to the direct cascade of free energy to high-$k_\perp$.

What we find concerning the parallel structure, is that in the absence of magnetic shear, the modes with $k_\parallel = 0$ become dominant. In the literature these are called convective cells, or flute modes. In Fig. 10.12, we see that the average amplitudes of the disturbances are nearly independent of s, and the transport, as expected, is maximum at $s = 0$. But the transport is positive even in the regions where the interchange forcing is negative. The mode structure is set up by the forcing where $\omega_B \cos s > 0$, and then the parallel dynamics spreads the disturbances out along the magnetic lines field such that it acquires a largely two dimensional structure. The slight structure in the amplitude envelopes arises from the sloshing behaviour in the parallel dynamics. There were no large differences observed in either the mode structure or the transport in companion cases with $\hat{\beta} = 3$, 10, and 30, just

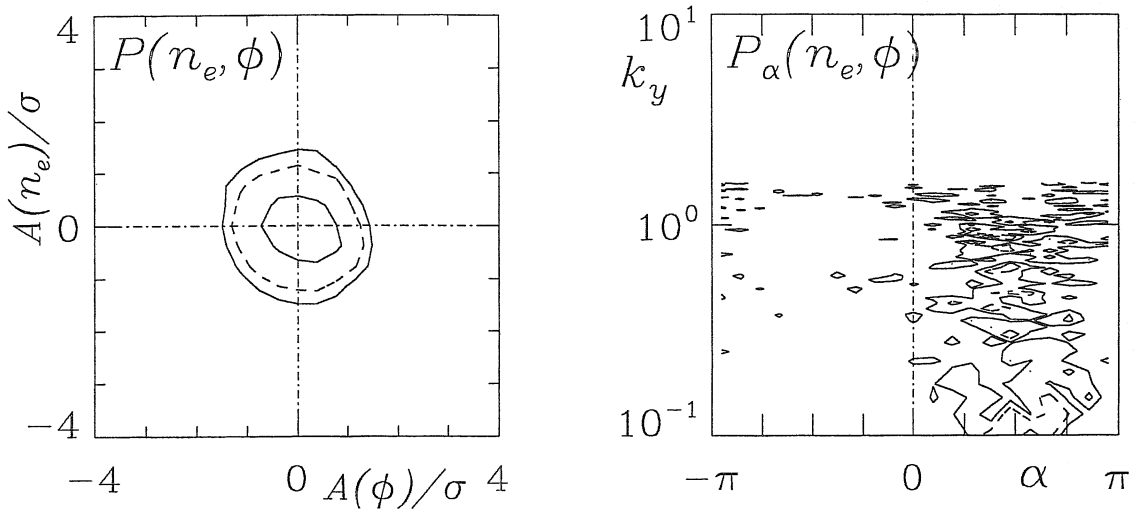

Figure 10.11. Cross coherence (left) and phase shift distributions (right), between $\widetilde{n}_e$ and $\widetilde{\phi}$, for three dimensional interchange turbulence. Compare with Fig. 10.7. These forms reflect the absence of an adiabatic response, by contrast to drift wave turbulence.

somewhat more parallel sloshing structure. The three dimensional morphology is shown in Fig. 10.13, wherein the flute mode character is obvious. There is no effect from the Alfvén dynamics on the pressure/density in this model, but the flute mode structure persists in $\widetilde{p}_e$ as well, since the principal effect in its equation is the nonlinear plus linear ExB advection, which obtains its flute mode structure from the effect of the Alfvén dynamics on $\widetilde{\phi}$.

10.XI. Summary

Interchange turbulence and its ballooning mode counterpart in three dimensions have a simpler physical basis and mode structure than drift wave turbulence. The quantity whose gradient is the free energy source develops disturbances via ExB advection in the gradient, and then nonlinear advection leads to the turbulence. The dynamics of the ExB flows arises from interchange forcing, which has the same physical role as Rayleigh-Taylor forcing on a neutral fluid, even though in this case the mechanism is a charge separation and does not constitute a potential energy source. The magnetic curvature which gives rise to the interchange forcing in fluid drift dynamics is a catalyst which allows free energy in the pressure disturbances to reach the electrostatic potential, and hence the ExB eddies. There is no strict cross coupling to consider, however, because the back reaction of the pressure on the ExB flows is smaller than the gradient drive level, by contrast to the

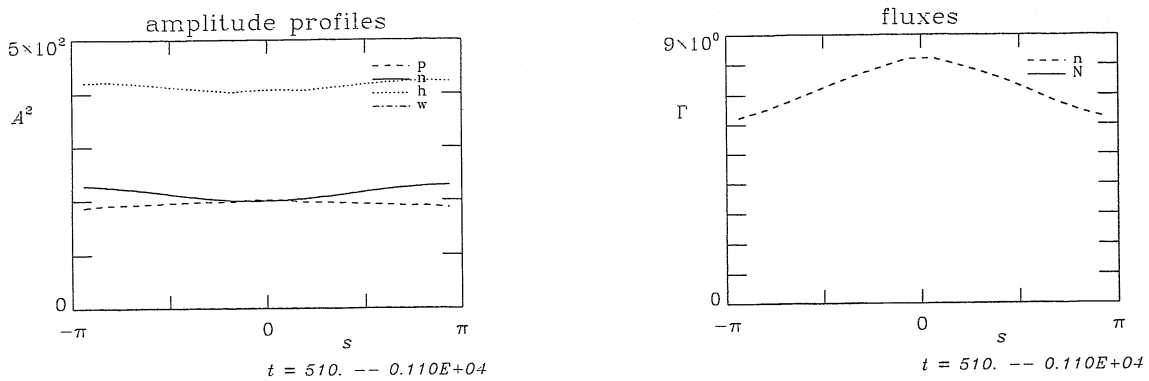

Figure 10.12. (left) Amplitude envelopes of $\widetilde{n}_e$, $\widetilde{h}_e$, $\widetilde{\phi}$, and $\nabla_\perp^2\widetilde{\phi}$, respectively labelled by 'n', 'h', 'p', and 'w'. This amplitude ordering $\widetilde{n}_e > \widetilde{\phi} > \widetilde{h}_e$ is a general feature of drift wave turbulence; to get $\widetilde{\phi} > \widetilde{n}_e$ requires the temperature. (right) Amplitude envelope of the ExB transport ('n'). The magnetic flutter transport is negligible on this scale.

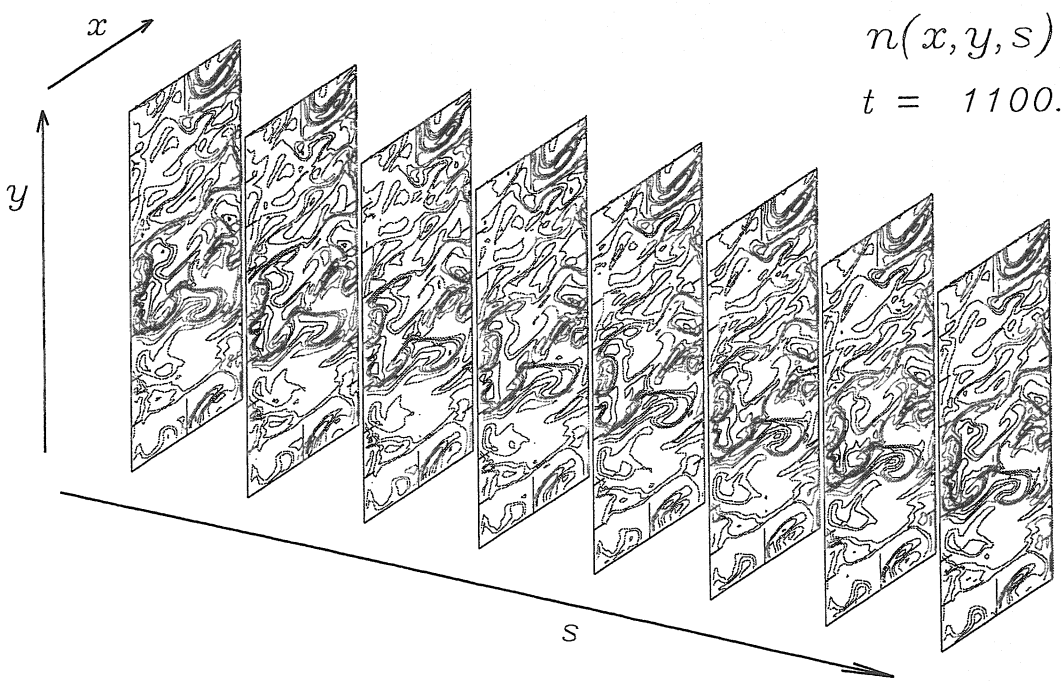

Figure 10.13. Three dimensional morphology of the density, $\widetilde{n}_e$, with the flux surface average subtracted out. Every second drift plane is shown. The flute mode is dominant, and the resulting morphology is the same as in the two dimensional cases even though the interchange forcing is positive only in the middle half of the flux tube.

situation with dissipative coupling. Relatively simple analytical modelling is therefore possible, comparable to what has been done in astrophysical fluid dynamics.

Interchange flows are primarily radial plumes, rather than more or less isotropic eddies. In a computation they are sensitive to the aspect ratio, and it is important to leave enough room in the purely periodic coordinate so as too avoid a spurious conclusion involving secondary instabilities of these flows — if the aspect ratio is too low, the widest possible radial flow is Kelvin-Helmholtz unstable and therefore the radial flows do not develop properly. Interchange turbulence has a wider spectrum than does drift wave turbulence, and in a situation where absolute transport levels are paramount one will require more resolution than was necessary here to investigate the basic physical properties.

We called the three dimensional interchange variant a ballooning mode because the interchange forcing is positive only on the outboard midplane region of a toroidal configuration. But the disturbances tend to build flute modes and only properly balloon when there is magnetic shear. We will see this in the next chapter, when we investigate both drift wave and interchange turbulence in a sheared toroidal magnetic field.

Further Reading

The ideal interchange and ballooning instabilities are treated in the texts on ideal MHD listed in Chapter 2. The resistive MHD paradigm for toroidally confined plasmas grows out of the reduced MHD model introduced by H. R. Strauss, in *Phys. Fluids* 20 (1976) 1354, and was advanced for fluidlike turbulence in toroidal magnetically confined plasmas by B. A. Carreras and P. H. Diamond, in *Phys. Fluids B* 1 (1989) 1011. MHD Interchange models in astrophysics are treated in the text by E. N. Parker, *Cosmical Magnetic Fields* (Clarendon Press, Oxford, 1979). For geophysical fluid dynamics see the text by J. Pedlosky, *Geophysical Fluid Dynamics* (Springer, 1992).

11. Drift Wave versus Interchange Turbulence

B. Scott

Jul 1999

11.I. Introduction — What to do with More Than One Eigenmode

We now treat a situation we have been delaying as long as possible. It is involved enough to study the properties of nonlinear drift wave turbulence or the radial flows of three dimensional interchange turbulence on their own. But in general we face situations in which there is potentially more than one type of instability, or even turbulence. We need to have developed the set of tools necessary to tell these apart before we address a multi-eigenmode situation, and we have done this in previous chapters. We now turn to a special but exemplary case, that of drift wave and interchange turbulence on closed, toroidal magnetic flux surfaces. We first establish the turbulence in saturated state and look at the mode structure. We then directly compare the multi-eigenmode situation to the two control cases we already know: drift wave or interchange turbulence acting in isolation. We also examine the differences between linear and nonlinear mode structure. Finally, we use these results to locate the boundaries in parameter space within which the MHD model is valid, or within which we must face the complication of drift wave dynamics. It is interesting to note that these regime boundaries can be different in turbulence than they are for linear instabilities.

11.II. Flux Tube Geometry for Toroidal Magnetic Surfaces

The simplest model of toroidal geometry adds the effects of the gradient and curvature of the magnetic field to the field line connection — toroidal topology and magnetic shear — which we introduced in Chapter 8. The details of the shape of flux surfaces in particular equilibria are neglected. We introduce the model heuristically, and note that it is a mathematical simplification of the general axisymmetric case, which is treated in Appendix B. It is the prototypical model of the tokamak concept (tokamak is an acronym for toroidal magnetic chamber in Russian), and so it is called the circular tokamak. The resulting localised magnetic geometry is the toroidal flux tube model. It is localised in the two perpendicular dimensions, in which the scale of the dynamics is small, but in the parallel direction the dynamics extends for an entire connection length, since parallel dynamics favours the longest allowed wavelengths, as we have already seen.

We assume nested, axisymmetric toroidal flux surfaces, whose cross section is circular, and for which the centers of the corresponding circles in the poloidal plane are all equal. For

a given surface, the minor radius is r and the major radius is R_0. While R_0 is a constant, r is a surface label and therefore useful as a coordinate. The other two coordinates are the angles θ and ζ, which are cyclic on the interval $[0, 2\pi]$.

The surface which has $r = 0$ is called the magnetic axis, and a reference surface at which the turbulence is to be evaluated has $r = a$, with a a constant. The aspect ratio of the reference volume is therefore R_0/a. The smallness parameter in which this model represents an expansion of an actual MHD equilibrium is

$$\epsilon = \frac{a}{R_0} \ll 1 \tag{11.1}$$

It is further assumed that finite pressure effects on the geometry are also negligible, which requires

$$\beta = \frac{8\pi p}{B^2} \ll 1 \tag{11.2}$$

The flux surfaces are therefore circular and concentric, and equilibrium quantities such as pressure are assumed to be functions of r only; equivalently, flux functions.

The only exception to this is the magnetic field, whose flux is a function of r only but whose strength varies inversely with $R = R_0 + r\cos\theta$. This is a result of geometry and is quite general for axisymmetric equilibria. The most general axisymmetric, divergence free vector field can be written in terms of the gradients of the toroidal angle and two scalar functions,

$$\mathbf{B} = I\nabla\zeta + \nabla\Psi\times\nabla\zeta, \tag{11.3}$$

where Ψ is independent of ζ and in order to avoid a toroidal component to $\mathbf{J}\times\mathbf{B}$ we require $I = I(\Psi)$. In the circular tokamak, we assume $\Psi = \Psi(r)$ and neglect all special features of the finiteness of a/R_0, except we face the fact that $\nabla\zeta$ generally varies inversely with R. This is the origin of the magnetic curvature effects in a toroidal field. Briefly, in an equilibrium where both ϵ and β are small, we can take I to be a constant and define the pitch parameter, $q(r)$, as

$$q = \frac{rB_{tor}}{RB_{pol}} \tag{11.4}$$

or equivalently

$$\frac{\partial\Psi}{\partial r} = \frac{I}{R}\frac{r}{q} \tag{11.5}$$

Both $p(r)$ and $q(r)$ can be chosen arbitrarily, since the changes to I necessary to maintain equilibrium are of order ϵ^2 and β. Among the finite ϵ departures from the circular tokamak model we are neglecting is the necessity of the circles to shift outward in the R-direction by an amount of order ϵa, the famous Shafranov shift, treated in elementary texts on MHD

and MHD equilibrium. In general, if this is important, so also are all the other finite ϵ effects.

Given the cylindrical coordinates (r, θ, ζ), we define slab like coordinates (x, y, s) to follow the unperturbed field lines:

$$x = r - a, \qquad y = \frac{a}{q_a}(q\theta - \zeta), \qquad s = q_a R_0 \theta, \tag{11.6}$$

where q_a is a normalising constant allowing y and s to be defined as simple distances. The factor of q in y is variable, allowing for shear through the parameter $\hat{s} = d\log q/d\log x$. The relationship of this model to the sheared slab of Chapter 8 is through the shear length, given by

$$L_s = \frac{qR_0}{\hat{s}} \tag{11.7}$$

The periodicity length $L_\parallel$ is replaced by $2\pi qR$, where the presence of q reflects the fact that the magnetic field lines close on a given flux surface poloidally, not toroidally, following from the use of y as a perpendicular coordinate.

The contravariant components of $\mathbf{B}$ are given by $B^\mu = \mathbf{B}\cdot\nabla x^\mu$, or

$$B^x = B^y = 0 \qquad B^s = B_0 = \frac{I}{R_0} \tag{11.8}$$

where B_0 is a flux function giving the strength of the magnetic field. In this low-ϵ model, B_0 like I is a constant. We therefore have x and y as perpendicular coordinates describing the drift plane, and s as a parallel coordinate.

We now specialise to drift ordering, and assume that the extent of the computational domain perpendicular to the magnetic field is small compared to a, so that we can neglect the difference between q and q_a except for the shear, and neglect the variability of factors of r in the coordinate metric. By computing the coordinate gradients ∇x^μ, with $x^\mu \in \{x, y, s\}$, we find the inverse metric components

$$g^{\mu\nu} = \nabla x^\mu \cdot \nabla x^\nu \tag{11.9}$$

and simplify using the assumptions that the perpendicular scale is small compared to a and to qR_0. This gives the perpendicular components of the inverse metric,

$$g^{xx} = 1 \qquad g^{xy} = \hat{s}\theta \qquad g^{yy} = 1 + \hat{s}^2\theta^2 \tag{11.10}$$

which are what we need to build the perpendicular Laplacian,

$$\nabla_\perp^2 = g^{xx}\frac{\partial^2}{\partial x^2} + 2g^{xy}\frac{\partial^2}{\partial x \partial y} + g^{yy}\frac{\partial^2}{\partial y^2} \tag{11.11}$$

Note that later, when we normalise s to $q_a R_0$, s becomes interchangeable with θ.

The magnetic curvature operator is given in general by

$$\mathcal{K} = -\nabla \cdot \frac{c\mathbf{B}\times\nabla}{B^2} = \mathcal{K}^x \frac{\partial}{\partial x} + \mathcal{K}^y \frac{\partial}{\partial y} \tag{11.12}$$

In a toroidal model with ϵ and β small, the only significant contribution to $\mathcal{K}$ arises from the action of the divergence upon the factor of B^2 in the denominator, which gives

$$\mathcal{K} = \nabla \log B^2 \cdot \frac{c\mathbf{B}\times\nabla}{B^2} \tag{11.13}$$

Instead of this combination of dot and cross products, it is often easier and safer to use the tensor formulation, according to which the magnetic part of the Maxwell stress tensor $\mathbf{F}$ is given by

$$\mathbf{F} = \epsilon \cdot \mathbf{B} \qquad\qquad F_{ij} = \epsilon_{ijk} B^k \tag{11.14}$$

where ϵ is the totally antisymmetric pseudotensor of rank three, and the subscripts and superscripts refer to the covariant and contravariant components. The pseudotensor has covariant components

$$\epsilon_{ijk} = \sqrt{g}\,[ijk] \tag{11.15}$$

where g is the determinant of the metric tensor,

$$g = \det g_{ij} = \left(\det g^{ij}\right)^{-1} \tag{11.16}$$

and $[ijk]$ is the sign of the permutation of the coordinate indices relative to $\{x, y, z\}$. In the circular tokamak model, we have $g = 1$, and so the contravariant and covariant components of ϵ are all either ± 1 or 0. Coordinate systems which have this property generally are called Hamada flux coordinates, which are treated in Appendix B, and for which the circular tokamak model is a mathematically consistent simplification. In the field aligned coordinate system, there is only one independent covariant component of $\mathbf{F}$,

$$F_{xy} = -F_{yx} = B_0 \tag{11.17}$$

We can now write down the curvature operator. Replacing the vector operations by their tensor counterparts yields

$$\mathcal{K} = \nabla \log B^2 \cdot \frac{c\mathbf{B}\times\nabla}{B^2} = \nabla_j \log B^2\, \epsilon^j{}_k{}^i \frac{cB^k}{B^2} \nabla_i \tag{11.18}$$

or in terms of the components,

$$\mathcal{K}^i = \hat{F}^{ij} \nabla_j \log B^2 \tag{11.19}$$

where the

$$\hat{F}^{ij} = \frac{cF^{ij}}{B^2} \tag{11.20}$$

are the contravariant components of the drift tensor. Under drift ordering the only significant one is

$$\hat{F}^{xy} = \frac{c}{B_0} \tag{11.21}$$

a constant. This is related to the fact that $\mathbf{B}$ is given in general by the Clebsch representation $f(\Psi)\nabla x \times \nabla y$. The constant comes from evaluating the flux function $f(\Psi)$ at the reference flux surface. Taking the field strength derivatives B^2 as given at $r = a$ by

$$\frac{\partial}{\partial r}\log B^2 = -\frac{2}{R}\cos\theta \qquad \frac{\partial}{\partial \theta}\log B^2 = \frac{2a}{R}\sin\theta \tag{11.22}$$

we find

$$\mathcal{K}^x = \frac{2}{R_0 B_0}\sin\theta \qquad \mathcal{K}^y = \frac{2}{R_0 B_0}(\cos\theta + \hat{s}\theta\sin\theta) \tag{11.23}$$

For a flux tube computation under drift ordering, the magnetic geometry is contained in the seven quantities

$$g^{xx} \qquad g^{xy} \qquad g^{yy} \qquad B^s \qquad B^2 \qquad \mathcal{K}^x \qquad \mathcal{K}^y \tag{11.24}$$

all functions of s only. The first three appear in the perpendicular Laplacian, B^s appears in parallel gradients and divergences, B^2 appears in the polarisation dynamics wherever ρ_s or the gyroradii control the response of the electrostatic potential, and the components of $\mathcal{K}$ appear in all the magnetic divergence terms. It is prudent to do the computations in this simplest toroidal flux tube model, and then with interest in the properties of particular equilibria we can simply drop in and replace these seven geometric quantities.

11.III. The DALF3 Model

We first present the model we need for this investigation in a self contained way. It consists of the above toroidal flux tube model, together with the dynamics to be treated in that geometry. The dynamics is the four field model under drift ordering which has as dependent variables the fluctuating electrostatic potential ($\widetilde{\phi}$), electron pressure ($\widetilde{p}_e$), parallel current ($\widetilde{J}_\parallel$), and parallel ion velocity ($\widetilde{u}_\parallel$). Their respective equations are the two conservation laws for charge ($\nabla \cdot \mathbf{J} = 0$), electron thermal energy, and then the equations of motion for the electrons and ions. The fluctuating parallel magnetic potential ($\widetilde{A}_\parallel$) is given by $\widetilde{J}_\parallel$ through Ampere's law, and then $\widetilde{\phi}$ and $\widetilde{A}_\parallel$ serve as stream functions for the ExB velocity and the magnetic field disturbances, respectively. The equations appear as

$$\frac{1}{B^2}\frac{d_E}{dt}\nabla_\perp^2\widetilde{\phi} = B\nabla_\parallel\frac{\widetilde{J}_\parallel}{B} - \mathcal{K}(\widetilde{p}_e) \tag{11.25}$$

$$\hat{\beta}\frac{\partial \widetilde{A}_{\parallel}}{\partial t} + \hat{\mu}\frac{d_E \widetilde{J}_{\parallel}}{dt} = \nabla_{\parallel}(p_e + \widetilde{p}_e - \widetilde{\phi}) - C\widetilde{J}_{\parallel} \tag{11.26}$$

$$\frac{d_E}{dt}(p_e + \widetilde{p}_e) = B\nabla_{\parallel}\frac{\widetilde{J}_{\parallel} - \widetilde{u}_{\parallel}}{B} - \mathcal{K}(\widetilde{p}_e - \widetilde{\phi}) \tag{11.27}$$

$$\hat{\epsilon}\frac{d_E \widetilde{u}_{\parallel}}{dt} = -\nabla_{\parallel}(p_e + \widetilde{p}_e) + \mu_{\parallel}\nabla_{\parallel}^2 \widetilde{u}_{\parallel} \tag{11.28}$$

and the Ampere's law is

$$\widetilde{J}_{\parallel} = -\nabla_{\perp}^2 \widetilde{A}_{\parallel} \tag{11.29}$$

serving as an auxiliary relation. One can think of either $\widetilde{A}_{\parallel}$ or $\widetilde{J}_{\parallel}$ as the flux dependent variable for the Alfvénic dynamics, with the other determined by Ampere's law.

The equations are normalised via

$$\widetilde{\phi} \leftarrow \delta^{-1}\frac{e\widetilde{\phi}}{T_e} \qquad \widetilde{p}_e \leftarrow \delta^{-1}\frac{\widetilde{p}_e}{p_e} \tag{11.30}$$

for the state variables, and

$$\widetilde{J}_{\parallel} \leftarrow \delta^{-1}\frac{\widetilde{J}_{\parallel}}{n_e e c_s}\frac{L_{\perp}}{qR} \qquad \widetilde{u}_{\parallel} \leftarrow \delta^{-1}\frac{\widetilde{u}_{\parallel}}{c_s}\frac{L_{\perp}}{qR} \qquad \widetilde{A}_{\parallel} \leftarrow \delta^{-1}\frac{\widetilde{A}_{\parallel}}{B\rho_s\hat{\beta}}\frac{L_{\perp}}{qR} \tag{11.31}$$

for the flux variables, where $\delta = \rho_s/L_{\perp}$ is the drift parameter, and $L_{\perp}$ is the background profile scale.

The advective and parallel derivatives are given by

$$\frac{d_E}{dt} = \frac{\partial}{\partial t} + \mathbf{v}_E \cdot \nabla \qquad \nabla_{\parallel} = \frac{1}{B}\mathbf{B}\cdot\nabla \tag{11.32}$$

where the ExB velocity and magnetic field are given by

$$\mathbf{v}_E = \frac{\mathbf{B}\times\nabla\widetilde{\phi}}{B^2} \qquad \frac{1}{B}\mathbf{B} = \frac{B^s}{B}\nabla s - \hat{\beta}\frac{\mathbf{B}\times\nabla\widetilde{A}_{\parallel}}{B^2} \tag{11.33}$$

and the perpendicular combinations of derivatives involve only x and y, so that

$$\mathbf{v}_E\cdot\nabla = \frac{\partial\widetilde{\phi}}{\partial x}\frac{\partial}{\partial y} - \frac{\partial\widetilde{\phi}}{\partial y}\frac{\partial}{\partial x} \qquad \frac{1}{B}\widetilde{\mathbf{B}}\cdot\nabla = -\hat{\beta}\left(\frac{\partial\widetilde{A}_{\parallel}}{\partial x}\frac{\partial}{\partial y} - \frac{\partial\widetilde{A}_{\parallel}}{\partial y}\frac{\partial}{\partial x}\right) \tag{11.34}$$

are the sole nonlinearities, as discussed in Chapter 6. The appearance of the background p_e under derivatives represents the gradient drive terms, so that

$$\mathbf{v}_E\cdot\nabla p_e = \omega_n\frac{\partial\widetilde{\phi}}{\partial y} \qquad \nabla_{\parallel}p_e = -\omega_n\hat{\beta}\frac{\partial\widetilde{A}_{\parallel}}{\partial y} \tag{11.35}$$

where ω_n is a parameter (note choosing $\omega_n = 1$ is equivalent to choosing $L_\perp = L_p$).

The appearance of the magnetic field strength B in the $\nabla_\parallel$ operations reflects the fact that some of the parallel gradient terms are actually divergences, so that, for example,

$$\nabla \cdot (\widetilde{J}_\parallel \mathbf{b}) = \nabla \cdot \left(\frac{\widetilde{J}_\parallel \mathbf{B}}{B} \right) = \mathbf{B} \cdot \nabla \frac{\widetilde{J}_\parallel}{B} = B \nabla_\parallel \frac{\widetilde{J}_\parallel}{B} \tag{11.36}$$

since $\nabla \cdot \mathbf{B} = 0$. By the same token, the double parallel derivative takes the form

$$\nabla_\parallel^2 = \nabla \cdot \mathbf{b}\mathbf{b} \cdot \nabla = B \nabla_\parallel \frac{1}{B} \nabla_\parallel \tag{11.37}$$

The appearance of B in the vorticity (Eq. 11.25) reflects the fact that the local ρ_s depends on it, since the original quantity this comes from is the polarisation current, given by

$$\nabla \cdot \frac{n_i M_i c^2}{B^2} \frac{d_E}{dt} \nabla_\perp \phi \tag{11.38}$$

(unnormalised). The two factors of B depend on s in a toroidal magnetic field, so they are kept. The equilibrium is otherwise assumed to be independent of s.

The magnetic geometry is contained in the seven quantities outlined in the previous section. We have the perpendicular Laplacian,

$$\nabla_\perp^2 = g^{xx} \frac{\partial^2}{\partial x^2} + 2 g^{xy} \frac{\partial^2}{\partial x \partial y} + g^{yy} \frac{\partial^2}{\partial y^2} = \left(\frac{\partial}{\partial x} + \hat{s} s \frac{\partial}{\partial y} \right)^2 + \frac{\partial^2}{\partial y^2} \tag{11.39}$$

the equilibrium magnetic field,

$$B^s = B^2 = 1 \tag{11.40}$$

and the curvature operator

$$\mathcal{K} = \omega_B \left[\sin s \frac{\partial}{\partial x} + (\cos s + g^{xy} \sin s) \frac{\partial}{\partial y} \right] \tag{11.41}$$

where ω_B, nominally equal to $2L_\perp / R_0$, is kept as a separate parameter.

In the computations, we use the shifted forms of these as discussed in Chapter 8, with y shifted on each drift plane according to

$$y_k = y - \hat{s} s_k x \tag{11.42}$$

with s_k constant so that $\mathbf{B} \cdot \nabla y_k = 0$ is maintained while setting

$$g_k^{xy} = 0 \qquad g_k^{yy} = 1 \qquad \text{at} \quad s = s_k \tag{11.43}$$

This adjusts the curvature vector according to the tensor transformation rules,

$$\mathcal{K}^x = \omega_B \sin s \qquad \mathcal{K}^y_k = \omega_B \cos s \qquad \text{at} \quad s = s_k \tag{11.44}$$

Parallel derivatives between two s-nodes, evaluated at the half-node position, are

$$\frac{\partial f}{\partial s}(x, y_{k+1/2}, s_{k+1/2}) = \frac{f(x, y_{k+1} - h_s \hat{s}x/2, s_{k+1}) - f(x, y_k + h_s \hat{s}x/2, s_k)}{h_s} \tag{11.45}$$

Parallel derivatives between two half-node positions, evaluated at a node, are

$$\frac{\partial f}{\partial s}(x, y_k, s_k) = f(x, y_{k+1/2} - h_s \hat{s}x/2, s_{k+1/2}) - f(x, y_{k-1/2} + h_s \hat{s}x/2, s_{k-1/2}) \tag{11.46}$$

Centered parallel derivatives between nodes are evaluated as

$$\frac{\partial f}{\partial s}(x, y_k, s_k) = f(x, y_{k+1} - h_s \hat{s}x, s_{k+1}) - f(x, y_{k-1} + h_s \hat{s}x, s_{k-1}) \tag{11.47}$$

All three forms take into account the fact that the coordinate systems used at each position in s are different although they are all globally valid.

The dependent variables are defined on a domain

$$-\pi/4K < x < \pi/4K \qquad -\pi/K < y < \pi/K \qquad -\pi < s < \pi \tag{11.48}$$

where K is a parameter. The boundary conditions are Dirichlet for x (dependent variables vanish at the boundaries), periodic for y, and in s they satisfy

$$f(x, y_{k+N}, s_{k+N}) = f(x, y_k, s_k) \tag{11.49}$$

where N is the number of nodes, noting that the two points are on differing coordinate systems, as in the parallel derivatives. At each location in s, including half-nodes, the coordinate system is the field aligned version, shifted in y such that $y = y_k$ at $s = s_k$, so that g^{xy} vanishes there.

The parameters are

$$\hat{\beta} = \frac{4\pi p_e}{B^2}\left(\frac{qR}{L_\perp}\right)^2 \qquad \hat{\mu} = \frac{m_e}{M_i}\left(\frac{qR}{L_\perp}\right)^2 \qquad C = 0.51\frac{\nu_e L_\perp}{c_s}\frac{m_e}{M_i}\left(\frac{qR}{L_\perp}\right)^2 \tag{11.50}$$

for the dissipative kinetic shear Alfvén dynamics, and

$$\omega_n = \frac{L_\perp}{L_p} \qquad \omega_B = \frac{2L_\perp}{R} \qquad \hat{\epsilon} = \left(\frac{qR}{L_\perp}\right)^2 \tag{11.51}$$

for the gradient drive, curvature, and the sound waves, with $\mu_\parallel$ an arbitrary parallel diffusion coefficient. Nominal values of the parameters, unless otherwise stated, are

$$\hat{\beta} = 1 \quad \hat{\mu} = 5 \quad C = 10 \quad \omega_n = 1 \quad \omega_B = 0.05 \quad \hat{\epsilon} = 18350 \quad \mu_\parallel = 1 \tag{11.52}$$

reflecting typical conditions in the edge of a magnetic confinement experiment. The grid for all cases consists of $64 \times 256 \times 16$ equidistant nodes in $\{x, y, s\}$, with a domain size of $20\pi \times 80\pi \times 2\pi$, respectively ($K = 0.025$). The time step is 0.05, and the initial state is the random phase one in Chapter 8, for $\widetilde{p}_e$, with $\widetilde{\phi} = \widetilde{A}_\parallel = \widetilde{u}_\parallel = 0$.

11.IV. DALF3 Energetics

Since the energetics of the DALF3 model will form a central part of the analysis, we review it once more, within the treatment of magnetic coordinates just outlined. To form the energy theorem we multiply Eqs. (11.25–11.28) by $-\widetilde{\phi}$, $\widetilde{J}_\parallel$, $\widetilde{p}_e$, and $\widetilde{u}_\parallel$, respectively, and integrate over the domain, assuming that total divergences vanish. We find the following, in which the integration operation is denoted by the angle brackets,

$$\frac{\partial}{\partial t}\left\langle \frac{1}{2}\frac{1}{B^2}\left|\nabla_\perp \widetilde{\phi}\right|^2 \right\rangle = \left\langle \widetilde{J}_\parallel \nabla_\parallel \widetilde{\phi} \right\rangle - \left\langle \widetilde{p}_e \mathcal{K} \widetilde{\phi} \right\rangle \tag{11.53}$$

$$\frac{\partial}{\partial t}\left\langle \frac{1}{2}\widetilde{J}_\parallel \left(\hat{\beta}\widetilde{A}_\parallel + \hat{\mu}\widetilde{J}_\parallel\right) \right\rangle = \left\langle \widetilde{J}_\parallel \nabla_\parallel \widetilde{p}_e \right\rangle - \left\langle \widetilde{J}_\parallel \nabla_\parallel \widetilde{\phi} \right\rangle - C\left\langle \frac{1}{2}\left|\widetilde{J}_\parallel\right|^2 \right\rangle \tag{11.54}$$

$$\frac{\partial}{\partial t}\left\langle \frac{1}{2}\left|\widetilde{p}_e\right|^2 \right\rangle = -\left\langle \widetilde{J}_\parallel \nabla_\parallel \widetilde{p}_e \right\rangle + \left\langle \widetilde{u}_\parallel \nabla_\parallel \widetilde{p}_e \right\rangle + \left\langle \widetilde{p}_e \mathcal{K} \widetilde{\phi} \right\rangle + \omega_n \left\langle -\widetilde{p}_e \frac{\partial \widetilde{\phi}}{\partial y} \right\rangle \tag{11.55}$$

$$\frac{\partial}{\partial t}\left\langle \frac{\hat{\epsilon}}{2}\left|\widetilde{u}_\parallel\right|^2 \right\rangle = -\left\langle \widetilde{u}_\parallel \nabla_\parallel \widetilde{p}_e \right\rangle + \omega_n \hat{\beta}\left\langle \widetilde{u}_\parallel \frac{\partial \widetilde{A}_\parallel}{\partial y} \right\rangle - \mu_\parallel \left\langle \left|\nabla_\parallel \widetilde{u}_\parallel\right|^2 \right\rangle \tag{11.56}$$

Terms appearing in two equations with opposite sign represent the transfer channels, while isolated terms reflect the sources and sinks. The only important source is the one in the pressure equation, ExB advection down the gradient. Sound wave motion down the gradient is always negligible. The sinks are resistive friction (C) and sound wave viscosity ($\mu_\parallel$). There are two ways for free energy to be channelled from the source in the pressure equation into the ExB turbulence: the drift wave mechanism, which goes from $\widetilde{p}_e \to \widetilde{J}_\parallel \to \widetilde{\phi}$ through the parallel dynamics, $\nabla_\parallel$, and the MHD compression mechanism, which goes directly from $\widetilde{p}_e \to \widetilde{\phi}$ through the curvature, $\mathcal{K}$. One of our tasks will be to determine which of these is the more prominent.

11.V. Direct Comparison to Resistive MHD

We now run computations within the full DALF3 model and compare them to the resistive MHD model at the same parameters. The MHD model is a reduced MHD case, in which under the drift approximation the ExB flow is dynamically incompressible, and so the perpendicular electric field is electrostatic, just as in the drift wave model. The pressure is the total pressure in MHD, but within a cold ion model the total pressure is simply p_e. The cold ion model without temperature effects is therefore the closest to the corresponding MHD case. The only difference at all is the coupling of $\widetilde{p}_e$ and $\widetilde{J}_\parallel$, in their respective equations. In the MHD model this coupling is absent, and the diamagnetic velocity is neglected in the pressure equation; the model is in all other respects identical to the DALF3 model. The MHD model appears as

$$\frac{1}{B^2}\frac{d_E}{dt}\nabla_\perp^2\widetilde{\phi} = B\nabla_\parallel\frac{\widetilde{J}_\parallel}{B} - \mathcal{K}(\widetilde{p}_e) \tag{11.57}$$

$$\hat{\beta}\frac{\partial\widetilde{A}_\parallel}{\partial t} + \hat{\mu}\frac{d_E\widetilde{J}_\parallel}{dt} = \nabla_\parallel(p_e + \widetilde{p}_e - \widetilde{\phi}) - C\widetilde{J}_\parallel \tag{11.58}$$

$$\frac{d_E}{dt}(p_e + \widetilde{p}_e) = -B\nabla_\parallel\frac{\widetilde{u}_\parallel}{B} + \mathcal{K}(\widetilde{\phi}) \tag{11.59}$$

$$\hat{\epsilon}\frac{d_E\widetilde{u}_\parallel}{dt} = -\nabla_\parallel(p_e + \widetilde{p}_e) + \mu_\parallel\nabla_\parallel^2\widetilde{u}_\parallel \tag{11.60}$$

with the Ampere's law,

$$\widetilde{J}_\parallel = -\nabla_\perp^2\widetilde{A}_\parallel \tag{11.61}$$

All other considerations are as above. Simple comparison to Eqs. (11.25–11.28) shows that the resistive MHD model is an entirely included subset of the DALF3 model.

We run both models with the fixed parameter set shown above, and vary C from very low to very high values. The cases shown are for $C = 2.55 \times \{0.3, 1.0, 3.0, 10.0, 30.0, 100.0\}$ (the values in braces are actually those of the normalised ν), and $\mu_\parallel = 0$ (allowing the numerical scheme to provide dissipation at the very shortest parallel wavelengths; cf. Appendix A).

The first quantities to show are the practical ones, the transport and the relative amplitudes between $\widetilde{\phi}$ and $\widetilde{p}_e$, since if the MHD model predicted these correctly the DALF3 model would represent unnecessary complication. We find that the transport scaling does in fact disagree, strongly. We also find that the rms amplitude ratios $\widetilde{\phi}/\widetilde{p}_e$ disagree. In drift wave dynamics, $\widetilde{p}_e$ and $\widetilde{\phi}$ are held together by the dissipative Alfvén couplings, but in MHD the Alfvén dynamics dissipates $\widetilde{\phi}$ only. Since MHD neglects the electron pressure in

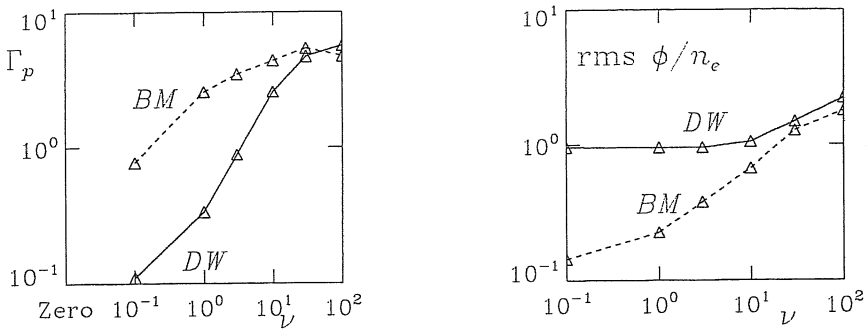

Figure 11.1. (left) Transport scaling of drift wave and interchange turbulence in toroidal geometry, labelled 'DW' and 'BM', respectively. Both are weaker at lower collisionality ($C = 2.55\nu$), but the drift wave cases drop off faster. At asymptotically large C the trends will merge, but that limit is not reached. (right) Amplitude ratio for the two sets of cases. Due to the adiabatic response, $\widetilde{\phi}$ tracks $\widetilde{p}_e = \widetilde{n}_e$ for drift wave turbulence, but in the MHD model of the interchange cases $\widetilde{p}_e$ is unaffected by the Alfvén dynamics, and so instead of $\widetilde{\phi}$ being forced towards $\widetilde{p}_e$ it is forced towards zero.

the Ohm's law, it implicitly assumes that $\widetilde{\phi} \gg \widetilde{p}_e$ in any situation in which the geometry sets the parallel scale as it does here. But with only $\widetilde{\phi}$ damped by the Alfvén effects, the MHD model actually delivers a result that $\widetilde{\phi} < \widetilde{p}_e$, which is contrary to the model's validity. The DALF3 model finds the result of the adiabatic response, namely, $\widetilde{\phi} \sim \widetilde{p}_e$. Both models give a power law for this amplitude ratio at low C. The position at which these two lines cross defines the regime boundary between the two models. For C larger than this critical value, both models find $\widetilde{\phi} > \widetilde{p}_e$. It follows that the resistive MHD model is valid only for C beyond this value. The transport curves both reach maxima and then saturate for very large C; this is due to the fact that both approach two dimensional interchange dynamics moderated only by sound waves for values of C so large that $\widetilde{J}_\parallel$ is essentially negligible.

Beyond the simple scalings, we turn to the mode structure in the transition range given by $\nu = \{3, 10, 30\}$. The most important diagnostics are the ones which tell us about the relationship between $\widetilde{\phi}$ and $\widetilde{p}_e$, since this is where the models are different. In Fig. 11.2 we examine the cross coherence between $\widetilde{p}_e$ and $\widetilde{\phi}$ for both models. The control cases appear in Chapters 7 and 8 for drift wave turbulence, and in Chapter 10 for interchange turbulence. We find that the MHD model shows uncorrelated behaviour for all three values of ν, while the DALF3 model shows moderate correlation even for the largest ν. The adiabatic response coupling $\widetilde{\phi}$ to $\widetilde{p}_e$ through $\widetilde{J}_\parallel$ is always significant in this parameter range.

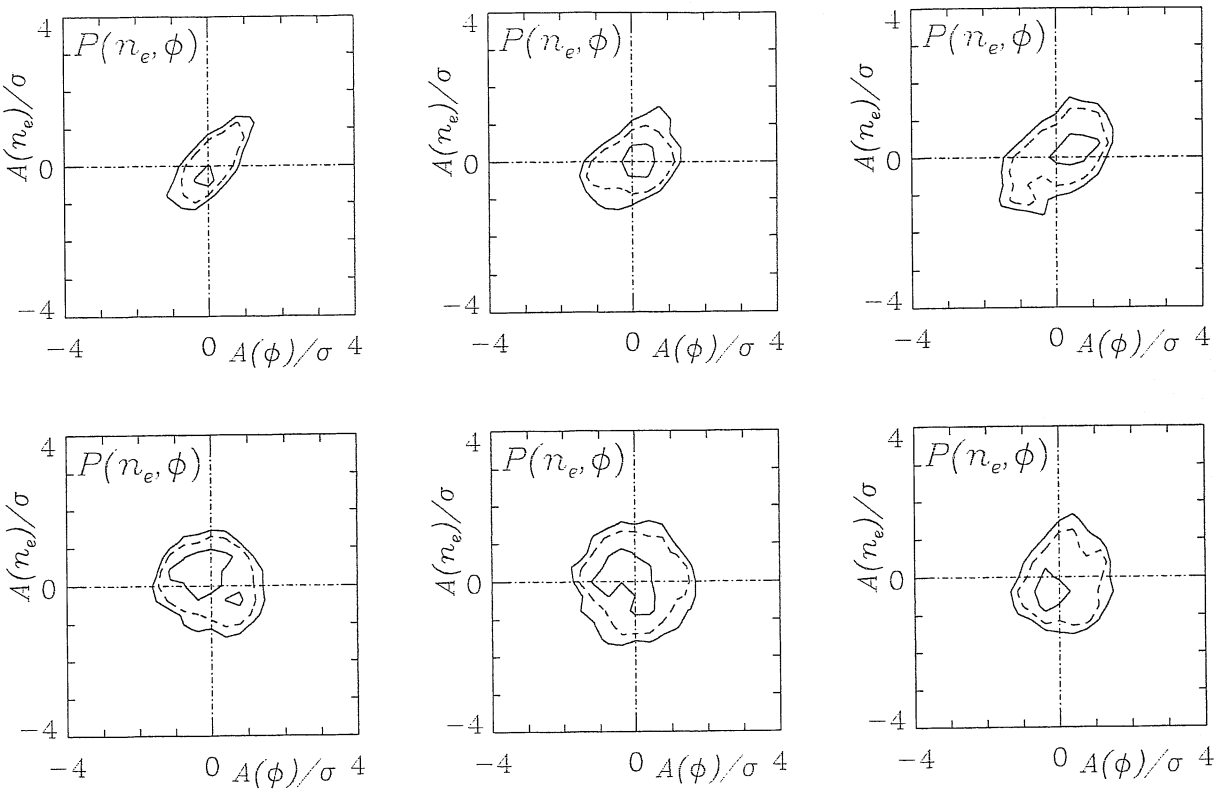

Figure 11.2. Cross coherence between $\widetilde{p}_e = \widetilde{n}_e$ and $\widetilde{\phi}$, for drift wave (top row) and interchange (bottom row) turbulence, for $\nu = 3$, 10, and 30 (left to right), where $C = 2.55\nu$. Compare with the results of Chapter 8 for drift wave and Chapter 10 for interchange turbulence. The DALF3 model results in drift wave mode structure especially for $\nu < 10$, while the MHD model always shows interchange mode structure.

Turning to the phase shift distributions for each k_y component in the spectrum, we find the MHD model predicting the ideally unstable values of $\alpha_{p\phi} = \pi/2$ for all k_y, while the DALF3 model shows the transition between 0 and $\pi/2$ at low k_y as ν is increased. We see why we need these two diagnostics together: the cross coherence reflects the turbulence as a whole, while the phase shift spectrum shows each component. We can see that the transition is in the longer wavelengths, while the cross coherence is influenced also by the smaller scale activity which remains in a drift wave mode structure. Moreover, it is not the case that part of the spectrum has MHD character (some mid range wavelength, for example) while the rest (longer and shorter wavelengths) has drift wave character, at least before the transition regime is reached. So we know that the entire system has drift wave mode structure and therefore character in the drift wave regime, not just in part of the

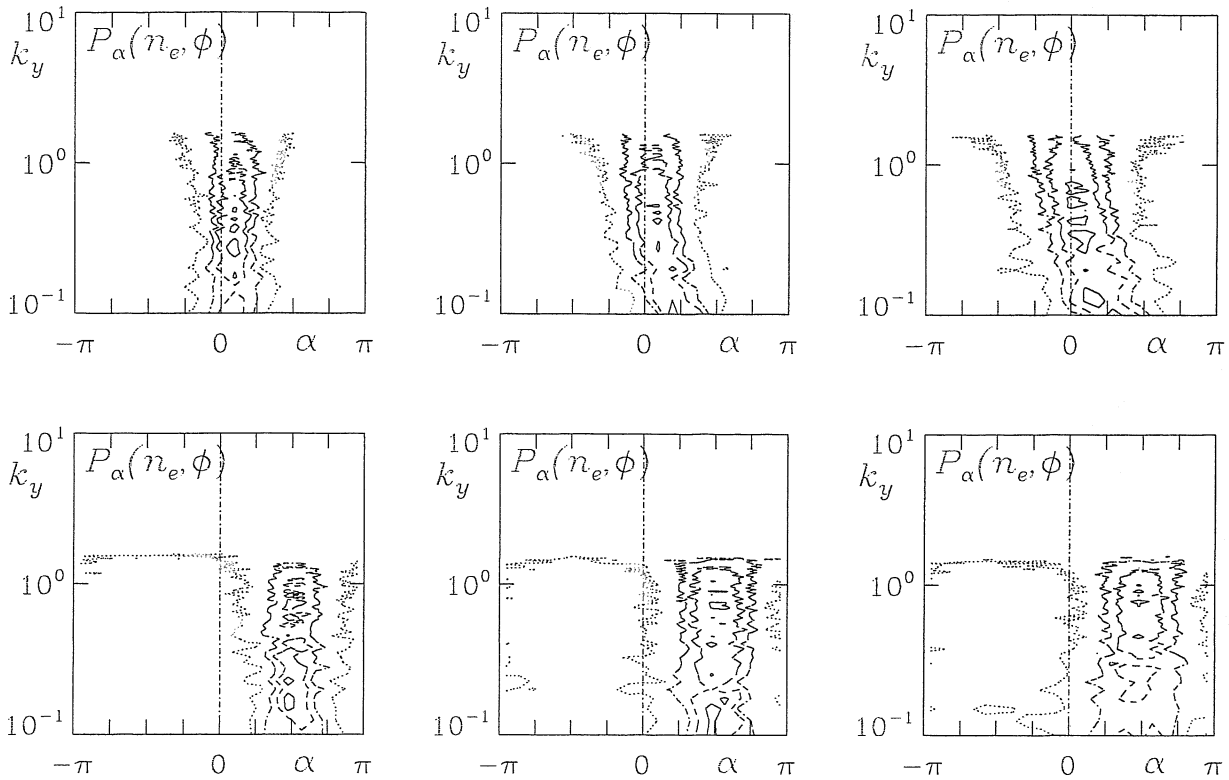

Figure 11.3. Phase shift distributions of $\widetilde{n}_e$ ahead of $\widetilde{\phi}$ at each k_y, for drift wave (top row) and interchange (bottom row) turbulence, for $\nu = 3$, 10, and 30 (left to right), where $C = 2.55\nu$. Compare with the results of Chapter 8 for drift wave and Chapter 10 for interchange turbulence. The DALF3 model begins the transition from drift wave to interchange mode structure for $\nu \sim 10$, in contrast to the MHD model which always shows interchange mode structure.

spectrum. And we know that it is principally the longer wavelengths which effect the transition to resistive ballooning character for increasing C.

For the fundamental reasons for this state of affairs we turn to the energetics. Recall that the only transfer mechanism between $\widetilde{p}_e$ and $\widetilde{\phi}$ in the MHD model is interchange forcing, in this model due to the curvature of the magnetic field lines. For drift wave turbulence in slab geometry this coupling occurs through the adiabatic response, mediated by $\widetilde{J}_\parallel$, and so the free energy liberated from the background gradient can only reach the ExB eddies through the parallel dynamics. In the DALF3 model both coupling mechanisms are available, and so the question arises as to which is most important energetically as well as in the correlations. In Fig. 11.4, we measure the energy transfer terms in the ExB energy equation, including the nonlinearity. As usual, the rms levels are what we ask

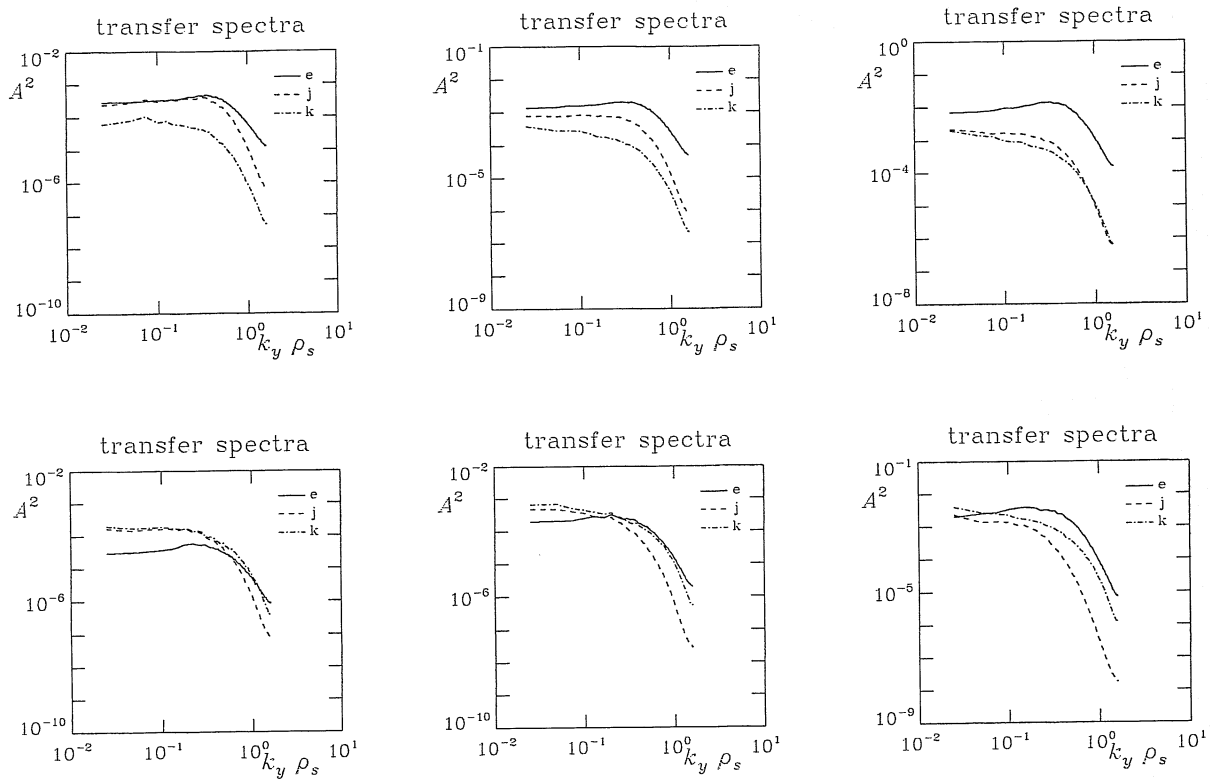

Figure 11.4. Spectra of the rms transfer dynamical levels for each k_y in the spectrum, comparing the sizes of $\widetilde{\phi}\nabla_{\parallel}\widetilde{J}_{\parallel}$ ('j'), $\widetilde{\phi}\mathcal{K}(\widetilde{p}_e)$ ('k'), and $\widetilde{\phi}\mathbf{v}_E \cdot \nabla\nabla_{\perp}^2\widetilde{\phi}$ ('e'), for drift wave (top row) and interchange (bottom row) turbulence, for $\nu = 3$, 10, and 30 (left to right), where $C = 2.55\nu$. Compare with the results of Chapter 8 for drift wave and Chapter 10 for interchange turbulence. For $\nu = 3$ we see the essential difference in mode structure; drift wave turbulence balances the vorticity and current dynamics, and interchange turbulence balances the dissipation of $\widetilde{\phi}$ by the parallel current with the curvature effects. Here even for $\nu = 10$ the drift wave coupling mechanism is clearly the stronger in the DALF3 model, while the MHD model contains only the interchange coupling.

for, not the averages, since the importance of these transfers to turbulence is in their maintenance of each part of the energetics at finite levels, whatever the sign. The results may be compared to those in Chapter 8 for drift wave turbulence and Chapter 10 for interchange turbulence. For the drift wave cases the polarisation drift ($\mathbf{v}_E \cdot \nabla\nabla_{\perp}^2\widetilde{\phi}$) and the nonadiabaticity ($\nabla_{\parallel}\widetilde{J}_{\parallel}$) are in rough balance, while the curvature ($\mathcal{K}\widetilde{p}_e$) is subdominant. For interchange turbulence, especially at low collisionality where the resistive dissipation keeps $\widetilde{\phi}$ small, the curvature and parallel current divergence are in rough balance, and when $\widetilde{\phi}$ and hence the polarisation drift is larger, the curvature becomes larger than the

nonadiabaticity. In the DALF3 model containing both eigenmode types, the transition from drift wave to interchange transfer dynamics occurs in the $\nu > 10$ range, at which all three effects are of comparable importance. This again stresses the regime boundary as one which determines the nature of the turbulence generally, as this conclusion is valid for the entire spectrum, not just part of it.

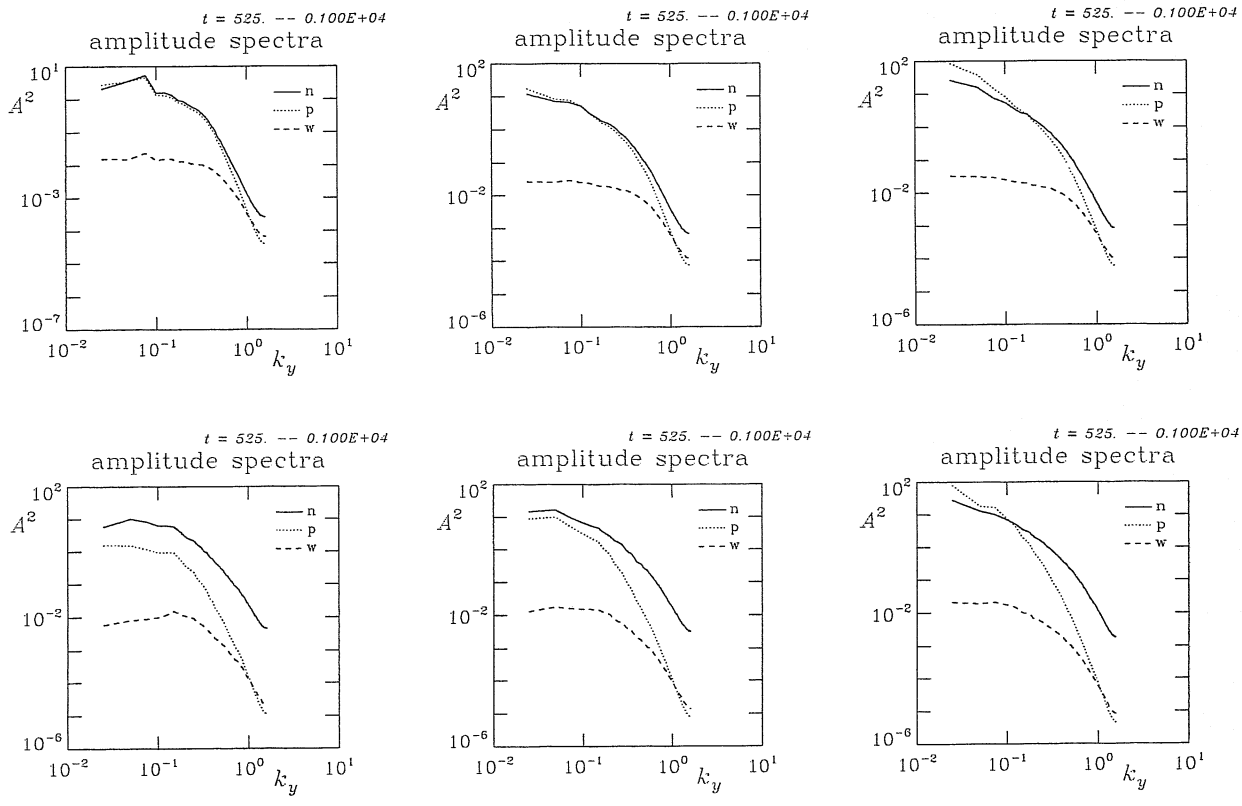

Figure 11.5. Amplitude spectra of $\widetilde{n}_e$, $\widetilde{\phi}$,and $\nabla_\perp^2\widetilde{\phi}$, respectively labelled by 'n', 'p', and 'w', for drift wave (top row) and interchange (bottom row) turbulence, for $\nu = 3$, 10, and 30 (left to right), where $C = 2.55\nu$. Compare with the results of Chapter 8 for drift wave and Chapter 10 for interchange turbulence. With only the density present one cannot distinguish the mode structure or dynamics, but if $\widetilde{\phi}$ is also present the amplitude ratio, shown in Fig. 11.1, is decisive.

We note now the important fact that if we look only at the morphology of one dependent variable, $\widetilde{n}_e$ for example, that we cannot easily see the difference between the two models. We can see this in the spectra and parallel structure, although if we have this data for both $\widetilde{n}_e$ and $\widetilde{\phi}$ the conclusion is obvious. We show the amplitude spectra for the same six cases, in Fig. 11.5. The spectra of $\widetilde{n}_e$ look quite similar for the three cases

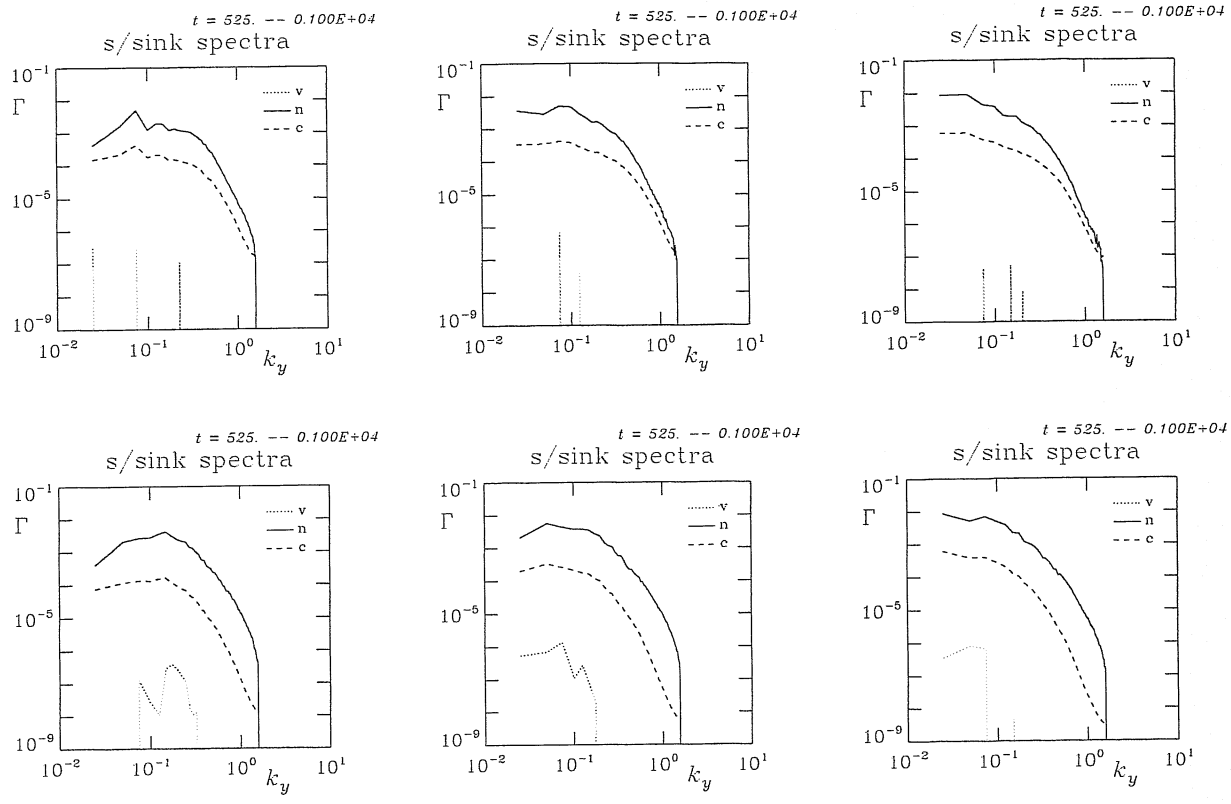

Figure 11.6. Spectra of the ExB gradient drive ('n'), dissipation ('c'), and the magnetic flutter drive ('v'), for drift wave (top row) and interchange (bottom row) turbulence, for $\nu = 3$, 10, and 30 (left to right), where $C = 2.55\nu$. Compare with the results of Chapter 8 for drift wave and Chapter 10 for interchange turbulence. These curves are all comparable, even though the information in previous figures shows the mechanism supporting the gradient drive to differ between the drift wave and interchange models.

$\nu = \{3, 10, 30\}$ in both models, but the relationship to $\tilde{\phi}$ is, as by now expected, different. In Fig. 11.6 the energetics is shown, and these too are very similar, this time for all the cases. Most importantly, the scale of motion is not a distinguishing factor. This means that experiments that measure the statistics or morphology only of density fluctuations, which are the most accessible in a hot plasma, can do little to ascertain what the dynamics of the turbulence actually is.

We find a similar state of affairs in the parallel structure. The amplitude envelopes of the state variables are shown in Fig. 11.7. Here we find that the outboard to inboard asymmetry of the density disturbance activity is also not a distinguishing factor, as the mere presence of interchange forcing, even at the low levels implied by $\omega_B = 0.05$, is sufficient to make a difference in the overall dynamics. But this difference is a quantitative

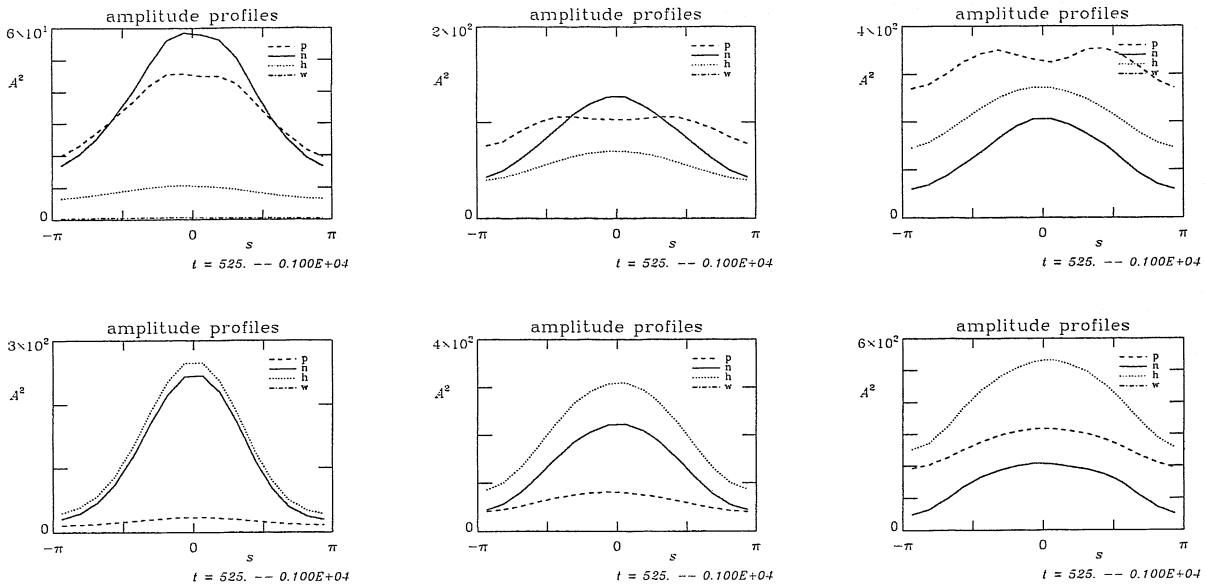

Figure 11.7. Amplitude envelopes of $\widetilde{n}_e$, $\widetilde{h}_e$, $\widetilde{\phi}$, and $\nabla_\perp^2\widetilde{\phi}$, respectively labelled by 'n', 'h', 'p', and 'w', for drift wave (top row) and interchange (bottom row) turbulence, for $\nu = 3$, 10, and 30 (left to right), where $C = 2.55\nu$. Compare with the results of Chapter 8 for drift wave and Chapter 10 for interchange turbulence. Drift wave mode structure is exemplary for $\nu = 3$ and 10 in the DALF3 model, with $\widetilde{h}_e$ much flatter than either $\widetilde{n}_e$ or $\widetilde{\phi}$. The ballooning (peaking near $s = 0$) is pronounced in all cases due to the combination of interchange forcing and magnetic shear. For $C < 30$ the contrast in the two models is nevertheless clear in the differing degree to which $\widetilde{\phi}$ and $\widetilde{n}_e$ are asymmetric.

difference. As we have just found, the qualitative difference of the DALF3 model with C less than about 30, to the three dimensional slab drift wave model in Chapter 8 is negligible. The basic mode structure features which are able to tell the difference between drift wave and interchange turbulence, as seen in Chapters 8 and 10, decide the contrast unequivocally for drift wave mode structure, and therefore dynamics.

11.VI. The Role of Interchange Forcing in Drift Wave Turbulence

It is instructive to examine the effect of the curvature terms, which do the interchange forcing, on the simple linear drift waves we looked at in Chapter 5. This version of the linearised equations takes a single Fourier component by setting $\nabla_\perp^2 \to -k_\perp^2$, and $\nabla_\parallel \to ik_\parallel$, and $\partial/\partial y \to ik_y$, and for the curvature $\mathcal{K} \to i\omega_B k_y$ as in Chapter 10. We recall from Section V of Chapter 5 that for the drift waves all we needed to know was the response of $\widetilde{h}_e$ to $\widetilde{\phi}$, in order to find the dispersion relation, and that the resulting phase

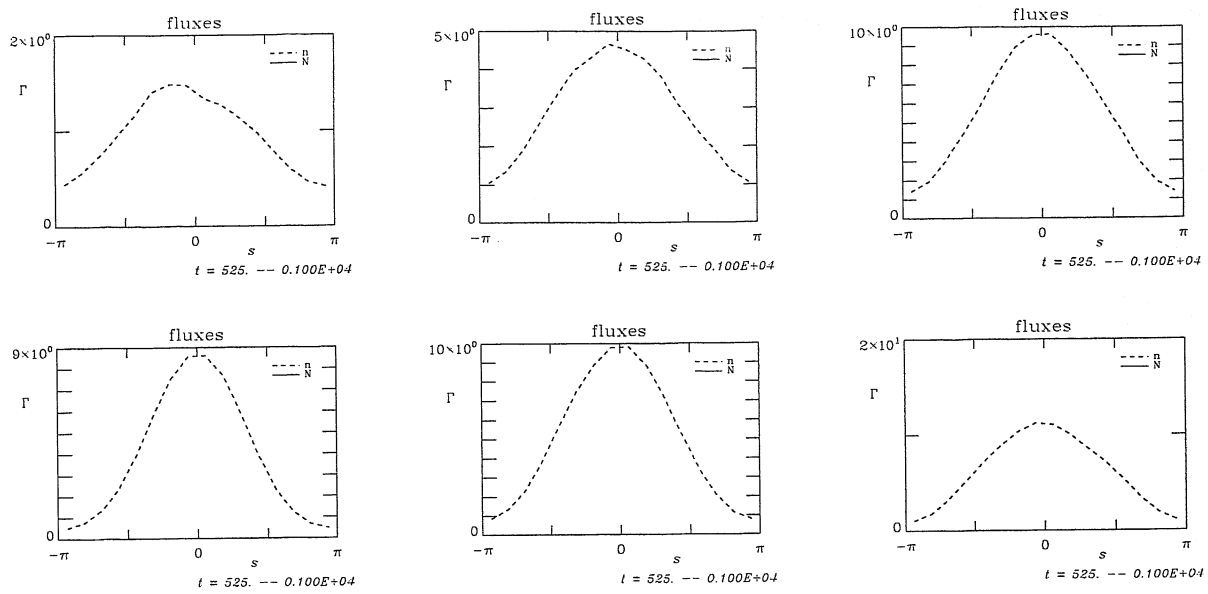

Figure 11.7. Amplitude envelope of the ExB transport ('n'), for drift wave (top row) and interchange (bottom row) turbulence, for $\nu = 3$, 10, and 30 (left to right), where $C = 2.55\nu$. The magnetic flutter transport is negligible on this scale. Compare with the results of Chapter 8 for drift wave and Chapter 10 for interchange turbulence. Drift wave mode structure is exemplary for $\nu = 3$ and 10 in the DALF3 model, with $\widetilde{h}_e$ much flatter than either $\widetilde{n}_e$ or $\widetilde{\phi}$. The ballooning in the transport is much more pronounced where the turbulence has interchange character.

shift was closely related to the linear growth rate. The vorticity equation and Ohm's law, Eqs. (11.25) and (11.26), are all we need. Using the relations $\omega_* = \omega_n k_y$ and $\omega_c = \omega_B k_y$, their linearised form is

$$\omega k_\perp^2 \widetilde{\phi}_{\mathbf{k}} = k_\parallel \widetilde{J}_{\parallel \mathbf{k}} - \omega_c \widetilde{p}_{e\mathbf{k}} \tag{11.62}$$

$$\hat{\beta}\,(\omega - \omega_*)\,\widetilde{A}_{\parallel \mathbf{k}} + (\hat{\mu}\omega + iC)\,\widetilde{J}_{\parallel \mathbf{k}} = -k_\parallel \left(\widetilde{p}_{e\mathbf{k}} - \widetilde{\phi}_{\mathbf{k}}\right) \tag{11.63}$$

which we can find by continuing from the end of Chapter 5, Section V, simply adding the single curvature term into the vorticity equation. Eliminating $\widetilde{J}_{\parallel \mathbf{k}}$, we find the equation for the response. It is simplest to do this in the collisional regime, where C is the dominant effect in Eq. (11.63). We then find

$$\widetilde{p}_{e\mathbf{k}} = \frac{k_\parallel^2 - iCk_\perp^2\omega}{k_\parallel^2 + iC\omega_c}\,\widetilde{\phi}_{\mathbf{k}} \tag{11.64}$$

As with drift waves proper, the consideration of the phase shift is only important when $k_\parallel$ is finite, enough so that $k_\parallel^2$ is the largest term in both numerator and denominator of

Eq. (11.64). If this is so, then the phase shift is small. It then follows that the eigenmode has the same properties as a drift wave, merely with a different excitation mechanism for the phase shift. But the role of the interchange forcing in this case is simply to excite a phase shift and thereby cause the turbulence to be driven by the background gradient. This is the same role the polarisation drift has for drift waves, and the same role its nonlinear version, the vorticity nonlinearity, has for drift wave turbulence. Even in this regime dominated by parallel dynamics, the interchange effects can win out and change the mode structure if they dominantly cause the phase shift. But we saw in the vorticity dynamical spectra in Fig. 11.4, that in turbulence this is not the case until the collisionality reaches what we found as the resistive ballooning threshold. The threshold is at about

$$(C\omega_B)_{\text{crit}} = 1.2 \tag{11.65}$$

which is the boundary beyond which the curvature effects overcome the adiabatic response, as seen in the denominator of the simple response in Eq. (11.64). At that threshold the transport does not sharply change, but the mode structure does so. So we can properly think of this transition as an eigenmode regime boundary, and of the turbulence to the low collisionality side of it as drift wave turbulence.

11.VII. Linear versus Nonlinear Mode Structure

The reason that the result of this investigation for the turbulence is somewhat other than what one might expect by looking at linear instabilities is that the character of drift wave turbulence, especially, is very different that its corresponding linear instabilities (or stable disturbances). The reason for this is of course the nonlinear polarisation drift — equivalently, the self advection of unsteady ExB vortices, or eddies — which is the mechanism through which the turbulence has such strengthened parallel current dynamics, and hence more net nonadiabaticity of the electrons than those linear eigenmodes.

We can investigate this directly by starting the dynamics with an initial state in the linear regime with a linear instability strongly driven by the magnetic curvature, and then tracking the evolution of the mode structure through the saturation phase, which is the transition from the linear regime towards the turbulence, and then into the fully developed turbulence in which there is no detailed memory of whatever transpires several correlation times before.

The initial state is the same as before, just with an amplitude of $a_0 = 3\times10^{-10}$ instead of the usual 3.0. We take a single case, that given by the nominal parameters above (with $\mu_{||} = 0$), but with $\nu = 10$ and hence $C = 25.5$. The time traces of the amplitudes, transport,

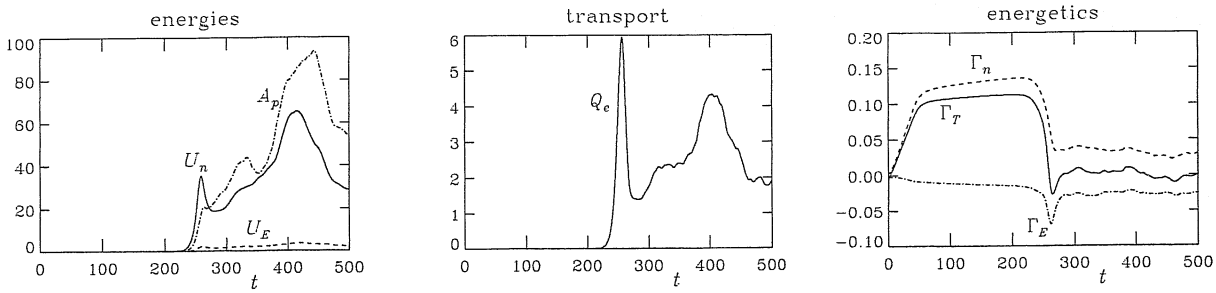

Figure 11.9a. Time evolution of the DALF3 case with $\nu = 10$ (or $C = 25.5$) out of a linear initial state at small amplitude. (left) Half squared amplitude of $\widetilde{\phi}$, denoted A_p and the free energy density components, U_E for the ExB eddies ($\widetilde{\phi}$) and U_n for the density, noting that U_n is also A_n. (center) The transport caused by the turbulence. (right) Growth rate (Γ_T), gradient drive rate (Γ_n), and total dissipation rate (Γ_E). The linear growth phase proceeds until the rapid saturation at about $t = 250$.

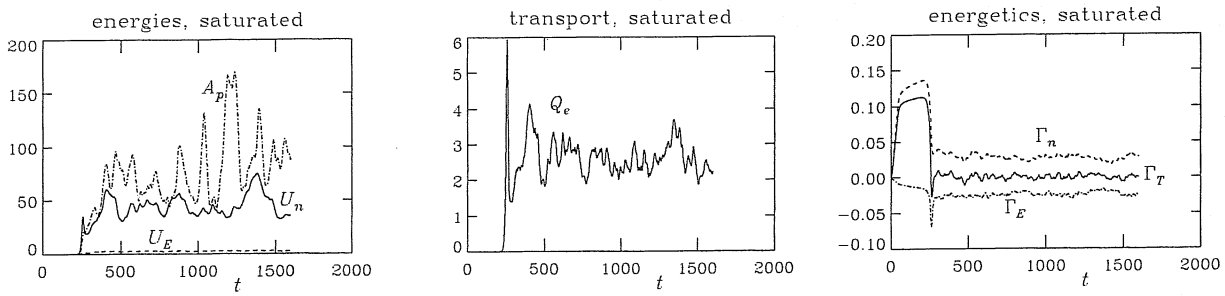

Figure 11.9b. Time evolution of the DALF3 case with $\nu = 10$ (or $C = 25.5$) out of a linear initial state at small amplitude, showing the eventual saturation. Compare to Fig. 11.9a. The amplitudes of $\widetilde{\phi}$ and $\widetilde{p}_e$ track each other until the onset of zonal flow activity, seen in the excursions of A_p. At late times there is no memory of the linear or initial saturation phases.

and energetics are shown in Figs. 11.9a and 11.9b. The linear instability develops, and reaches a constant growth rate which is quite large, about 0.15 in the units of $c_s/L_\perp$. Then, the growth rate rapidly drops to zero. This is the onset of saturation. Then, the growth rate begins to fluctuate, rises away from zero for a short while, and then approaches zero again up to some statistical fluctuation on the scale of a correlation time. The manifestation of this is a large overshoot in the transport, before it settles to statistical fluctuation. Actual saturation in terms of a statistically stationary state takes place only after $t = 500$, in a somewhat longer term memory of the very violently overshooting process of saturation.

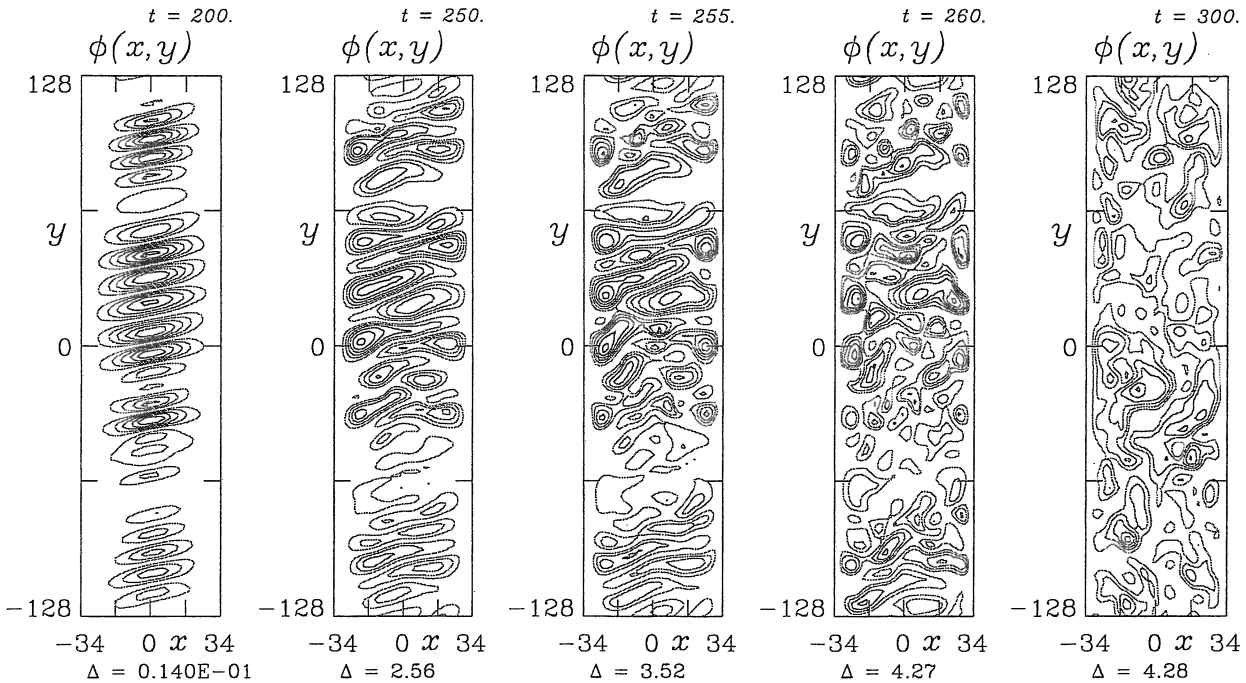

Figure 11.10. Saturation and transition to turbulence, as seen in the morphology of the ExB eddies, for $t = 200$, 250, 255, 260, and 300. Refer to Fig. 11.9a. The linear stage shows radial flows of the interchange type, comparable to those seen in Chapter 10. Saturation near $t = 250$ is extremely rapid, after which the turbulence acquires the more isotropic appearance of drift wave turbulence. The statistically stationary state is only reached after $t = 500$, as the larger scale flows settle out more slowly.

This is the stage of fully developed turbulence, which we can see has a very distinct separation in time from the prior two states. The spatial morphology of the flows shows a substantial change during saturation, as shown in Fig. 11.10. Up until initial saturation, the qualitative character of the eigenmode growth and the initial nonlinear deformations due to secondary instabilities, the properties of radial interchange flows are pronounced, with the spatial morphology looking very much like Figure 10.3. But once the turbulence is well established, it looks more like Figure 6.8. This visual change is cemented by the diagnosis we just did with the transfer spectra. This is the motivation of the statement that the properties of linear instabilities have no *a priori* relevance to the turbulence. But to really find out whether the linear phase is relevant, we have to examine the mode structure in both regimes.

The diagnostics we have been using for the turbulence show important differences between the linear, saturation, and fully developed turbulence stages. The vorticity dy-

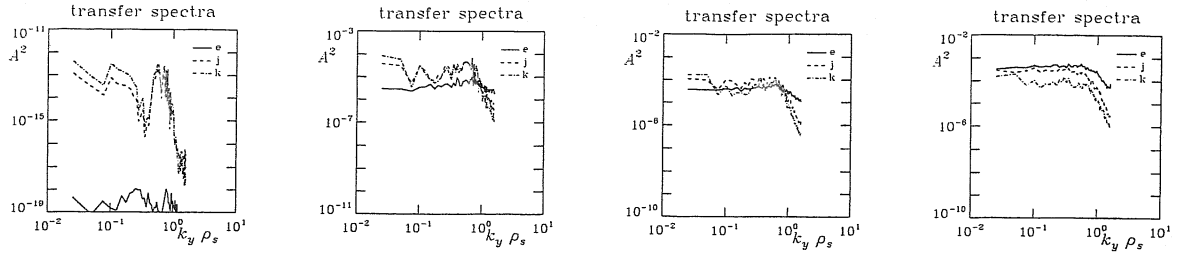

Figure 11.11. Saturation and transition to turbulence, as seen in the dynamical transfer spectra for the ExB vorticity, for $t = 200$, 250, 255, and 260. Compare with Fig. 11.4. Initially the eigenmode is controlled by interchange forcing, with the linear polarisation drift negligible. See Eq. (11.64). But as the dynamics becomes nonlinear the vorticity nonlinearity, the same one which causes the drift wave nonlinear instability, emerges to become the principal agent for maintaining nonadiabatic electron dynamics. The transition is extremely rapid, barely captured on the snapshot interval of $\Delta t = 5$.

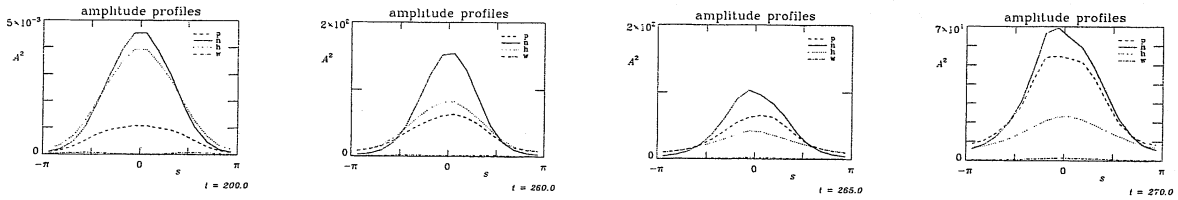

Figure 11.12. Saturation and transition to turbulence, as seen in the parallel envelope structure, for $t = 200$, 260, 265, and 270. Compare with Fig. 11.7. This transition between linear and nonlinear mode structure takes place slightly delayed compared to the underlying nonlinear dynamics, but is just as rapid. In the linear stage $\widetilde{\phi} < \widetilde{n}_e$, with $\widetilde{h}_e \sim \widetilde{n}_e$, but in the nonlinear stage the drift wave coupling is much more effective. The degree of asymmetry is also reduced.

namical spectra are shown for the transition phase in Fig. 11.11, noting that the state after about $t = 300$ approaches what we see in Fig. 11.4. The nonlinear polarisation drift is obviously negligible in the linear stage, where there is a tight balance between curvature and nonadiabaticity. But it is interesting to note that the linear polarisation drift (not shown because it has a time derivative) is also negligible. As in the interchange turbulence cases, the linear state of the DALF model shows a close balance between interchange forcing and the parallel current divergence. We therefore have a curvature dominated linear instability. Through the saturation phase, the polarisation drift enters, and in the end state the polarisation drift has become the dominant cause of nonadiabaticity. That the

nonadiabaticity is still important conceptually is shown by the fact that this case exhibits the high degree of cross coherence and low phase shifts shown in Figs. 11.2 and 11.3. The parallel structure, displayed in Fig. 11.12, also shows interesting changes between the linear and turbulent stages. The degree of ballooning, especially in $\widetilde{h}_e$ is markedly reduced in turbulence. It does not make sense to discuss coherence in a nonrandom system such as a linear eigenmode, but we can say that the degree of drift wave coupling through the adiabatic response is much more effective in turbulence as for the original instability. With the short correlation time of the turbulence, the initial state with which the turbulence is reached is not relevant to consideration of its mode structure or underlying dynamics.

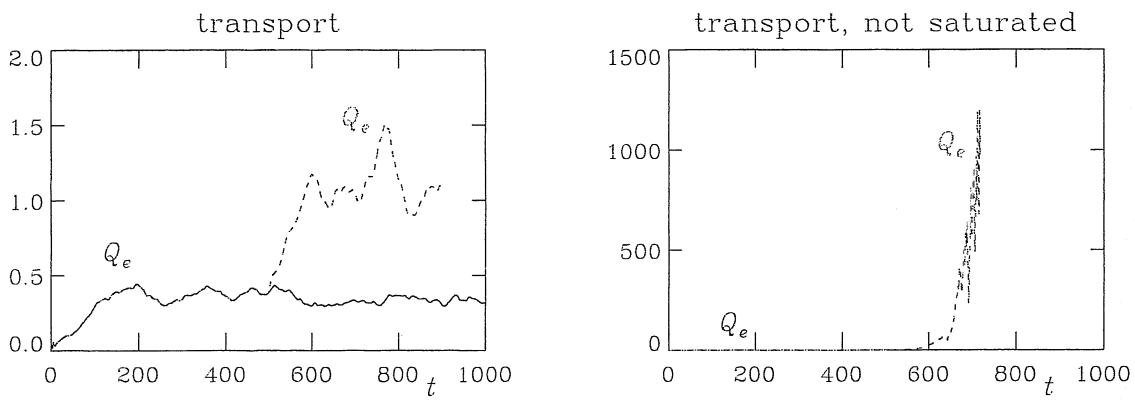

Figure 11.13. Nonlinear mechanisms of excitation and saturation, for fully developed drift wave turbulence with $C = 2.55$ in toroidal geometry, with interchange forcing present. Restarting from $t = 500$ and leaving out the vorticity (left) or pressure (right) nonlinearities, we find that the vorticity nonlinearity always excites the turbulence (right), while the pressure nonlinearity always saturates it (left). Compare to the results of Figs. 8.8 and 8.13 of Chapter 8 to find that this is the same behaviour as in pure drift wave turbulence.

Finally, we investigate the various roles of the main ExB pressure and vorticity nonlinearities. Taking the case with $C = 2.55$, with other parameters at their nominal values, we establish the run to $t = 1000$ with all terms present in the equations. We then restart from $t = 500$ taking the evolved state there as the initial condition for two test cases, leaving out $\mathbf{v}_E \cdot \nabla \widetilde{p}_e$ or $\mathbf{v}_E \cdot \nabla \nabla_\perp^2 \widetilde{\phi}$ in turn. The results are shown in Fig. 11.13. We find that removal of the pressure nonlinearity leads to a situation in which the vorticity nonlinearity modifies the mode structure as we just saw, but it acts alone. This case grows indefinitely showing no signs of eventual saturation. The run was terminated with the transport well over 1000 in normalised units, compared to the nominal value of about 0.4. Comparing to Figs. 8.8

and 8.13 of Chapter 8, we find that this is the same result as for drift wave turbulence in either the two or three dimensional models. Alternatively we find that removal of the vorticity nonlinearity, which leaves the balance between interchange forcing and parallel dynamics in the vorticity dynamics unchanged from the linear regime, leads to a somewhat higher transport but nevertheless does lead to eventual saturation at a transport of about 1.2. The linear eigenmode is after all quite strongly driven, with a growth rate of about 0.12. This result naturally differs from that of Figs. 8.8 and 8.13, because by contrast to the drift wave case, this one has the linear instability. However, we do find that the special roles of these two nonlinearities is the same as for the pure drift wave models: the vorticity always very powerfully excites the turbulence by enlarging its available space of nonadiabaticity, while the pressure nonlinearity always acts to provide saturation by mixing the pressure disturbances and thereby delivering the thermal free energy to arbitrarily small scales. Toroidal geometry therefore brings no qualitative changes to the dynamics of the fully developed drift wave turbulence with regard to the mechanisms of excitation, energy transfer, or saturation. All of this results from the fact that the vorticity nonlinearity (nonlinear polarisation current) overshadows the interchange forcing.

11.VIII. Summary — Drift Turbulence in Context

What these results show is that it is important to consider the turbulence in context when making judgments about its character, especially when in a situation like this there is more than one possible mode structure into which it can arrange itself. We find in the basic case a strong change in this physical character as the linear instability makes the transition into turbulence. Since the turbulence has no detailed memory beyond several correlation times (typically about 100 in these units), the character the dynamics has in the linear regime is not only not relevant, it delivers an incorrect paradigm as to understanding of the basic nature of the turbulence. This illustrates clearly the danger of relying on linear instability theory in the formative stages of a body of work whose aim is to understand turbulence and transport, something well worth to keep in mind.

The important thing to note about these results is that they all speak together; there are no contradictions. In all cases, the mode structure for low collisionality and low beta is clearly of drift wave character, and the transition to resistive MHD was found to start for $\nu > 10$. Therefore, having examined the properties of the turbulence in its native context (*i.e.*, with measurements of its state rather than generalised considerations of how the equations scale), we can determine where the MHD model begins to be valid, and where we need the drift wave model not only for computation but for fundamental understanding. Where the MHD model loses validity due to the adiabatic response becoming important,

it also loses usefulness as a paradigm, because the basic physics of how the disturbances in pressure and ExB flow communicate undergoes fundamental changes. Generally, MHD is found when the interchange forcing on the pressure overcomes the adiabatic response. For ideal MHD the regime boundary is the ballooning limit at the critical value of $\alpha_M = q^2 R |\nabla \beta|$ for the particular geometry; in the circular tokamak model it is near $\alpha_{M\,\mathrm{crit}} = \hat{s}$. We will show an example of this in the next two chapters, treating the effects of the electron and ion temperatures. For resistive ballooning the ideal Alfvén response is replaced by the dissipative adiabatic response, and the boundary is near $C\omega_B = 1$. The factors of unity will vary with magnetic geometry and some of the complications of the temperatures, but generally for the low beta and moderate collisionality regime in which fusion plasmas are found, one either finds drift wave turbulence if the equilibrium is steady, or ideal ballooning phenomena when there are disruptive events which typically collapse the pressure gradient.

Further Reading

For nonlinear drift wave turbulence and field aligned coordinate systems see the Further Reading section of Chapter 8. The latest version of the flux tube model for general flux tube geometry appears in Appendix B. Some of these results have appeared in *Plasma Phys. Contr. Fusion* 39 (1997) 471, and in "Electromagnetic Gyrofluid Turbulence in Tokamak Edge Geometries" from *Theory of Fusion Plasmas* (Societa Italiana di Fisica, Bologna, 1998), p. 359, and in *Phys. Plasmas* 7 (2000) 1845, all by B. Scott.

12. Effects of the Electron Temperature

B. Scott

Jul 1999

12.I. Introduction — Temperature as Dissipation

In the preceding chapters concerning the results, we have kept to the simplest model of the basic physics which is still capable of capturing the principal effects of fluid drift turbulence driven by the pressure gradient. But in reality the state of the plasma even as two fluids is more complicated than a set of simple ideal or isothermal gases. Especially in the drift wave dynamics regime which is most germane to turbulence in laboratory magnetised plasmas, the compressibility of the parallel electron dynamics leads us to consider nonideal effects in the generalised response of the currents to the pressure and electrostatic potential gradients. We consider the electron and ion temperatures separately, since unlike the ion temperature, the electron temperature does not introduce new eigenmode types, that is, dynamical mechanisms of substantially different character than what we have already seen. The electron temperature is important especially at very low collisionality, where resistive friction is not by itself sufficient to establish appreciable nonadiabatic character in the electron response, and the mechanism for that is Landau damping, a kinetic process which we have to model by extending the fluid paradigm past its regime of formal validity. Even in strongly collisional regimes, the additional physics of the temperature makes the nonlinear drift wave dynamics more robust than otherwise, increasing the relevance of this type of physics to realistic situations. Other than that, the qualitative character of the temperature disturbances is the same as the nonadiabatic part of the density, and therefore there are no changes to the qualitative character of the turbulence itself. More specifically, the mechanisms of free energy transfer between electron pressure and ExB flow disturbances do not change with the addition of the electron temperature.

We first discuss some basic effects the electron temperature has while the fluid model is still formally valid, and then move on to the necessary steps for treatment of the weakly collisional regime.

12.II. Ideal Effects

The electron temperature has a number of ideal effects, which we can think of as those which alter the thermodynamics without introducing actual dissipation. These are the kinetic shear Alfvén dispersion relation, and the diamagnetic heat flux, which in the fluid model is purely reactive. The changes these introduce are minimal, simply a matter of quantitative modification at moderate to small scales.

We studied the kinetic shear Alfvén wave properties in terms of the adiabatic response in Chapter 4. The force potential is $(\widetilde{p}_e - \widetilde{\phi})$, and the response is in $\widetilde{J}_{\|}$. When the temperature is present, the normalised pressure disturbance consists of both density and temperature contributions,

$$\widetilde{p}_e = \widetilde{n}_e + \widetilde{T}_e \tag{12.1}$$

and so we must consider what happens to $\widetilde{T}_e$ in the dynamics. The linearised equations for the electrons as an ideal fluid and the ions as a cold fluid are what we find by taking the linear kinetic shear Alfvén model of Chapter 4, and recovering the temperature equation from Chapter 3, while still neglecting the heat flux. The model is the same as in Chapter 4, except we split $\widetilde{p}_e$ into its two pieces, finding

$$\frac{\partial}{\partial t}\nabla_{\perp}^2\widetilde{\phi} = \frac{\partial \widetilde{J}_{\|}}{\partial s} \tag{12.2}$$

$$\frac{\partial \widetilde{n}_e}{\partial t} = \frac{\partial \widetilde{J}_{\|}}{\partial s} - \frac{\partial \widetilde{u}_{\|}}{\partial s} \tag{12.3}$$

$$\frac{3}{2}\frac{\partial \widetilde{T}_e}{\partial t} = \frac{\partial \widetilde{J}_{\|}}{\partial s} - \frac{\partial \widetilde{u}_{\|}}{\partial s} \tag{12.4}$$

$$\hat{\beta}\frac{\partial \widetilde{A}_{\|}}{\partial t} + \hat{\mu}\frac{\partial \widetilde{J}_{\|}}{\partial t} = \frac{\partial \widetilde{p}_e}{\partial s} - \frac{\partial \widetilde{\phi}}{\partial s} - 0.51\hat{\mu}\nu\widetilde{J}_{\|} \tag{12.5}$$

$$\hat{\epsilon}\frac{\partial \widetilde{u}_{\|}}{\partial t} = -\frac{\partial \widetilde{p}_e}{\partial s} + \mu_{\|}\frac{\partial^2 \widetilde{u}_{\|}}{\partial s^2} \tag{12.6}$$

with $\widetilde{J}_{\|} = -\nabla_{\perp}^2\widetilde{A}_{\|}$ and $\widetilde{p}_e = \widetilde{n}_e + \widetilde{T}_e$, under local drift ordering and normalisation in terms of ρ_s, c_s, and $qR/L_{\perp}$. Since $\widetilde{n}_e$ and $\widetilde{T}_e$ combine, we obtain the same four modes we had before, namely, the two sound waves and kinetic shear Alfvén waves with the ratio of specific heats $\Gamma = 5/3$. Since there are five equations there is a fifth mode, which we can find simply by showing that without the background gradients, curvature terms, and extra dissipation channels, the combination $\widetilde{n}_e - (3/2)\widetilde{T}_e$ does not change. This mode is damped by thermal conduction, as we will see below. So to this point all $\widetilde{T}_e$ does is set

Γ to 5/3, following the factor of 3/2 in front of $\partial \widetilde{T}_e/\partial t$. If this factor is changed to an arbitrary constant c_f, then Γ becomes $(1+c_f)/c_f$.

The other dissipation free effect is the diamagnetic heat flux. If we take the simple two dimensional interchange model of Chapter 10, adding the effects due to $\widetilde{T}_e$ (background gradient, where $\omega_t = L_\perp/L_{Te}$, contribution of $\widetilde{T}_e$ to $\widetilde{p}_e$, and the diamagnetic heat flux), we find

$$\frac{d_E}{dt}\nabla_\perp^2 \widetilde{\phi} = -\omega_B \frac{\partial \widetilde{p}_e}{\partial y} \tag{12.7}$$

$$\frac{d_E \widetilde{n}_e}{dt} = -\omega_n \frac{\partial \widetilde{\phi}}{\partial y} - \omega_B \frac{\partial}{\partial y}\left(\widetilde{p}_e - \widetilde{\phi}\right) \tag{12.8}$$

$$\frac{3}{2}\frac{d_E \widetilde{T}_e}{dt} = -\frac{3}{2}\omega_t \frac{\partial \widetilde{\phi}}{\partial y} - \omega_B \frac{\partial}{\partial y}\left(\frac{5}{2}\widetilde{T}_e + \widetilde{p}_e - \widetilde{\phi}\right) \tag{12.9}$$

The term involving the factor of 5/2 is the diamagnetic heat flux, as derived in Chapter 3. All this does is to change the reactivity of the ExB flows to the overall gradient, given by

$$\frac{L_\perp}{L_p} = \omega_n + \omega_t \tag{12.10}$$

The long wavelength limit is not changed at all, except instead of ω_n we now have $\omega_n + \omega_t$. The ideal interchange growth rate is still given by $\gamma_I^2 = c_s^2/L_B L_p$, leaving little modification to the turbulence, since although the dispersion relation changes for higher $k_\perp$ the turbulence is dominated by the largest scales. Generally, this factor of 5/2 is $c_f + 1$, or $\Gamma/(\Gamma - 1)$.

12.III. Dissipation – Damping of Kinetic Shear Alfvén Waves

Keeping to the collisional fluid model, we can introduce the conductive heat flux and investigate its effect on linear kinetic shear Alfvén waves. We take the same model as in Eqs. (12.2–12.6) above, and add the conductive heat flux from the Braginskii model,

$$\frac{3}{2}\frac{\partial \widetilde{T}_e}{\partial t} = \frac{\partial \widetilde{J}_\parallel}{\partial s} - \frac{\partial \widetilde{q}_{e\parallel}}{\partial s} - \frac{\partial \widetilde{u}_\parallel}{\partial s} \tag{12.11}$$

$$\widetilde{q}_{e\parallel} = -0.71\widetilde{J}_\parallel - \frac{3.2}{\hat{\mu}\nu}\frac{\partial \widetilde{T}_e}{\partial s} \tag{12.12}$$

while taking care to include the thermal force (the Onsager symmetric counterpart to the thermal heat flux, $0.71\widetilde{J}_\parallel$) in the Ohm's law,

$$\hat{\beta}\frac{\partial \widetilde{A}_\parallel}{\partial t} + \hat{\mu}\frac{\partial \widetilde{J}_\parallel}{\partial t} = \frac{\partial \widetilde{p}_e}{\partial s} + 0.71\frac{\partial \widetilde{T}_e}{\partial s} - \frac{\partial \widetilde{\phi}}{\partial s} - 0.51\hat{\mu}\nu\widetilde{J}_\parallel \tag{12.13}$$

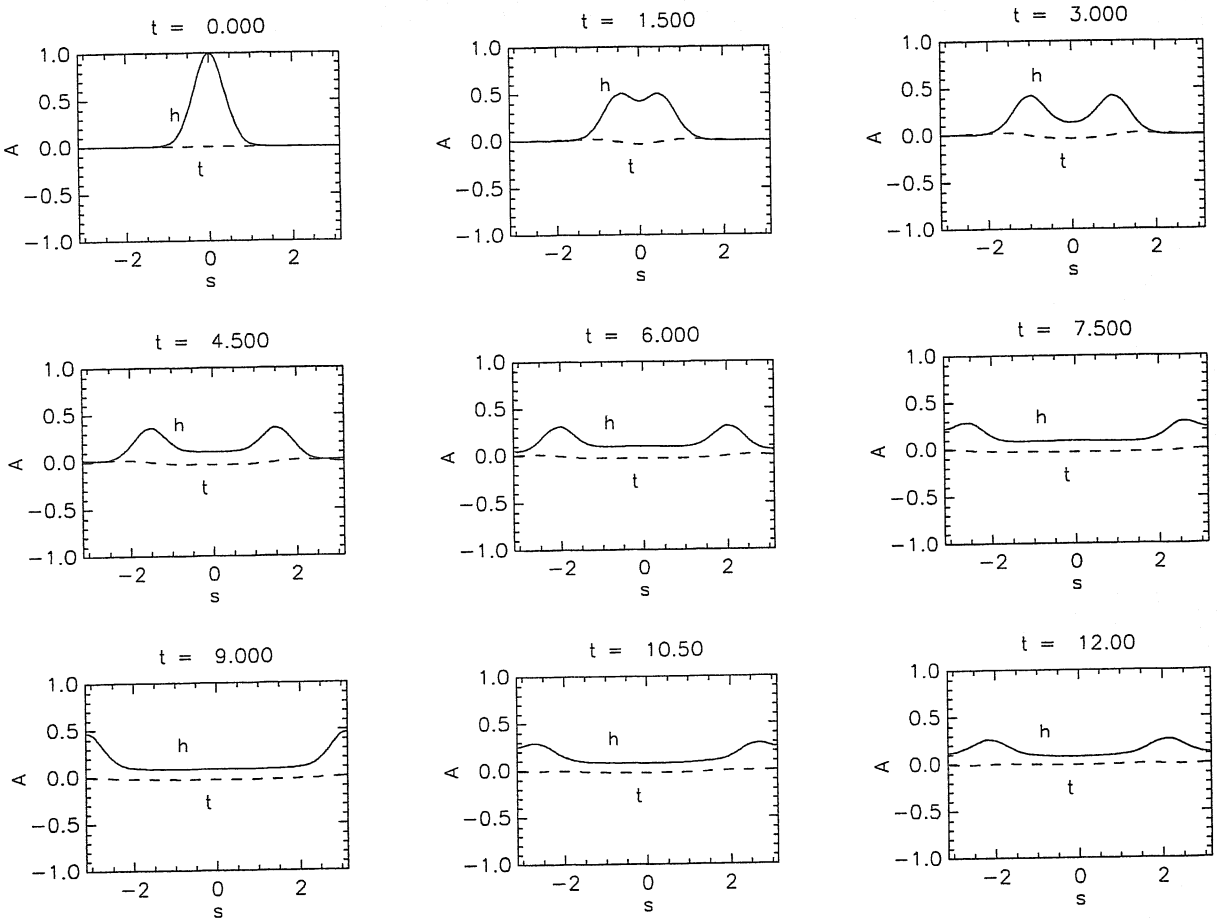

Figure 12.1. A kinetic shear Alfvén wave oscillation, for the electromagnetic case, showing only $\widetilde{h}_e = \widetilde{n}_e - \widetilde{\phi}$ ('h') and $\widetilde{T}_e$ ('t'). The temperature damps quickly, leaving an isothermal wave to oscillate and damp on a resistive time scale. Compare with Fig. 4.10.

We have the same five modes as before, but now the combination $\widetilde{n}_e - (3/2)\widetilde{T}_e$ will damp since the $\widetilde{T}_e$ part is damped by $\widetilde{q}_{e\|}$, and the $\widetilde{n}_e$ part damps through the action of resistivity on $\widetilde{J}_{\|}$. Taking this system of five dynamical equations, we illustrate the effect using the initial value examples from Chapter 4. In these normalised units, the periodicity length in s is simply 2π, with the connection length built into the parameters via the factors of $qR/L_\perp$. For an electromagnetic case, we take the parameter set

$$\hat{\beta} = 10 \quad \hat{\mu} = 5 \quad \nu = 1 \quad \hat{\epsilon} = 18350 \quad \mu_{\|} = 10 \tag{12.14}$$

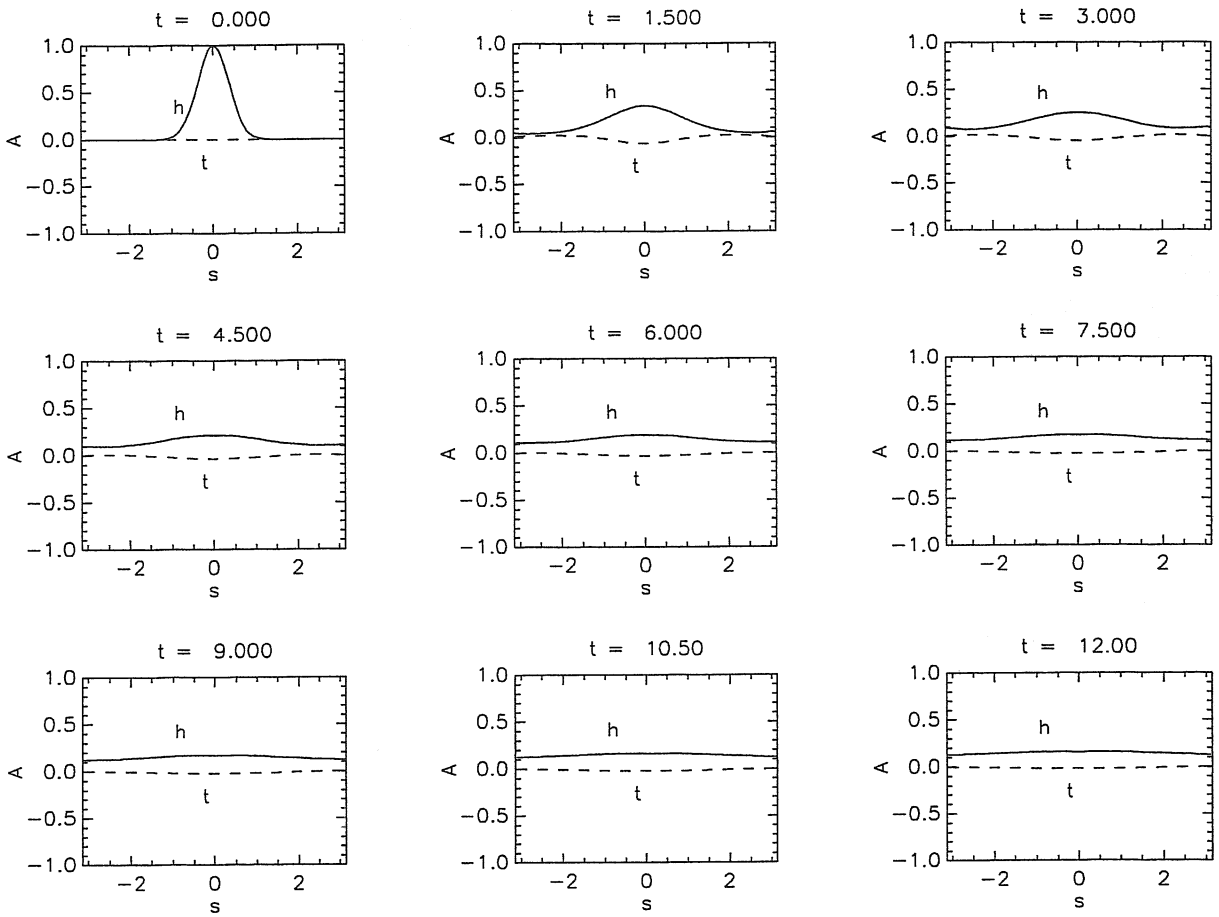

Figure 12.2. A kinetic shear Alfvén wave oscillation, for the electrostatic case, showing only $\widetilde{h}_e = \widetilde{n}_e - \widetilde{\phi}$ ('h') and $\widetilde{T}_e$ ('t'). Both quantities diffuse resistively, at comparable rates.

and investigate the fate of initial density disturbances with $K = 0.7$ where we are replacing $\nabla_\perp^2$ with $-K^2$, and setting

$$\widetilde{n}_e = \exp(-2s^2) \tag{12.15}$$

with all other dependent variables zero, at $t = 0$. The initial response is shown in Fig. 12.1. With this small value of ν we find that the temperature is the first quantity to damp, followed by the main Alfvén quantities $\widetilde{n}_e - \widetilde{\phi}$ and $\widetilde{J}_\parallel$, followed by the isothermal sound wave quantities $\widetilde{n}_e$ and $\widetilde{u}_\parallel$. This is the basic feature of thermal conduction on the parallel dynamics: the tendency to have things isothermal. On the other hand, if we take a

collisional electrostatic case,

$$\hat{\beta} = 0.1 \quad \hat{\mu} = 1 \quad \nu = 10 \quad \hat{\epsilon} = 3670 \quad \mu_{\|} = 10 \tag{12.16}$$

we find from the initial response in Fig. 12.2 that the damping rates of $\widetilde{n}_e - \widetilde{\phi}$ and $\widetilde{T}_e$ are similar, since deep into this regime we have

$$\widetilde{J}_{\|} = C^{-1}\nabla_{\|}[1.71\widetilde{T}_e + \widetilde{n}_e - \widetilde{\phi}] \tag{12.17}$$

$$1.71\widetilde{J}_{\|} - \widetilde{q}_{e\|} = C^{-1}\nabla_{\|}\left[(1.6 + 1.71^2)\widetilde{T}_e + 1.71(\widetilde{n}_e - \widetilde{\phi})\right] \tag{12.18}$$

in which the symmetry is obvious.

12.IV. The Problem of Closure

The problem with the collisional diffusive flux model is that it is limited not only temporally but also spatially. If we neglect the temperatures as in previous chapters this is not a concern because the sole dissipation mechanism is resistive friction of the parallel current, which involves time scales only. But if we face situations in which the collisionality is very low, we have to expand the model to include other dissipation mechanisms. These usually spring from kinetic effects even though we will model them in fluid equations — similarly to the way we already derived the collisional diffusive flux model in Chapter 2.

For the collisional diffusive flux model to be valid, the mean free path λ_{mfp} must satisfy $k_{\|}\lambda_{mfp} \ll 1$, in addition to the temporal limit of $\omega \ll \nu_e$. For drift wave turbulence in almost any interesting regime, at least the latter limit fails, and usually both limits are violated, especially for the Alfvénic transients which have frequencies at least as large as $c_s/L_{\perp}$. What happens when either or both of these limits is violated is that dissipation is taken over by a process called Landau damping — particles with a velocity specifically close to the phase velocity of the wave will interact resonantly with the wave, with those slightly faster being slowed and those slightly slower being accelerated. Since in a Maxwellian distribution of velocities there are more of the slower particles, the net effect is for the wave to damp and the background to heat. Since this is a heating effect with no net particle transfer, its fundamental physics is the same as thermal conduction. So when we extend the fluid model to try to capture this effect, it is natural that we do so using the parallel heat flux. Additionally, the time delays inherent in motion over one mean free path taking a finite time compared to the overall forcing of the dynamics means that this parallel heat flux has to become time dependent. We could do that through an integral formula including time delays, but that is a very expensive proposition in a computation.

What is better is to construct a dynamical equation for $\widetilde{q}_{e\|}$, treating it as a dependent variable interacting with $\widetilde{T}_e$ on the same basis of self consistency that we already follow in the interaction of $\widetilde{J}_\|$ with $\widetilde{p}_e$ and $\widetilde{\phi}$.

The way we do this is to construct a moment equation for $\widetilde{q}_{e\|}$ extending the moment approach to deriving the fluid equations by one level additional to the three that are usual. We motivate the process by noting that the standard collisional formulae are merely the largest terms in the equations we end with, for the limit that ν is arbitrarily large. So we reformulate the collisional equations for $\widetilde{J}_\|$ and $\widetilde{q}_{e\|}$, treating damping rates instead of conductivities. The collisional, electrostatic formulae for the parallel current and heat flux become

$$0 = V_e^2 \nabla_\| \left(\frac{\widetilde{p}_e}{p_e} - \frac{e\widetilde{\phi}}{T_e} \right) - \nu_e \left[0.51 \frac{\widetilde{J}_\|}{n_e e} + \frac{0.71}{3.2} \left(\frac{\widetilde{q}_{e\|}}{n_e T_e} + 0.71 \frac{\widetilde{J}_\|}{n_e e} \right) \right] \tag{12.19}$$

$$0 = -V_e^2 \nabla_\| \frac{\widetilde{T}_e}{T_e} - \frac{1}{3.2} \nu_e \left(\frac{\widetilde{q}_{e\|}}{n_e T_e} + 0.71 \frac{\widetilde{J}_\|}{n_e e} \right) \tag{12.20}$$

for small disturbances in scaled physical units. Here we have simply rearranged things such that the parallel gradients of the state variables are the forcing terms and the parallel flux variables are acted upon by a dissipation matrix. The dissipation matrix is nondiagonal because the two particle Coulomb collision frequency depends on relative velocity (*i.e.*, the mean free path is a function of the velocity). We saw this as the origin of the thermal forces, or thermoelectric effect, in Chapter 2, Section X.

What we have to do now is to add the time derivatives to take care of the frequency domain, and an extra dissipation operator on $\widetilde{q}_{e\|}$ to treat the long mean free path regime. The numerical factors on the time derivatives are set by the moment expansion, and the dissipation operator will be set by approximating the kinetic damping rates as closely as possible. The forms we use are given by

$$\frac{\partial}{\partial t} \frac{e\widetilde{A}_\|}{m_e c} + \frac{d_E}{dt} \frac{\widetilde{J}_\|}{n_e e} = V_e^2 \nabla_\| \left(\frac{\widetilde{p}_e}{p_e} - \frac{e\widetilde{\phi}}{T_e} \right) - \nu_e \left[0.51 \frac{\widetilde{J}_\|}{n_e e} + \frac{0.71}{3.2} \left(\frac{\widetilde{q}_{e\|}}{n_e T_e} + 0.71 \frac{\widetilde{J}_\|}{n_e e} \right) \right] \tag{12.21}$$

$$\frac{d_E}{dt} \frac{\widetilde{q}_{e\|}}{n_e T_e} = -\frac{5}{2} V_e^2 \nabla_\| \frac{\widetilde{T}_e}{T_e} - a_{Le} \left(\frac{\widetilde{q}_{e\|}}{n_e T_e} \right) - \frac{5/2}{3.2} \nu_e \left(\frac{\widetilde{q}_{e\|}}{n_e T_e} + 0.71 \frac{\widetilde{J}_\|}{n_e e} \right) \tag{12.22}$$

where a_{Le} is the Landau damping operator and as usual d/dt is the ExB advective derivative. The factors of $5/2$ in the equation for $\widetilde{q}_{e\|}$ comes from the moment hierarchy considerations just mentioned.

We can easily verify the reactive part of this by applying the moment approach to the one dimensional drift kinetic equation for electrons,

$$\frac{d_E f_e}{dt} = -w_\parallel \nabla_\parallel f_e + \frac{e}{m_e} E_\parallel \frac{\partial f_e}{\partial w_\parallel} \tag{12.23}$$

We neglect the perpendicular dynamics but allow three degrees of freedom in the velocities, as in the treatments in Chapter 2. The first five moments, needed for the first four moment equations (due to the $w_\parallel \nabla_\parallel$ term), are given by

$$n_e = \int d^3w\, f_e \tag{12.24}$$

$$n_e v_\parallel = \int d^3w\, w_\parallel f_e \tag{12.25}$$

$$n_e \frac{m_e v^2}{2} + \frac{3}{2} p_e \quad \rightarrow \quad \frac{3}{2} p_e = \int d^3w\, \frac{m_e w^2}{2} f_e \tag{12.26}$$

$$\left(\frac{5}{2} p_e + n_e \frac{m_e v^2}{2}\right) v_\parallel + q_{e\parallel} \quad \rightarrow \quad \frac{5}{2} p_e v_\parallel + q_{e\parallel} = \int d^3w\, \frac{m_e w^2}{2} w_\parallel f_e \tag{12.27}$$

$$\frac{5}{2}\frac{p_e T_e}{m_e} + \left(n_e \frac{m_e v^2}{2} + \frac{3}{2} p_e\right) v_\parallel^2 + m_e \frac{v^2}{2} v_\parallel^2 + R_\parallel \quad \rightarrow \quad \frac{5}{2}\frac{p_e T_e}{m_e} + R_\parallel = \int d^3w\, \frac{m_e w^2}{2} w_\parallel^2 f_e \tag{12.28}$$

neglecting $m_e v^2$ and $m_e v_\parallel^2$ compared to $(3/2)p_e$. Closure is the term used for the procedure for truncating this hierarchy. If f_e is a drifting Maxwellian, then $q_{e\parallel}$ and $R_\parallel$ are zero and we obtain the ideal fluid equations. What we do is take an approximation: keep all of these moments and then replace the last one by a formula given by the lower moments. We could simply set $R_\parallel$ to zero, but this would give a reactive equation for $q_{e\parallel}$ in the limit that $\nu \rightarrow 0$, which we do not want. For the nonlinear, perpendicular part we simply add the magnetic flutter contributions to $\nabla_\parallel$ acting on densities and temperatures, and add the ExB advection contribution to d/dt.

We need some guidance for the dissipation, $R_\parallel$, and the way to get it is to look at the electrostatic kinetic problem. The normalised drift kinetic equation for electrons under this limit is

$$\frac{\partial \widetilde{f}_e}{\partial t} = -\omega_T v_D f^M \frac{\partial}{\partial y}\frac{e\widetilde{\phi}}{T_e} - w_\parallel \nabla_\parallel \left(\widetilde{f}_e - f^M \frac{e\widetilde{\phi}}{T_e}\right) \tag{12.29}$$

where $v_D = \rho_s c_s / L_\perp$ is the diamagnetic drift velocity, and f^M is the local Maxwellian and ω_T is the velocity space combination of the background gradients, given by

$$f^M = \pi^{-3/2} \frac{n_e}{v_t^3} e^{-w^2/v_t^2} \qquad \omega_T = \omega_n + \left(\frac{w^2}{v_t^2} - \frac{3}{2}\right)\omega_t \tag{12.30}$$

and ω_n and ω_t the normalised gradient strengths as above, and $v_t^2 = 2T_e/m_e$.

We can Fourier transform this and then simply solve it for $\widetilde{f}_e$, and then express the density response as

$$\frac{\widetilde{n}_e}{n_e} = \int d^3w\, \widetilde{f}_e = \pi^{-3/2} \int \frac{d^3w}{v_t^3} \frac{k_\parallel w_\parallel - \omega_T v_D k_y}{k_\parallel w_\parallel - \omega} e^{-w^2/v_t^2} \frac{e\widetilde{\phi}}{T_e} \tag{12.31}$$

As we saw in Chapter 5, such an expression of the linear response ($\widetilde{n}_e$ in terms of $\widetilde{\phi}$) is sufficient to obtain the drift wave dispersion relation. But in this case it is enough to have $\widetilde{f}_e$ so that we can find the necessary disturbances in the moment hierarchy. Integrals of the form in Eq. (12.31) are solved in terms of the plasma dispersion function, or simply Z-function, given by

$$Z(y) = \pi^{-1/2} \int_{-\infty}^{\infty} \frac{dw\, e^{-w^2}}{w - y} \tag{12.32}$$

The parallel Landau closure is obtained by setting up the moments such that this Z-function is properly approximated to a given desired order. It can be shown (see Further Reading) that a three moment expansion, in which all moments are expressed in terms of the first three of $\widetilde{n}_e$, $\widetilde{v}_\parallel$, $\widetilde{T}_e$, is equivalent to a three pole expansion of the Z-function in terms of w. By extending the set of moments to four variables including $\widetilde{q}_{e\parallel}$, we are using a four pole expansion. This is obtained in the high and low frequency limits using the asymptotic forms of the Z-function,

$$\lim_{y\to 0} Z(y) = i\pi^{1/2} \qquad \lim_{y\to\infty} Z(y) = -y^{-1} \tag{12.33}$$

by setting

$$\widetilde{R}_\parallel = -D_0 \frac{V_e}{|k_\parallel|} ik_\parallel \widetilde{q}_{e\parallel} + D_1 \frac{p_e}{m_e} \widetilde{T}_e \tag{12.34}$$

such that the native damping rate of $\widetilde{q}_{e\parallel}$ is given by

$$\frac{\partial \widetilde{q}_{e\parallel}}{\partial t} \to -D_0 \left|k_\parallel V_e\right| \widetilde{q}_{e\parallel} \tag{12.35}$$

where D_0 and D_1 are numerical constants of order unity. For a one-degree of freedom model with $\Gamma = 3$ and hence the 5/2 and 3/2 factors in the moment hierarchy (Eqs. 12.24–12.28) changing to 3/2 and 1/2, the values of the constants are $D_0 = (8\pi)^{1/2}/(3\pi - 8)$ and $D_1 = (32 - 9\pi)/(6\pi - 16)$, respectively (a truly collisionless model will treat parallel and perpendicular temperatures separately by using $w_\parallel^2$ and $w_\perp^2$ respectively in Eq. 12.26.) We note that the extra piece involving $\widetilde{T}_e$ acts to speed up the thermal relaxation in

the $\{\widetilde{T}_e, \widetilde{q}_{e\|}\}$ subsystem, capturing the fact that the perturbed distribution function is somewhat non-Maxwellian, with the faster particles in an enhanced role.

If we could do all computations in Fourier space we could just use this as a formula for $\widetilde{R}_\|$. In general, however, we need to stay in configuration space since not only do we not always have periodicity in the parallel direction, we also have to face the fact that $\nabla_\|$ is a nonlinear operator involving derivatives of $\widetilde{A}_\|$, that is, one of the dependent variables. The best we can do in this circumstance is to make a model, and check that it gives the correct behaviour. The model we use here is to neglect the extra $\widetilde{T}_e$ piece in $\widetilde{R}_\|$, and to replace a_{Le} by a constant plus a second order differential operator, such that the longest wavelengths are damped at the correct rate (similar to V_e/qR), and the damping rate increases towards shorter wavelength. In a computation with a given step size in the s-direction, the fastest damping rate should be similar to V_e/h_s. A first order upwind numerical scheme gives a damping rate of $2V_e/h_s$ (diffusion coefficient of $h_sV_e/2$ times the numerical squared wavenumber of $4/h_s^2$), which we can compare to the Fourier rate of $2D_0V_e/h_s$. There is some freedom on how to set the constant, as the simple forms above are valid for the case with only one degree of freedom and we are using an isotropic temperature more relevant to moderate to high collisionality, and the substitute for long wavelength damping is a matter of modelling anyway. We set the constant in front of V_e/qR to unity as a model.

12.V. The DALFTE Model of Landau Fluid Drift Dynamics

In Chapter 11, we presented the DALF3 four field collisional model of drift wave turbulence in general flux tube geometry, for the most basic treatments involving $\widetilde{\phi}$, $\widetilde{p}_e$, $\widetilde{J}_\|$, and $\widetilde{u}_\|$. We now add $\widetilde{T}_e$ and $\widetilde{q}_{e\|}$ to this set, and replace $\widetilde{p}_e$ with $\widetilde{n}_e$ as a dependent variable, with $\widetilde{p}_e$ given by $\widetilde{n}_e + \widetilde{T}_e$. Except for the model equations, all other considerations in the outline of the DALF3 model apply. The equations are

$$\frac{1}{B^2}\frac{d_E}{dt}\nabla_\perp^2\widetilde{\phi} = B\nabla_\|\frac{\widetilde{J}_\|}{B} - \mathcal{K}\left(\widetilde{p}_e\right) \tag{12.36}$$

$$\hat{\beta}\frac{\partial\widetilde{A}_\|}{\partial t} + \hat{\mu}\frac{d_E\widetilde{J}_\|}{dt} = \nabla_\|\left(p_e + \widetilde{p}_e - \widetilde{\phi}\right) - \hat{\mu}\nu\left[0.51\widetilde{J}_\| + \frac{0.71}{3.2}\left(\widetilde{q}_{e\|} + 0.71\widetilde{J}_\|\right)\right] \tag{12.37}$$

$$\frac{d_E}{dt}\left(n_e + \widetilde{n}_e\right) = B\nabla_\|\frac{\widetilde{J}_\| - \widetilde{u}_\|}{B} - \mathcal{K}\left(\widetilde{p}_e - \widetilde{\phi}\right) \tag{12.38}$$

$$\hat{\epsilon}\frac{d_E\widetilde{u}_\|}{dt} = -\nabla_\|\left(p_e + \widetilde{p}_e\right) + \mu_\|\nabla_\|^2\widetilde{u}_\| \tag{12.39}$$

$$\frac{d_E}{dt}\left(T_e + \widetilde{T}_e\right) = B\nabla_\|\frac{\widetilde{J}_\| - \widetilde{u}_\| - \widetilde{q}_{e\|}}{B} - \mathcal{K}\left(\widetilde{p}_e - \widetilde{\phi} + \frac{5}{2}\widetilde{T}_e\right) \tag{12.40}$$

$$\hat{\mu}\frac{d_E\widetilde{q}_{e\|}}{dt} = -\frac{5}{2}\nabla_\|\left(T_e+\widetilde{T}_e\right) - a_{Le}\left(\widetilde{q}_{e\|}\right) - \frac{5/2}{3.2}\hat{\mu}\nu\left(\widetilde{q}_{e\|}+0.71\widetilde{J}_\|\right) \tag{12.41}$$

with auxiliaries

$$\widetilde{p}_e = \widetilde{n}_e + \widetilde{T}_e \qquad \widetilde{J}_\| = -\nabla_\perp^2\widetilde{A}_\| \qquad \frac{d_E}{dt} = \frac{\partial}{\partial t} + \mathbf{v}_E\cdot\nabla \tag{12.42}$$

$$\mathbf{v}_E\cdot\nabla = \frac{\partial\widetilde{\phi}}{\partial x}\frac{\partial}{\partial y} - \frac{\partial\widetilde{\phi}}{\partial y}\frac{\partial}{\partial x} \qquad \nabla_\| = \frac{B^s}{B}\frac{\partial}{\partial s} - \hat{\beta}\left(\frac{\partial\widetilde{A}_\|}{\partial x}\frac{\partial}{\partial y} - \frac{\partial\widetilde{A}_\|}{\partial y}\frac{\partial}{\partial x}\right) \tag{12.43}$$

$$\nabla_\|^2 = \nabla\cdot\mathbf{bb}\cdot\nabla = B\nabla_\|\frac{1}{B}\nabla_\| \tag{12.44}$$

The flux surface geometry ($\nabla_\perp^2$, B^s, B^2, $\mathcal{K}$, shifts to make g_k^{xy} vanish) and computational domain remain as before. Drive terms appear wherever $\partial/\partial x$ acts upon p_e or T_e, with

$$\frac{\partial n_e}{\partial x} \to -\omega_n \qquad \frac{\partial T_e}{\partial x} \to -\omega_t \qquad \frac{\partial p_e}{\partial x} \to -(\omega_n+\omega_t) \tag{12.45}$$

representing $L_\perp/L_n$, $L_\perp/L_{Te}$, and $L_\perp/L_{pe}$, respectively. The Landau damping operator is

$$a_{Le} = \hat{\mu}^{1/2}\left(1-0.2\nabla_\|^2\right) \tag{12.46}$$

12.VI. Energetics of the DALFTE Model

The energetics of this model is very similar to that for the DALF3 model; we simply add complexity to the already existing transfer channels, as well as the extra source and sink represented by ∇T_e and $\widetilde{q}_{e\|}$. To form the energy theorem we multiply Eqs. (12.36–12.41) by $-\widetilde{\phi}$, $\widetilde{J}_\|$, $\widetilde{n}_e$, $\widetilde{u}_\|$, $\widetilde{T}_e$, and $(2/5)\widetilde{q}_{e\|}$, respectively, and integrate (as an average, as in Chapter 7) over the domain. We find the following, in which the integration/averaging operation is denoted by the angle brackets,

$$\frac{\partial}{\partial t}\left\langle\frac{1}{2}\frac{1}{B^2}\left|\nabla_\perp\widetilde{\phi}\right|^2\right\rangle = \left\langle\widetilde{J}_\|\nabla_\|\widetilde{\phi}\right\rangle - \left\langle\widetilde{p}_e\mathcal{K}\widetilde{\phi}\right\rangle \tag{12.47}$$

$$\begin{aligned}\frac{\partial}{\partial t}\left\langle\frac{1}{2}\widetilde{J}_\|\left(\hat{\beta}\widetilde{A}_\|+\hat{\mu}\widetilde{J}_\|\right)\right\rangle = \left\langle\widetilde{J}_\|\nabla_\|\widetilde{p}_e\right\rangle - \left\langle\widetilde{J}_\|\nabla_\|\widetilde{\phi}\right\rangle - \\ - 0.51\hat{\mu}\nu\left\langle\left|\widetilde{J}_\|\right|^2\right\rangle - \hat{\mu}\nu\left\langle 0.71\widetilde{J}_\|\frac{\widetilde{q}_{e\|}+0.71\widetilde{J}_\|}{3.2}\right\rangle\end{aligned} \tag{12.48}$$

$$\frac{\partial}{\partial t}\left\langle\frac{1}{2}\left|\widetilde{n}_e\right|^2\right\rangle = -\left\langle\widetilde{J}_\|\nabla_\|\widetilde{n}_e\right\rangle + \left\langle\widetilde{u}_\|\nabla_\|\widetilde{n}_e\right\rangle + \left\langle\widetilde{n}_e\mathcal{K}\widetilde{\phi}\right\rangle - \left\langle\widetilde{n}_e\mathcal{K}\widetilde{T}_e\right\rangle + \omega_n\left\langle-\widetilde{n}_e\frac{\partial\widetilde{\phi}}{\partial y}\right\rangle \tag{12.49}$$

$$\frac{\partial}{\partial t}\left\langle \frac{\hat{\epsilon}}{2}\left|\widetilde{u}_{\parallel}\right|^2\right\rangle = -\left\langle \widetilde{u}_{\parallel}\nabla_{\parallel}\widetilde{p}_e\right\rangle + (\omega_n+\omega_t)\hat{\beta}\left\langle \widetilde{u}_{\parallel}\frac{\partial \widetilde{A}_{\parallel}}{\partial y}\right\rangle - \mu_{\parallel}\left\langle \left|\nabla_{\parallel}\widetilde{u}_{\parallel}\right|^2\right\rangle \tag{12.50}$$

$$\begin{aligned}\frac{3}{2}\frac{\partial}{\partial t}\left\langle \frac{1}{2}\left|\widetilde{T}_e\right|^2\right\rangle = &-\left\langle \widetilde{J}_{\parallel}\nabla_{\parallel}\widetilde{T}_e\right\rangle + \left\langle \widetilde{q}_{e\parallel}\nabla_{\parallel}\widetilde{T}_e\right\rangle + \left\langle \widetilde{u}_{\parallel}\nabla_{\parallel}\widetilde{T}_e\right\rangle + \\ &+\left\langle \widetilde{T}_e\mathcal{K}\widetilde{\phi}\right\rangle + \left\langle \widetilde{n}_e\mathcal{K}\widetilde{T}_e\right\rangle + \frac{3}{2}\omega_t\left\langle -\widetilde{T}_e\frac{\partial\widetilde{\phi}}{\partial y}\right\rangle\end{aligned} \tag{12.51}$$

$$\begin{aligned}\frac{2}{5}\frac{\partial}{\partial t}\left\langle \frac{\hat{\mu}}{2}\left|\widetilde{q}_{e\parallel}\right|^2\right\rangle = &-\left\langle \widetilde{q}_{e\parallel}\nabla_{\parallel}\widetilde{T}_e\right\rangle + \omega_t\hat{\beta}\left\langle \widetilde{q}_{e\parallel}\frac{\partial\widetilde{A}_{\parallel}}{\partial y}\right\rangle - \\ &-\frac{2}{5}\left\langle \widetilde{q}_{e\parallel}a_{Le}(\widetilde{q}_{e\parallel})\right\rangle - \hat{\mu}\nu\left\langle \widetilde{q}_{e\parallel}\frac{\widetilde{q}_{e\parallel}+0.71\widetilde{J}_{\parallel}}{3.2}\right\rangle\end{aligned} \tag{12.52}$$

Terms appearing in two equations with opposite sign represent the transfer channels, while isolated terms reflect the sources and sinks. Sinks also appear in combinations which are positive definite (*e.g.*, $|\widetilde{J}_{\parallel}^2|$ in Eq. 12.48). Some of the transfer effects also appear in such combination; an example is the kinetic Alfvén transfer dynamics, in which the pieces of $\widetilde{p}_e$ multiplying $\widetilde{J}_{\parallel}$ in the equations for $\widetilde{n}_e$ and $\widetilde{T}_e$ combine to balance $\widetilde{J}_{\parallel}\nabla_{\parallel}\widetilde{p}_e$ in the Ohm's law. There is also a curvature mediated transfer between $\widetilde{n}_e$ and $\widetilde{T}_e$ through the diamagnetic current, but this keeps free energy in the overall thermal content,

$$U_p = U_n + U_t = \frac{1}{2}\left\langle \left(\left|\widetilde{n}_e\right|^2 + \frac{3}{2}\left|\widetilde{T}_e\right|^2\right)\right\rangle \tag{12.53}$$

In general we have

$$U = U_e + U_n + U_t + U_u + U_B + U_q \tag{12.54}$$

for the free energy, with pieces given by

$$U_e = \frac{1}{2}\left\langle \frac{1}{B^2}\left|\nabla_{\perp}\widetilde{\phi}\right|^2\right\rangle \qquad U_n = \frac{1}{2}\left\langle \left|\widetilde{n}_e\right|^2\right\rangle \qquad U_t = \frac{1}{2}\left\langle \frac{3}{2}\left|\widetilde{T}_e\right|^2\right\rangle \tag{12.55}$$

$$U_u = \frac{1}{2}\left\langle \hat{\epsilon}\left|\widetilde{u}_{\parallel}\right|^2\right\rangle \quad U_B = \frac{1}{2}\left\langle \left(\hat{\beta}\left|\nabla_{\perp}\widetilde{A}_{\parallel}\right|^2 + \hat{\mu}\left|\widetilde{J}_{\parallel}\right|^2\right)\right\rangle \quad U_q = \frac{1}{2}\left\langle \frac{2}{5}\hat{\mu}\left|\widetilde{q}_{e\parallel}\right|^2\right\rangle \tag{12.56}$$

and

$$\frac{1}{2U}\frac{\partial U}{\partial t} = \Gamma_n + \Gamma_t + \Gamma_m - \Gamma_c - \Gamma_k - \Gamma_l - \Gamma_s \tag{12.57}$$

with sources and sinks given by

$$\Gamma_n = \frac{1}{2U}\left\langle -\omega_n\widetilde{n}_e\frac{\partial\widetilde{\phi}}{\partial y}\right\rangle \qquad \Gamma_t = \frac{1}{2U}\left\langle -\frac{3}{2}\omega_t\widetilde{T}_e\frac{\partial\widetilde{\phi}}{\partial y}\right\rangle \tag{12.58}$$

$$\Gamma_m = \frac{1}{2U}\left\langle \omega_t \hat{\beta}\widetilde{q}_{e\|}\frac{\partial \widetilde{A}_\|}{\partial y} + (\omega_n+\omega_t)\hat{\beta}\widetilde{u}_\|\frac{\partial \widetilde{A}_\|}{\partial y}\right\rangle \tag{12.59}$$

$$\Gamma_c = \frac{1}{2U}\left\langle 0.51\hat{\mu}\nu\left|\widetilde{J}_\|\right|^2\right\rangle \qquad \Gamma_k = \frac{1}{2U}\left\langle \frac{\hat{\mu}\nu}{3.2}\left|\widetilde{q}_{e\|}+0.71\widetilde{J}_\|\right|^2\right\rangle \tag{12.60}$$

$$\Gamma_l = \frac{1}{2U}\left\langle \widetilde{q}_{e\|}a_{Le}(\widetilde{q}_{e\|})\right\rangle \qquad \Gamma_s = \frac{1}{2U}\left\langle \mu_\|\left|\nabla_\|\widetilde{u}_\|\right|^2\right\rangle \tag{12.61}$$

all normalised as growth or damping rates. Note the split of the total collisional dissipation into $\Gamma_c+\Gamma_k$, the resistive and conductive pieces.

12.VII. Temperature and the Nonlinear Drift Wave Instability

In both collisional and collisionless regimes, the electron temperature physics strengthens the basic drift wave turbulence in a sheared magnetic field. This is due to the fact that while thermal conduction is added to the dissipation, the temperature gradient is added to the sources. Furthermore, the phase shift between $\widetilde{T}_e$ and $\widetilde{\phi}$ is typically greater than that between $\widetilde{n}_e$ and $\widetilde{\phi}$, since while the parallel dynamics forces $\widetilde{n}_e$ towards $\widetilde{\phi}$, it merely forces $\widetilde{T}_e$ towards zero. For equal gradient strengths ($\omega_n = \omega_t = 1$) we often find the temperature doing more of the drive even though its fluctuation is smaller than that for the density. DALFTE is a Landau fluid model, applicable also at low to zero collisionality, where the principal dissipation mechanism is Landau damping directly on $\widetilde{T}_e$ and $\widetilde{q}_{e\|}$ but also indirectly on $\widetilde{J}_\|$, as we saw from the linear kinetic shear Alfvén dynamics. When this mechanism is important, we are required to keep the electron temperature physics in order to treat drift waves and their associated turbulence.

The stronger drift wave turbulence resulting from the action of ∇T_e and $\widetilde{T}_e$ is a general result, applicable to both slab and toroidal geometry, as we will develop in the next two sections. The temperature physics changes no aspect of the mode structure, and the principal effects are quantitative. At low beta, the mostly electrostatic turbulence is always stronger than the four field model suggests. However, as beta is raised, the magnetic flutter and induction effects become appreciable, and in toroidal geometry so does the ideal interchange effect. In some cases the combined effect of ∇T_e and finite β_e is stabilising. In toroidal geometry, however, the onset of ideal ballooning enters to restrict the drift wave turbulence regime to regions where the turbulence and transport become stronger with rising β_e, if expressed in physical (unnormalised) units.

12.VIII. Temperature and Drift Wave Turbulence in a Toroidal, Sheared Magnetic Field

We repeat the runs of the previous chapter comparing drift wave and interchange (MHD) turbulence in toroidal flux tube geometry to see what effect the electron temperature might have on the transition regime boundary. We simply apply the DALFTE model to the same cases (geometry, domain, parameters) as before. We will not go into so much detail, as most of the work has been done. But there are a few observations that further shed light on the overall physics besides the specific role of the temperature.

We also compare the turbulence from the Landau fluid model in DALFTE to one with the same set of equations under the Braginskii model for collisional electrons. Both models follow $\widetilde{T}_e$ and $\widetilde{q}_{e\|}$, but the Landau model keeps the time dependent and dissipative Landau damping, while the Braginskii model replaces the parallel heat flux with a thermal diffusive damping on the temperature, keeping the thermoelectric effect,

$$\widetilde{q}_{e\|} + 0.71\widetilde{J}_{\|} = -\frac{3.2}{\hat{\mu}\nu}\nabla_{\|}\left(T_e + \widetilde{T}_e\right) \tag{12.62}$$

ultimately applying both parallel derivatives implied in $\nabla_{\|}\widetilde{q}_{e\|}$ to the combination of the disturbance and the background profile of the temperature. The Ohm's law is not changed, since we have combined the thermal force in terms of $\widetilde{q}_{e\|} + 0.71\widetilde{J}_{\|}$ under the collision frequency in Eq. (12.37). Without Landau damping, we might expect the turbulence at low collisionality to be weaker, but this will depend on how much the thermal response to $J_{\|}$ affects the overall physics. We choose the following parameter set,

$$\hat{\beta} = 1 \quad \hat{\mu} = 5 \quad \omega_n = \omega_t = 1 \quad \hat{\epsilon} = 18350 \quad \omega_B = 0.05 \quad \hat{s} = 1 \tag{12.63}$$

and sweep ν through the values $\{1, 3, 10, 30\}$ for the Braginskii cases and from zero to 100 for the Landau cases. The results can be compared to those of the DALF3 isothermal model in the previous chapter. Also, for comparison to those cases we set $\mu_{\|} = 0$ herein as well.

The results for the transport scaling and relative amplitudes $\widetilde{\phi}/\widetilde{n}_e$ and $\widetilde{\phi}/\widetilde{T}_e$ are shown in Fig. 12.3. At moderate to large collisionality the results are qualitatively the same as for the DALF3 model. The relationship between the resistive MHD cases (neglecting the $\widetilde{p}_e \leftrightarrow \widetilde{J}_{\|}$ coupling and the diamagnetic fluxes in the thermodynamics) and the DALFTE cases show the same disagreement as in the four field DALF3 model regarding the transport and the amplitude ratios. We find drift wave mode structure for $\nu \leq 10$, that is, $C \leq 25$, as the amplitudes of all the state variables track each other. Only for $\nu > 10$ does $\widetilde{\phi}$ become much larger than $\widetilde{p}_e$, signalling the onset of the resistive MHD regime.

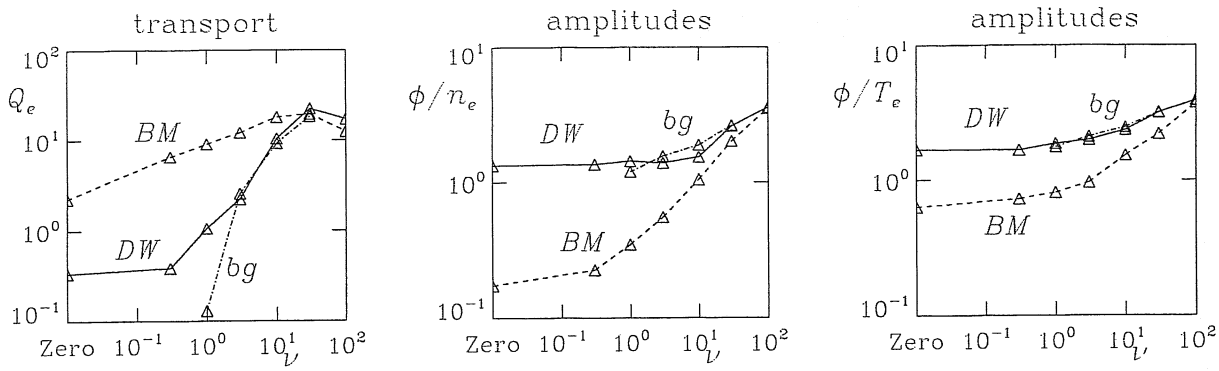

Figure 12.3. (left) Transport scaling of drift wave and interchange turbulence in toroidal geometry under the DALFTE model, labelled 'DW' and 'BM', respectively. Both are weaker at lower collisionality ($C = 2.55\nu$), but the drift wave cases drop off faster. The DALFTE Braginskii cases, labelled 'bg', drop sharply for $\nu < 3$. At asymptotically large C the trends will merge, but that limit is not reached. (center and right) Amplitude ratio $\widetilde{\phi}/\widetilde{n}_e$ and $\widetilde{\phi}/\widetilde{T}_e$ for the three sets of cases. Due to the adiabatic response, $\widetilde{\phi}$ tracks $\widetilde{p}_e = \widetilde{n}_e + \widetilde{T}_e$ for drift wave turbulence, but in the MHD model of the interchange cases $\widetilde{p}_e$ is unaffected by the Alfvén dynamics, and so instead of $\widetilde{\phi}$ being forced towards $\widetilde{p}_e$ it is forced towards zero. Compare with Fig. 11.1

At low collisionality the differences between the Landau and Braginskii closures on the electron temperature become apparent. The turbulence under the Landau fluid model reaches a floor, but that under the Braginskii model continues to drop with ν. This is the effect of Landau damping in drift wave turbulence: to replace thermal conduction with a different kind of dissipation, one which has the same physical role but does not vanish when ν does. The Braginskii model leads to strong turbulence only for moderate to high collisionality, as $\nu = 3$ corresponds to $C = 7.55$. If ν is any lower than this then the Braginskii model significantly overestimates the conductive dissipation of $\widetilde{T}_e$. One often concludes on this basis that drift wave turbulence is limited to regimes of high collisionality, but as we can see from the Landau model at low ν this is not the case. It is the assumptions behind the Braginskii closure that are limited, not drift wave turbulence as such. Other than that, the Braginskii model has no qualitative problems, as it yields the same mode structure as the Landau model in all respects.

We find that the DALFTE model leads to stronger turbulence than does the DALF3 model at the same parameters. The heat transport is larger, as we might expect simply because there are now two gradients driving the turbulence. The particle and heat transport

are given by

$$F_n = \langle \widetilde{n}_e \widetilde{v}_E^x \rangle \qquad\qquad Q_e = \frac{3}{2} \langle \widetilde{p}_e \widetilde{v}_E^x \rangle \tag{12.64}$$

normalised in terms of n_e and $n_e T_e$ times $c_s \rho_s^2 / L_\perp^2$, respectively, where $\widetilde{v}_E^x = -\partial \widetilde{\phi} / \partial y$. Note especially that $Q_e = F_n$ are synonymous for DALF3. For $\nu = \{1, 3, 10\}$ we find $Q_e = \{0.336, 0.885, 2.59\}$ for DALF3 and $Q_e = \{1.06, 2.25, 10.4\}$ for DALFTE, but for the particle flux in the latter we find $F_n = \{0.134, 0.459, 3.07\}$. The error bars on all these numbers are about 15 to 20 percent. At low collisionality, the temperature and its gradient really dominate the energetics, even though the actual amplitude of $\widetilde{T}_e$ is smaller than $\widetilde{n}_e$. When this happens, there is not so much selection as to whether a particular density disturbance should have a specific relation to the flow field, and so the average phase shifts for the density are smaller.

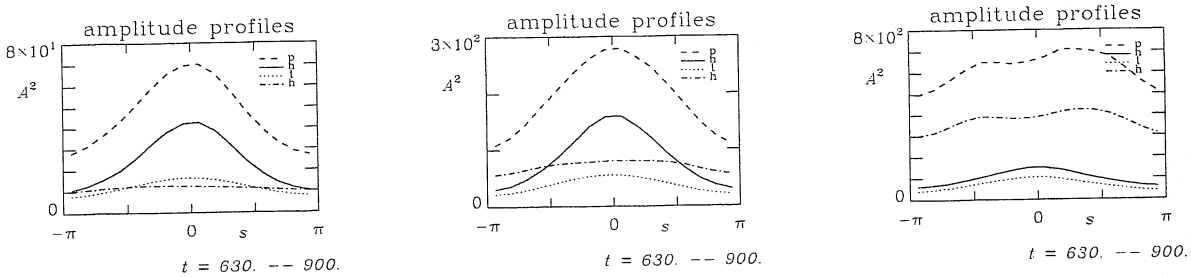

Figure 12.4. Amplitude envelopes of $\widetilde{\phi}$, $\widetilde{n}_e$, $\widetilde{T}_e$, and $\widetilde{h}_e$, respectively labelled by 'p', 'n', 't', and 'h', for drift wave turbulence, for $\nu = 3$, 10, and 30 (left to right), where $C = 2.55\nu$. Comparing with Fig. 11.7, we find the transition to ballooning mode structure for the same $\nu > 10$. For the two drift wave cases (left, center) $\widetilde{h}_e$ gives the flattest curve; for the interchange case (right) it is the curve below that of $\widetilde{\phi}$. Note that $\widetilde{T}_e$ plays the same role in the physics as $\widetilde{h}_e$, part of the overall nonadiabatic dynamics. The asymmetry in $\widetilde{T}_e$, like $\widetilde{h}_e$, is less than for $\widetilde{n}_e$ for drift wave mode structure but is similar for ballooning mode structure, where the amplitude of $\widetilde{\phi}$ becomes relatively larger.

The envelopes of the squared amplitudes of the three state variables in the s-direction is shown in Fig. 12.4, for the three Landau DALFTE cases across the MHD regime boundary, $\nu = \{3, 10, 30\}$. Comparing these to the results in the previous chapter, we find that $\widetilde{T}_e$ has the same structure as $\widetilde{h}_e$, less asymmetric than either $\widetilde{\phi}$ or $\widetilde{n}_e$ at lower ν, and asymmetric to about the same degree as $\widetilde{n}_e$ for $\nu = 30$ at the onset of the MHD regime. We always have $\widetilde{\phi} > \widetilde{n}_e$ because of the presence of $\widetilde{T}_e$, since in the adiabatic response $\widetilde{\phi}$ tracks $\widetilde{p}_e = \widetilde{n}_e + \widetilde{T}_e$. The MHD regime signifies the statistical independence of $\widetilde{\phi}$ versus

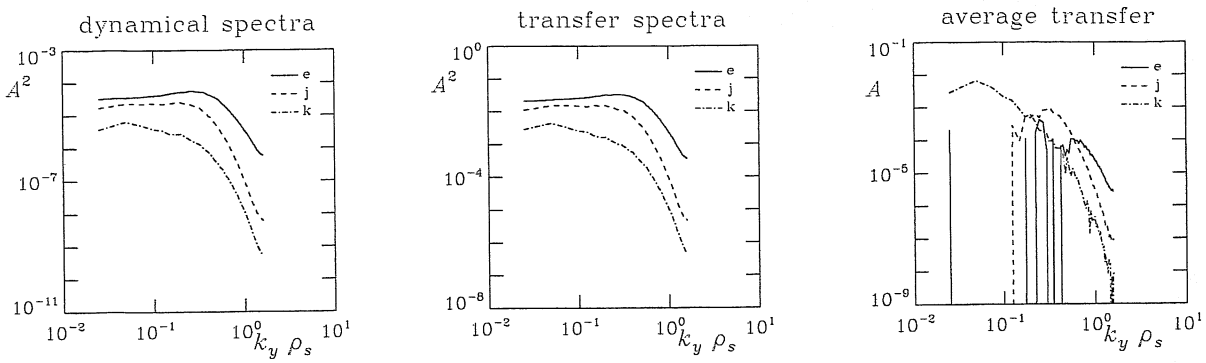

Figure 12.5. ExB dynamical spectra of the polarisation drift ('e'), nonadiabaticity ('j'), and curvature ('k') effects, for drift wave turbulence under the Braginskii closure, for $\nu = 10$, or $C = 25$. (left) Rms spectra of the terms in the vorticity equation, as in Fig. 11.4. (center) Rms spectra of the transfer terms in the ExB energetics, also as in Fig. 11.4. (right) Average spectra of the transfer terms in the ExB energetics. Although the curvature is significant in the average transfer (where it balances the nonadiabaticity, not seen because it is negative at low-k_y), it is not the principal cause of adiabaticity. Note that the rms level of $\mathbf{v}_E \cdot \nabla \nabla_\perp^2 \widetilde{\phi}$ is what is important, not the average. The rms level of $\nabla_\parallel \widetilde{J}_\parallel$ is still larger than $\mathcal{K}(\widetilde{p}_e)$ at all wavelengths, reflective of drift wave dynamics. As ν rises, the curvature balances $\nabla_\parallel \widetilde{J}_\parallel$ and the mode structure makes the transition to the resistive ballooning regime.

the other state variables, which is felt in all the mode structure measurements presented in Chapter 11.

In Fig. 12.5, three versions of the spectra of the ExB transfer dynamics are shown for the Landau DALFTE case $\nu = 10$. In the leftmost frame we have the dynamical spectra, which give the rms levels of $\mathbf{v}_E \cdot \nabla \nabla_\perp^2 \widetilde{\phi}$ (polarisation drift), $\nabla_\parallel \widetilde{J}_\parallel$ (nonadiabaticity), and $\mathcal{K}(\widetilde{p}_e)$ (curvature) for each k_y. The polarisation, reflecting the vorticity nonlinearity which causes the drift wave nonlinear instability, is the largest, followed by the nonadiabaticity, followed by the curvature, at all wavelengths. In the center frame, we have the transfer spectra, which give the rms levels of $\widetilde{\phi}(\mathbf{v}_E \cdot \nabla \nabla_\perp^2 \widetilde{\phi})$ (random scattering), $-\widetilde{\phi}(\nabla_\parallel \widetilde{J}_\parallel)$ (adiabatic coupling), and $\widetilde{\phi}\mathcal{K}(\widetilde{p}_e)$ (interchange forcing) for each k_y. The same size ordering as in DALF3 is found. In the rightmost frame, we have the averages rather than the rms levels of these transfer effects. In the average transfer effects, the complex conjugate of $\widetilde{\phi}(k_y)$ is multiplied by the k_y component of the quantity in parentheses. The rms level measures the average size of a quantity whose mean value may be zero. For the vorticity

nonlinearity the average value is especially small compared to the mean even for any individual k_y, since this is a purely randomising effect. If all we measured were its average, we would miss its importance. We find that the rms nonadiabaticity is larger than the curvature forcing at every wavelength, which means it has to have been caused by the random scattering of the vorticity, not the curvature. This is why the drift wave mode structure persists far into what would have been the resistive MHD regime for linear instabilities. Ultimately, this random scattering of the vorticity is the reason we have drift wave turbulence even in toroidal geometry with significant interchange forcing. Although the turbulence is ballooned for all ν, the physics is still drift wave physics until the resistive ballooning threshold is reached at about

$$(C\omega_B)_{\text{crit}} = 1.2 \tag{12.65}$$

which merely gives the relative strengths of curvature and adiabatic forcing on the vorticity for a given pressure disturbance, as discussed in the previous chapter.

12.IX. Electromagnetic Effects on Drift Wave Turbulence

We have been running cases with both small and finite β_e, which normalises to $\hat{\beta}$ in the models, but have not yet addressed the effect this has on the turbulence. There are two effects to consider: the magnetic induction, represented by $\partial \widetilde{A}_{\|}/\partial t$ in the parallel electric field, and the magnetic flutter, represented by $\widetilde{\mathbf{B}} \cdot \nabla_\perp$ in the parallel gradient. We recall from the linear analysis of Chapter 5, that these effects were destabilising and stabilising, respectively. Moreover, in the four field model, DALF3, they tend to cancel, since the diamagnetic frequency in that model comes from the pressure/density gradient only, that is, the same gradient involved in the magnetic flutter in the Ohm's law. In the regime of small phase shifts these two tend to cancel, leaving a small overall effect. We saw this as well for the self sustained drift wave turbulence in the three dimensional slab, under the four field model, in Chapter 8. Up to very large values, $\hat{\beta} = 30$, the transport was found to be nearly independent of $\hat{\beta}$. It is interesting to return to this effect when ∇T_e and $\widetilde{T}_e$ are considered, since the propagation frequencies tend to go with ω_n while the flutter effect goes with $\omega_n + \omega_t$ (if multiplied by k_y, these are the normalised diamagnetic frequencies). So the temperature gradient might enter to break this cancellation. The other effect to watch out for while increasing the plasma beta holding the other parameters fixed is the onset of the ideal ballooning instability discussed in Chapter 10. In the case we looked at there, the magnetic shear was zero and so we found ballooning turbulence in the MHD

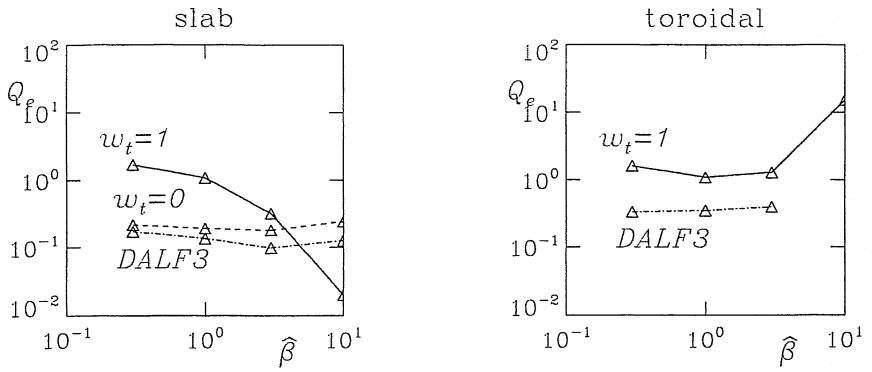

Figure 12.6. Transport scaling of drift wave turbulence as a function of $\hat{\beta}$. (left) Slab geometry results for the DALFTE model with $\omega_t = 1$ (solid line), with $\omega_t = 0$ (dashed line), and the DALF3 result of Chapter 8 (dotted line). The magnetic induction and flutter effects cancel for $\omega_t = 0$, but for $\omega_t = 1$ the flutter effect stablises the turbulence. Except when so stabilised, slab turbulence is stronger when the T_e effects are retained. (right) Toroidal geometry results for the DALFTE model for $\omega_t = 1$. The lightly falling trend is not enough to yield a falling trend in physical units. The interchange forcing effects compensate the magnetic flutter stabilisation. Magnetic flutter transport is close to zero for the three drift wave cases (see text), and about one third of Q_e for the ideal ballooning case.

model for all $\hat{\beta}$. With magnetic shear and toroidal geometry, the nominal ideal ballooning threshold is at

$$(\alpha_M)_{\text{crit}} = \hat{s} \tag{12.66}$$

where $\alpha_M = \hat{\beta}\omega_B(\omega_n + \omega_t)$ in the DALFTE model. We can expect violent activity above this boundary, judging from the results of Chapter 10 for ideal interchange turbulence.

For the investigation in three dimensional slab geometry we use the same setup as in Chapter 8, ultimately comparing to the results in Fig. 8.23 for the DALF3 model. The parameters for the nominal case were $\hat{\beta} = 1$, $\hat{\mu} = 5$, and $\nu = 1.0$, giving $C = 2.5$, and $\hat{\epsilon} = 18350$, $\hat{s} = 1$, and $K = 0.025$. The grid resolution was $64 \times 256 \times 16$ in $\{x, y, s\}$, with Dirichlet boundary conditions in x. We recall that for linear drift waves the magnetic flutter effect entered to stabilise the eigenmodes but had to compete with the destabilising effect of the magnetic induction. Both effects carry over to the turbulence. In the left frame of Fig. 12.6, we find the results for the transport in the slab geometry, for $\omega_t = 0$ and $\omega_t = 1$ in the DALFTE model, and the same DALF3 model results already shown at the end of Chapter 8. By varying the temperature gradient (ω_t), we can check the effect of this cancellation, since the propagation frequency for the turbulence as for the linear

eigenmodes at low collisionality is close to ω_n, the contribution to ω_* due to ∇n_e in these units. With $\omega_t = 0$ we find the same relatively flat scaling as in the DALF3 model. But setting $\omega_t = 1$ has the same effect that artificially doubling the magnetic flutter terms did in Chapter 5, Section IX. The induction effect scaling with ω_n only is overcome by the flutter effect scaling with $\omega_n + \omega_t$. The result is the stabilisation of the slab drift wave turbulence that we find.

In toroidal geometry we take the same setup except for setting $\omega_B = 0.05$ as in the study in the previous section. Holding $\nu = 1$, we sweep $\hat{\beta}$ upward to a value of 10. The flatness of the scaling below the disruption at $\hat{\beta} = 10$ is remarkable, showing that the magnetic curvature effects cancel out the magnetic flutter effects that suppress the slab turbulence for the same parameters. Interestingly, we find the same effect in the DALF3 model, in which both the slab and toroidal trends below the onset of ideal ballooning are flat. It is important to note that the flat trend we see is in normalised units. In physical units, sweeping β_e at fixed $\nu_e L_\perp / c_s$ and fixed $L_\perp$ also means sweeping the drift scale normalisation as $\beta_e^{1/2}$, due to $\beta_e \propto n_e T_e$ and $\nu_e / c_s \propto n_e / T_e^2$, and then $\rho_s^2 c_s \propto T_e^{3/2}$. So in physical units these trends actually rise at all β_e. We will find the same thing for warm ion turbulence in the next chapter. The disruption at $\hat{\beta} = 10$ marks the onset of ideal ballooning in the DALFTE model, where for these parameters $\alpha_M = 1$. In other cases run in the past we find the actual boundary perhaps slightly lower, but not lower than about 0.6. The fact that this disruption takes place only with larger $\hat{\beta}$ and finite ω_B in combination indicates that the boundary does indeed scale with α_M and not with either $\hat{\beta}$ or ω_B by themselves.

One important result of these computations is the finding that the transport directly due to magnetic flutter is much smaller than that due to the ExB turbulence, and the magnetic flutter transport is often even negative. The ExB transport is defined in Eq. (12.64), while the flutter transport effects arising from parallel sound wave and thermal conduction are given by

$$F_n(M) = \hat{\beta} \left\langle \widetilde{u}_\parallel \frac{\partial \widetilde{A}_\parallel}{\partial y} \right\rangle \qquad Q_e(M) = \hat{\beta} \left\langle \widetilde{q}_{e\parallel} \frac{\partial \widetilde{A}_\parallel}{\partial y} \right\rangle + \frac{5}{2} F_n(M) \tag{12.67}$$

with a similar correspondence to the source terms in the energetics as for the ExB transport (cf. Eqs. 12.58 and 12.64, and Eqs. 12.59 and 12.67). For the four toroidal DALFTE cases discussed here (Fig. 12.6, right frame), the four values of $F_n(M)$ were $\{-0.032, -0.085, -0.30, 3.99\} \times 10^{-3}$ and the four values of $Q_e(M)$ were $\{-0.013, -0.020, -0.029, 2.97\}$, compared to $F_n = \{0.24, 0.14, 0.22, 6.0\}$ and $Q_e = \{1.6, 1.1, 1.3, 15.3\}$ for the electrostatic

transport, all respectively for $\hat{\beta} = \{0.3, 1.0, 3.0, 10.0\}$. The magnetic flutter transport is negligible in the drift wave regime and only becomes appreciable in the ideal MHD regime.

Although the turbulence causes robust disturbances in the magnetic field line direction, with $\widetilde{B}^x/B$ approaching 5×10^{-4}, the phase correlations between $\widetilde{B}^x$ and $\widetilde{q}_{e\|}$ and $\widetilde{u}_{\|}$ are more or less random since the turbulence is directly driven by the ExB advection. Although the $\{\widetilde{T}_e, \widetilde{q}_{e\|}\}$ subsystem would indeed give rise to a net transport in a prescribed $\widetilde{B}^x$ disturbance, the fact that for drift wave turbulence $\widetilde{B}^x$ is a self consistent product of the overall dynamics renders such a simple analysis inapplicable, and indeed the magnetic flutter effect on the current is more important. The result is that magnetic flutter is net stabilising, and the fact that the various flutter effects tend to cancel each other renders the direct transport via magnetic flutter negligible. So although the internal dynamics of the turbulence is electromagnetic, the transport itself is essentially electrostatic. This situation changes only when the ideal MHD ballooning regime is encountered, but in that regime the turbulence leads to a disruption of the profiles rather than steady transport.

12.X. Temperature and Toroidal Effects on Sheared ExB Flows

The temperature does not strongly affect the dynamics of the zonal ExB flows treated in Chapter 9. We find the same layering in the $k_y = 0$ component of $\widetilde{\phi}$ in both models, especially at low collisionality. All of the cases presented in slab geometry in the previous section are strongly affected by zonal flows. On the other hand, self generation of coherent zonal flow layers is inhibited in toroidal geometry by coupling of the zonal flow mode to global kinetic shear Alfvén modes with $k_y = 0$ but $k_{\|} \neq 0$. Indeed, except at extremely low collisionality ($C < 1$) the zonal flows are not evident in the ExB flow morphology. Nevertheless, setting the zonal flow generation through $\mathbf{v}_E \cdot \nabla \nabla_\perp^2 \widetilde{\phi}$ to zero as in Chapter 9 results in stronger transport for moderate collisionality. But the effects are not as severe as in slab geometry.

The effect of magnetic curvature on zonal flows is part of the reason the turbulence is less sensitive to either $\hat{\beta}$ or ν in toroidal geometry than in slab geometry. The more pronounced nature of the zonal flows in slab geometry is obvious from the spatial morphology of the density, which we show for both high and low-$\hat{\beta}$ cases for both geometries in Fig. 12.7. The left two frames show the slab results, in which the vertical striping morphology caused by zonal flows stands out. The low-$\hat{\beta}$ toroidal case (second from right) looks the most like the standard drift wave morphology seen in Chapter 6. The toroidal case with $\hat{\beta} = 10$ (rightmost) is across the ideal ballooning threshold (cf. Fig. 12.6) with $\alpha_M = 1$, and exhibits the corresponding radial flow effects. But even for the clear drift wave turbulence case of $\hat{\beta} = \nu = 1$, which has $\alpha_M = 0.1$ and $C\omega_B = 0.13$, the toroidal

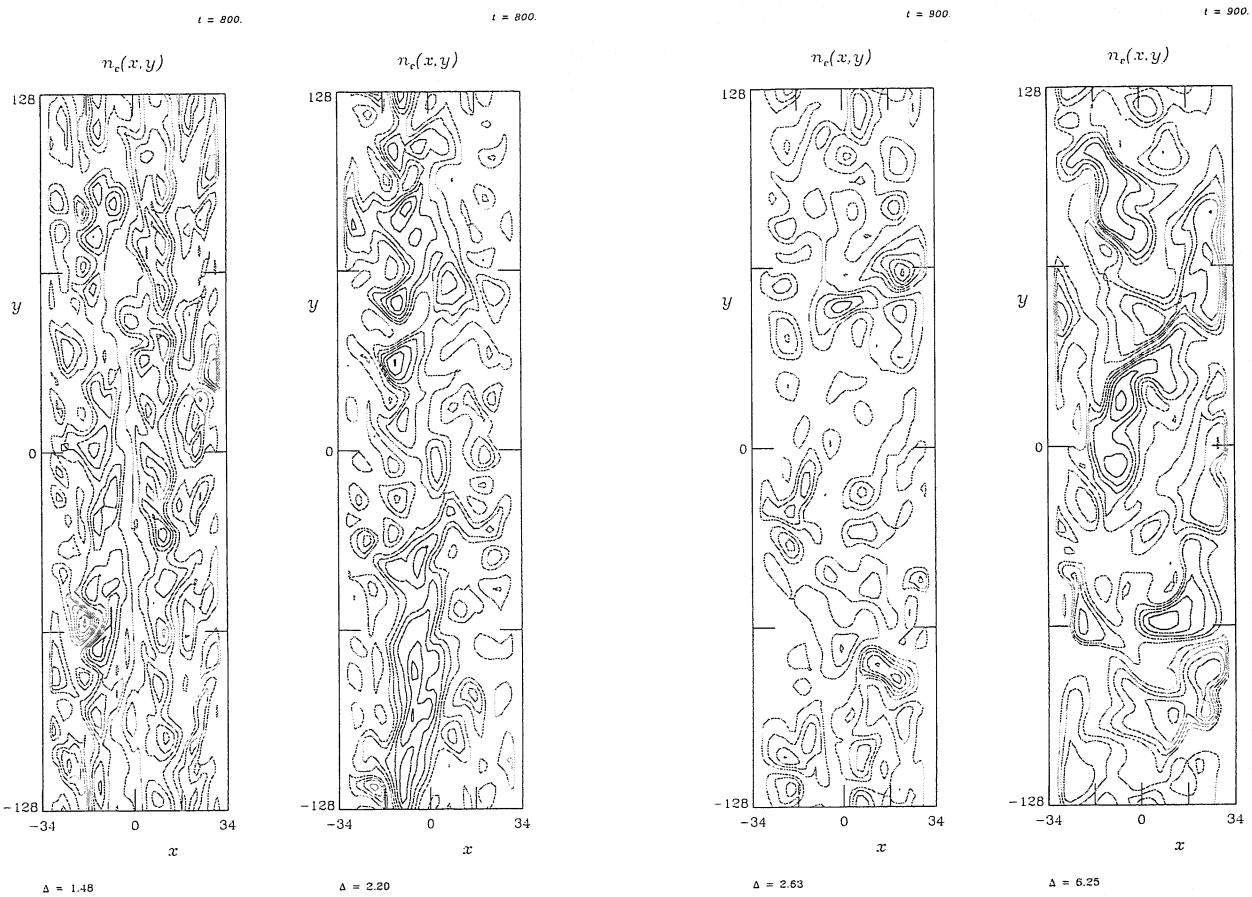

Figure 12.7. Density contours for slab (left two cases) and toroidal geometry (right two cases). In each pair, the case on the left has $\hat{\beta} = 1$ and the case on the right has $\hat{\beta} = 10$. Zonal flow effects (vertical striping) are visible in both slab cases, and the $\hat{\beta} = 10$ toroidal case shows the effects of radial flows expected in this case which has crossed the ideal ballooning threshold.

coupling to the global Alfvén modes is sufficient to prevent the buildup of long-lived zonal flow layers.

12.XI. Summary

The principal effect of the temperature on fluid drift dynamics is to introduce Landau damping as an additional dissipation mechanism, besides the more obvious effects of the temperature gradient and the generalisation of collisional dissipation to include thermal conduction. Landau damping functions merely as an extension to thermal conduction, preserving the general role of dissipation at low collisionality. The effects on simple interchange turbulence are negligible, merely changing the ratio of specific heats. The dynamics

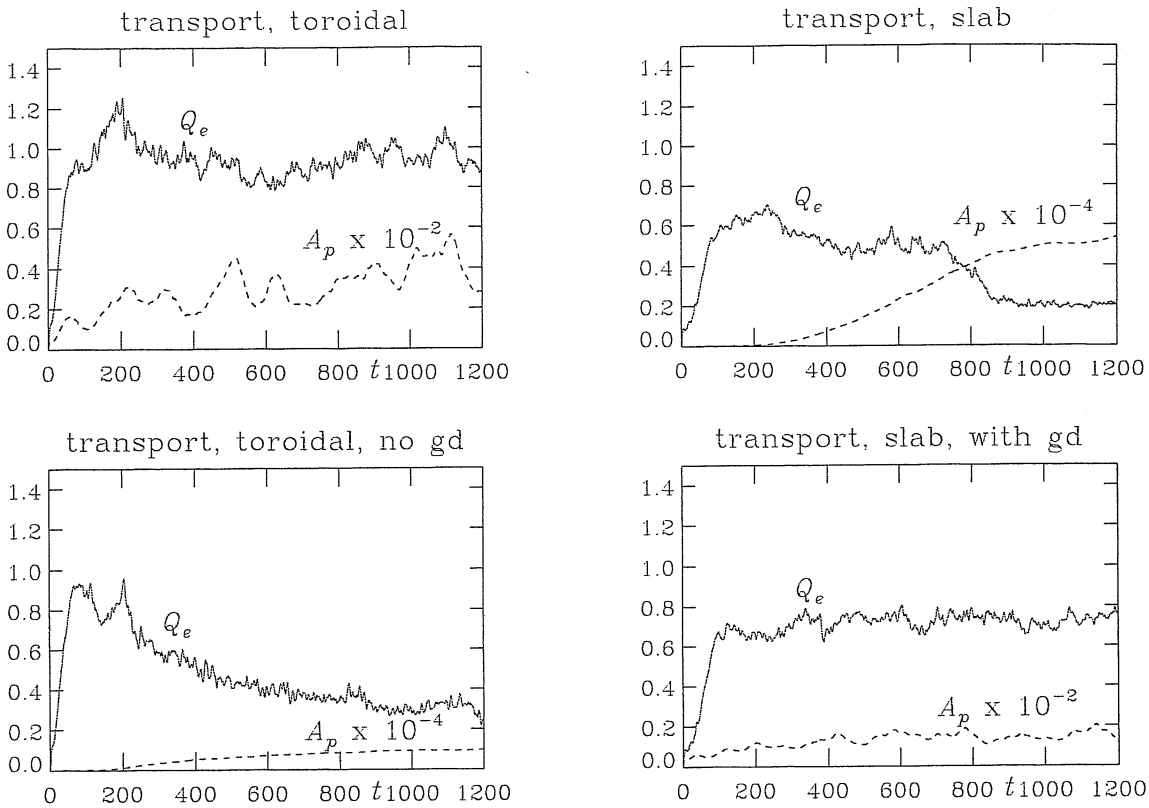

Figure 12.8. Time traces of the transport (Q_e) and mean squared $\widetilde{\phi}$ amplitude (A_p) for the DALF3 model with $C = 7.55$ for the slab and toroidal cases (left to right, top row), and for the toroidal case with geodesic curvature removed for the $k_y = 0$ modes (bottom left), and for the slab case with geodesic curvature inserted for the $k_y = 0$ modes (bottom right). This shows that most of the difference between the slab and toroidal cases is this zonal flow depletion via coupling to global Alfvén modes through the geodesic curvature; the value of A_p for the cases without geodesic curvature is two orders of magnitude larger than for those with it. The effect of the interchange forcing directly on the turbulence is given by the difference between the top left and bottom right frames.

of the density and temperature in interchange turbulence are identical and may be replaced by the pressure, returning to the models treated in Chapter 10. The effect of the temperature on drift wave turbulence is to strengthen it, especially at low collisionality where due to the Landau damping the applicability of the model becomes unbounded. In all respects the temperature has the same role and same mode structure as the nonadiabatic part of the density. Together, both form the force potential for the adiabatic response. In situations with limited computational resources the isothermal model is an adequate replacement up

to the fact that one often has to apply an unrealistic collisionality parameter in order to reflect the robustness of the turbulence. The physics of the nonlinear instability and the interactions with zonal ExB flows do not change. If the temperature is the stronger gradient then the turbulence becomes more sensitive to the magnetic flutter effect with increasing plasma beta (pressure gradient strength). In finite beta toroidal turbulence, however, this is overshadowed by the curvature effects, leaving the basic trend of the transport with plasma beta largely unaffected, until the ideal MHD instabilities are reached. The basic result of the MHD regime boundaries at $\alpha_M = \hat{s}$ (ideal) and $C\omega_B = 1$ (resistive) are not changed by the presence of the electron temperature. The ideal boundary is slightly lower than the nominal value, and the resistive boundary is slightly higher.

Qualitatively, the same turbulence takes place under both the Braginskii and Landau closure approximations on the electron temperature. But it is important to have found that finite collisionality is not necessary for electron drift wave turbulence to lead to significant disturbance activity and transport.

Further Reading

Temperature effects on two dimensional slab turbulence are compared between the isothermal model of B. Scott, H. Biglari, P. W. Terry, and P. H. Diamond, *Phys. Fluids B* 3 (1991) 51, and B. Scott, *Phys. Fluids B* 4 (1992) 2468. It was then believed that the temperature effects were required to find the nonlinear instability but with the more modern numerical techniques discussed in Chapter A, which are less dissipative for the same resolution, this is found not to be true. The role of the temperature in three dimensional drift wave mode structure is discussed by B. Scott in *Plasma Phys. Contr. Fusion* 39 (1997) 471, and in *Plasma Phys. Contr. Fusion* 39 (1997) 1635, which introduces the DALFTE model.

The Landau closure model follows the four pole expansion to the Z-function derived by G. Hammett and F. Perkins, in *Phys. Rev. Lett.* 64 (1990) 3019. It is also discussed in more detail by W. Dorland and G. Hammett, in *Phys. Fluids B* 5 (1993) 812, which contains references to the earlier literature. An alternative model perhaps better applicable to situations where wavelike behaviour is not expected (fronts, etc.) is given by E. M. Epperlein and R. W. Short, in *Phys. Fluids B* 3 (1991) 3092, which also contains several earlier references.

The result that the transport directly due to the disturbances of the magnetic field lines is negligible compared to that due to the ExB eddies was found by R. E. Waltz, in *Phys. Fluids* 28 (1985) 577, and confirmed in three dimensions by B. Scott, in *Plasma Phys. Contr. Fusion* 39 (1997) 1635.

13. Effects of the Ion Temperature

B. Scott

Jul 1999

13.I. Introduction

In all the models we have been considering up to now, we have been neglecting the effects of the ion temperature even though in Chapter 3 we derived a general set of equations. Having investigated the run of gradient driven turbulence with the four field model neglecting all temperature effects, and then having introduced the electron temperature in the previous chapter, we now turn to the ions. In contrast to the electron temperature disturbances, whose properties are the same as those of the nonadiabatic part of the density disturbances, the ion temperature as a dependent variable introduces new eigenmodes. Rather than the general pressure gradient, these have specifically the ion temperature gradient as their free energy source, and a coupling between the ion temperature disturbances and the ExB eddies as their defining transfer mechanism setting up their mode structure. These modes are called ITG modes in the literature, with ITG denoting "ion temperature gradient driven" modes. They have a somewhat generalised character in either of the two possibilities for the coupling mechanism — either through parallel dynamics or through the magnetic divergences. The eigenmode character does not strongly change because in both of these cases the coupling is relatively weak, no stronger than the dynamics itself, whereas in the electron dynamics cases the coupling through the parallel dynamics is strong. The classic realm of these ITG modes is in the case where the electrons are adiabatic, leaving the ion temperature gradient as the only remaining energy source, and the ion temperature disturbance as the only state variable not in a prescribed relationship to the electrostatic potential (the density is adiabatic, and the electron temperature is zero). But in the case of turbulence driven by steep enough gradients to keep the electrons nonadiabatic, the mode structure contains both drift wave and ITG mode aspects. Investigation of this interesting situation will form the bulk of this chapter. But first we have to discuss the ion temperature as such more fundamentally, for this is the place where we can no longer avoid the issue of finite gyroradius effects, and the need to have these treated by the fluid model in a reasonable way.

13.II. The Larmor Radius and Gyro Averaging

If dynamics at the drift scale, ρ_s, is active in drift wave turbulence, and the electron and ion temperatures are comparable, this means we also have dynamics at the scale of the ion gyroradius, ρ_i. These scales are given by

$$\rho_s^2 = \frac{c^2 M_i T_e}{e^2 B^2} \qquad \rho_i^2 = \frac{c^2 M_i T_i}{e^2 B^2} \tag{13.1}$$

obviously related by the parameter controlling the ion/electron temperature ratio,

$$\tau_i \equiv \frac{T_i}{T_e} \qquad \rho_i = \tau_i^{1/2} \rho_s \tag{13.2}$$

We therefore have to face the physical effects of a finite gyroradius in the dynamics we are considering, and as we have noted in Chapter 3 this actually puts pressure on the validity of the fluid model. This model formally breaks down if for perpendicular wavenumbers $k_\perp$ we have $k_\perp \rho_i \sim 1$. But as we noted in the previous chapter, kinetic effects like this can be incorporated by extending the fluid model provided their role is a simple one. We treated Landau damping as a dissipation mechanism by considering the parallel heat flux as a dynamical variable and adding a dissipative correction at the level of the moment hierarchy where the fluid moments higher than levels two (pressure, temperature) and three (heat flux) were called for. The fourth moment was replaced by a combination involving second moments (pT) plus the damping operator on the heat flux ($a_L q_\parallel$).

The fluid model treats finite Larmor radius effects by retaining the off diagonal components of the pressure tensor, whose "collisionless" part we called the gyroviscosity, noting that it is actually a diamagnetic momentum flux. But before discussing this in detail we look at what the gyroradius actually does at the kinetic level in altering the flow velocity when the state variables combining to serve as its stream function have small scale character. For simplicity we can consider heuristically a test particle whose drift is given solely by the ExB velocity, whose stream function is ϕ. If ϕ has no significant structure at the level of ρ_i, the picture we draw of the dynamics leading to the ExB velocity (Figure 1.5) contains smooth equipotential lines, and over the gyroradius the electric field is nearly constant. A more realistic picture of the flow in an ExB eddy disturbance is given in Fig. 13.1. If the size of an ExB eddy, $\Delta_\perp$, is closer to ρ_i, the variations of $\mathbf{E}_\perp$ must be considered in constructing the drift. If we can do this perturbatively we introduce the effects scaling as $k_\perp^2 \rho_i^2$ as corrections, so we still formally expect that $\Delta_\perp \gg \rho_i$. Since the ExB drift is a linear problem, it is possible to drop the small-ρ_i ordering.

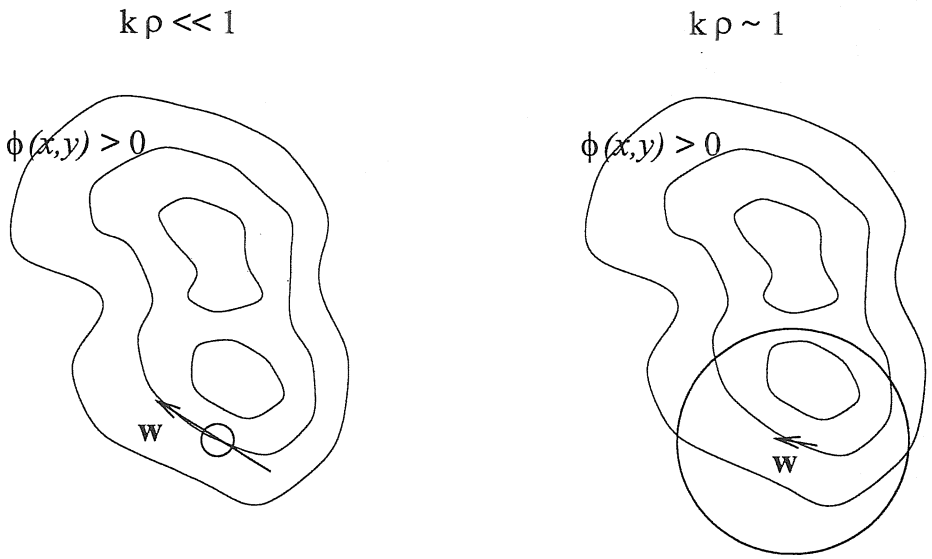

Figure 13.1. Gyroaveraging due to finite Larmor radius of an ion in a potential field. The circles give the size of the Larmor radius. The sense of the ExB drift for an ion is clockwise. If the Larmor radius is small (left), then the drift velocity of the gyrocenter will follow the ExB drift, instantaneously along a contour of $\widetilde{\phi}$. If the Larmor radius is comparable to the size of the disturbance, then the particle will feel an average electric force corresponding to the various places along its gyro orbit. Its velocity will typically be slower than the nominal ExB velocity, and may be in a different direction.

13.III. Gyroaveraging versus Gyroviscosity

In the fluid model, the effects of a finite Larmor radius are introduced by the diamagnetic fluxes, specifically, the gyroviscosity. But as we will see, while finite Larmor radius effects develop from the gyroviscosity tensor, *true* gyroaveraging in the sense of the ions and electrons having different drift velocities at small scales does not enter. The purely perpendicular part of this gyroviscosity contains three pieces: one which cancels the diamagnetic velocity $\mathbf{u}_*$ out of the advection, one which properly cancels divergences of the diamagnetic flow and heat flux, leaving only negligible magnetic divergence terms of order ρ_i/L_B, and one which is a true finite gyroradius reduction of all the flows themselves. In a homogeneous magnetic field we can write these as

$$\begin{aligned} -\left(\nabla_\perp \cdot \mathbf{\Pi}_*\right)_\perp = \mathbf{b}\times\nabla_\perp \frac{p_i}{\Omega_i} \cdot \nabla \mathbf{u}_\perp - \\ - \mathbf{b}\times\nabla_\perp \left(\frac{p_i}{2\Omega_i}\nabla_\perp \cdot \mathbf{u}_\perp\right) + \nabla_\perp \left(\frac{p_i}{2\Omega_i}\nabla \cdot \mathbf{u}_\perp \times \mathbf{b}\right) \end{aligned} \tag{13.3}$$

respectively, where $p_i/\Omega_i = n_i M_i (cT_i/eB)$ signifies the action of p_i and gyroviscosity as a finite Larmor radius effect, once the first term has cancelled $\mathbf{u}_* \cdot \nabla \mathbf{u}_\perp$. In a case where ∇T_i

or $\widetilde{T}_i$ is significant, then the gyroviscosity acquires extra terms arising from the diamagnetic heat flux, which is the same size as the diamagnetic velocity for $n_i \nabla T_i \sim T_i \nabla n_i$ (see Further Reading). The second term drops down to higher order in $k_\perp L_B$ as a result, where L_B is the scale of the magnetic field. The third term appears as a finite Larmor radius correction to the Lorentz force,

$$\nabla_\perp \left(\frac{p_i}{2\Omega_i} \nabla \cdot \mathbf{u}_\perp \times \mathbf{b} \right) = \nabla_\perp \left[n_i e \frac{\rho_i^2}{2} \nabla_\perp \cdot \left(\frac{\mathbf{u} \times \mathbf{B}}{c} \right) \right] \tag{13.4}$$

However, taking the drift operation $-\nabla \cdot \mathbf{b} \times$ on Eq. (13.3) as we do to construct the fluid drift equations (Chapter 3), we find that since it is given by the perpendicular gradient of a scalar this gyroreduction piece is annihilated by the drift divergence up to inhomogeneous magnetic field effects, leaving

$$\begin{aligned} \nabla \cdot \mathbf{b} \times \left[\left(\nabla_\perp \cdot \boldsymbol{\Pi}_* \right)_\perp + n_i M_i \mathbf{u}_* \cdot \nabla \mathbf{u}_\perp \right] = \\ = \nabla_\perp^2 \left(\frac{p_i}{2\Omega_i} \nabla_\perp \cdot \mathbf{u}_\perp \right) + \nabla \cdot \mathbf{b} \times \nabla \left(\frac{p_i}{2\Omega_i} \nabla \cdot \mathbf{u}_\perp \times \mathbf{b} \right) \end{aligned} \tag{13.5}$$

Both terms on the right side, representing contributions to the polarisation drift equation, are small by measure of ρ_i / L_B, and so as a finite-T_i gyroviscosity effect we only have the cancellation of $\mathbf{u}_* \cdot \nabla \mathbf{u}_\perp$, with no additional corrections.

This serves to highlight the fluid equations as an expansion in $k_\perp \rho_i$, which the gyroviscosity ultimately is: If we use the Chapman-Enskog procedure to derive the diamagnetic fluxes we find they come from the expansion of the kinetic equation to first order in $k_\perp^2 \rho_i^2$. The true gyroaveraging corrections only come in at higher order. Attempts to continue the expansion approaches discussed in Chapter 2 end in failure for the finite gyroradius effects. The expansion to first order usually breaks down for $k_\perp \rho_i \approx 1/2$. The expansion to second order will do better but still fail before $k_\perp \rho_i = 1$. Further effort must come from a different approach. The one which has borne the most fruit is called the gyrofluid model. It starts from the gyrokinetic equation, which is a generalisation of the drift kinetic equation for zero Larmor radius guiding centers to a kinetic equation for finite Larmor radius gyrocenters, in which the force potentials leading to the drifts are explicitly gyroaveraged in a way that preserves the Hamiltonian structure of the equations. Then, it builds a moment hierarchy and applies a closure model. In short, it takes the drift approximation at the kinetic level first before constructing fluid equations, which is opposite to the way the fluid drift equations are built. In the end, numerical treatments of the gyrofluid model are better behaved in the region $k_\perp \rho_i \sim 1$ than the fluid model. But it is beyond the scope of this work to go as deep into the kinetic theory as is necessary to build that model. Instead, a set of references are given in Further Reading.

We will retain the fluid drift equations as a model which, although formally breaking down at $k_\perp \rho_i \sim 1$, is well behaved with rigorous conservation laws everywhere in the spectrum. Validity is argued for by the fact that for most situations the dominant part of the spectrum has $k_\perp \rho_i$ well below unity, as we have seen for drift wave turbulence, in some contrast to the linear instabilities in a homogeneous magnetic field. The model we use is a normalised version of the local fluid drift model derived in Chapter 3, finally with all the terms.

13.IV. Effects on Cold Ion Dynamics

As with the electron temperature, taking into account the ion temperature changes the ratio of specific heats for the ion fluid, and therefore the sound velocity changes. In contrast to a neutral fluid, the sound waves in a plasma can exist when the ions are cold, because the electrons to which they are coupled through the electric field still have a finite temperature, and this leads to the sound speed c_s. The ion temperature enters the parallel dynamics of the ions exactly as T_e does for the electrons as discussed in the previous chapter, with the result that idealised sound waves with adiabatic electrons have a propagation velocity corresponding to the remaining available degrees of freedom. The effects of the two fluids add, because their pressures add in the total force on fluid elements, and so the propagation velocity is given by

$$\left(V_s^2\right)_{\text{adiabatic}} = \frac{T_e + (5/3)T_i}{M_i} \tag{13.6}$$

where the factor of 5/3 reflects the action of the disturbance $\widetilde{T}_i$ in the dynamics. The electrons add a factor of unity because they are isothermal due to the fact that they are adiabatic. Recall that adiabatic in the context of parallel dynamics (force balance, with $\widetilde{p}_e \to n_e e\widetilde{\phi}$ and $\widetilde{T}_e \to 0$) is different from the concept of adiabaticity in thermodynamics. The latter concept is the one of an ideal fluid in which dissipation mechanisms are small; here, adiabatic electrons refers to quasistatic parallel force balance.

The ion temperature effects on ideal interchange dynamics are the same as for the electrons. If the scale of motion is larger than ρ_i, then the picture of the ideal interchange remains. As in the case of the electrons, we can simply sum up all the pieces of the total pressure disturbance,

$$\widetilde{p} = \widetilde{p}_e + \widetilde{p}_i = (T_e + T_i)\,\widetilde{n}_e + n_e\left(\widetilde{T}_e + \widetilde{T}_i\right) \tag{13.7}$$

and then work with a model using only the two variables $\widetilde{p}$ and $\widetilde{\phi}$. In the same way as for the disturbances, the pieces of the pressure gradients add,

$$\nabla p = \nabla p_e + \nabla p_i = (T_e + T_i)\,\nabla n_e + n_e\,(\nabla T_e + \nabla T_i) \tag{13.8}$$

Using a profile scale $L_\perp$, the normalised total pressure gradient is then

$$\frac{L_\perp}{L_p} = \omega_n + \omega_t + \tau_i(\omega_n + \omega_i) \tag{13.9}$$

with the three normalised gradients defined as

$$\omega_n = \frac{L_\perp}{L_n} \qquad \omega_t = \frac{L_\perp}{L_{T_e}} \qquad \omega_i = \frac{L_\perp}{L_{T_i}} \tag{13.10}$$

and with the ion /electron temperature ratio

$$\tau_i = \frac{T_i}{T_e} \tag{13.11}$$

All of these become parameters in local drift equations. With the ideal interchange model neglecting diamagnetic velocities and fluxes in the pressure equation, we have the same model as in Chapter 10.

The ion temperature also has an indirect role in kinetic shear Alfvén dynamics, but only near $k_\perp \rho_i \sim 1$. This is due to the the divergence of the ion polarisation velocity appearing in the ion density and temperature equations. We recall that the interesting effects in this Alfvénic activity enter when $k_\perp^2 \rho_s^2$ becomes appreciable. This is due to $\nabla_\perp^2 \widetilde{\phi}$ in the ion polarisation divergence, and enters through ρ_s and not ρ_i because $\widetilde{\phi}$ follows T_e as a result of the adiabatic response of the electrons. Due to quasineutrality the ion and electron densities are the same; the effects on the Alfvénic activity follow from $\nabla_\parallel \widetilde{J}_\parallel$ and equivalently $\nabla \cdot \mathbf{u}_p$, which ultimately also couples $\widetilde{T}_i$ to the parallel electron dynamics. Since $\widetilde{T}_i$ enters in the equation for $\widetilde{\phi}$ scaling with ρ_i (cf. Chapter 3), it will add finite Larmor radius corrections to the kinetic shear Alfvén dynamics. As is the case with $\widetilde{T}_e$, however, the qualitative nature of those effects is not different from those of the $\widetilde{n}_e \leftrightarrow \widetilde{\phi}$ coupling already present in the four field model, and so the physics of the waves does not change.

13.V. New Eigenmodes — Ion Temperature Gradient Turbulence

The situation gets interesting when we consider not yet dissipation, but the fact that we have a new regime possible with the interchange turbulence. Suppose that the plasma is hot enough to keep the electrons adiabatic. We saw in the previous chapter that in a cold ion model the interchange turbulence becomes drift wave turbulence in a toroidal magnetic field at still very high values of collisionality and then is reduced to low amplitude as the collision frequency goes to zero. The interchange effects on the turbulence are mostly absent, even as the toroidal coupling of zonal flows to global shear Alfvén modes hinders

the buildup of zonal flows and therefore leads to more vigorous transport. When the electrons become adiabatic, the ion density is also removed from the energetics because of quasineutrality, $Zn_i = n_e$ and $Z\widetilde{n}_i = \widetilde{n}_e$ for charge state Z. But now we have the ion temperature, and that means we now have a state variable with a background gradient acting as a free energy source, but which does not feel the adiabatic response if the electrons are adiabatic. The ion temperature could still participate in interchange dynamics even if the electrons are adiabatic, and the ion parallel dynamics might still be too slow to alter the results. The instability we find in this regime is called the ITG-interchange mode, or in a toroidal magnetic field the toroidal ITG mode, where ITG stands for ion temperature gradient since ∇T_i is now the only available free energy source.

The simplest form of the ITG model combines the two dimensional adiabatic model of Chapter 6 and the two dimensional interchange model of Chapter 10. The electrons are assumed to be kept adiabatic by an arbitrarily fast Alfvén dynamics, while the ions are assumed to remain hydrodynamic due to an arbitrarily slow sound wave dynamics, as in the classic drift ordering with which the simplest drift wave models are built, as in Chapter 5. The equations are those for the ion density and temperature, with the ExB flows determined by the adiabatic constraint. We may simplify to a singly charged fluid and use n_e for n_i, and hence $\widetilde{\phi}$ for $\widetilde{n}_i$. We take a single Fourier component for the homogeneous linear problem as in the ideal interchange, with k_y and $k_\perp^2$ as parameters. Keeping the polarisation drift in both equations, we have

$$\frac{\partial}{\partial t}\left(\widetilde{\phi} + k_\perp^2 \widetilde{w}\right) = -i\omega_n k_y \widetilde{\phi} + i\omega_B k_y \widetilde{w} \tag{13.12}$$

$$\frac{\partial}{\partial t}\left(\frac{3}{2}\widetilde{T}_i + \tau_i k_\perp^2 \widetilde{w}\right) = -i\tau_i \omega_i k_y \widetilde{\phi} + i\tau_i \omega_B \left(\widetilde{w} + \frac{5}{2}\widetilde{T}_i\right) \tag{13.13}$$

where $\widetilde{w}$ is the stream function for the total perpendicular velocity,

$$\widetilde{w} = \widetilde{p}_i + \widetilde{\phi} = \widetilde{T}_i + (1 + \tau_i)\widetilde{\phi} \tag{13.14}$$

and τ_i emerges as a parameter because the adiabatic response scales $\widetilde{\phi}$ with T_e.

Interchange instabilities usually involve only the largest scales possible in a given domain, due to the fact that the purely hydrodynamic ideal interchange mode has the same growth rate for all k_y as $k_y \to 0$. But we recall the inhibition of large scale activity in $\widetilde{\phi}$ in the adiabatic model in Chapter 6; the same result takes place here. The presence of a factor of order unity in addition to $k_\perp^2$ in both of Eqs. (13.12,13.13) has the same effect — as all forcing terms scale with k_y, the growth rate will be proportional to k_y as $k_y \to 0$.

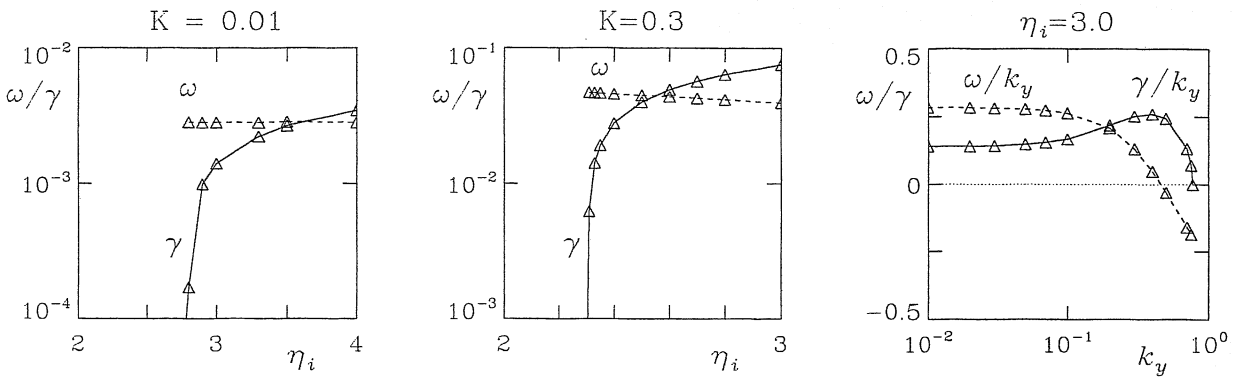

Figure 13.2. (left and center) Adiabatic ITG-interchange growth rate and mode frequency as a function of $\eta_i = \omega_i/\omega_n$, for $k_y = 0.3$ and 0.01. The threshold is similar but sharper for higher k_y. (right) For $\eta_i = 3$, the growth rate and mode frequency normalised to k_y, showing the robust region $k_y \sim 0.5$, and the threshold before $k_y = 1$ is reached. The mode frequency would be k_y if T_i/T_e were zero, but ∇T_i enters to give a negative contribution which increases towards $k_y = 1$.

We investigate this briefly with two values of k_y, with $k_\perp^2 = k_y^2$. We set $\omega_n = \tau_i = 1$ and $\omega_B = 0.1$, and vary ω_i to find the instability. The resulting mode frequencies and growth rates are shown in Fig. 13.2. The first case is with $k_y = 0.3$, in the range at which we have been finding the strongest free energy source rates in drift wave turbulence. We find no instability whatsoever for $\eta_i = \omega_i/\omega_n \lesssim 2.3$. This is a situation akin to buoyant convection in a neutral fluid, due to subtle details in the energetics there is no free energy gain for exchanging fluid elements until a threshold is reached. The threshold is not dissipative, with γ smoothly going through zero, but it is a case where ω^2 changes from real to complex values. Unlike a Hermitian problem where ω^2 is always real, Eqs. (13.12,13.13) may be Fourier transformed in time and solved for the eigenmodes, and this yields a quadratic equation for ω. The threshold is reached when the discriminant of that equation becomes negative. This always has some manifestation in the energetics, and in this case the threshold results from the adiabatic constraint on the electrons, which is what makes this situation different from the ideal interchange instability. The adiabatic constraint results in an initial disturbance being shifted away in the y-direction due to the diamagnetic drift, before it can liberate sufficient energy from ∇T_i. Here, we note that for the adiabatic ITG-interchange mode ∇T_i is the sole free energy source, so there is a competition between a radial flow tapping the free energy, and its tendency to drift away from the $\widetilde{T}_i$ disturbances

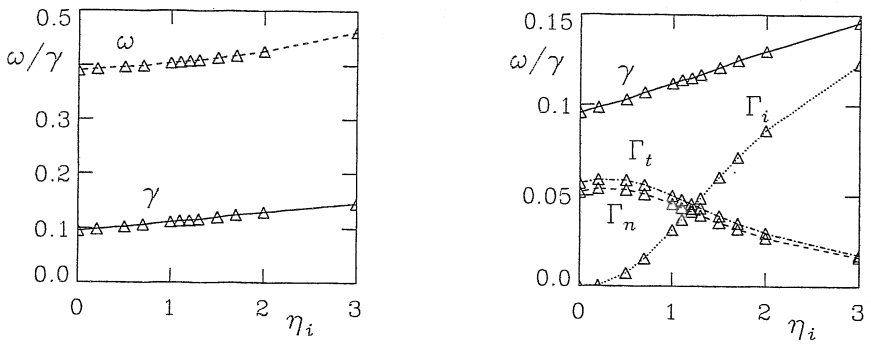

Figure 13.3. Electromagnetic drift wave with ITG-interchange forcing, as a function of η_i for $k_y = 0.3$. The mode frequency and growth rate (left) show no transition, but the mode structure does. The contributions to the total growth rate (right), due to ∇n ('n'), ∇T_e ('t'), and ∇T_i ('i') show a transition from an electron to an ion dominated eigenmode.

it causes before they can grow. For $\eta_i = 1$ the adiabatic ITG-interchange mode is nearly always stable.

We can see the effect of the adiabatic constraint on the threshold by relaxing it, and taking the case of a general situation containing both drift wave and interchange dynamics, plus the parallel ion dynamics. We take a parameter set in the regime of interest to the drift wave turbulence in toroidal geometry investigated in Chapters 11 and 12,

$$\hat{\beta} = 1 \quad \hat{\mu} = 2.7 \quad \nu = 1 \quad \hat{\epsilon} = 10^4 \quad \mu_{\parallel} = 10 \quad \omega_B = 0.1 \tag{13.15}$$

together with $\omega_n = \omega_t = \tau_i = 1$, and sweep ω_i for $k_y = 0.3$. The mode frequencies and growth rates are shown in Fig. 13.3, together with the three contributions to the overall gradient drive, Γ_n from ω_n, and Γ_t from ω_t, and Γ_i from ω_i. We find that the electron parallel dynamics is not negligible, but relatively small, with the collisional dissipation at about 0.01. The ion parallel dynamics is negligible. The eigenmodes found are healthily driven interchange modes, making a smooth transition towards ITG-mode character as η_i crosses about 1.0, and we note that this is well below the adiabatic ITG-interchange threshold for this ω_B and k_y. The threshold basically disappears when there is significant electron activity, as there is here. We recall from Chapter 11 that while the linear eigenmodes in toroidal geometry have an interchange character shaped by radial flows, the turbulence turned out to have a clear drift wave character for this value of ν, about a factor of 10 below the transition to resistive MHD and interchange mode structure. But what we have learned here is that the existence of an ITG-interchange threshold is due to adiabatic electrons, and as we move away from that state we also lose the threshold. It

will be interesting to investigate this further for turbulence, as one of the things we might expect is that while the electron dynamics goes over into drift wave mode structure, the dynamics of $\widetilde{T}_i$ might remain with interchange character. We will do this after presenting the ion/electron Landau fluid model.

One further point of note is that there is also a version of this ITG instability in slab geometry, in terms of which the ITG mode was first discovered. It is a combination of an adiabatic sound wave and the ion temperature gradient and disturbance effects. Assuming an ideal fluid at large scales, we neglect the polarisation drift entirely, so that

$$\frac{\partial \widetilde{\phi}}{\partial t} = -i\omega_n k_y \widetilde{\phi} - ik_{\|}\widetilde{u}_{\|} \tag{13.16}$$

$$\hat{\epsilon}\frac{\partial \widetilde{u}_{\|}}{\partial t} = -ik_{\|}\left[(1+\tau_i)\widetilde{\phi} + \widetilde{T}_i\right] \tag{13.17}$$

$$\frac{\partial \widetilde{T}_i}{\partial t} = -i\left[(1+\tau_i)\omega_n + \tau_i\omega_i\right]k_y\widetilde{\phi} - \frac{2}{3}ik_{\|}\widetilde{u}_{\|} \tag{13.18}$$

Taking the Fourier transform in time as well, we can manipulate this into the following cubic equation for ω,

$$\left[\omega - \omega_n k_y\right]\left[\hat{\epsilon}\omega^2 - \left(1+\frac{5}{3}\tau_i\right)k_{\|}^2\right] = \left[1+\tau_i(1+\eta_i)\right]\omega_n k_y k_{\|}^2 \tag{13.19}$$

The two quantities in brackets on the left side represent the adiabatic drift wave and sound waves in the low-k_y limit, with a coupling term on the right side. Due to this coupling term there is a threshold in η_i, before this term can compete with the ω-independent term on the left side, enough to force two of the roots into the upper and lower complex plane, off the real axis. This gives the slab branch of the ITG mode, unstable for $\eta_i = 2/3$ for three degrees of freedom (isotropic temperature). For one degree of freedom (a kinetic situation with a parallel temperature disturbance only), the threshold is at $\eta_i = 2$.

13.VI. Landau Closure for Ions — the DALFTI Model

Before writing down the model equations, we briefly note that besides the finite Larmor radius effects we also have the same parallel dynamics closure problem as for the ions, regarding the dissipation of the temperature disturbances. We recall that the electrons are usually either in the low frequency limit or the marginal range, comparing ω to $k_{\|}V_e$; conventional drift ordering has $\omega \ll k_{\|}V_e$. But for the ions the conventional drift ordering has $\omega \gg k_{\|}V_i$, due to the small size of m_e/M_i. So not only are the ions, like the electrons, in the marginal or weakly collisional regime regarding the mean free path, they are always

in the *high* frequency regime regarding Landau damping. We already included the time dependence of $\widetilde{q}_{e\parallel}$ in the electron model; we merely do the same for $\widetilde{q}_{i\parallel}$ the ion model and then we are done. There is no thermoelectric effect in the ions, and hence no direct coupling to $\widetilde{u}_{\parallel}$. The Landau closure neither helps nor hinders the model regarding finite Larmor radius effects, so we simply carry over the fluid model and insert the Landau model for the parallel heat flux, just as we did for the electrons.

The resulting set of warm ion Landau fluid drift equations is called the DALFTI model, basically extending DALFTE to include $\widetilde{T}_i$ and $\widetilde{q}_{i\parallel}$. There are now eight dependent variables, $\{\widetilde{\phi}, \widetilde{A}_{\parallel}, \widetilde{n}_e, \widetilde{u}_{\parallel}, \widetilde{T}_e, \widetilde{q}_{e\parallel}, \widetilde{T}_i, \widetilde{q}_{i\parallel}\}$, whose equations are

$$\frac{1}{B^2}\nabla\cdot\frac{d_E}{dt}\nabla_\perp\widetilde{w} = B\nabla_\parallel\frac{\widetilde{J}_\parallel}{B} - \mathcal{K}\left(\widetilde{p}_e+\widetilde{p}_i\right) \tag{13.20}$$

$$\hat{\beta}\frac{\partial\widetilde{A}_\parallel}{\partial t} + \hat{\mu}\frac{d_E\widetilde{J}_\parallel}{dt} = \nabla_\parallel\left(p_e+\widetilde{p}_e-\widetilde{\phi}\right) - \hat{\mu}\nu_e\left[0.51\widetilde{J}_\parallel + \frac{0.71}{3.2}\left(\widetilde{q}_{e\parallel}+0.71\widetilde{J}_\parallel\right)\right] \tag{13.21}$$

$$\frac{d_E}{dt}\left(n_e+\widetilde{n}_e\right) = B\nabla_\parallel\frac{\widetilde{J}_\parallel-\widetilde{u}_\parallel}{B} - \mathcal{K}\left(\widetilde{p}_e-\widetilde{\phi}\right) \tag{13.22}$$

$$\hat{\epsilon}\frac{d_E\widetilde{u}_\parallel}{dt} = -\nabla_\parallel\left(p_e+p_i+\widetilde{p}_e+\widetilde{p}_i\right) + \mu_\parallel\nabla_\parallel^2\widetilde{u}_\parallel \tag{13.23}$$

$$\frac{d_E}{dt}\left(T_e+\widetilde{T}_e\right) = B\nabla_\parallel\frac{\widetilde{J}_\parallel-\widetilde{u}_\parallel-\widetilde{q}_{e\parallel}}{B} - \mathcal{K}\left(\widetilde{p}_e-\widetilde{\phi}+\frac{5}{2}\widetilde{T}_e\right) \tag{13.24}$$

$$\hat{\mu}\frac{d_E\widetilde{q}_{e\parallel}}{dt} = -\frac{5}{2}\nabla_\parallel\left(T_e+\widetilde{T}_e\right) - a_{Le}\left(\widetilde{q}_{e\parallel}\right) - \frac{5/2}{3.2}\hat{\mu}\nu_e\left(\widetilde{q}_{e\parallel}+0.71\widetilde{J}_\parallel\right) \tag{13.25}$$

$$\frac{d_E}{dt}\left(T_i+\widetilde{T}_i\right) = B\nabla_\parallel\frac{\tau_i(\widetilde{J}_\parallel-\widetilde{u}_\parallel)-\widetilde{q}_{i\parallel}}{B} - \tau_i\mathcal{K}\left(\widetilde{p}_e-\widetilde{\phi}-\frac{5}{2}\widetilde{T}_i\right) \tag{13.26}$$

$$\hat{\epsilon}\frac{d_E\widetilde{q}_{i\parallel}}{dt} = -\frac{5}{2}\tau_i\nabla_\parallel\left(T_i+\widetilde{T}_i\right) - a_{Li}\left(\widetilde{q}_{i\parallel}\right) - \frac{5/2}{3.9}\hat{\epsilon}\nu_i\widetilde{q}_{i\parallel} \tag{13.27}$$

with auxiliaries

$$\widetilde{J}_\parallel = -\nabla_\perp^2\widetilde{A}_\parallel \qquad \frac{d_E}{dt} = \frac{\partial}{\partial t} + \mathbf{v}_E\cdot\nabla \tag{13.28}$$

$$\mathbf{v}_E\cdot\nabla = \frac{\partial\widetilde{\phi}}{\partial x}\frac{\partial}{\partial y} - \frac{\partial\widetilde{\phi}}{\partial y}\frac{\partial}{\partial x} \qquad \nabla_\parallel = \frac{B^s}{B}\frac{\partial}{\partial s} - \hat{\beta}\left(\frac{\partial\widetilde{A}_\parallel}{\partial x}\frac{\partial}{\partial y} - \frac{\partial\widetilde{A}_\parallel}{\partial y}\frac{\partial}{\partial x}\right) \tag{13.29}$$

$$\nabla_\parallel^2 = \nabla\cdot\mathbf{bb}\cdot\nabla = B\nabla_\parallel\frac{1}{B}\nabla_\parallel \tag{13.30}$$

$$\widetilde{p}_e = \widetilde{n}_e + \widetilde{T}_e \qquad \widetilde{p}_i = \tau_i\widetilde{n}_e + \widetilde{T}_i \qquad \widetilde{w} = \widetilde{\phi} + \widetilde{p}_i \tag{13.31}$$

The flux surface geometry ($\nabla_\perp^2$, B^s, B^2, $\mathcal{K}$, shifts to make g_k^{xy} vanish) and computational domain remain as before. Drive terms appear wherever $\partial/\partial x$ acts upon pressures or temperatures, with

$$\frac{\partial n_e}{\partial x} \to -\omega_n \qquad \frac{\partial T_e}{\partial x} \to -\omega_t \qquad \frac{\partial p_e}{\partial x} \to -(\omega_n + \omega_t) \tag{13.32}$$

for the electrons, and

$$\frac{\partial T_i}{\partial x} \to -\tau_i \omega_i \qquad \frac{\partial p_i}{\partial x} \to -\tau_i(\omega_n + \omega_i) \tag{13.33}$$

for the ions, representing $L_\perp/L_n$, $L_\perp/L_{Te}$, $L_\perp/L_{pe}$, $\tau_i L_\perp/L_{Ti}$, and $\tau_i L_\perp/L_{pi}$, respectively. The factors of τ_i throughout reflect the normalisation in terms of T_e, from the time scale to ρ_s and to the gradients; some of the terms in Eq. (13.26) have two factors of τ_i due to the fact that the fourth moment in the hierarchy scales as $p_i T_i$. The presence of electron based divergence terms in Eq. (13.26) are due to the use of Eq. (13.20) to cancel the polarisation drift compression, as explained in Chapter 3. The factors of ν_e and ν_i in the equations are still normalised, but now we must distinguish between electron and ion collisional dissipation, as with Landau damping. The normalised collision frequencies are

$$\nu_e \leftarrow \frac{\nu_e L_\perp}{c_s} \qquad \nu_i \leftarrow \frac{\nu_i L_\perp}{c_s} = 2^{-1/2}\mu_e^{1/2}\tau_i^{-3/2}\nu_e \tag{13.34}$$

and the Landau damping operators are

$$a_{Le} = \hat{\mu}^{1/2}\left(1 - 0.2\nabla_\parallel^2\right) \qquad a_{Li} = (\tau_i\hat{\epsilon})^{1/2}\left(1 - 0.2\nabla_\parallel^2\right) \tag{13.35}$$

One thing deserves further comment: the treatment of the gyroviscosity. The diamagnetic cancellation results in the total ion drift velocity being advected by the ExB velocity. Among other things, this breaks vorticity conservation. Energy conservation is preserved with the total inertial drift energy proportional to $|\nabla_\perp \widetilde{w}|^2$. In the numerical treatment we can no longer simply advect the vorticity as another state variable using an ExB characteristic equation. While this is part of the treatment we use, it has to be corrected to give the entire term on the left side of Eq. (13.20). This term is evaluated as

$$\frac{\partial}{\partial t}\nabla_\perp^2 \widetilde{w} = -\mathbf{v}_E \cdot \nabla\nabla_\perp^2 \widetilde{w} - (\nabla_\perp \mathbf{v}_E) : (\nabla\nabla_\perp \widetilde{w}) \tag{13.36}$$

The last term on the right side is called the gyroviscous correction. For the cold ion models this correction vanishes because for $\tau_i = 0$ we have $\widetilde{w} = \widetilde{\phi}$, and then the combination of

derivatives vanishes due to the cross product in the ExB velocity. So in the correction we replace $\widetilde{w}$ with $\widetilde{p}_i$, and in the numerics we apply

$$\frac{\partial}{\partial t}\nabla_\perp^2\widetilde{w} = -\mathbf{v}_E\cdot\nabla\nabla_\perp^2\widetilde{w} - (\nabla_\perp\mathbf{v}_E):(\nabla\nabla_\perp\widetilde{p}_i) \tag{13.37}$$

evaluating the ExB advection with the same MUSCL scheme of Appendix A as in the DALF3 and DALFTI models, and apply the gyroviscous correction as a forcing term. We note that each factor of $\widetilde{\phi}$ and $\widetilde{p}_i$ in this equation appears under two derivatives, and so there are no gradient terms. There is still a background gradient effect on the vorticity dynamics, however, due to the ultimate presence of ω_n and ω_i in $\partial\widetilde{p}_i/\partial t$.

13.VII. Energetics of the DALFTI Model

The energetics of DALFTI expands that of DALFTE to finite ion temperature. All of the electron based source, transfer, and sink mechanisms are still present, and we do not need to write them here. The electron collisional sinks generally scale with $C = 0.51\hat{\mu}\nu_e$, and the ion sinks scale with $\hat{\epsilon}\nu_i$. The part of the energetics differing from the outline of the DALFTE model in the previous chapter is

$$\frac{\partial}{\partial t}\left\langle\frac{1}{2}\frac{1}{B^2}\left|\nabla_\perp\widetilde{w}\right|^2\right\rangle = \cdots + \left\langle\widetilde{J}_\parallel\nabla_\parallel\widetilde{p}_i\right\rangle - \left\langle\widetilde{p}_i\mathcal{K}\widetilde{\phi}\right\rangle + \left\langle\widetilde{p}_i\mathcal{K}\widetilde{p}_e\right\rangle \tag{13.38}$$

$$\begin{aligned}(1+\tau_i)\frac{\partial}{\partial t}\left\langle\frac{1}{2}\left|\widetilde{n}_e\right|^2\right\rangle = \cdots &- \left\langle\widetilde{J}_\parallel\nabla_\parallel(\tau_i\widetilde{n}_e)\right\rangle + \left\langle\widetilde{u}_\parallel\nabla_\parallel(\tau_i\widetilde{n}_e)\right\rangle + \\ &+ \left\langle(\tau_i\widetilde{n}_e)\mathcal{K}\widetilde{\phi}\right\rangle - \left\langle(\tau_i\widetilde{n}_e)\mathcal{K}\widetilde{p}_e\right\rangle + \tau_i\omega_n\left\langle-\widetilde{n}_e\frac{\partial\widetilde{\phi}}{\partial y}\right\rangle\end{aligned} \tag{13.39}$$

$$\frac{\partial}{\partial t}\left\langle\frac{\hat{\epsilon}}{2}\left|\widetilde{u}_\parallel\right|^2\right\rangle = \cdots - \left\langle\widetilde{u}_\parallel\nabla_\parallel\widetilde{p}_i\right\rangle + \tau_i(\omega_n+\omega_i)\hat{\beta}\left\langle\widetilde{u}_\parallel\frac{\partial\widetilde{A}_\parallel}{\partial y}\right\rangle \tag{13.40}$$

$$\begin{aligned}\frac{3}{2}\frac{\partial}{\partial t}\left\langle\frac{1}{2}\tau_i^{-1}\left|\widetilde{T}_i\right|^2\right\rangle = &-\left\langle\widetilde{J}_\parallel\nabla_\parallel(\widetilde{T}_i)\right\rangle + \tau_i^{-1}\left\langle\widetilde{q}_{i\parallel}\nabla_\parallel\widetilde{T}_e\right\rangle + \left\langle\widetilde{u}_\parallel\nabla_\parallel(\widetilde{T}_i)\right\rangle + \\ &+ \left\langle(\widetilde{T}_i)\mathcal{K}\widetilde{\phi}\right\rangle - \left\langle(\widetilde{T}_i)\mathcal{K}\widetilde{p}_e\right\rangle + \frac{3}{2}\omega_i\left\langle-\widetilde{T}_i\frac{\partial\widetilde{\phi}}{\partial y}\right\rangle\end{aligned} \tag{13.41}$$

$$\begin{aligned}\frac{2}{5}\tau_i^{-2}\frac{\partial}{\partial t}\left\langle\frac{\hat{\epsilon}}{2}\left|\widetilde{q}_{i\parallel}\right|^2\right\rangle = &-\tau_i^{-1}\left\langle\widetilde{q}_{i\parallel}\nabla_\parallel\widetilde{T}_i\right\rangle + \omega_i\hat{\beta}\left\langle\widetilde{q}_{i\parallel}\frac{\partial\widetilde{A}_\parallel}{\partial y}\right\rangle - \\ &- \frac{2}{5}\tau_i^{-2}\left\langle\widetilde{q}_{i\parallel}a_{Li}(\widetilde{q}_{i\parallel})\right\rangle - \frac{\hat{\epsilon}\nu_i}{3.9}\tau_i^{-2}\left\langle\left|\widetilde{q}_{i\parallel}\right|^2\right\rangle\end{aligned} \tag{13.42}$$

Factors of $\tau_i\widetilde{n}_e$ and $\widetilde{T}_i$ appearing in parentheses are the pieces of $\widetilde{p}_i$ terms that transfer energy between $\widetilde{u}_{\|}$ and $\widetilde{p}_i$ through sound wave channels, and between $\widetilde{\phi}$ and $\widetilde{p}_i$ through the ExB and polarisation compression. These effects are relatively negligible for drift wave turbulence, but the ion sources represented by ω_n and ω_i operating on $\tau_i\widetilde{n}_e\widetilde{v}_E^x$ and $\widetilde{T}_i\widetilde{v}_E^x$ are significant, and the transfer channel over the curvature on $\widetilde{T}_i\mathcal{K}(\widetilde{\phi})$ is important as this is the mechanism for the ITG-interchange drive in transferring the ion temperature free energy into the ExB flows. The transfer terms involving $\widetilde{J}_{\|}$ and $\nabla_{\|}\widetilde{p}_i$ represent transfer between $\widetilde{\phi}$ and $\widetilde{p}_i$ through polarisation compression. In slab geometry this can become significant, but in an inhomogeneous magnetic field it is overshadowed by the interchange coupling. The ion dissipation channels through $\widetilde{q}_{i\|}$ and $\widetilde{T}_i$, in other words, thermal conduction and Landau damping, scale similarly to the sound waves, which we found to be subdominant in Chapter 8. The important sources are Γ_n and Γ_t for the electrons, and $\tau_i\Gamma_n$ and $\tau_i\Gamma_i$ for the ions, where

$$\Gamma_n = \omega_n \left\langle \widetilde{n}_e\widetilde{v}_E^x \right\rangle \qquad \Gamma_t = \frac{3}{2}\omega_t \left\langle \widetilde{T}_e\widetilde{v}_E^x \right\rangle \qquad \Gamma_i = \frac{3}{2}\omega_i \left\langle \widetilde{T}_i\widetilde{v}_E^x \right\rangle \tag{13.43}$$

where $\widetilde{v}_E^x = -\partial\widetilde{\phi}/\partial y$ The important sinks are all in the electron parallel dynamics, Γ_c, Γ_k, and Γ_l as in the DALFTE model plus ion thermal conductive contributions to Γ_k and Γ_l (the terms with two factors of $\widetilde{q}_{i\|}$ in Eq. 13.42), and in the ExB direct cascades in $\widetilde{n}_e$, $\widetilde{T}_e$, and $\widetilde{T}_i$.

13.VIII. Warm Ion Drift Wave Turbulence in a Toroidal, Sheared Magnetic Field

We now turn to the situation which is of greatest interest and is still a central topic of current research: drift wave turbulence in toroidal geometry in the edge regions of magnetically confined fusion devices. While we established for electron dynamics by itself under the DALF3 and DALFTE models that the turbulence preserves drift wave mode structure in the collisionality regimes occupied by the experiments, we need to find out of the ion temperature changes those conclusions. At the very least, we get two more factors of background scale length going into the ideal ballooning limit, as for warm ions we now have

$$\alpha_M = \hat{\beta}\omega_B[(1+\tau_i)\omega_n + \omega_t + \tau_i\omega_i] \tag{13.44}$$

and so if the gradient scale lengths and temperatures are all equal we have $4\hat{\beta}\omega_B$ instead of ω_B. This brings the ideal ballooning threshold uncomfortably close to the parameter region of interest, and ultimately results in the need to do computations in a realistic geometry rather than the circular tokamak model developed in Chapter 11. Nevertheless,

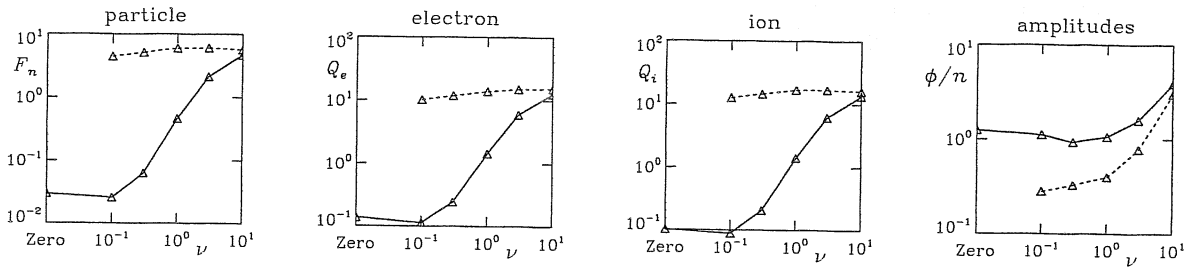

Figure 13.4. Transport scaling (left three frames) and amplitude ratios (right) of drift wave (solid lines) and resistive MHD (dashed lines) turbulence in toroidal geometry under the DALFTI model. The MHD model, which neglects the drift wave coupling terms between $\widetilde{p}_e$ and $\widetilde{J}_{||}$, is insensitive to collisionality ($C = 2.55\nu_e$) because although $\widetilde{\phi}$ is too small, $\widetilde{p}_i$ is too large, compared to the drift wave model. The transition to the MHD regime at a lower $\nu_e > 3$ is assisted by the ITG-interchange physics, since $\widetilde{T}_i$ does not feel the adiabatic response. Compare with Figs. 11.1 and 12.3

the place to investigate the resistive ballooning boundary is below this limit, and so we can still apply the same models as in the previous two chapters to the situation here.

We take the same cases as run under the DALFTE model, and simply set $\omega_n = \omega_t = \omega_i = \tau_i = 1$, placing the electrons and ions on equal footing. Nominal parameters are

$$\hat{\beta} = 1 \qquad \hat{\mu} = 5 \qquad \nu_e = 1 \qquad \hat{\epsilon} = 18350 \qquad \omega_B = 0.05 \qquad \hat{s} = 1 \tag{13.45}$$

noting that $C = 0.51\hat{\mu}\nu_e$. It is sufficient to summarise the results, as the plan follows the outlines in the previous two chapters for the DALF3 and DALFTE models. The results for the transport scaling and relative amplitudes $\widetilde{\phi}/\widetilde{n}_e$ are shown in Fig. 13.4. At moderate to large collisionality the results are qualitatively the same as for the DALF3 model. The relationship between the resistive MHD cases (neglecting the $\widetilde{p}_e \leftrightarrow \widetilde{J}_{||}$ coupling and the diamagnetic fluxes in the thermodynamics) and the DALFTI cases show the same disagreement as in the DALF3 and DALFTE models regarding the transport and the amplitude ratios. However, the transition range is much broader than in the models without the ion temperature, which we can see by comparing to Figs. 11.1 and 12.3. The particle and electron and ion heat transport are given by

$$F_n = \langle \widetilde{n}_e \widetilde{v}_E^x \rangle \qquad Q_e = \frac{3}{2} \langle \widetilde{p}_e \widetilde{v}_E^x \rangle \qquad Q_i = \frac{3}{2} \langle \widetilde{p}_i \widetilde{v}_E^x \rangle \tag{13.46}$$

normalised in terms of n_e and $n_e T_e$ times $c_s \rho_s^2 / L_\perp^2$, respectively. The level of the transport is about the same as in the DALFTE model, higher for Q_e by somewhat less than 50

percent, and slightly higher still for Q_i, which is of course zero in DALFTE. Both the ion and electron pressures are involved in the interchange forcing, and so the regime boundary for the transition to resistive MHD is lowered to somewhat above 3 rather than somewhat above 10.

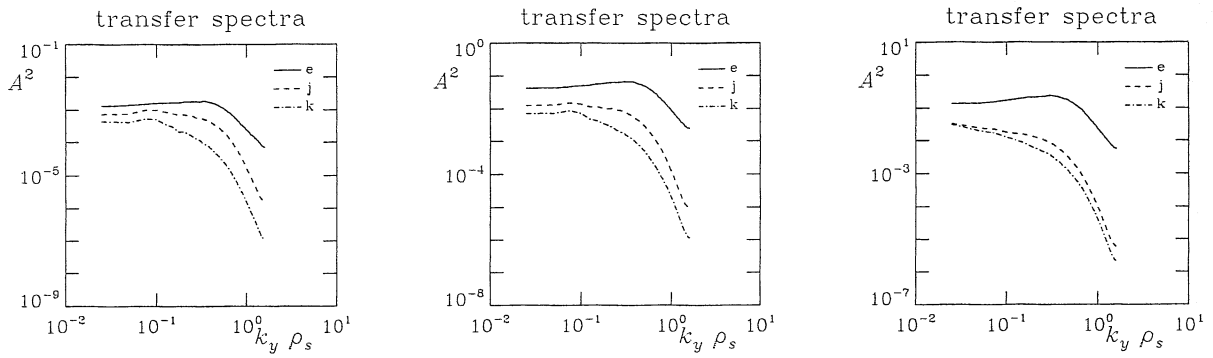

Figure 13.5. Spectra of the rms transfer dynamical levels for each k_y in the spectrum, comparing the sizes of $\widetilde{\phi}\nabla_{\parallel}\widetilde{J}_{\parallel}$ ('j'), $\widetilde{\phi}\mathcal{K}(\widetilde{p}_i+\widetilde{p}_e)$ ('k'), and $\widetilde{\phi}\mathbf{v}_E\cdot\nabla\nabla_{\perp}^2\widetilde{\phi}$ ('e'), for drift wave turbulence, for $\nu_e = 1$, 3, and 10 (left to right), where $C = 2.55\nu_e$. Compare with Fig. 11.4. For $\nu_e = 10$ the curvature catches up to the parallel dynamics at long wavelength, establishing this as the first resistive ballooning case.

Fig. 13.5 shows where this boundary should lie. The spectra of the ExB transfer dynamics is shown for the three cases $\nu_e = \{1, 3, 10\}$, and we find that the transfer between $\widetilde{p}_e$ and $\widetilde{\phi}$ over the current is still stronger than over the curvature for $\nu_e = 3$, by about the same margin as in the DALFTE model for $\nu_e = 10$, as we find by comparing to Fig. 12.5. The average transfer for the curvature has the same form, however, telling us that $\nu_e = 3$ for DALFTI is equivalent in the transition to $\nu_e = 10$ for DALFTE.

The envelopes of the squared amplitudes of the four state variables in the s-direction is shown in Fig. 13.6, for the three Landau DALFTI cases across the MHD regime boundary, $\nu_e = \{1, 3, 10\}$. We can compare this to Fig. 12.4. It still holds that $\widetilde{T}_e$ behaves like $\widetilde{h}_e$, but $\widetilde{T}_i$ is strong in all cases and behaves like $\widetilde{n}_e$. The dual role of $\widetilde{n}_e$ as an electron and ion density, forming part of the pressure, means that it leans more towards ITG-interchange physics than in the DALFTE model, and we can attribute to this the fact that the transition to resistive MHD lies lower, at about

$$(C\omega_B)_{\text{crit}} = 0.4 \tag{13.47}$$

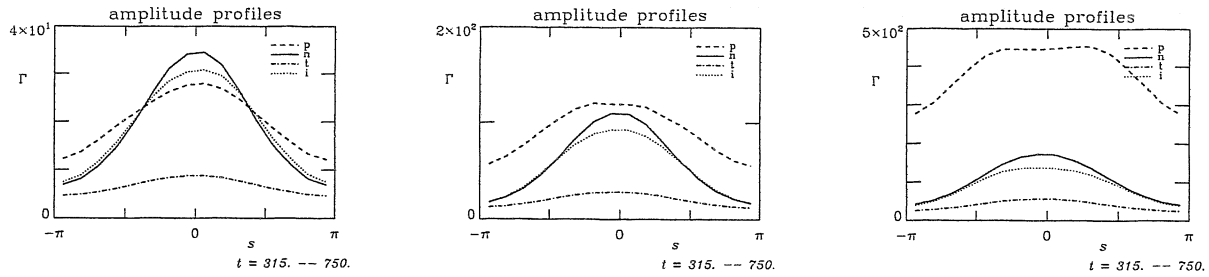

Figure 13.6. Amplitude envelopes of $\widetilde{\phi}$, $\widetilde{n}_e$, $\widetilde{T}_e$, and $\widetilde{T}_i$, respectively labelled by 'p', 'n', 't', 'i', for drift wave turbulence, for $\nu_e = 1$, 3, and 10 (left to right), where $C = 2.55\nu_e$. Comparing with Fig. 11.7, we find the transition to ballooning mode structure at lower $\nu_e > 3$. Note that $\widetilde{T}_e$ plays the same role in the physics as $\widetilde{h}_e$, part of the overall nonadiabatic dynamics (cf. Fig. 12.4), but that $\widetilde{T}_i$ involves purely ITG-interchange dynamics. This lowers the regime boundary. These results correspond well to those of Fig. 13.5, but we note again that with only the density to hand we could not discern any differences.

The competing roles of curvature and adiabatic forcing on the electron dynamics is the same; it is just that there is now twice as much total pressure gradient, and since $\widetilde{T}_i$ is larger than $\widetilde{T}_e$ the boundary is a factor of about three lower.

For the ideal ballooning transition we find that the ion temperature dynamics lowers the threshold by about the same amount as for resistive ballooning, and the threshold is now clearly well below unity, as seen in Fig. 13.7. These cases started with the $\nu_e = 1$ nominal cases for the three DALF models and took several values of $\hat{\beta}$. Sweeping $\hat{\beta}$ at constant ν_e also means raising the drift normalisation scale $\rho_s^2 c_s/L_\perp$ in the measure of $\hat{\beta}^{1/2}$, as noted in the previous chapter. This is important, because it rules out scenarios according to which the magnetic flutter effect which is so effective in slab geometry (cf. Fig. 12.6) should lead to transport regime transitions at some lowered collisionality. We now find an ideal ballooning threshold somewhere between

$$0.2 < (\alpha_M/\hat{s})_{\text{crit}} < 0.6 \tag{13.48}$$

with α_M defined in Eq. (13.44), and this is significantly lower than the conventional linear analysis suggests. Ideal ballooning is now enough of a problem that for quantitative investigations one has to turn to very realistic models of flux surface geometry, and then the focus departs from basic physics and enters modelling. We can nevertheless learn much about the physics of fluid drift turbulence without having to resort to such complication.

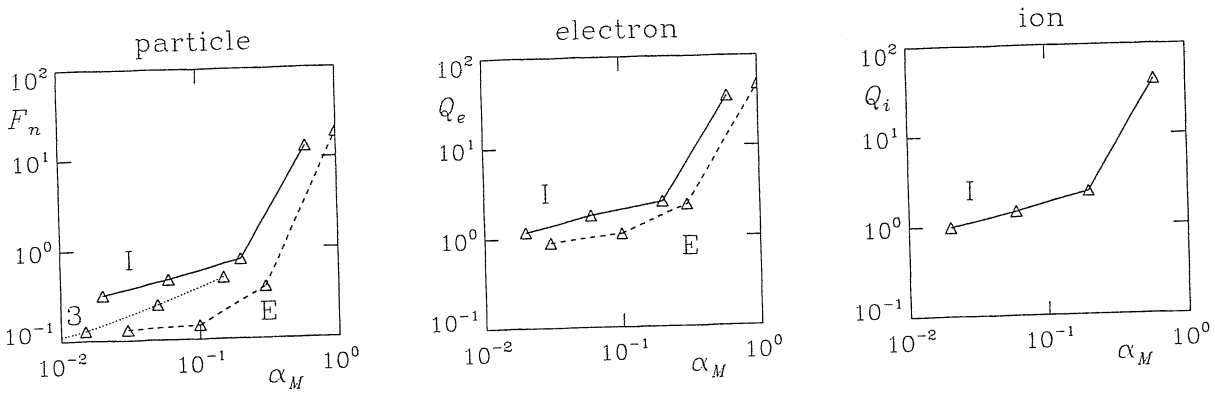

Figure 13.7. Transport scaling (left three frames) as a function of the total pressure gradient $\nabla\beta$, or the ideal ballooning parameter α_M, for the DALF3 ('3'), DALFTE ('E'), and DALFTI ('I') models. The collisionality was $C = 2.55$, in the drift wave regime. The transport is in physical, but arbitrary units, compensating for the effect of varying $\hat{\beta}$ on the normalisation scale $\rho_s^2 c_s / L_\perp$. The ion temperature assists the transition to ideal MHD in the measure and for the same reason as for the resistive ballooning cases: more total pressure gradient, and $\widetilde{T}_i > \widetilde{T}_e$. But the ideal ballooning threshold now between 0.2 and 0.6, is lowered by a factor of at least two relative to the linear analysis.

In the overall drive levels, it is interesting to note that $Q_e \approx Q_i$ for $\omega_n = \omega_t = \omega_i$ and $\tau_i = 1$, even though $\widetilde{T}_e$ is much smaller than $\widetilde{T}_i$, as Fig. 13.6 shows. The electron temperature is more closely coupled to the ExB flows through the parallel dynamics than $\widetilde{T}_i$, which is more involved in the relatively incoherent interchange dynamics. It is important to note this contrast if experimental information concerning $\widetilde{T}_i$ ever becomes available.

13.IX. Warm Ions and Sheared ExB Flows

It is of interest in magnetically confined fusion research to know to what extent an externally applied ExB shear layer of several centimeters thickness is able to suppress fluid drift turbulence so that some of the observed transport regime transitions can be attributed to this scenario.

In Fig. 13.8 we can see the spatial morphology of $\widetilde{T}_i$ when a constant background ExB vorticity is applied, as in Chapter 9. The parameter is $V' = (c_s/L_\perp)(\partial v_0^y/\partial x)$. The suppression is clearly observed, as the disturbances are about half as strong with $V' = 0.1$ as for $V' = 0$. We note that this is right in the experimentally observed range of ExB shear layer strengths at the time of the most famous transport regime transition, between the experimental regimes known as the L-mode and H-mode, for low and high confinement,

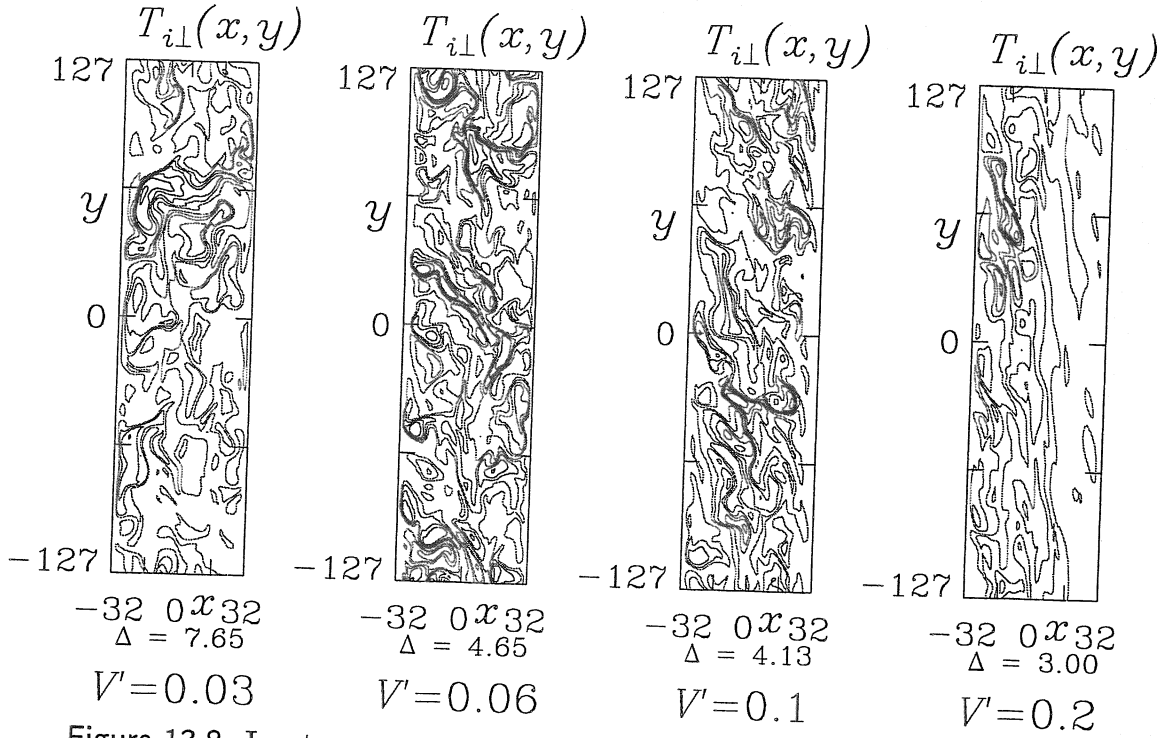

Figure 13.8. Ion temperature contours in ITG turbulence in toroidal geometry with $\hat{\beta} = 2$, $C = 2$, $\omega_n = 0.5$, $\hat{\epsilon} = 14680$, and other parameters nominal, subjected to externally applied flows parameterised by V'. The tendency to rip apart and suppress the disturbances is clear, as the maximum absolute value in each case is 6Δ.

respectively. While a fully self consistent model is not yet to hand, it is interesting that this background shear layer can do what the self generated flows cannot: reach a high enough level to suppress the turbulence. For modellers, this points to the need to incorporate the physics determining the equilibrium electric field structure and the turbulence into the same scheme. For those more interested in fundamental physics, it is indicative of a rich level of self consistency, not only in the turbulence but also between the turbulence and the profile gradients giving rise to it. It is a situation reminiscent of the most interesting topics in geophysical fluid dynamics and the understanding of the Earth's climate.

Zonal flows as time dependent ExB shear layers which are part of the turbulence is an ongoing theme of this research. The studies shown in Chapters 8 and 12 have not been done in the DALFTI model yet, but it is expected that there should be noticeable effect on the total transport. We should expect a result more similar to the one in Chapter 12 than to the slab cases, as we have already found that the toroidal coupling to global

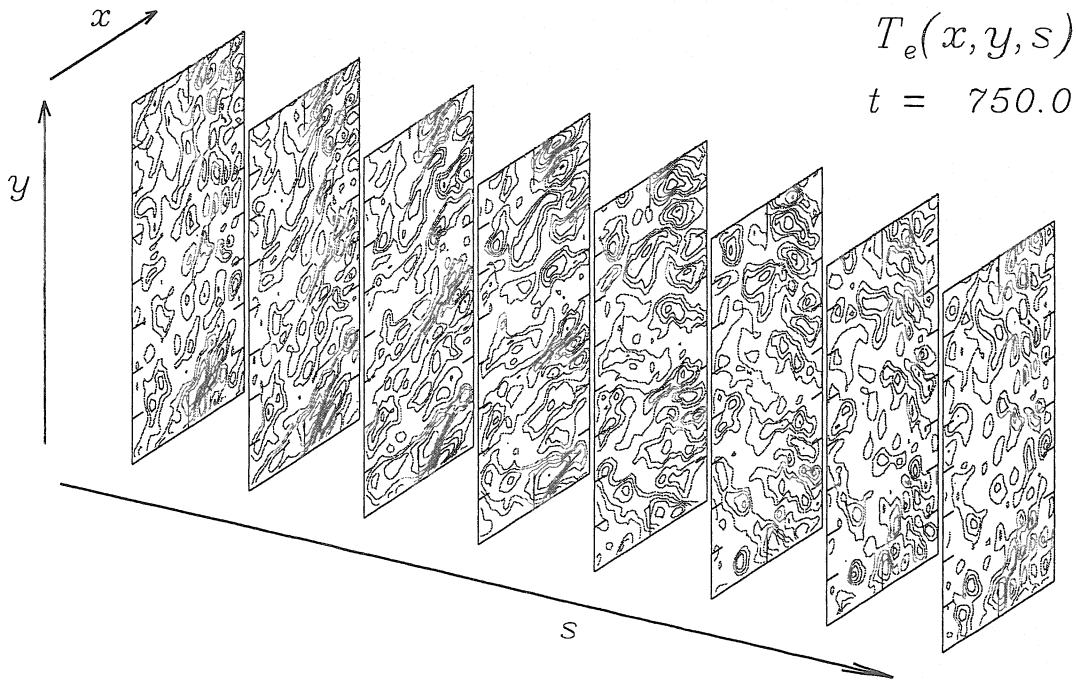

Figure 13.9. Three dimensional morphology of the electron temperature for drift wave turbulence at the nominal parameters, with the flux surface average subtracted out. Every second drift plane is shown. The disturbances follow the field lines well, commensurate with the moderate collisionality of $C = 2.55$. Note that the field lines are sheared, in the s-direction but tilting towards negative y, for positive x.

shear Alfvén modes inhibits zonal flow generation. Interchange turbulence tends to be more sensitive to externally applied flows, but the situation for electromagnetic drift wave and ITG mode turbulence is more complicated. This situation bears further study, with a wider range of parameter variation than has been the case up to now.

13.X. Summary

The principal effect of the ion temperature on fluid drift dynamics is to add two new types of eigenmode which compete to form the turbulence. These are the ITG modes, the classical versions of which consist of adiabatic electrons and an accessibility mechanism for the ion temperature gradient. The slab branch is a thermal sound wave, while the interchange branch is a radial flow mode existing in an inhomogeneous magnetic field. In both cases, a threshold exists for the relative gradient strength ratio between the ion temperature and the density, termed η_i. The threshold results from the tendency for an

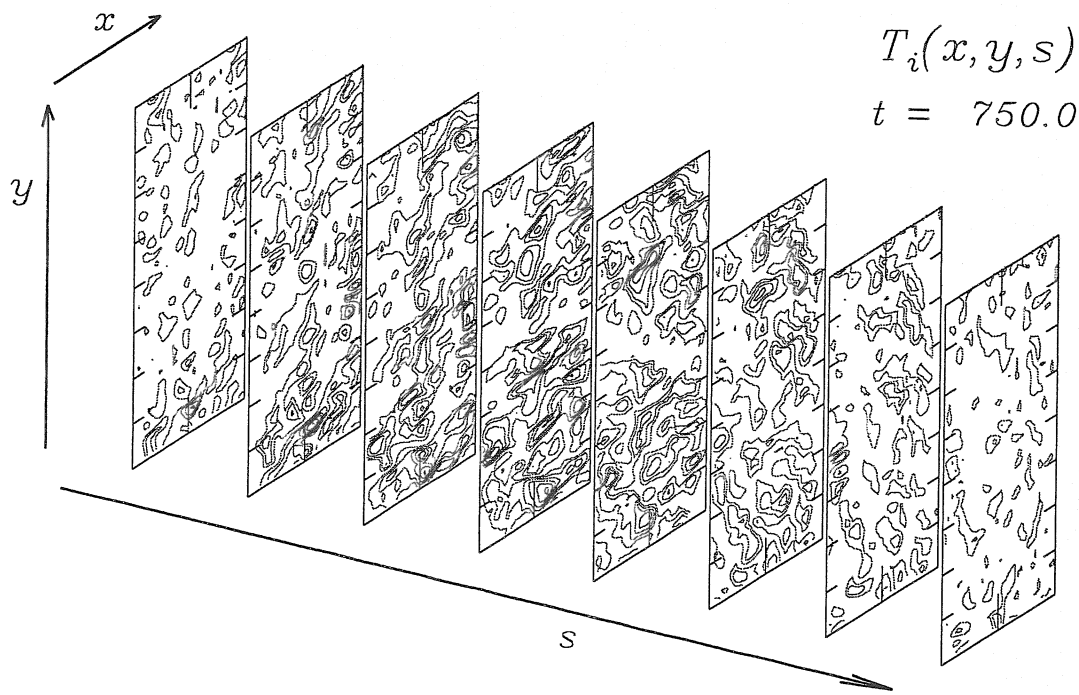

Figure 13.10. Three dimensional morphology of the ion temperature, with the flux surface average subtracted out, for the same case as in Fig. 13.9. Every second drift plane is shown. The tendency to follow the field lines is much less pronounced than for $\widetilde{T}_e$, and the amplitude asymmetry with s is much greater, corresponding to $\widetilde{T}_i$ as the principal agent for interchange dynamics. Note that the field lines are sheared, in the s-direction but tilting towards negative y, for positive x.

ExB eddy to drift out of the way of an emerging ion temperature disturbance, for smaller values of η_i. For strongly nonadiabatic regimes, the threshold disappears, but the transition to an ITG mode structure characterised by $\widetilde{T}_i$ being the largest normalised disturbance still persists. This can emerge in turbulence as well, but investigation of that regime has just started.

For fluid drift turbulence in toroidal geometry, the mode structure is either drift wave or ballooning like, depending on the resistive and ideal limits given in Eqs. (13.47) and (13.48), respectively. The resistive limit corresponds to a level of collisionality somewhat higher than the average experimental regime, with some tokamaks having an empirical density limit well below this threshold. Taking this together with the observations that a more realistic model of flux tube geometry than the circular tokamak model tends to be less sensitive to ballooning at the same parameters, it appears that the experiments are

operating well to the drift wave side of the resistive MHD regime boundary. For the ideal threshold the situation is much clearer: the operation regimes are limited experimentally by what appears to be a pressure gradient threshold which follows a similar scaling to Eq.(13.48), but with a higher critical value usually attributed to the strongly shaped flux surface geometry causing an effectively stronger magnetic shear. This makes drift wave turbulence a very relevant model for understanding the physics of those experiments, and it is fortunate that a qualitative understanding can be obtained from much simpler models, like those in earlier chapters.

Further Reading

The complications of the finite ion Larmor radius for drift instabilities and turbulence have been known for a long time, and are also discussed in the two reviews mentioned earlier, by W. M. Tang, in *Nucl. Fusion* 18 (1978) 1089, and by P. C. Liewer, in *Nucl. Fusion* 25 (1985) 543. Several models for finite Larmor radius fluid equations were in use by that time, and one of the most important is the one by F. L. Hinton and C. W. Horton, Jr., in *Phys. Fluids* 14 (1971) 116, mentioned also in Chapters 2 and 3. It is important to note that in those days MHD ordering was still common, with a pure ExB advection equation for $\widetilde{p}_i$ used to alter the form of the gyroviscous cancellation so that only $\widetilde{\phi}$ appears under the time derivative and $\nabla_\perp^2$; this is only valid in the ballooning regimes in which $\widetilde{\phi} \gg \widetilde{p}_i$ in the normalised equations.

The gyrofluid model mentioned in the text has become standard in regions of weak collisionality, where various kinetic dissipation mechanisms beyond those discussed here are needed in addition to several finite Larmor radius modifications generally involving polarisation. The original idea of using a polarisation density instead of a polarisation current, for gyrocenter instead of particle fluid elements, appears in an article by G. Knorr, F. R. Hansen, J. P. Lynov, H. L. Pécseli, and J. Juul Rasmussen, in *Physica Scripta* 38 (1988) 829. A systematic treatment through the heat flux equations by W. Dorland and G. Hammett, in *Phys. Fluids B* 5 (1993) 812, is a useful starting place. The state of the art for toroidal geometry is presented by M. A. Beer and G. W. Hammett, in *Phys. Plasmas* 3 (1996) 4046. For an electromagnetic model based on the Beer and Hammett equations but with self consistent electrons, see B. Scott, *Phys. Plasmas* 7 (2000) 1845.

The gyrofluid models are based on the gyrokinetic equation which has been recently formalised in terms of Lie transforms of the original Vlasov equation for the kinetic distribution function, suitable for any magnetic geometry, following the work by R. Littlejohn for the drift kinetic equation, detailed in *J. Plasma Phys.* 29 (1983) 111. A concise version for the electrostatic theory in a homogeneous magnetic field was given by T. S. Hahm, in *Phys.*

Fluids 31 (1988) 2670. The entire model was rebuilt in the framework of a Lagrangian field theory, including the Maxwell equations as well as the Vlasov equation, by H. Sugama, in *Phys. Plasmas* 7 (2000) 466, which contains all the principal references. The current status of gyrofluid and gyrokinetic computation for adiabatic electrons is well represented in the review by A. Dimits *et al*, in *Phys. Plasmas* 7 (2000) 969.

14. The Character of Transport Caused by the Turbulence

B. Scott

Jul 1999

14.I. Introduction — Transport as Turbulent Diffusion

We have been studying small scale turbulence under the drift approximation, which assumes that the fluctuations in the variables involved in the turbulence are small compared either to their background values (for the thermodynamic variables) or to the quantities against which they are typically scaled (for the electrostatic potential, or the parallel fluxes). The general statement of this is that quantities such as $e\widetilde{\phi}/T_e$ or $\widetilde{p}_e/p_e$ should be small even if robustly nonlinear. Even if this is true for the turbulence, it is not true for the evolution of the background, should this be put under consideration. We have been treating turbulence, not transport. Specifically, although we have computed the transport as a function of parameters, we have not been computing transport *per se*, that is, we have not considered the effect the turbulence has on the background, beyond fluctuations in the profiles which are actually part of the turbulence. Herein, we derive some general results concerning the character of this transport, and how it differs in character from the simple thermodynamic diffusion which results from random thermal motion and inter-particle collisions. To do this, we have to address what sort of equations one should treat transport with.

Transport of thermal energy and particles in magnetically confined, laboratory plasmas is well known to be anomalous: much larger than transport by collisional diffusion and appearing with different scaling characteristics. Modelling of this transport is usually done in terms of the two fluid Braginskii equations, but by substituting either empirical or theoretical turbulence models for the diffusivity coefficients. The ExB turbulence is supposed to act as a set of small, random displacements according to which the quantities they transport are diffused down these quantities' gradients.

It is important to note that the transport process is assumed by such a model to have the same character as the collisional diffusion process, including the prospect that Onsager symmetry should hold. Onsager symmetry is a general result of nonequilibrium thermodynamics, which considers how the thermodynamic equilibrium (minimum entropy, no entropy gradients) is approached. It rests on two standard assumptions: that the problem can be linearised, that is, that the system is close enough to equilibrium that the entropy can be expressed as a quadratic functional of the disturbances of all the state

variables away from their equilibrium values; and that the disturbances in all the state variables are mutually uncorrelated. Gradient driven transport in magnetised plasmas breaks both of these assumptions. We have seen that in drift wave turbulence, the cross coherence among the dependent variables can be significant even if the ExB eddies as such (that is, $\widetilde{\phi}$) show a Gaussian distribution. Furthermore, the problem is strongly nonlinear even though the amplitudes are small, a consequence of the smallness of the drift parameter, $\delta = \rho_s/L_\perp$. We have seen how important the nonlinear polarisation drift is to the ExB flow energetics. This is equivalent to the statement that third and higher order expressions are as important as second order ones in the energy theorem; their rms values are large even if their mean values are small. This is our first signpost that the turbulence may act very differently than randomised thermal motion of uncorrelated particles, in causing transport. But there are even more important properties to consider.

14.II. The Basic Character of Small Scale ExB Flow Transport

There are a number of fundamental properties of ExB drift turbulence which suggest that the transport they cause should be qualitatively different from random thermal transport. First, if conventional drift ordering holds — the scale of the turbulence is short compared to that of the background gradients and the relative amplitude of the fluctuations in the thermodynamics quantities is small — the velocity can be thought of as nearly incompressible. If the magnetic field is straight then the divergence $\nabla\cdot\mathbf{v}_E$ vanishes entirely. In a toroidal device, the divergence carries the scale of the major radius:

$$\nabla\cdot\mathbf{v}_E = \nabla\cdot\frac{c}{B^2}\mathbf{B}\times\nabla\phi \approx -\mathbf{v}_E\cdot\nabla\log B^2 \sim R^{-1}\mathbf{v}_E \tag{14.1}$$

Since in the confinement zone the pressure scale length, L_p is much smaller, we have

$$\mathbf{v}_E\cdot\nabla\widetilde{p} \gg \widetilde{p}\nabla\cdot\mathbf{v}_E \qquad \text{if} \quad L_p \ll R \tag{14.2}$$

Here, we assume that the scale of a significant divergence of the transport flux is L_p rather than the much smaller scale of ExB disturbances, because such a state should be approached on the time scale of the turbulence, not the transport. By contrast, a diffusive flux of the form $n_e\mathbf{v}_D = -D\nabla n_e$ is always compressible, as it can be derived from a potential.

The second important characteristic is that the ExB velocity is also involved in the Poynting energy flux,

$$\mathbf{v}_E = \frac{c}{B^2}\mathbf{E}\times\mathbf{B} = \frac{1}{\rho v_A^2}\,c\frac{\mathbf{E}\times\mathbf{B}}{4\pi} \tag{14.3}$$

with ρ the mass density and v_A the Alfvén velocity. Due to the close force balance for small scale disturbances in drift dynamics, there is a cancellation between the Poynting flux and one factor of $p\,\mathbf{v}_E$ in the total thermal energy flux. This has the consequence that alone among transport mechanisms, for ExB drift turbulence the advective part of the thermal energy flux appears with a factor of 3/2, not 5/2, times the temperature times the particle flux. More specifically, its energetic coupling to the thermal reservoir is mediated through its small, quasistatic divergence, so that the pressure does little work on elemental volumes of the fluid.

A third characteristic of ExB flows is that they cannot cause magnetic flux diffusion unless there is a significant amount of reconnection of magnetic field lines in the presence of a current gradient (that is, the drive mechanism should be this current gradient, rather than the thermal gradients as for drift turbulence). The magnetic flux occurs through the inductive part of the electric field in the force balance for electrons, that is, $\partial A_\parallel/\partial t$. Neglecting dissipation and electron inertia the Ohm's law is

$$\frac{1}{c}\frac{\partial A_\parallel}{\partial t} = \frac{\nabla_\parallel p_e}{n_e e} - \nabla_\parallel \phi \tag{14.4}$$

In an average over a closed flux surface the right hand side vanishes unless there are appreciable magnetic disturbances. When the disturbances follow from drift dynamics the relative phase shifts are such that magnetic transport effects tend to cancel out of the flux surface averages. Only when the current gradient is available as an energy source do these processes lead to appreciable transport, even if the thermal transport is robustly anomalous. By contrast, random thermal diffusion transports magnetic flux by the same mechanism as for particles and energy, and the flux diffusivity, $\eta_\parallel c^2/4\pi$, is even larger than the fluid diffusivities, proportional to $D_e = \rho_e^2 \nu_e$, by a factor of β_e^{-1}.

Two further considerations involve the development of large scale ExB flows within the flux surfaces (we assume that the equilibrium is quiescent enough that there is no bulk flow across flux surfaces beyond the existence of the turbulence). Under ExB drift turbulence, the disturbances as well as the background are deeply quasineutral. Charge differences are neutralised on time and space scales which are effectively arbitrarily small, so that while there can be nonvanishing electric fields, there is no significant charge density for dynamics at drift scales. In this context it is meaningless to speak of a radial electric field generated by the divergence of a radial current. Rather, we have the constraint that the total current is divergence free, so that various pieces of the current which might have a divergence are balanced by a divergence in the polarisation current of the ions. We have seen this already in Chapter 2 in a general sense, but will develop it here specifically for

the problem of mean flow generation which we encountered in Chapter 9. If source or loss mechanisms for either of the charge species are considered, these should be thought of as a torque on the ExB vorticity rather than a charge generation.

Finally, anomalous transport in the ExB vorticity results fundamentally from anomalous viscosity, either the fluid Reynolds stress or some process arising from gyroviscosity. Under flux surface and short time scale averaging, it is a matter of the total radial polarisation drift (linear plus nonlinear) necessarily vanishing. An anomalous resistivity cannot lead to anomalous transport of ExB flows or, equivalently, generation of a radial electric field. This is a direct consequence of the fact that resistivity is a momentum conserving friction between electrons and ions.

In the rest of this chapter, we address the general equations of transport by small scale drift turbulence via mean field theory, and then underscore the above points via analysis of these equations.

14.III. Global Fluid Drift Equations and Energy Conservation

The general derivation of fluid drift equations for large scale motion proceeds similarly to the local treatment; the difference is mainly that we must keep track of the variability of the coefficients which depend on densities or temperatures. The density is the most important of these. It carries the consequence that the ion polarisation drift must be retained in advection if exact energy conservation is to hold.

We begin with a neutral, single-component plasma with ions of mass M_i and charge state Z and electrons of mass m_e. For this treatment we will neglect electron inertia but keep m_e in combination with ν_e in the formulae for the dissipative fluxes. The densities satisfy $n_e = Zn_i$. We assume that the local drift parameter, $\delta = \rho_s/L_p$, and the electron beta, $\beta_e = 4\pi p_e/B^2 = c_s^2/v_A^2$, are small. In contrast to the familiar situation with drift equation models, no assumption concerning flute mode ordering in the derivatives is made during the derivation of the equations themselves and their energy theorem concerning spatial scales, even for $\mathbf{B}$. The more familiar assumption of $k_\parallel \ll k_\perp$, or for a toroidally confined plasma $L_p \ll R$, is reserved for evaluating the properties of the transport considering that the disturbances involved in the turbulence do indeed satisfy local drift ordering.

As in the local treatments, we start by assuming an electric field whose perpendicular components are electrostatic but with a parallel component which includes induction,

$$\mathbf{E}_\perp = -\nabla_\perp \phi \qquad E_\parallel = -\frac{1}{c}\frac{\partial A_\parallel}{\partial t} - \nabla_\parallel \phi \tag{14.5}$$

Correspondingly, the total magnetic field, $\mathbf{B}_t$, is given by the background, plus the principal disturbance arising from $A_\parallel$, plus a small compressional piece which evolves quasistatically, plus an even smaller correction needed to ensure that $\nabla \cdot \mathbf{B}_t = 0$,

$$\mathbf{B}_t = \mathbf{B} - \frac{\mathbf{B}}{B}\times\nabla A_\parallel + \widetilde{B}\frac{\mathbf{B}}{B} - \nabla\alpha \tag{14.6}$$

respectively. The symbols $\mathbf{B}$ and B give the equilibrium magnetic field and its magnitude, while $\mathbf{b}$ is reserved for the combination of $\mathbf{B}$ and the piece involving $A_\parallel$, given by

$$\mathbf{B}_\perp = -\frac{\mathbf{B}}{B}\times\nabla A_\parallel \tag{14.7}$$

so that in describing parallel components we use

$$\mathbf{b} = \frac{1}{B}(\mathbf{B} + \mathbf{B}_\perp) \qquad\qquad \nabla_\parallel = \mathbf{b}\cdot\nabla \tag{14.8}$$

Perpendicular components are described by the background field only,

$$\nabla_\perp = -\mathbf{B}\times\frac{\mathbf{B}\times\nabla}{B^2} \qquad\qquad \nabla_\perp^2 = \nabla\cdot\nabla_\perp \tag{14.9}$$

so we must note that with these definitions we cannot write $\nabla = \nabla_\perp + \mathbf{b}\nabla_\parallel$, for example. The Ampere's law involving $A_\parallel$ is written with $\nabla_\perp^2$,

$$\nabla_\perp^2 A_\parallel = -\frac{4\pi}{c}J_\parallel \tag{14.10}$$

The compressional part of the magnetic field, involving $\widetilde{B}$, is used only to evaluate the Poynting energy flux in the energy theorem. The divergence correction, involving α, is never used; it is written only to preserve $\nabla\cdot\mathbf{B}_t = 0$, and in practice it is always negligibly small.

We start with the ExB and diamagnetic drift velocities, replacing n_i with n_e in $\mathbf{u}_*$,

$$\mathbf{v}_E = \frac{c}{B^2}\mathbf{B}\times\nabla\phi \qquad \mathbf{v}_* = -\frac{c}{B^2}\mathbf{B}\times\frac{\nabla p_e}{n_e e} \qquad \mathbf{u}_* = \frac{c}{B^2}\mathbf{B}\times\frac{\nabla p_i}{n_e e} \tag{14.11}$$

We form the lowest order perpendicular fluid velocities resulting from these drifts,

$$\mathbf{u}_\perp = \mathbf{v}_E + \mathbf{u}_* \qquad\qquad \mathbf{v}_\perp = \mathbf{v}_E + \mathbf{v}_* \tag{14.12}$$

or in terms of the state variables,

$$\mathbf{u}_\perp = \frac{c}{B^2}\mathbf{B}\times\left(\nabla\phi + \frac{\nabla p_i}{n_e e}\right) \qquad\qquad \mathbf{v}_\perp = \frac{c}{B^2}\mathbf{B}\times\left(\nabla\phi - \frac{\nabla p_e}{n_e e}\right) \tag{14.13}$$

The total velocities are therefore given by

$$\mathbf{u} = \mathbf{u}_\perp + u_\parallel \mathbf{b} + \mathbf{u}_p \qquad \mathbf{v} = \mathbf{v}_\perp + v_\parallel \mathbf{b} \tag{14.14}$$

For the ions we keep the polarisation drift, which as we will see is required in the advection process in the polarisation and ion pressure dynamics to conserve energy. Together, the parallel velocities give the parallel current,

$$J_\parallel = n_e e \left(u_\parallel - v_\parallel \right) \tag{14.15}$$

which is used to eliminate $v_\parallel$ from the equations for the electron dynamics. We can express the polarisation drift in terms of a potential,

$$\mathbf{u}_p = -\frac{M_i c^2}{ZeB^2} \nabla_\perp \chi = \frac{M_i}{Ze} \frac{c}{B^2} \mathbf{B} \times \left(\frac{c}{B^2} \mathbf{B} \times \nabla \chi \right) \tag{14.16}$$

following from the fact that it is primarily proportional to gradients of scalars,

$$n_e e \mathbf{u}_p = n_i M_i \frac{c}{B^2} \mathbf{B} \times \left(\frac{\partial}{\partial t} + \mathbf{u} \cdot \nabla \right) \left[\frac{c}{B^2} \mathbf{B} \times \left(\nabla \phi + \frac{\nabla p_i}{n_e e} \right) \right] + \frac{c}{B^2} \mathbf{B} \times (\nabla \cdot \boldsymbol{\Pi}_*) \tag{14.17}$$

where we keep the gyroviscosity explicitly instead of just using the part which cancels $\mathbf{u}_* \cdot \nabla$, in order to preserve its symmetry. By contrast to the local treatments, the polarisation drift does indeed appear in the inertia, but only in the advection. On the other hand, the inertial velocity itself is the lowest order version, whose perpendicular component is $\mathbf{u}_\perp$. Consequently, we construct the components of $\boldsymbol{\Pi}_*$ using only the lowest order velocities, $\mathbf{u}_\perp + u_\parallel \mathbf{b}$, as we will need to use the fact that $\boldsymbol{\Pi}_* : \nabla \mathbf{u}$ vanishes, for whichever vector $\mathbf{u}$ is used to construct $\boldsymbol{\Pi}_*$.

We now form the polarisation equation,

$$-\nabla \cdot n_e e \mathbf{u}_p = \nabla \cdot \left(J_\parallel \mathbf{b} \right) + \nabla \cdot \frac{c}{B^2} \mathbf{B} \times \nabla \left(p_e + p_i \right) \tag{14.18}$$

Where we need to evaluate $\mathbf{u}_p$ in the ion equations, we may use,

$$\nabla \cdot \frac{n_i M_i c^2}{B^2} \nabla_\perp \chi = \nabla \cdot \left(J_\parallel \mathbf{b} \right) + \nabla \cdot \frac{c}{B^2} \mathbf{B} \times \nabla \left(p_e + p_i \right) \tag{14.19}$$

which we solve for χ.

The rest of the equations are formed using the same procedure as in Chapter 3: the drifts are substituted in for the perpendicular fluxes, and the parallel velocities are left as dependent variables. The polarisation inertia is evaluated using the lowest order velocities except for the fact that we have to keep it in the advection. As usual, $v_\parallel$ is eliminated

in favor of $J_\parallel$, which is related to $A_\parallel$ through Ampere's law. We do neglect the electron mass, assuming that all relevant scales are larger than the collisionless skin depth.

The resulting model is given by

$$-\nabla\cdot\left\{n_iM_i\frac{c}{B^2}\mathbf{B}\times\left(\frac{\partial}{\partial t}+\mathbf{u}\cdot\nabla\right)\left[\frac{c}{B^2}\mathbf{B}\times\left(\nabla\phi+\frac{\nabla p_i}{n_ee}\right)\right]+\frac{c}{B^2}\mathbf{B}\times(\nabla\cdot\mathbf{\Pi}_*)\right\}=$$

$$=\nabla\cdot\left(J_\parallel\mathbf{b}\right)+\nabla\cdot\frac{c}{B^2}\mathbf{B}\times\nabla\left(p_e+p_i\right) \quad (14.20)$$

$$\frac{\partial n_e}{\partial t}+\nabla\cdot\left[n_e\mathbf{v}_E+n_e\left(u_\parallel-\frac{J_\parallel}{n_ee}\right)\mathbf{b}-\frac{c}{B^2}\mathbf{B}\times\nabla\frac{p_e}{e}\right]=0 \quad (14.21)$$

$$\frac{1}{c}\frac{\partial A_\parallel}{\partial t}=\frac{\nabla_\parallel p_e}{n_ee}-\nabla_\parallel\phi-R_{ei} \quad (14.22)$$

$$\frac{\partial}{\partial t}\frac{3}{2}p_e+\nabla\cdot\left[\frac{3}{2}p_e\mathbf{v}_E+\frac{5}{2}p_e\left(u_\parallel-\frac{J_\parallel}{n_ee}\right)\mathbf{b}+q_{e\parallel}\mathbf{b}-\frac{c}{B^2}\mathbf{B}\times\nabla\frac{5}{2}\frac{p_eT_e}{e}\right]=$$

$$=u_\parallel\nabla_\parallel p_e-\frac{J_\parallel}{n_ee}\nabla_\parallel p_e-p_e\nabla\cdot\mathbf{v}_E+J_\parallel R_{ei} \quad (14.23)$$

$$n_iM_i\left(\frac{\partial}{\partial t}+\mathbf{u}\cdot\nabla\right)u_\parallel+\mathbf{b}\cdot(\nabla\cdot\mathbf{\Pi}_*)=-\nabla_\parallel\left(p_e+p_i\right)+\nabla\cdot\left(\mu_\parallel\mathbf{b}\nabla_\parallel u_\parallel\right) \quad (14.24)$$

$$\frac{\partial}{\partial t}\frac{3}{2}p_i+\nabla\cdot\left[\frac{3}{2}p_i\mathbf{v}_E+\frac{5}{2}p_iu_\parallel\mathbf{b}+q_{i\parallel}\mathbf{b}+\frac{5}{2}p_i\mathbf{u}_p+\frac{c}{B^2}\mathbf{B}\times\nabla\frac{5}{2}\frac{p_iT_i}{e}\right]=$$

$$=u_\parallel\nabla_\parallel p_i+\mathbf{u}_p\cdot\nabla p_i-p_i\nabla\cdot\mathbf{v}_E+\mu_\parallel\left|\nabla_\parallel u_\parallel\right|^2 \quad (14.25)$$

where except for $\nabla\cdot\mathbf{v}_E$ the magnetic divergences are written explicitly. The dissipative momentum transfer,

$$R_{ei}=\eta_\parallel\left[J_\parallel+\frac{\alpha}{\kappa_e}\left(\alpha J_\parallel+\frac{e}{T_e}q_{e\parallel}\right)\right] \quad (14.26)$$

and parallel heat fluxes,

$$q_{e\parallel}+\alpha\frac{T_e}{e}J_\parallel=-\kappa_en_e\frac{V_e^2}{\nu_e}\nabla_\parallel T_e \qquad q_{i\parallel}=-\kappa_in_i\frac{V_i^2}{\nu_i}\nabla_\parallel T_i \quad (14.27)$$

are given by the Braginskii model, with the resistivity and electron and ion thermal velocities given by

$$\eta_\parallel=\eta\frac{m_e\nu_e}{n_ee^2} \qquad V_e=\left(\frac{T_e}{m_e}\right)^{1/2} \qquad V_i=\left(\frac{T_i}{M_i}\right)^{1/2} \quad (14.28)$$

respectively, with numerical constants for $Z=1$

$$\eta=0.51 \qquad \alpha=0.71 \qquad \kappa_e=3.2 \qquad \kappa_i=3.9 \quad (14.29)$$

We note that this is an approximate treatment, but as we will now show, it conserves global energy. We first make a few remarks. First, the reason for including $\mathbf{u}_p$ in advection is conservation of the inertial energy due to $\mathbf{u}_\perp$. We must manipulate this such that the density is brought under both the time derivative and under a resulting total divergence. Since it starts out as a multiplier on $\partial/\partial t$ as well as on the advecting velocity, the continuity demands require that we keep $\mathbf{u}_p$ in this advection if we keep it in the density equation. This chain of demands starts at the presence of $\nabla_\parallel p_e$ in the Ohm's law, continues with $\nabla_\parallel J_\parallel$ in the electron pressure equation and hence the density equation, and finally with the fact that the divergences of $J_\parallel$ and $\mathbf{u}_p$ go together in the continuity. The ordering and conservation are preserved by keeping $\mathbf{u}_p$ in the advection, but not in the actual inertial velocity. Second, although the perpendicular and parallel components of vectors are set up differently, they are kept separate in all computations so that there is no violation of energy conservation. Finally, one sees that part of the drift ordering is expressed in the fact that the equations are written only for the lowest order components of the ion velocity and magnetic field, but the operations involving those velocities and gradients include all components in order to conserve energy.

The energy theorem is formed by multiplying Eqs. (14.20,14.24) for the vorticity and parallel velocity by $-\phi$ and $u_\parallel$, and Eq. (14.22) for the magnetic potential by $J_\parallel$, respectively. The total energy density is

$$U = \int d^3x \left(n_i M_i \frac{|\mathbf{u}_\perp|^2}{2} + n_i M_i \frac{u_\parallel^2}{2} + \frac{3}{2} p_e + \frac{3}{2} p_i + \frac{|\mathbf{B}_\perp|^2}{8\pi} \right) \tag{14.30}$$

We will call these pieces the drift energy, sound wave energy, electron and ion thermal energy, and magnetic energy, respectively.

The first consideration is how polarisation works under the drift approximation. We have already seen this in the fluctuation free energy theorem for the local drift equations, in Chapter 3, Section VII. The formulation for global energy is similar, since velocities and the magnetic disturbances enter squared in both treatments. But in this case we multiply the polarisation equation by ϕ only, to obtain

$$\phi \nabla \cdot \mathbf{J} = \nabla \cdot \phi \mathbf{J} - \mathbf{J} \cdot \nabla \phi = 0 \tag{14.31}$$

where $\mathbf{J}$ includes all three pieces, $J_\parallel \mathbf{b} + \mathbf{J}_* + \mathbf{J}_p$. The form of this that we actually use is

$$-\mathbf{J}_p \cdot \nabla \phi + \nabla \cdot \phi \mathbf{J} - \mathbf{J}_* \cdot \nabla \phi = J_\parallel \nabla_\parallel \phi \tag{14.32}$$

where the first piece will give part of the drift energy, the next two pieces will be combined into a total flux plus a transfer term, and the piece on the right side is already a transfer term. We manipulate

$$\mathbf{J}_* \cdot \nabla\phi = \left(\frac{c}{B^2}\mathbf{B}\times\nabla p\right)\cdot\nabla\phi = -\left(\frac{c}{B^2}\mathbf{B}\times\nabla\phi\right)\cdot\nabla p = -\mathbf{v}_E\cdot\nabla p \tag{14.33}$$

where $p = p_e + p_i$ is the total pressure, and then combine with the total divergence to write

$$-\mathbf{J}_p\cdot\nabla\phi + \nabla\cdot(\phi\mathbf{J} + p\mathbf{v}_E) = J_{\|}\nabla_{\|}\phi + p\nabla\cdot\mathbf{v}_E \tag{14.34}$$

We note that in general the divergence of $\phi\mathbf{J}$ is equivalent to part of the Poynting flux,

$$\nabla\cdot\phi\mathbf{J} = \nabla\cdot\left(\frac{c}{4\pi}\phi\nabla\times\mathbf{B}_t\right) = -\nabla\cdot\left(\frac{c}{4\pi}\nabla\phi\times\mathbf{B}_t\right) \tag{14.35}$$

dropping a divergence of a curl. The near cancellation with $p\mathbf{v}_E$ is called the Poynting cancellation,

$$\nabla\cdot(\phi\mathbf{J} + p\mathbf{v}_E) \approx 0 \tag{14.36}$$

and results in the fact that the ExB thermal transport eventually appears with a factor of 3/2, so that the ExB divergence, not an ExB advection, is the term with which transfer with the thermal reservoir occurs. We will show this in Section V, together with the other characteristics of ExB transport.

The pressure piece in the drift energy is found by subtracting $\mathbf{u}_p\cdot\nabla p_i$ from both sides of Eq. (14.34), to find

$$-\mathbf{J}_p\cdot\left(\nabla\phi + \frac{\nabla p_i}{n_e e}\right) + \nabla\cdot(\phi\mathbf{J} + p\mathbf{v}_E) = J_{\|}\nabla_{\|}\phi + (p_e + p_i)\,\nabla\cdot\mathbf{v}_E - \mathbf{u}_p\cdot\nabla p_i \tag{14.37}$$

Finally, substituting in for $\mathbf{J}_p$ and noting how the combination in parentheses gives rise to $\mathbf{u}_\perp$, we have

$$\frac{\partial}{\partial t}\left(n_i M_i\frac{|\mathbf{u}_\perp|^2}{2}\right) + \nabla\cdot\left[n_i M_i\frac{|\mathbf{u}_\perp|^2}{2}\mathbf{u} + \mathbf{u}_\perp\cdot\mathbf{\Pi}_* + \phi\mathbf{J} + p\mathbf{v}_E\right] =$$

$$= \mathbf{\Pi}_* : \nabla\mathbf{u}_\perp + J_{\|}\nabla_{\|}\phi + (p_e + p_i)\,\nabla\cdot\mathbf{v}_E - \mathbf{u}_p\cdot\nabla p_i \tag{14.38}$$

in which the transport terms are the ones under the divergence operator on the left side, and the transfer terms are those on the right side. We note that the reason that $\mathbf{u}$ must include all components of the ion velocity is to bring the factor of n_i under both the partial time derivative and the divergence operator simultaneously. In other words, whatever we

keep in the velocity divergence in the density equation must also be kept in the advection in the polarisation equation, and in all the ion fluid equations as well.

We now find where the energy transferred out of this drift energy goes. The next subtlety is the magnetic energy. We multiply Eq. (14.22) by $J_\parallel$ and manipulate the divergence to obtain

$$\frac{\partial}{\partial t}\frac{1}{8\pi}\left|\nabla_\perp A_\parallel\right|^2 + \nabla\cdot\left(\nabla_\perp A_\parallel \frac{1}{4\pi c}\frac{\partial A_\parallel}{\partial t}\right) = \frac{J_\parallel}{n_e e}\nabla_\parallel p_e - J_\parallel \nabla_\parallel \phi - J_\parallel R_{ei} \tag{14.39}$$

The terms on the right side are the Alfvénic transfer effects and resistive dissipation, as we have already seen. The divergence term is the inductive part of the Poynting energy flux, as we can see by evaluating the projection operations implicit in the $\nabla_\perp$ operators,

$$\nabla\cdot\left(\nabla_\perp A_\parallel \frac{1}{4\pi c}\frac{\partial A_\parallel}{\partial t}\right) = \nabla\cdot\frac{c}{4\pi}\left[\frac{1}{c}\frac{\mathbf{B}}{B}\frac{\partial A_\parallel}{\partial t}\times\left(\frac{\mathbf{B}}{B}\times\nabla A_\parallel\right)\right] \tag{14.40}$$

Substituting $\mathbf{B}_\perp$ for $A_\parallel$, this gives the conservation law for the perturbed magnetic energy

$$\frac{\partial}{\partial t}\frac{|\mathbf{B}_\perp|^2}{8\pi} - \nabla\cdot\frac{c}{4\pi}\left(\frac{1}{c}\mathbf{b}\frac{\partial A_\parallel}{\partial t}\times\mathbf{B}_\perp\right) = \frac{J_\parallel}{n_e e}\nabla_\parallel p_e - J_\parallel\nabla_\parallel\phi - J_\parallel R_{ei} \tag{14.41}$$

where we note that the inductive electric field appears with $\mathbf{b}$ since the term it is crossed into is $\mathbf{B}_\perp$.

The sound wave energy is found by multiplying Eq. (14.24) by $u_\parallel$, noting that here also the need to put the factor of n_i under the time derivative and the divergence requires keeping $\mathbf{u}_p$ in the advection terms. We obtain

$$\frac{\partial}{\partial t}\left(n_i M_i\frac{u_\parallel^2}{2}\right) + \nabla\cdot\left(n_i M_i\frac{u_\parallel^2}{2}\mathbf{u} + u_\parallel\mathbf{b}\cdot\boldsymbol{\Pi}_* - u_\parallel\mathbf{b}\,\mu_\parallel\nabla_\parallel u_\parallel\right) =$$

$$= \boldsymbol{\Pi}_* : \nabla\left(u_\parallel\mathbf{b}\right) - u_\parallel\nabla_\parallel\left(p_e + p_i\right) - \mu_\parallel\left|\nabla_\parallel u_\parallel\right|^2 \tag{14.42}$$

noting that the gyroviscosity term cancels properly with the one in Eq. (14.38) because $\boldsymbol{\Pi}_* : \nabla(\mathbf{u}_\perp + u_\parallel\mathbf{b})$ vanishes. Gyroviscosity thereby represents a diamagnetic momentum flux which acts to transfer energy between parallel and perpendicular fluid motion.

The thermal energy comes next. These are simply the pressure equations, with some of the advection terms evaluated piece by piece. For the electrons we have Eq. (14.23), in which the transfer effects with other equations are now obvious: Alfvénic transfer ($J_\parallel\nabla_\parallel p_e$) and resistive frictional heating ($J_\parallel R_{ei}$) with the magnetic energy, acoustic coupling ($u_\parallel\nabla_\parallel p_e$) with the sound waves, and the ExB divergence ($p_e\nabla\cdot\mathbf{v}_E$) with the drift energy through polarisation. For the ions we have Eq. (14.25), in which the transfer effects

are thermal coupling ($u_{\|}\nabla_{\|}p_i$) and viscous heating (the $\mu_{\|}$ term) with the sound waves, and the ExB divergence ($p_i\nabla\cdot\mathbf{v}_E$) through polarisation and the polarisation advection ($\mathbf{u}_p\cdot\nabla p_i$) with the drift energy.

The total energy theorem is then given by

$$\frac{\partial U}{\partial t}+\nabla\cdot\Bigg[\frac{3}{2}(p_e+p_i)\mathbf{v}_E+\left(q_{e\|}+q_{i\|}\right)\mathbf{b}+$$

$$+\frac{5}{2}\left(p_e v_{\|}+p_i u_{\|}\right)\mathbf{b}+\frac{5}{2}p_i\mathbf{u}_p+\frac{c}{B^2}\mathbf{B}\times\nabla\frac{5}{2}\frac{p_iT_i}{e}-\frac{c}{B^2}\mathbf{B}\times\nabla\frac{5}{2}\frac{p_eT_e}{e}+$$

$$+n_iM_i\frac{|\mathbf{u}_{\perp}|^2+u_{\|}^2}{2}\mathbf{u}+\mathbf{\Pi}_*\cdot\left(\mathbf{u}_{\perp}+u_{\|}\mathbf{b}\right)+(\phi\mathbf{J}+p\mathbf{v}_E)-\frac{c}{4\pi}\frac{1}{c}\mathbf{b}\frac{\partial A_{\|}}{\partial t}\times\mathbf{B}_{\perp}\Bigg]=0 \qquad (14.43)$$

The transport effects are written in order of their usual importance; in practical situations only the terms in the first line need be kept. In situations where transport by Pfirsch-Schlüter currents (generally caused by nonzero magnetic divergences involving the equilibrium pressure) is relevant, the second line would have to be kept as a unit, since the divergences of all the currents go together. The diamagnetic fluxes are combined into the terms involving the drift operator. The terms in the last line are negligible unless there are transonic or supersonic flows.

The dominant transport effect across the magnetic flux surfaces is the ExB advection, $(3/2)p_e\mathbf{v}_E$, which appears with the factor of 3/2 due to the Poynting cancellation, Eq. (14.36). For the parallel transport, the principal effects are the electron and ion heat fluxes, $B^{-1}(q_{e\|}+q_{i\|})\mathbf{B}_{\perp}$. We also have the ion advection, $(5/2B)p_iu_{\|}\mathbf{B}_{\perp}$, appearing with the factor of 5/2 due to the compressibility of the parallel flows. For the electrons this effect is small because $A_{\|}$ is the stream function for $\mathbf{B}_{\perp}$ and it is also related to $J_{\|}$ through Ampere's law, but here we also have the acoustic advective effect, $(5/2B)p_eu_{\|}\mathbf{B}_{\perp}$. These parallel advective effects are small, however, as we saw for drift waves in Chapter 5.

To summarise, we have a set of drift equations following the drift ordering as to magnetic compression but allowing for an arbitrary scale of motion and with it, interactions with the thermal gradient of the background. The conservation of total energy is exact, but at the price that the total velocity must be kept in advection. The extra piece, that is, the polarisation drift, is given in terms of the dependent variables through a constitutive relation, Eq. (14.19).

14.IV. A One Dimensional Mean Field Model of Transport by ExB Turbulence

In this section we construct a mean field transport model which we will need to discuss the properties of ExB turbulent transport in Section V. The model involving anomalous transport of one dimensional profiles that are flux functions solely by ExB turbulence is the simplest case and will form the framework for this discussion. This allows the neglect of such subtle effects as transport within the flux surface and polarisation effects on the pressures, of which the Pfirsch-Schlüter current is the prototypical example. The transport due to these effects is usually small anyway, and consideration of it would unduly sacrifice clarity.

We can construct a mean field model of background evolution through turbulent transport by ExB eddies or magnetic flutter. We note that for purely electrostatic dynamics, useful as a model within which to understand the ExB transport, the magnetic flutter (entering via $\widetilde{A}_{\|}$) vanishes. The background magnetic field ($\mathbf{B}$) is assumed to lie in nested flux surfaces in which field aligned coordinates based on a flux surface label (r), a parallel coordinate (s), and a third coordinate which labels field lines (ξ), can be well defined. This third coordinate is called the drift angle. The first coordinate is also called the radius. A flux function is a function of radius only, while a two dimensional profile would depend on both the radial and parallel coordinates. The background dependent variables are assumed to be flux functions. With the profile of ϕ dependent on r only, there are no radial flows in the equilibrium, and hence there is no transport by equilibrium flows.

Disturbances in all the dependent variables are allowed, with arbitrary dependence on all three coordinates. We take the ensemble average (basically a short time average over several coherence times of the turbulence) according to which only quadratic nonlinearities survive. For these quadratic nonlinearities, which are either transport fluxes or anomalous transfer effects (*e.g.*, heating), we will be able to substitute model formulae in terms of the background parameters, including the gradients. The equations for the disturbances will contain background drive terms, which conserve particles and energy by transferring them against the background. It is only necessary to write explicit equations for the disturbances which enter the energy density quadratically (vorticity, current, sound waves), since the pressures enter linearly and hence with no mean field contribution from the disturbances. Magnetic divergences can be nonzero, but only for the disturbances. Linear terms arising from magnetic divergences vanish in the ensemble average.

The equations for the profiles are those derived in the previous section, simplified by the symmetry assumptions, but with the addition of the ensemble averaged transport

effects. For the disturbances we mainly have to declare what is kept in order to satisfy energy conservation. We start with the polarisation equation. For the profiles we have

$$\begin{aligned}\nabla\cdot\frac{n_iM_ic^2}{B^2}\frac{\partial}{\partial t}\left(\nabla_\perp\phi+\frac{\nabla_\perp p_i}{n_ee}\right)=\\ =\nabla\cdot\frac{c}{B^2}\mathbf{B}\times\left(M_i\left\langle\widetilde{n}_i\widetilde{\mathbf{v}}_E\right\rangle\cdot\nabla\mathbf{u}_\perp+n_iM_i\left\langle\widetilde{\mathbf{v}}_E\cdot\nabla\widetilde{\mathbf{v}}_E\right\rangle\right)\end{aligned}\tag{14.44}$$

in which the only effects are nonlinear forcing. The more familiar linear terms are all in the equation for the disturbances,

$$\begin{aligned}\nabla\cdot\frac{n_iM_ic^2}{B^2}\frac{\partial}{\partial t}\nabla_\perp\widetilde{\phi}=\nabla\cdot\frac{c}{B^2}\mathbf{B}\times\left(n_iM_i\mathbf{v}_E\cdot\nabla\widetilde{\mathbf{v}}_E+n_iM_i\widetilde{\mathbf{v}}_E\cdot\nabla\mathbf{v}_E\right)\\ +\nabla\cdot\left(\widetilde{J}_\parallel\mathbf{b}\right)-\mathcal{K}(\widetilde{p})\end{aligned}\tag{14.45}$$

here keeping only $\widetilde{\phi}$ in the vorticity, as the ExB contributions to the Reynolds stress are dominant.

Next comes the density equation. Here we have to be careful to set up the model such that the density and polarisation equations work together properly in conservation, not only of energy but also of particles. For the profiles we have

$$\frac{\partial n_e}{\partial t}+\nabla\cdot\left\langle\widetilde{n}_e\widetilde{\mathbf{v}}_E\right\rangle=0\tag{14.46}$$

where neglect of polarisation is allowed by the neglect of two dimensional profile effects. For the disturbances, necessary because of the polarisation dynamics, we have

$$\frac{\partial\widetilde{n}_i}{\partial t}+\nabla\cdot\left(n_i\widetilde{\mathbf{v}}_E+n_i\widetilde{\mathbf{u}}_p\right)=0\tag{14.47}$$

The electron and ion pressure equations are somewhat easier, since they are already written in conservative form. We keep the most important quadratic fluxes, plus all the transfer effects of the disturbances. For the electrons we have

$$\begin{aligned}\frac{3}{2}\frac{\partial p_e}{\partial t}+\nabla\cdot\left(\frac{3}{2}\left\langle\widetilde{p}_e\widetilde{\mathbf{v}}_E\right\rangle+\left\langle\widetilde{q}_{e\parallel}\widetilde{\mathbf{b}}_\perp\right\rangle+\frac{5}{2}p_e\left\langle\widetilde{u}_\parallel\widetilde{\mathbf{b}}_\perp\right\rangle\right)=\\ =\left\langle\widetilde{u}_\parallel\nabla_\parallel\widetilde{p}_e\right\rangle-\frac{1}{n_ee}\left\langle\widetilde{J}_\parallel\nabla_\parallel\widetilde{p}_e\right\rangle-\left\langle\widetilde{p}_e\nabla\cdot\widetilde{\mathbf{v}}_E\right\rangle+\left\langle\widetilde{J}_\parallel\widetilde{R}_{ei}\right\rangle\end{aligned}\tag{14.48}$$

neglecting the magnetic flutter transport involving $\widetilde{J}_\parallel$. Note that this also allows the neglect of polarisation transport for the ions. For the ions we have

$$\begin{aligned}\frac{3}{2}\frac{\partial p_i}{\partial t}+\nabla\cdot\left(\frac{3}{2}\left\langle\widetilde{p}_i\widetilde{\mathbf{v}}_E\right\rangle+\left\langle\widetilde{q}_{i\parallel}\widetilde{\mathbf{b}}_\perp\right\rangle+\frac{5}{2}p_i\left\langle\widetilde{u}_\parallel\widetilde{\mathbf{b}}_\perp\right\rangle\right)=\\ =\left\langle\widetilde{u}_\parallel\nabla_\parallel\widetilde{p}_i\right\rangle-\left\langle\widetilde{p}_i\nabla\cdot\widetilde{\mathbf{v}}_E\right\rangle+\left\langle\widetilde{\mathbf{u}}_p\cdot\nabla\widetilde{p}_i\right\rangle+\mu_\parallel\left|\nabla_\parallel\widetilde{u}_\parallel\right|^2\end{aligned}\tag{14.49}$$

The sound wave and magnetic energies now enter only through the disturbances, and are important only for the transfer effects,

$$\frac{\partial}{\partial t}\left(\frac{n_i M_i}{2}\left\langle \widetilde{u}_{\parallel}^2\right\rangle\right) = -\left\langle \widetilde{u}_{\parallel}\nabla_{\parallel}\widetilde{p}_e\right\rangle - \left\langle \widetilde{u}_{\parallel}\nabla_{\parallel}\widetilde{p}_i\right\rangle - \mu_{\parallel}\left|\nabla_{\parallel}\widetilde{u}_{\parallel}\right|^2 \tag{14.50}$$

$$\frac{\partial}{\partial t}\frac{1}{8\pi}\left\langle \left|\mathbf{B}_{\perp}\right|^2\right\rangle = \frac{1}{n_e e}\left\langle \widetilde{J}_{\parallel}\nabla_{\parallel}\widetilde{p}_e\right\rangle - \left\langle \widetilde{J}_{\parallel}\nabla_{\parallel}\widetilde{\phi}\right\rangle - \left\langle \widetilde{J}_{\parallel}\widetilde{R}_{ei}\right\rangle \tag{14.51}$$

since we are neglecting temporal changes in the magnetic geometry.

The key question is what to do with the equations for the disturbed energies in a transport model. A reasonable treatment is to note that over an ensemble average the partial time derivatives are zero. We can then order the drift and sound wave energies with the ions, and the magnetic energy with the electrons, merely a matter of solving for some of the transfer effects in terms of others. In contrast to the rms transfer levels which we saw (esp. Chapters 8 and 11) were important to the underlying dynamics of the turbulence, the profiles sense only the average transfer and transport. Some of the transfer effects cancel as the two equations they appear in are summed, most notably the kinetic shear Alfvén transfer between the electron thermal and magnetic energies. This transport model may be written as follows:

$$\frac{\partial n_e}{\partial t} + \nabla\cdot\left\langle \widetilde{n}_e\widetilde{\mathbf{v}}_E\right\rangle = 0 \tag{14.52}$$

$$\begin{aligned}\frac{3}{2}\frac{\partial p_e}{\partial t} + \nabla\cdot\left(\frac{3}{2}\left\langle \widetilde{p}_e\widetilde{\mathbf{v}}_E\right\rangle + \left\langle \widetilde{q}_{e\parallel}\widetilde{\mathbf{b}}_{\perp}\right\rangle + \frac{5}{2}p_e\left\langle \widetilde{u}_{\parallel}\widetilde{\mathbf{b}}_{\perp}\right\rangle\right) = \\ = \left\langle \widetilde{u}_{\parallel}\nabla_{\parallel}\widetilde{p}_e\right\rangle - \left\langle \widetilde{p}_e\nabla\cdot\widetilde{\mathbf{v}}_E\right\rangle - \left\langle \widetilde{J}_{\parallel}\nabla_{\parallel}\widetilde{\phi}\right\rangle\end{aligned} \tag{14.53}$$

$$\begin{aligned}\frac{3}{2}\frac{\partial p_i}{\partial t} + \nabla\cdot\left(\frac{3}{2}\left\langle \widetilde{p}_i\widetilde{\mathbf{v}}_E\right\rangle + \left\langle \widetilde{q}_{i\parallel}\widetilde{\mathbf{b}}_{\perp}\right\rangle + \frac{5}{2}p_i\left\langle \widetilde{u}_{\parallel}\widetilde{\mathbf{b}}_{\perp}\right\rangle\right) = \\ = -\left\langle \widetilde{u}_{\parallel}\nabla_{\parallel}\widetilde{p}_e\right\rangle + \left\langle \widetilde{p}_e\nabla\cdot\widetilde{\mathbf{v}}_E\right\rangle + \left\langle \widetilde{J}_{\parallel}\nabla_{\parallel}\widetilde{\phi}\right\rangle - n_i M_i\left\langle \widetilde{\mathbf{v}}_E\widetilde{\mathbf{v}}_E\right\rangle:\nabla\mathbf{u}_{\perp}\end{aligned} \tag{14.54}$$

$$\begin{aligned}\nabla\cdot\frac{n_i M_i c^2}{B^2}\frac{\partial}{\partial t}\left(\nabla_{\perp}\phi + \frac{\nabla_{\perp}p_i}{n_e e}\right) = \\ = \nabla\cdot\frac{c}{B^2}\mathbf{B}\times\left(M_i\left\langle \widetilde{n}_i\widetilde{\mathbf{v}}_E\right\rangle\cdot\nabla\mathbf{u}_{\perp} + \nabla\cdot n_i M_i\left\langle \widetilde{\mathbf{v}}_E\widetilde{\mathbf{v}}_E\right\rangle\right)\end{aligned} \tag{14.55}$$

Arranging the energy in sound waves and ExB disturbances with the ions carries with it the appearance of anomalous transfer effects between the electron and ion temperatures. The electron thermal gradient drives drift waves, which couple directly to ion pressure disturbances or to sound waves, which dissipate viscously into the ion thermal energy. Strictly speaking, this requires a finite T_i in the first place, as otherwise there would be

no ion pressure to do work and besides $\mu_{\|}$ would vanish. But in a Landau fluid model we can have Landau damping on the sound waves (which is never exactly zero) heat the ions to finite temperature. If the temperatures start out of similar order but significantly different (*e.g.*, $T_i/T_e = 2$ or 3), then this anomalous transfer becomes quite sensible. We still have a Reynolds stress transfer between ExB profile and turbulence to worry about. With the ExB energy added into the ion thermal bath this becomes a transfer between drift and ion thermal energy, which adds to the transfer due to the ExB divergence coupling which is already there. The most important of these transfer effects, however, is $\left\langle \widetilde{J}_{\|} \nabla_{\|} \widetilde{\phi} \right\rangle$, representing compression of the polarisation drift in the ions and parallel currents in the electrons. It is significant even for $T_i = 0$.

We note that the Reynolds stress terms in the equations for ϕ and p_i account for the contribution of the disturbances to the polarisation drift energy transfer we have been discussing. It can be modelled as a stress tensor because $\widetilde{u}_{\perp}^2$ is neglected in the energetics. But in order for the total flow energy to be conserved against $(3/2)p_i$ we must still keep the polarisation transfer term due to the time changes in the stream function (ϕ and p_i) of the rotation profile. However, in this one-dimensional model we have Eq. (14.55), which says that the total polarisation divergence vanishes (we keep $J_{\|}$ and J_* only in the disturbances). By Eq. (14.16) the total profile J_p also vanishes (*i.e.*, the total flux surface averaged radial current vanishes, as in many treatments), and so in this case the polarisation transfer term is zero.

14.V. The Characteristics of Transport Caused by ExB Turbulence

In this section we confirm the main points of Section 14.II concerning the special nature of ExB turbulent transport, compared with the more familiar random scattering via Coulomb collisions.

The first point is the simplest: the ExB velocity is nearly divergence free,

$$\nabla \cdot \mathbf{v}_E \approx 0 \tag{14.56}$$

and in a homogeneous magnetic field it is divergence free. For some laboratory configurations, cylindrical plasma geometry at very low beta bounded by plates at the ends, for example, this can be taken to be exact. The result is something we can see in the fluid thermodynamics in Chapter 2: in a divergence free velocity field the pressure does not do work on the fluid elements. The transfer of energy between the pressure and the velocity becomes small. Note that for interchange turbulence (cf. Chapter 10) the work done by the pressure on the ExB velocity divergence is responsible for the principal forcing effect on

the velocity. But for the profiles this is overshadowed by the other transfer effects. A divergence free transporting velocity is something very different from the model in collisional kinetics, by which the velocity is given by diffusion,

$$n_e \mathbf{v}_D = -D(n_e, T_e)\nabla n_e \tag{14.57}$$

for example. This velocity is only divergence free for specific dependences of D on the parameters. For example, the scale of the velocity divergence for a constant diffusion is the same as the scale of the density profile. But $\mathbf{v}_E$ is exactly or nearly divergence free according to the magnetic geometry, regardless of what form $n_e(r)$ or $T_e(r)$ take.

The second point is the Poynting cancellation, Eq. (14.36). The presence of $p\mathbf{v}_E$ in the transport with the factor of 3/2 is true for total energy, but what we want to know is if that is just a result of formal manipulation. We recall that an ideal pressure equation may be written in terms of a transport term $[(5/2)p\mathbf{v}]$ and a work term $[\mathbf{v}\cdot\nabla p]$, or alternatively in terms of a transport term $[(3/2)p\mathbf{v}]$ and a divergence $[p\nabla\cdot\mathbf{v}]$. If the divergence is small, as we showed for $\mathbf{v}_E$, then the second form is more germane. But it is even more interesting to know how the transport works for each piece of the energy rather than the total. The quantity $(\phi\mathbf{J}+p\mathbf{v}_E)$ appears in the transport equation for the drift energy, Eq. 14.38. In modelling transport terms we usually write down the lowest order forms, which still conserve energy properly. We know that the diamagnetic current is at the same order as $\mathbf{v}_E$ if $n_e e\mathbf{E}_\perp$ is comparable to ∇p, so $\phi\mathbf{J}$ is generally the same size as $p\mathbf{v}_E$. In fact they are close enough for the remnant to be negligible. A particularly useful form of the Poynting cancellation turns out to be the one with the diamagnetic current,

$$\nabla\cdot(\phi\mathbf{J}_* + p\mathbf{v}_E) = \nabla\cdot\left[\frac{c}{B^2}\mathbf{B}\times\nabla(\phi p)\right] \tag{14.58}$$

This is a magnetic divergence, and it is now down to the next smallest row of terms in Eq. (14.43) as its scale is L_B (or R in toroidal geometry), and the scale of interest is $L_\perp$. It is therefore a fundamental property of ExB transport that its contribution to the total energy transport is

$$\mathbf{Q}_e + \mathbf{Q}_i = \frac{3}{2}\left\langle(\widetilde{p}_e + \widetilde{p}_i)\,\widetilde{\mathbf{v}}_E\right\rangle \tag{14.59}$$

given that there are no radial equilibrium flows. The physical point of this is that the energy due to the fluid perpendicular velocities presents a transfer term of the form $p\nabla\cdot\mathbf{v}_E$, rather than the more usual form $\mathbf{v}_E\cdot\nabla p$, to the thermal energy reservoir, due to the Poynting cancellation, so that the actual transport is due to the remaining $(3/2)p\mathbf{v}_E$. This role of the Poynting cancellation is what makes the ExB velocity somewhat "special" compared to all the others.

A third point concerns magnetic flux diffusion. It is an interesting measured property of magnetically confined plasma experiments that the electron thermal transport is anomalous by more than two orders of magnitude, but the magnetic flux diffusion is neoclassical (classical diffusion, modified by toroidal drifts of particles whose parallel motion is in the long mean free path regime). If we write the mean field Ohm's law neglecting resistivity, however, we instantly see why this should be true for ExB turbulence,

$$\frac{1}{c}\frac{\partial A_\parallel}{\partial t} = \frac{1}{n_e e}\nabla \cdot \left\langle \tilde{p}_e \tilde{\mathbf{b}}_\perp \right\rangle - \nabla \cdot \left\langle \tilde{\phi}\tilde{\mathbf{b}}_\perp \right\rangle \tag{14.60}$$

If the magnetic disturbances are small, then the flux diffusion is small, and if the turbulence were electrostatic the flux diffusion would be zero. We have already seen that $\left\langle \tilde{q}_{e\parallel}\tilde{\mathbf{b}}_\perp \right\rangle$ contributes negligibly to transport for drift wave turbulence in either slab or toroidal geometry, and it then follows that the anomalous flux diffusion should be small. With $J_\parallel$ determined by $A_\parallel$, this holds as well for the current diffusion. Anomalous current diffusion can only result from the ExB nonlinearity in the electron inertia, and this is small compared to the mechanisms by which currents in a specifically current carrying plasma are generated. This is another nice contrast to classical diffusion, for in that case the flux diffusivity is much *greater* than the particle diffusivity. Neglecting $\tilde{\mathbf{b}}_\perp$, the mean field Ohm's law is now classical,

$$\frac{\partial A_\parallel}{\partial t} = \frac{\eta_\parallel c^2}{4\pi}\nabla_\perp^2 A_\parallel \tag{14.61}$$

with the term on the right representing resistivity, neglecting thermal forces. Comparing the classical diffusivities, we find

$$\frac{\eta_\parallel c^2}{4\pi} = \frac{0.51}{\beta_e}\rho_e^2\nu_e = \frac{0.51}{\beta_e}D_e \tag{14.62}$$

With $\beta_e \sim 10^{-4}$ in the edge regions of fusion plasmas, this classical diffusivity is as large as the anomalous electron thermal diffusivity if not larger. An interesting consequence is that the MHD equilibrium in this regime is resistive. If the pressure gradient changes during a transport event it is not the case that the magnetic structure evolves isentropically through its successive equilibria. This point has been largely ignored in edge transport modelling, which takes the magnetic structure to be fixed as we have been doing herein.

The fourth point is the various mechanisms of ExB flow generation. We discussed the self consistent interaction with the turbulence in Chapter 9, where it was clear that the evolution proceeded by means of fluid dynamics. But for closed, toroidal geometry a sheared ExB velocity profile also means a radial electric field with radial dependence.

In other words, a finite divergence and hence a finite charge density. But within low frequency fluid drift motion at scales larger than the Debye length, the charge density is always small, specifically, much less than $n_e e$, the charge density of the electrons. Not only that, as we also saw in Chapter 2, it is small in all phases of the dynamics. Writing simple continuity equations for both fluids using the velocities in Eqs. (14.11–14.14), we find a charge continuity equation given by

$$\frac{\partial \rho_{ch}}{\partial t} + \nabla \cdot (\rho_{ch} \mathbf{v}_E) + \nabla \cdot \left(J_{\parallel} \mathbf{b} + \mathbf{J}_* + \mathbf{J}_p \right) = 0 \tag{14.63}$$

where $\rho_{ch} = n_e e - n_i Z e$ is the charge density. Taking into account that $\mathbf{v}_E \cdot \nabla \sim \partial / \partial t$, the first two terms are the same size. But the polarisation current can be written next to them,

$$-\frac{\partial \rho_{ch}}{\partial t} - \nabla \cdot (\rho_{ch} \mathbf{v}_E) - \nabla \cdot \mathbf{J}_p = \nabla \cdot \left(J_{\parallel} \mathbf{b} + \mathbf{J}_* \right) \tag{14.64}$$

As we have already seen, the polarisation divergence and the charge density term have the same form, and the polarisation divergence is larger by a factor of c^2/v_A^2, since $\nabla_\perp^2 \phi = 4\pi \rho_{ch}$. All of the terms involving ρ_{ch} are then negligible, and we are left with $\nabla \cdot \mathbf{J} = 0$ as before. This underscores the strictness of the quasineutral character of the dynamics. It holds pointwise, not just in an averaged sense. We then conclude that any mechanism which should build up an electric field does so under the ExB fluid dynamics and not due to transport of charges by currents. The total charge transport itself has to vanish. This leads to what happens as a result of any charged particle source or sink mechanisms. It is quite possible to have source terms on the right side of Eq. (14.64), but instead of accumulating charge we then have a balance between sources and transport,

$$-\nabla \cdot \mathbf{J}_p = \nabla \cdot \left(J_{\parallel} \mathbf{b} + \mathbf{J}_* \right) + S_e - S_i \tag{14.65}$$

so that the charge content remains small. This is the high throughput regime for electric charge, similar to the situation with free energy in drift wave turbulence where the current transfers thermal and drift free energy back and forth but the magnetic energy always remains small. In the high throughput regime for charges, quasineutrality is maintained and these source mechanisms act as a torque on the ExB vorticity. Taking charges out of a flux tube causes the flux tube to rotate, since while the small but finite $\nabla_\perp^2 \phi$ leads to no appreciable charge density, it the ExB vorticity it does lead to has a significant role. Ultimately, the source of this angular momentum, as is the case for perpendicular momentum in general in fluid drift motion, is the background magnetic field, as we saw in Chapter 2.

The last point concerns anomalous momentum transport. With the ExB vorticity proportional to the small but nonzero charge density, transport of angular momentum takes place through the Reynolds stress, which is nothing more than the nonlinear polarisation current. But in modelling the transport of this current one should not use an anomalous conductivity in a simple radial Ohm's law. Conductivity, or better its inverse, resistivity, is a friction between the two fluids which conserves total momentum. Resistivity leads to particle diffusion, as the magnetic Lorentz force balancing resistive friction,

$$\frac{\mathbf{v}\times\mathbf{B}}{c} = \eta_\perp \mathbf{J} \tag{14.66}$$

with perpendicular resistivity $\eta_\perp = m_e\nu_e/n_e e^2$, gives rise to a collisional drift velocity which acts as a diffusion, once the MHD equilibrium constraint, $\mathbf{J}\times\mathbf{B} = c\nabla p$, is set in,

$$\mathbf{v}_D = -\frac{D_e}{T_e}\nabla_\perp p \tag{14.67}$$

(in the neglect of thermal forces). But in the momentum equation, the resistive friction cancels, as

$$\frac{\partial}{\partial t} n_e m_e \mathbf{v} + \nabla\cdot(\cdots) = \mathbf{R}_{ie} - \nabla p_e - n_e e\left(\mathbf{E} + \frac{\mathbf{v}}{c}\times\mathbf{B}\right) \tag{14.68}$$

$$\frac{\partial}{\partial t} n_i M_i \mathbf{u} + \nabla\cdot(\cdots) = -\mathbf{R}_{ie} - \nabla p_i + n_i Z e\left(\mathbf{E} + \frac{\mathbf{u}}{c}\times\mathbf{B}\right) \tag{14.69}$$

add to become approximately

$$\frac{\partial}{\partial t}\rho\mathbf{u} + \nabla\cdot(\cdots) = -\nabla p + \frac{\mathbf{J}\times\mathbf{B}}{c} \tag{14.70}$$

The only phenomenon left to transport momentum is the Reynolds stress (cf. Eq. 14.44), which is the dominant effect in the momentum flux terms we did not write down. The JxB force remains as a transfer mechanism between fluid and Poynting momentum, with the background magnetic field acting as an anchor.

To summarise, transport of the background profile quantities by small scale ExB turbulence can still be diffusive, provided the scale of motion is small compared to $L_\perp$. But its fundamental properties are qualitatively different from those of a kinetic diffusion via random thermal motions, and these should be taken into account when constructing transport models. Attempts to extend conventional edge transport models, which are able to treat the parallel fluxes as well as the radial transport since the profiles are no longer flux functions in their regime, to incorporate these effects are ongoing.

Further Reading

General transport modelling is not within the scope of this work, although it provides a major part of directed research into magnetically confined fusion plasmas. For a series of reviews, one can start with the special December 1990 issue of *Physics of Fluids B*, which is dedicated to that topic. From the experimental side, the older review by J. Hugill, in *Nucl. Fusion* 23 (1983) 331, gives a clear introduction to the basic concepts. Current research on transport modelling may be found in recent issues of *Nuclear Fusion, Journal of Nuclear Materials, Plasma Physics and Controlled Fusion*, or *Physics of Plasmas* (formerly *Physics of Fluids*, then *Physics of Fluids B*).

Symmetry in the thermodynamic variables during approach to equilibrium was shown by L. Onsager, in *Phys. Rev.* 38 (1931) 2265. Onsager symmetry in an electrically coupled plasma was treated in a rigorous way by A. Boozer, in *Phys. Fluids B* 4 (1992) 2845. Onsager symmetry for the collisional diffusion process was treated by S. I. Braginskii, in *Reviews of Plasma Physics*, M. A. Leontovich, ed. (Consultants Bureau, New York, 1965), Vol. 1, p. 205, and generally by R. Balescu, *Transport Processes in Plasmas*, 2 Vols., (North Holland, Amsterdam, 1988). Its applicability to turbulence was questioned by Balescu, in *Phys. Fluids B* 2 (1990) 2100. It is still not known whether turbulent transport should follow Onsager symmetry, as clear demonstrations in either direction are lacking. The article by Boozer is a good starting reference for further study.

A. Computational Methods for Drift Alfvén Turbulence

B. Scott

Jul 1999

A.I. Introduction

The fundamental character of drift Alfvén turbulence, the electromagnetic generalisation of drift wave turbulence, is of turbulent ExB advection taking place among a set of state variables in drift planes perpendicular to the magnetic field, with the state variables coupled together by parallel currents which flow between the planes along magnetic field lines. These currents are excited whenever their force potential is different on different drift planes. This force potential is the difference between the electron pressure and the electrostatic potential, and the electrostatic potential is also the stream function for the ExB velocity which does the advection. This builds a self consistent coupling between the turbulence in the drift planes and a wave system of mostly hyberbolic character along the field lines, which due to the relationship between magnetic potential and current (Ampere's law) are ergodically deformed by fluctuating components perpendicular to the background field. The wave system is therefore itself nonlinear. What we have to do is build a numerical scheme which can accurately treat arbitrary levels of this dynamics which is also inherently stable.

Both parts of this dynamics lend themselves to what has become a standard method in the field of computational fluid dynamics: higher order upwind schemes. Advection is easy to treat when the velocity is known; the scheme is a set of simple formulae into which we simply drop the spatially variable ExB velocity. For wave systems we have to split the dynamics into components which travel in opposite directions; in this case the electron force potential and current split into two eigenfunctions which travel at a specific velocity in opposite directions along the magnetic field. This split is in general called a Riemann solve, after the first rigorous treatments of shock waves in an ideal fluid. We have an easier situation than that: dynamics which is linearised in the sense that the wave speed is a constant. The corresponding Riemann solve is a simple combination of state variable and flux variable, and the upwind scheme is constructed in the same way as advection; we simply transport each eigenfunction with the characteristic wave speed in the proper direction. For sound waves this is trivial. The only problem we have to face is that the Riemann solve for the kinetic shear Alfvén waves cannot be exact, because the wave velocity depends on the perpendicular scale. We studied the properties of these waves in Chapter 4. Here we take that insight into account while building the numerical scheme.

A.II. The Second Order MUSCL Upwind Scheme

The basic scheme we use is the linearised form of the MUSCL scheme of Colella (1990). This builds a conservative flux form of the equations, such that at each grid node $\{x_i, y_j, s_k\}$ we take differences between flux values at each half node. At each node there are six half nodes, halfway to each of the six nearest neighbors. The Taylor expansion is used to approximate the variables at these half nodes, advanced by half a time step. At each half node there are two extrapolations to consider, one from each neighboring node. For example, values at the half node $\{x_i, y_j, s_{k+1/2}\}$ are extrapolated from node $\{x_i, y_j, s_k\}$ and from node $\{x_i, y_j, s_{k+1}\}$. The ambiguity is resolved by building the eigenfunctions transported in a given direction from the variables on the appropriate side of the half node. These approximate values are then used to build the fluxes at each half node. If all the derivatives are centered, the scheme is second order. Near extrema of the transported quantities (*e.g.*, the eigenfunctions split according to direction of transport), where numerical instabilities take hold, the order of accuracy is dropped smoothly towards first order such that no spurious extrema form (a clear indication of numerical trouble for wave systems). The result is a scheme which is both more stable and more accurate than older methods one usually finds in textbooks prior to about 1990.

We outline this for ExB advection of a quantity f, given by

$$\frac{d_E f}{dt} = \frac{\partial f}{\partial t} + \mathbf{v}_E \cdot \nabla f = 0 \tag{A.1}$$

since the transported quantity is obvious and we can concentrate on the formulation. The extrapolation from node $\{x_i, y_j, s_k\}$ to half node $\{x_i, y_j, s_{k+1/2}\}$ at mid time step for transported quantity f is given by

$$f_{i,j,k+1/2} = f_{i,j,k} + \frac{h_s}{2}\left.\frac{\partial f}{\partial s}\right|_{i,j,k} + \frac{\tau}{2}\left.\frac{\partial f}{\partial t}\right|_{i,j,k} \tag{A.2}$$

where the discretisation is in terms of a time step τ and equidistant spatial step sizes h_x, h_y, and h_s. We evaluate the time derivative with the equation itself to find

$$f_{i,j,k+1/2} = f_{i,j,k} - \left(\frac{\tau v^s_{Ei,j,k}}{2} - \frac{h_s}{2}\right)\left.\frac{\partial f}{\partial s}\right|_{i,j,k} - \frac{\tau v^x_{Ei,j,k}}{2}\left.\frac{\partial f}{\partial x}\right|_{i,j,k} - \frac{\tau v^y_{Ei,j,k}}{2}\left.\frac{\partial f}{\partial y}\right|_{i,j,k} \tag{A.3}$$

The derivatives in the half node direction (here, s) are called longitudinal, and the others (here, x and y) are called transverse. The latter are evaluated according to simple upwinding rules, for example,

$$h_x \left.\frac{\partial f}{\partial x}\right|_{i,j,k} = \begin{cases} f_{i+1,j,k} - f_{i,j,k} & \text{if } v^x_{Ei,j,k} < 0 \\ f_{i,j,k} - f_{i-1,j,k} & \text{if } v^x_{Ei,j,k} > 0 \end{cases} \tag{A.4}$$

The longitudinal derivative is handled differently since it is taken in the direction of transport for that half node. We use the Van Leer (1979) slope limiting method,

$$h_s \left.\frac{\partial f}{\partial s}\right|_{i,j,k} = \frac{1}{2}\,\mathrm{sign}\,(\Delta_p + \Delta_m)\,\mathrm{Min}\,(4\,|\Delta_p|\,, 4\,|\Delta_m|\,, |\Delta_p + \Delta_m|) \tag{A.5}$$

which we limit again by setting

$$h_s \left.\frac{\partial f}{\partial s}\right|_{i,j,k} = 0 \qquad \text{if} \quad \Delta_p \Delta_m < 0 \tag{A.6}$$

that is, we use simple first order extrapolation at extrema, second order (centered) extrapolation where there is no limiting at all, with a continuous transition in regions where the extrapolation on either side would yield a value outside the interval of the value at the node and either of its neighbors. That is, we do the extrapolations to both half nodes $\{x_i, y_j, s_{k+1/2}\}$ and $\{x_i, y_j, s_{k-1/2}\}$ simultaneously. An illustration of how this slope limiting works appears in Fig. A.1.

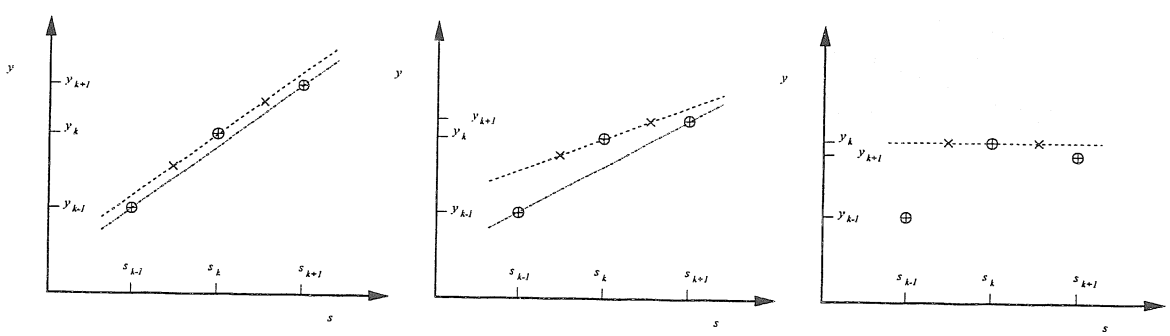

Figure A.1. Illustration of the Van Leer slope limiting method. In smooth regions, the function values are extrapolated to the half node positions according to the difference between the two neighboring values, and there is no limiting (left). Where the second derivative is larger, the slope is limited such that the extrapolated values lie within the interval given by the neighboring points (center). At extrema, where the differences on each side are of opposite sign, the slope is set to zero, and the scheme reduces all the way to first order (right). It is important to note that when the slope is limited, the extrapolations to both neighboring half nodes are affected.

At each half node there are two possible values, one from each neighboring node. At half node $\{x_i, y_j, s_{k+1/2}\}$, for example, the values are extrapolated from nodes $\{x_i, y_j, s_k\}$

and $\{x_i, y_j, s_{k+1}\}$. We resolve this ambiguity by the simple upwinding rules, taking

$$\hat{f}_{i,j,k+1/2} = \begin{cases} f^R_{i,j,k} & \text{if } v^s_{Ei,j,k} + v^s_{Ei,j,k+1} > 0 \\ f^L_{i,j,k+1} & \text{if } v^s_{Ei,j,k} + v^s_{Ei,j,k+1} < 0 \\ 0 & \text{if } v^s_{Ei,j,k} + v^s_{Ei,j,k+1} = 0 \end{cases} \tag{A.7}$$

where $f^R_{i,j,k}$ is the "rightward" extrapolation from node $\{x_i, y_j, s_k\}$ and $f^L_{i,j,k+1}$ is the "leftward" extrapolation from node $\{x_i, y_j, s_{k+1}\}$.

Finally, we advance the quantity f, by evaluating the fluxes conservatively. At the half node $\{x_i, y_j, s_{k+1/2}\}$ the flux is given by

$$U_{i,j,k+1/2} = \hat{f}_{i,j,k+1/2} \frac{v^s_{Ei,j,k} + v^s_{Ei,j,k+1}}{2} \tag{A.8}$$

The flux difference is then summed into the change of f,

$$S_{i,j,k} \leftarrow S_{i,j,k} - \frac{U_{i,j,k+1/2} - U_{i,j,k-1/2}}{h_s} \tag{A.9}$$

When each piece of the dynamics has been summed into S, the new f is evaluated as

$$f_{i,j,k} \leftarrow f_{i,j,k} + \tau S_{i,j,k} \tag{A.10}$$

For the entire scheme, we have not only the three components of the ExB advection but also each component of all the other pieces of the dynamics. The ExB advection actually takes place only within the drift planes, involving extrapolation and derivative computation only in the x and y coordinates. The wave systems are three dimensional and involve the s coordinate as well. Derivatives in the s-direction are complicated by x-dependent shifting in the y-direction between the coordinate systems used on each drift plane (see Chapters 8 and 11, and Appendix B).

A.III. The MUSCL Scheme for Linearised Wave Systems

The scheme for the simple wave systems we treat is exactly the same as for advection, except that instead of one transported quantity we have a pair of transported eigenfunctions. For the four field DALF3 model these are the sound waves,

$$\frac{\partial \widetilde{p}_e}{\partial t} + \mathbf{b} \cdot \nabla \widetilde{u}_{\|} = 0 \qquad \hat{\epsilon} \frac{\partial \widetilde{u}_{\|}}{\partial t} + \mathbf{b} \cdot \nabla \widetilde{p}_e = 0 \tag{A.11}$$

and the kinetic shear Alfvén waves,

$$\hat{\beta} \frac{\partial \widetilde{A}_{\|}}{\partial t} + \hat{\mu} \frac{\partial \widetilde{J}_{\|}}{\partial t} + \mathbf{b} \cdot \nabla \left(\widetilde{\phi} - \widetilde{p}_e \right) \qquad \nabla^2_{\perp} \frac{\partial}{\partial t} \left(\widetilde{\phi} - \widetilde{p}_e \right) + \left(1 - \nabla^2_{\perp} \right) \mathbf{b} \cdot \nabla \widetilde{J}_{\|} = 0 \tag{A.12}$$

where as far as the subsystems with which we approximate the quantities ultimately needed are concerned, we neglect the distinction between $\mathbf{b}\cdot\nabla\widetilde{J}_{\|}$ and $\nabla\cdot\mathbf{b}\widetilde{J}_{\|}$. When the final differences are taken, this distinction is treated properly. Also, the scheme is presented as if there were no background gradient terms, but when these are present we integrate them into the scheme by taking, for example, $\widetilde{p}_e \rightarrow \widetilde{p}_e - \omega_p x$.

The sound waves we can easily transform into the eigenfunctions travelling parallel and antiparallel to the field lines,

$$\left(\frac{\partial}{\partial t} \pm V_s \mathbf{b}\cdot\nabla\right)\left(\widetilde{p}_e \pm \frac{\widetilde{u}_{\|}}{V_s}\right) = 0 \tag{A.13}$$

where the wave speed V_s is given by

$$V_s^2 = \frac{1}{\hat{\epsilon}} \tag{A.14}$$

This is a pair of advection equations with velocity $\pm V_s\mathbf{b}$, with which we advance the eigenfunctions

$$u^{\pm} = \widetilde{p}_e \pm \widetilde{u}_{\|}/V_s \tag{A.15}$$

with the same scheme as in the previous section. Having extrapolated each of these to the half nodes and resolved the direction of transport (which an change sign in the x and y directions according to the total $\mathbf{b}$), we then recover the state variable and flux variable according to

$$\hat{p}_{ei,j,k+1/2} = \frac{\hat{u}^+ + \hat{u}^-}{2} \qquad \hat{u}_{\|i,j,k+1/2} = \frac{\hat{u}^+ - \hat{u}^-}{2/V_s} \tag{A.16}$$

The differences in the original wave equations are taken with these approximate values at half node and mid time step, with the known transport velocity $V_s\mathbf{b}$. The difference between parallel gradient and divergence is treated properly, with

$$S_p \leftarrow S_p - \frac{b^s_{i,j,k+1/2}\hat{u}_{\|i,j,k+1/2} - b^s_{i,j,k-1/2}\hat{u}_{\|i,j,k-1/2}}{h_s} \tag{A.17}$$

$$S_u \leftarrow S_u - b^s_{i,j,k}\frac{\hat{p}_{ei,j,k+1/2} - \hat{p}_{ei,j,k-1/2}}{h_s} \tag{A.18}$$

in the s-direction, for example.

For the kinetic shear Alfvén waves, we have the problem that the factors of $\nabla_{\perp}^2$ give a wave speed dependent on the perpendicular scale. We therefore use a Riemann solve based on the approximate equations

$$\left(\frac{\partial}{\partial t} \pm V_a\mathbf{b}\cdot\nabla\right)\left[\left(\widetilde{\phi} - \widetilde{p}_e\right) \pm V_a\left(\hat{\beta}\widetilde{A}_{\|} + \hat{\mu}\widetilde{J}_{\|}\right)\right] = 0 \tag{A.19}$$

where the wave velocity V_a is given by

$$V_a^2 = \text{Max}\left(\frac{1}{\hat{\beta}}, \frac{1+K_m^2}{\hat{\beta}+\hat{\mu}K_m^2}\right) \tag{A.20}$$

and K_m is the maximum perpendicular wavenumber on the grid, given by

$$K_m^2 = 4\,\text{Max}\left(\frac{g^{xx}}{h_x^2} + \frac{g^{yy}}{h_y^2}\right) \tag{A.21}$$

for the shifted metric procedure by which g^{xy} is eliminated on each drift plane for the coordinate system referenced at that plane. Given this approximate solve, we extrapolate

$$v^{\pm} = \left(\widetilde{\phi} - \widetilde{p}_e\right) \pm V_a\left(\hat{\beta}\widetilde{A}_{\|} + \hat{\mu}\widetilde{J}_{\|}\right) \tag{A.22}$$

according to the transport velocity $\pm V_a \mathbf{b}$, and find the half node variables,

$$\hat{\phi}_{i,j,k+1/2} - \hat{p}_{ei,j,k+1/2} = \frac{\hat{v}^+ + \hat{v}^-}{2} \qquad \hat{A}_{i,j,k+1/2} = \frac{\hat{v}^+ - \hat{v}^-}{2V_a} \tag{A.23}$$

We then find the estimated parallel current via Helmholtz solve,

$$\hat{J}_{\|\,i,j,k+1/2} = \left(\hat{\beta} - \hat{\mu}\nabla_{\perp}^2\right)^{-1}\left(-\nabla_{\perp}^2\hat{A}_{i,j,k+1/2}\right) \tag{A.24}$$

The differences in the original wave equations are taken on with these approximate values, with the known transport velocity $V_a\mathbf{b}$.

A.IV. Overall Outline of the Time Step

The above scheme is used to evaluate the ExB advection and parallel dynamics terms independently. In each case the three dimensions are integrated together as a whole in the algorithm, and in cases where there is a background gradient term, this is also integrated into the scheme. For example, ExB advection of the electron pressure is set up like this,

$$\frac{\partial\widetilde{p}_e}{\partial t} = -\mathbf{v}_E \cdot \nabla\left(\widetilde{p}_e + p_e\right) \tag{A.25}$$

where the background gradient term is

$$p_e = -\omega_p x \tag{A.26}$$

Derivatives of this in the y and s-directions have no effect, while in the x-direction we recover the linear gradient term, $-\omega_p\partial\widetilde{\phi}/\partial y$. This is a useful method because the slope

limiting and upwind decisions are made not by the behaviour of $\widetilde{p}_e$, but of the whole, $\widetilde{p}_e + p_e$. The resulting scheme is the same as it would be without splitting between background and disturbances. One important note is that if there is background ExB shear in the model case under consideration, it is also integrated into the general ExB advection scheme.

The basic order of operations in one time step of the DALF models is as follows.

1. The ExB advection terms. The four equations are treated separately, but within each, all three dimensions and the background and disturbances are treated together. In cases involving background ExB shear, that is also integrated into this step.

1a. Gyroviscous corrections in DALFTI.

1b. Profile maintenance, dissipation of the y-independent parts of disturbances of quantities which have background gradients towards zero in the profile screening zone. This step is absent if the x direction is periodic.

2. All forms of external forcing. In DALF3 this means only the curvature terms. In the other models it also includes collisional dissipation, slow time scale coupling, and external drive mechanisms. In DALF3 there is only the one resistive dissipation term, and it is treated implicitly.

3. Parallel dynamics. In DALF3 the sound waves and kinetic shear Alfvén waves are treated separately, but in each case the dimensions and background gradient terms are all integrated into the scheme. In DALF3 and in the Braginskii versions of DALFTE/I the resistivity term is integrated into the Alfvén scheme to second order, by keeping it in all Helmholtz solves involving $\hat{\beta} - \hat{\mu}\nabla_\perp^2$. In DALFTE/I proper, all collisional dissipation is treated in step 2. In either version of DALFTI the ion thermal conduction is treated as a third part of this step. Electron thermal conduction is left out of step 3 but put into step 5, below.

4. Helmholtz solve operations. The equations actually step the quantities $\nabla_\perp^2 \widetilde{\phi}$ and $\hat{\beta}\widetilde{A}_\parallel + \hat{\mu}\widetilde{J}_\parallel$. The dependent variables $\widetilde{\phi}$ and $\widetilde{J}_\parallel$, and $\widetilde{A}_\parallel$, are recovered from these quantities via Helmholtz solve. In the Ohm's law, the right side is operated on by $-\nabla_\perp^2$, and then the Helmholtz solve of $\hat{\beta} - \hat{\mu}\nabla_\perp^2$ yields $\widetilde{J}_\parallel$. An additional Helmholtz solve of $-\nabla_\perp^2$ then yields $\widetilde{A}_\parallel$.

5. Electron thermal dissipation, absent in DALF3 but present in models treating $\widetilde{T}_e$. In DALFTE/I proper the dissipative wave system involving $\widetilde{T}_e$ and $\widetilde{q}_{e\parallel}$, with Landau

dissipation on $\widetilde{q}_{e\|}$, is solved with the same scheme as above except to better model the Landau damping the upwinding is kept to first order. In the Braginskii version of DALFTE/I this step simply does thermal conduction dissipation of $\widetilde{T}_e$. However, in both versions the background gradient and disturbance in T_e are treated together, allowing for thermal conduction down a gradient when there are magnetic disturbances. Step 5 is separate from the rest because in many cases it has faster time scales than the rest of the problem. This is equivalent to using an implicit scheme for electron thermal conduction.

A.V. Further Notes

Some of the above requires clarification. The gyroviscous correction is already discussed in Chapter 13. Here we expand the descriptions of what is done for profile maintenance, how thermal conduction is treated, and the use of $\nabla_\perp^2$ in the Helmholtz solve operations involving $\widetilde{A}_\|$ and $\widetilde{J}_\|$.

1b. Profile maintenance is a matter of ensuring that the average gradient drive is kept up so that the transport as a function of a given gradient can be evaluated. With periodic boundaries in the x direction this is automatic, as the integral of any dependent variable over the xy-plane is then zero, so that the y-independent part (the profile piece) averages to zero, leaving the average of the overall gradient unchanged. As periodic boundaries are not always desirable (and in some cases, *e.g.*, externally imposed ExB shear, impossible), we require a way to compute turbulence and transport as a function of parameters with Dirichlet boundaries as well. If nothing is done, the typical result is to completely flatten the gradient via turbulent mixing, leaving all of it in a region one or two grid nodes wide at the boundaries. Simply diffusing this zone turns out to do to much dissipation of the turbulence, directly or even indirectly in the case that only the profile piece is diffused. The best solution is to damp this profile piece near the boundary and let the turbulence do the mixing on its own. Using the electron pressure as an example, the profile maintenance is done as follows,

$$\frac{\partial \widetilde{p}_e}{\partial t} = \cdots - S_0 p_s(x) \oint \frac{dy}{L_y} \widetilde{p}_e \tag{A.27}$$

where the profile damping envelope is given by

$$p_s(x) = \exp\left[-(x + x_L)^2/\Delta_s^2\right] + \exp\left[-(x - x_L)^2/\Delta_s^2\right] \tag{A.28}$$

where the boundaries are at $x = \pm x_L$, and the width of the damping region is $\Delta_s = 0.2x_L$. The damping rate is set to $S_0 = 0.1$.

4. The actual equation for $J_{||}$ in ideal MHD is found by taking the curl of the equation for $\mathbf{B}$,

$$\frac{4\pi}{c}\frac{\partial \mathbf{J}}{\partial t} = \nabla\times\frac{\partial \mathbf{B}}{\partial t} = \nabla\times\nabla\times(\mathbf{u}\times\mathbf{B}) \tag{A.29}$$

After some manipulation, we find that

$$\mathbf{B}\cdot\frac{4\pi}{c^2}\frac{\partial \mathbf{J}}{\partial t} = \nabla^2\left(\mathbf{B}\cdot\nabla\phi\right) \tag{A.30}$$

if we can replace the velocity in terms of ϕ under the drift approximation. This result generalises appropriately in the two fluid case, with $\mathbf{B}\cdot\nabla\phi \to \mathbf{B}\cdot\nabla\phi - (n_e e)^{-1}\mathbf{B}\cdot\nabla p_e$ This means that the actual Ohm's law under the drift approximation is

$$\nabla_\perp^2\left[\hat{\beta}\frac{\partial \widetilde{A}_{||}}{\partial t} + \hat{\mu}\frac{d_E \widetilde{J}_{||}}{dt}\right] = \nabla_\perp^2\left[\mathbf{b}\cdot\nabla\left(p_e + \widetilde{p}_e - \widetilde{\phi}\right) - C\widetilde{J}_{||}\right] \tag{A.31}$$

(in the four field model in which there are no thermal forces), that is, with $\nabla_\perp^2$ acting on both sides of the equation(s) we have been writing. The point is, the potentials description of the velocities and the magnetic field makes sense only in finite domains (*i.e.*, not necessarily for infinite plane waves). With periodic boundaries in the xy-plane this makes no difference, as the component with an eigenvalue of $\nabla_\perp^2 \to 0$ vanishes anyway. But with Dirichlet boundaries this action of $\nabla_\perp^2$ is necessary to remove a piece which might have s-dependence but be constant or linear in the xy-plane. So, once the right hand side of the discretised Ohm's law has been evaluated into S_A, we have

$$\nabla_\perp^2\left(\hat{\beta}\widetilde{A}_{||} + \hat{\mu}\widetilde{J}_{||}\right) = \nabla_\perp^2 S_A = -S_J \tag{A.32}$$

which we rewrite using Ampere's law as

$$\left(\hat{\beta} - \hat{\mu}\nabla_\perp^2\right)\widetilde{J}_{||} = S_J \tag{A.33}$$

This equation is solved for $\widetilde{J}_{||}$ and then Ampere's law is solved for $\widetilde{A}_{||}$. The general Helmholtz solve is performed separately on each xy-plane, by Fourier transforming y such that the resulting equation is the standard tri-diagonal matrix. For equidistant discretisation and an orthonormal metric

$$-\frac{\hat{\mu}}{h_x^2}J_{i-1,l,k} + \left(\hat{\beta} + 2\frac{\hat{\mu}}{h_x^2} + 2l^2K^2\right)J_{i,l,k} - \frac{\hat{\mu}}{h_x^2}J_{i+1,l,k} = S_{i,l,k} \tag{A.34}$$

on the k-th drift plane at the i-th node in the x-direction for the l-th Fourier component, where $h_x = 2x_L/N$ is the step size for N x-nodes, and K is the parameter giving the size of the y-domain as $2\pi/K$. This equation is solved using standard matrix techniques with boundary values $J_1 = J_N = 0$ in the Dirichlet case. If x is periodic, then the matrix acquires an extra column and an extra row at its bottom and right hand edges, due to the identity between nodes 0 and N, and 1 and $N+1$, respectively. Then, $\widetilde{J}_{\|}$ is found via inverse Fourier transform.

5a. We take the electron temperature as an example of how to treat thermal conduction dissipation. In the Braginskii model this is a simple diffusion operation along the known magnetic field. We therefore have a diffusion tensor equation,

$$\frac{3}{2}\frac{\partial \widetilde{T}_e}{\partial t} = \frac{\partial}{\partial x^\mu} D^{\mu\nu} \frac{\partial T}{\partial x^\nu} \tag{A.35}$$

where $T = \widetilde{T}_e - \omega_t x$ includes the gradient piece, $D^{\mu\nu}$ is the diffusion tensor given by

$$D^{\mu\nu} = \frac{3.2}{\hat{\mu}\nu} b^\mu b^\nu \tag{A.36}$$

and b^μ are the contravariant components of the magnetic field including the disturbances,

$$b^s = \frac{B^s}{B} \qquad b^x = \hat{\beta}\hat{F}^{xy}\frac{\partial \widetilde{A}_{\|}}{\partial y} \qquad b^y = \hat{\beta}\hat{F}^{yx}\frac{\partial \widetilde{A}_{\|}}{\partial x} \tag{A.37}$$

The equation is solved conservatively, with the flux at the half node $\{x_i, y_j, s_{k+1/2}\}$, for example, given by

$$U_{i,j,k+1/2} = b^s \left(b^s \frac{T_{i,j,k+1} - T_{i,j,k}}{h_s} + b^x \frac{T_{i+1,j,k+1/2} - T_{i-1,j,k+1/2}}{2h_x} + \right. \tag{A.38}$$

$$\left. + b^y \frac{T_{i,j+1,k+1/2} - T_{i,j-1,k+1/2}}{2h_y} \right) \tag{A.39}$$

with values of T and b^μ at half node positions given by linear interpolation. The shifted metric geometry (Appendix B) is taken into account appropriately. In this manner, considerations of interplay between the background gradient and fluctuation along perturbed field lines are taken into account automatically.

5b. In the Landau fluid models thermal conduction is a dissipative wave system. As noted in Chapter 12, it is impossible to use $k_{\|}$ in formulae as is done in the electrostatic models, where the damping is expressed in terms of the absolute value, $|k_{\|} V_e|$, which

in normalised units is $\hat{\mu}^{-1/2}\left|k_{\|}\right|$. We use the best approximation to this possible with three grid nodes, such that the dissipation at each node is given by a constant plus a step size dependent diffusion. The constant ensures that the dissipation at long parallel wavelength follows $\left|k_{\|}qR\right| \to 1$, while at the shortest wavelengths the first order upwinding ensures the correct amount of dissipation. In between, the dissipation is somewhat less. For $\widetilde{T}_e$ have the wave system

$$c_f \frac{\partial \widetilde{T}_e}{\partial t} = -\mathbf{b}\cdot\nabla\widetilde{q}_{e\|} \qquad \hat{\mu}\left(\frac{\partial}{\partial t} + \hat{\mu}^{-1/2}a_L\right)\widetilde{q}_{e\|} = -c_1\mathbf{b}\cdot\nabla\left(\widetilde{T}_e - \omega_t x\right) \quad \text{(A.40)}$$

including the gradient piece in the temperature, where $\hat{\mu}$ is the constant parameter giving the parallel thermal transit frequency, and c_f, c_1, and a_L are constants. The standard value of a_L is 1.0, and for the isotropic temperature models we are using, $c_f = 3/2$ and $c_1 = 5/2$. The wave part of the system is split such that

$$\left(\frac{\partial}{\partial t} \pm V_q\mathbf{b}\cdot\nabla\right)\left(c_f\widetilde{T}_e - c_f\omega_t x \pm c_1\frac{\widetilde{q}_{e\|}}{V_q}\right) = 0 \quad \text{(A.41)}$$

with wave speed V_q given by $V_q^2 = c_1/c_f\hat{\mu}$. It is treated via first order upwinding as above (the first order scheme neglects all spatial derivatives in the extrapolation step). Then, the constant damping piece is treated implicitly,

$$\widetilde{q}_{e\|} \to \left(1 + \tau\hat{\mu}^{-1/2}a_L\right)^{-1}\widetilde{q}_{e\|} \quad \text{(A.42)}$$

where τ is the time step. For the ions, everything is the same as for the electrons except in the Landau scheme $\hat{\mu}$ is replaced by $\hat{\epsilon}$ and there is an extra factor of τ_i in front of $\mathbf{b}\cdot\nabla\left(\widetilde{T}_i - \tau_i\omega_i x\right)$. For the ions under the Braginskii model the coefficient $3.2/\hat{\mu}\nu_e$ is replaced by $3.9/\hat{\epsilon}\nu_i$, where $\nu_i = 2^{-1/2}\mu_e^{1/2}\tau_i^{-3/2}\nu_e$

5c. The electron thermal dissipation is sub cycled on a time step given by the minimum of τ and $0.8h_\mu/b^\mu V_q$ for each coordinate x^μ. adjusted downward such that the number of sub steps is an integer. The overall time step τ is limited by ExB and Alfvén dynamics, given by the minimum of a prescribed value τ_0 compared to each of $0.8h_\mu/v_E^\mu$ and $0.8h_\mu/b^\mu V_a$. For $\hat{\beta} > 1$ the constant in front of $h_\mu/b^\mu V_a$ is reduced to 0.5.

References

P. Colella, *J. Comput. Phys.* 87 (1990) 171.

B. Van Leer, *J. Comput. Phys.* 32 (1979) 101.

B. The Treatment of Flux Surface Geometry in Flux Tube Computations

B. Scott

Jul 1999

Note

This is a detailed explanation of how one takes an MHD equilibrium, finds field aligned flux tube coordinates and sets up the seven geometric quantities one needs in a computation, and finally how one applies coordinate shifts in the drift direction (the one which remains purely periodic) in order to avoid the deleterious effects of coordinate cell deformation in the drift plane. It is a paper recently appearing in *Physics of Plasmas*.

B.I. Introduction, Field Aligning and Deformation

During recent activity involving turbulence computations of particle and energy transport in magnetised fusion plasmas, it has become usual to set up the coordinate system so that derivatives along the magnetic field lines involve only one of the three coordinates [1–5]. This takes advantage of the strong anisotropy of drift scale dynamics (fluid, gyrofluid, gyrokinetic), especially regarding parallel electron dissipation, which gives the dynamics a strong flute mode character,

$$\nabla_{\parallel}^2 \ll \nabla_{\perp}^2 \tag{B.1}$$

for the components of the gradients parallel and perpendicular to the magnetic field, $\mathbf{B}$, respectively. Even for electromagnetic dynamics, in which case $\nabla_{\parallel}$ necessarily involves all three coordinates, the perturbed magnetic field and scales are such that

$$\widetilde{\mathbf{B}}_{\perp} \cdot \nabla \sim \mathbf{B} \cdot \nabla \tag{B.2}$$

which preserves the flute mode character. Aligning the coordinates to the magnetic field brings the benefit that relatively few grid nodes are needed in what becomes the parallel coordinate, even though very high resolution is needed in the perpendicular plane, represented by the remaining two coordinates [4,6–9].

A simple example of the idea can be given using a periodic cylindrical model, described by coordinates (r, θ, ζ) such that

$$0 \le r \le a \qquad -\pi \le \theta \le \pi \qquad -\pi \le \zeta \le \pi \tag{B.3}$$

with periodicity length $2\pi R$, where a and R are constants. It is assumed that the equilibrium plasma pressure is a function of r only, $p = p(r)$, and that its gradient is everywhere

finite. The conditions of magnetic equilibrium then demand that $\mathbf{B}$ lie in the nested flux surfaces described by the full domain of (θ, ζ) at each r. The topology of these surfaces is that of 2-tori, with the result that if $\mathbf{B}$ has finite pitch the field lines in general cover the entire surface. The magnetic field in a given flux surface is

$$\mathbf{B} = (B^\theta, B^\zeta) = B\left(\frac{r}{qR}, 1\right) \tag{B.4}$$

which defines $q = q(r)$ as the pitch parameter.

Aligning to the magnetic field is simply a method to make one of these contravariant components vanish, so that $\mathbf{B} \cdot \nabla = B^j \nabla_j$ involves only one coordinate. We can transform the flux surface coordinates from (θ, ζ) to (ϑ, ξ), according to the rules

$$\begin{aligned} \xi &= \zeta - q\theta & \qquad \zeta &= \xi + q\vartheta \\ \vartheta &= \theta & \qquad \theta &= \vartheta \end{aligned} \tag{B.5}$$

We can compute the new contravariant components B^j according to the tensor transformation rules, $B^j(\mathbf{X}) = (\partial X^j / \partial x^k) B^k(\mathbf{x})$, to find

$$B^\vartheta = B^\theta \qquad B^\xi = 0 \tag{B.6}$$

This defines ξ as the drift angle: $\nabla\xi$ is in the ion drift direction, $\mathbf{B}\times\nabla p$, for $\partial p/\partial r < 0$ and $B > 0$. We now have r and ξ as perpendicular coordinates, requiring high resolution. But ϑ is now purely parallel, since

$$\mathbf{B} \cdot \nabla = B^\vartheta \frac{\partial}{\partial \vartheta} \tag{B.7}$$

and hence in this coordinate we require relatively few grid nodes. We have r as a flux surface label, ξ as a field line label within the flux surface, and ϑ as a position along the field line.

The drawback of this transformation is that the coordinate cells become severely deformed if there is appreciable shear. The global shear parameter for the cylinder model is defined as

$$\hat{s} = \frac{r}{q}\frac{\partial q}{\partial r} \tag{B.8}$$

Although the original coordinates were orthogonal,

$$\nabla r \cdot \nabla\theta = \nabla r \cdot \nabla\zeta = \nabla\theta \cdot \nabla\zeta = 0 \tag{B.9}$$

the transformed ones are not. Under drift ordering the parallel derivatives are neglected in perpendicular dynamics (*e.g.*, $\nabla_\perp^2$ or $\mathbf{v}_E \cdot \nabla$, where $\mathbf{v}_E$ is the ExB velocity), so the

nonorthogonality involving $\nabla\vartheta$ is not an issue. However, the magnetic shear introduces nonorthogonality in the two perpendicular coordinates: the corresponding inverse metric element is

$$g^{r\xi} \equiv \nabla r \cdot \nabla \xi = -\vartheta \frac{\partial q}{\partial r} |\nabla r|^2 = -\vartheta \frac{\partial q}{\partial r} \tag{B.10}$$

What takes place geometrically is that the difference in the field line pitch for neighboring flux surfaces gives the gradient of the drift angle a component out of the flux surface. If the "reference position" of the aligning transformation is $\vartheta = 0$ as it is here (the position at which $\zeta = \xi$ and the coordinates are orthogonal), then two field lines at different r going through $\vartheta = \xi = 0$ (hence $\theta = \zeta = 0$) have a purely radial displacement. But at positions up or down these same field lines, at a given poloidal position $\vartheta \neq 0$, the two field lines now also have a toroidal displacement: at the two radii, r_1 and r_2, with q values q_1 and q_2, respectively, the points at the same values of $\vartheta \neq 0$ and $\xi = 0$ are at $\zeta = q_1\vartheta$ and $q_2\vartheta$, respectively. Since these positions are at the same value of ξ, the ξ-constant plane is no longer normal to the flux surface. The existence of both a radial and secular poloidal displacement of the two field lines leads to the nonorthogonality $\nabla r \cdot \nabla \xi \neq 0$. Indeed, the derivative of this metric element with ϑ gives the local shear

$$S = -\frac{r}{q}\frac{\partial g^{r\xi}}{\partial \vartheta} \tag{B.11}$$

which is equal to the global shear $\hat{s}$ in the cylinder model. It is important to note that this coordinate cell deformation is a consequence of periodicity and shear only; no special toroidal effects beyond the basic topology are fundamental to it.

The consequence of this coordinate deformation is to give a distorted set of eigenvalues to the perpendicular Laplacian,

$$\nabla_\perp^2 = g^{rr}\frac{\partial^2}{\partial r^2} + 2g^{r\xi}\frac{\partial}{\partial r}\frac{\partial}{\partial \xi} + g^{\xi\xi}\frac{\partial^2}{\partial \xi^2} \tag{B.12}$$

when taken as a difference operator on a discrete grid in r and ξ. Basic to drift dynamics, either fluid or kinetic, is the fact that the electrostatic potential, ϕ, is not only the stream function for the ExB flow but also a force potential ("state variable") for the parallel electron dynamics. In local treatments (which neglect variation of the background with r except for gradient drive terms) the ExB advection in field aligned coordinates has the form of a Poisson bracket,

$$\mathbf{v}_E \cdot \nabla = \frac{\partial \phi}{\partial \xi}\frac{\partial}{\partial r} - \frac{\partial \phi}{\partial r}\frac{\partial}{\partial \xi} \tag{B.13}$$

in suitably normalised units. This poses no difficulty for numerical treatments given a rectangular grid in r and ξ. But the polarisation dynamics, the simplest case of which

is the ExB vorticity given by $\nabla_\perp^2 \phi$ in a fluid treatment, will react differently at different positions ϑ, due to the different set of eigenvalues $\nabla_\perp^2$ has for the differing metric elements $g^{r\xi}$ and $g^{\xi\xi}$. Experience shows that this leads to increased numerical dissipation at larger ϑ, and hence spurious dependence of the turbulence statistics on ϑ. This is important in toroidal geometry due to several physical effects which cause a ϑ-dependence; if we want to quantify the ϑ-dependence we have to have a numerical treatment which will not corrupt the results.

The rest of this paper is the description of such a treatment. We take advantage of the fact that the perpendicular dynamics is solved at discretely various ϑ in a computation. At each position ϑ we can arbitrarily shift the grid in the ξ-direction, since the ξ-coordinate remains simply periodic. This shift can depend on r, but not on ϑ even though a different shift is used for different, discrete positions in ϑ. This is not the same thing as simply undoing the original transformation, since the field aligning shift depends on both r (through q) and ϑ. After the shift we are still left with a field aligned coordinate system in the vicinity of each perpendicular plane. We must merely take into account the different shifts at different ϑ while taking parallel derivatives. What results is a procedure which can treat arbitrary shear and toroidal flux surface shaping without suffering from the consequences of twisting deformation of the grid cells.

In the next section we outline a procedure by which Hamada coordinates and then field aligned coordinates may be constructed from a given axisymmetric equilibrium. In the following sections the shifted metric procedure is outlined for the local, thin flux tube limit, and the advantages are shown using some simple example computations. Following that, the shifted metric procedure for global models is developed. Appendices then show how to deal with radial (cross flux surface) periodicity and with computational methods requiring evaluations of the dependent variables between grid nodes along the magnetic field.

B.II. Field Aligned Hamada Coordinates, Global and Local

In this section we describe the procedure by which Hamada coordinates are constructed from an axisymmetric, separatrix free tokamak equilibrium. Next comes the transform which aligns the coordinates to the magnetic field. The effects on the boundary conditions are briefly described. This completes the construction of the global version of field aligned Hamada coordinates. Following that, we restrict the domain to make it radially local; that is, the radial dependence of the metric and auxiliary information is neglected, and a rescaling transformation presents the coordinates, metric, and auxiliary information in a form usable by local, thin flux tube computations. Much of this material

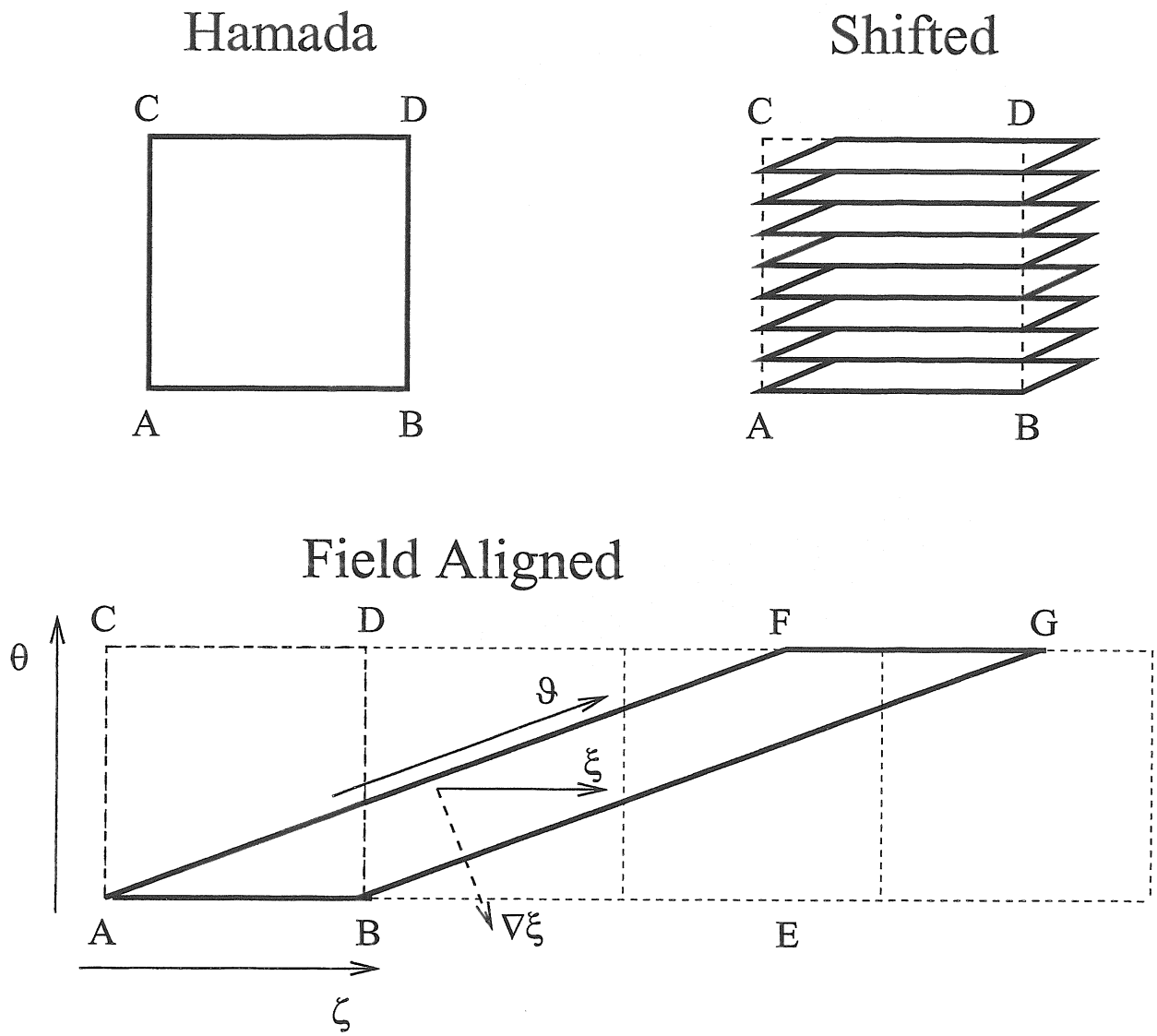

Figure B.1. The sense of the shifted metric coordinate system. The closed flux surface is the 2-torus ABDC with poloidal and toroidal angles θ and ζ, respectively. The field aligning transformation uses the covering space ABGF, defining a parallel coordinate ϑ and drift angle ξ, such that $\mathbf{B} \cdot \nabla \xi = 0$. The coordinate system is nonorthogonal. Due to the simple periodicity in ξ holding ϑ fixed, each subspace with fixed ϑ may be shifted arbitrarily in ξ. The shifted metric coordinate system chooses these shifts such that the coordinate system is orthogonal at a particular value of ϑ. At each ϑ, one is on a different coordinate system, but each of them is still field aligned.

has been developed elsewhere, both in papers and in textbooks, but the purpose is to give a complete if concise documentation of the numerical methods used in the construction of these coordinates by recent electromagnetic gyrofluid computations in globally consistent

geometry [10]. This will also provide a useful review of the preparations for the shifted metric procedure.

One of the viable definitions of the Hamada coordinates is the demand that the contravariant components of the magnetic field are flux functions [11]. That is, we assume the existence of an equilibrium described by nested, closed surfaces within which the magnetic field lines lie, so that the flux surfaces may be labelled monotonically from the magnetic axis (defined as the surface which has zero enclosed volume), to some specified boundary surface. As is well known, the surfaces must be 2-tori — covered by the specification of two coordinates whose domains are cyclic. For the coordinates to remain nonsingular, there must be no separatrices in the equilibrium — for an axisymmetric equilibrium this means that the poloidal field must not vanish.

We use the standard representation of an axisymmetric magnetic field on closed surfaces,

$$\mathbf{B} = I\nabla\phi + \nabla\Psi\times\nabla\phi \tag{B.14}$$

defined on poloidal planes with $0 < R < \infty$ and $-\infty < z < \infty$ each of which is labelled by a toroidal angle $0 < \phi < 2\pi$. The variables $\Psi(R,z)$ and $I(\Psi)$ are scalar fields. Any quantity which is a function of Ψ only is called a flux function. The flux variable Ψ is assumed to be zero on a specified boundary curve in (R,z), whose surface of revolution about $R=0$ is the boundary flux surface. It is assumed that $\Psi > 0$ interior to the boundary curve, rising to a single maximum $\Psi = \Psi_0$. The flux surface $\Psi = \Psi_0$ is the magnetic axis.

The equilibrium is determined via the Grad Shafranov equation,

$$-R^2\nabla\cdot\frac{\nabla\Psi}{R^2} = \frac{\partial}{\partial\Psi}\left(\frac{I^2}{2} + 4\pi R^2 p\right) \tag{B.15}$$

the well known consequence of $\mathbf{J}\times\mathbf{B} = c\nabla p$. We solve this using the HELENA code [12]. The normalisation removes central values from profile shapes by defining $\bar{\Psi} = 1 - \Psi/\Psi_0$ as the flux surface variable and by using the auxiliary flux functions

$$\Pi(\bar{\Psi}) = -\frac{4\pi}{B_0^2}\frac{\partial p}{\partial\bar{\Psi}} \qquad \Gamma(\bar{\Psi}) = \frac{1}{B_0^2 a^2}\frac{\partial}{\partial\Psi}\left(\frac{I^2}{2} + 4\pi R_0^2 p\right) \tag{B.16}$$

where a and R_0 are the reference minor and major radii, respectively, (the boundary curve is specified in terms of $R - R_0$ and z), and B_0R_0 is the value of I on the boundary curve. The equilibrium is determined by specified choices for the boundary curve $\bar{\Psi} = 1$, and the profiles $p(\bar{\Psi})$ and $I(\bar{\Psi})$. We use the simple parameterisations

$$\Pi = \frac{\beta_0}{2}\left(\frac{q_1}{q_0}\right)^{\bar{\Psi}} \qquad \Gamma = \frac{2}{q_0}\left(\frac{q_1}{q_0}\right)^{-2\bar{\Psi}} \tag{B.17}$$

with β_0, q_0 and q_1 the input constants which determine the central beta, the central q and approximately the edge q (it is possible to iterate on q_1 within HELENA to obtain a desired edge q, so as to do a parameter sweep with self consistently changing equilibria). HELENA's Grad Shafranov equation is then

$$-R^2\nabla\cdot\frac{\nabla\bar{\Psi}}{R^2}=A\left[\Gamma+A\Pi\left(R^2-R_0^2\right)\right] \tag{B.18}$$

with R normalised in terms of a, and with $A=B_0a^2/\Psi_0$. In the simplest case of a circular boundary surface with arbitrarily small a/R_0, one obtains a high aspect ratio circular torus with p and q parabolic in the minor radius r, given by $V=2\pi^2r^2R_0+O[(a/R_0)^2]$, with $p(r)\propto(1-r^2/a^2)$ and $q(r)=q_0+(q_1-q_0)r^2/a^2$.

The Hamada coordinates (V,θ,ζ) are defined by

$$\mathbf{B}\cdot\nabla V=0\qquad\mathbf{B}\cdot\nabla\theta=\hat{\chi}(V)\qquad\mathbf{B}\cdot\nabla\zeta=\hat{\psi}(V)=q(V)\hat{\chi}(V) \tag{B.19}$$

such that V is the volume enclosed by surface Ψ, and θ and ζ are cyclic on $[0,1]$. Here, q is the global pitch parameter, also a flux function. The coordinate Jacobian is

$$g^{-1/2}=\nabla V\times\nabla\theta\cdot\nabla\zeta=1 \tag{B.20}$$

where

$$g=\det g_{jk} \tag{B.21}$$

is the determinant of the covariant components of the metric tensor.

Given the representation of $\mathbf{B}$ in Eq. (B.14), the coordinate definitions in Eq. (B.19) may be used to construct the coordinates from a specified equilibrium (here we use the procedure in Refs. [2] and [6]). The integrals are done using the third order Hermitian element machinery in HELENA. The position around each flux surface is parameterised in terms of the poloidal grid nodes, normalised in terms of the domain $0<\eta<2\pi$, and $\hat{\chi}(\bar{\Psi})$ and $\theta(\bar{\Psi},\eta)$ are computed via

$$\hat{\chi}^{-1}=\int_0^{2\pi}\frac{d\eta'}{\mathbf{B}\cdot\nabla\eta'}\qquad\qquad\theta=\hat{\chi}\int_0^{\eta}\frac{d\eta'}{\mathbf{B}\cdot\nabla\eta'} \tag{B.22}$$

The volume $V(\bar{\Psi})$ is computed via

$$V=\oint_{\bar{\Psi}}R d\phi\,dz\,dR \tag{B.23}$$

where the integral is over the region enclosed by the surface $\bar{\Psi}(R,z,\phi)=\bar{\Psi}$. It is clear that $(R,z)\rightarrow(\bar{\Psi},\eta)\rightarrow(V,\theta)$ are one-to-one and onto maps.

With V and θ to hand we may find ζ via

$$\zeta = \frac{\phi}{2\pi} + \frac{I}{2\pi\hat{\chi}} \int_0^\theta d\theta' \left(\left\langle \frac{1}{R^2} \right\rangle - \frac{1}{R^2} \right) \tag{B.24}$$

where the flux surface average denoted by the angle brackets is simply

$$\left\langle \frac{1}{R^2} \right\rangle = \int_0^1 d\theta' \frac{1}{R^2} \tag{B.25}$$

This flux surface average operator leads to the evaluation of the pitch parameter $q(\bar{\Psi})$, via

$$q = \frac{I}{2\pi\hat{\chi}} \left\langle \frac{1}{R^2} \right\rangle \tag{B.26}$$

The Hamada coordinates are transformed into their field aligned versions with the same Eqs. (B.5) as for the simple cylinder model. This works because q is a flux function and so are the B^j. The boundary conditions for both Hamada coordinate systems are

$$\begin{aligned} f(V,\theta+1,\zeta) &= f(V,\theta,\zeta) & \qquad f(V,\vartheta+1,\xi-q) &= f(V,\vartheta,\xi) \\ f(V,\theta,\zeta+1) &= f(V,\theta,\zeta) & \qquad f(V,\vartheta,\xi+1) &= f(V,\vartheta,\xi) \end{aligned} \tag{B.27}$$

The top row gives poloidal periodicity in the physical sense, and the bottom row gives toroidal periodicity. For the field aligned version, this is the periodicity constraint which enters due to the combined influence of toroidal topology and field line pitch [13].

The globally consistent procedure for truncating this domain on the full flux surface down to a thin flux tube was given in Ref. [5]. Given the poloidal and toroidal periodicity, the only way to ensure that the flux tube contains no degrees freedom not existing on the full flux surface is to divide the domain in ξ into an integer k_0 equal parts and enforce periodicity on each of them. Even though the ends of a given flux tube one poloidal cycle (in ϑ) apart lie in general at different positions ξ, the flux tubes in which they fall are identical and so the poloidal periodicity must be enforced after that one cycle. This was proved in Ref. [5] using the fact that poloidal periodicity applies to each component in a Fourier decomposition of the ξ domain on the full flux surface, and therefore to each such component incorporated into the truncation, since the latter is a wholly contained subset of the former. Periodicity in a truncated domain is then

$$f(V,\vartheta+1,\xi-q) = f(V,\vartheta,\xi) \qquad f(V,\vartheta,\xi+1/k_0) = f(V,\vartheta,\xi) \tag{B.28}$$

In terms of the Fourier components, we have

$$f(V,\vartheta,\xi) = \sum_l f_l(V,\vartheta)\, e^{-2\pi i l \xi} \qquad f_l(V,\vartheta+1) = f_l(V,\vartheta)\, e^{-2\pi i l q} \tag{B.29}$$

with $l \in \{0, \pm 1, \pm 2, \pm 3, \ldots\}$ on the full flux surface or $l \in \{0, \pm k_0, \pm 2k_0, \pm 3k_0, \ldots\}$ on the truncated flux tube.

In general for such an axisymmetric equilibrium the metric elements are functions of V and θ and hence V and ϑ. In addition we require the magnetic field strength, the divergence of the unit vector $\mathbf{b}$, and the curvature operator

$$\mathcal{K} \equiv \mathcal{K}^j \nabla_j \equiv \nabla \cdot \frac{c}{B^2} \mathbf{B} \times \nabla \approx -\nabla \log B^2 \cdot \frac{c}{B^2} \mathbf{B} \times \nabla = \frac{c}{B^2} B^k \epsilon_k{}^{lj} \nabla_l \log B^2 \nabla_j \tag{B.30}$$

where ϵ_{ijk} is the totally antisymmetric pseudotensor of rank three. In field aligned Hamada coordinates the unit vector has the contravariant component and divergence

$$b^\vartheta = \frac{\hat{\chi}}{B} \qquad \nabla \cdot \mathbf{b} = \mathbf{B} \cdot \nabla \frac{1}{B} = -\frac{\hat{\chi}}{B} \frac{\partial}{\partial \vartheta} \log B = -b^\vartheta \frac{\partial}{\partial \vartheta} \log B \tag{B.31}$$

In a local computation using drift ordering the dependence of this geometrical information on V is neglected except where derivatives are taken with respect to V. Additionally, due to the flute mode character, Eq. (B.1), derivatives with respect to ϑ are neglected except in parallel derivatives and where $\partial B / \partial \vartheta$ is needed. Following Ref. [5], the coordinates are rescaled as $x = x(V)$, $y = y(\xi)$, and $s = s(\vartheta)$ such that

$$\begin{aligned} V &= V_0 + V' x, & x &= (V - V_0)/V', \\ \vartheta &= s/L_\parallel, & y &= -\xi V'/L_\parallel, \\ \xi &= -y L_\parallel / V', & s &= \vartheta L_\parallel, \end{aligned} \tag{B.32}$$

where V_0, V', and $L_\parallel = B_0/\hat{\chi}$ are constants (note the change in coordinate order, the sign in $\xi \leftrightarrow y$ which indicates both systems are right handed, and that $\hat{\chi}$ at the local flux surface has become a constant due to the drift ordering). The boundary conditions become

$$f(x, y + 2\pi/K, s) = f(x, y, s) \qquad f(x, y + 2\pi \hat{s} x, s + L_\parallel) = f(x, y, s) \tag{B.33}$$

where the drift direction periodicity length and global shear parameter are given by

$$2\pi/K = V'/k_0 L_\parallel \qquad \hat{s} = V' q'/2\pi L_\parallel \qquad q' = \frac{\partial q}{\partial x} \tag{B.34}$$

In the simple models we have the more familiar relations $L_\parallel = 2\pi q R$ and $K = k_0 q/R$ and $\hat{s} = r q'/q$, which follow from the cylinder volume $V = 2\pi^2 r^2 R$ at a given minor radius r with periodicity length $2\pi q R$.

In a local computation, the necessary geometrical information is reduced to the seven quantities

$$g^{xx}(s) = \nabla x \cdot \nabla x \qquad g^{xy}(s) = \nabla x \cdot \nabla y \qquad g^{yy}(s) = \nabla y \cdot \nabla y \tag{B.35}$$

for the metric,

$$\rho^2(s) = \frac{B_0^2}{B^2} \qquad b^s(s) = \frac{B_0}{B} \tag{B.36}$$

for the magnetic field, and

$$\mathcal{K}^x(s) = \frac{B_0 L_\perp}{B^2}\mathbf{B}\cdot\nabla\log B^2\times\nabla x \qquad \mathcal{K}^y(s) = \frac{B_0 L_\perp}{B^2}\mathbf{B}\cdot\nabla\log B^2\times\nabla y \tag{B.37}$$

for the curvature operator, where $L_\perp$ is the local perpendicular profile scale used to normalise the dynamical equations of the model in question. We note in particular that ρ serves as a normalised gyroradius or drift scale, taking into account the variation of this scale around the flux surface, which has been shown to have strong impact on drift wave turbulence in tokamak edge geometry [6].

B.III. Shifted Metric Procedure for Local Computations

With the treatment given in the previous section one can extend a local flux tube computation to axisymmetric, separatrix free equilibria which are otherwise general. Once an equilibrium is chosen, a given flux surface is chosen as the reference for the computation, and normalised units are established in terms of the physical parameters (temperature, *etc.*) at that radial location ("radial" of course refers simply to the V-coordinate). The computation is constructed exactly as for a simplified sheared flux tube model (see, *e.g.*, Refs. [8,9]), except that the flux tube parameters K and $\hat{s}$ in Eqs. (B.33,B.34) and the seven geometrical quantities in Eqs. (B.35–B.37) are now computed from the specified equilibrium. This means that the shifted metric procedure used in the Introduction can be carried over almost intact to a computation in a realistic flux surface geometry. This is what was done in Ref. [10]. It remains only to properly document this treatment.

The desired property of the shifted metric geometry is simply that the metric elements describing nonorthogonality in the coordinates vanish. We apply an arbitrary shift α_k, which depends only on x, to the y-coordinate,

$$y_k = y - \alpha_k(x) \tag{B.38}$$

such that

$$g_k^{xy} = g^{xy} - \alpha_k' g^{xx} = 0 \tag{B.39}$$

where the prime denotes $\partial/\partial x$. We still have field aligned coordinates,

$$\mathbf{B}\cdot\nabla y_k = \mathbf{B}\cdot\nabla y - \alpha_k'\mathbf{B}\cdot\nabla x = 0 \tag{B.40}$$

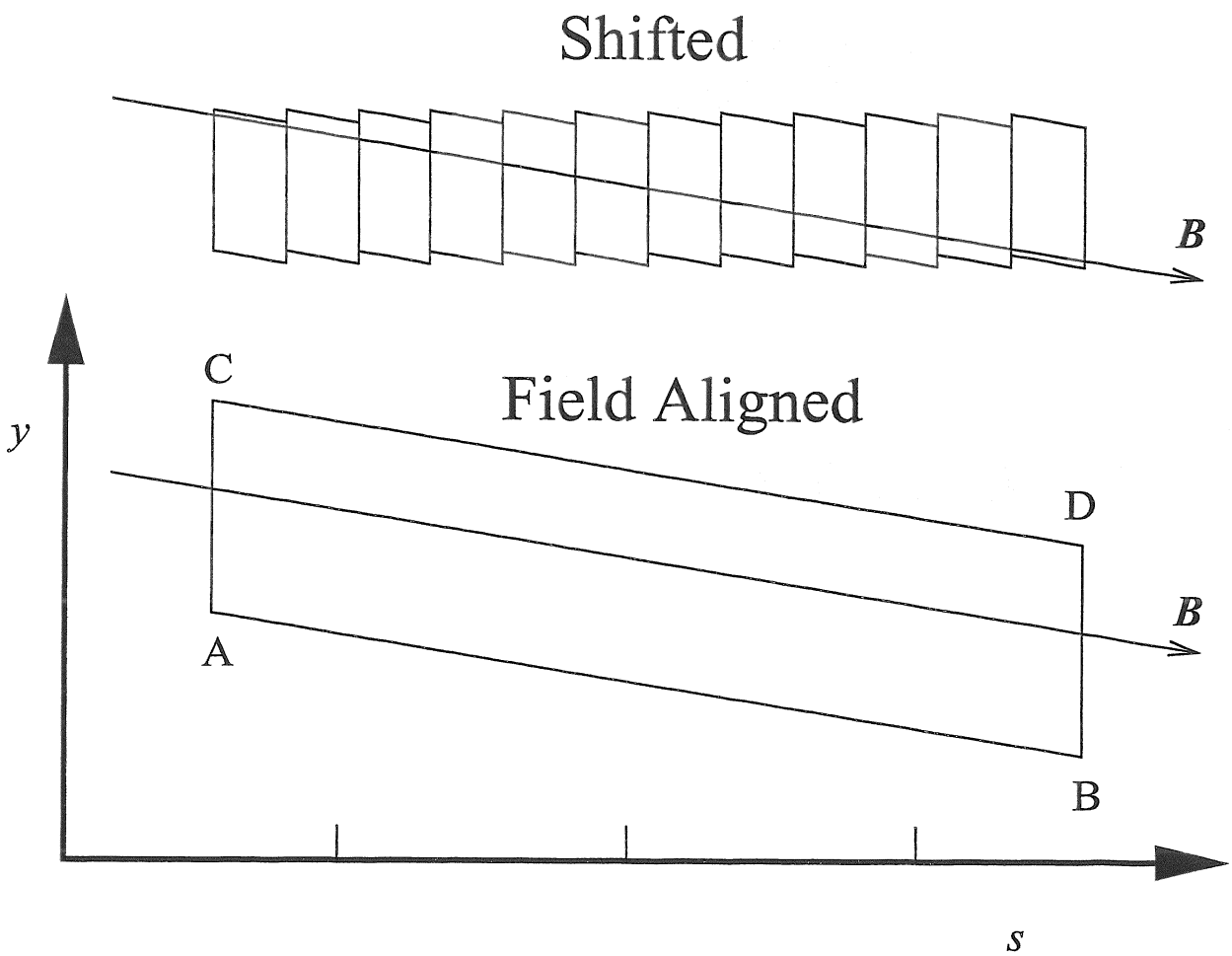

Figure B.2. The sense of the shifted metric coordinate system for flux tube geometry. The field aligned domain ABDC contains a global shift due to the pseudo periodic boundary condition in the s-direction, as explained in the text leading up to Eq. (B.33). This shift is split into pieces which become the local shifts between each of the drift planes in the upper figure. Due to the simple periodicity in y holding s fixed, these shifts can be chosen to set the off diagonal metric element to zero while preserving the field aligned nature of the coordinate system. The shifts are functions of x only (the coordinate perpendicular to the flux surface). Magnetic shear therefore only appears in the connection between perpendicular (drift) planes occurring as a result of dynamics parallel to the field lines (represented by the lines drawn with an arrow).

because α_k does not depend on s. It is very important to note that this shift does not merely reverse the field aligning transformation; it does so only at a single point in s. As noted in the Introduction, this serves merely to generalise the field aligning transformation such that

it is referenced at an arbitrary value of s, not just at $s = 0$. Each member of the family of systems (x, y_k, s) still has the property that g^{xy} departs secularly from zero as the position in s moves away from $s = s_k$. The relationship between the Hamada, field aligned, and shifted metric coordinate systems is sketched in Figure B.1. The corresponding relationship between the flux tube field aligned and shifted metric coordinate systems is sketched in Figure B.2.

The difference between the simple cylinder/slab geometry of the Introduction and a general flux tube is that we no longer have the properties that g^{xx} is independent of s and g^{xy} is linear in s. Instead, these quantities have arbitrary s dependence. So we must solve for the local shift. Since we are using each k-th coordinate system (x, y_k, s) only at $s = s_k$, we do the relevant integral along x at fixed s, noting that all geometric quantities are independent of y. We therefore have

$$\alpha_k = \alpha'_k x \qquad\qquad \alpha'_k = \left.\frac{g^{xy}}{g^{xx}}\right|_{s=s_k} \tag{B.41}$$

with the result that the shifts are not merely proportional to the value of s at which they are referenced.

The consequence of this shifted metric procedure is that all perpendicular operations are computed separately at each value of s, in the field aligned coordinate system referenced to that value of s. Since $g^{xy}_k = 0$ at $s = s_k$, and $\partial/\partial y = \partial/\partial y_k$ everywhere, we have

$$\nabla^2_{\perp k} = g^{xx}\frac{\partial^2}{\partial x^2} + g^{yy}_k \frac{\partial^2}{\partial y^2} \tag{B.42}$$

that is, an orthogonal grid on which to discretise $\nabla^2_\perp$. It is important to note that this also affects the curvature operator, especially $\mathcal{K}^y$ which involves pieces which enter through g^{xy}. In the simple slab/cylinder model with curvature terms added, this means that the secularly varying piece drops out of the standard ballooning form,

$$\begin{gathered}\mathcal{K}^y = \omega_B\left(\cos s + s\sin s\right) \rightarrow \mathcal{K}^y_k = \omega_B\left(\cos s + [s - s_k]\sin s\right) \\ \mathcal{K}^y \rightarrow \mathcal{K}^y_k(s = s_k) = \omega_B \cos s\end{gathered} \tag{B.43}$$

since it is used only at $s = s_k$ (here, ω_B, nominally equal to $2L_\perp/R$, is the parameter through which the curvature terms enter [8,9]). More generally, $\mathcal{K}^x$ and $\mathcal{K}^y$ are still constructed according to Eq. (B.30), but with the new metric.

There is the additional consequence that discretised parallel derivatives are now taken across grid nodes on which the coordinate systems are different. The effect of the shifts on parallel derivatives is sketched in Figure B.3. Only the part of the parallel derivative taken

with respect to the unperturbed field is affected, since $\partial/\partial x$ and $\partial/\partial y$ remain unchanged. The unshifted discretisation of $\partial/\partial s$ is

$$\frac{\partial f}{\partial s}(x, y, s_k) = \frac{f(x, y, s_{k+1}) - f(x, y, s_{k-1})}{s_{k+1} - s_{k-1}} \tag{B.44}$$

After the shifting transformation is applied at each node in s, we have

$$\frac{\partial f}{\partial s}(x, y_k, s_k) = \frac{f(x, y_k, s_{k+1}) - f(x, y_k, s_{k-1})}{s_{k+1} - s_{k-1}} \tag{B.45}$$

that is, the derivative is taken along s at constant y, in this case y_k. After shifting each y_k into its own particular coordinate system, this discretisation becomes

$$\frac{\partial f}{\partial s}(x, y_k, s_k) = \frac{f(x, y_{k+1} - \Delta_k^+, s_{k+1}) - f(x, y_{k-1} - \Delta_k^-, s_{k-1})}{s_{k+1} - s_{k-1}} \tag{B.46}$$

with shifts $\Delta_k^{\pm}(x)$ given by

$$\Delta_k^{\pm} = \alpha_{k\pm1} - \alpha_k = \left(\alpha'_{k\pm1} - \alpha'_k\right) x \tag{B.47}$$

The manifestation of magnetic shear in the shifted metric coordinate system is this dependence of the α_k and hence the $\Delta_k^{\pm}$ on x, which represents a local twist. In other words, magnetic shear in the shifted metric coordinate system appears only when coupling the various drift planes together via the dynamics along the magnetic field; perpendicular dynamics as such are not affected. We therefore find that the shifted metric coordinate system gives an optimal representation of the effects of magnetic shear.

Finally, the parallel boundary conditions are affected. The global shift represented by the periodicity constraint is now replaced by these local shifts. Beginning with Eq. (B.33), we shift the drift planes at $s = s_k$ and $s = s_k + L_{\|} = s_{k+N}$ onto their own coordinate systems,

$$f(x, y_{k+N} - \alpha_{k+N} + 2\pi\hat{s}x, s_{k+N}) = f(x, y_k - \alpha_k, s_k) \tag{B.48}$$

and then since

$$\alpha_{k+N} - \alpha_k = 2\pi\hat{s}x \tag{B.49}$$

we have

$$f(x, y_{k+N}, s_{k+N}) = f(x, y_k, s_k) \tag{B.50}$$

where N is the number of grid nodes in s covered by a change $s \to s + L_{\|}$, that is, one poloidal connection length. This divides up the global shift in Eq. (B.33) applied once, into the local shifts α_k, applied at every grid node in s. The local shifts, of course, add

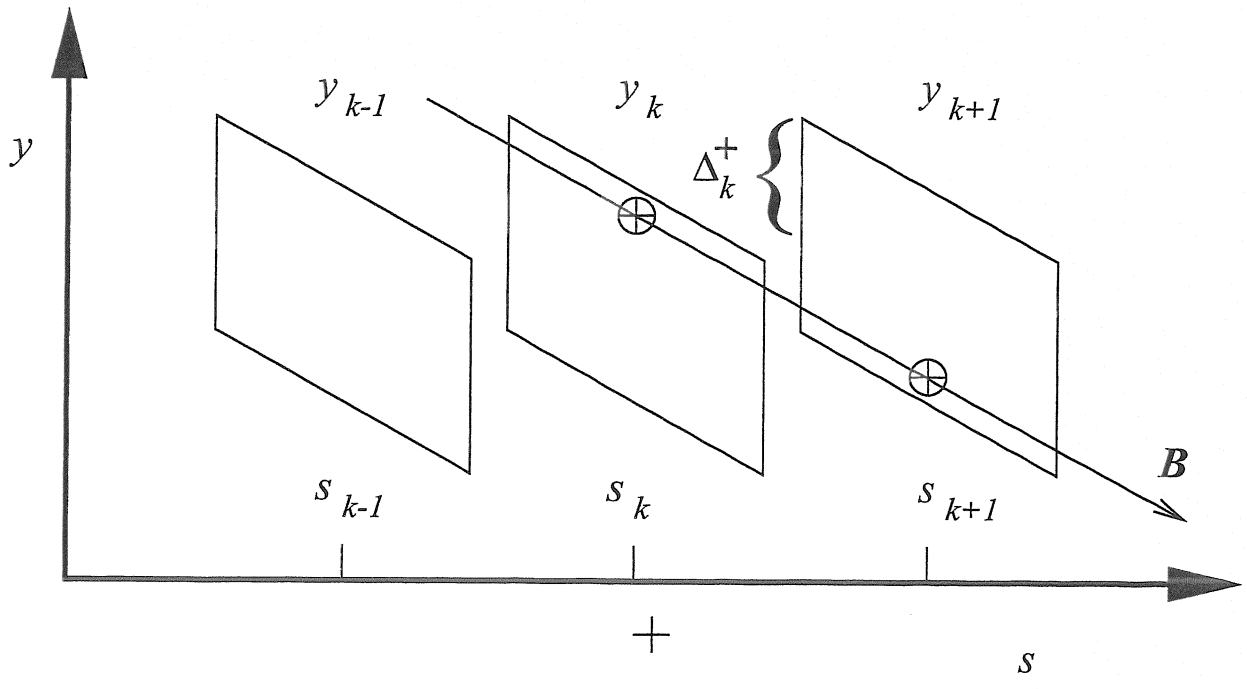

Figure B.3. The effect of the shifted metric coordinate system on parallel derivatives. A finite difference between the two points marked with crossed circles proceeds along the magnetic field line drawn with an arrow. Since the two points are reckoned in two different coordinate systems, $\{x, y_k, s\}$ and $\{x, y_{k+1}, s\}$, the shift Δ_k^+ is required in the finite difference, as in Eqs. (B.46,B.47).

up to the global shift, which is what Eq. (B.49) represents. This is easily proved using the relationship between α'_k and $g^{xy}(s_k)$, and the fact that the integral of g^{xy}/g^{xx} over s from $-L_\parallel$ to $L_\parallel$ gives the total shift of the parallel boundary condition, $2\pi\hat{s}x$ as per Eq.(B.33). The cancellation of the total shift by the sum of the α_k is valid generally, not just for a slab or cylinder. This is of course the result of the general definitions of K and $\hat{s}$ in Eq. (B.34).

The effect of these shifts α_k is that there must be interpolation in the parallel derivatives in Eq. (B.46). We note that there is always such interpolation, due to the fact that if we do not apply the shifting transformations we have a shift at the ends of the s-domain anyway [cf. Eqs. (B.33,B.49)], due to the fact that the field aligning transformation itself involves a shift. As noted, this merely distributes this interpolation equally among all the s-nodes. Testing shows indeed that in the turbulence it makes no difference if this interpolation in the y-direction is linear, third-order Lagrange, or by means of finite Fourier transforms (which is exact up to machine accuracy). The same is true for the shifting in Eq. (B.33), which is the version in common use.

The shifted metric procedure has not eliminated any geometrical information. It has merely replaced the coordinate twists g^{xy} of the original field aligned system by the shifts α_k. So instead of g^{xy} we must carry the α'_k; there are still seven quantities to carry in a computation.

B.IV. Illustration of Coordinate Deformation and its Remedy

We illustrate the effects of the coordinate deformation produced by a flux tube metric using a single field aligning transform ("straight metric") as in Section II, or alternatively the shifted metric as in Section III, with computations of drift wave turbulence in a simplified four field model. The model is chosen in order to illustrate the qualitative properties of electromagnetic drift wave (that is, drift Alfvén) turbulence while neglecting the more subtle properties of various closure schemes which are necessary to treat the temperatures. The geometry is a simple three dimensional sheared slab, as in the Introduction, in which the magnetic field is taken to be homogeneous except for the shear. This isolates the role of the interaction between parallel (kinetic shear Alfvén waves) and perpendicular dynamics (incompressible ExB turbulence), without the additional complications represented by magnetic curvature or other toroidal effects. Additionally, drift wave dynamics is isolated by neglecting the ion temperature. The electron temperature is taken to be a background constant which simply sets the parameters. In this context, the density, the electron density, and the electron pressure are all equivalent. The basic equations are the same as those used to treat drift tearing modes in a sheared slab with the addition of the electron inertia [14]:

$$\frac{nM_ic^2}{B^2}\frac{d_E}{dt}\nabla_\perp^2\widetilde{\phi} = \nabla_\parallel \widetilde{J}_\parallel \tag{B.51}$$

$$\frac{d_E\widetilde{p}_e}{dt} + \mathbf{v}_E\cdot\nabla p_e = \frac{T_e}{e}\nabla_\parallel\widetilde{J}_\parallel - p_e\nabla_\parallel\widetilde{u}_\parallel \tag{B.52}$$

$$\frac{ne}{c}\frac{\partial\widetilde{A}_\parallel}{\partial t} + \frac{m_e}{e}\left(\frac{d_E}{dt} + 0.51\nu_e\right)\widetilde{J}_\parallel = \nabla_\parallel\left(\widetilde{p}_e + p_e\right) - ne\nabla_\parallel\widetilde{\phi} \tag{B.53}$$

$$nM_i\frac{d_E\widetilde{u}_\parallel}{dt} = -\nabla_\parallel\left(\widetilde{p}_e + p_e\right) \tag{B.54}$$

$$\widetilde{J}_\parallel = -\frac{c}{4\pi}\nabla_\perp^2\widetilde{A}_\parallel \tag{B.55}$$

where the tilde symbols identify the dependent variables, the background is homogeneous except for the action of $\mathbf{v}_E\cdot\nabla$ and $\nabla_\parallel$ on the pressure, and the derivatives are given by

$$\frac{d_E}{dt} = \frac{\partial}{\partial t} + \mathbf{v}_E\cdot\nabla \qquad \mathbf{v}_E\cdot\nabla = \frac{c}{B}\left(\frac{\partial\widetilde{\phi}}{\partial x}\frac{\partial}{\partial y} - \frac{\partial\widetilde{\phi}}{\partial y}\frac{\partial}{\partial x}\right) \tag{B.56}$$

$$\nabla_{\parallel} = \frac{\partial}{\partial s} - \frac{1}{B}\left(\frac{\partial \widetilde{A}_{\parallel}}{\partial x}\frac{\partial}{\partial y} - \frac{\partial \widetilde{A}_{\parallel}}{\partial y}\frac{\partial}{\partial x}\right) \tag{B.57}$$

and the background gradient is in the minus x-direction,

$$\nabla p_e = -\frac{p_e}{L_{\perp}}\nabla x \tag{B.58}$$

The geometry for the straight metric is the one given in Section II, with

$$g^{xx} = 1 \qquad g^{xy} = \hat{s}\frac{s}{qR} \qquad g^{yy} = g^{xx} + (g^{xy})^2 \tag{B.59}$$

and with no curvature terms. For the shifted metric it is as in Section III, with

$$\alpha_k' = \hat{s}\frac{s_k}{qR} \qquad g^{xx} = g_k^{yy} = 1 \qquad g_k^{xy} = 0 \tag{B.60}$$

Both models assume a homogeneous magnetic field except for the shear, with

$$\rho^2 = 1 \qquad b^s = 1 \tag{B.61}$$

The numerical method is purely explicit except for the collisional dissipation, which is implicitly incorporated into the Alfvén dynamics. The dynamical subsystems representing ExB advection ($\mathbf{v}_E \cdot \nabla$), kinetic shear Alfvén waves ($\nabla_{\parallel}$ acting on $\widetilde{J}_{\parallel}$ and on $\widetilde{p}_e + p_e$ and $\widetilde{\phi}$ together), and sound waves ($\nabla_{\parallel}$ acting on $\widetilde{u}_{\parallel}$ and on $\widetilde{p}_e + p_e$ alone) are separated and discretised independently, with $\mathbf{v}_E \cdot \nabla$ acting in two dimensions (x and y) and $\nabla_{\parallel}$ acting in all three (x, y, and s). In each case the multi-dimensional second order upwind scheme ("MUSCL") of Colella is used [15], which is numerically stabilised by the slope limiting method of Van Leer [16]. For $\mathbf{v}_E \cdot \nabla$ the upwinding is straightforward. For the Alfvén waves and sound waves it splits the wave pair into two oppositely travelling eigenfunctions and applies the upwinding and slope limiting to each eigenfunction [17].

The cases used to illustrate the shifted metric procedure consisted of one run each with the shifted metric and straight metric, using the following parameters,

$$\hat{\beta} = \frac{4\pi n T_e}{B^2}\left[\frac{qR}{L_{\perp}}\right]^2 = 1.0 \qquad \hat{\mu} = \frac{m_e}{M_i}\left[\frac{qR}{L_{\perp}}\right]^2 = 5.0 \tag{B.62}$$

$$\hat{\epsilon} = \left[\frac{qR}{L_{\perp}}\right]^2 = 18350.0 \qquad \nu = \frac{\nu_e L_{\perp}}{c_s} = 10.0 \qquad \hat{s} = 1.0 \tag{B.63}$$

with the following computational domain,

$$-10\pi\rho_s < x < 10\pi\rho_s \qquad -40\pi\rho_s < y < 40\pi\rho_s \qquad -\pi qR < s < \pi qR \tag{B.64}$$

where the drift scale ρ_s and sound speed c_s are defined by

$$\rho_s^2 = \frac{c^2 M_i T_e}{e^2 B^2} \qquad\qquad c_s^2 = \frac{T_e}{M_i} \tag{B.65}$$

reflecting the combination of electron mobility and ion inertia. The spatial grid was $32 \times 128 \times 16$ in the x-, y-, and s-directions, respectively. The time step was $0.05 L_\perp / c_s$, the runs were carried to $1000 L_\perp / c_s$, and measurements were averaged over the interval $500 < c_s t / L_\perp < 1000$, referred to below as the saturated phase.

The boundary conditions in the s-direction were as in Eqs. (33) and (46), for the straight and shifted metric cases, respectively. The y-direction was periodic, and the x-direction was Dirichlet with the dependent variables set to zero at the boundaries. The background profile was maintained by damping the y-averaged component of $\widetilde{p}_e$ within a Gaussian envelope of half-width $2\rho_s$ centered at each x-boundary. The profile damping rate was $0.1 c_s / L_\perp$ times this envelope function. The fluctuations represented by the components with y-dependence were not dissipated artificially, except for the action of the numerical scheme itself.

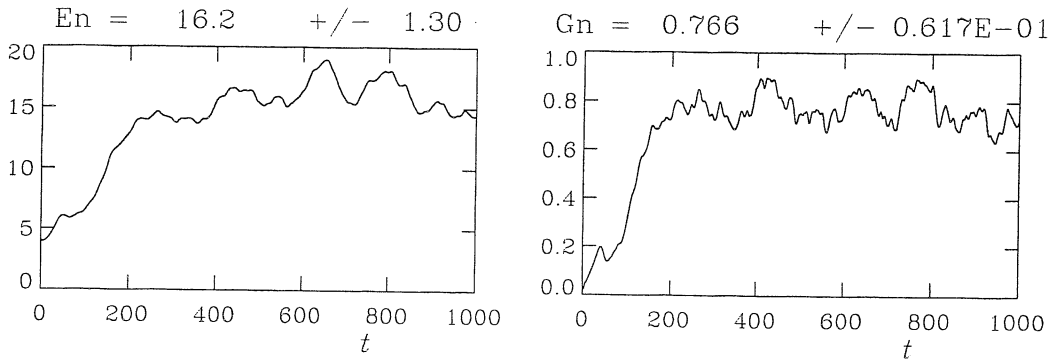

Figure B.4. Time traces of the squared amplitude $\widetilde{p}_e / p_e$ and the transport Q_e, normalised to gyro Bohm units as in the text, showing saturation. Statistics are taken from 500 to 1000 in $c_s t / L_\perp$.

As the reference case we use the result from the shifted metric. The squared amplitude of $\widetilde{p}_e / p_e$, normalised to $\rho_s^2 / L_\perp^2$, and the transport rate $Q_e = \langle \widetilde{p}_e \mathrm{v}_E^x \rangle$, normalised to the gyro Bohm units $p_e c_s \rho_s^2 / L_\perp^2$, as a function of time are shown in Fig. B.4, showing saturation before $t = 500 L_\perp / c_s$. This is by now a standard result: a nonlinear initialisation exciting self sustained drift wave turbulence by means of nonlinear instability [18].

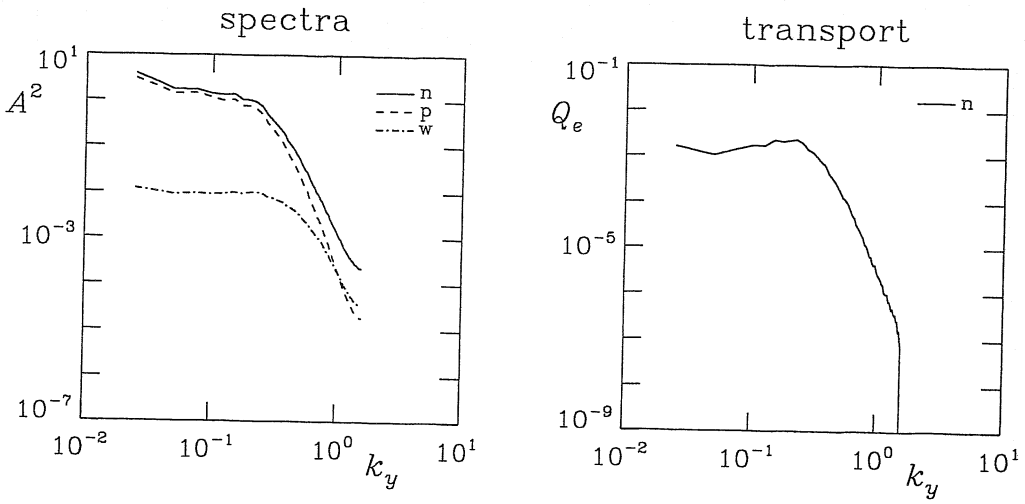

Figure B.5. Spectra of the squared amplitudes (left) of $\widetilde{p}_e/p_e$ (n), $e\widetilde{\phi}/T_e$ (p), and the vorticity, $\rho_s^2\nabla_\perp^2 e\widetilde{\phi}/T_e$ (w), and (right) of the transport Q_e (n), normalised to gyro Bohm units as in the text, showing the drive peak near $k_y\rho_s = 0.2$.

The spectra of pressure and vorticity fluctuations, and of the transport are shown in Fig. B.5. Here it is important to note that the vorticity spectrum is much flatter than that of the pressure (or any other basic quantity except for the current, which has similar form). The ExB vorticity nonlinearity ($\mathbf{v}_E \cdot \nabla\nabla_\perp^2\widetilde{\phi}$) is what causes the turbulence to self sustain, and this gives the smaller scales (wavelengths down to a few ρ_s) their importance. Also of note is the transport peak near $k_y\rho_s = 0.2$, showing that the free energy is generated at scales somewhat smaller than those implied by the pressure fluctuation spectrum. This result is also standard [18].

Of particular interest to this illustration is the structure in the s-direction, here normalised such that one connection length $L_\parallel$ ranges from $-\pi$ to π. The envelopes of the transport and the squared amplitudes of $e\widetilde{\phi}/T_e$ and $\widetilde{p}_e/p_e$, and the nonadiabatic response and the vorticity, normalised to $\rho_s^2/L_\perp^2$ and averaged over the spatial domain and over the saturated phase as a function of s are shown in Fig. B.6. Up to statistical deviations (there were 25 snapshots taken over the phase $500 < c_s t/L_\perp < 1000$), these envelopes are flat, as they should be, particularly the transport. In slab geometry, all locations along a given field line are equivalent.

Now, we turn to the case using the straight metric, with its strong s-dependence of the eigenvalues of $\nabla_\perp^2$ on the discrete grid. The increased numerical dissipation is reflected in a lower transport rate: for the shifted metric we obtain $Q_e = 0.766 \pm 0.062$, while the

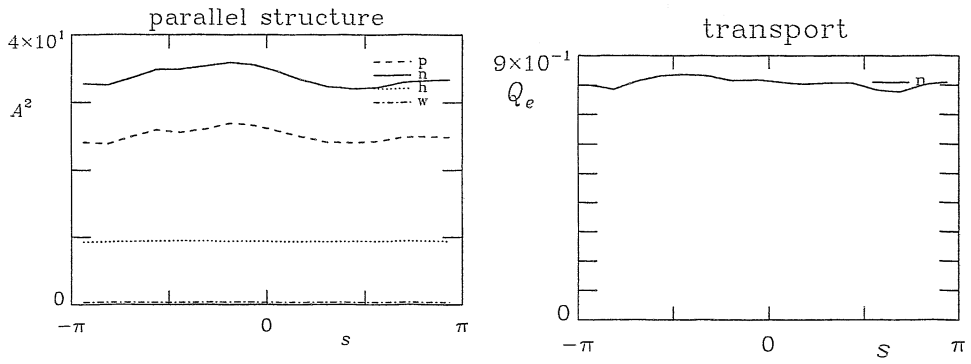

Figure B.6. Parallel structure of the squared amplitudes (left) of $e\widetilde{\phi}/T_e$ (p), $\widetilde{p}_e/p_e$ (n), the nonadiabatic response $\widetilde{p}_e/p_e - e\widetilde{\phi}/T_e$ (h), and the vorticity, $\rho_s^2\nabla_\perp^2 e\widetilde{\phi}/T_e$ (w), and (right) of the transport Q_e (n), normalised to gyro Bohm units as in the text, showing the equivalence of various positions along the field lines in slab geometry.

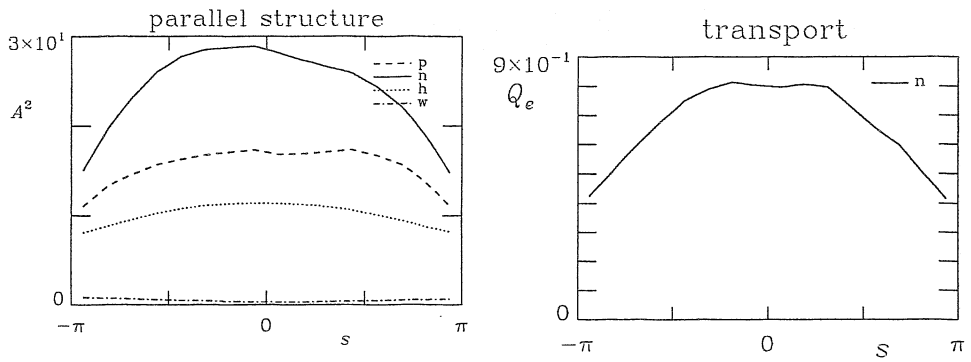

Figure B.7. Parallel structure of the squared amplitudes (left) of $e\widetilde{\phi}/T_e$ (p), $\widetilde{p}_e/p_e$ (n), the nonadiabatic response $\widetilde{p}_e/p_e - e\widetilde{\phi}/T_e$ (h), and the vorticity, $\rho_s^2\nabla_\perp^2 e\widetilde{\phi}/T_e$ (w), and (right) of the transport Q_e (n), normalised to gyro Bohm units as in the text, now for the straight metric case, showing the spurious parallel structure introduced by the coordinate deformation associated with the dependence of the degree of nonorthogonality on s. This is what the shifted metric has been introduced to remedy.

straight metric gives $Q_e = 0.632 \pm 0.053$, in units of $p_e c_s(\rho_s/L_\perp)^2$. It is interesting to find that both cases give the same pressure fluctuation amplitude, about $5.7\rho_s/L_\perp$, but the shifted metric case has a larger ExB energy amplitude: 2.49 ± 0.14 versus 1.67 ± 0.22 for

the straight metric, given in units of $p_e(\rho_s/L_\perp)^2$. Since most of the large to small scale cascade goes through the vorticity, it is not surprising to find that larger eigenvalues of $\nabla_\perp^2$ for the same resolution lead to a decreased ExB flow energy.

The structure in the s-direction of the straight metric case is even more revealing. The envelopes of the averaged transport and squared amplitudes are shown for that case in Fig. B.7. In contrast to the shifted metric case in Fig. B.6, these envelopes are sharply bowed, with decreased levels at larger values of $|s|$. We expect this for $\widetilde{\phi}$ but we find that it is even more pronounced for $\widetilde{p}_e$. The vorticity is increased for larger $|s|$, due mostly to the increased g^{yy} there. The additional numerical dissipation associated with this leads to the parallel structure, which is obviously spurious — all field line positions are equivalent in slab geometry. Indeed, this spurious parallel structure can compete with the ballooning one obtains in toroidal geometry, which is also often a factor of two in the transport.

The clear result of this illustration is that the more familiar straight metric for flux tube geometry gives rise to increased numerical dissipation for the same resolution, leading to decreased transport and turbulence and most especially to a spurious result for the structure in the s-direction. Both problems are effectively solved by using the shifted metric procedure.

B.V. Shifted Metric Procedure for Global Computations

Herein we outline a procedure by which the above shifted metric technique may be generalised to global computations. In this context, global means only that we no longer neglect the dependence of geometric quantities on V. The dynamical equations themselves may still be either local or nonlocal, according to the given model situation. Since the local and global field aligned coordinate systems have trivial differences in form, all the necessary work has already been done except for one thing. The global metric has arbitrary radial as well as poloidal dependence, so to compute the shifts in the ξ-coordinate we have to do the integral implied in Eq. (B.41).

One further change is useful in keeping the machinery transparent: we can treat the global and local shear effects separately. If we were using the simple cylinder model, for which there is no effect from local shear variations as distinct from the global shear represented by the radial variation of q, we would simply add a factor $q\theta_k$ to the definition of ξ in Eq. (B.5) such that the transformation is referenced at $\theta = \theta_k$ rather than $\theta = 0$. So the shift we need at position $\vartheta = \vartheta_k$ is given by this global shear correction $q\vartheta_k$, which we already know, and a local shear correction $\Delta\alpha_k(V)$ for which we have to solve. The expression for the shifts in the global coordinate system is

$$\alpha_k(V) = q(V)\theta_k + \Delta\alpha_k(V) \tag{B.66}$$

where V-dependence is denoted explicitly, and they are applied as

$$\xi_k = \xi + \alpha_k(V) \tag{B.67}$$

noting the fact that ∇y and $\nabla \xi$ are oppositely oriented. These can be combined in the form

$$\xi_k = \zeta - q(V)\,(\theta - \theta_k) + \Delta\alpha_k(V) \tag{B.68}$$

explicitly giving the relationship between the shifted field aligned coordinate system and the original Hamada one. The shifts are determined by the requirement that the purely perpendicular off diagonal metric element vanish at $\vartheta = \vartheta_k$,

$$g_k^{V\xi} = g^{V\xi} + \frac{\partial \alpha_k}{\partial V} g^{VV} = 0 \tag{B.69}$$

which when expressed in terms of the original Hamada coordinate system reads

$$g_k^{V\xi} = g^{V\zeta} - q g^{V\theta} + \frac{\partial \Delta\alpha_k}{\partial V} g^{VV} = 0 \tag{B.70}$$

discarding the piece proportional to $(\vartheta - \vartheta_k)$, since all quantities are evaluated at $\vartheta = \vartheta_k$. Since the quantities we actually compute directly from the HELENA equilibrium are the metric elements in the original Hamada coordinate system, we can go directly from that to the shifted system to write the equation for the local shear corrections,

$$\frac{\partial \Delta\alpha_k}{\partial V} = \frac{q g^{V\theta} - g^{V\zeta}}{g^{VV}} \tag{B.71}$$

which are oscillatory in ϑ_k.

The main shift due to the global shear is simply given by $q\vartheta_k$, and if there were no local shear effects, the Hamada metric would be orthogonal, and $g^{V\theta}$ and $g^{V\zeta}$ and hence $\Delta\alpha_k$ would vanish. The point from which the integral for $\Delta\alpha_k$ is computed is therefore arbitrary, and so we can do it from the center to each specific flux surface V,

$$\alpha_k(V) = q(V)\vartheta_k + \Delta\alpha_k(V) = q(V)\vartheta_k + \int_0^V dV' \left.\frac{q g^{V\theta} - g^{V\zeta}}{g^{VV}}\right|_{\vartheta=\vartheta_k} \tag{B.72}$$

with the integral for each $\alpha_k(V)$ being taken along V at fixed $\vartheta = \vartheta_k$.

In this form the oscillatory local shear correction, $\Delta\alpha_k$,is separated from the secular global shear shifts, $q\vartheta_k$, making it convenient to switch between the simple cylinder model and one using a computed flux surface geometry. In a cylinder model there is no orthogonality in the original Hamada coordinates, since $g^{V\theta}$ and $g^{V\zeta}$, and therefore the $\Delta\alpha_k$,

vanish, and this leaves $\alpha_k \to q\vartheta_k$. We therefore have $q\vartheta_k$ as the result of global shear, and $\Delta\alpha_k$ as the result of finite aspect ratio and flux surface shaping. Due to the separation there are no $\partial q/\partial V$ pieces in the integral, and this reduces the amount of numerical noise in the metric elements. We can however have $\Delta\alpha_k$ rather larger than $q\vartheta_k$, for equilibria with very strong local shear, such as occurs near the X-point of a diverted geometry. Such regions would incur enormous dissipation effects if the shifted metric procedure were not used.

Finally, this task of setting up the shifts mathematically makes the technique more general than simply following a field line between poloidal planes for taking parallel derivatives. By solving for $\alpha_k(V)$ such that $g_k^{V\xi}$ vanish, we can also eliminate the local shear deformation which would still be present in the resulting model, for any finite aspect ratio or shaping. We therefore reliably eliminate coordinate nonorthogonality from all local shear effects as well as the more obvious contribution from the global shear. The benefit is that not only simple models but also general ones with finite aspect ratio and shaping can be treated without twist deformations appearing at lowest order in the drift ordering in $\nabla_\perp^2$.

B.References

[1] K. V. Roberts and J. B. Taylor, *Phys. Fluids* 8 (1965) 315.

[2] R. L. Dewar and A. H. Glasser, *Phys. Fluids* 26 (1983) 3038.

[3] S. C. Cowley, R. M. Kulsrud, and R. N. Sudan, *Phys. Fluids B* 3 (1991) 2767.

[4] M. A. Beer, S. C. Cowley, and G. W. Hammett, *Phys. Plasmas* 2 (1995) 2687.

[5] B. Scott, *Phys. Plasmas* 5 (1998) 2334.

[6] B. Scott, in *Proceedings of the 22th European Conference on Controlled Fusion and Plasma Physics, Bournemouth, 1995* (European Physical Society, Bournemouth, 1995), p I-229; *Plasma Phys. Contr. Fusion* 39 (1997) 471.

[7] A. Zeiler, D. Biskamp, J. F. Drake, P. N. Guzdar, *Phys. Plasmas* 3 (1996) 2951.

[8] B. Scott, *Plasma Phys. Contr. Fusion* 39 (1997) 1635, and references to earlier versions therein.

[9] B. Scott, *Plasma Phys. Contr. Fusion* 40 (1998) 823.

[10] B. Scott, "Electromagnetic Gyrofluid Turbulence in Tokamak Edge Geometries," in Theory of Fusion Plasmas ISPP-18 (Societa Italiana di Fisica, Bologna, 1998), J.W. Connor, E. Sindoni, and J. Vaclavik, eds., pp 359-372; see also B. Scott, *Phys. Plasmas* 7, 1845 (2000), which contains an outline of the numerical scheme.

[11] S. Hamada, *Kakuyugo Kenkyu* 1 (1958) 542, cited and discussed by J. M. Greene and J. L. Johnson, *Phys. Fluids* 5 (1962) 510.; S. Hamada *Nucl. Fusion* 2 (1962) 23.

[12] G. Huijsmans, Ph.D. thesis, Vrije Universiteit Amsterdam (1991), External resistive modes in tokamaks.

[13] J. W. Connor, R. J. Hastie, and J. B. Taylor, *Phys. Rev. Lett.* 40 (1978) 396.

[14] B. Scott, A. B. Hassam, and J. F. Drake, *Phys. Fluids* 28 (1985) 275.

[15] P. Colella, *J. Comput. Phys.* 87 (1990) 171.

[16] B. Van Leer, *J. Comput. Phys.* 32 (1979) 101.

[17] B. Scott, *Phys. Plasmas* 7 (2000) 1845.

[18] B. Scott, *Phys. Rev. Lett.* 65 (1990) 3289; *Phys. Fluids B* 4 (1992) 2468.

B.A. Radial Periodicity and Shifting

In some cases, the ideal way to treat homogeneous turbulence in a background gradient is to take the gradient as a constant, as usual, and also to treat the domain in the downward direction of the gradient (x) as periodic. One expects identical conditions to prevail throughout the drift plane (x, y), and one avoids the need to maintain the background gradient against the net transport produced by the turbulence. Magnetic shear ($\hat{s}$) may be present, so long as it is also treated as constant.

It is already known [4] that the combined action of radial periodicity and the parallel boundary condition,

$$f(x, y, s) = f(x + L_x, y, s) = f(x, y + 2\pi\hat{s}x, s + L_{\|}) \tag{B.73}$$

places a condition on the periodicity lengths (L_x, L_y) of the drift plane:

$$f(x, y + 2\pi\hat{s}x + L_y, s + L_{\|}) = f(x + L_x, y + 2\pi\hat{s}x + 2\pi\hat{s}L_x + L_y, s + L_{\|}) \tag{B.74}$$

For these relations all to be consistent implies that $2\pi\hat{s}L_x$ be an integral multiple of L_y, or

$$L_x = (\text{integer}) \times \frac{L_y}{2\pi\hat{s}} \tag{B.75}$$

What this means is that the available parallel wavelengths on one side of the domain (x) and one periodicity length away ($x + L_x$) must be the same, so that there are no jump discontinuities at the box boundaries when taking parallel gradients. Additionally, the periodicity in y must also be regular. In simple terms, the homogeneous domain must equally sample all regions relative to main rational surfaces (where $2\pi\hat{s}x$ is an integral multiple of L_y). Therefore, L_x must be an integral multiple of the distance between main rational surfaces. Under this constraint, the straight metric sheared geometry may be given simple periodicity in the x-direction.

When transforming to the shifted metric geometry, the condition that the parallel gradient have no jump discontinuities, as a consequence of domain periodicity, must be retained. If the shear were so large that $2\pi\hat{s}L_x/NL_y$ could reasonably be an integer, where N is the number of drift planes (s-nodes) kept in the computations, then we could keep simple radial periodicity (note, though, that this would require no variation of the underlying geometry in $\nabla_\perp^2$ in the s-direction, *i.e.*, we would be restricted to the simple sheared slab/cylinder model except for the presence or absence of curvature terms). Unfortunately, with typical values of N in the range 16 to 32, this would place undue restrictions on the ratio L_y/L_x for typical $\hat{s}$ values near unity. Therefore, we have to actually follow the periodicity condition in the x-direction,

$$f(x + L_x, y, s) = f(x, y, s) \tag{B.76}$$

through the shifting transform,

$$f(x + L_x, y_k - \alpha_k' x - \alpha_k' L_x, s) = f(x, y_k - \alpha_k' x, s) \tag{B.77}$$

arriving at

$$f(x + L_x, y_k - \alpha_k' L_x, s) = f(x, y_k, s) \tag{B.78}$$

as the radial periodicity condition under the shifted metric geometry.

This may be implemented in Poisson/Helmholtz solvers by following it through the Fourier transform in the y-direction, under which Eq. (B.78) becomes

$$f(x + L_x, k_y, s) = f(x, k_y, s) e^{i\alpha_k' L_x k_y} \tag{B.79}$$

in which we remember not to confuse k_y with y_k. Unfortunately, the x-direction may no longer be transformed via simple FFT, since we now have a pseudo-periodic constraint much like the one for the parallel boundary condition in the straight metric, Eq. (B.29). Fourier coefficients are therefore offset away from integers by a phase factor that is in general irrational. This renders two-dimensional FFT methods inapplicable to Poisson/Helmholtz solves under the shifted metric.

Tridiagonal solvers are still applicable, provided the "wing elements" (last column and last row) are retained in addition to the three diagonals, as in the case of simple periodicity, and provided the matrix elements be set up as complex rather than simply real. At each i-th node in the x-direction we have, for example,

$$(f_{i-1} - 2f_i + f_{i+1}) - h_x^2 \hat{k}_y^2 f_i = h_x^2 S_i \tag{B.80}$$

for each Fourier component k_y, for the Poisson equation $\nabla_\perp^2 f = S$, where h_x is the equidistant step size in the x-direction, and

$$\hat{k}_y^2 = k_y^2 \frac{2(1 - \cos k_y^2 h_y^2)}{k_y^2 h_y^2} \tag{B.81}$$

is the modified Fourier coefficient for equidistant step size h_y in the x-direction (this modification of k_y^2 is necessary to keep the solution method as an inverse to the usual 5-point stencil for $\nabla_\perp^2$). For the first ($i = 1$) and last ($i = M$) nodes the matrix equation becomes

$$\left(e^{-i\alpha'_k L_x k_y} f_M - 2f_1 + f_2\right) - h_x^2 \hat{k}_y^2 f_1 = h_x^2 S_1 \tag{B.82}$$

$$\left(f_{M-1} - 2f_M + e^{i\alpha'_k L_x k_y} f_1\right) - h_x^2 \hat{k}_y^2 f_M = h_x^2 S_M \tag{B.83}$$

respectively. These phase factors ensure that the matrix fill-in process will render most elements complex.

B.B. Computational Methods Requiring Mid-Node Values

Finite difference approximations of order two and higher for the original partial differential equations typically call for evaluations of the dependent variables not only at the node positions but also at intermediate positions between the nodes. If operations involving $\nabla_\perp^2$ are needed at these inter-node positions ("interfaces"), then the shifted metric procedure must be applied at the interfaces as well as at the nodes, in the s-direction. For N s-nodes this means we must carry the geometrical information in Eqs. (B.35–B.37) at $2N$ positions in the s-direction, for example for centered second order schemes like that in

Ref. [15]. The best way to do this is to actually compute the geometry for each additional position, as simple interpolation is not always sufficiently accurate (especially for strongly shaped equilibria). If we were to linearly interpolate the shifts, then an evaluation of $\nabla_\parallel$ at position $s_{k+1/2}$ would involve

$$\frac{\partial f}{\partial s}(x, y_{k+1/2}, s_{k+1/2}) = \frac{f(x, y_{k+1} - \Delta_{k+1/2}, s_{k+1}) - f(x, y_k + \Delta_{k+1/2}, s_{k-1})}{s_k - s_{k-1}} \tag{B.84}$$

where the half shifts are given by

$$\Delta_{k+1/2} = \alpha_{k+1} - \alpha_k \tag{B.85}$$

(compare to Eqs. B.46,B.47). With $2N$ evaluations of the geometry, we would rather use

$$\frac{\partial f}{\partial s}(x, y_{k+1/2}, s_{k+1/2}) = \frac{f(x, y_{k+1} - \Delta^+_{k+1/2}, s_{k+1}) - f(x, y_k + \Delta^-_{k+1/2}, s_{k-1})}{s_k - s_{k-1}} \tag{B.86}$$

with the (differing) half shifts given by

$$\Delta^+_{k+1/2} = \alpha_{k+1} - \alpha_{k+1/2} \qquad \Delta^-_{k+1/2} = \alpha_{k+1/2} - \alpha_k \tag{B.87}$$

as in Eqs. (B.46,B.47).